Active Tectonics and Palaeoseismicity of the Northern Tien Shan and Dzhungaria

Chia-Hsin (Wendy) Tsai

Thesis submitted to the University of Oxford

for the degree of Doctor of Philosophy

in

Earth Sciences

Department of Earth Sciences and University College,

University of Oxford

Hilary, 2023

Supervised by Prof. Richard Walker,

Dr. Christoph Grützner and Dr. Simon Daout

Declaration

The contents of this thesis are all my own work, except where otherwise stated. The views and opinions expressed herein are mine and not necessarily those of any other person or body unless so attributed.

This thesis is dedicated to those who lost their lives and loved ones in the many earthquakes in history.

May science one day free us from the sufferings and bring us harmony with Nature.

Abstract

Active Tectonics and Palaeoseismicity of the Northern Tien Shan and Dzhungaria

Chia-Hsin Tsai
University College, Oxford

Hilary Term, 2023

This thesis focuses on the active tectonics and the palaeoseismicity around the Dzhungarian Basin. The study of surface ruptures is crucial to comprehending the earthquake occurrences of faults. I investigate geomorphic displacements along the boundary strike-slip Dzhungarian Fault using high-resolution drone and Pléiades satellite imagery. The results reveal possible single-event fault slip along the Dzhungarian Fault in the most recent earthquake. I suggest this earthquake is likely linked with a previously identified palaeo-earthquake rupture on the Lepsy Fault. With a joint rupture of the two faults, it could generate an earthquake with a magnitude up to Mw 8.4, which would be amongst the largest magnitude inferred for a continental earthquake. I further use Quaternary dating techniques and InSAR time-series analysis to determine the geological and geodetic slip rates of the Dzhungarian Fault. The results show that the northern Dzhungarian Fault has a long-term uplift rate of 0.6 ± 0.2 mm/yr, whilst the southern Dzhungarian Fault has geological and geodetic strike-slip rates consistent with a range of 2.1 – 4.7 mm/yr. I also re-investigate three historical earthquakes with magnitudes greater than Mw 7.0: the 1812 Nilke, the 1906 Manas and the 1944 Xinyuan Earthquakes in the Borohoro Shan. By re-analysing source parameters and integrating published data, seismological analysis results, and remote-sensing mapping, the study demonstrates the significance of both reverse and strike-slip faulting in the regional seismotectonics, which also indicates the deformation kinematics of the Borohoro Shan as being in a transpressional zone. I collate my results with those from the literature to propose updated earthquake scaling relationships of intra-continental earthquakes. Finally, this study suggests that the Dzhungarian Basin and its surrounding tectonic units are rotating anticlockwise to accommodate both the N-S crustal shortening and the left-lateral shearing within a large-scale zone from the SW Tien Shan to the Altay Mountains.

Extended Abstract

Active Tectonics and Palaeoseismicity of the Northern Tien Shan and Dzhungaria

Chia-Hsin Tsai
University College, Oxford

Hilary Term, 2023

This thesis aims to enhance our understanding of intra-continental earthquakes and the potential seismic hazards they could pose. To achieve this, I focus on the northern Tien Shan and Dzhungarian regions, which are ideal natural laboratories for studying intra-continental earthquakes due to their well-preserved palaeo-earthquake ruptures. My investigation centres on the active tectonics and palaeoseismicity in the Dzhungarian Alatau, the Borohoro Shan, and other surrounding areas on the edges of the rigid Dzhungarian Basin. Chapter 1 provides a brief introduction to the characteristics of intra-continental earthquakes and the tectonic settings of the northern Tien Shan and Dzhungaria in Central Asia. Chapters 2, 3, and 4 present independent research, each with its own objectives and conclusions. Results are synthesised in Chapter 5 to expand our knowledge of intra-continental earthquake scaling and the regional deformation kinematics.

Chapter 2 is focused on the earthquake occurrence on the major boundary strike-slip faults in the Dzhungarian Alatau. I investigate the > 400 km-long palaeo-earthquake ruptures on the Dzhungarian and Lepsy Faults using digital elevation models (DEMs) from the High Mountain Asia (HMA) and derived from structure-from-motion analysis of drone and Pléiades satellite imagery. I provide direct age constraints from the displaced alluvial terraces and indirect dating from morphological analysis of the scarps. The findings reveal that the southern 250 km of the Dzhungarian Fault likely ruptured in a single event 2,000–4,000 years ago, with displacements of 10–15 m, and potentially up to 20 m at one site. I suggest that the Dzhungarian and Lepsy Faults likely had a joint rupture through a system of splays in the intervening highlands. I propose different rupture scenarios and find that rupture on the Dzhungarian Fault alone is likely to have exceeded Mw 8, and the combined Lepsy-Dzhungarian rupture scenario may have been up to Mw 8.4. Despite being at the upper end of inferred continental earthquake magnitudes, the

proposed scenario combining the 375 km of the Dzhungarian and Lepsy ruptures yields a slip-to-length ratio consistent with global averages.

To understand more of the Dzhungarian Fault kinematics, Chapter 3 deals with the geological and geodetic constraints on average Quaternary rates of the fault slip. A comprehensive sample collection covers both the northern and southern parts of the fault, and optically/infrared stimulated luminescence and cosmogenic nuclide dating were applied to determine the age of cumulative fault displacements. Time-series analysis was conducted on interferometric synthetic aperture radar (InSAR) data from the Sentinel-1 satellite to estimate the present-day slip rate of the fault. The results indicate that the geological and geodetic strike-slip rates on the southern Dzhungarian Fault are consistent with each other and range from 2.1 to 4.7 mm/yr since approximately 100 ka. This finding implies that the southern portion of the fault accommodates roughly 25 ± 10% of the total crustal shortening in the region. The study also estimates the vertical slip rate on the northern Dzhungarian Fault as 0.6 ± 0.2 mm/yr over the last 5–60 ka. The decrease in total slip rates towards the northwestern Dzhungarian Fault is likely due to the proximity to the fault tip and the presence of other active structures that accommodate most of the crustal shortening in the northern Dzhungarian Alatau.

Chapter 4 is dedicated to re-investigate the major (Mw > 7) historical earthquakes that have occurred in the Borohoro Shan. The 1906 Manas Earthquake is the largest earthquake recorded since 1900 in the Borohoro Shan. Reported magnitudes range from 7.2 to 8.3, and yet subtle surface ruptures and ambiguous epicentres underline confusion about the size, mechanism, and responsible fault for this event. Such confusion can also be highlighted for the 1812 Nilke and the 1944 Xinyuan Earthquakes, which are the only other Mw > 7 earthquakes occurring in the Borohoro Shan. I compile published data and remote sensing mapping for these three historical events, and I integrate them into the re-analysis results of the source parameters of the 1906 Manas and 1944 Xinyuan Earthquakes using bulletins and digitised seismic records. The re-estimated seismic magnitude of the 1906 event is Mw 7.7 ± 0.2 with the relocated hypocentre at 43.96°N, 84.93°E. I interpret this event as nucleating on a steeply south-dipping basement reverse fault beneath the Borohoro Shan margin, but with the slip that propagated northward to the surface across a shallow decollement. The seismological analysis of the 1944 earthquake indicates it is a double event including an Mw 6.5 ± 0.3 foreshock and an Mw 7.2 ± 0.2 main shock, both with dominant strike-slip motion, and likely on the major right-lateral Kashihe Fault. I suggest there is an overestimation of magnitude from intensity measurements of the 1812 earthquake, and this event possibly involves both reverse and right-lateral slip along the Kashihe Fault as well as a splay from it. These earthquakes highlight

the importance of the seismic-induced landslides regarding the potential seismic hazards in this region and the right-lateral and reverse faulting in the seismotectonics of the Borohoro Shan.

In Chapter 5, I first present the surface ruptures of palaeo- and historical earthquake in the north of the Dzhungarian Basin. The ruptures on the Northern Tacheng Fault and Zaisan NE Fault, which are ~ 50 km and ~ 85 km in length, respectively, are investigated using DEMs derived from Pléiades satellite imagery. I also summarise the previous findings of the Irtysh Fault and the Fuyun Fault. Subsequently, I compiled fault parameters, including magnitudes, displacements, and surface rupture lengths, of intra-continental earthquakes in Central Asia and other regions worldwide to update the earthquake scaling relationships for intraplate faults. My findings reveal that the scaling relationships related to displacements are more variable between different tectonic settings and that there are scaling differences between earthquakes in stable continental regions (SCR) and tectonically active continental regions (TCR). This suggests that intraplate faults behave differently under different intra-continental settings. Finally, I synthesise all the findings in this thesis and previous research to discuss the deformation kinematics of the Dzhungarian Basin. The pattern of faulting and topography indicate a counterclockwise rotation of the triangular Dzhungarian Basin and its surrounding tectonic units under compression and left-lateral shearing, in a large-scale zone from the southwestern Tien Shan to the Altay Mountains.

Chapter 6 concludes the thesis by summarising research outcomes and suggesting the directions for future work. This thesis presents significant findings on the active tectonic and seismological characteristics of the northern Tien Shan and Dzhungaria, highlighting the importance of a multi-disciplinary approach in earthquake research and the need for further investigation in intra-continental earthquakes.

Acknowledgements

Firstly, I would like to express my gratitude to my supervisors, Richard Walker, Christoph Grützner, and Simon Daout for their unwavering support and guidance. Richard, I am grateful for the opportunity you gave me to explore the Tien Shan, a place I have yearned to visit since childhood. Your patience, hospitality, and encouragement have been helping me navigate the challenges of my DPhil and gain confidence in my work. Thank you for sharing your encyclopaedic knowledge of intra-continental faults in Central Asia and for guiding me in developing new research ideas that ensured the survival of this thesis despite the cancellation of all fieldwork. Christoph, every meeting with you over the years has been inspiring and encouraging. I must say that I am impressed by your prompt replies to every email. Thank you for sharing lots of your previous work and samples in Dzhungaria, which saved this thesis from being defeated by the pandemic. I am lucky to have such a warm and helpful collaborator and supervisor like you. Simon, thank you for all the support and guidance in the InSAR processing and time-series analysis. As a beginner, it was tough to learn these techniques, but your patience and professionalism always put me at ease. Thank you for enduring my silly questions and challenging me to maximise my potential. I am truly fortunate to have you all as my supervisors. I am also very grateful for the advice and guidance from John Elliott and Austin Elliott. Additionally, I would like to thank the examiners, James Hollingsworth and Conall Mac Niocaill, for their valuable comments on this work.

I would like to extend my gratitude to all the people who have been part of the Oxford COMET group during my time here, including all the faculties, postdocs and students. Barry, Philip and Jess, I am grateful for your advice from every group meeting. Eleanor and Nick, thank you for sharing the tutorials and scripts that were crucial for the analysis in this research. Jingxing, thank you for always promptly replying to my literature requests. JD, thank you for always staying late in the office, making me feel less lonely when working at night. Roberta, thank you very much for being my coursemate, proofreader, lab work partner, sample collector, and more. Tamarah, thank you so much for being such a supportive and proactive group member. I am glad to have the company of you both as female members of the group during the second half of my course. Our time together in the Kazakhstan field trip is unforgettable to me. Ben and Neill, thank you for helping me with coding, mapping, and computer restarting of my PC. Ian, thank you for teaching me photogrammetry and providing practical advice. A special thanks goes to Qi who has been incredibly generous with her time and expertise. Her kindness and hospitality mitigated my anxiety and made me feel at home when I first joined the group. Qi, thank you for being my tutor when

my brain malfunctioned, my driver when I was too lazy to cycle, and even my host when I had nowhere to stay. Through all the ups and downs, I am glad to have your company in my DPhil journey. Furthermore, I would like to thank Steve for handling many of my computational problems. I would also like to express my gratitude to our collaborators who helped with my visa issues and field trip logistics in Kazakhstan and Kyrgyzstan. Kanatbek, Aidyn, Ainagul, Ruslan and Sultan, thank you all for your assistance and contributions.

Next, I thank all the friends who I have made at Oxford University Taiwanese Student's Society, which has been an important cohort during my time here. I am lucky to have had Pei-Hsin and Tzu-Hao as my hanging-out buddies when I first arrived at Oxford. Bo-Shiuan and Kuo-Lun, I miss those days we spent chilling out together. Julie, thank you for being such a wonderful housemate. I am also very grateful for every invitation from Yu-Wen and Min-Erh to travel, attend festival feasts, housewarming parties, and more. Yu-Wen, thank you for taking care of us as a grandmother in Oxford. I appreciate the company from Ming-Shan, Ta-Chun, Kwan Chee and Tin Hang during the second half of my course. Thank you for bringing joy and laughter to my stressful DPhil life. I would like to express my sincere gratitude to Tin Hang, who has been my friend, mentor, chef, and B&B host. Thank you for all the emotional, technical, and nutritional support. Through trials and tribulations, thank you for seeing me through. A special thanks also goes to Tsai-Wei and Pei-Chen who have been my comrades for more than a decade. Moreover, I would also like to thank Yi-Ting, Ying-Hung, Yu-Hsuan, Yu, Pei-Yu, Kuang-Ting, Hung-Po, and everyone in TaiGE. To all of you and all the others not mentioned, thank you for reminding me that I am not alone in Oxford/UK and helping me get through those difficult times during the lockdown.

I thank all the friends I have made at the department, University College, 19 Rectory Road, and Oxford University Badminton Club (OUBaC) and Company of Archers (OUCofA). Annika, Anna, Kirsty, Matthew, Raphael, David and Michael, thank you for all the peer support and for chatting with me during the coffee/lunch breaks. Eunice and Run Yu, I will not forget my very first birthday cake at Oxford was from you both, and I cherish the memories of playing badminton and strolling on the streets of Cowley with you. I would also like to thank all my teammates at OUBaC, especially those in W2, and OUCofA. Moreover, I acknowledge the support of scholarships from University College, the Ministry of Education, Taiwan, and various grants that have made my Oxford journey possible.

Last but not least, I would like to express my heartfelt gratitude to my parents, sister, and other members of my family, whom I love the most in this world. I am thankful to my sister for being my best

listener, protector, and friend. I would like to thank my parents for their support, for enduring not having me around for years, and for their endless love.

Contents

List of Figures

List of Tables

Chapter 1

Introduction

1.1 Motivation and Background

It has been proposed that faults and earthquakes within intra-continental and plate-boundary settings behave differently from each other. Unlike the boundaries of tectonic plates where seismicity and deformation are concentrated in narrow zones, the continental interiors typically have widespread earthquakes. There is a further potential for spatial and temporal clustering of earthquakes within the deforming regions (Q. Li et al., 2009; Stein et al., 2009; Thatcher, 2009; M. Liu et al., 2011; M. Liu & Stein, 2016) (Figure 1-1). Due to the diffused strain and the heterogeneity within the continental crust, the intraplate fault types and the kinematics of intra-continental deformation are complex (Molnar & Tapponnier, 1975a; McKenzie & Jackson, 1983; Cunningham, 2005; Gatinsky & Prokhorova, 2014; Middleton et al., 2016; Grützner et al., 2019; H. Yang et al., 2021). The generally longer recurrence interval of intraplate earthquakes also means fewer examples are available for their study in comparison to plate boundaries. Since earthquakes within continental interiors are also destructive and often unanticipated, and have resulted in massive loss of life in history (England & Jackson, 2011), it is essential to expand our knowledge of intra-continental earthquakes and the potential seismic hazards they might cause.

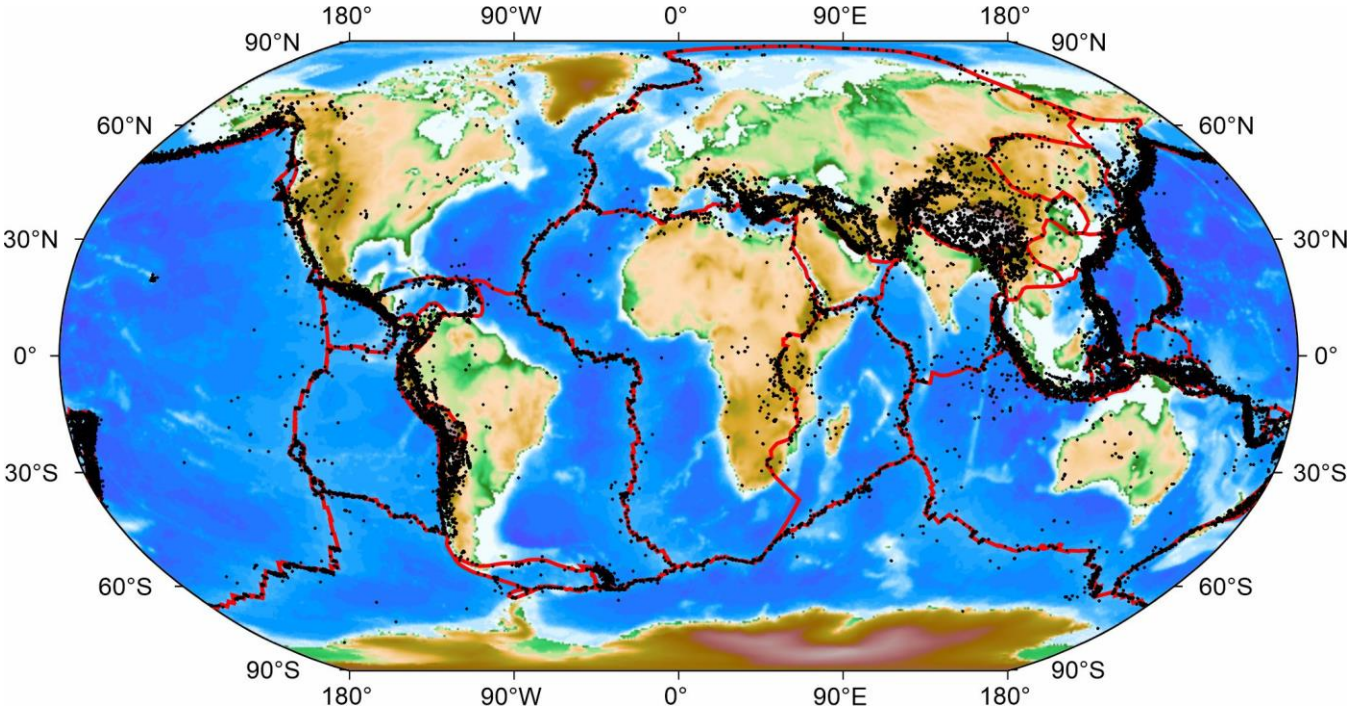

Figure 1-1. Map of global earthquakes, black dots from International Seismological Centre-Global Earthquake Model (ISC-GEM) catalogue (from 1904 – 2018 with magnitudes > 5.0), and plate boundaries (red lines) defined by Bird (2003).

Central Asia, extending from the Caspian Sea to western China, is an intra-continental region within Eurasia where abundant large historical earthquakes have been recorded (Kalmeteva et al., 2009; Bindi et al., 2014) (Figure 1-2 and Figure 1-3). One of the most active seismogenic belts in Central Asia is the Tien Shan, which is a ~ 2500-km long mountain with the latest orogenesis caused by the India-Eurasia collision since the Late Cenozoic (Molnar & Tapponnier, 1975a; Tapponnier & Molnar, 1979; Windley et al., 1990; Abdrakhmatov et al., 2001). The India-Eurasia collision has a convergence rate of ~ 35 mm/yr and this crustal shortening is not only accommodated within the vicinity in the Tibetan Plateau, but also affects a larger surrounding area from the Tien Shan to the Altay (or Altai) Mountains (Tapponnier & Molnar, 1979; Abdrakhmatov et al., 1996; England & Molnar, 1997; Thompson et al., 2002; Bayasgalan et al., 2005; Zheng et al., 2017) (Figure 1-2). The interior of the Tien Shan has a shortening rate of 15 – 22 mm/yr but it decreases towards its northern and eastern boundaries where the rate may be as little as 2 – 3 mm/yr based on the global navigation satellite system (GNSS) velocities (Abdrakhmatov et al., 1996; Zubovich et al., 2010; Zheng et al., 2017) (Figure 1-3a). Despite the low convergence rate in the northeast Tien Shan and around the neighbouring Dzhungarian Basin, several large historical earthquakes have occurred and palaeo-earthquake ruptures are observed (e.g. Avouac et al., 1993; Klinger et al., 2011), but

have been studied less in comparison to the interior of Tien Shan. Due to the arid climate, the northern Tien Shan and Dzhungaria have a pristine landscape that preserves prominent surface ruptures over several thousands of years and are ideal natural laboratories for examining intra-continental earthquake occurrences.

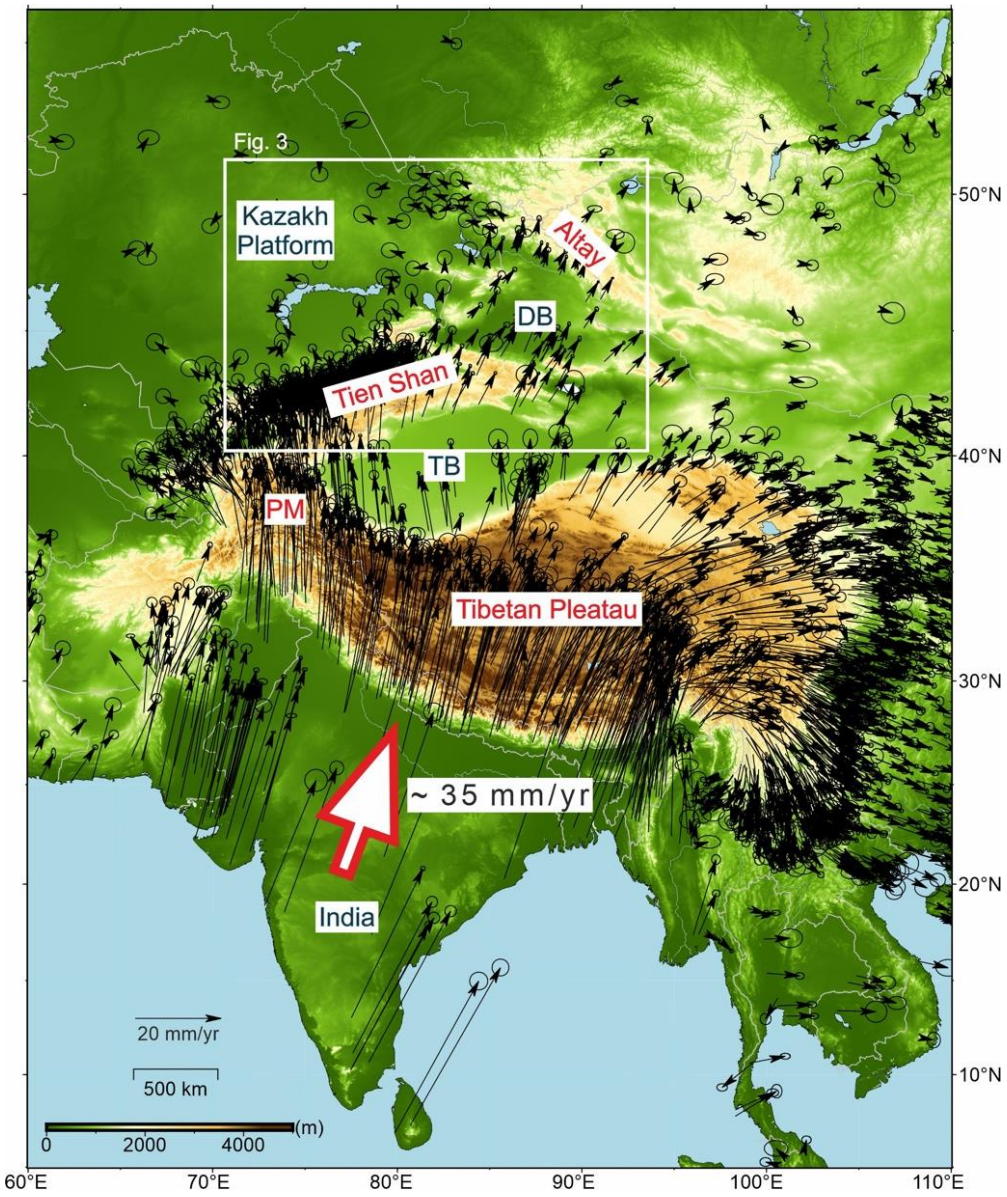

Figure 1-2. Topographic map with GNSS velocities in Central Asia, Tibet and India. The India Plate is moving northwards at ~ 35 mm/yr and is colliding with the Eurasian Plate (Abdrakhmatov et al., 1996; England & Molnar, 1997). Crustal shortening created by this collision is accommodated by the crustal thickening in Tibetan Plateau and also the Tien Shan and Altay Mountains. Regions with low relief between the mountains, such as the Tarim Basin (TB) and the Dzhungarian Basin (DB), appear to behave as rigid blocks. PM: Pamir. (GNSS data are from C. Rollins, pers comm., 2022.)

The two main sub-ranges of the northern Tien Shan are the Dzhungarian Alatau in the west and the Borohoro Shan in the east, which are also the boundaries with the Kazakh Platform and the Dzhungarian Basin, respectively (Figure 1-3a). The edges of the Dzhungarian Alatau are bounded by faults with lengths of hundreds of kilometres (Campbell et al., 2013, 2015), and with palaeo-earthquake ruptures but without historical or instrumental records of large (Mw > 6) seismicity (Figure 1-3b). On the other hand, abundant seismicity including several Mw > 7 earthquakes has been recorded at the edge and within the Borohoro Shan (Avouac et al., 1993; ISC, 2021), but where fewer surface ruptures can be recognised in the landscape (Figure 1-3b). As the northern Tien Shan in China has a rapid urban development and has become an important route of Asia-Europe transportation (such as the Eurasian Railway) (Figure 1-3a), it is necessary to understand the potential seismic impacts from investigating both the palaeo-earthquake ruptures and the historical events in this region.

To the north of the Tien Shan lies the Dzhungarian Basin, which is a rigid block with very little internal strain but concentrated crustal deformation, caused by the northwards motion of the India Plate, around its margin (Kreemer et al., 2014; Zheng et al., 2017) (Figure 1-3a). Seismicity with depths over 30 km is observed around the basin, especially at its southern edge connecting the northern Tien Shan and its foreland (Sloan et al., 2011; Wimpenny & Watson, 2020), which indicates the potentially large seismogenic depth of the intraplate earthquakes in this region. The 1931 Mw 7.9 Fuyun Earthquake occurred at its eastern margin and other poorly known palaeo-earthquake ruptures can be recognised around the basin (e.g. Klinger et al., 2011; Baize et al., 2019; Yu et al., 2021) (Figure 1-3b).

This thesis aims to reveal the patterns of active faulting and slip rates in the less-studied slow-moving intraplate region of the northern Tien Shan and Dzhungaria with data spanning a range of spatial and temporal scales. A combination of seismology, geomorphology, remote sensing, Quaternary geology and geochronology methods are used in the investigation with an incorporation of the previous findings to improve our understanding of intra-continental earthquakes.

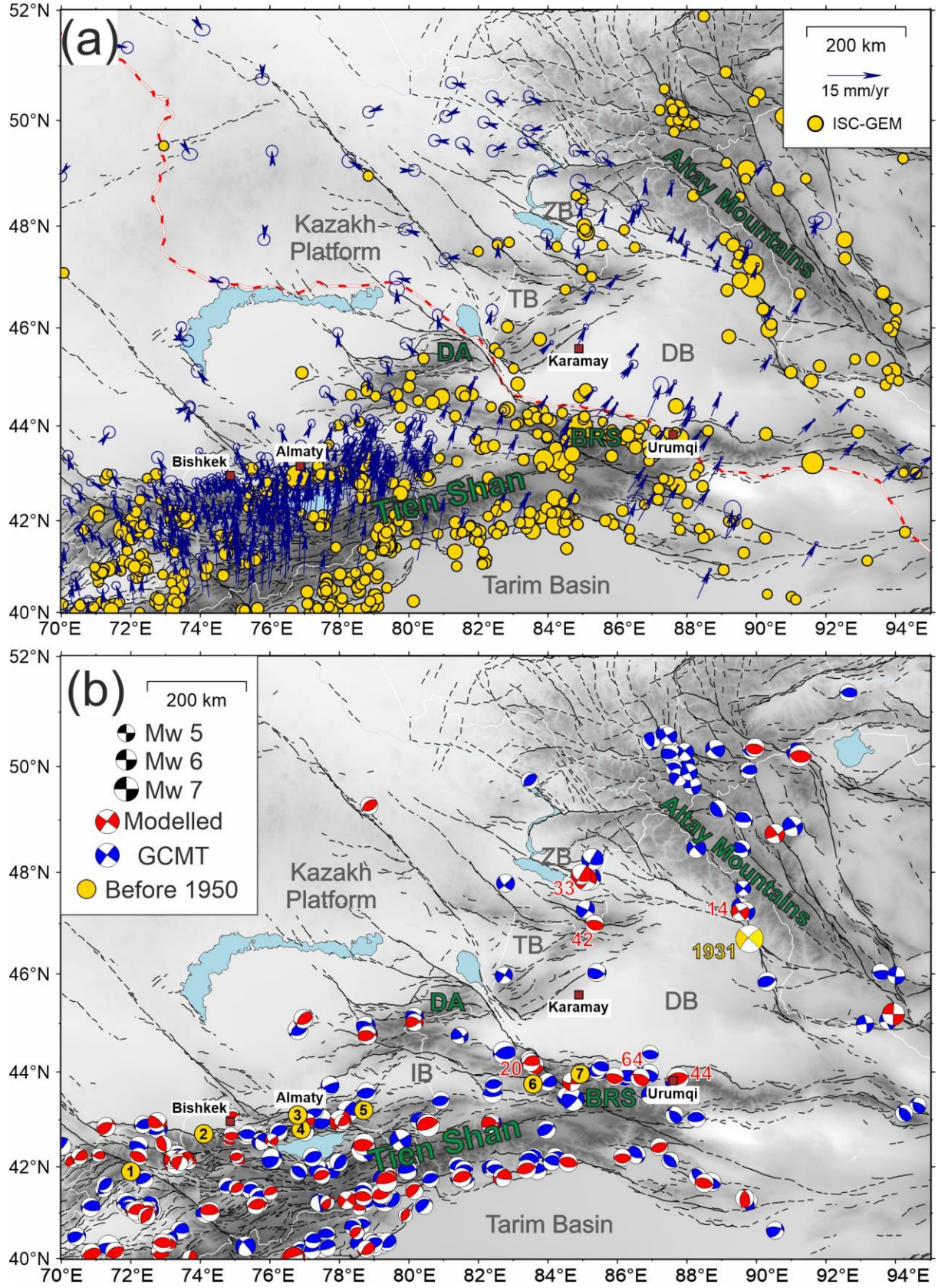
(a)
200 km
15 mm/yr
ISC-GEM
Kazakh Platform
ZB
TB
DA
DB
Karamay
Altay Mountains
BRS
Urumqi
Bishkek
Almaty
Tien Shan
Tarim Basin
52°N
50°N
48°N
46°N
44°N
42°N
40°N
70°E
72°E
74°E
76°E
78°E
80°E
82°E
84°E
86°E
88°E
90°E
92°E
94°E
(b)
200 km
Mw 5
Mw 6
Mw 7
Modelled
GCMT
Before 1950
Kazakh Platform
ZB
TB
DA
DB
IB
Karamay
Altay Mountains
BRS
Urumqi
Bishkek
Almaty
Tien Shan
Tarim Basin
1931
1
2
3
4
5
6
7
20
33
42
64
44
1-4

Figure 1-3. (a) Map of seismicity in Tien Shan and around the Dzhungarian Basin (DB) for Mw ≥ 5.0 earthquakes from 1904 to 2018 from ISC-GEM catalogue. GNSS data are from C. Rollins, pers comm., (2022). Red dashed line is the Eurasia Railway (from World Food Programme (WFP), https://geonode.wfp.org/layers/geonode%3Awld_trs_railways_wfp) that goes through the range front of the Borohoro Shan (BRS) and the Dzhungarian Alatau (DA), which are the main study areas in this thesis. (b) Map of seismicity with Mw ≥ 5 and their focal mechanisms compiled from Global Centroid Moment Tensor (GCMT) (blue circles) from 1976 to 2021 (Ekström et al., 2012) and modelled using body-waveform (red circles with red texts showing seismic depth for several events), mostly from 1962 – 2019 by Wimpenny & Watson (2020). Yellow circles represent the epicentres for destructive events with Mw ≥ 7.0 before 1950 with (1) 1946 Chatkal earthquake, (2) 1885 Byelovoda (Belovod) earthquake, (3) 1887 Verny earthquake, (4) 1911 Chon-Kemin earthquake, (5) 1889 Chilik earthquake, (6) 1812 Nilke earthquake, and (7) 1906 Manas earthquake (G. Yin et al., 2006; Kalmeteva et al., 2009; Kulikova & Krüger, 2015; Krüger et al., 2017). The 1931 Mw 7.9 Fuyun Earthquake is labelled with its focal mechanism (Klinger et al., 2011). Brown squares represent the cities and towns in this region with their names annotated. ZB: Zaisan Basin; TB: Tacheng Basin; IB: Ili Basin.

1.2 Overview of this thesis

In Chapter 2, I investigate the earthquake occurrence of the major boundary faults of the northern Tien Shan. I examine the displacements and possible seismic magnitudes of the palaeo-earthquakes along the right-lateral strike-slip Dzhungarian and Lepsy Faults, bounding the eastern and northern Dzhungarian Alatau, respectively. Previous preliminary investigations of the two faults suggested a higher slip-to-length ratio for the Lepsy palaeo-earthquake (Campbell et al., 2013, 2015). I re-assess the palaeo-earthquake ruptures along the two faults using the latest high-resolution topographic imagery along with the field survey and I estimate the likely coseismic displacements in the most recent earthquake of the > 300 km long Dzhungarian Fault. In addition, I provide possible earthquake scenarios and their corresponding rupture patterns with a re-estimated slip-to-length ratio of the boundary faults at the Dzhungarian Alatau.

In Chapter 3, I further investigate both the long-term geological and the short-term geodetic slip rates of the Dzhungarian Fault to understand how this principal structure in the northern Tien Shan is accommodating the crustal shortening. Since only limited results of slip rates estimated from a certain section of the Dzhungarian Fault have been reported, I calculate the slip rates based on a wider sample coverage and by using various methods in this thesis. Quaternary dating techniques including optically/infrared stimulated luminescence and cosmogenic nuclide dating are applied to constrain the age of the cumulative fault displacements for the long-term slip rates. Time-series analysis on the interferometric synthetic aperture radar (InSAR) data is used for estimating short-term strain accumulation.

The variation of slip rates along the Dzhungarian Fault and its regional tectonic implications are then discussed.

In Chapter 4, I look at the seismotectonics of the Borohoro Shan by examining and reviewing three large historical earthquakes: the 1812 Nilke, the 1906 Manas and the 1944 Xinyuan Earthquakes. I compile the previously reported surface ruptures of these three events, which are mostly only recorded in Chinese literature published decades ago, with my own investigation from modern satellite imagery. I further incorporate the reanalysis results of the source parameters of the 1906 Manas (Mw 7.7) and the 1944 (Mw 7.2) Xinyuan Earthquakes. These geological, macroseismic and seismological observations are integrated to discuss the responsible faults for these historical earthquakes and to highlight the types of surface damages and behaviours of active faulting in the Borohoro Shan.

In Chapter 5, I take a broader examination of the palaeo-earthquake ruptures around the Dzhungairan Basin. I identify and map surface ruptures in the northern Tacheng and Zaisan Basins for the first time using high-resolution Pléiades imagery. I also summarise the palaeo-earthquake ruptures of the Irtysh and Fuyun Faults, located at the northern and eastern margins of the Dzhungarian Basin. The findings in this thesis along with other previous studies of intra-continental earthquakes are then compiled to update the earthquake scaling relationships for intraplate faults. A synthesis of the intra-continental earthquake occurrences from the aspect of seismic depths and the kinematics of the Dzhungarian Basin are then discussed.

In Chapter 6, I briefly conclude the overall findings of this thesis and suggest directions for future research.

1.3 Publication arising from this thesis

Chapter 2 has been published in Tsai et al. (2022) as:

Tsai, C.-H., Abdrakhmatov, K., Mukambayev, A., Elliott, A., Elliott, J., Grützner, C., Rhodes, E., Ivester, A., Walker, R. T., & Wilkinson, R. (2022). Probing the upper end of intra-continental earthquake magnitude: a prehistoric example from the Dzhungarian and Lepsy faults of Kazakhstan. *Tectonics*, *41*, e2022TC007300, https://doi. org/10.1029/2022TC007300

Chapter 3 will be submitted as:

Tsai, C.-H., Grützner, C., Daout, S., Abdrakhmatov, K., Mukambayev, A., Fitzsimmons, K., Carr, A. S., Rhodes, E., Ivester, A., Rood, A. H., Rood D. H., Wilkinson, R., & Walker, R. T. Geological and Geodetic Constraints on Average Quaternary Rates of the Dzhungarian Fault Slip.

Chapter 4 will be submitted as:

Tsai, C.-H., Kulikova, G., Krüger, F. & Walker, R. T. Source Parameters of the 1906 Manas (Mw 7.7), 1944 Xinyuan (Mw 7.2) and 1812 Nilke Earthquakes and Seismotectonics of the Borohoro Shan, Western China.

The earthquake scaling content in Chapter 5 will be drafted independently as a scientific journal paper.

Chapter 2

Probing the Upper End of Intra-continental Earthquake Magnitude: a Prehistoric Example from the Dzhungarian and Lepsy Faults of Kazakhstan

2.1 Introduction

There is a growing realization that active faults deep within the continental interiors behave in ways that are unexpected given the present understanding of global earthquakes and fault rupture (Wells & Coppersmith, 1994; Bilham & England, 2001; Schmidt & Bürgmann, 2006; Leonard, 2010; Copley et al., 2011; Campbell et al., 2015; Walker et al., 2017). Observation of destructive earthquakes in such regions from historical to recent times show some evidence of spatial and temporal clustering, presenting challenges in the application of standard time-independent models of earthquake occurrence (Shimazaki & Nakata, 1980; Sieh, 1996; Stein et al., 2009; M. Liu & Stein, 2016; Salditch et al., 2020). Earthquake ruptures in continental interiors can be complex, and several examples show the potential for very large earthquakes to occur on a network of multiple short faults, which may be of particular importance for rupture within diffuse networks of critically-stressed faults, as commonly observed in plate interior settings (Abdrakhmatov et al., 2016; Ainscoe et al., 2019; King et al., 2019; Ross et al., 2019). More fundamentally, there is uncertainty in 1) the degree to which the recent and historical records of earthquakes encompass the maximum likely magnitude of future events (Hu et al., 2021; Pierce et al., 2021; Walker et al., 2021), and 2) the relationships between rupture length, average and maximum surface slip, and magnitude (Manighetti et al., 2007; Wesnousky, 2008; Leonard, 2010; Thingbaijam et al., 2017; Ou et al., 2020).

Some faults in continental interiors rupture in earthquakes with total fault slip significantly larger than expected for their length, according to a common slip-to-length ratio estimated as 10^{-4} to 10^{-5} (Scholz, 1982; Scholz et al., 1986; Wells & Coppersmith, 1994; Leonard, 2010). For example, the 2001 M_w 7.6 Bhuj earthquake in India involved ~10 m of slip on a fault extending for 20 – 30 km laterally, and 20 km in depth (Schmidt & Bürgmann, 2006; Copley et al., 2011), and the 1897 M_w 8.1 earthquake in Assam, India, involved slip of 11 – 25 m on a 110 km long fault (Bilham & England, 2001). The occurrence of unusually large amounts of slip may be related to the structural maturity of the faults since it has been proposed that more immature faults tend to fail in more energetic ruptures (e.g. Manighetti et al., 2007). The large seismogenic thicknesses encountered in some intraplate regions are also likely to affect the measured slip, due to larger fault plane area for a given fault length (Stockmeyer et al., 2014; Lu et al., 2018; Jackson et al., 2021). The classification, modelling, and eventual understanding of earthquake occurrence in continental interiors have direct impacts on modern approaches to seismic hazard assessment (Q. Li et al., 2009; M. Liu & Stein, 2016). However, there are a limited number of examples of earthquakes that demonstrate particular behaviours, or that are studied in sufficient detail to help refine scaling relationships for continental interiors. It is therefore important to re-examine the historical record, and to explore the palaeoseismic record to provide databases of sufficiently long duration (e.g. Wallace, 1970; K. E. Sieh, 1978; Pantosti et al., 1993; Zhang et al., 2005; McCalpin & Carver, 2009; Rizza et al., 2015; Abdrakhmatov et al., 2016; Walker et al., 2017; Baize et al., 2019; Bi et al., 2020; Hu et al., 2021).

The Tien Shan region of Central Asia is important as a natural laboratory for examining plate-interior earthquake occurrence, with a pristine natural landscape across much of the region providing the potential to record discrete earthquake ruptures which occurred in the past several thousands of years (e.g. Avouac et al., 1993; Thompson et al., 2002; Grützner, Carson, et al., 2017; Grützner, Walker, et al., 2017; Campbell et al., 2019; Rizza et al., 2019; Wu et al., 2020). There is also a historical and early-instrumental record of very large, apparently clustered, and sometimes complex earthquake ruptures (Abdrakhmatov et al., 1996, 2002; Thompson, 2001; Kalmeteva et al., 2009). The northern Tien Shan region, in particular, experienced a series of large earthquakes (M6.9 – 8.3) comprising the 1885 Belovod, 1887 Verny, 1889 Chilik, 1911 Chon-Kemin, and 1938 Chu earthquakes (Hay, 1888; Mushketov, 1890; Bogdanovich et al., 1914; Vilgelmzon, 1947; Molnar & Ghose, 2000; Arrowsmith et al., 2017; Krüger et al., 2017). The 1889 Chilik earthquake is the largest of this apparent sequence, with a moment-magnitude estimated at 8.0-8.3 (Krüger et al., 2017), and apparent rupture on three discrete faults, including both left and right-lateral slip, and with slip of up to 10 m on the central 35-km-long section. The ~175 km of surface ruptures

identified from satellite imagery and field surveys are shorter than expected for the estimated instrumental magnitude relative to global compilations (Abdrakhmatov et al., 2016). The broad distribution of the isoseismals suggests a deep focus of up to ~40 km (Bindi et al., 2014). Earthquake centroid depths of up to 40 km are determined for some recent earthquakes in the foreland of the main Tien Shan (Chen & Molnar, 1983; Sloan et al., 2011), and it is possible that equivalent rupture depths are possible in the northernmost parts of the Tien Shan itself, though modern-day seismicity in the mountain interior is typically in the range 15-30 km (Figure 2-1a) (Sloan et al., 2011; Alinaghi & Krüger, 2014).

The remarkable size and complexity of the 1889 Chilik earthquake, and the other earthquakes within the northern Tien Shan sequence (e.g. Abdrakhmatov et al., 2016; Arrowsmith et al., 2017), prompt an investigation of the longer-term behaviour of faults in the Tien Shan foreland region. Such studies are required to shed light on the occurrence of large intraplate earthquakes in general, and to better understand the seismic risks posed to the fast-growing cities along the northern Tien Shan margin, which would be susceptible to shaking from large earthquakes at the margin and in the foreland (e.g. Mosca et al., 2019; Amey et al., 2021). Few pre-19th century earthquakes in the Tien Shan and its surroundings are recorded in detail (e.g. Mushketov & Orlov, 1893; Kondorskaya & Shebalin, 1977; Seismological Bureau of Xinjiang, 1985), meaning that the identification and mapping of ruptures are of importance in extending the record further back in time (e.g. Grützner, Carson, et al., 2017; Campbell et al., 2019).

A particularly striking single-event earthquake rupture is described by Campbell et al. (2015) on the Lepsy Fault, which is an oblique right-lateral and reverse fault in the Kazakh Platform (Figure 2-1b). The Lepsy ruptures are notable for their size, with slips of up to 14 m, and an unusually large slip-to-length ratio, given the mapped length of 120 km (Figure 2-2). The measurements of slip, length, and an assumption that rupture extended to a maximum depth of 35 km were used to estimate a magnitude in the range of M_w 7.5 – 8.2. The Lepsy Fault branches westwards from the Dzhungarian Fault. The Dzhungarian Fault is a ~300-km-long right-lateral strike-slip fault and one of the major structures in the eastern Tien Shan region (Figure 2-1). Campbell et al. (2013) interpreted a single-event rupture along one ~30 km section of the northern part of the Dzhungarian Fault, but suggested that the remainder of the fault no longer retains clear evidence for slip in the most recent surface rupturing event.

In the following sections we undertake a new analysis, using the morphology of the scarps, of the Lepsy rupture, and examine the evidence for its continuation onto the neighbouring Dzhungarian Fault. We assess the distribution of slip in single and cumulative event offsets along the length of the Dzhungarian Fault, using a combination of Pléiades satellite imagery (https://www.intelligence-

airbusds.com/imagery/constellation/pleiades/), digital elevation models derived from the satellite imagery and field-based structure-from-motion surveys, and field measurements and sample collection. We estimate the slip vector and net slip of the most recent event from the mapped surface ruptures, and propose possible rupture scenarios of palaeo-earthquakes based on fault segmentation and displacements. Finally, we discuss the co-seismic rupture pattern in terms of its implication for seismic hazard and earthquake scaling relationships within intra-continental regions.

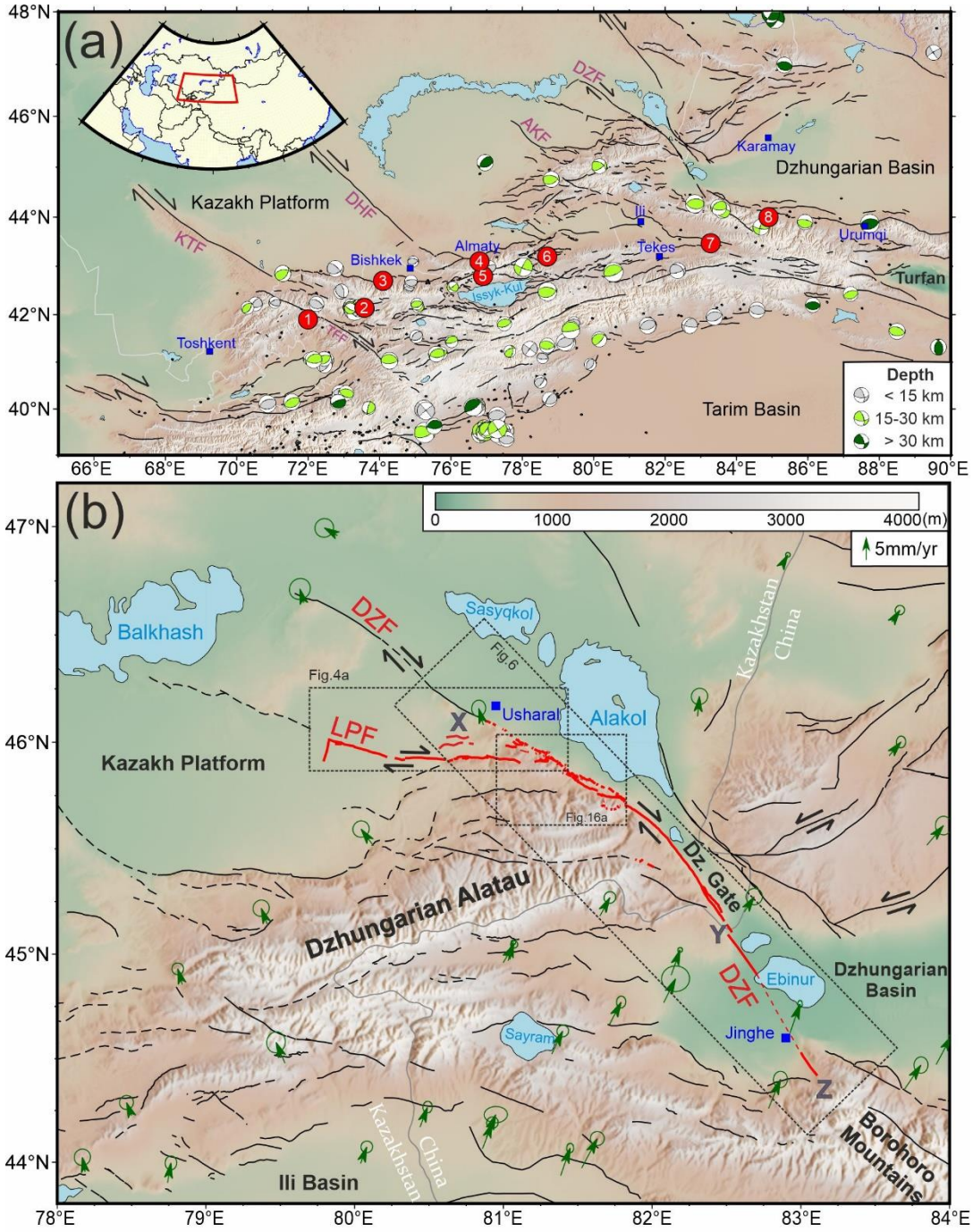

Figure 2-1. (a) Topography, active faults and selected historical earthquakes in the Tien Shan. Earthquake centroid depths and fault plane solutions are constrained by body wave inversion (Mw > 5) from Sloan et al. (2011) and references therein. Black dots are Mw > 4 events from 1965-2019 from the Global Centroid-Moment-Tensor (CMT) data (Dziewonski et al., 1981; Ekström et al., 2012). Numbered red circles represent the epicentres for destructive events in this region with 1) 1946 Chatkal earthquake, 2) 1992 Suusamyr earthquake, 3) 1885 Byelovoda (Belovod) earthquake, 4) 1887 Verny earthquake, 5) 1911 Chon-Kemin earthquake, 6) 1889 Chilik earthquake and 7) 1812 Nilke earthquake. 8) 1906 Manas earthquake. (Dziewonski et al., 1981; G. Yin et al., 2006; Kalmeteva et al., 2009; Ainscoe et al., 2019;

Tsai et al., 2021). (b) The Dzhungarian Fault (DZF), the Lepsy Fault (LPF), and other active structures in the northern Tien Shan with GPS velocity vectors with respect to Eurasia from Zubovich et al., (2010). Red lines are the mapped surface ruptures in this study. Points X and Y are the boundaries for the three main sections (NW, central and SE) of the DZF defined by Campbell et al. (2013). The coverage of the Pléiades satellite images used in our study extends from point X to Z. Blue squares are the major cities within the area. KTF: Karatau Fault, DHF: Dzhalair-Naiman Fault, AKF: Aktas Fault, DZF: Dzungarian Fault, TFF: Talas-Fergana Fault.

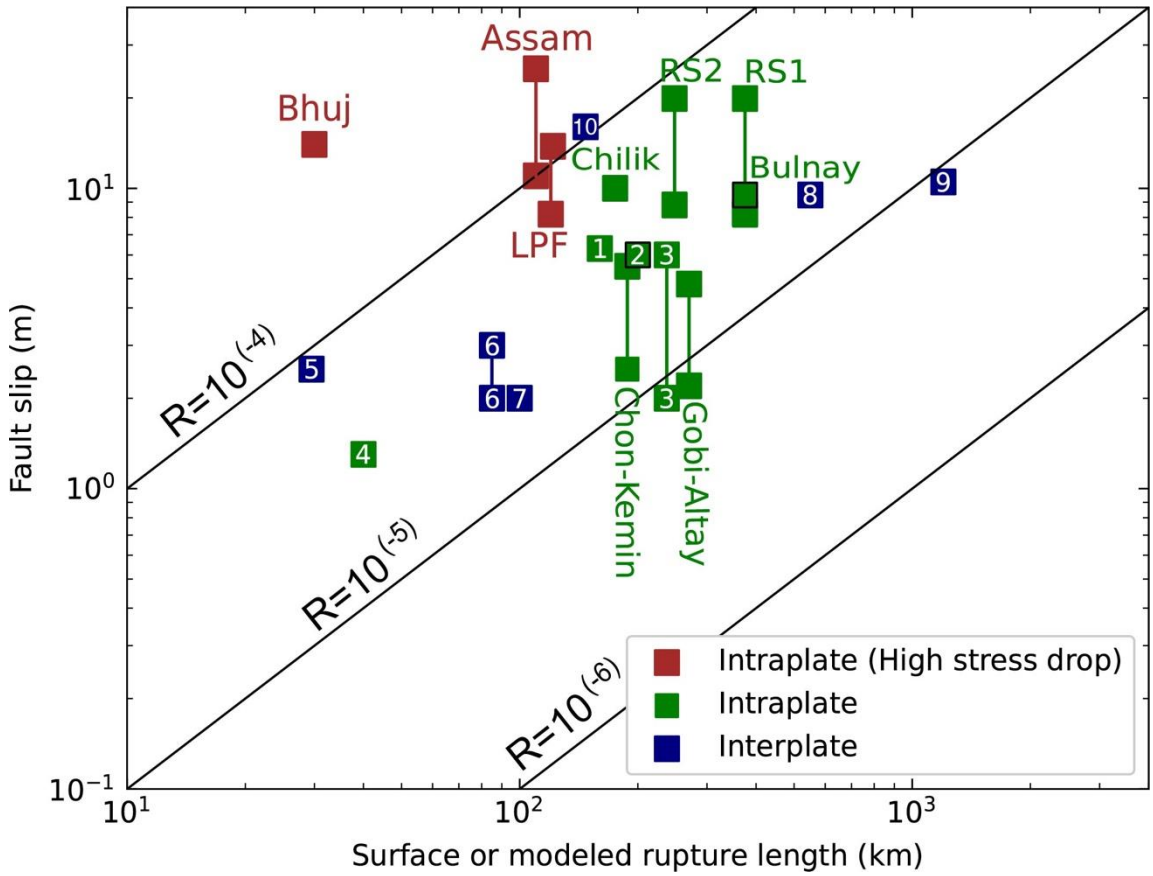

Figure 2-2. Earthquake scaling for fault slip (averaged or from minimum to maximum) against surface or modelled rupture length with slip-to-length ratio (R) plotted for $10^{(-4)}$, $10^{(-5)}$ and $10^{(-6)}$. Great intraplate and several renowned interplate historical earthquakes are presented along with the proposed two rupture scenarios in this study. High stress drop intraplate events are labelled in brown for the 1897 Assam (Mw 8.1), the 2001 Bhuj (Mw. 7.6) and the single Lepsy Fault rupture (LPF) (Mw 8.1-8.2) (Bilham & England, 2001; Negishi et al., 2002; Campbell et al., 2015). High-magnitude intraplate events and the proposed two rupture scenarios (RS1 and RS2) are labelled in green and are highlighted by their names on (the 1889 Mw. 8.0-8.3 Chilik, the 1905 Mw 8.2-8.5 Bulnay, the 1911 Mw 7.8-8.0 Chon-Kemin, the 1957 Mw 8.1 Gobi-Altay earthquakes) (Kulikova & Krüger, 2015; Rizza et al., 2015; Abdrakhmatov et al., 2016; Arrowsmith et al., 2017; Krüger et al., 2017; Kurtz et al., 2018). Other intraplate events (green) and renowned interplate (blue) are labelled by numbers for (1) the 1931 Fuyun (Mw 7.9), (2) the 2013 Balochistan (Mw 7.7), (3) the 1920 Haiyuan (Mw 7.9), (4) the 1967 Mogod (Mw 7.1), (5) the 2010 Darfield (Mw 7.1), (6) the 1992 Landers (Mw 7.3), (7) the 1999 Chi-Chi (Mw 7.6), (8) the 2005 Sumatra (Mw ~9), (9) the 2011 Tohoku (Mw ~9) and (10) the 1855 Wairarapa earthquakes (Sieh et al., 1993; Ma

& Mori, 2000; Catherine et al., 2005; Rodgers & Little, 2006; Klinger et al., 2011; Quigley et al., 2012; Satake et al., 2013; Avouac et al., 2014; Ou et al., 2020; Bollinger et al., 2021).

2.2 Tectonic Background

The Tien Shan is the longest mountain range in Central Asia, extending east-west for 2500 km between longitudes 70°E to 90°E. It has experienced two major orogenic processes, with the first occurring in the Late Palaeozoic and the second, ongoing, phase beginning in the Cenozoic (Windley et al., 1990, 2007). The majority of the E-W parallel ranges which make up the Tien Shan are composed of the Precambrian and Palaeozoic metamorphic and structurally-deformed igneous rocks resulting from the amalgamation of island arc terranes during the Late Palaeozoic Variscan/Hercynian orogeny (Voytovich, 1965; Burtman, 1975). After a relatively quiescent tectonic environment during the Mesozoic, the India-Eurasia collision reactivated the Late Palaeozoic structures and has resulted in significant surface deformation since ~25 Ma (Molnar & Tapponnier, 1975a; Tapponnier & Molnar, 1979; Avouac et al., 1993; Abdrakhmatov et al., 2001; De Grave et al., 2007). This latest phase of orogenesis is thought to have started in the late Oligocene in the west and central Tien Shan, whereas the onset of mountain building in the northern Tien Shan occurred later, in the Miocene (Windley et al., 1990; Hendrix et al., 1992; Abdrakhmatov et al., 2001; De Grave et al., 2007). The Tien Shan is bounded to the south by the Tarim Basin and to the north by the Kazakh Platform and Dzhungarian Basin. A wide fold-and-thrust belt runs along the southern margin of the range (Burchfiel et al., 1999; Burtman, 2008; Sloan et al., 2011), whereas the northern margin is typified by basement-cored steep reverse faults (e.g. Wang et al., 2004; Selander et al., 2012). The range interior contains several fault-bounded intermontane basins (e.g. Issyk-Kul Basin) filled with up to 10 km of Cenozoic sediments (Figure 2-1a) (Hendrix et al., 1992). Strike-slip faults are also widespread within the Tien Shan, with left-lateral faults parallel to the range, and NNW-SSE trending right-lateral faults cutting obliquely through it. Two of the most prominent right-lateral faults are the Talas-Fergana and Dzhungarian Faults (Figure 2-1a). The Talas-Fergana Fault has a late Quaternary slip rate of 2.2 – 6.3 mm/yr (Rizza et al., 2019) and the Dzhungarian Fault slips at 1.4 – 4.6 mm/yr (Voytovich, 1969; England & Molnar, 1997; Campbell et al., 2013; Z. Hu, Yang, et al., 2021).

Permanent and campaign GNSS velocity measurements show the western Tien Shan accommodates 15 – 22 mm/yr of the current convergence, which is half the total shortening rate measured across the whole India-Eurasia collision. The rate of shortening decreases eastwards, whereas range-parallel left-lateral shearing increases (Abdrakhmatov et al., 1996; Zubovich et al., 2010). GNSS data and geological

investigation indicate that N-S shortening is accommodated by active E-W reverse structures, both at the margins and within the interior, of the range (e.g. Thompson et al., 2002). The major right-lateral strike-slip faults that cut obliquely through the Tien Shan, such as the Talas-Fergana and Dzhungarian Faults, may also accommodate some shortening by rotation around a vertical axis (Campbell et al., 2013; Rizza et al., 2019; C. Wu et al., 2021). About 1 – 3 mm /yr of shortening is observed across the Dzhungarian Alatau, which is a mountain range north of the main Tien Shan (Figure 2-1b). Approximately 2 mm/yr of shortening is accommodated north of the mountainous regions, within the Kazakh Platform (Abdrakhmatov et al., 1996; Zubovich et al., 2010).

Some destructive earthquakes have occurred within the last two centuries within and around the Tien Shan (Kalmeteva et al., 2009), with the causative faults and source parameters constrained to varying degrees. These earthquakes include the 1812 M 8.0 Nilke (G. Yin et al., 2006; C. Wu et al., 2020) and the 1906 M_w 7.7 Manas (P. Zhang, Deng, Xu, Peng, et al., 1994) earthquakes adjacent to the Borohoro Shan in the eastern parts of the Tien Shan (Figure 2-1). The northern margin of the Tien Shan, including regions close to the cities of Bishkek and Almaty, was damaged by several events starting with the 1885 Byelovoda (M 6.9) earthquake, with an epicentral zone west of Bishkek (Molnar & Ghose, 2000), and then continuing with the 1887 Verny earthquake (M 7.3), which caused damage and widespread landslide west of Almaty (Hay, 1888), the 1889 Chilik earthquake (M_w 8.0-8.3) (Krüger et al., 2017), and the 1911 Chon-Kemin earthquake (M_w 8.0) (Bogdanovich et al., 1914; Delvaux et al., 2001; Kulikova & Krüger, 2015; Arrowsmith et al., 2017). More westerly parts of the Tien Shan have produced the 1946 Chatkal earthquake (M 7.6) (Simpson et al., 1981) and the 1992 Suusamyr (M_w 7.2) earthquake (Ghose et al., 1997; Ainscoe et al., 2019). Of all these earthquakes, only the 1911 and 1992 have ruptures that were identified and mapped by contemporary sources (Arrowsmith et al., 2017; Ainscoe et al., 2019), though probable ruptures from the 1812, 1889 and 1946 earthquakes have also been found (Simpson et al., 1981; Abdrakhmatov et al., 2016; C. Wu et al., 2020). There are relatively few large instrumentally-recorded earthquakes adjacent to the Dzhungarian Alatau (Figure 2-1), and yet there is abundant evidence of significant surface-rupturing events in the pre-historic past (Yang & Shen, 2000; Shen et al., 2011; Cording et al., 2014; Hu et al., 2021), including 120 km of surface rupture with ~8 – 14 m slip along the Lepsy Fault (Campbell et al., 2015) and 70 km of surface rupture with 8 m slip near Tekes (Yang et al., 1988; Rogozhin et al., 2015) (Figure 2-1a), both of which have been suggested as the potential source of a large earthquake in 1716 (Mushketov & Orlov, 1893).

2.3 Methods

2.3.1 Image Processing and Field Acquisition

We combined both remote-sensing and field-based measurements of surface ruptures. We mapped the faults and measured the surface displacements using open-source imagery hosted on Google Earth (https://earth.google.com/) and Bing Maps (https://ge-map-overlays.appspot.com/bing-maps) as well as commercial Pléiades optical satellite data in a strip along the Dzhungarian Fault. We analysed the terrain using the 8-m-resolution High Mountain Asia (HMA) digital elevation model (DEM) provided by the National Aeronautics and Space Administration (NASA) (Shean, 2017), which covers the part of our study area west of 81.8° E and south of 46°N and was used for the first time to investigate the surface ruptures along the Lepsy Fault. We also produced metre-resolution DEMs from stereo Pléiades satellite images along the Dzhungarian Fault. We produced decimetre resolution DEMs of key field sites from photographs taken in the field during unmanned aerial vehicle (UAV) field surveys. All imagery and topographic datasets are archived as outlined in our FAIR data statement.

Fifteen patches of bi-stereo Pléiades optical images were acquired during the snow-free season in May 2016, June 2016 and June 2019. These satellite images totally cover > 1350 km^2 with a 270 km length from 46.1°N – 44.4°N and a ~5 km width across the Dzhungarian Fault. Each patch has a pair of acquisitions from two different aspects, and both contain a 0.5-metre resolution panchromatic band and four 2-metre resolution multispectral bands (Red, Green, Blue, Near infrared). We constructed high-resolution DEMs and orthorectified imagery using the Leica Photogrammetry Suite built in Erdas Imagine software via the following procedure (Middleton et al., 2015; Y. Zhou et al., 2015; Ainscoe et al., 2019). First, dozens of tie points were identified both manually and automatically on the pairing panchromatic images to resolve the relationship between the image coordinates and the ground coordinates. Second, pixel-by-pixel matching was implemented for the two images. Third, we used the Enhanced Automatic Terrain Extraction tool with the 3-D point positions determined from the previous steps to extract the point clouds. Fourth, the resulting point clouds were gridded at 1 m spacing. Finally, the panchromatic images and the DEMs were used to produce pan-sharpened orthorectified multispectral images which we used in our mapping.

Field surveys were conducted between July and September in 2015, 2016 and 2019 at individual sites along the Dzhungarian Fault. We collected low-altitude aerial photographs taken by a digital camera attached to the bottom of a DJI Phantom 4 quadcopter at a flying altitude of 90 – 100 m. Artificial ground

control markers were widely distributed and measured by differential GPS (dGPS) for photographic correlation and scaling in the photogrammetry processes. We generated ~10-cm resolution orthophotos and dense point clouds by using the structure-from-motion method with Agisoft Photoscan Pro software (Westoby et al., 2012). The resulting point clouds were gridded at 10 cm spacing to generate the raster DEMs.

2.3.2 Offset Measurement

To define the size of displacements from the surface ruptures, we measured both lateral and vertical offsets from the Bing Map, Google Earth and ortho-panchromatic Pléiades imagery using QGIS software (http://qgis.osgeo.org). Lateral offsets are mostly in the form of displaced stream channels. We manually measured the channel offsets because the resolution of our imagery is insufficient for the dedicated code to implement stable and high-quality measurements (Zielke & Arrowsmith, 2012; Stewart et al., 2018). We followed the methods and assumptions described in Elliott et al. (2015), with the preferred, maximum and minimum permissible lateral offsets defined from the distances across the fault between the channel thalwegs (the lowest elevation within the channel), the outer levees, and the inner levees, respectively (Figure 2-3a). We also categorized the measurements into three quality categories (high, medium and low) based on the sinuosity and the sharpness of the channels (Kurtz et al., 2018). Each measurement was further incorporated as an individual probability density function (PDF) displayed as a fixed area triangle (Figure 2-3b) and stacked to form a Cumulative Offset Probability Distribution function, or COPD, which can be used to identify peaks in measured offset values that may result from individual earthquakes, an established methodology used in Klinger et al., 2011; Elliott et al., 2015; Kurtz et al., 2018; Ou et al., 2020; Dodds et al., 2022). A total of 260 laterally-dislocated channels were measured in this study including 179 channels along the southern part of the Dzhungarian Fault, where the slip appears to be predominantly right-lateral (see supporting material for the detailed lateral offset data and locations in https://agupubs.onlinelibrary.wiley.com/doi/abs/10.1029/2022TC007300).

Vertical offsets refer to the heights of the scarps across the fault. Since we do not know the precise location of the fault projection at the surface, we defined the fault position to be at the steepest point on the scarp (Campbell et al., 2015; Grützner et al., 2017). The scarp profiles are either measured by dGPS in the field or extracted from the structure-from-motion DEMs using the Terrain Profile Tool in QGIS, with 100 – 200 m-long single-tracked profiles aligned approximately perpendicular to the scarps. The

boundaries between fans and scarps were defined manually by identifying the apparent change in curvature along the profiles, avoiding the undulatory features caused by erosion or collapse. We applied a least-squares linear regression to estimate gradients of the fan surface on both sides of the fault and took the offset between the two fitted lines at the fault position as the scarp height. To account for the uncertainties introduced by the image processing and the subjective selection of scarp, fan and fault position, we applied a Monte Carlo approach. We sampled a range of points with reasonable bounds of extent on each fan surface and fault position for 10,000 times for each profile. We used standard deviation in these multi-calculated offsets as our estimation of the uncertainty. Nevertheless, it should be noted that this estimation still neglects the uncertainty caused by the landform geometry and variability in scarp heights along strike (Mackenzie & Elliott, 2017), so multiple profiles were measured at each site.

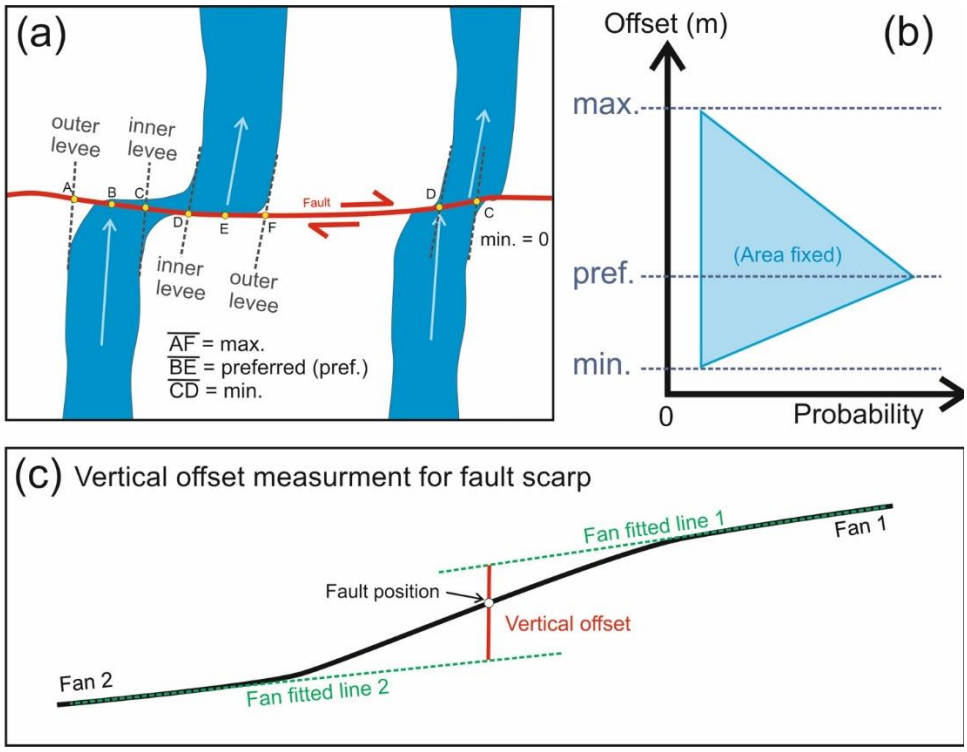

Figure 2-3. (a) Illustration of determining lateral offset measurements for stream channels estimated using satellite imagery. For each offset stream, the levees and thalweg, which is mostly in the middle of the channel, were projected to the fault. The preferred offset was assigned based upon realignment of the thalweg of the channel (distance $\overline{BE}$). Minimum ($\overline{CD}$) and maximum ($\overline{AF}$) offsets were assigned from the alignment of inner and outer levees. If the preferred offset is smaller than the minimum offset, as is the case for the channel on the right, the minimum offset is set to zero. (b) Illustration of how each measurement is plotted as a triangle for demonstrating its probability density function. (c) Illustration of determining the vertical offset measurements for the fault scarps. Red line is the vertical offset estimated based on the fault position and the fan fitted lines.

2.3.3 Quaternary Dating

Age constraints on displaced terraces were obtained from radiocarbon dating of gastropod shells where such material was encountered, and through post-infrared infrared stimulated luminescence dating (post-IR IRSL) of single grains of K-feldspar from within sediment. All age data are presented in Table 2-1. IRSL sediment sample was collected in stainless steel tubes hammered into vertical sections of silty sediment or loess. Sample preparation was similar to that described in Grützner, Carson, et al. (2017), incorporating a density separation at 2.58 gcm^{-3} applied to either 125-212 μm sieve fractions to extract K-feldspar grains. Single grain post-IR IRSL signals were measured in the luminescence laboratory at the University of Sheffield following the procedures described in Rhodes (2015) and Zinke et al. (2017). Based on previous experience from age-controlled single grain samples from Australian geoarchaeological sites (Rhodes et al., 2010), an overdispersion value of 15% was used in age estimation for all samples. No significant systematic IRSL fading was observed after assessment for every grain measured. Environmental dose rates were estimated using ICP-OES for K and ICP-MS for U and Th. Corrections were made for water content and grain size attenuation, and the dose rate estimation assumed an internal K content of 12.5 ± 2.5% (Huntley & Baril, 1997).

Table 2-1. Radiocarbon and IRSL Dating Results.

Radiocarbon Ages						
Sample name	Site	Lon. (°E)	Lat. (°N)	Materials	Calibrated Range	Age (Cal. Years B.P.)
RC1	Bear River Site	81.37651	45.90390	Gastropod Shell	A.D. 1435 to A.D. 1490 A.D. 1605 to A.D. 1610	515-460 345-340
RC2	Bear River Upstream	81.36473	45.89720	Gastropod Shell	B.C. 2025 to B.C. 1885	3975-3835
Luminescence Ages						

Sample name	Site	Lon. (°E)	Lat. (°N)	Depth (m)	Water (%)	Total Dose rate (Gy/ka)	De (Gy)	IRSL Age (ka)
DZH1	Section S3 graben	81.66034	45.75066	0.65	6.9	3.91 ± 0.24	66.5 ± 2.0	17.0 ± 1.1

2.3.4 Morphological Scarp Dating

A scarp's morphology can be used to estimate its formation age. The principle of this dating technique, reviewed by Hanks (2000), can only be applied to single-event scarps and is based on the hypothesis that the scarp degrades as a simple diffusive process through time. Following this assumption, we calculated the diffusion age (kt), given in m^2, from the morphology of the scarp and its adjacent fan surfaces for each fault-orthogonal topographic profile. We applied a mass diffusivity of 4.19 ± 0.65 m^2/kyr, estimated from the nearby and climatically similar Borohoro Shan (Pang et al., 2021), to calculate how long the scarp has been going through the diffusion process. It may take hundreds of years before a scarp transitions to diffusive degradation from non-diffusive degradation processes such as slumping and collapse (Wallace, 1977; Colman & Watson, 1983; Spelz et al., 2008). At the onset of the diffusive stage, the initial scarp angle (repose angle) is assumed to be 30° – 35°, meaning that scarps steeper than this angle might be relatively young (Carson & Kirkby, 1972; Nash, 1980; K. L. Pierce & Colman, 1986). In this study, we set the initial angle as 35° and implemented the morphological dating for the "likely" single-event scarps that show a clear single step without beveling along the scarps or adjacent fan surfaces, which might result from earlier scarp-forming events. Moreover, we only applied this method to the profiles from the dGPS measurements or from the drone-derived DEMs, which illustrate the scarp morphology better due to their higher image resolution, and we used the mean diffusion age averaged from multiple scarps to define the diffusion age at each investigated site (Fig. S1-2 – S1-7) (Grützner, Carson, et al., 2017; Walker et al., 2017).

2.4 Geomorphology of the Dzhungarian Alatau and the Major Boundary Faults

The Dzhungarian Alatau is a roughly east-west-oriented mountain range geographically separate from, though tectonically related to, the eastern Tien Shan (Figure 2-1a). It has an overall asymmetry with steep relief at its southern and eastern margins, with a maximum of 2000 m relief above the surrounding sedimentary basins, and gradually diminishing relief to the west and north. The mountain summits preserve an extensive peneplain surface, which is incised by deep E-W canyons. Offsets and folding of the peneplain surface indicate the presence of reverse faulting within the range interior (Campbell et al., 2013). The east-west ridges of the Dzhungarian Alatau are bounded by reverse faults, though right-lateral strike-slip faults with orientation NNW-SSE to NW-SE are also present, either bounding the edges of the high topography, as is the case for the Dzhungarian Fault, or cutting through the range interior (Figure 2-1b).

The Dzhungarian right-lateral fault, also known as the Bolokenu-Aqikekuduk (or Bo-A) Fault in Chinese literature, runs along the boundary of the northern Tien Shan and the southwestern Dzhungarian Basin, straddling the border of Kazakhstan and China. The Dzhungarian Fault has existed since at least mid-Palaeozoic as a structure dividing the Hercynian tectonic zones and it has been reactivated since the Late Cenozoic as a dextral strike-slip fault with reverse slip component (Voytovich, 1965; Campbell et al., 2013). The fault is ~400 km long, and extends from the east of Lake Balkhash, Kazakhstan, in the north to the Borohoro Shan, China, in the south. It trends NNW-SSE in its southern part, and NW-SE in the north. It separates the Dzhungarian Alatau mountains and the western margin of the Dzhungarian Basin, and runs along the western side of the Dzhungarian Gate, a major low-level pass through the ranges of the eastern Tien Shan.

The Dzhungarian fault has been separated into three main geomorphological sections by Campbell et al. (2013) (Figure 2-1b). The northwestern section is the NW ~150 km low-relief portion north of Usharal Town within the Kazakh Platform. The central section is the ~160 km portion truncating the eastern margin of the Dzhungarian Alatau, with a ~20° gradual change in strike near Lake Alakol. Oblique slip components with reverse and strike-slip components separated onto two subparallel branches are found in this central section (Campbell et al., 2013) and there is a relief of ~2000 m across the fault. The southeastern section extends for ~90 km across the basin of Lake Ebinur to the margin of the Borohoro Shan. There is very little relief (~10 m) across the fault in the Ebinur basin, suggesting that the kinematics

are almost purely strike-slip. The Dzhungarian Fault ends in the SE either within the Borohoro Shan, as shown in our maps, or continues through the Borohoro Shan to end in the Turfan depression (e.g. Yang & Shen, 2000; Shen et al., 2011; Hu et al., 2021). Shen et al. (2011) and Hu et al., (2021) estimate slip rates of ~5 mm/yr during the last 300 ka and 3.2 + 1.4/ - 1.1 mm/yr during the last 100 ka, respectively, in the southern portion of the fault, in China, and Campbell et al. (2013) estimate a slip rate of 2.2 ± 0.8 mm/yr during the last 26 ka at the southern end of the central section, just north of the Kazakh border, where a long-term slip rate of 3 ± 1 mm/yr is also estimated from a 7 km offset of Pliocene-age deposits (Voytovich, 1965; England & Molnar, 1997). In this study, we examine the Dzhungarian Fault from its northern end to where it enters the Borohoro Shan. We separate the fault into eight sections mainly based on the geomorphological characteristics and the unique property within each section, as described in Section 2.5.2 in detail.

The Lepsy Fault has an approximate 110° strike and extends from the Dzhungarian Alatau into the low-relief Kazakh Platform. It dips ~50° to the south and possesses both reverse and dextral slip components, with a slip-vector azimuth of 317-343° (Campbell et al., 2015). The eastern part of the Lepsy Fault, close to the Dzhungarian Fault, of the Lepsy Fault shows a clear long-term expression of faulting, with an uplift to the south. West of the Shynzhyly River, where the fault enters the low-relief Kazakh Platform, there is only a very subtle long-term expression of faulting in the geomorphology. Fresh palaeo-earthquake ruptures extend for the entire ~120 km mapped length of the Lepsy Fault (Campbell et al., 2015). We provide additional mapping and description of these ruptures in Section 2.5.1.

2.5 Palaeo-earthquake Ruptures on the Lepsy Fault and the Dzhungarian Fault

2.5.1 The Lepsy Fault

The 120 km length of ruptures along the Lepsy Fault are separated into the east, central and west sections, with the boundaries at the Shynzhyly (Shingildy) River and the Tentek River (Campbell et al., 2015, Figure 2-4a). The vertical displacement is easily recognised along the entire fault length whereas the significant right lateral component is only apparent in a few locations in the eastern and central sections. The eastern section of the Lepsy Fault is sited within the relatively high mountainous topography of the Dzhungarian Alatau. Campbell et al. (2015) visited the eastern section near Jaxa-Kol Lake (Figure 2-4a). Here, a series of southward-flowing ephemeral gullies and intervening ridges have been displaced, with

drainage now ponded against a north-facing scarp 9 – 13 m in height, and with right-lateral displacements of 4 – 6 m. Campbell et al. (2015) excavated a pit into one of the dry ponds formed where one of the channels has been blocked by the scarp. The base of the ponded sediment was not reached within the pit but a bulk soil radiocarbon sample from 1.05 m deep indicates that the scarp has been present in some form for at least 2000 years. The fresh scarps can be traced eastwards on satellite imagery to longitude 81.2°E, ~10 km from the trace of the Dzhungarian Fault (Figure 2-4a).

The central section of the Lepsy Fault runs along the base of the Chirindy mountains, an east-west sub-range of the Dzhungarian Alatau (Figure 2-4a). West of the Tentek River, Campbell et al. (2015) identified a 6 – 9 m high scarp with ~7 m lateral offset that they inferred to result from a single earthquake, which is consistent with our own measurements of 7 – 10 m scarp height from terraces adjacent to the Tentek River (Figure 2-4a,c,d). The north-facing scarps of the Lepsy Fault continue westwards along the base of the Chirindy mountains and are accompanied by additional discontinuous fresh scarps within the southern, uplifted, block. We measured apparent right-lateral stream offsets of 5 – 9 m across some of these scarps (Figure 2-4e-h). Close to the western end of the central section, the Lepsy Fault bends to the south, forming a restraining bend between its central and western sections. At this transpressional bend the north-facing scarps along the range-front end, and are replaced by a south-facing scarp ~5 m high that is clearly visible in the High Mountain Asia DEM (Shean, 2017) (Figure 2-4a,b,d). The High Mountain Asia DEM also reveals additional steep scarps north of the main fault trace, adjacent to the transpressional bend, near the village of Kyzylashi, (Figure 2-4a,b). These scarps, which were not identified by Campbell et al. (2015), reach heights of 10 – 15 m. We have not visited these scarps in the field, and do not know if they represent single-event or cumulative displacements. The main Lepsy scarp was measured by Campbell et al. (2015) at 7.4 m high where it crosses the Shynzhyly River. Folded and thrusted Tertiary sediments exposed in the uplifted southern side of the fault attest to long-term shortening. Their radiocarbon and OSL samples from river gravels uplifted in the southern, hanging-wall, of the fault suggest these deposits were uplifted at least ~5,000 years ago, though there is no direct constraint on whether the scarp here is formed from one or more earthquakes.

West of the Shynzhyly River (Figure 2-4a), the Lepsy ruptures cross into the low-relief steppe of the Kazakh Platform, with only subtle evidence for prior Quaternary fault movement. The fault trace is linear, trending 107°, and composed of a number of short en-echelon segments uplifted to the south, and with small sag-ponds at their ends. Scarp heights reach up to ~10 m (Campbell et al., 2015). At Ayak-Kol a now abandoned and exposed channel of the Lepsy River (Figure 2-4a and Figure 2-5) has been uplifted

at the fault scarp, which it should thus predate. From radiocarbon dating of reeds and optically-stimulated luminescence of cross-bedded sands forming the upper part of the exposed fluvial sequence, Campbell et al., (2015), estimate that the scarp, which is 5 – 7 m high at this site, formed within the past 400 years B.P. Deeper fluvial units that have been deformed by soft-sediment deformation yielded a radiocarbon age of 5328–4931 calibrated radiocarbon years B.P. (Campbell et al., 2015). A second ~2 m high scarp to the south of Ayak-Kol has been incised by the now abandoned river channel, suggesting that it formed in an earlier earthquake that predates the channel abandonment. A pit dug into the abandoned fluvial channel here yielded OSL ages of 2245 ± 480 years and 1810 ± 400 years B.P, which suggest may be contaminated by sands derived from older uplifted fluvial deposits exposed in the adjacent channel walls (Campbell et al., 2015). East of Ayak-Kol the two scarps merge to form a single ~ 9 m high scarp, which is suggested to be a composite of two events given that the two parallel scarps are of different ages (Campbell et al., 2015) (Figure 2-5).

The age results from the Lepsy Fault are mixed from Campbell et al. (2015). In the one location (Ayak-Kol) where the geomorphology indicates a single-event scarp and has suitable material for age dating, the scarp appears to be no more than 400 years old (profiles A3 and A4 in Figure 2-5). At several other sites, however, there is evidence that the scarp is significantly older, with ponding against the scarp near Jaxa-Kol from at least 2000 years ago, and 5000-year-old fluvial sediments uplifted by the scarp at the Shynzhyly River (Figure 2-4a). At Ayak-Kol there was also evidence for soft-sediment deformation of possible seismic origin affecting sediments containing organic material of age 5328–4931 calibrated radiocarbon years B.P. (profile A5 in Figure 2-5). We performed morphological scarp dating on the dGPS profiles A3 and A4, which were likely produced in a single event simultaneously, from Ayak-Kol measured by Campbell et al. (2015). These yield a mean diffusion age (kt) of 18.0 ± 0.9 m^2, implying they formed between 5.3 ka – 3.5 ka when applying a mass diffusivity of 4.19 ± 0.65 m^2/kyr (Pang et al., 2021) (Figure 2-5). The morphological dating suggests a much older age than the 400 years suggested by Campbell et al. (2015), but overlapping with the ~5000-year ages found from the Shynzhyly River and from older sediments at Ayak-Kol.

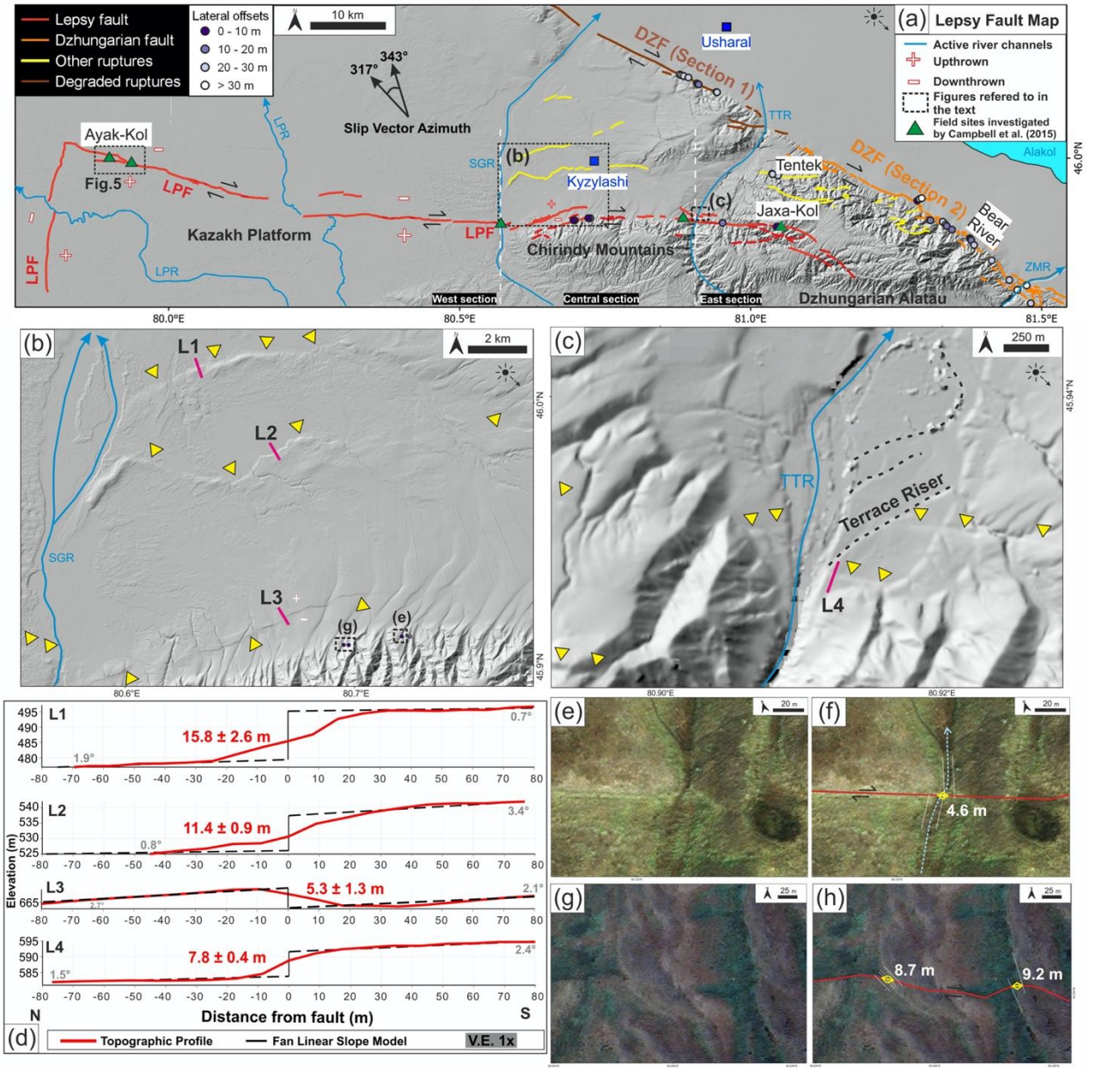

Figure 2-4. (a) Shaded relief High Mountain Asia (HMA) digital elevation model (DEM) showing the Lepsy Fault (red) and a part of the Dzhungarian Fault (orange). "Other ruptures" include secondary fractures, lineament and other fault scarps not directly associated with the DZF and LPF. The dashed white lines separate the three main sections of the Lepsy Fault. Locations of lateral offset measurement are shown as dots). The range of estimated slip vector azimuth of 317° – 343° from Campbell et al. (2015) are shown. LPR: Lepsy River; SGR: Shynzhyly River; TTR: Tentek River, ZMR: Zhamanty River. (b) Secondary scarps in the central section of the Lepsy Fault (see 'a') with the positions of three topographic profiles (L1, L2 and L3) shown by short red lines. (c) Ruptures adjacent to the Tentek River, marked by yellow arrows, with topographic profile (L4) labelled. Dotted black lines are river terrace risers. (d) Topographic profiles extracted from the HMA DEM with no vertical exaggeration (V.E. 1x). (e) and (g) Satellite images of the smallest lateral offset features found along the Lepsy Fault, see 'b' for location, with offset values annotated in (f) and (h).

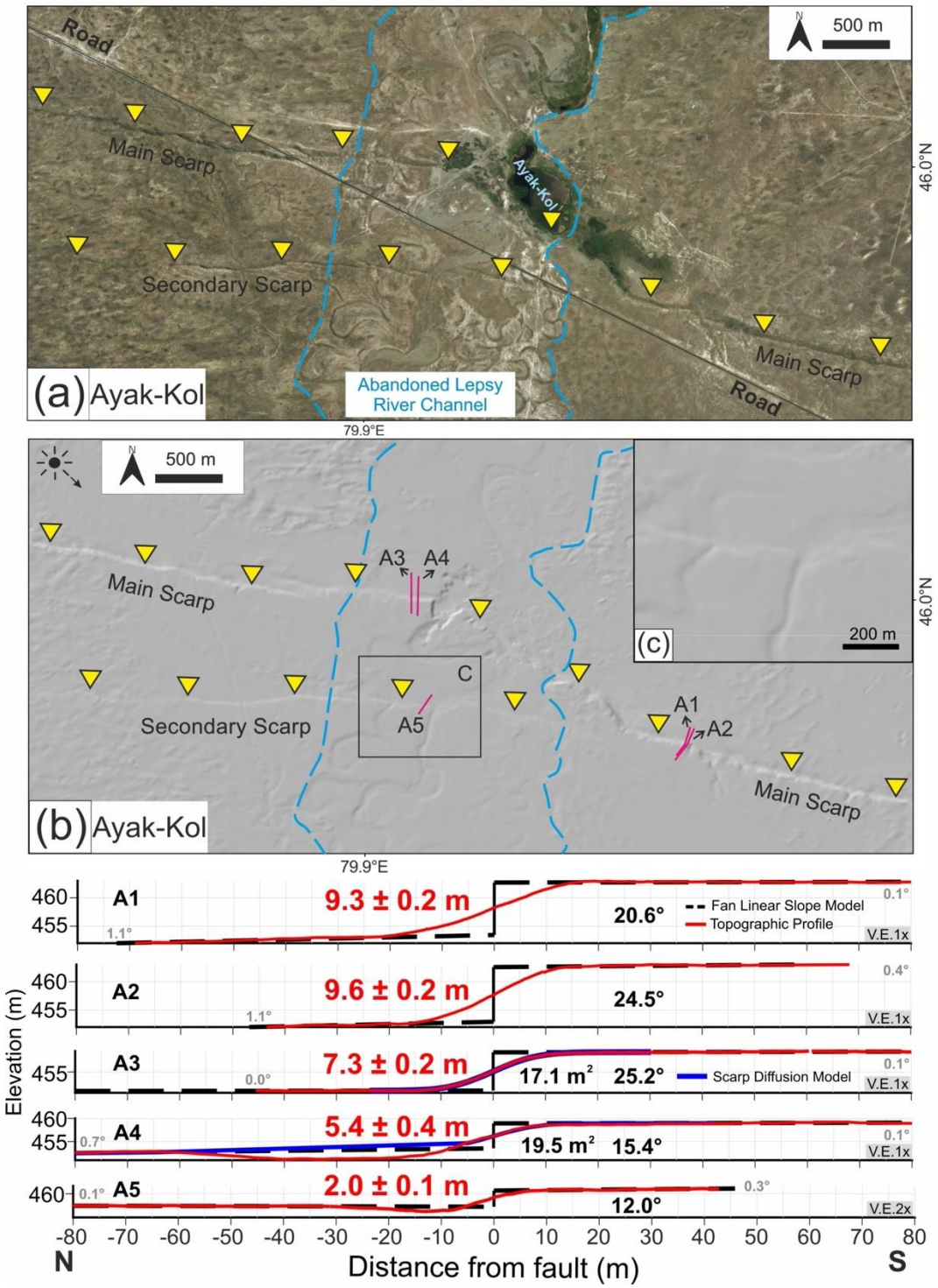

Figure 2-5. (a) Bing Map imagery and (b) shaded relief HMA DEM showing the abandoned river channel (bounded by blue dashed lines) and fresh scarps (marked by yellow arrows) at Ayak-Kol (Campbell et al., 2015; Fig. 2-4a for location). Five differential GPS topographic profiles (A1-A5) are shown below with their scarp heights (red text, in metres), maximum scarp slopes (black text, in degrees) and fan slopes (grey text, in degrees) annotated. Blue lines show the scarp diffusion model for profiles A3 and A4, the likely single-event scarps, with their diffusion ages (black text, in square metres) annotated and black lines

show the fan linear slope model. Note that profile A4 have dry ponds at the base of the scarps, so those areas were excluded in the estimation of the fan linear slope model. All the profiles except A5 are plotted without vertical exaggeration. (c) Close-up HMA DEM showing the secondary scarp incised by the abandoned river channel.

2.5.2 The Dzhungarian Fault

We divide the Dzhungarian Fault into eight sections based on the geomorphological characteristics, fault continuity, the width of the fault zone, the freshness of surface ruptures, and the distribution of offsets (Figure 2-6), as described in Table 2-2. The fault geomorphology and sense of slip vary along strike with a gradual change from almost pure right-lateral strike-slip faulting in the southeast, where the fault trends at ~330°, to oblique slip with a substantial vertical component of motion in the northwest, where the strike is ~300°. Sections S0 and S1 extend from the south of Usharal to the northwestern end of the fault (Figure 2-6). The tectonic geomorphology of these two sections is noticeably different from that of Section S2 southwards, in that the fault along S0 and S1 is manifest only as degraded scarps and much of the evidence for faulting has been completely removed by fluvial erosion during the deposition of the youngest generation of alluvial fans along the range front (Figure 2-7c-d). No discrete earthquake ruptures can be identified along S0 and S1. In contrast, the scarps along S2 are well-preserved and continuous, even within the young alluvial deposits (Figure 2-7b,e,f). Campbell et al. (2013) inferred that the scarps along S2 were produced by a single earthquake. Here we investigate the potential for that single event rupture to extend much further south along the Dzhungarian Fault by at least 200 km including Section S3 which is composed of two main branches and Section S4-S7 where the fault appears to be pure strike-slip. We also identify additional fresh scarps between the Lepsy and Dzhungarian Faults, and describe clusters of bedrock land sliding within adjacent highlands. We start our description in the south, where the fault appears to be predominantly strike-slip, before addressing the evidence for single event slip in the more northerly and complicated oblique slip sections (S2 and S3).

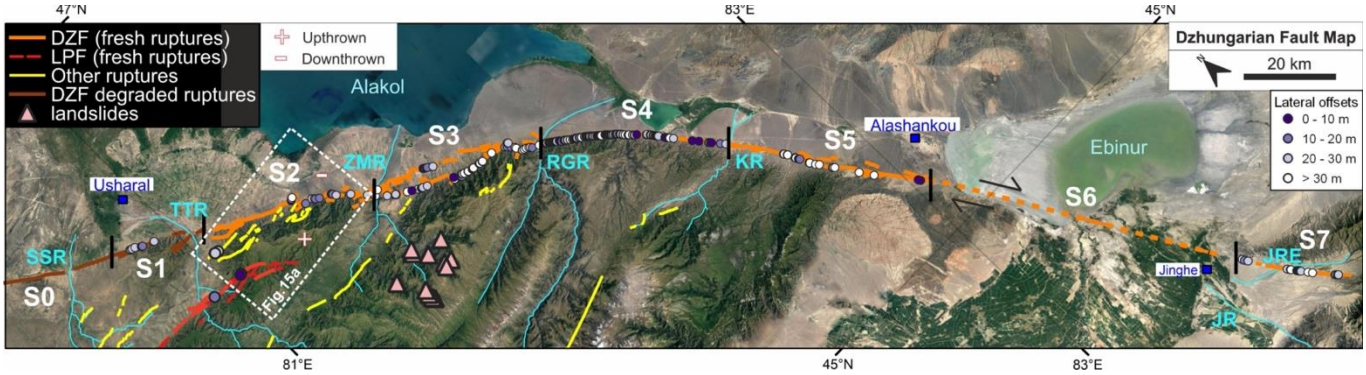

Figure 2-6. Google Earth imagery showing the Dzhungarian Fault (DZF), eastern Lepsy Fault (LPF), other ruptures (explained in Fig. 2-4), and mapped landslides (pink triangles) within the Dzhungarian Alatau mountains (west of the DZF). Lateral offset measurements are labelled by dots. The Dzhungarian Fault is divided into eight sections from northwest to southeast (S0 – S7) as represented by upright black lines with section numbers annotated. Zoomed-in images of each section are shown in Fig. 2-7, 2-8, 2-9 and 2-11. Towns are marked as blue squares. SGR: Shynzhyly River; TTR: Tentek River; ZMR: Zhamanty River; RGR: Rygayty River; KR: Kokty River; JR: Jing River; JRE: Jing River East.

Table 2-2. Characteristics of Section S0 to S7 along the Dzhungarian Fault.

	Type of offsets	Continuity	Strike	Length (km)	Notes
Section S0	Vertical	Fine	274°-300°	140	Degraded scarps
Section S1	Vertical and Lateral	Fine	300°	20	Degraded scarps and cumulative lateral displacements
Section S2	Vertical and Lateral	Fine	300°	35	Fresh scarps and many small branches
Section S3	Vertical and lateral	Fine	300°#	40	Two main branches
Section S4	Mostly lateral	Good	306°-326°	40	Gradual strike changing with narrow fault zone
Section S5	Mostly lateral	Good	327°	43	Many relay zones with several secondary faults
Section S6	Mostly lateral	(Unknown)	327°#	67	Fault traces mostly obscured by sediments and the lake / lowest topographic relief
Section S7	Mostly lateral	Good	324°	23	Low-quality offset features

[#]Strike of S3 is defined by the linearity connecting the end of S2 and the top of S4. Strike of S6 is defined by the linearity connecting the end of S5 and the top of S7.

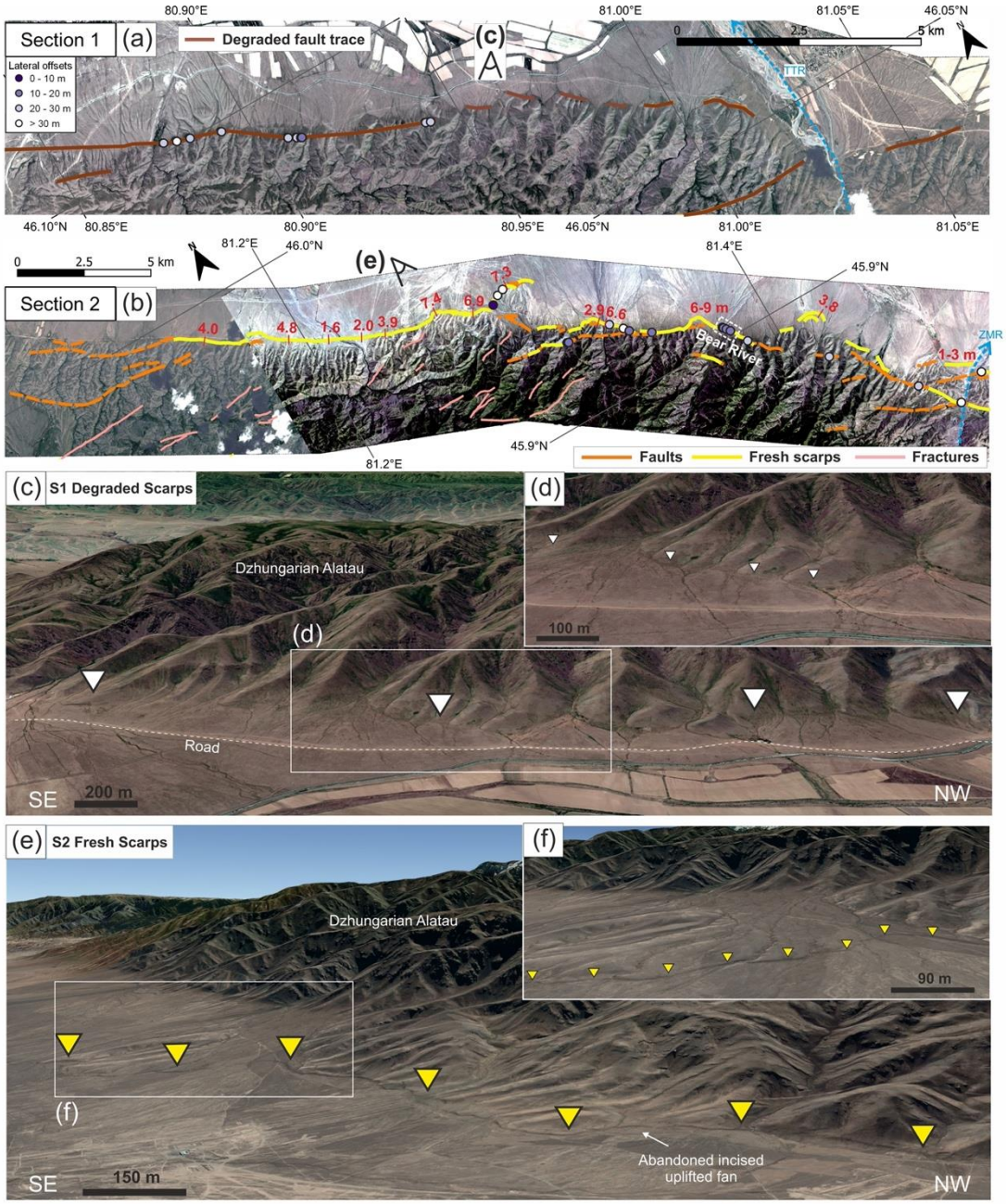

Figure 2-7. Orthorectified Pléiades imagery showing (a) Section S1 and (b) Section S2 of the Dzhungarian Fault with mapped fault traces and offsets (see Fig. 2-6 for locations, TTR: Tentek River, ZMR: Zhamanty River). Heights of the fresh scarps are annotated in red text with short red lines showing the measured locations. (c) and (e) are Google Earth satellite images looking obliquely SW along Section S1 and Section S2 with close-up details shown in (d) and (f) respectively, showing the different levels of scarp degradation and morphology at the range front between these two sections. Degraded scarps are pointed by white arrows; fresh scarps are pointed by yellow arrows.

2.5.2.1 Borohoro Shan to the Rygayty River (Sections S7-S4)

From where it exits the Borohoro Shan in the south to where it crosses the Rygayty River, the Dzhungarian Fault is generally straight and continuous without major branches (Campbell et al. 2013), though it can be separated into four sections (S7-S4) based upon its geomorphological characteristics. Section S7 is defined as the part of the fault from the Borohoro Shan to Jinghe Town. In this section the fault tracks through terraces and tributaries of the river in the east of the Jing River (named Jing River East (JRE) in this study). Most of the streams along S7 are oblique (25 – 30°) to the fault, which poses challenges in measuring the precise channel offset. Vertical offsets are restricted to short transpressional and transtensional relays (Campbell et al., 2013; Z. Hu, Yang, et al., 2021). Although the laterally offset features along S7 are mostly defined as low quality, our measurements based on Pléiades imagery show the smallest offsets are around 6.9 – 8.4 m (Figure 2-8b,e and f). These values happen to be similar to the 6 – 9 m single-event offset interpreted by Hu (2019) from examining high-resolution drone imagery in this area and their further COPD analysis. Adjacent to the Ebinur lake basin the fault becomes hard to trace, leading us to separate this part into a separate section S6 (Figure 2-8a). To the south of Lake Ebinur, the fault trace is mostly obscured by widespread agriculture. However, we recognised a linear fault trace right at the south of the shoreline and a likely pull-apart basin following the same trend in the further south (Figure 2-8a,c,d), which potentially have recorded the ruptures on S6. To the north of the lake the fault is visible cutting through palaeo-shorelines, but there are no geomorphic features from which lateral displacements can be measured.

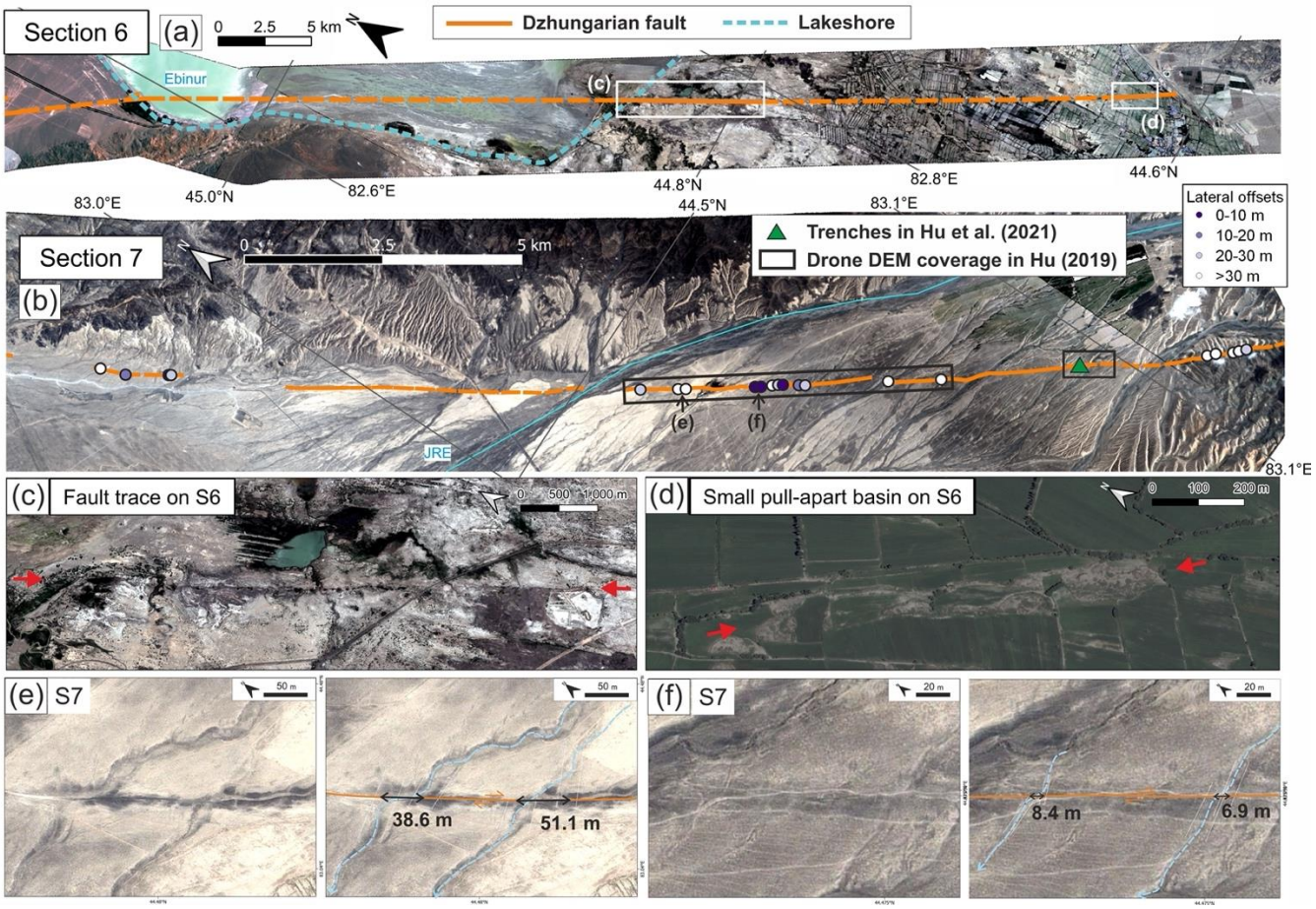

Figure 2-8. Orthorectified Pléiades imagery showing (a) Section S6 and (b) Section S7 with mapped fault traces and offsets measurement sites annotated. The maximum extent shoreline of Ebinur is shown by a blue dashed line in 'a'. Dashed orange lines are the inferred fault trace. (c) The linear fault trace (pointed by red arrows) at the south of the Ebinur Lake. (d) A pull-apart basin (pointed by red arrows) cutting through the fields. Locations of the trench and coverage of the high-resolution drone imagery from Hu (2019) and Hu et al. (2021) are labelled in 'b'. (e) and (f) are the lateral offset channels with the interpretations found along Section S7. JRE: Jing River East.

We defined S5 as the section of the fault from Lake Ebinur northwards to the Kokty River (Figure 2-9b). This section has an average strike of 327°. There are several < 2 km-long pressure ridges and pull-apart basins plus some ~5 km-long subsidiary faults 2 km eastwards of the primary fault. Several high-quality laterally-offset channels are found with the smallest displacement measured at 7.9 m (Figure 2-9i-j). Vertical offsets are only found within the relay zones. On the subsidiary faults, there are some < 1 m vertical displacements but no lateral offsets were identified.

Section S4 runs from the Kokty River northwards to the Rygayty River (Figure 2-9a). Within this section, the strike of the fault gradually changes from 326° in the southeast to 306° in the northwest. Despite the strike change, the fault zone remains the narrowest (mostly < 100 m) among its adjacent

sections, and is well defined and continuous. Numerous and widely distributed laterally offset channels are found. Vertical displacements are restricted to small relay zones. The smallest high-quality lateral offsets along a single strand found on this section are in the range of 6.9 – 8.8 m (Figure 2-9c-h).

Overall, the Dzhungarian Fault along sections S7-S4, south of the Rygayty River, is relatively continuous and appears to be predominantly strike-slip, with an average slip vector azimuth of ~328°. The smallest lateral offsets measured from a single strand along these sections are in the range of 6.9 – 8.8 m based on individual measurements (Figure 2-9). Due to the lack of historical coseismic slip data along this fault, we infer that these smallest offsets are likely to represent the slip in the most recent surface-rupturing earthquake, which is the working assumption based on the models developed for other historical earthquakes (e.g. Kurtz et al., 2018; Klinger et al., 2011). To calculate the average slip and to assess the evidence for prior offsets we produced a cumulative offset probability density (COPD) from the stacked triangular PDF of individual offsets along the single fault trace on sections S4 and S5 (Figure 2-10), where the fault has good continuity and where the measured high-quality smallest offset values remain similar along the fault (Zielke et al., 2010; Klinger et al., 2011; Kurtz et al., 2018). The COPD plot shows three peaks at 8.8 m, 15.2 m and 23.7 m, which we infer to result from slip in the 3 most recent earthquakes. This corresponds to slip of 8.8 m, 6.4 m and 8.5 m in the most recent, penultimate and antepenultimate events respectively (Figure 2-10c). Although the COPD peaks are not prominent, the inferred amounts for the past coseismic slip generally fit with the smallest lateral offsets of 6.9 – 8.8 m from individual measurements from the imagery.

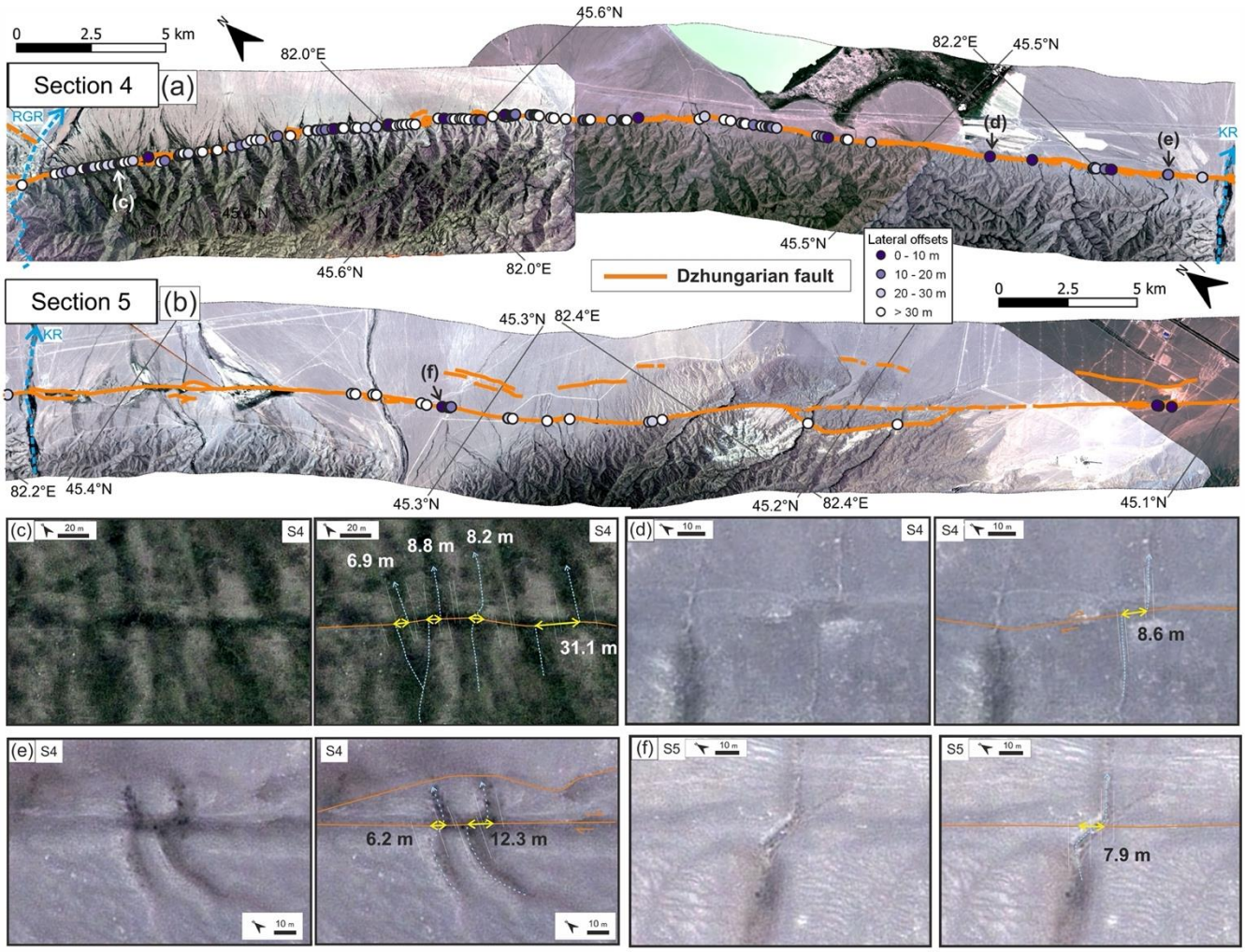

Figure 2-9. Orthorectified Pléiades imagery showing (a) Section S4 and (b) Section S5 of the Dzhungarian Fault with mapped fault traces and offset measurement sites annotated. (c)-(f) Close-up Pléiades imagery showing the smallest high-quality offset channels along sections S4 and S5 with the displacements annotated in metres. Example (e) shows closely-spaced probable single event and cumulative offsets. There is a second fault splay at location (e), such that the measured offset may underestimate earthquake displacement and these kinds of measurements would be excluded from the probability density plot and the COPD analysis.

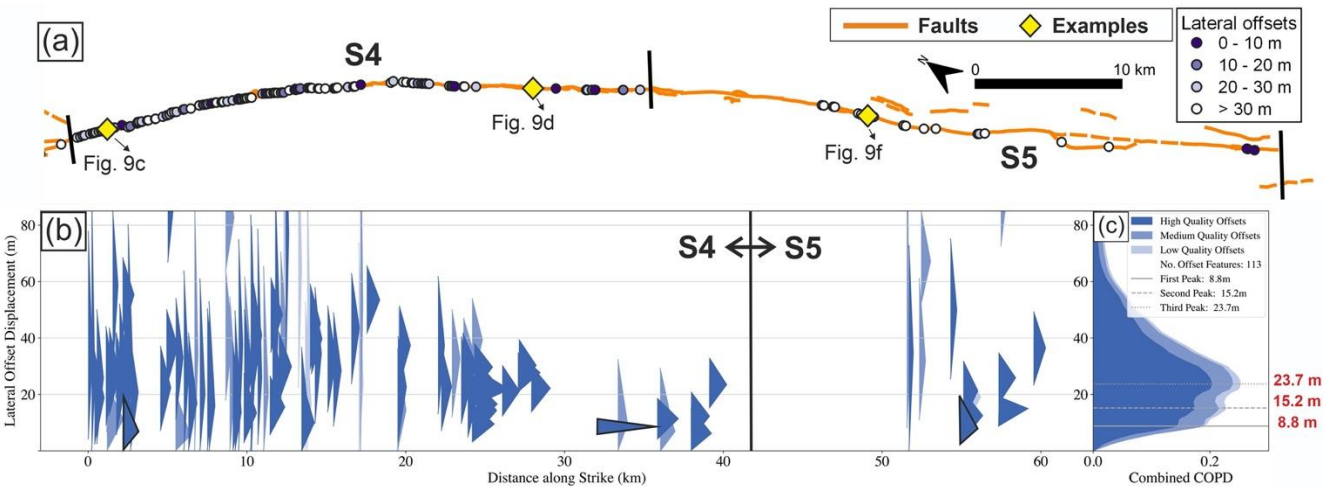

Figure 2-10. (a) Fault trace of sections S4 and S5 of the Dzhungarian Fault. Examples of high-quality smallest offset measurements are marked by yellow diamonds and their corresponding triangular PDFs framed by black lines in 'b'. (b) Probability density plot for the 113 dextral offset channels along the single fault trace of S4 and S5. Each triangle represents an individual offset PDF with dark blue to light blue colours representing high to low quality of the offset measurement. (c) Stacked cumulative offset probability density (COPD) with values of the three peaks annotated in red.

2.5.2.2 From the Rygayty River to the Zhamanty River (Section S3)

Between the Rygayty and Zhamanty Rivers the Dzhungarian Fault splits into two prominent branches, which is a unique geometry along this fault (Figure 2-11a). We defined this portion as section S3 with an average strike of 300°. On the northern branch, vertical displacements dominate, though several apparently right-laterally offset channels are also observed (Figure 2-11a). The scarp along the northern branch cuts through a number of different generations of alluvial fans, with the most widespread one having a scarp of ~14 m high (Figure 2-11j-l).

The southern fault branch tracks into the foothills of the Dzhungarian Alatau and appears to be predominantly right-lateral strike-slip, with abundant offsets of ridges and streams (Figure 2-11b,c). The smallest lateral offsets that we found along the southern branch are 7.3 – 9.2 m (Figure 2-11d-i). A small (~1-km-long) transtensional graben along the southern fault trace is shown in Figure 2-12. The south side of the graben is bounded by a north-facing steep fault scarp that displaces a low-relief alluvial surface. Five topographic profiles (B1-B5) extracted across this scarp from a drone-derived SfM digital model (Figure 2-12) show it to be 8 – 12 m high, except in Profile B4 where it is only ~6 m high. We note that Profile B4 goes across a small channel and a road on the upper fan, which might have modified the original scarp shape, though we cannot exclude an interpretation of this lower scarp value reflecting the true scarp offset. The topographic profiles show the scarp to be a single step, suggestive of a single-event rupture,

though the nearby 6-m measurement might instead indicate that where the scarp is higher, it resulted from a minimum of two events. We collected a single IRSL sample (DZH1) from a loess exposure under the terrace surface on the upthrown side of the southern fault. The sample was taken at a depth of 65 cm and yielded an age of 17.0 ± 1.1 ka (Figure 2-12e; Table 2-1), which should predate the formation of the basin scarps. Morphological scarp dating, excluding Profile B4 whose original shape might be modified, yielded a mean diffusion age (kt) of 19.9 ± 3.2 m^2 and a scarp age of 6.5 ka – 3.5 ka (Figure 2-12g).

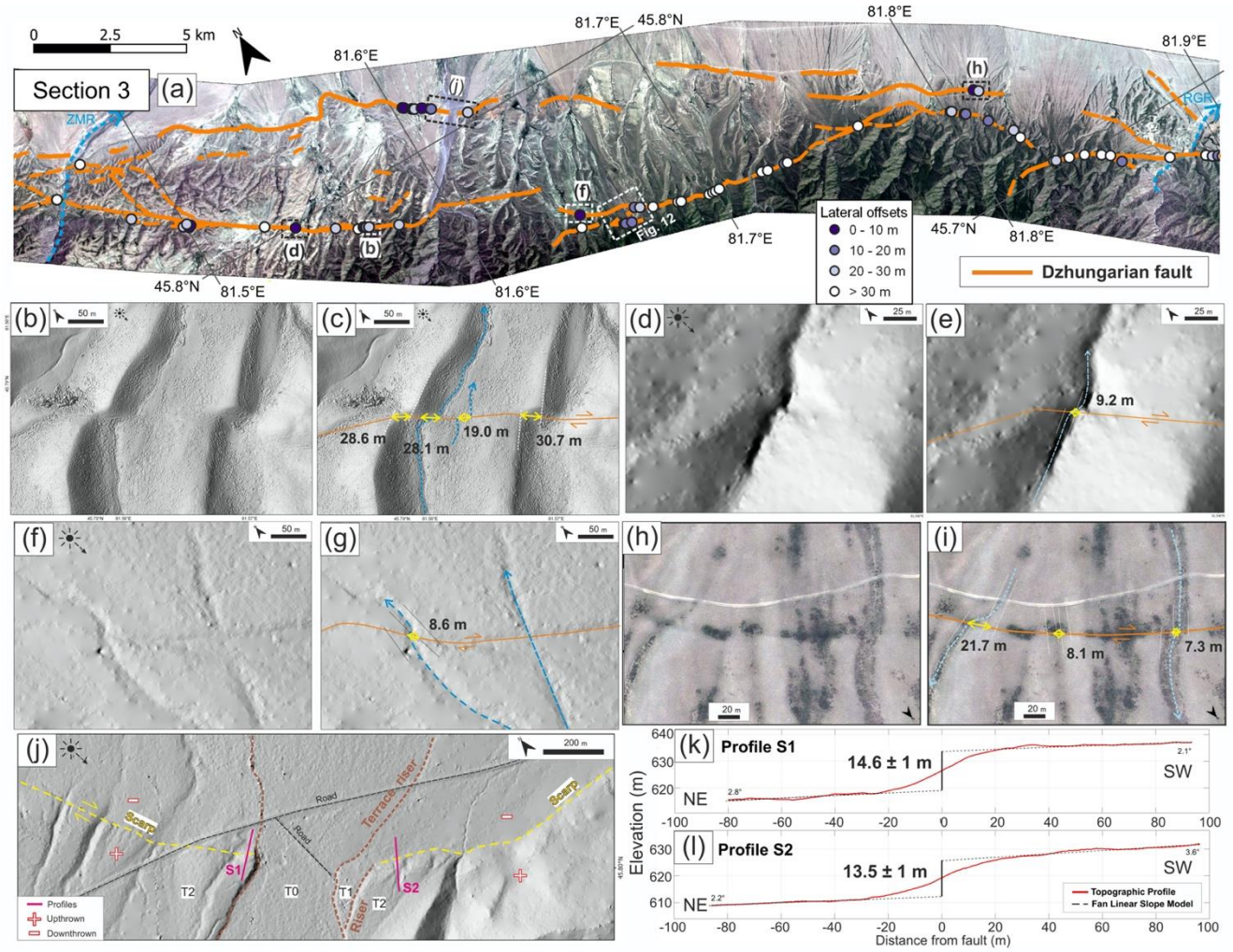

Figure 2-11. (a) Orthorectified Pléiades imagery showing Section S3 of the Dzhungarian Fault (See Fig. 2-6 for location) with mapped fault traces and offsets measurement sites annotated. (b)-(i) Orthorectified and shaded-relief topography derived from Pléiades imagery of the laterally-offset channels along S3 with the amounts of displacements annotated; see 'a' for locations. (j) Shaded-relief topography derived from Pléiades imagery showing the terraces T2-T0, from old to young, and the ~ 14 m scarps along the northern fault branch, with locations of the two profiles (S1 and S2) labelled; see 'a' for location. (k)-(l) Topographic profiles S1 and S2 from Pléiades-derived DEMs with their heights annotated.

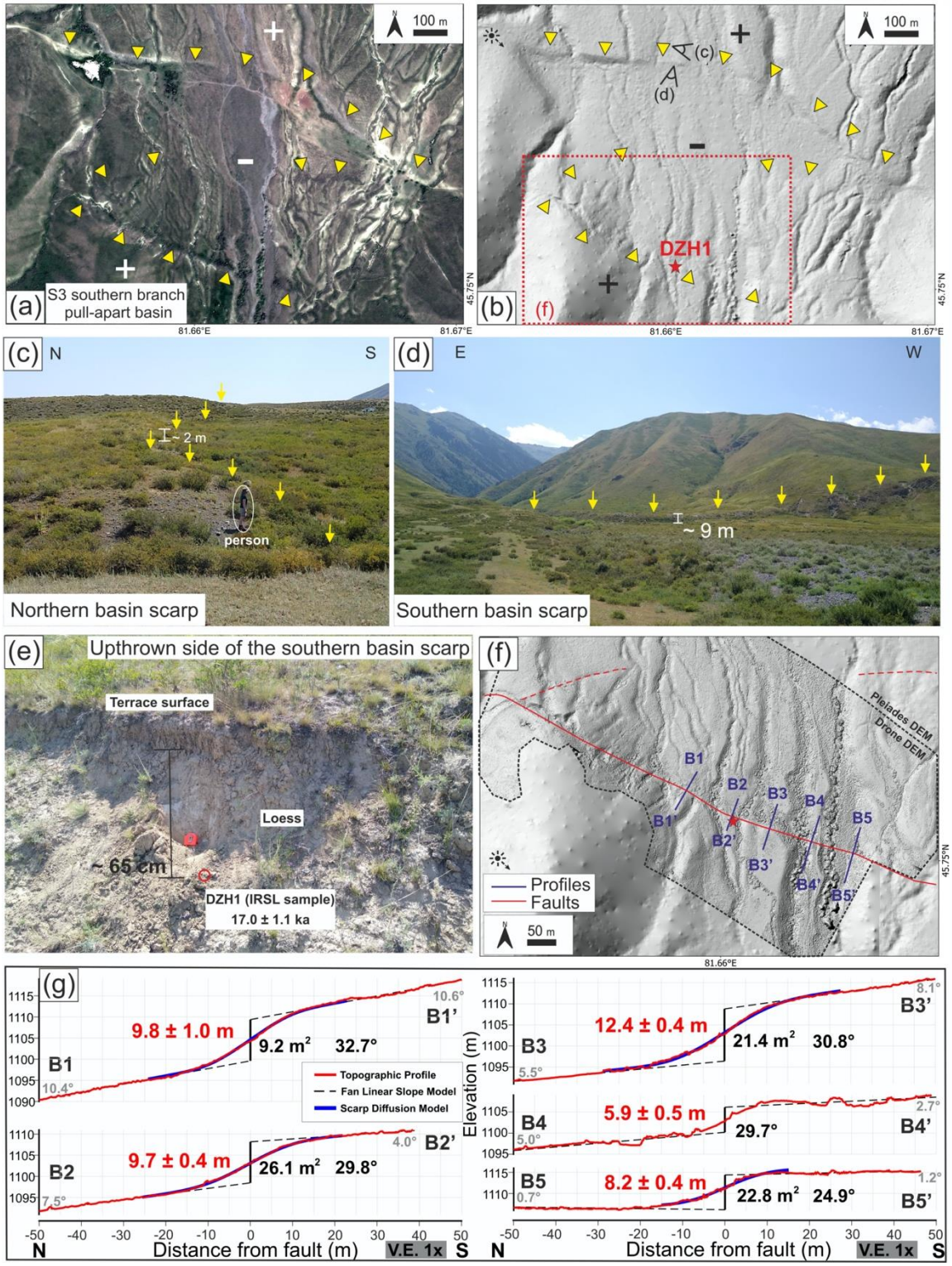

Figure 2-12. Pull-apart basin along the southern branch of Section S3 of the Dzhungarian Fault (see Fig. 2-11a for location). (a) Orthorectified Pléiades imagery with scarps marked by yellow arrows. (b) Shaded-relief topography derived from Pléiades imagery, with the location (red star) of Sample DZH1 labelled. (c) and (d) Field photographs of the northern and the southern basin scarps (marked by yellow arrows;

viewing perspective shown in 'b'). (e) Field photo of where the IRSL sample DZH1 was collected from loess at a depth of ~65 cm below the terrace surface on the upthrown, southern, side of the fault (see 'b'). The IRSL age is shown. (f) Drone-derived shaded-relief topography showing the five topographic profiles (B1-B5) labelled in blue. (g) Topographic profiles with their scarp heights (red text, in metres), diffusion ages (black text, in square metres), maximum scarp slopes (black text, in degrees) and fan slopes (grey text, in degrees).

2.5.2.3 From the Zhamanty River to the Tentek River (Section S2)

Section S2 of the Dzhungarian Fault extends from the Zhamanty River in the south to the Tentek River in the north with a strike of 300°. The fault in this section has a substantial vertical component, which is accommodated along a single main oblique fault, though minor fresh scarps are also distributed within adjacent foothills (Figure 2-7b).

The 'Bear River' site (Figure 2-13) is important in showing the potential slip in the most recent event on the fault. The Dzungarian fault crosses upper (T2) and lower (T1) alluvial surfaces, adjacent to the active river terrace (labelled T0 in Figure 2-13c), that have been displaced obliquely by the fault. Streams on the upper surface appear to have been displaced dextrally by ~12 m, with one stream potentially showing as much as 15.7 m offset (Figure 2-13d). The riser between T2 and T1 is right-laterally displaced by 13 m. There are no reliable markers of lateral offset on T1, probably covered by the sedimentation in the downthrown side. Six topographic profiles extracted from a drone-derived SfM model show a single step without beveling and with similar heights, with an average of ~7.9 m, on both the older and younger terraces (Figure 2-13b,e,f). Profile P2 has a double scarp morphology that we infer to result from localized slumping along the scarp, as represented by dotted red lines in Figure 2-13c.

The similarity in scarp heights in both T1 and T2 at the Bear River site, and the similarity in right-lateral offset of streams in the T2 surface and the T1-T2 riser suggest that both terraces have experienced the same amount of displacement. Furthermore, the scarp morphologies suggest, at a qualitative level, that the displacement possibly occurred in a single earthquake event, which is also supported by the consistency in scarp height measured more widely along S2, as described earlier. Morphological scarp dating for all profiles except P2, which we excluded due to the possibility of slumping, yielded a mean diffusion age (kt) of 24.2 ± 1.8 m^2, implying a scarp age of 7.3 – 4.6 ka. On the upthrown side of the scarp, a snail sample (RC1) extracted from ~1 m below the upper terrace (T2) surface (Figure 2-13a) was collected and yielded radiocarbon ages of 515 – 460 and 345 – 340 calibrated radiocarbon years B.P. (Table 2-1).

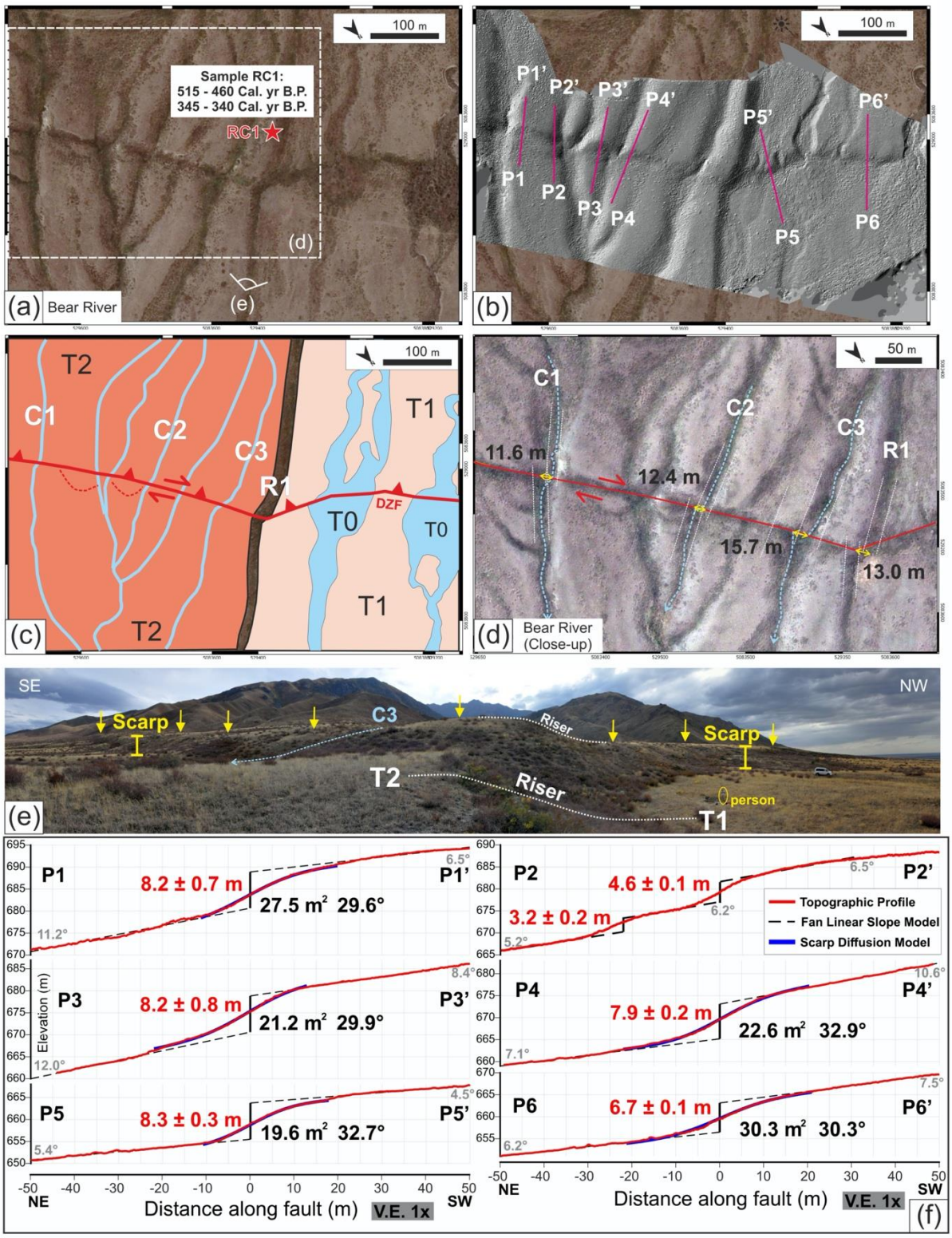

Figure 2-13. (a) Orthorectified Pléiades imagery showing fault scarp and offset channels at the Bear River site (81.37°E, 45.90°N) within Section S2 of the Dzhungarian Fault (see 'Fig. 2-7b' or "Fig. 2-14a" for location). The location (red star) and age of Sample RC1 is annotated. (b) Drone-derived shaded relief DEM showing the same view as in 'a'. Locations of topographic profiles are shown. (c) Geomorphic map

showing the extents of two terraces (T1 and T2) and the riser (R1) between them. (T0 is the current river channel.) (d) Close-up Pléiades image showing the three offset channels (C1, C2 and C3) and the terrace riser (R1) with amounts of dextral offsets annotated in metres. (e) Panoramic field photograph showing the scarp, which is of similar height in both terraces T1 and T2. See 'a' for viewing perspective. (f) The six topographic profiles (P1-P6) extracted from drone DEMs showing scarp heights (red text, in metres), diffusion ages (black text, in square metres), maximum scarp slopes (black text, in degrees) and fan slopes (grey text, in degrees).

Upstream of the main Bear River scarp, a second scarp was found with a height of 4.4 ± 0.6 m (Figure 2-14a-b). This scarp has a diffusion age (kt) of 15.9 ± 2.9 m^2, implying a scarp age of 5.3 – 2.7 ka (Figure 2-14b). Another snail sample (RC2) embedded within fluvial deposits at a depth of ~1 m on the upthrown, southern, side of the fault yielded a radiocarbon age of 3975 – 3835 calibrated radiocarbon years B.P. (Figure 2-14c-d) (Table 2-1).

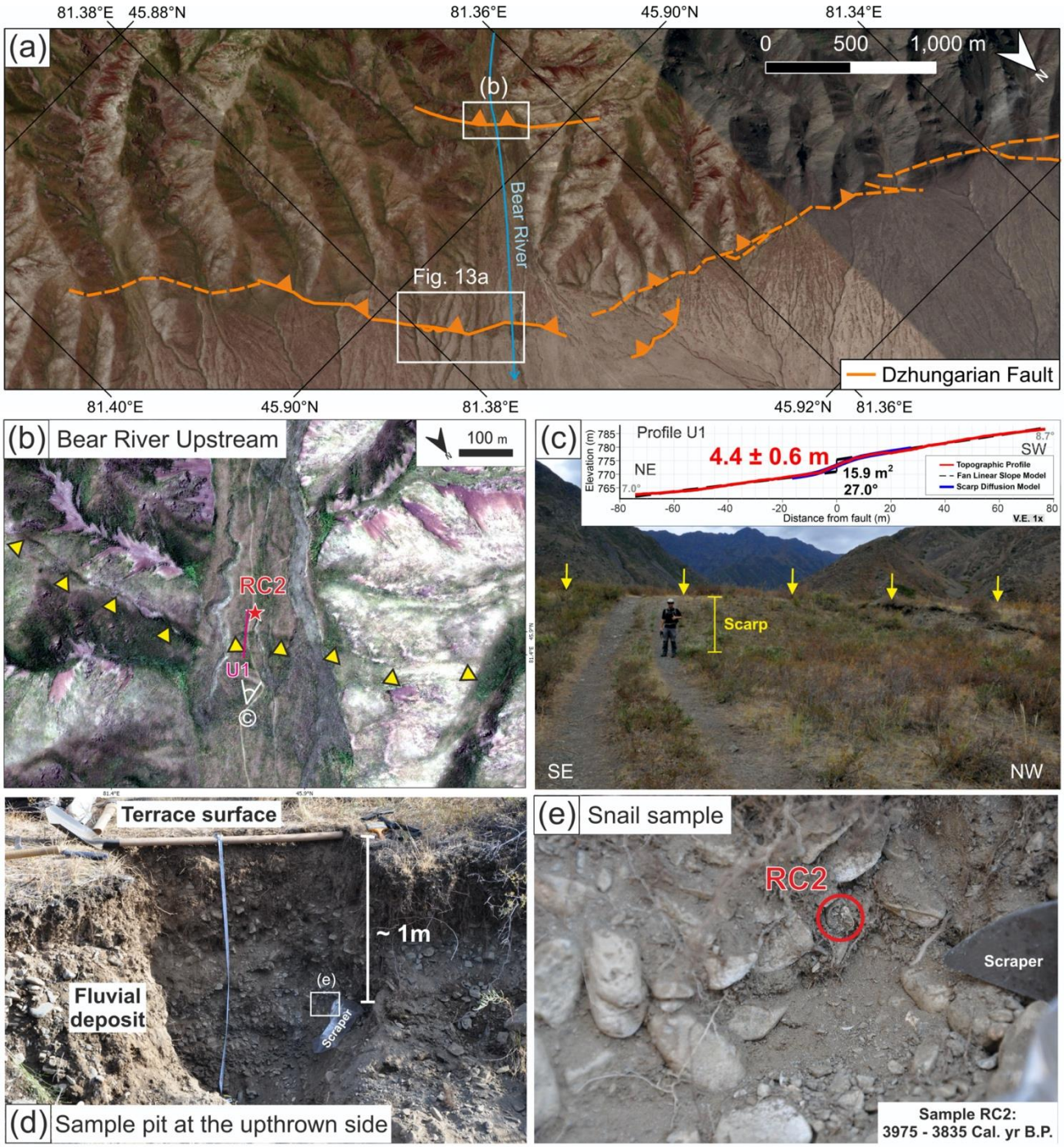

Figure 2-14. (a) Orthorectified Pléiades imagery showing the second scarp (yellow arrows) upstream from the Bear River site (81.36°E, 45.90°N). The locations of Sample RC2 (red star) and the dGPS profile (short red line) are marked. (b) Field photo of the scarp with the dGPS topographic profile and morphological scarp dating results shown as an inset. (c)-(d) Field photographs of the sample pit and the gastropod sample RC2 (red circle) along with its calibrated radiocarbon age.

We measured the scarp heights along the length of S2 from topographic profiles through the Pléiades-derived digital elevation model, primarily at sites where the scarp crosses small river catchments. We found consistent 6 – 9 m-high scarps for the southern twelve kilometres of S2 (Figure 2-7b), including the Bear River site as described above. Occasional lower scarp heights of 1 – 4 m are all sited on small splays rather than the main fault. The absence of scarps less than 6-9 m on the main fault, despite the wide preservation of scarps and the abundance of young faulted alluvial deposits, suggests that the 6-9 m scarps were formed in a single earthquake. For the northern seven kilometres of S2, however, the scarps abruptly reduce in height to < 5 m-high. Campbell et al. (2013) visited this part of the rupture and inferred a single-event origin of scarps measured at 1.6 ± 0.2 m high. The 'fresh' scarps end at the transition from S2 to S1, with the morphology of S1 and S0, as described below, being much more subdued.

2.5.2.4 North of the Tentek River (Sections S1 and S0)

We defined S1 as the section of the fault from the Tentek River northwards to ~46.10°N with a strike of 300°. On Section S1, the total topographic relief is up to 600 m with several dextral offsets of around 20 – 30 m, but no fresh scarps were found. (Fig. S2-1). Section S0 is defined as the part of the fault north of 46.10°N. This section also generally trends 300° but it bends to the south at 46.67°N to a strike of 240°. The topographic relief on Section S0 is mostly less than 200 m with no fresh scarps, laterally offset features or fractures, which do not have apparent or extensive offset but have obvious linearity.

2.5.2.5 Faulting, Fracturing and Landsliding within the Dzhungarian Alatau Foothills

The abrupt decrease in scarp height from 6-9 m to < 5 m within S2 coincides with significant splay faults and associated fracture that runs ENE into the Dzhungarian Alatau and exits into the lowlands east of the Tentek River, northeast of the Lepsy rupture (Figure 2-15a). We visited one of the splay faults at the 'Tentek River East' site (Figure 2-15a) where we surveyed steep north-facing scarps preserved within a small stream catchment. The present-day stream has cut a narrow gorge through the uplifted block, leaving the remainder of the scarp well preserved. The scarp height in individual topographic profiles ranges from 4.0 to 10.2 m along strike, but most heights are > 8 m and all show a single topographic step without beveling, meaning they might be single earthquake displacements (Figure 2-15e). Features offset by > 20 m could be found along these scarps. We conducted morphological scarp dating of seven profiles

at this site. We found that Profile T4 has over twice the diffusion age of the others. The mean diffusion age (kt) from all profiles except T4 is 11.3 ± 1.6 m^2, implying a scarp age between 3.6 ka – 2 ka. Apart from these high and fresh fault scarps, some small and fresh fractures are also recognised at the range margins within this transition area between the Dzhungarian and Lepsy Faults (Figure 2-15 and Figure 2-16) and are widespread within the foothills of the Dzhungarian Alatau, especially adjacent to S2 and S3 (Figure 2-16a). These scarps are clearly visible in the satellite imagery though we did not find any indicators of lateral offset (Figure 2-16b-f). We also identify a number of large rock avalanches within the Dzhungarian Alatau adjacent to S3 (Figure 2-16a and g). The landslides have occurred on steep west and north-facing slopes, and the debris have formed small lakes within adjacent valley bottoms.

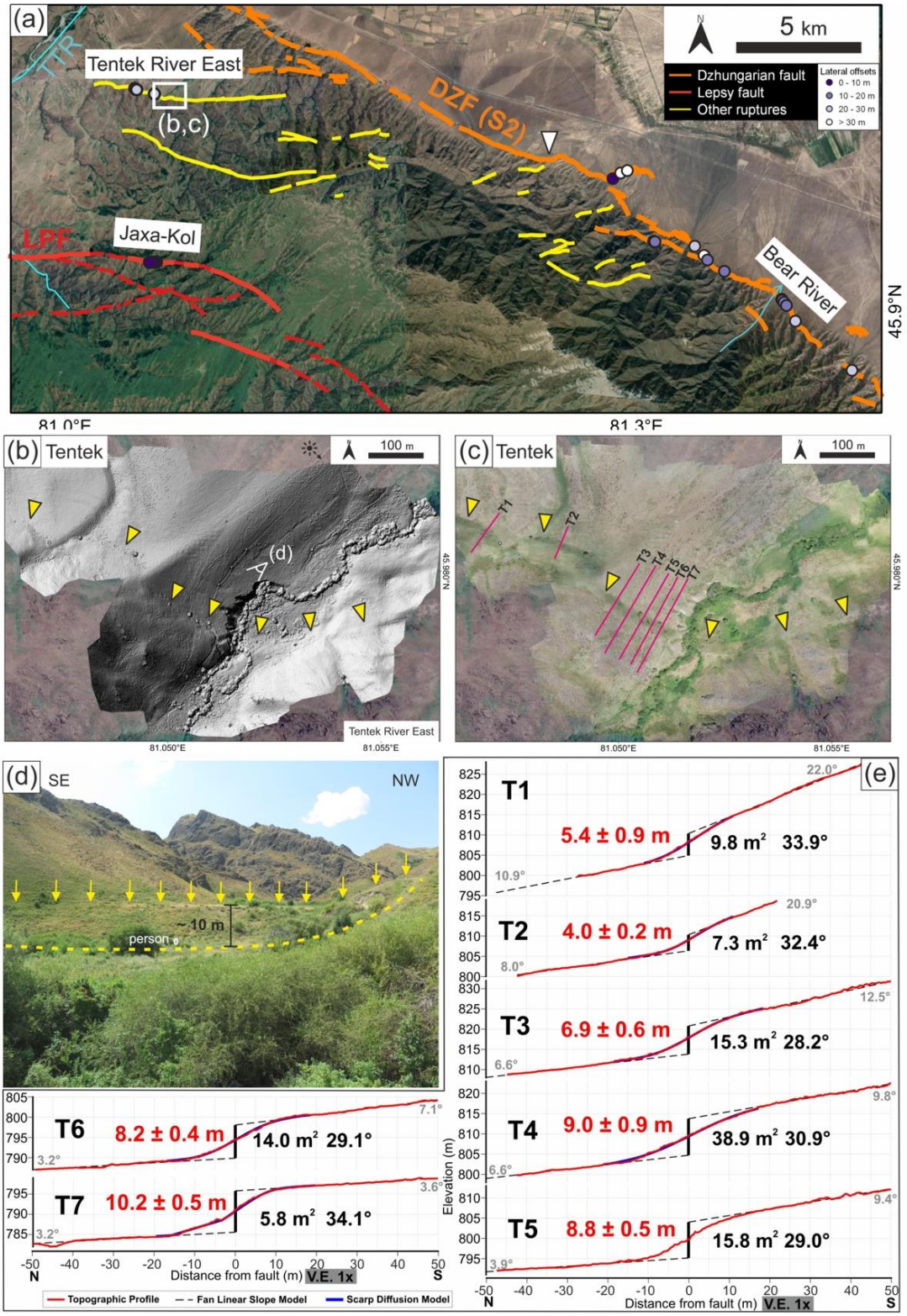

Figure 2-15. (a) Bing Map imagery showing the transition area between the Lepsy and Dzhungarian Faults. The white triangle marks the transition where the heights of the S2 fresh scarps drop from 6-9 m to < 5 m. (b)-(c) Drone-derived shaded-relief topography and orthorectified imagery showing the fresh scarps (marked by yellow arrows) and the locations of the seven topographic profiles (T1-T7) at the Tentek River

(TTR) East site (81.05°E, 46.00°N). (d) Field photograph of the scarp, marked by yellow arrows on top and a dashed line at the bottom (see 'b' for viewing perspective). (e) The seven profiles T1-T7 with their morphological scarp dating results.

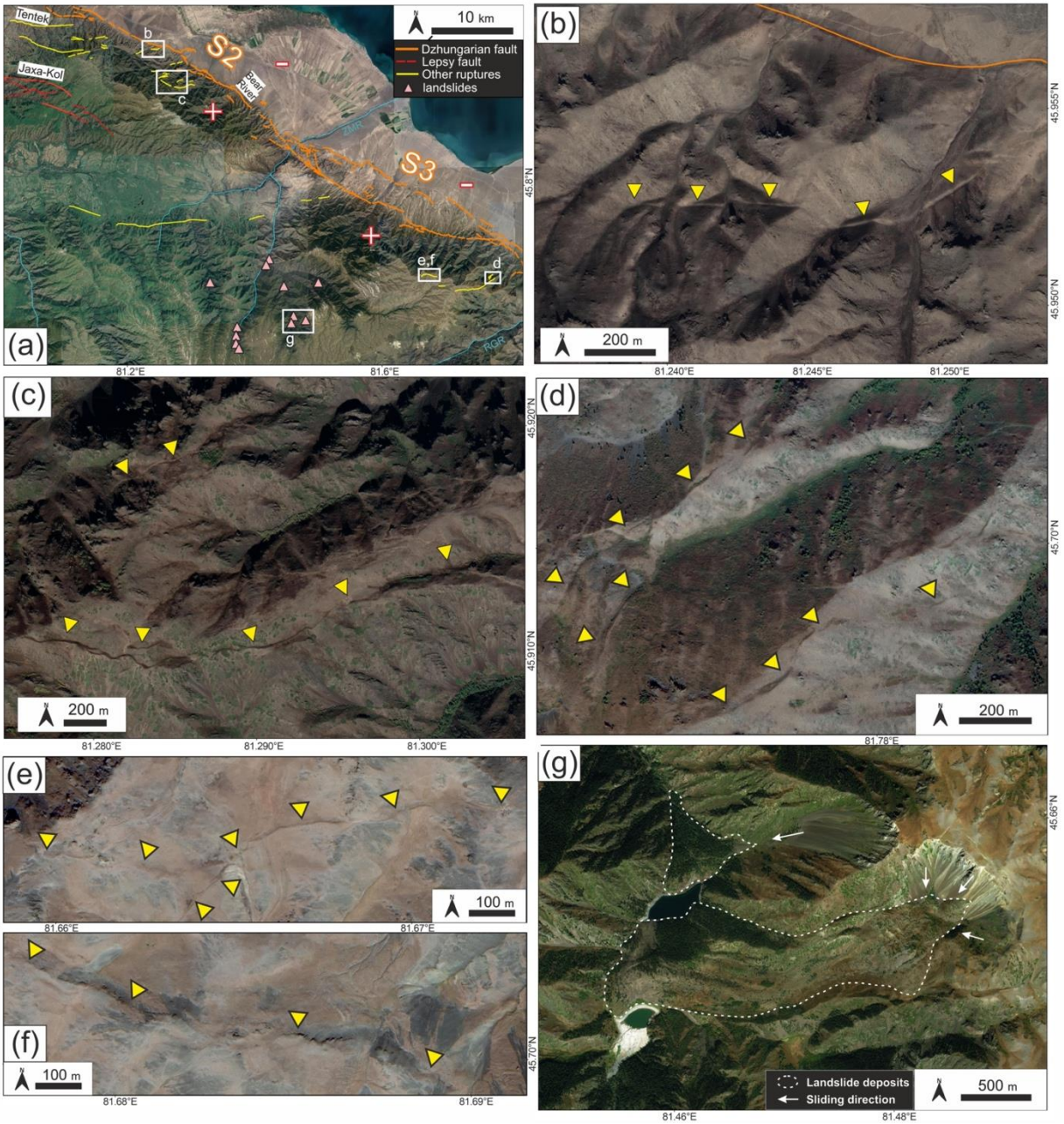

Figure 2-16. (a) Bing Map imagery showing the northern Dzhungarian Alatau with locations of mapped fault traces, other ruptures and landslides. (b)-(f) Google Earth imagery showing fresh fractures (marked by yellow arrows) on the hill surfaces close to S2 (near 81.29°E, 45.92°N) and S3 (near 81.77°E, 45.70°N). (g) Bing Map imagery showing examples of large bedrock landslides (at 81.47°E, 45.65°N).

2.6 Discussion

2.6.1 Palaeo-earthquake Rupture in the Most Recent Event

We have described evidence for young geomorphic displacements that we interpret to have resulted from single earthquakes along the Dzhungarian and Lepsy Faults, along with a number of splay faults that occupy the mountainous region between them. The southern parts of the Dzhungarian Fault (sections S7-S4) trend ~328° and are predominantly right-lateral strike-slip. Section S3 has a trend of ~300° and is oblique slip, with right-lateral and reverse components partitioned onto parallel structures separated by up to 6 km. Section S2 is a single oblique-slip range-front fault with splays branching westwards into the Dzhungarian Alatau. Sections S1 and S0 do not appear to have been reactivated since the deposition of the youngest widespread generation of alluvial fans, which is not displaced by faulting along these sections. Campbell et al. (2015) estimated the fault slip in the eastern part of the Lepsy Fault to be 8.2 – 13.8 m and a slip vector azimuth of 317°-343° from a site where they could measure both vertical and lateral components of slip, along with an independent estimate of fault dip (50°S). The similarity in slip-vector azimuth between that determined by Campbell et al. (2015) on the Lepsy Fault, and the 328° slip-vector azimuth implied by the trend of the southern Dzhungarian Fault, where the slip is predominantly right-lateral strike-slip, lead us to assume that the slip-vector azimuth is constant along the lengths of the Dzhungarian and Lepsy Faults, as is seen in other ruptures with significant strike changes such as the 2002 Denali Fault Earthquake and the 1999 Chi-Chi Earthquake (Lee et al., 2002; Haeussler et al., 2004).

To estimate the distribution of slip representing the most recent surface rupture(s) along the Dzhungarian Fault we use different approaches in the south and north. In the south (Sections S7-S4) where the slip is predominantly right-lateral, we use high-resolution satellite imagery to identify and measure numerous stream displacements, yielding an average of 8.8 m of right-lateral displacement in the most recent event along this section (Figure 2-10). Although we do find streams having offset less than 6 m in Section S5 near Alashankou as mentioned in Hu et al. (2021), they are mostly located in an area with multiple fault splays. Thus, we suggest that the widespread ~ 6 – 9 m displacements found along Section S7-S4 in this study at sites where the fault has a single surface trace better represent the most recent surface rupture along the main fault. Along Section S2 we found consistent 6 – 9 m high scarps that appear to result from a single rupture event. At the 'Bear River' site the fault strike is 300°, and the scarps of height 6.7 – 8.9 m are associated with lateral displacements of 11.6 – 15.7 m. The smallest lateral displacements found on Section S2 is close to the world's largest coseismic pure strike-slip offset as ~15.5 m (Rodgers

& Little, 2006), and considering the oblique slip component on S2, the total fault slip would be even higher. By assuming a slip-vector azimuth of 328°, these measurements yield slip of 14.7 – 19.9 m on a fault plane dipping 39° – 55° to the south, based on a geometrical fault model presented in Figure 2-17. For Section S3 the complexity of faulting makes estimation of net slip more challenging, though minimum lateral displacements of 7.3 – 9.2 m were found along the main strike-slip segment. Assuming the fault dips 47° to the south, as having a similar dipping angle to Section S2, the average strike of 300°, and a slip vector azimuth of 328°, we calculate a fault slip of 9.3 – 11.7 m, though note that this range is a minimum and does not take into account any slip on the numerous secondary faults within the region. We follow a similar approach to estimate the slip across the 6.9 – 10.2 m scarps on the splay fault at the Tentek River East site, in the transition zone between the Dzhungarian and the Lepsy Faults. This fault is parallel to the Lepsy Fault, with a trend of 280°. We estimate a fault slip of 10.4 – 15.4 m by assuming a slip vector azimuth of 328° and a fault dip of 50°S, as was found for the adjacent Lepsy Fault (Campbell et al., 2015). These values imply a lateral slip of 5.2 – 7.7 m. A compilation of fault geometry and slip estimation of each section is in Table 2-3.

The continuity of scarps along the Dzhungarian Fault, their fresh morphology, and the large interpreted single-event offsets all point to an earthquake that ruptured most of the fault, from S7 in the south to S2 in the north, for a length of at least 250 km. Overall, the fault slip resulting from the most recent slip event on the Dzhungarian Fault appears to increase from the southeast to the northwest with the largest slip in the central Section S2, and possibly in S3 where we do not have constraints on single-event offset for both branches. This region of high slip is at the transition between NW-SE to almost W-E striking segments. It is also adjacent to a zone of splay faults branching westwards from the Dzhungarian Fault towards the Lepsy Faults. Although there is no direct linkage of rupture between the Dzhungarian and Lepsy Faults, the widely distributed Holocene faults between them are each separated by no more than 3 km, raising the possibility that the two main faults ruptured simultaneously during a single earthquake, which would have a rupture length of at least 375 km (RS1 in Table 2-3).

Relatively complex multi-fault rupture patterns have been observed in a number of recent events in which slip has occurred on several splays or branched fault systems, such as in the 1992 Landers earthquake (Sieh et al., 1993), the 2010 Darfield earthquake (Quigley et al., 2019) and the 2016 Kaikoura earthquake (Hollingsworth et al., 2017). In this last example, large (> 10 m) multi-fault ruptures with displacement changing from strike-slip to thrust motion along strike were observed (Hollingsworth et al., 2017; W. Xu et al., 2018), which is similar to the scenario we have presented here. We note that scenarios

with shorter rupture lengths cannot be discounted, and we also consider a scenario in which the Dzhungarian Fault ruptured alone during its latest earthquake from Section S7-S2, with a rupture length of 248 km (RS2 in Table 2-3).

Table 2-3. The two rupture scenarios proposed in this study.

Sections	Length (km)	Strike	Dip	Measured Minimum Lateral Slip (m)	Measured Minimum Vertical Slip (m)	Inferred Average Slip (AD) (m)	
LPF	120*	290°*	50°S*	5 – 9*	5 – 9*	8.2 – 13.8*	
TRE	7	280°	50°S	-	6.9 – 10.2	10.4 – 15.4	
S2	35	300°	39 °- 55°S	11.6 – 15.7	6.7 – 8.9	14.7 – 19.9	
S3	40	300°	47°S	7.3 – 9.2	-	9.3 – 11.7	
S4-S7	173	328°	90°	8.8	-	8.8	
Scenarios	**Rupture Sections**	**SRL[#] (km)**	**AD (m)**	**Mw from AD[†]**	**Mw from SRL[+]**	**Mw from Seismic Moment**	**Slip-to-Length Ratio**
RS1	LPF+TRE +(S2-S7)	375	8.2 – 19.9	7.9 – 8.2	8.1	8.1 – 8.4	2.6×10^{-5} – 3.7×10^{-5}
RS2	S2-S7	248	8.8 – 19.9	7.9 – 8.2	7.8	7.9 – 8.2	4.0×10^{-5} – 5.5×10^{-5}

*The parameters of the Lepsy Fault (LPF) are all from Campbell et al. (2015).
[#]SRL: Surface Rupture Length
[†]Mw is calculated from Mw = 7.04 + 0.89log(AD) in Wells and Coppersmiths (1994).
[+]Mw is calculated from log(SRL) = -2.943 + 0.681Mw in Thinbaijam et al. (2017).
TRE: Tentek River East

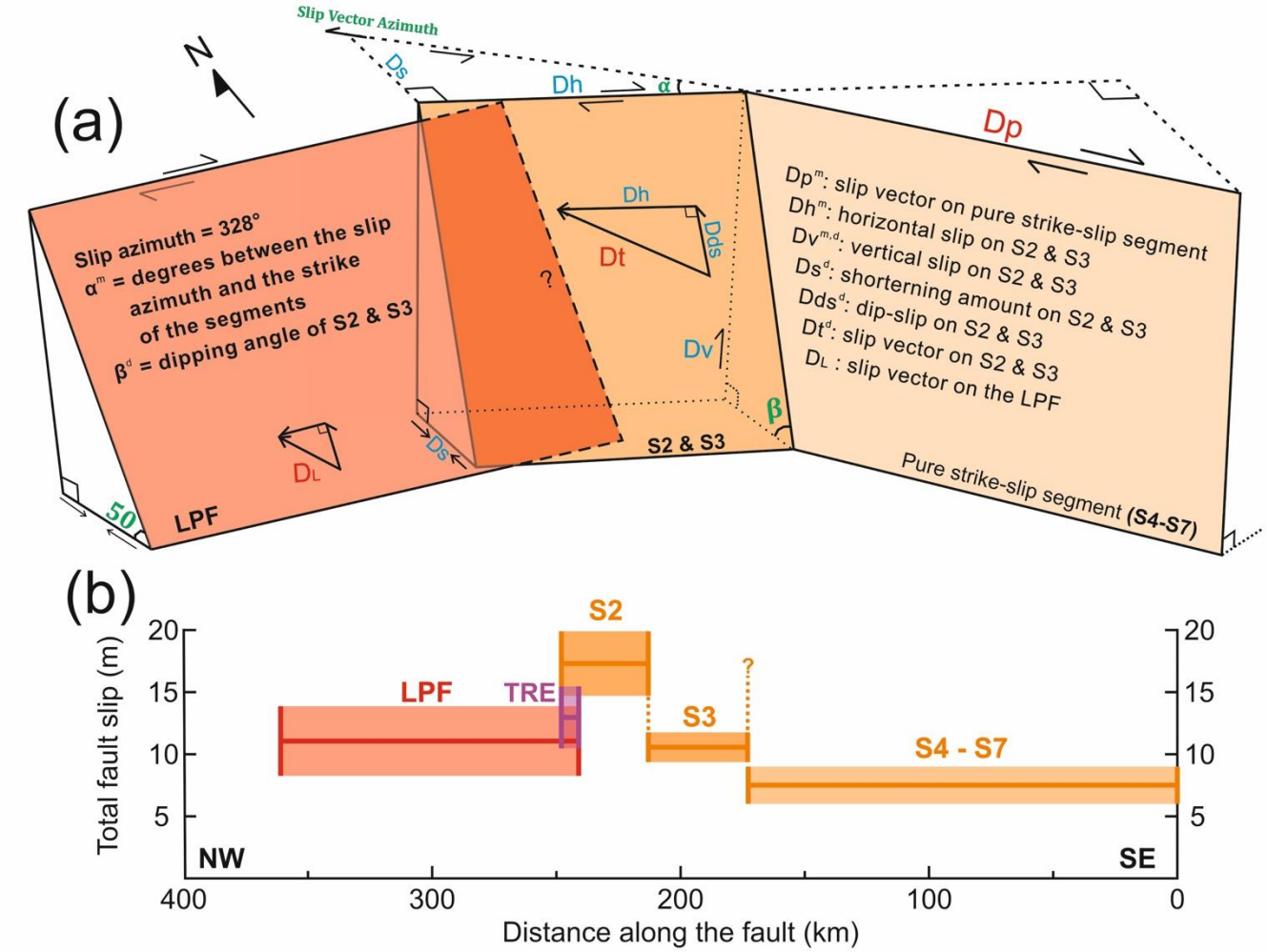

Figure 2-17. (a) Sketch showing the simplified fault geometry including the Lepsy Fault and sections S2-S7 of the Dzhungarian Fault. The slip on sections S2 and S3, which includes substantial vertical as well as horizontal components of slip, are estimated assuming a constant slip vector azimuth of 328˚ for all the segments. The superscript "m" and "d" mean the "measured" and "derived" components, respectively. Note that the vertical slip was measured on S2 but was derived on S3. Note that slip vector azimuth (D_L) for the LPF has been determined independently based on the interpretations by Campbell et al. (2015) and is consistent with the assumed value used here. (b) Total fault slip interpreted as being from the most recent event on different segments in this multi-fault system, including Dzhungarian Fault (orange), Lepsy (red) and the Tentek River East scarps (TRE; purple).

2.6.2 Earthquake Chronology

We have relatively limited constraints on the timing of the most recent event on the Dzhungarian and Lepsy Faults. The most detailed palaoeseismic information so far comes from Hu et al. (2021), who recognise four events from a trench along S7 (Figure 2-8b), with the most recent rupture after 6.6 ka, a

penultimate event in the range 12.2-6.6 ka, a third in the range 19.4-17.3 ka, and a fourth either prior to ~19.4 ka, or occupying the same 19.4-17.3 ka range as the following event. Hu et al., (2021) provide an average recurrence time of ~4-6 ka. From our fieldwork, we have a single IRSL sample DZH1 from a displaced terrace along S3 that is dated to 12 ka which must predate the most recent event (Figure 2-12). At the primary and secondary scarps at the Bear River site (Section S2), two radiocarbon samples (RC1 and RC2) from the displaced terraces yield ages of ~400 Cal. yr B.P. and ~4000 Cal. yr B.P. respectively (Figure 2-13 and Figure 2-14). We note that both our snail samples for radiocarbon dating might not represent the terrace abandoned ages since it is likely that they dug into the gravel layer a long time after gravel deposition although snail ages do show consistency with terrace deposition age in other region (e.g. Stahl et al., 2022). Though limited, our age results may be compatible with those of Hu et al. (2021), if we assume that the older (~4000 Cal. yr B.P.) rather than younger (~400 Cal. yr B.P.) age from the Bear River site is more representative of terrace deposition age. In that case, our age data support a single large earthquake rupture along the Dzhungarian Fault, occurring within the last ~4 ka. It is possible that this is the only earthquake to have occurred in the last ~17 ka, if we consider the scarps along the pull-apart basin in S3 shown in Figure 2-12 to result from a single event, as implied by the absence of beveling at the top of the scarp. One profile at that site showed a lower amount of slip that, if real, would mean that more than one earthquake has occurred within the last 17 ka.

Campbell et al. (2015) infer a large surface-rupturing earthquake along the Lepsy Fault within the last 400 years, which they tentatively assign to an earthquake in 1716 described in Mushketov and Orlov's catalogue (1893). The evidence for this < 400-year age comes from one location (Ayak-Kol). Our morphological dating, however, suggests that the scarps at Ayak-Kol might be substantially older, in the range of 5.3 ka – 3.5 ka. At several sites, Campbell et al, (2015) find evidence for deformation within that older range: ponded sediments near Jaxa-Kol date to at least 2000 years ago, 5000-year-old fluvial sediments are uplifted by the scarp at the Shynzhyly River, and soft-sediment deformation at Ayak-Kol has affected sediments dated at 5328–4931 calibrated radiocarbon years B.P. In summary, the available age data indicates a rupture on the Lepsy Fault within the last ~5000 years, but suggests the < 400-year constraint previously interpreted from Ayak-Kol is too young. Further investigation may confirm whether the young ages at Ayak-Kol are erroneous, or whether the scarp profiles appear anomalously old.

In summary, the majority of available evidence is consistent with a single rupture along the Dzhungarian and Lepsy Faults that displaced terraces that are as little as 4000 years in age, and which has caused ponding against the scarps for at least 2000 years. A later earthquake within the last 400 years may

have occurred along the Lepsy Fault, as suggested by dating at Ayak-Kol, but morphological scarp dating at all of our sites, including those along the Lepsy Fault, are 10 – 24 m^2 in average (Fig. S2-S5), indicating an onset of scarp degradation in the range 6 – 2 ka.

Our COPD analysis for the sections S4 and S5 of the Dzhungarian Fault yielded peaks in lateral offset at 8.8 m, 15.2 m and 23.7 m, which we inferred to represent slip in the last three earthquakes, with amounts of 8.8 m, 6.4 m and 8.5 m respectively. Hu et al. (2021) interpret three or four earthquakes to have occurred in the southern Dzhungarian Fault over the last 19.4-17.3 ka with an average recurrence interval of 4 – 6 ka. Further investigations may determine whether the most recent event was closer to 4000 or 2000 years ago. If the last three earthquakes have accrued an average slip of 23.7 m, and if those earthquakes have occurred within the last 19.4 –17.3 ka with an average recurrence interval of 4-6 ka, the inferred lateral slip rate would be 1.2 – 1.4 mm/yr and the age of 25.7 ± 5.8 ka for ~50 m of offset measured by Campbell et al. (2013) is plausible.

2.6.3 Earthquake Magnitudes and Scaling

We consider the likely magnitudes in two palaeo-earthquake scenarios. Rupture Scenario 1 (RS1) assumes the Lepsy Fault, Dzhungarian Fault, and the faults within the transition zone between them ruptured together in a single event. In Rupture Scenario 2 (RS2) only Sections S2-S7 of the Dzhungarian Fault ruptured together. We first use the empirical relationships in Wells & Coppersmith (1994) and Thingbaijam et al. (2017). By using the mean coefficients for strike-slip faulting from the average slip (AD), which is the range of AD on each ruptured sections, we calculate moment-magnitudes of M_w 7.9 – 8.2 for both scenarios (Table 2-3). Applying the scaling relationship between magnitude and surface rupture length (SRL) yields M_w 8.1 for RS1 and M_w 7.8 for RS2. We also calculate the magnitudes based on the combining seismic moment (M_o) released from each rupture segment:

$$M_w = \frac{2}{3} log M_o - 6.06, \text{ where } M_o = \mu AD,$$

Where μ is the shear modulus $3 \times 10^{10}\ Nm^2$, D is the average slip and A is the rupture area on the fault plane (Aki, 1966; Kanamori, 1977). We assume the depth is 15 – 30 km given typical earthquake depths within the Tien Shan, though we note that event depths down to ~40 km have been modelled in the adjacent Kazakh steppe (Sloan et al., 2011; Alinaghi & Krüger, 2014) (Figure 2-1a). Applying the range of depths and the other source parameters listed in Table 2-3 yields the moment magnitudes in the range of M_w 8.1 – 8.4 for the combined Lepsy and Dzhungarian Faults (RS1), and M_w 7.9 – 8.2 for the

Dzhungarian Fault alone (RS2). The ranges of the estimated moment magnitudes are similar to magnitudes found for the 1889 Chilik (M_w 8.0 – 8.3), and the 1911 Chon-Kemin (M_w 7.8 – 8.0) earthquakes (Kulikova & Krüger, 2015; Abdrakhmatov et al., 2016; Arrowsmith et al., 2017; Krüger et al., 2017), which suggests the northern Tien Shan could have similarly large magnitude earthquakes as the central Tien Shan despite the slower strain rate in the north.

We calculate the ranges of the slip-to-length ratios for each scenario from the average minimum slip and the average maximum slip among each ruptured segment and then divided by the total rupture length. Rupture of the Dzhungarian Fault alone yields a ratio of 4.0×10^{-5} – 5.5×10^{-5}, the combined Lepsy-Dzungarian rupture yields a ratio of 2.6×10^{-5} – 3.7×10^{-5} (Table 2-3). These ratios are generally compatible with global scaling relationships which are in the range of 1–10 x 10^{-5} (Scholz et al., 1986; Wells & Coppersmith, 1994; Wesnousky, 2008) (Figure 2-2). That the Dzhungarian Fault is inferred to follow global scaling relationships between slip and length, even though it is within an intra-continental and relatively slowly deforming setting, might be due to the structural maturity of the Dzhungarian Fault since it is a re-activated fault that has formed since the Palaeozoic (Voytovich, 1965; Manighetti et al., 2007; Campbell et al., 2015).

Comparing the two rupture scenarios with renowned great intraplate earthquakes that have well-studied surface ruptures, the combined Dzhungarian-Lepsy rupture length is similar to those in the 1905 Bulnay (375 km) and the 1957 Gobi-Altay (360 km) earthquakes (Rizza et al., 2015; Kurtz et al., 2018) but fault slip in the Dzhungarian-Lepsy rupture is larger (Figure 2-2). Adding our findings of prehistorical ruptures along the Dzhungarian Alatau to the other examples of giant intraplate earthquake ruptures, we find them roughly in line with the global scaling relationships and do not find many discrepancies with plate-boundary earthquakes (Figure 2-2). There are several high stress drop events, meaning more energy is released for a given-magnitude earthquake, such as the Bhuj and the Assam earthquakes as having large slip and rupture area (Bilham & England, 2001; Negishi et al., 2002; Copley et al., 2011). Some studies also stated stress drops for intraplate earthquakes tend to be higher than for interplate ones (Kanamori & Anderson, 1975; Allmann & Shearer, 2009); however, the compilation of great earthquakes in the Tien Shan and Mongolia in this study and some stable continental earthquake examples in Yang et al. (2021) seem to disagree with this idea. We suggest the various settings for intraplate faults such as their maturity, local lithology, crustal thickness and slip heterogeneity might cause variability in stress drop and slip-to-length ratio (Thingbaijam et al., 2017 and the references therein). Therefore, whether intra-continental

faults do have particular rupture behaviours and how different they are from faults in plate boundary settings still requires further investigation.

2.6.4 Implications for Intraplate Earthquakes and Faulting in the Tien Shan Region

It is worth noting that the latest rupture does not propagate along the general strike of the Dzhungarian Fault into Section S1 and S0 but instead goes along the Lepsy Fault whose strike is misoriented to the inferred slip vector of ~328°. It is possible that multi-fault ruptures start at the Lepsy Fault and further trigger movement along the central to SE Dzhungarian Fault, which might explain the absence of fresh ruptures in the northern Dzhungarian Fault and the additional fault splays between the Lepsy and Dzhunfarian faults adjacent to the central part of the Dzhungarian Fault (S2 and S3). Several cases globally (e.g. the 2010 El Mayor-Cucapah and the 2010 Darfield earthquakes) have shown that misoriented faults can trigger cascading ruptures across the fault network (Fletcher et al., 2016; Quigley et al., 2019), which might also be the case for the combined Dzhungarian-Lepsy rupture. Moreover, the increasing component of shortening from the southern part of the Dzhungarian Fault to the Lepsy Fault is consistent with the regional pattern of deformation in the Dzhungarian Alatau and wider Tien Shan region (Figure 2-1b) (Abdrakhmatov et al., 1996; Zubovich et al., 2010) and the misoriented segments like the Lepsy Fault might be the primary structures for the mountain building process in this region as they have a similar trend to the E-W oriented ridges of the Dzhungarian Alatau. Our data imply that a major boundary fault in the region could have a joint rupture with shorter local structures, which is still likely to trigger larger-magnitude earthquakes than expected for single-fault ruptures.

2.7 Conclusions

Our results provide a valuable example of a palaeo-earthquake which ruptured a major intra-continental strike-slip fault. Our observations and analysis of the palaeo-earthquake ruptures from satellite imagery and field surveys indicate that a great earthquake likely occurred in the last 4000 years on the Dzhungarian Fault, with a rupture length of up to 375 km for a combined Dzhungarian-Lepsy rupture. We interpret this complex earthquake to have involved slip on two separate faults and distributed faulting in between. The total fault slip is up to ~20 m on the northern oblique-slip sections and 6 – 9 m on the southern pure strike-slip section. Our estimated palaeo-earthquake magnitudes for a combined rupture of

the Dzhungarian and Lepsy Faults reach up to M_w 8.4, which would place it amongst the largest known intra-continental earthquakes. Despite these particularly large parameters, this palaeo-earthquake is consistent with the global scaling relationships between slip and length, as are other large intra-continental earthquakes in Tien Shan and Mongolia. We show that the Lepsy Fault may not have a high slip-to-length ratio as previously suggested and we demonstrate the importance of meticulous fault mapping for the estimation of accurate scaling relationships. More examples from either historical or pre-historical earthquakes would be helpful to further analyse and summarize fault behaviours within intra-continental settings.

2.8 Appendices

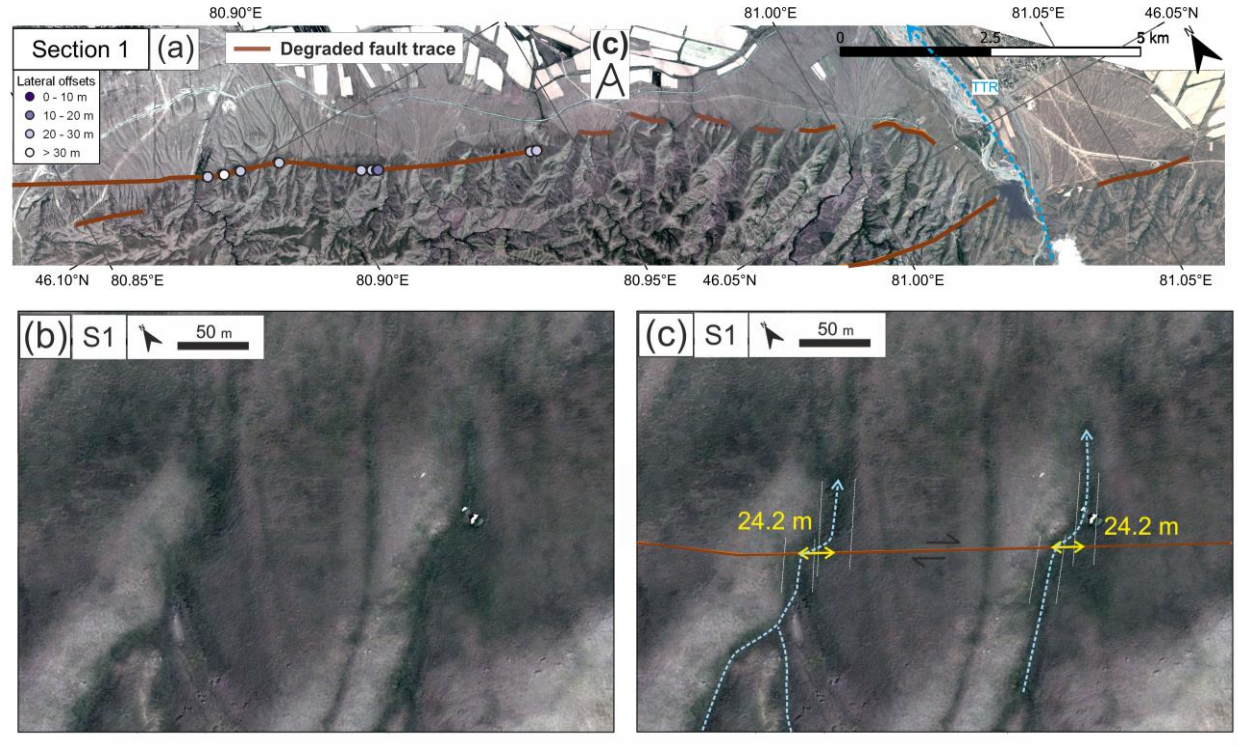

Figure S2-1. The 20-30 m offset channels found at Section S1 of the Dzhungarian Fault.

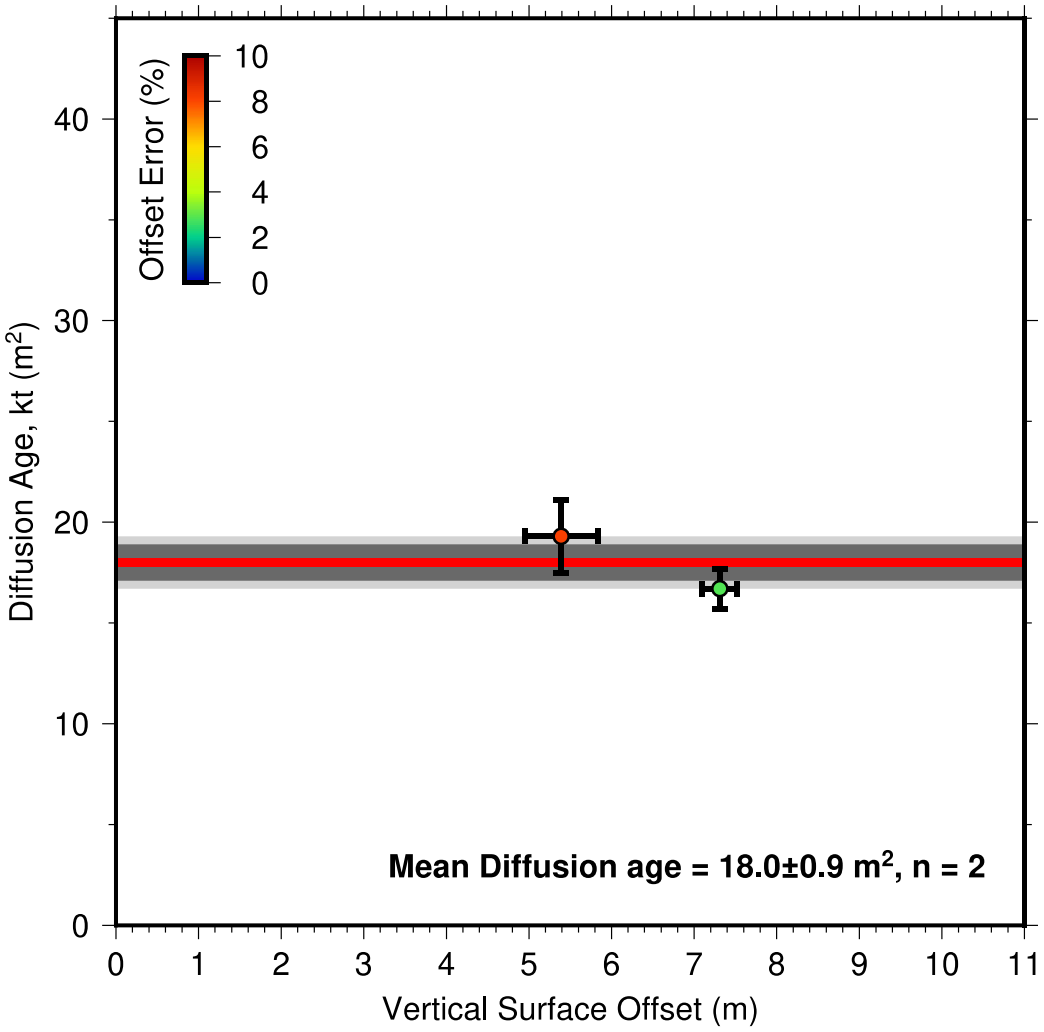

Figure S2-2. Calculated diffusion age (kt) for the three DGPS scarp profiles (A3 and A4) at Ayak-Kol along the Lepsy fault. Points are coloured according to their percentage errors in the estimation of vertical fault offsets. The mean kt value of 18.0 m^2 is denoted by the red line, with 1 σ standard deviation shown by the light grey area and the standard error (0.9 m^2) of the mean value shown by the dark grey area.

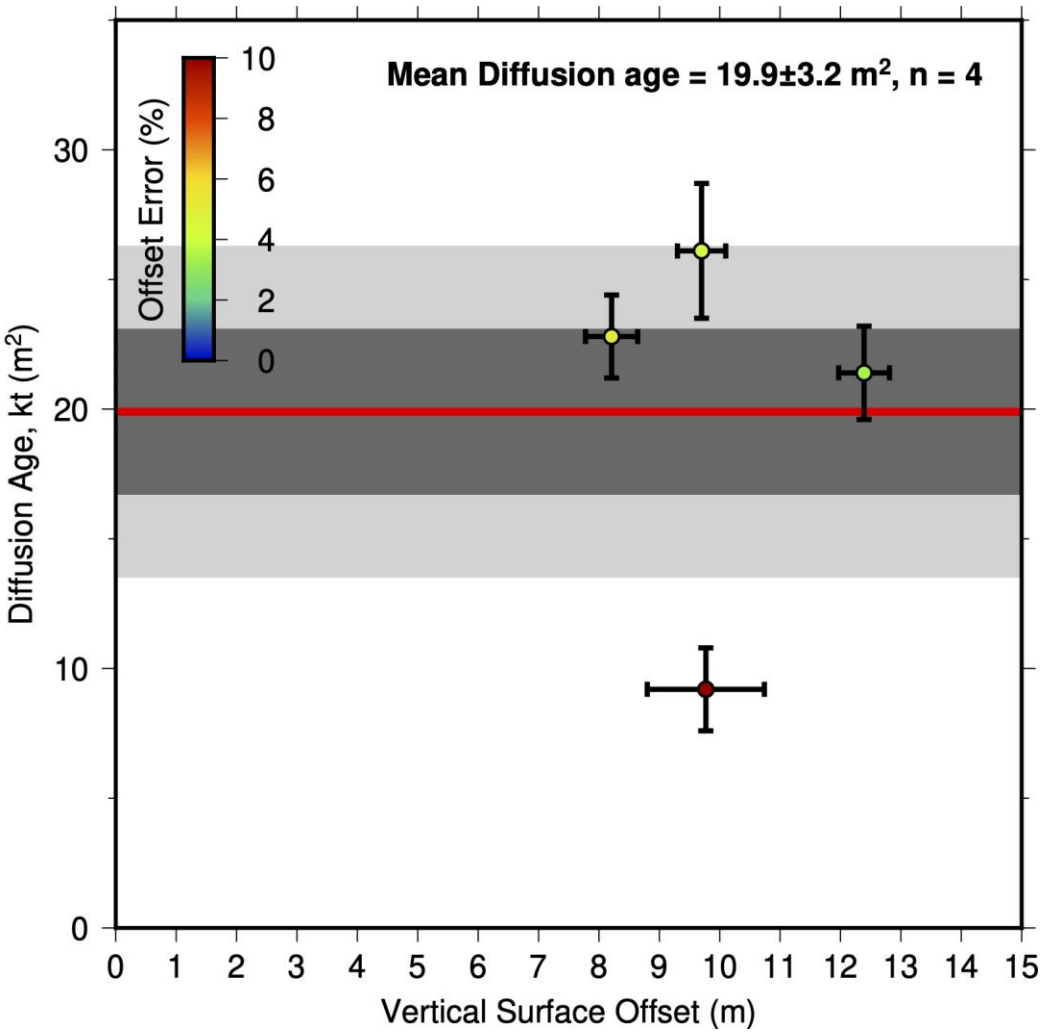

Figure S2-3. Calculated diffusion age (kt) for the four profiles (B1, B2, B3 and B5) of the southern basin scarps at Section S3 on the Dzhungarian fault. Points are coloured according to their percentage errors in the estimation of vertical fault offsets. The mean kt value of 19.9 m^2 is denoted by the red line, with 1 σ standard deviation shown by the light grey area and the standard error (3.2 m^2) of the mean value shown by the dark grey area.

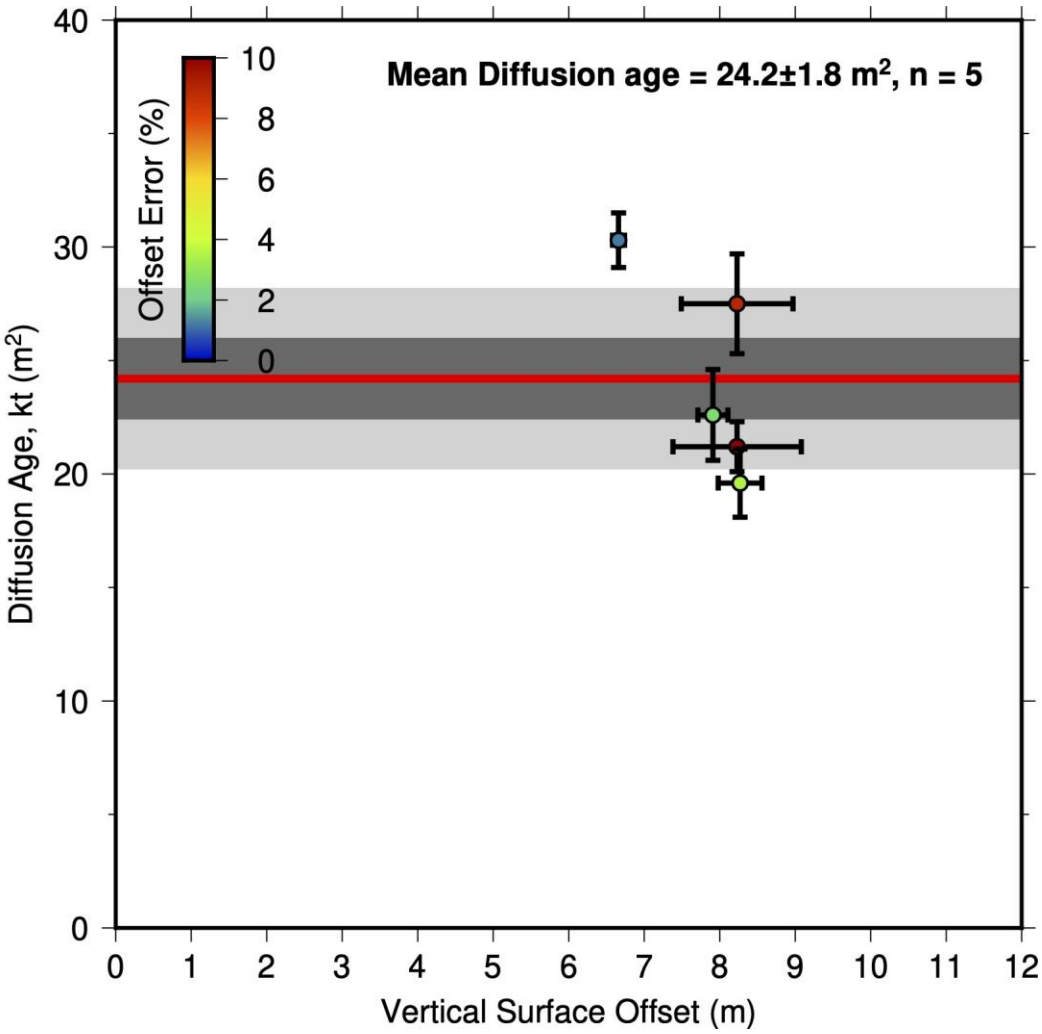

Figure S2-4. Calculated diffusion age (kt) for the five profiles (P1 and P3-P6) of the Bear River scarps at Section S2 on the Dzhungarian fault. Points are coloured according to their percentage errors in the estimation of vertical fault offsets. The mean kt value of 24.2 m^2 is denoted by the red line, with 1 σ standard deviation shown by the light grey area and the standard error (1.8 m^2) of the mean value shown by the dark grey area.

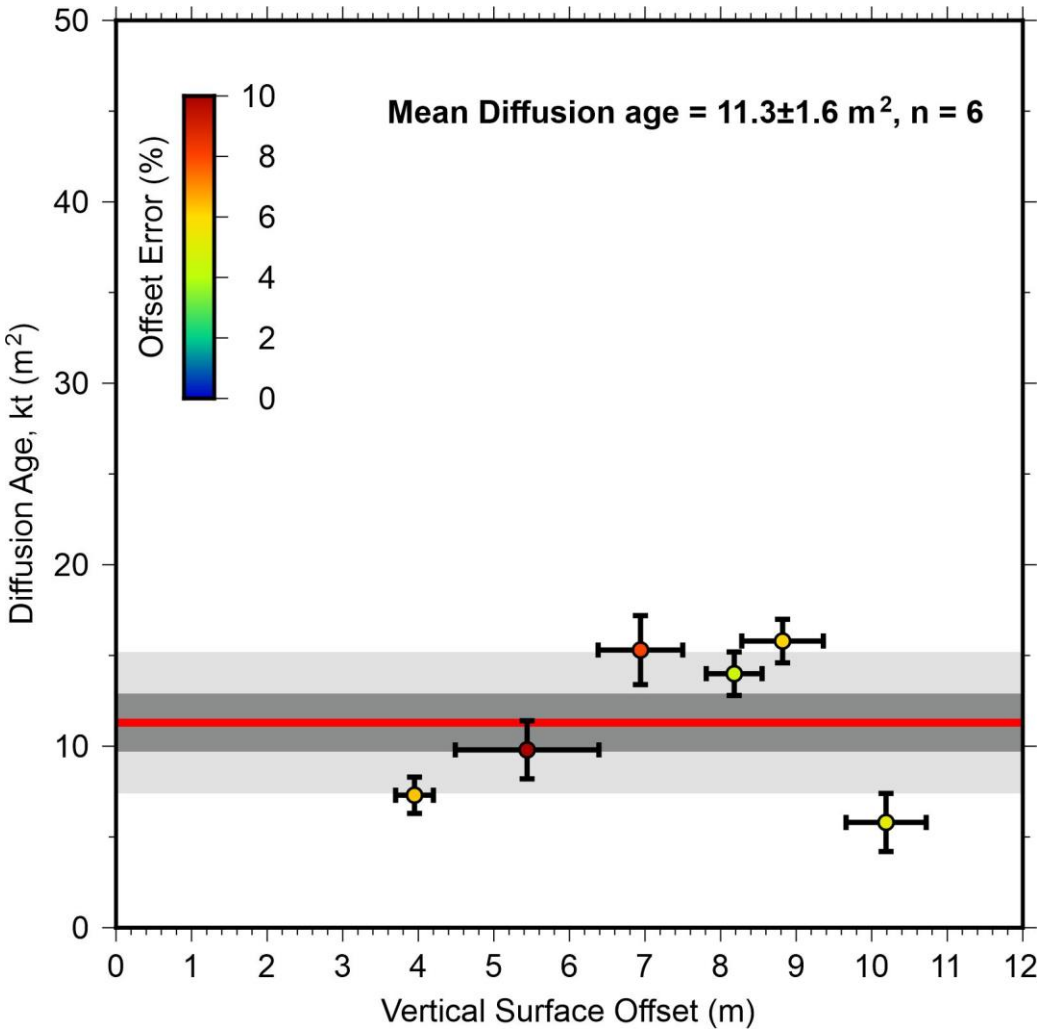

Figure S2-5. Calculated diffusion age (kt) for the six profiles (T1-T3 and T5-T7) of the scarps at the Tentek River East site. Points are coloured according to their percentage errors in the estimation of vertical fault offsets. The mean kt value of 11.3 m^2 is denoted by the red line, with 1 σ standard deviation shown by the light grey area and the standard error (1.6 m^2) of the mean value shown by the dark grey area.

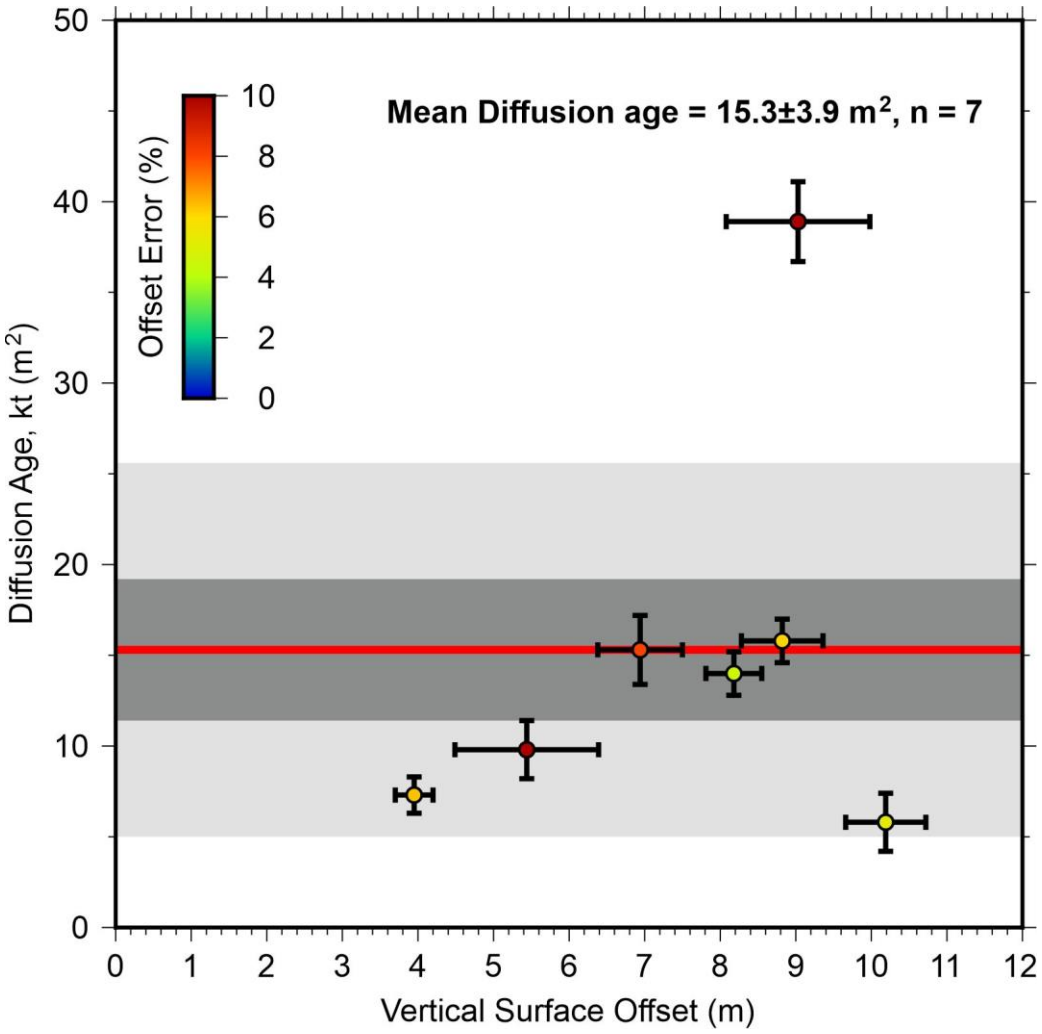

Figure S2-6. Calculated diffusion age (kt) for all seven profiles (T1-T7) of the scarps at the Tentek River East site. Points are coloured according to their percentage errors in the estimation of vertical fault offsets. The mean kt value of 15.3 m^2 is denoted by the red line, with 1 σ standard deviation shown by the light grey area and the standard error (3.9 m^2) of the mean value shown by the dark grey area. We took the largest kt value (Profile T4) as an outlier for this site and excluded it for the mean diffusion age calculation.

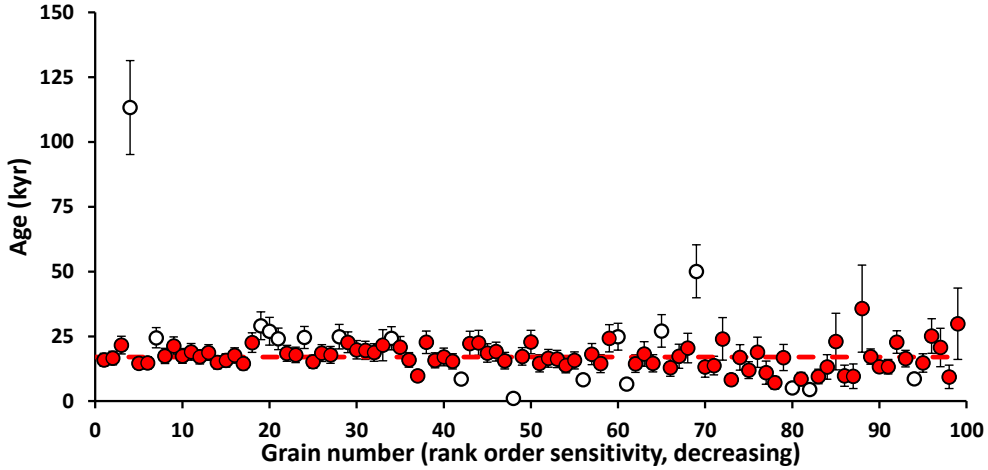

Figure S2-7. Single grain K-feldspar post-IR IRSL data for sample DZH1 illustrated as grain age vs. rank IRSL sensitivity. Grains shown in red represent those included in the age calculation. Grains shown in white represent those rejected from the age calculation, either interpreted as poorly bleached (too old) or as intrusive grains (too young). The grain numbers are 400,99,81,7 respectively for those measured, those gave results, those included in the age calculation and those rejected as intrusive.

Statement of Authorship for joint/multi-authored papers for PGR thesis

To appear at the end of each thesis chapter submitted as an article/paper

The statement shall describe the candidate's and co-authors' independent research contributions in the thesis publications. For each publication there should exist a complete statement that is to be filled out and signed by the candidate and supervisor **(only required where there isn't already a statement of contribution within the paper itself).**

Title of Paper	Probing the Upper End of Intracontinental Earthquake Magnitude: A Prehistoric Example From the Dzhungarian and Lepsy Faults of Kazakhstan
Publication Status	■Published □ Accepted for Publication □Submitted for Publication □Unpublished and unsubmitted work written in a manuscript style
Publication Details	Tsai, C.-H., Abdrakhmatov, K., Mukambayev, A., Elliott, A., Elliott, J., Grützner, C., Rhodes, E., Ivester, A., Walker, R. T., & Wilkinson, R. (2022). Probing the upper end of intra-continental earthquake magnitude: a prehistoric example from the Dzhungarian and Lepsy faults of Kazakhstan. Tectonics, 41, e2022TC007300, https://doi. org/10.1029/2022TC007300

Student Confirmation

Student Name:	Chia-Hsin Tsai		
Contribution to the Paper	Performed mapping and analysis on the topographic data, interpreted data, wrote manuscript		
Signature	蔡佳欣	Date	06.03.2023

Supervisor Confirmation

By signing the Statement of Authorship, you are certifying that the candidate made a substantial contribution to the publication, and that the description described above is accurate.

Supervisor name and title: Prof. Richard T. Walker		
Supervisor comments		
Signature 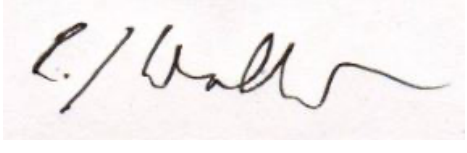	Date	7 March 2023

This completed form should be included in the thesis, at the end of the relevant chapter.

Chapter 3

Geological and Geodetic Constraints on Average Quaternary Rates of the Dzhungarian Fault Slip

3.1 Introduction

The slip rate of a fault is an important parameter for understanding fault behaviour both temporally and spatially, and is essential information for investigating fault activities and their related seismic hazards. Slip rates of faults can help uncover the regional crustal deformation and kinematics (e.g. Duvall & Clark, 2010; Middleton et al., 2016; Rizza et al., 2019; Pierce et al., 2021; Walker et al., 2021; Zebari et al., 2021). Comparisons of geological (up to hundreds of thousands of years) and geodetic (decadal) slip rates also help give insights into the rheological properties and earthquake cycles of the faults (Savage & Prescott, 1978; Dixon et al., 2003; Papanikolaou et al., 2005; Chéry & Vernant, 2006; Chuang & Johnson, 2011; He et al., 2013; Meade et al., 2013; Tong et al., 2014; Dolan & Meade, 2017; Lifton et al., 2020). As Quaternary dating and remote sensing techniques have developed, we are now able to determine both geological and geodetic rates of fault slip for those with the geochronological and remote-sensing data available (e.g. Hubert-Ferrari et al., 2002; Cowgill et al., 2009; Walters et al., 2011; Mousavi et al., 2021; Liu et al., 2022).

The Tien Shan in Central Asia is one of the most active intra-continental seismogenic belts globally, with ongoing crustal shortening caused by the India-Eurasia collision since ~ 25 Ma (Molnar & Tapponnier, 1975b; Tapponnier & Molnar, 1979; Abdrakhmatov et al., 2001). Global Navigation Satellite System (GNSS) velocities show the convergence rate across the western Tien Shan is 15 – 22 mm/yr

(Abdrakhmatov et al., 1996; Zubovich et al., 2010), which is more than 50 % of the total convergence rate of ~ 33 mm/yr between India and Eurasia (Argus et al., 2010). The shortening rate decreases to the northeast, and range-parallel left-lateral shearing increases (Zubovich et al., 2010). Shortening in the Tien Shan is thought to be accommodated by a combination of fold and thrust belts within the range and at its margins, and block rotations. These block rotations highlight the important role that strike-slip faulting plays in the regional kinematics and the associated seismicity (Thompson et al., 2002; A. Yin, 2010; Zubovich et al., 2010; Campbell et al., 2013, 2019; Bosboom et al., 2014; Goode et al., 2014; Bande et al., 2017; Grützner et al., 2019; C. Wu et al., 2021).

Many of the major strike-slip faults in the Tien Shan are NW-SE-oriented right-lateral faults which are thought to accommodate N-S shortening through counterclockwise block rotations. These right-lateral faults include, from southwest to northeast, the Talas-Ferghana Fault (Rizza et al., 2019), the Dzhalair-Naiman Fault (Hollingsworth et al., 2016), the Kashihe Fault (C. Wu et al., 2020), the Aktas Fault (Suvorov, 1964) and the Dzhungarian Fault (Figure 3-1a). The Talas-Ferghana Fault and the Dzhungarian Fault extend through the Tien Shan interior and their prominent geomorphic expression suggests they have been active in the Holocene. However, there are few large historical earthquakes known to have ruptured these two major right-lateral faults.

The Late Quaternary slip rate of the ~ 400-km-long Talas-Ferghana Fault in the southern Tien Shan has been studied in detail using various methods with a result of 2.2 – 6.3 mm/yr (Bande et al., 2017; Rust et al., 2018; Rizza et al., 2019). Although the palaeoseismicity and fault geomorphology of the Dzhungarian Fault have been studied (Campbell et al., 2013; G. Hu et al., 2021; Tsai et al., 2022), there are limited and discrepant data reported for slip rates of the fault (England & Molnar, 1997; X. Yang & Shen, 2000; Jie Li et al., 2010; J. Shen et al., 2011; Campbell et al., 2013; G. Li et al., 2016; Z. Hu, Yang, et al., 2021). Large surface ruptures along the Dzhungarian Fault indicate its potential to generate earthquakes with magnitude > Mw 8.0 (Tsai et al., 2022), demonstrating the potential seismic hazard posed by this fault.

In this chapter, we estimate both the geological and geodetic slip rates of the Dzhungarian Fault, to aid our understanding of its role in the regional tectonics and potential for earthquakes. We analyse a collection of samples from multiple field sites covering the area north of Alashankou and the Rygayty River (Figure 3-2), to reveal both the vertical and dextral slip rate of the Dzhungarian Fault. We dated these samples using luminescence dating, with the detailed procedures described in Section 3.3.2.1. In addition, we used cosmogenic nuclides (details in Section 3.3.2.2) to date the samples collected near

Alashankou, in order to examine the reliability of the slip rate suggested by Campbell et al. (2013). For the geodetic approach, we used Interferometric Synthetic Aperture Radar (InSAR) time-series analysis to estimate the modern strike-slip rate of the Dzhungarian Fault. The processing and results from radar data and the related technical details are elaborated in Section 3.4. A comparison of the long-term and short-term slip rates with further implications is discussed in Section 3.5.

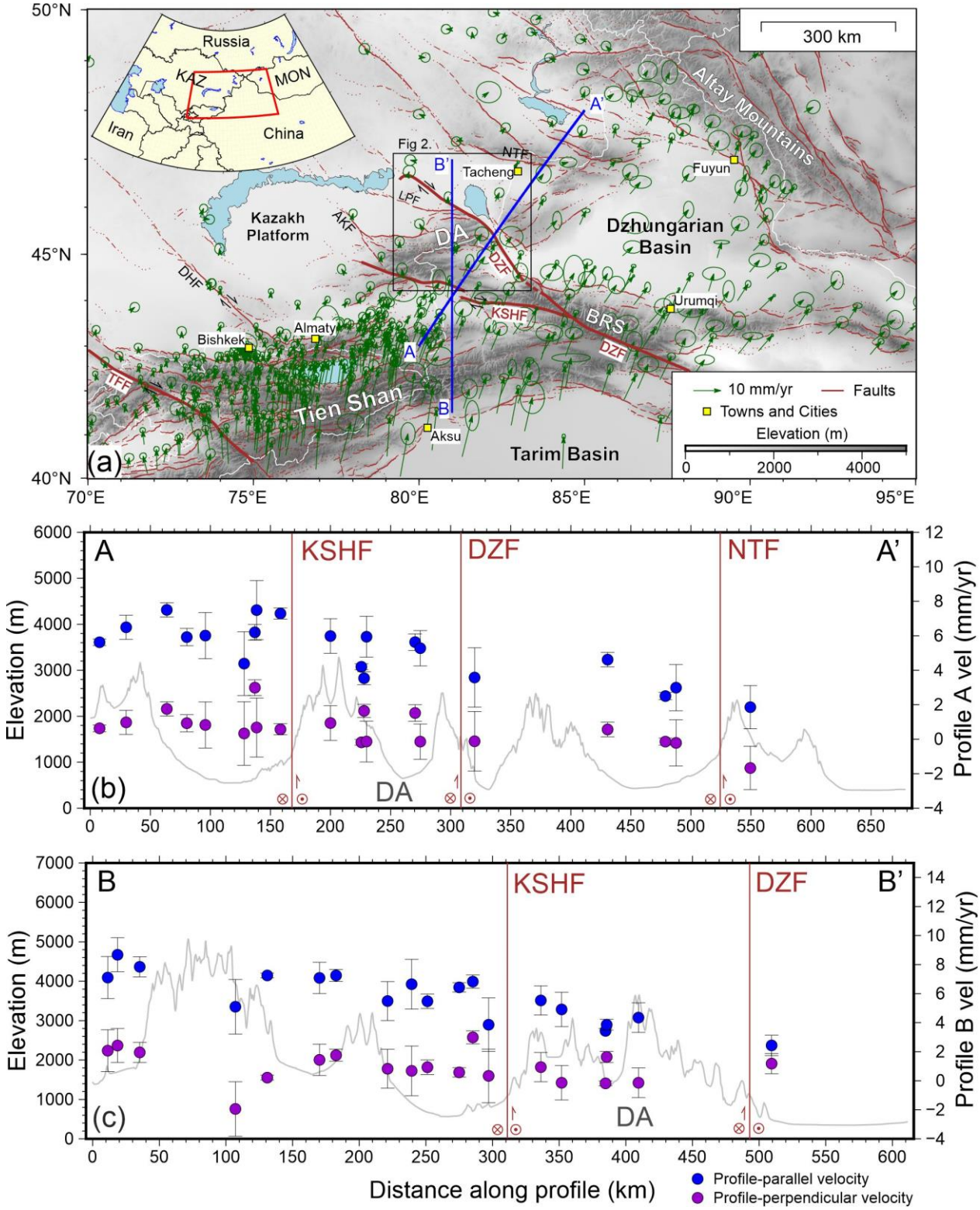

Figure 3-1. (a) Overview of the Tien Shan and its surrounding regions. The fault database (Zelenin et al., 2021) is shown by brown lines with confidence levels C and D displayed in dashed and dotted styles, respectively. Thick brown lines show the major dextral strike-slip faults in the Tien Shan. The GNSS velocity data (green arrows) are from Zheng et al. (2017). Blue lines are the locations of profiles A and B

shown in panels (b) and (c). TFF: Talas-Fergana Fault; DHF: Dzhalair-Naiman Fault; KSHF: Kashihe Fault; AKF: Aktas Fault; LPF: Lepsy Fault; DZF: Dzhungarian Fault; NTF: North Tacheng Fault; DA: Dzhungarian Alatau; BRS: Borohoro Shan; MON: Mongolia, KAZ: Kazakhstan. (b) The GNSS velocity components parallel to (blue dots) and perpendicular to (purple dots) Profile A-A'. (b) The GNSS velocity components parallel to (blue dots) and perpendicular to (purple dots) Profile B-B'. Positive value of velocity represents northwards and westwards direction of the velocity vector. Elevation data are from GEBCO (https://www.gebco.net/data_and_products/gridded_bathymetry_data/) and are plotted in grey in (b) and (c). Note that the Dzhungarian Fault has been suggested to continue to the south of Urumqi (J. Shen et al., 2003; Jie Li et al., 2010; G. Li et al., 2016; Z. Hu, Yang, et al., 2021), but in this study, we only discuss the Dzhungarian Fault north of the Borohoro Shan.

3.2 Review of the Dzhungarian Fault Slip Rates

The Dzhungarian Fault can be separated into a southern part with pure strike-slip motion and a northern oblique-slip segment, with the boundary between the two sites near the Rygayty River (Tsai et al., 2022) (Figure 3-2). Previous investigations of geological strike-slip rate are all restricted to the pure strike-slip segment. England & Molnar (1997) suggested a strike-slip rate of 3 ± 1 mm/yr using the 7 km right-lateral displacement of the Pliocene stratigraphy as previously estimated by Voytovich, (1969). A higher strike-slip rate of ~ 5 mm/yr since the Late Pleistocene was proposed by Yang & Shen (2000) and Shen et al. (2011) who examined the offsets among five levels of terraces, from Alashankou (Zhalanashkol) to Jing River East, and their corresponding abandonment ages based on the climatic history presented in Zhang et al. (1995) and Deng et al., (2000). In the same region along the Jing River East (Figure 3-2), Hu et al. (2021) used optically stimulated luminescence and cosmogenic nuclide dating methods to better constrain the ages of terraces and suggested a strike-slip rate of 3.2 +1.4/-1.1 mm/yr. A minimum late Quaternary rate of 2.2 ± 0.8 mm/yr was also been suggested by Campbell et al. (2013), based on the measured offset (53 ± 7 m) of an inactive alluvial fan to the south of Lake Alakol and one estimate of its abandonment age (25.7 ± 5.8 ka) from luminescence dating (Figure 3-2).

For geodetic slip rates, two studies have reported dextral strike-slip rates for the same portion of the Dzhungarian Fault, from the south of Lake Ebinur to the south of Jing River East, inferred from GNSS measurements. J. Li et al. (2010) suggested a slip rate of 1.5 – 1.8 mm/yr, whereas G. Li et al. (2016) suggested the rate to be ~ 4.8 mm/yr. These discrepancies between existing geodetic results and some of the geological results further highlight the ambiguity in the strike-slip rates of the Dzhungarian Fault.

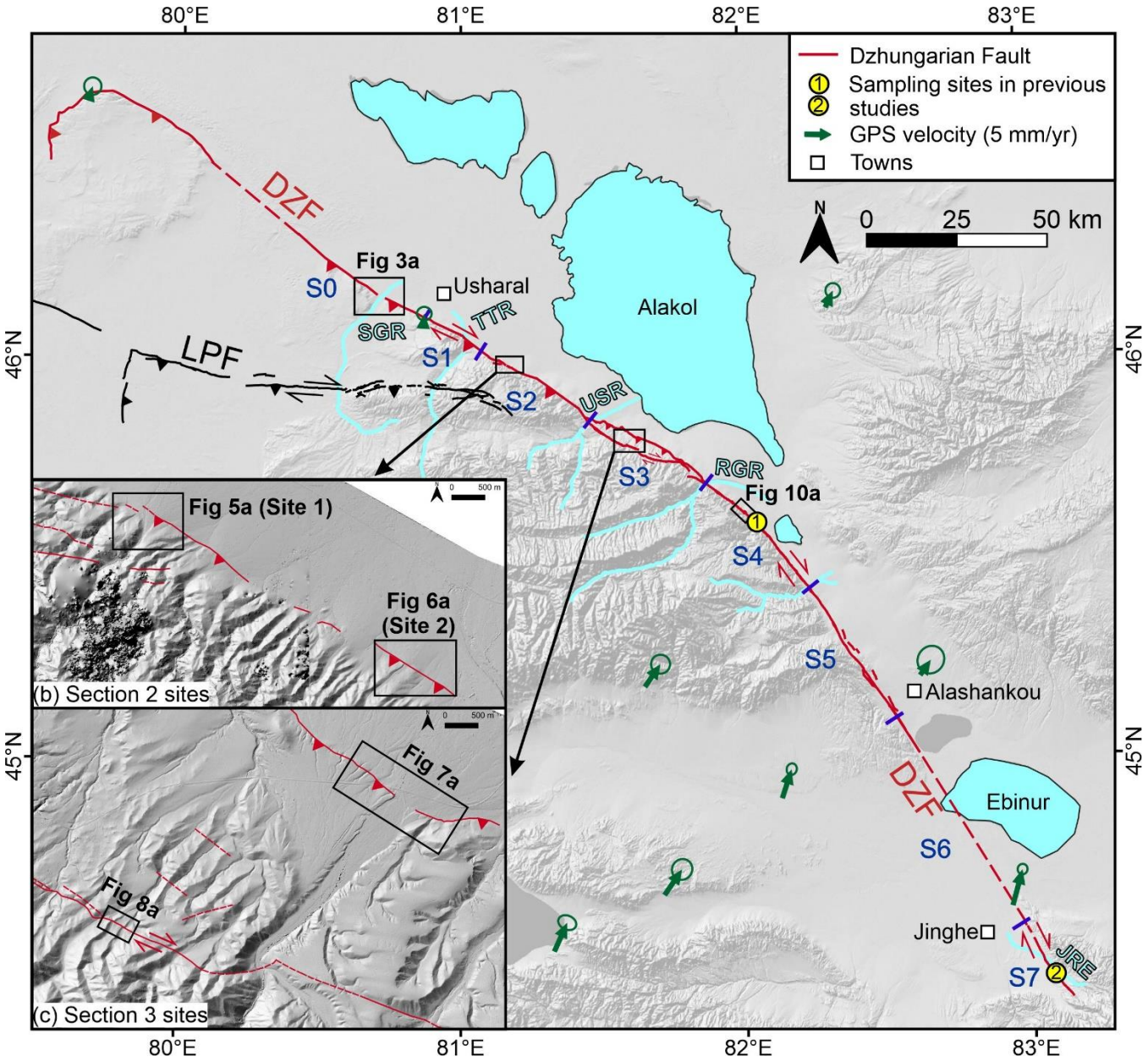

Figure 3-2. (a) Overview of the Dzhungarian Fault (red lines; DZF) and the Lepsy Fault (black lines; LPF). Yellow circles are the sampling sites with "1" from Campbell et al. (2013) and "2" from Hu et al. (2021). GNSS velocity vectors (green arrows) are from Zheng et al. (2017). S0 to S7 are the eight sections of the Dzhungarian Fault defined in Tsai et al. (2022) with section boundaries labelled with short purple lines. Lakes and rivers are labelled in light blue. (b) and (c) are the zoomed-in Pléiades DEM showing the sampling sites from this study on Section S2 and Section S3. SGR: Shynzhyly River; TTR: Tentek River; USR: Ulken Sengyrly River; RGR: Rygayty River; JRE: Jing River East.

3.3 Geological Slip Rates

3.3.1 Offset Measurements

The geological slip rate, commonly referred to the long-term fault slip rate, is derived from the absolute dating of displaced geomorphic features. Thus, the amount of displacement, or offset, is of critical information required for estimating the slip rate. In Chapter 2, we outlined the types of imagery, the techniques of photogrammetry, and the implementation of topographic analysis that we used for measuring the offsets in this chapter. However, horizontal offset measurements for channels were determined differently from the approach described in Chapter 2, which produces large uncertainties, which is suitable for COPD analysis but not ideal for slip rate estimation. In this chapter, we determined the channel offset by averaging three measured displacements: the offset of the thalwegs and the offsets of both levees across the fault. For lateral offsets across the ridges, we fitted straight lines manually to the ridge crests on both sides of the fault and measured the distance between them along the fault strike. Details of the ridge offset measurements are described in Section 3.3.3.2. We measured vertical offsets by drawing profiles across the fault scarps, extracting the elevations from the DEMs and fitting lines on both sides of the scarps, as explained in Chapter 2. Some profiles were made based on the *in situ* differential GPS (dGPS) field measurements, instead of DEMs, but we used the same method to estimate the heights of the scarps for both data types.

3.3.2 Dating Methods

Due to the arid climate, organic materials are rare and the commonly used radiocarbon method is less applicable in our study area. Therefore, samples collected in this study are mostly for luminescence dating since silty and sandy fluvial sediments are relatively abundant in the alluvial fans. We used cosmogenic nuclide dating to determine the ages of quartz-rich boulders at one site. We describe both methods below.

3.3.2.1 Luminescence Dating

3.3.2.1.1 General Background

Luminescence dating measures when currently buried sediments were last exposed to sunlight. The principle of this method relates to the trapping, accumulation and release of electrons within minerals. Radiation from the natural environments, such as from the decay of radioisotopes in rocks, causes the

bonding electrons inside minerals to be promoted from the valence band to the conduction band. Some of these excited electrons become trapped at defects in the crystal lattice during this movement. The trapped electrons accumulate very slowly over 10^1-10^5 years; however, it only takes 10^0-10^2 seconds for additional energy to evict electrons from the traps (Rhodes, 2011). This energy includes heat, visible light, and infrared radiation. The evicted electrons emit photons as a luminescence signal (Huntley et al., 1985). Therefore, we can determine the burial age of sediment by measuring the intensity of its stimulated luminescence signal as a function of the total dose of radiation (equivalent dose, De). Nevertheless, the strength of the natural radiation, affecting how much dose is received per year during the burial of sediments, varies in different environments. It depends on the concentration of radioisotopes (e.g. ^{40}K, ^{232}Th, ^{235}U and ^{238}U), the water content, the burial depth and the grain size of samples. The final burial age is equal to De divided by the environmental dose rate.

The most commonly used approach to determine the burial age is optically-stimulated luminescence (OSL) on quartz grains using a single aliquot regenerative dose (SAR) protocol (Huntley et al., 1985; Murray & Wintle, 2000, 2003). In this approach, each aliquot contains a few quartz grains and is measured for the natural luminescence signal first, and then exposed to a couple of known doses of radiation and re-measured each time to build a luminescence growth curve. This curve allows the natural luminescence signal to be converted into an equivalent dose (Rhodes, 2011). One of the issues with luminescence dating is incomplete bleaching, which means trapped electrons in minerals are not fully evicted by daylight exposure, mostly due to rapid fluvial transportation and deposition. However, the SAR protocol helps to calibrate for this effect by applying statistical models (Murray & Roberts, 1997; Rhodes et al., 2010).

Infrared-stimulated luminescence (IRSL) on feldspar is another widely used approach to date sediments (Hütt et al., 1988; Clarke & Rendell, 1998; Lamothe et al., 2003). Quartz from certain environments, including mountainous rocky environments such as those encountered within our study, where the grains have eroded from nearby outcrops, can have low OSL sensitivities. This means the luminescence signals have a low response to radiation exposure, so the OSL signal is low in answer to a unit of dose. K-feldspar has much higher sensitivities, leading it to be potentially useful in such settings, although it has issues with anomalous fading, a leaking of the accumulated luminescence signal, that could cause age underestimation (Wintle, 1973; Visocekas, 1985; Huntley & Lamothe, 2001). The main experimental procedures of IRSL are similar to those of OSL including the initial measurement of natural luminescence signals, the re-measurements of stimulated signals and the construction of a luminescence

growth curve. The post-infrared infrared stimulated luminescence (post-IR IRSL) dating, first implemented in Buylaert et al. (2009), with the "single-grain" SAR protocol was later found to be able to overcome the limitation caused by anomalous fading by isolating less stable signal components (Smedley et al., 2012, 2015; Trauerstein et al., 2012, 2014; Rhodes, 2015a). The post-IR approach applies a low temperature (50°C) IRSL measurement to evict easily-fading electrons first, and then immediately applies a high temperature (225°C) IRSL measurement to access signals from more stable electrons (Jain et al., 2015).

Luminescence samples are typically collected by hammering steel tubes into sediment sections horizontally and are processed under subdued red light in the laboratory. In this study, we collected twelve samples for luminescence dating for the slip rates. These samples were collected in 2015, 2016 and 2019[1], noted on their sample names in Table 3-1, and thus were processed and measured in different laboratories. Post-IR IRSL was performed following the procedures in Rhodes (2015) and quartz OSL was implemented following the methods in Wintle & Murray (2006) since some of the feldspar samples in our study area produced very little luminescence signal for unknown reasons.

3.3.2.1.2 Implementation of OSL

The 2015 samples were collected from the river terraces of the Shynzhyly River near Usharal by a group led by Dr Christoph Grützner and Dr Austin Elliott. These samples were processed and analysed for equivalent doses in the Department of Human Evolution, Max Planck Institute for Evolutionary Anthropology, Leipzig, Germany by Prof. Kathryn Fitzsimmons. The dose rates were determined based on high-resolution germanium gamma spectrometry (HRGS) undertaken at the Radiation Protection, Analytics & Disposal Inc. (VKTA) in Dresden, Germany. In the first processing step, 1 – 2 cm of sediment were removed from both ends of the sample tube for moisture content and environmental dose rate analysis. The processes for sample pre-treatment involve hydrochloric acid digestion, sieving and settling, density separation, and etching in 48% fluorosilicic acid solution for 45 minutes to extract and purify the targeting grain size of quartz (Rhodes, 1988; Timar et al., 2010). Sufficient amounts of quartz remained from all samples except DZH15-OSL3. Equivalent dose (De) was measured from 4-11 µm fine-grain quartz in 18 aliquots using an automated Risø TL-DA-20 reader with blue LEDs for stimulation. OSL signals were detected by an EMI 9235QA photomultiplier tube with a coated Hoya U340 glass filter. Laboratory

[1]Samples were collected by my colleagues before I began my DPhil in 2015 and 2016, and then in 2019 under my remote instructions and guidance as I was unable to attend the field survey in Kazakhstan in person due to visa issues.

irradiation was delivered by a calibrated $^{90}Sr/^{90}Y$ beta source (Bøtter-Jensen et al., 2000). The preheat and cutheat temperatures were set as 240°C and 220°C respectively. The measurements were conducted following the SAR protocol and the analyses consisted of a 6 or 7 regeneration point sequence, including a zero and a repeated regeneration dose point, to construct the luminescence growth curve. The equivalent dose values were estimated using a Central Age Model (Galbraith et al., 1999). Dose rates were converted from the activity of radioisotopes (K, Th, U) (Adamiec & Aitken, 1998; Guérin et al., 2011), the Beta dose-rate attenuation caused by water content (Mejdahl, 1979), and the cosmic-ray dose based on sediment depth, location and altitude (Prescott & Hutton, 1994). In general, the 2015 samples yield reliable ages in Table 3-1 with most of the aliquots responding well to the SAR protocol and the luminescence stimulation.

The 2016 samples were collected ~ 5 km SE of the Tentek River by the same group in 2015. These samples were processed and analysed in the School of Geography, Geology and the Environment, University of Leicester, UK by Dr Andrew S. Carr and their dose rates were determined via inductively coupled plasma mass spectrometry (ICP-MS) for U and Th and via inductively coupled plasma optical emission spectroscopy (ICP-OES) for K at the same institution. The procedures of sample pre-treatment, the equipment for measuring equivalent dose, and the laboratory irradiation are the same as for the 2015 samples except that the analysed grain size is 90-250 μm coarse-grain quartz. The results of the 2016 quartz samples are presented in Table 3-1. Sample DZH16-07 showed no luminescence signal when analysed and all the other samples showed low sensitivities, which might be due to the contamination of the non-quartz signal or/and the presence of the low quartz OSL components. In addition, these samples showed significant inter-aliquot scatter. Thus, aliquots with the least precise equivalent dose estimates were further removed based on a "fast ratio" criterion, which determines the relative contribution of the OSL fast component to the total signal (Durcan & Duller, 2011). However, applying this criterion resulted in only a limited number (< 10) of aliquots being accepted for some samples such as DZH16-06, DZH16-08 and DZH16-10.

3.3.2.1.3 Implementation of IRSL

The 2019 samples were prepared and analysed in the Department of Geography at the University of Sheffield, UK. The processes for sample pre-treatment are similar to those in the OSL experiments but a sodium polytungstate solution with a density of 2.58 g/cm^3 was applied for extracting K-feldspars in a density seperation. The equivalent dose (De) was measured from 125-212 μm K-feldspar grains using the single-grain SAR protocol by a Risø TL-DA automated reader with blue LEDs for luminescence

stimulation. For each sample, at least 200 K-feldspar grains were measured independently under the reader and SAR cycles were used to construct the growth curve. We used an overdispersion value of 15% in age estimation for all IRSL samples and we observed no significant systematic IRSL fading in any of the measured grains. The post-IR IRSL measurements and the other detailed procedures all followed the descriptions in Rhodes, (2015) and Zinke et al. (2017). Environmental dose rates were measured using ICP-MS for U and Th, and ICP-OES for K with an assumed internal K content of 12.5 ± 2.5% for dose rate correction (Huntley & Baril, 1997). Water content in each sample and grain size attenuation were also used for corrections.

Table 3-1. Luminescence Dating Results

Location	Name	Lon. (°E)	Lat. (°N)	Elevation (m)	Depth (m)	Method	Equivalent Dose (Ge)	Dose Rate (mGe/yr)	Age (ka)
Section 0	DZH15 - 01	80.69705	46.15756	466	1.04	OSL (GER)	166 ± 8	2.48 ± 0.22	66.9 ± 6.9
Section 0	DZH15-02	80.69705	46.15756	466	0.75	OSL (GER)	131 ± 6	2.92 ± 0.26	44.9 ± 4.5
Section 0	DZH15-03	80.69705	46.15756	466	1.55	OSL (GER)	Insufficient quartz remained		
Section 0	DZH15-04	80.72015	46.15183	419	0.53	OSL (GER)	20.9 ± 0.3	3.52 ± 0.27	5.9 ± 0.5
Section 0	DZH15-05	80.72015	46.15183	419	0.64	OSL (GER)	20.5 ± 0.3	3.58 ± 0.25	5.7 ± 0.4
Section 2	DZH16-06	81.19401	45.97215	537	0.8	OSL (LCT)	55.4 ± 4.8	2.27 ± 0.11	20.4 ± 1.9
Section 2	DZH16-07	81.14626	45.99134	577	1.5	OSL (LCT)	No luminescence signal yielded		
Section 2	DZH16-08	81.14626	45.99134	577	1.1	OSL (LCT)	198 ± 24	3.35 ± 0.15	59.1 ± 7.6
Section 2	DZH16-09	81.14534	45.99234	554	2.1	OSL (LCT)	65.8 ± 6.3	3.15 ± 0.15	20.9 ± 2.2
Section 2	DZH16-10	81.14534	45.99234	554	0.7	OSL (LCT)	22.9 ± 4.2	3.27 ± 0.15	7.0 ± 1.3

Section 3	DZH19-02	81.56556	45.78886	893	0.85	IRSL (SFD)	46.1 ± 1.2	4.11 ± 0.26	11.2 ± 0.8
Section 3	DZH19-03	81.61800	45.80521	705	0.74	IRSL (SFD)	131.2 ± 9.3	4.44 ± 0.27	29.6 ± 2.8

GER/ LCT/ SFD: Sample processed in Germany/Leicester/Sheffield.

3.3.2.2 Cosmogenic Nuclide Dating

3.3.2.2.1 General Background

Cosmogenic nuclide dating can be used to determine how long a rock has been exposed at the surface (Cerling & Craig, 1994; Gosse & Philips, 2001; Darvill, 2013; Schaefer et al., 2022). When primary cosmic radiation, mostly protons, hits the Earth's atmosphere from space, it triggers cascading particle reactions that produce secondary cosmic rays such as neutrons and muons. When secondary cosmic radiation reaches the Earth's surface, it then interacts with atoms within the minerals near the surface and generates terrestrial cosmogenic nuclides (TCN). Since different minerals are composed of different atoms, they produce different TCN. The most commonly used target mineral for cosmogenic nuclide dating is quartz which consists of O and Si which produce ^{10}Be and ^{26}Al in their reaction pathways with secondary cosmic radiation (e.g. Rizza et al., 2019; Shnizai et al., 2020; Ren et al., 2021). These TCN (or radioactive isotopes) accumulate in the target minerals as they remain exposed to the open sky, so their surface exposure ages can be estimated from a calculation involving the concentration of nuclides, the rates of nuclides production, and the rates of radioactive decay of the isotopes (half-life). The concentration of nuclides is usually measured by accelerator mass spectrum (AMS) in a form of a ratio such as ^{10}Be/^{9}Be (Gosse & Philips, 2001; Dunai, 2010; Jull & Burr, 2014). The rate of nuclide production is related to a couple of factors including latitude, altitude, and the local topography, which influence the energy of secondary cosmic rays and the effect of shielding (cosmic rays blocked by topography) (Gosse et al., 1995; Dunne et al., 1999; Balco et al., 2008; Hetzel, 2013). The sample ages are potentially affected by earlier periods of exposure higher in the catchment, which would produce an anomalously old age, and by post-deposition modification and erosion of the landform, which can cause the sample to look younger than it actually is. In this study, we assume no post-depositional erosion, due to the pristine geomorphology and resistant quartz boulders, which means the ages we obtain represent the minimum exposure ages.

3.3.2.2.2 Implementation of Cosmogenic Nuclide Dating

In this study, six samples from the top of quartz-rich boulders and three samples from amalgamated smaller quartz cobbles were collected from the levees of offset channels to determine the exposure ages via their accumulated ^{10}Be concentration. These samples were crushed and dry-sieved in the Department of Earth Sciences at the University of Oxford to retain grains with a size of 250-500 μm. The rest of the sample preparation was carried out in the CosmIC Laboratory at Imperial College London. We used magnetic separation followed by acid etching for purifying the samples to SiO_2 mineral separates. Beryllium was extracted from the separates by anion and ion exchange. The detailed procedures all followed the descriptions in Corbett et al. (2016) and Rood et al. (2020). ^{10}Be/^{9}Be ratios were measured at the Australian Nuclear Science and Technology Organisation (ANSTO) using AMS in May 2022 (Wilcken et al., 2017). The AMS measured ^{10}Be/^{9}Be data were normalized to standard KN 01-5-2 with an assumed ^{10}Be/^{9}Be ratio of 8.558×10^{-12} (Nishiizumi et al., 2007). The total number of ^{10}Be atoms was corrected by subtracting the total number of ^{10}Be atoms in the process blank, which contains only the beryllium carrier that was added to each sample, with uncertainties (1σ) in sample and blank propagated in quadrature. Topographic shielding was estimated using a 30-m digital elevation model from the Shuttle Radar Topography Mission (SRTM) and yielded a shielding factor of 0.985 for all our samples. We assumed a rock density of 2.7 g cm^{-3} and no post-depositional erosion or soil inflation. Final surface exposure ages were estimated using the online CRONUS-Earth calculator (Balco et al., 2008) with a Be half-life of 1.36 Ma (Nishiizumi et al., 2007) and other information including the sample locations, elevations, thickness, shielding factors and measured ^{10}Be concentrations. A constant production rate model with a ^{10}Be production rate of 4.132 ± 0.218 atoms g^{-1} and the "St" scaling scheme for spallation was used in the age calculation (Lal, 1991; Stone, 2000; Borchers et al., 2016).

Table 3-2. Cosmogenic Nuclide Dating Results

Sample	Latitude	Longitude	Elevation (m)	[^{10}Be] (atoms g^{-1})	1σ (atoms g^{-1})	Exposure Age (yr)	1σ internal (yr)
DZH-1	45.60588	82.02567	644	53933	1978	8036	295
DZH-2	45.60597	82.02575	640	83574	1989	12717	304
DZH-3	45.60597	82.02584	640	75868	1978	11352	297
DZH-4	45.60614	82.02654	632	96656	2441	14939	379
DZH-5	45.60515	82.02511	658	110824	2989	16487	446
DZH-6	45.60612	82.02650	637	79406	1997	12212	308

DZH-7	45.60603	82.02660	637	95757	2215	14375	334
DZH-8	45.60590	82.02569	642	95258	2899	14357	439
DZH-9	45.60521	82.02410	637	118423	2714	17793	410
Notes: See Appendices Tables S3-1 and S3-2 for inputs to concentration and age calculations.							

3.3.3 Results

3.3.3.1 Vertical Slip Rate

3.3.3.1.1 Section S0: Shynzhyly River

In Chapter 2, we separate the Dzhungarian Fault into eight sections from S0 to S7 based on the geomorphology (Figure 3-2). Along Section S0, cumulative vertical displacements can be found from the degraded fault scarps along the uplifted terraces at the Shynzhyly River, though fresh fault scarps and lateral offset features are not identified in the youngest generation of alluvial fans. From the satellite images and field observation near the range front of the Dzhungarian Alatau, we identified three main Quaternary river terraces (T1 to T3) on the northwest side of the river with a small intermediate terrace (Tm) between T1 and T2 (Figure 3-3a,b). These three river terraces (T1 to T3) are also present on the southeast Shynzhyly Riverbank. We measured dGPS topographic profiles across T3 and T2 on the northwest side of the river (Figure 3-3). Profile P1 indicates a cumulative vertical displacement of 26.7 ± 1.4 m in the highest terrace (T3) (Figure 3-3e), assuming it had the same elevation as the fans on the footwall before being uplifted. Profile P2 indicates a cumulative vertical displacement of 14.5 ± 2.5 m in terrace T2 based on the same assumption (Figure 3-3e). We do not have dGPS measurements or any high-resolution DEMs that cover the terraces on the southeast side of the river. A rough estimation from the topographic profile P3, derived from the SRTM DEM, indicates a cumulative vertical displacement of ~ 3 m in the lowest terrace T1 (Figure 3-3e).

We excavated Pit 1 on the northwest T3 surface at the edge of the terrace riser at 80.69705°E, 46.15756°N (Figure 3-3b). The top 40 cm of Pit 1 was composed of soil and loose loess with roots. The sediment from 40 cm to ~1 m depth consisted of loess and clay-rich layers with carbonate cement, and a few thin (< 10 cm) sand layers with several small clasts. Luminescence sample DZH15-02 was collected on the north wall at a depth of 75 cm from this layer and yielded an age of 44.9 ± 4.5 ka (Figure 3-4a). Another sample DZH15-01 was collected from the same layer on the E-wall at a depth of 1.04 m that directly overlaid the uppermost gravel layer and yielded an age of 66.9 ± 6.9 ka (Figure 3-4a). Below ~1 m depth, the sediments exposed in Pit 1 were fine-medium rounded gravels with fine-medium sand lenses.

Luminescence sample DZH15-03 was collected on the E-wall at a depth of 1.55 m from a medium sand layer, but it did not yield any ages due to the lack of sufficient quartz grains as mentioned in Section 3.3.2.1.2 (Figure 3-4a and Table 3-1).

Pit 2 was excavated on the southeast T1 surface at the edge of the terrace riser at 80.72015°E, 46.15183°N (Figure 3-3b and Figure 3-4f). The topsoil layer is 20 cm thick, below which a cemented loess layer without gravel extends to a depth of 58 cm. Luminescence sample DZH15-04 was collected from this loess layer at a depth of 53 cm and yielded an age of 5.9 ± 0.5 ka (Figure 3-4f). Beneath 58 cm in Pit 2, we encountered fluvial loess to fine sands with several rounded gravels. A luminescence sample DZH15-05 was collected from this layer at a depth of 64 cm and yielded an age of 5.7 ± 0.4 ka (Figure 3-4f). Below 2 m depth in Pit 2 we found fluvial gravel layers.

The stratigraphic change in both Pit 1 and Pit 2 shows rounded gravel layers capped at sharp contacts by finer fluvial to aeolian loess (or sand) sediments (Figure 3-3c,d). These contacts might reflect the transition of river activity. The incision for these terraces might begin when deposition gradually happaned only during the overbank flooding events and eventually ended up with merely aeolian sediments. Hence, samples collected from these finer capped sediments could provide age estimations for the timing of abandonment of the terraces. Two luminescence samples from the T3 capped sediments yielded ages of 44.9 ± 4.5 ka and 66.9 ± 6.9 ka respectively. The age difference (22 ka) is large considering they are only separated by 29 cm depth so it is likely that the deeper sample DZH15-01 has incomplete bleaching and thus shows an apparent older age. We suggest the shallower sample age is closer to the fan abandoned age.

Assuming the uplift of T3 started after the fan abandonment and using the cumulative vertical displacement of 26.7 ± 1.4 m (Figure 3-3), we calculate a minimum uplift rate of 0.6 ± 0.1 mm/yr, if post-uplift deposition in the footwall is assumed to be negligible. Using the deeper sample age of 66.9 ± 6.9 ka as the T3 abandoned age yields a minimum uplift rate of 0.4 ± 0.1 mm/yr. The same assumption and estimation could be used for T1. Two luminescence samples from the T1 capped sediments have similar ages which indicates the fan abandoned age is 5.3 – 6.4 ka. Using this age with cumulative vertical displacement of ~3 m yields a minimum uplift rate of 0.5 – 0.6 mm/yr, again assuming negligible post-uplift deposition in the footwall (Figure 3-3). The inferred uplifted rates from the higher (T3) and lower (T1) terraces are consistent within their errors, with a range of 0.6 ± 0.1 mm/yr at this Shynzhyly River site. However, we note that calculating slip rates (or uplift rates) from small offsets and young ages could come with large uncertainties since the timing of the next earthquake will change the slip rate significantly.

For example, if the next earthquake occurs five thousand years from now but only creates < 1 m vertical offset, the uplift rate estimated from the same sample from T1 will be about twice lower than what we calculate currently.

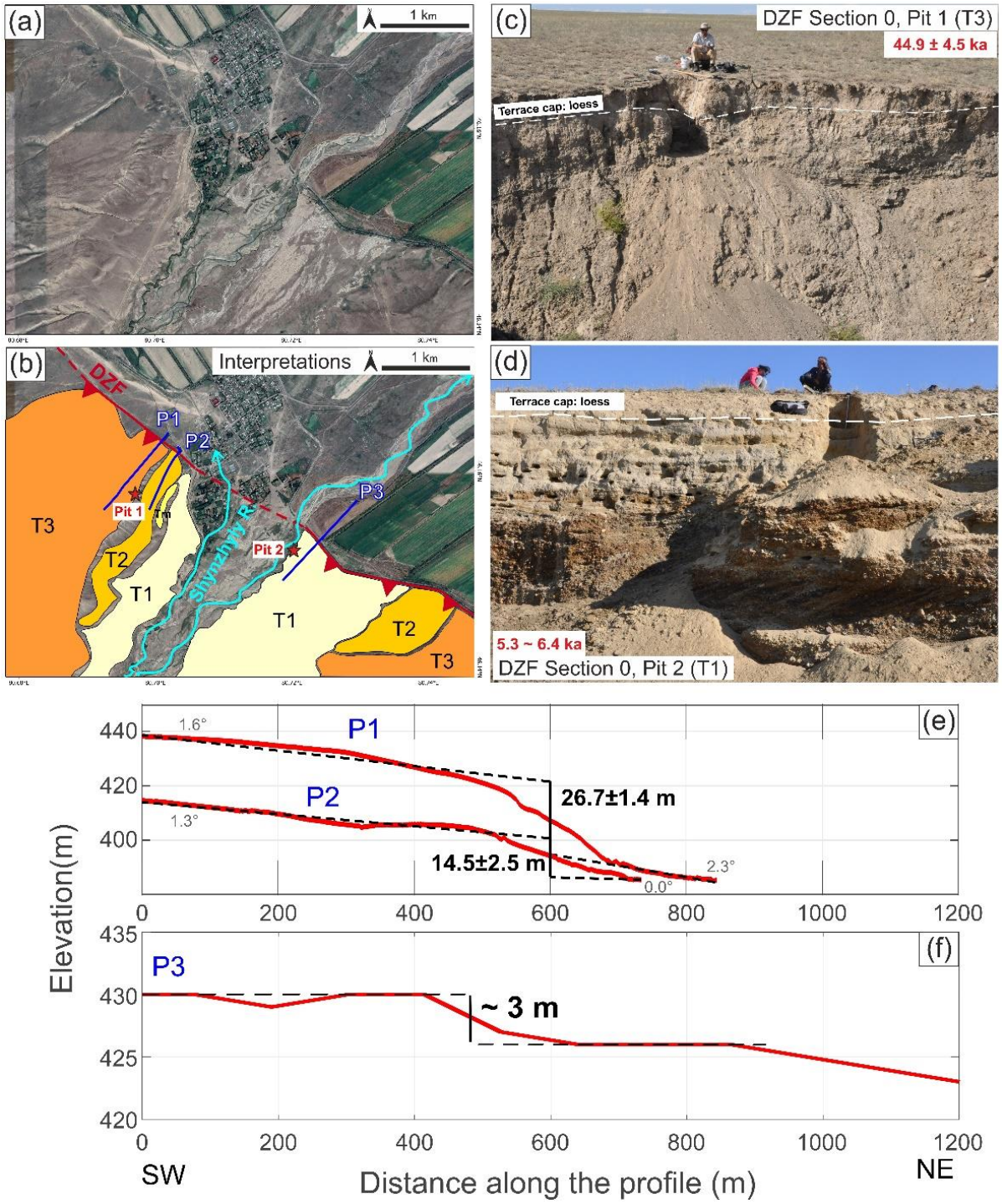

Figure 3-3. (a) Google Earth imagery showing the terraces at the Shynzhyly River (light blue) with the interpretations, fault trace (red line), profiles (blue lines), and sample pits (red stars) labelled in (b). Terraces level from high to low is noted as T3, T2, Tm and T1. (c) Field photograph of Pit 1 on the highest terrace T3 with its likely abandonment age noted in red. (d) Field photograph of Pit 2 on the lowest terrace T1 with its likely abandonment age noted in red. (e) Topographic profiles P1 and P2, from the dGPS survey, with their vertical displacements noted in black and the fan slopes noted. (f) Topographic profile P3 derived from SRTM, with its vertical displacement noted in black.

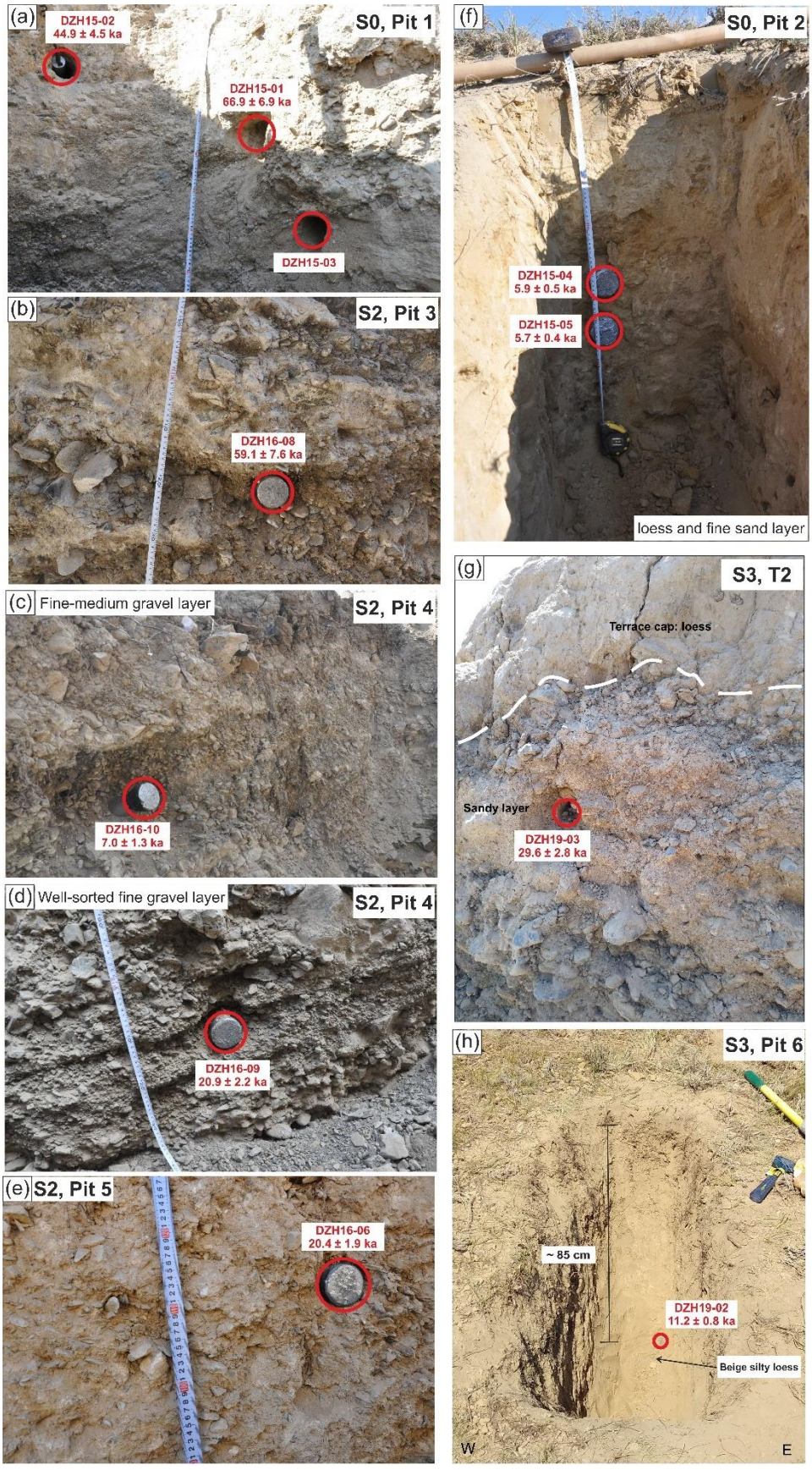
(a)
DZH15-02
44.9 ± 4.5 ka
S0, Pit 1
DZH15-01
66.9 ± 6.9 ka
DZH15-03
(b)
S2, Pit 3
DZH16-08
59.1 ± 7.6 ka
(c)
Fine-medium gravel layer
S2, Pit 4
DZH16-10
7.0 ± 1.3 ka
(d)
Well-sorted fine gravel layer
S2, Pit 4
DZH16-09
20.9 ± 2.2 ka
(e)
S2, Pit 5
DZH16-06
20.4 ± 1.9 ka
(f)
S0, Pit 2
DZH15-04
5.9 ± 0.5 ka
DZH15-05
5.7 ± 0.4 ka
loess and fine sand layer
(g)
S3, T2
Terrace cap: loess
Sandy layer
DZH19-03
29.6 ± 2.8 ka
(h)
S3, Pit 6
~ 85 cm
DZH19-02
11.2 ± 0.8 ka
Beige silty loess
W
E

Figure 3-4. Photographs of the *in situ* luminescence sampling location (red circles) and the ages they yield. See context and other figures for a detailed description. (a) Three samples from Section S0 T3 Pit 1. (b) One sample from Section S2 (Site 1) T2 Pit 3. (c) The shallower sample from Section S2 (Site 1) T1 Pit 4. (d) The deeper sample from Section S2 (Site 1) T1 Pit 4. (e) One sample from Section S2 (Site 2) T2 Pit 5. (f) Two samples from Section S0 T1 Pit 2. (f) One sample from Section S3 T2. (g) One sample from Section S3 Pit 6.

3.3.3.1.2 Section S2: Site 1

In Chapter 2, we mention that Section S2 has a substantial vertical component of motion accommodated along a main oblique fault, and it shows fresh scarps at the range front. Along the northwestern portion of S2 at 81.145°E, 45.992°N (Figure 3-2), two levels of uplifted terraces (T1 and T2) were found at Site 1 (Figure 3-5a,b). We do not have dGPS measurements at this site, but we have the high-resolution Pléiades and drone-derived DEMs for extracting topographic profiles here. Assuming that the uplift of terraces relative to the footwall is entirely caused by the vertical fault movement, Profile P4 indicates a cumulative vertical displacement across the fault for the lower terrace T1 of 13.8 ± 0.3 m (Figure 3-5b,c). On the higher terrace T2, a part of the surface was eroded by the newly formed river channels, which modify the original terrace morphology. Thus, the cumulative vertical displacement of 29.6 ± 2.0 m in T2 was inferred from a non-linear Profile P5, which tracks the unmodified terrace surface on the hanging wall (Figure 3-5b,c).

We excavated Pit 3 on the flat surface of terrace T2 at 81.146°E, 45.991°N (Figure 3-5a,b). The topsoil layer is 30 cm thick followed by a caliche layer with fine gravel to a depth of 1 m. Below the caliche layer, Pit 3 shows horizontal alluvial gravels aligned with sand layers (Figure 3-4b). Luminescence sample DZH16-08 was collected at a depth of 1.1 m from a fine gravel and medium sand mixed layer and yielded an age of 59.1 ± 7.6 ka (Figure 3-4b). Another sample DZH16-07 was collected at a depth of 1.5 m from a fine gravel and fine sand mixed layer but it did not yield any luminescence signal (Table 3-1).

Pit 4 was excavated on the flat surface of terrace T1 at 81.145°E, 45.992°N (Figure 3-5). The topsoil layer is 40-cm thick, followed by a 20 cm thick caliche layer to a depth of 60 cm. Below the caliche layer, Pit 4 is composed of horizontal fine-to-coarse gravel layers (Figure 3-4c,d). Luminescence sample DZH16-10 was collected at a depth of 0.7 m from a fine-to-medium gravel layer and yielded an age of 7.0 ± 1.3 ka (Figure 3-4c). Another sample DZH16-09 was collected at a depth of 2.1 m from a well-sorted fine gravel layer and yielded an age of 20.9 ± 2.2 ka (Figure 3-4d).

Unlike the sample pits at the Shynzhyly River, Pit 3 and Pit 4 at Section S2 do not show thick loess layers capping the fluvial gravels which indicate terrace abandonment. Therefore, we could only use the

available luminescence sample ages as the terrace abandoned ages, but we note that the real abandonment ages should postdate the sample ages since they were collected below the surface. Considering this assumption and the neglect of post-uplift sediments in the footwall, the uplift rate inferred from our data should be a lower bound. Using the cumulative vertical displacement of 29.6 ± 2.0 m for the higher terrace T2 and its abandoned age of 59.1 ± 7.6 ka from Pit 3 (Figure 3-5), we calculate a minimum uplift rate of 0.5 ± 0.1 mm/yr. The cumulative vertical displacement for the lower terrace T1 is 13.8 ± 0.3 m and by using the shallower and deeper luminescence sample ages of 7.0 ± 1.3 ka and 20.9 ± 2.2 ka (Figure 3-5), we calculate the minimum uplift rates of 2.0 ± 0.5 mm/yr and 0.7 ± 0.1 mm/yr, respectively. We note that the shallower sample (DZH16-10) from Pit 4 indicates a much higher uplift rate than the deeper sample. Since sample DZH16-10 has a low luminescence sensitivity and a limited number of accepted aliquots as mentioned in Section 3.3.2.1.2, we have lower confidence in this sample age and we suggest that the uplift rate inferred from sample DZH16-09, although it is deeper, is a more robust result.

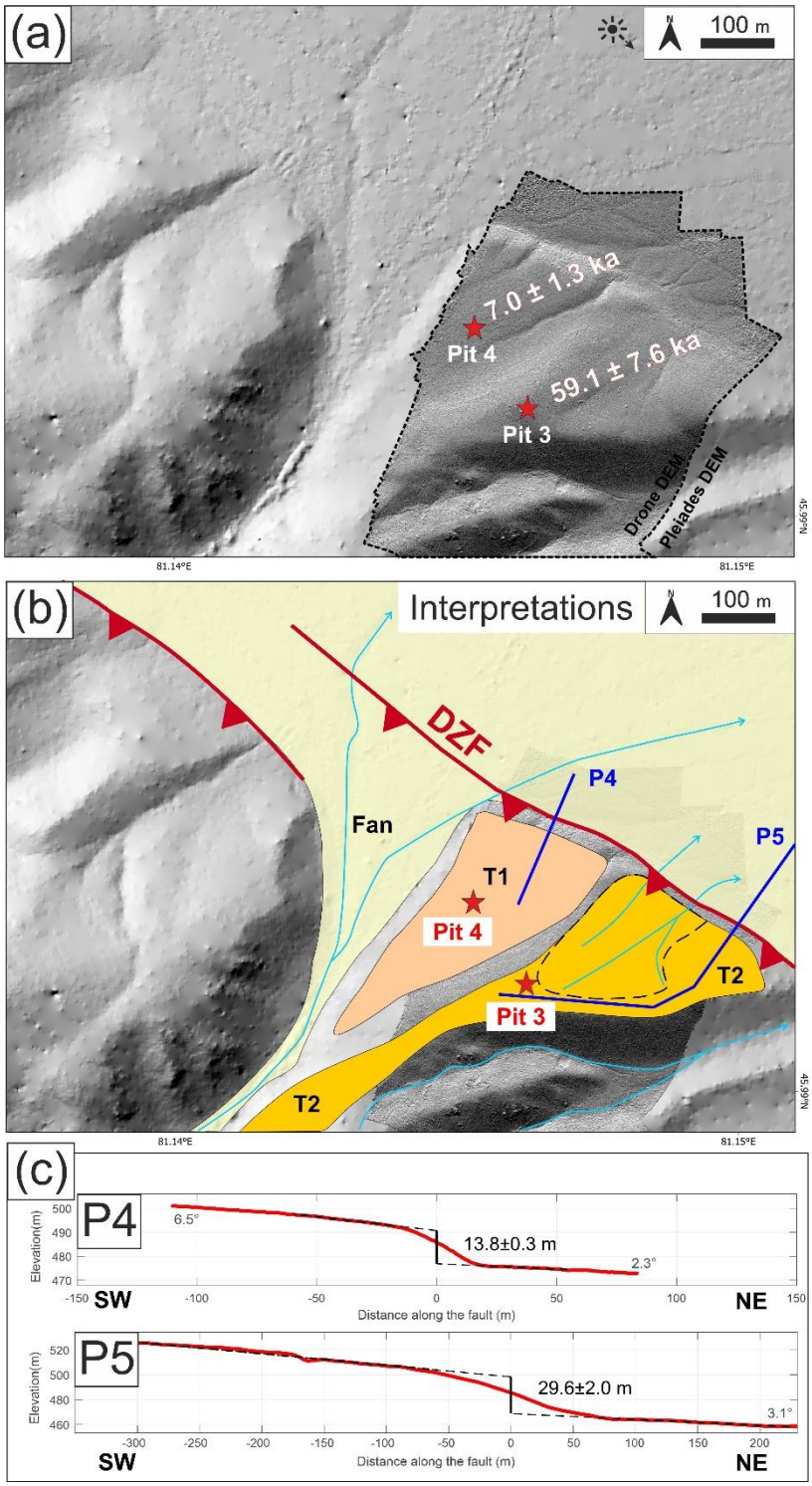

Figure 3-5. (a) Shaded-relief topography derived from both Pléiades imagery and drone photographs showing the uplifted terraces, with the sampling pits (red stars) and the abandonment ages labelled, at Section S2 Site 1. (b) Interpretations with current channels (light blue lines with arrows), fault traces (red lines), topographic profiles (blue lines), and sampling pits (red stars) labelled. The terrace surface within the dashed black line in (b) has been modified by the current river channels. (c) The scarp heights for the

lower (T1) and upper (T2) terraces from topographic profiles P4 and P5, which are extracted from drone-derived and Pléiades-imagery-derived DEMs respectively. The slopes of the fan surfaces across the fault are in grey text.

3.3.3.1.3 Section S2: Site 2

Site 2 is at 81.194°E, 45.972°N, which is about 5 km southeast of S2 Site 1 (Figure 3-2b). Two levels of uplifted terraces (T1 and T2) were found here (Figure 3-6a,b). The topographic profiles at this site are extracted from Pléiades and drone-derived DEMs due to a lack of dGPS measurements. Assuming that the uplift of the terraces is solely due to vertical fault movement, Profiles P6 and P7 show that the cumulative vertical displacements across the fault are 18.7 ± 0.5 m and 9.8 ± 0.4 m on terraces T2 and T1, respectively (Figure 3-6c). Profile P8 shows a 2.3 ± 0.2 m-high fault scarp which is thought to be caused by the latest event as mentioned in Chapter 2 and Campbell et al. (2013) (Figure 3-6c).

We excavated Pit 5 on the terrace T2 surface at 81.19401°E, 45.97215°N (Figure 3-6). The topsoil layer is 40 cm thick followed by a caliche layer with fine gravel up to a depth of 0.7 m. Below the caliche layer, there is a 20-cm thick layer of fine sand with fine gravel where sample DZH16-06 was collected from at the depth of 0.8 m and yielded an age of 20.4 ± 1.9 ka (Figure 3-4e). From a depth of 1 m and below we found interbedded medium gravel and fine gravel layers down to the bottom of Pit 5.

Similar to Site 1, terrace T2 at Site 2 shows no thick loess layer capping on top of the fluvial gravels or sand. Thus, we could only use the available sample age as the terrace abandonment age and we note that this provides a lower bound for the uplift rate as explained previously. Using the cumulative vertical displacement of 18.7 ± 0.5 m for the higher terrace T2 and its abandonment age of 20.4 ± 1.9 ka from sample DZH16-06 (Figure 3-6), we obtain a minimum uplift rate of 0.9 ± 0.1 mm/yr.

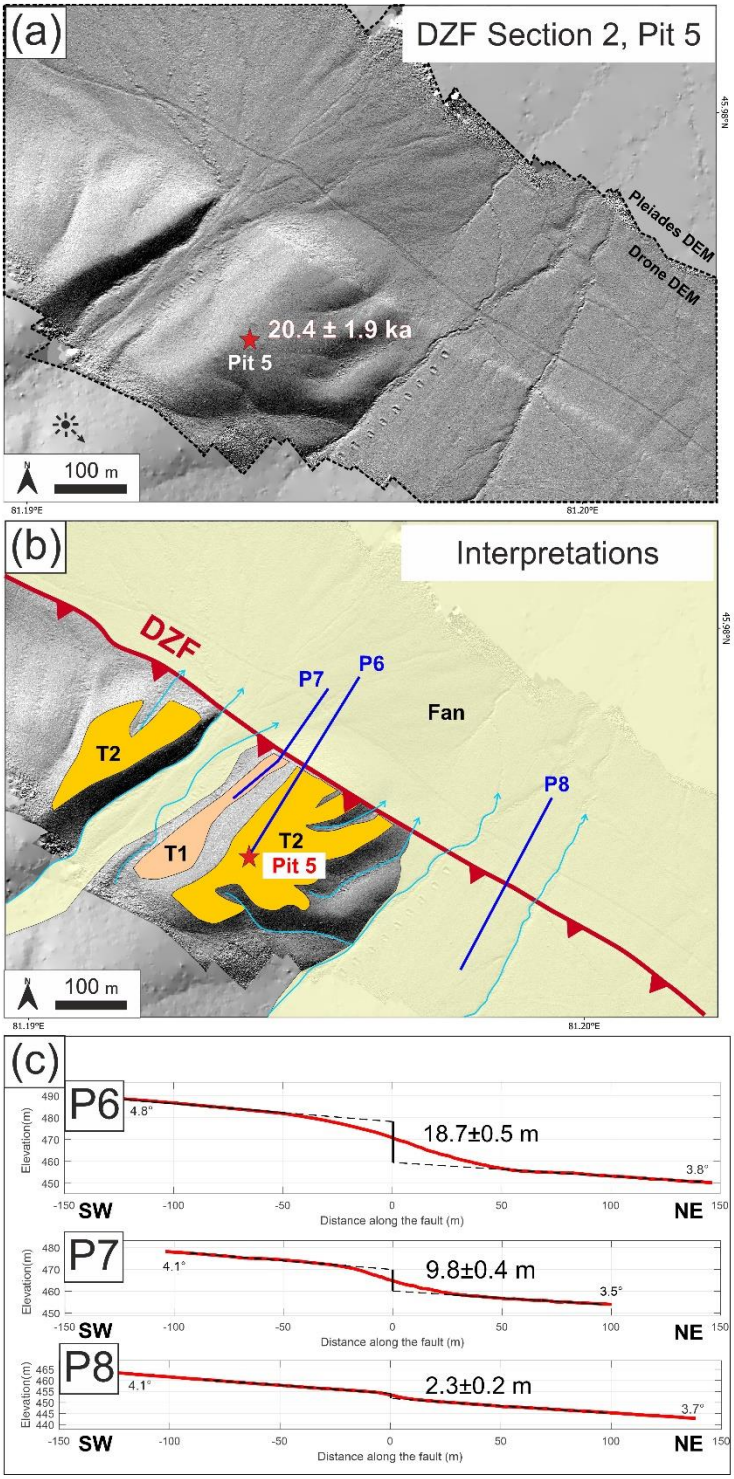

Figure 3-6. (a) Shaded-relief topography derived from both Pléiades imagery and drone photographs showing the uplifted terraces, with the sampling pit (red star) and the abandonment age labelled, at Section S2 Site 2. (b) Interpretations with current channels (light blue lines with arrows), fault traces (red lines), topographic profiles (blue lines), and sampling pits (red stars) labelled. (c) Profiles P6 and P7 extracted from drone-derived DEMs showing the scarp heights for the upper (T2) and lower (T1) terraces. Profile P8 shows the likely single-event fault scarp. The slopes of the fan surfaces across the fault are in grey text.

3.3.3.1.4 Section S3: Northern Branch

Section S3 of the Dzhungarian Fault is characterised by slip-partitioning and consists of two main branches. The northern branch shows a prominent reverse component whereas the southern branch is dominated by strike-slip movements (Figure 3-2c). Along the northern branch at the Ulken Sengyrly River (at 81.619°E, 45.805°N), two main series of terraces (T1 and T2) can be recognised. Terrace T2 extends to both sides of the river and has been uplifted by the Dzhungarian Fault (Figure 3-7a,b). Assuming that the uplift of T2 is totally controlled by fault movement, the cumulative vertical displacement on T2 is around 13-16 m as indicated by Profiles S1 and S2, which were constructed from the Pléiades-imagery-derived DEMs (Figure 3-7d,e). From the cross-section of the T2 terrace riser, we collected sample DZH19-03 at a depth of 0.74 m from a sandy layer with small clasts which is bounded by coarse-and-rounded gravel layers above and below, and all layers are capped by a ~50-cm-thick loess layer on the very top (Figure 3-4g and Figure 3-7c). Since this sandy layer predates the upper gravel layer that should have been deposited before the uplift of terrace T2, the abandonment age of T2 should be younger than the age of sample DZH19-03. Thus, using the cumulative vertical displacement of 14.6 ± 1 m from Profile S1 and the age of 29.6 ± 2.8 ka of this sample, we calculate a minimum uplift rate of 0.5 ± 0.1 mm/yr.

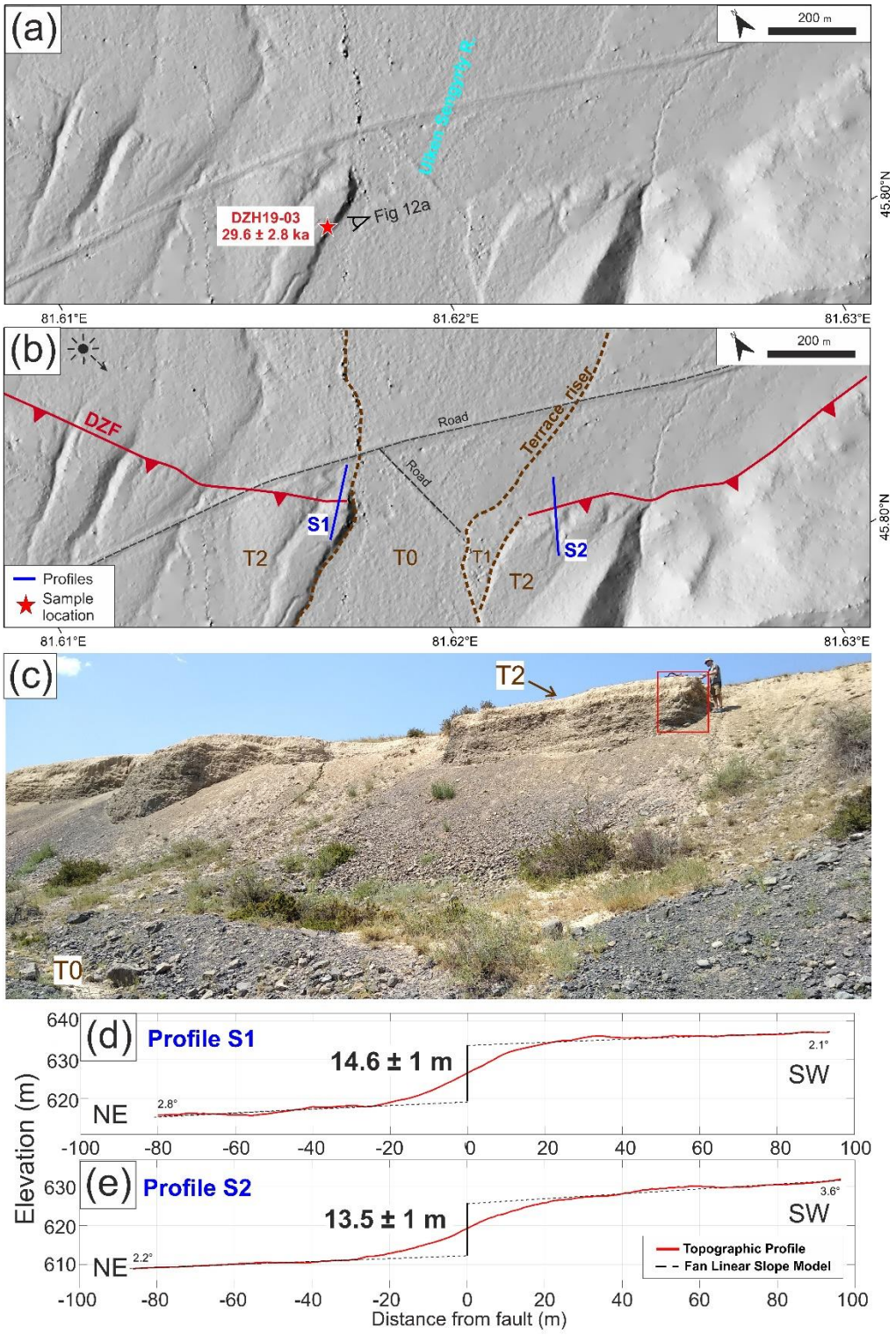

Figure 3-7. (a) Shaded-relief topography derived from Pléiades imagery showing the uplifted terraces on both sides of the Ulken Sengyrly River with the interpretations annotated in (b). (c) IRSL sample DZH19-03, marked by red star with yielded ages noted in (a), was collected within the red rectangle at the riser of terraces T0 and T2. The height of the T0-T1 riser is ~3 m; the height of the T0-T2 riser is ~7-8 m. The topographic profiles S1 and S2 are shown in (d) and (e), respectively.

The vertical slip rates implied from the uplifted terraces along Section S0, S2, and the northern branch of S3 are mostly consistent with each other with an average rate of 0.7 ± 0.3 mm/yr, except for sample DZH16-10 from Pit 4, which produces a rate of 2.0 ± 0.5 mm/yr. We suggest this exceptionally high rate is an overestimate. As mentioned in Section 3.3.2.1.2, the age from sample DZH16-10 is based on a limited number of accepted aliquots, and we suggest that it yields an inaccurate age. Therefore, from here onwards, we exclude this result from our analysis and discussion.

3.3.3.2 Lateral Slip Rate

3.3.3.2.1 Section S3 Southern Branch

Clear right-lateral strike-slip offset features are found at the southern branch of Section S3 (45.789°N, 81.565°E) where the fault is dominated by strike-slip motion (Figure 3-2a,c). Ridge A and Ridge B are excellent offset markers showing a cumulative pure strike-slip displacement of ~ 30 m (Figure 3-8a). We made DEMs from drone photographs for estimating the precise offsets. Using the elevation contours, we drew fitting lines for the ridge crests and the eastern slopes, where the gradients are more consistent across the fault (Figure 3-8c). We estimated the offsets by measuring the distances between the corresponding fitting lines along the fault strike. The average displacement for the two ridges is 29.9 +0.8/-1.3 m. Between the two ridges, Channel A and Channel B also show cumulative lateral displacements of 28.3 ± 0.4 m and 19.2 ± 0.6 m respectively (Figure 3-9).

The IRSL sample DZH19-02 was taken from Pit 6 at 45.789°N, 81.566°E, which was dug on the uplifted fan surface between Channel A and Channel B (Figure 3-9b). Pit 6 consists of an upper brown soil layer with roots followed by a ~1-m-thick silty loess layer. IRSL sample DZH19-02 was collected at a depth of 85 cm and yielded an age of 11.2 ± 0.8 ka (Figure 3-4f). We did not reach continuous gravel layers in Pit 6. The collected material is from a layer containing small clasts above a silty loess layer.

The relationship between this sample age and its corresponding cumulative offset is hard to define. The cumulative offset of 19 m from Channel B might be the best constraint for estimating the slip rate using the sample age of DZH19-02. Channel B is a relatively young geomorphic feature with shallower incision and smaller length and width comparing to Channel A or other major rivers nearby. Therefore, we suggest that Channel B formed after the abandonment of this peneplain. Considering the youth of Channel B and the thick loess layer above the collected sample, the cumulative offset recorded by Channel B should postdate the sample age of DZH19-02. Dividing the channel offset (19.2 ± 0.6 m) by the age of 11.2 ± 0.8 ka yields a minimum lateral slip rate of 1.7 ± 0.2 mm/yr. On the other hand, the age of 11.2 ±

0.8 ka should be seen as the minimum age for the larger ~ 30 m offset of Ridges A and B since this aeolian sample should postdate the formation of the ridges. Based on this data, we calculate a maximum lateral slip rate of 2.7 ± 0.3 mm/yr using the cumulative offset of 29.9 + 0.8/- 1.3 m and the age of 11.2 ± 0.8 ka.

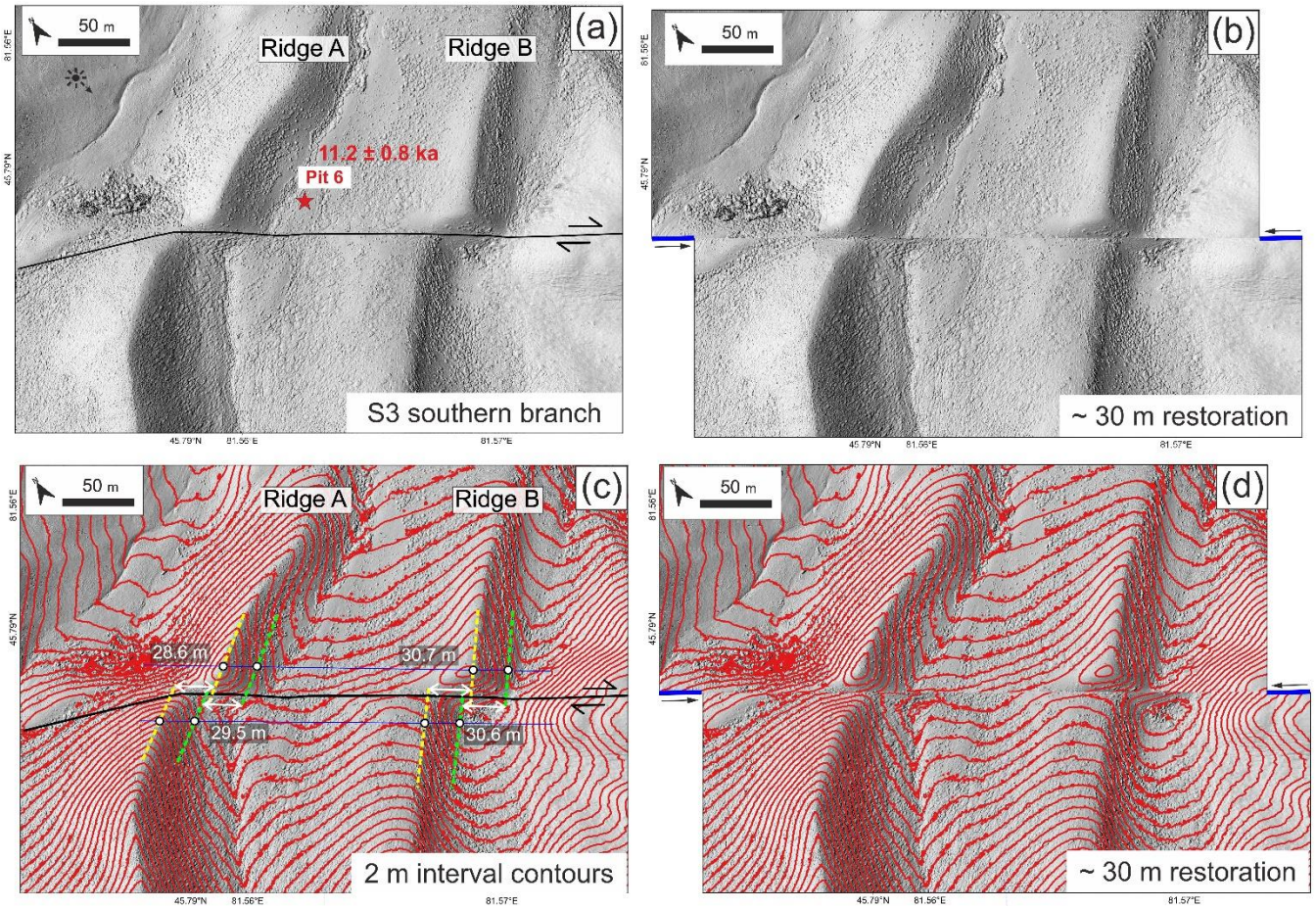

Figure 3-8. (a) Shaded-relief topography derived from the drone DEM at 45.79°N, 81.57°E showing the displaced Ridges A and B at the southern branch on Section S3 with 30 m restoration of the right lateral offset in (b) and (d). Red star marks the location of sampling Pit 6 with the measured age noted, and the black line is the fault trace of the Dzhungarian Fault. (c) Contour (red lines) map with shaded-relief topography in the background. Dashed yellow lines are the fitting lines for the ridge crests. Thin blue lines are 20-m away from and parallel to the fault and are the guidelines for placing the slope fitting lines (dashed green). The slope fitting line (dashed green) intercepts the point (white, on the slopes) that is 10-m lower than the crest along the guideline. The fitting line for each slope (dashed-green) is parallel to the slope of the corresponding ridge crest. White arrows denote the measurements of each corresponding fitting line with the amount of displacement annotated in metres.

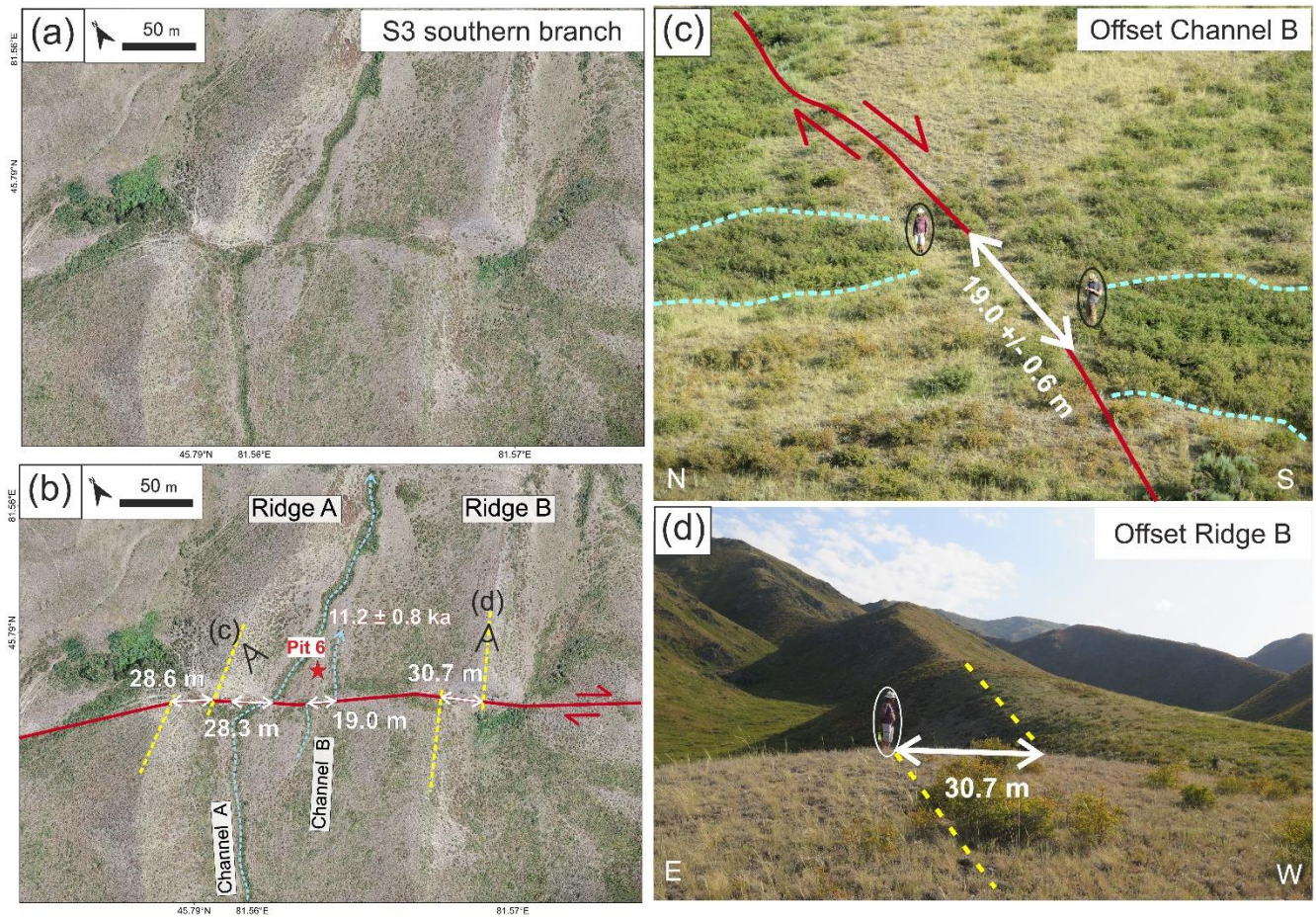

Figure 3-9. (a) Orthorectified drone imagery, showing the identical area as in Figure 3-8a, with the right-laterally displaced Channel A and B and Ridges A and B. (b) Same as (a) with data locations and interpretations, including sampling Pit 6 (red star) and its measured age, the fault trace (red lines), the offset river channels (dashed blue lines) and ridge crests (yellow dashed lines) with their displacements labelled. (c) and (d) Field photographs showing the displaced Channel B and Ridge B. Offset measurements are annotated in white.

3.3.3.2.2 Section S4

A minimum slip rate of 2.2 ± 0.8 mm/yr has been reported based on an alluvial fan on Section S4 at 45.59°N, 82.05°E, displaced ~ 50 m and dated ~ 26 ka from OSL dating (Figure 3-2) (Campbell et al., 2013). To test the validity of this slip rate, which is based on only limited data, we collected samples from quartz cobbles and boulder tops on a displaced fan located ~ 2.5 km NW of the previously investigated site in Campbell et al. (2013) (Figure 3-2). We applied the approach of cosmogenic nuclide dating to constrain the fan age for re-estimating the lateral slip rate of the fault section.

Our sample site, which was identified but not dated in Campbell et al. (2013), is at 45.61°N, 82.02°E, where an alluvial fan, channels, and pronounced channel levees are displaced by ~ 50 m (Figure

3-2 and Figure 3-10). It is difficult to determine the absolute displacements and uncertainties for all these offset geomorphic features because of the diffuse channel levees or fan edges. We measure the offsets only from the three best-defined features (Channel C, Channel D and Fan A in Figure 3-10c,d). We determined the offset in our sampling site to be 49.4 ± 8.0 m by averaging our measurements of these three offset features with error estimates defined by the maximum observed error among all the measurements.

Nine samples for cosmogenic nuclide dating were collected at the levees of Channel D for their surface exposure ages as an indication of the age of the displaced channel and fan (Figure 3-10b). Among them, six samples (DZH-1 to DZH-6) were collected from quartz cobbles (Figure 3-11a-f) and the other three samples (DZH-7, -8 and -9) consist of amalgamated smaller quartz cobbles (Figure 3-11g-i). The dating procedures are introduced in Section 3.3.2.2 with the results shown inTable 3-2. All the obtained ^{10}Be ages from both amalgamated and non-amalgamated samples are in relatively close agreement with each other except sample DZH-1, which is a clear outlier. Removing sample DZH-1 from the final age calculation yields an average age of 14.3 ± 2.0 ka (1 sigma; n=8) (Figure 3-10e). When combined with the total lateral offset of 49.4 ± 8.0 m, this age corresponds to a minimum lateral slip rate of 3.6 ± 1.1 mm/yr.

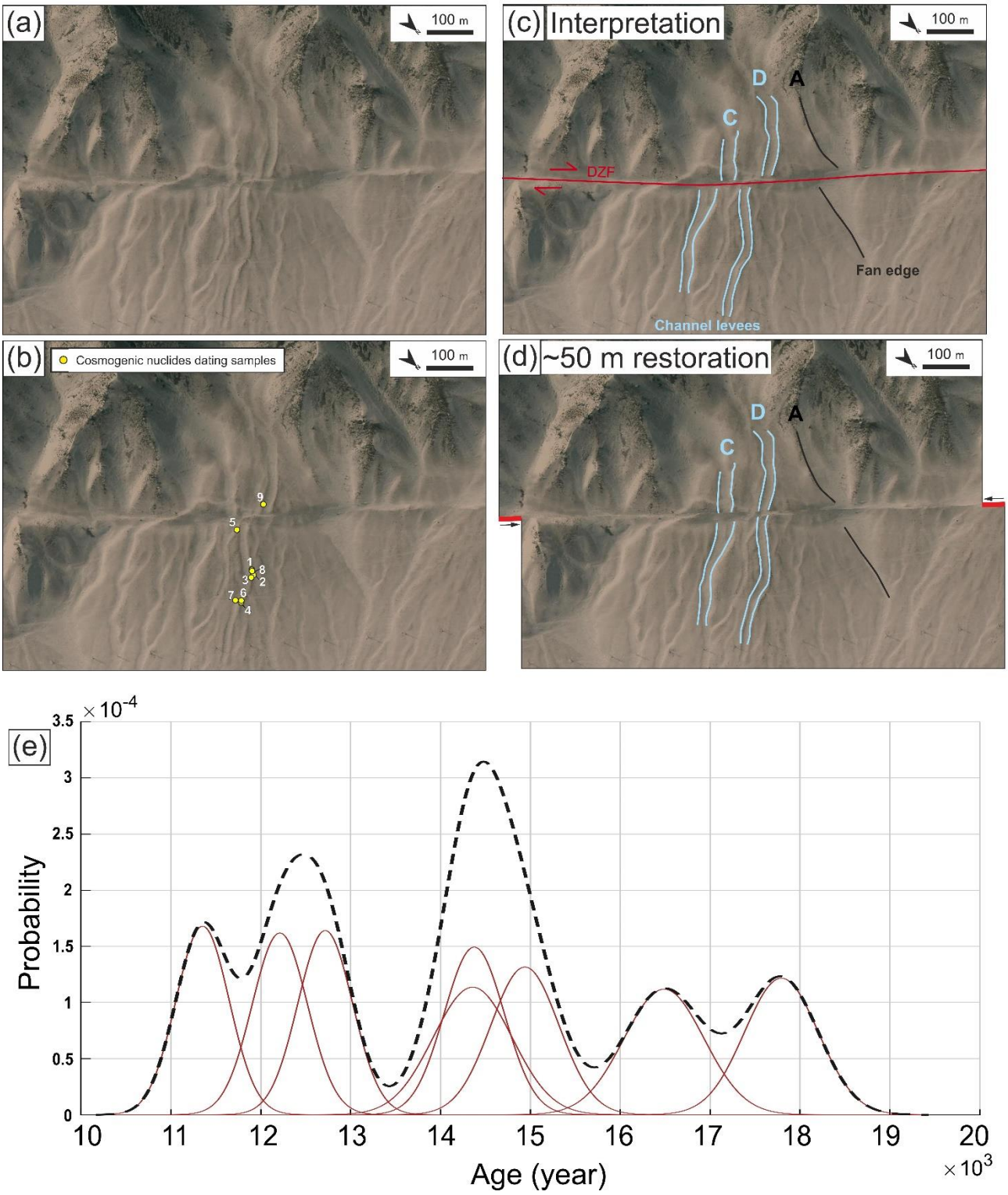

Figure 3-10. (a) Satellite imagery from Google Earth showing the right-laterally offset fan and channels at ~ 45.61°N, 82.02°E (see Figure 3-2 for regional location). (b) Locations of the nine samples (yellow dots) collected for cosmogenic nuclide dating with their sample numbers annotated. (c) Interpretations for the geomorphic features with displaced channel C, channel D (in blue) and the edge of Fan A (in black)

marked. (d) Restoration of the displaced geomorphic features for ~ 50 m. (e) Individual probability density functions (red lines) of the eight cosmogenic exposure ages and their aggregated probability density function (dashed black line). Plotting method adapted from http://depts.washington.edu/cosmolab/pubs/gb_pubs/camelplot.m

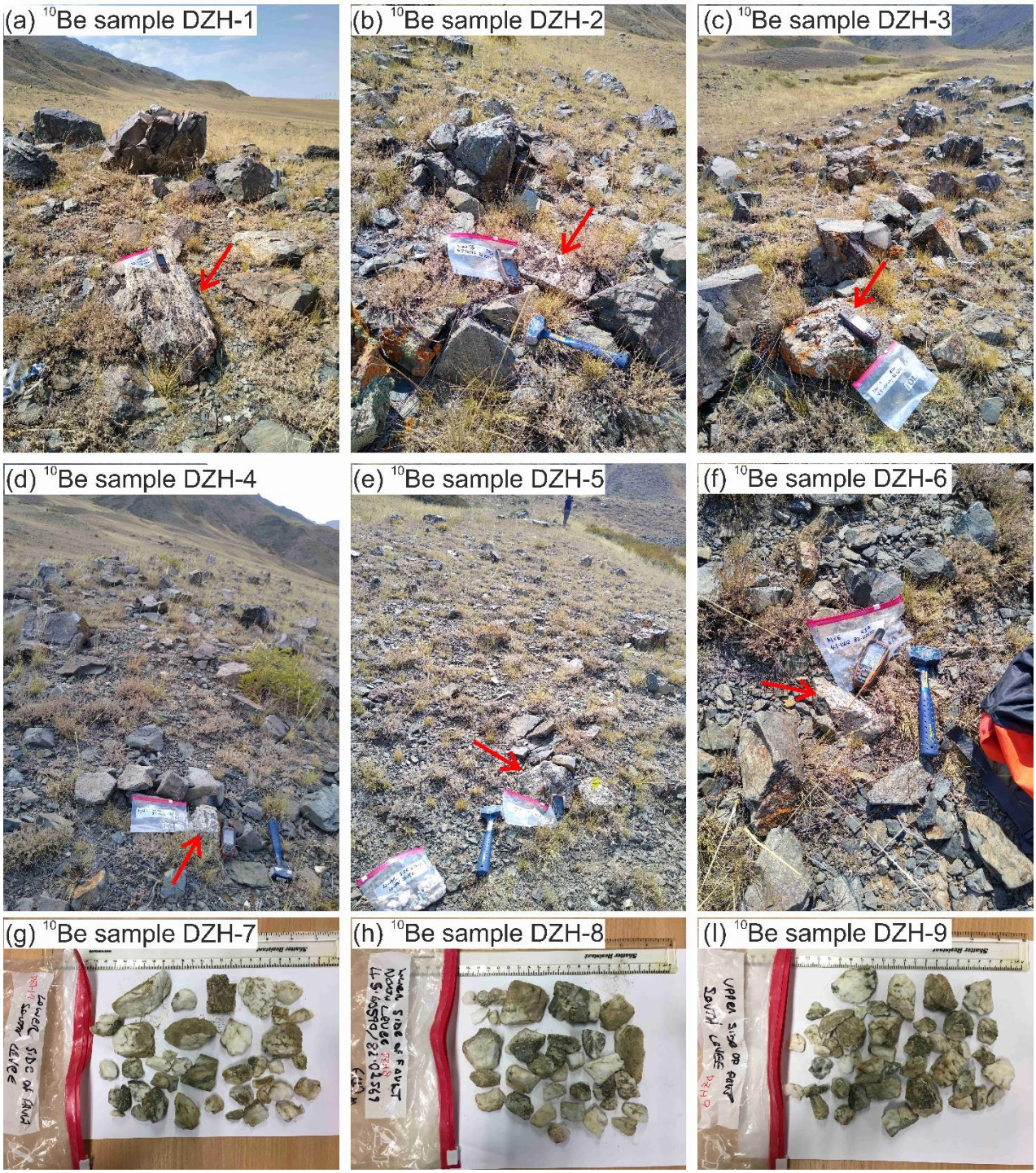

Figure 3-11. (a) – (f) Photographs of the *in situ* cosmogenic sampling locations and the collected quartz cobbles (red arrows pointed) (g) – (i) Photographs of the amalgamated smaller quartz cobbles samples.

3.3.4 Summary

By plotting the vertical offsets of the uplifted river terraces against the measured abandonment ages, we produce a best-fitting regression, which gives an uplift rate of 0.6 +0.4/-0.2 mm/yr since ~ 60 ka, including all the uncertainty ranges (Figure 3-12a). Examining the results from individual sampling locations, the uplift rates on Sections S0, S2, and the northern branch of S3 are 0.6 ± 0.1 mm/yr, 0.7 ± 0.3 mm/yr and 0.5 ± 0.1 mm/yr, respectively. Using the weighted mean for these three results yields the same mean uplift rate of 0.6 mm/yr with an uncertainty of 0.2 mm/yr since ~ 60 ka (Figure 3-12b). The uplift rate may vary in the period for which we do not have data coverage. However, most of our sampling sites agree with a single rate of uplift, supporting the conclusion that the uplift rate has remained consistent along the northern part of the DZF, from the Shynzhyly River to the Rygayty River, over the last ~ 5 to 60 ka.

Based on the ^{10}Be exposure age dating of the laterally-offset alluvial fan, we calculate a lateral slip rate of 3.6 ± 1.1 mm/yr since ~14 ka on the southern pure strike-slip Section S4 of the DZF. This lateral slip rate is consistent with the rate of 3.2 +1.4/-1.1 mm/yr estimated from the ^{10}Be depth profile dating of the fans since ~ 100 ka on Section S7 (Z. Hu, Yang, et al., 2021), and the 3 ± 1 mm/yr estimated by England & Molnar (1997) for all the strike-slip portion, suggesting that the right-lateral slip rates remain consistent along the southern part (S4 to S7) of the DZF. The slightly higher geological lateral slip rates of ~ 5 mm/yr suggested by Yang & Shen (2000) and Shen et al. (2011) might be a result of a less precise fan age estimation methodology, which is based solely on the climatic history rather than direct dating of fan sediments (P. Zhang et al., 1995; Deng et al., 2000). The two lateral slip rates calculated using ^{10}Be cosmogenic nuclide dating in this study and Hu et al. (2021) are larger than the rate of 2.2 ± 0.8 mm/yr (since ~ 26 ka) obtained from luminescence dating (Campbell et al., 2013), though the rates do overlap within the uncertainty ranges. Given the 50 m offset of the fan in Campbell et al. (2013), and its proximity to the other ~ 50 m offset dated in this study, we suggest the seemingly lower slip rate calculated from the luminescence dating might be due to the overestimation of the fan abandonment age, through incomplete bleaching of the luminescence sample or sampling of pre-fan abandonment sediments. Our dated fan age of ~ 14 ka is also more consistent with other Quaternary fan depositions dated from several intermontane basins within Tien Shan as well (Thompson et al., 2002).

Therefore, we suggest the geological lateral slip rate on the southern DZF should be 2.1 – 4.7 mm/yr since ~ 100 ka as obtained from the two ^{10}Be studies (Hu et al., 2021; this study). In contrast, the right-lateral slip rate we obtained further north, from luminescence dating on the southern branch of S3,

is bracketed between 1.7 ± 0.2 mm/yr and 2.7 ± 0.3 mm/yr since ~ 11 ka. This range of values may represent the lower bound of the strike-slip rate of the southern DZF, though as Section S3 consists of two main branches it is possible that the southern branch only accounts for a portion of the total slip rate on S3. Also, as S3 has a significantly different strike to the more southerly sections, the component of strike-slip across it should be reduced, with larger reverse components instead. Given a 28° change in the fault strike, the 2.1 – 4.7 mm/yr strike-slip rate of the southern DZF yields a strike-slip rate of 1.9 – 4.1 mm/yr on Section S3.

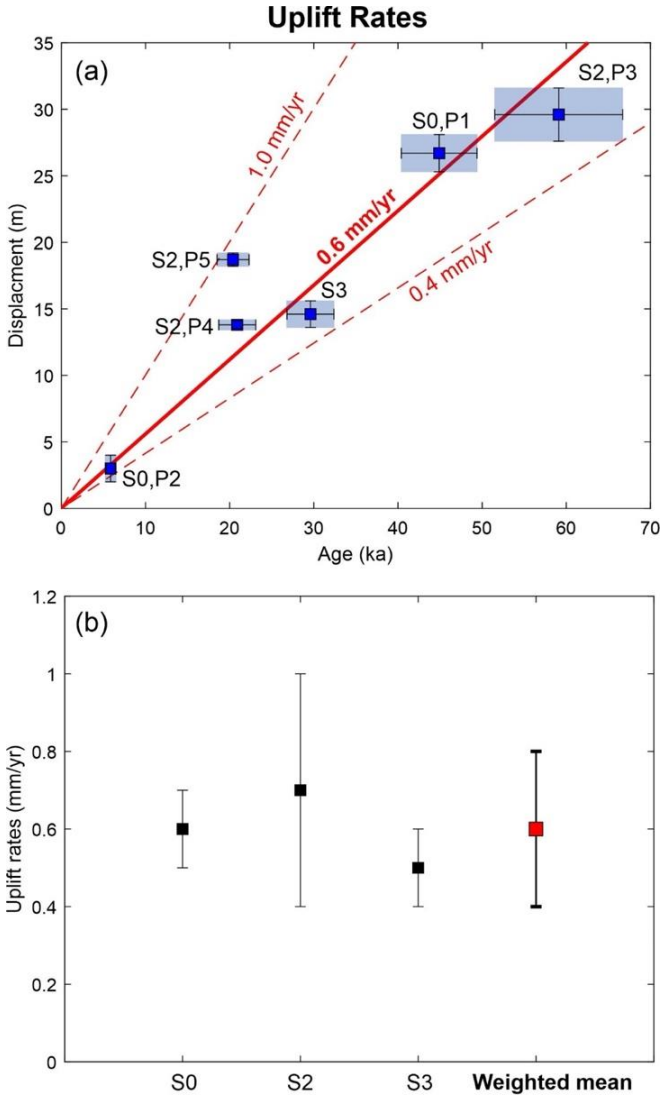

Figure 3-12. (a) Uplift rates estimated from the displaced terraces and their abandonment age. Six data points with sampling sites annotated are shown in blue squares with light blue rectangles illustrating the uncertainty. The least-squares best fitting line for all points is shown in a thick red line with the mean rate annotated (0.6 mm/yr). The least-squares best fitting lines for the maximum and minimum rates are shown in dashed red lines with rates annotated. (b) The weighted mean rate and uncertainty (red square) from the rates of the three Sections S0, S2 and S3 (black squares).

3.4 Geodetic Slip Rates

3.4.1 Introduction

Geodetic slip rates refer to the present or short-term slip rates observed by space-geodesy measurements. These measurements include the Global Navigation Satellite System (GNSS) and Interferometric Synthetic Aperture Radar (InSAR) that measure the ground movement within a particular time. These measurements can further be used for quantifying the spatial distribution of tectonic strain release and accumulation. GNSS measurements have been commonly applied for investigating crustal deformation due to their high observation precision in horizontal (~ 1 mm) components (Guohua Gu & Wang, 2013). However, the disadvantages of GNSS techniques are the less precise vertical components and, more practically, the need for station installation in the field. In contrast, InSAR allows measurement of surface displacements at a large scale and with a high spatial resolution with precision down to a few mm/yr and high sensitivity to vertical components, without the need to go to the field.

InSAR has been applied in recent decades to study short-term coseismic slip and long-term subtle crustal deformation. Researchers can measure precise coseismic displacements and rupture patterns after an earthquake from differential interferograms to infer fault geometry and slip at depth (e.g. Hamiel & Fialko, 2007; Copley et al., 2011; Sreejith et al., 2016; Xu et al., 2020). InSAR has also been widely used to examine inter-seismic slip rates (e.g. Elliott et al., 2008; Walters et al., 2011; Daout et al., 2019). Inter-seismic surface deformation is mainly due to elastic deformation caused by steady-state slip at depth, and reflects the smooth deformation gradient of the locked shallower parts of faults (Scholz, 2002). Several recent studies have used InSAR with improvements made for large-scale and automatic processing to investigate inter-seismic deformation and strain concentration (e.g. Hussain et al., 2016; Weiss et al., 2020; Thollard et al., 2021; Ou et al., 2022), which are fundamental to seismic hazard assessments. These uses of InSAR all highlight that it has become a powerful geodetic tool in studying fault behaviours and their associated seismic characteristics.

In this study, since GNSS stations along the Dzhungarian Fault (DZF) are relatively scarce (Figure 3-13), we explore the use of InSAR time-series approaches to estimate the lateral variation of the inter-seismic strain of the DZF and to increase the spatial resolution provided by GNSS measurements.

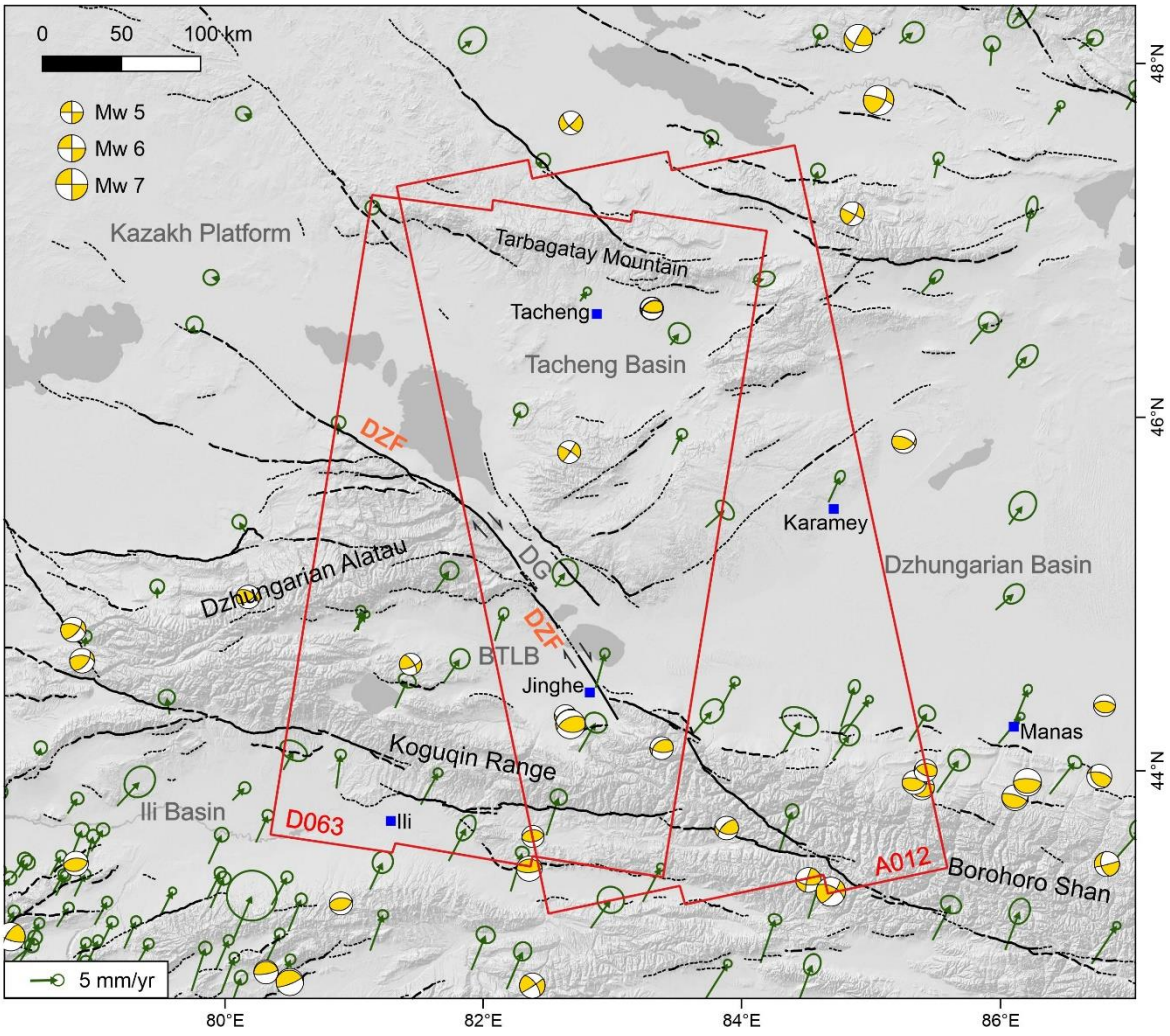

Figure 3-13. Overview of the InSAR data coverage from tracks D063 and A012 (red frames) used in this study. The Dzhungarian Fault (DZF) is mapped within this study. The other fault traces and slip rates are from the Active Faults of Eurasia Database (AFEAD) (Zelenin et al., 2021). Faults with slip rates higher and lower than 1 mm/yr (as defined in the database) are delineated by black solid and dashed lines respectively. Faults delineated by thinner dashed lines have lower reliability of activity. Focal mechanisms are from the database of the Global Centroid-Moment-Tensor (GCMT) Project (Dziewonski et al., 1981; Ekström et al., 2012). GPS velocity vectors are shown in green arrows (Zheng et al., 2017). Towns are labelled with blue squares with their names. DG: Dzhungarian Gate; BTLB: Bortala Basin

3.4.2 InSAR Processing

3.4.2.1 Interferogram Principle

SAR-bearing satellites travel around the Earth periodically along sun-synchronous near-polar orbits with high sensitivity to orbit-perpendicular (~east-west) displacements and low sensitivity to orbit-parallel (~north-south) displacements (Figure 3-14a). These satellites have right-looking antennae that

transmit electromagnetic waves of certain wavelengths to the Earth's surface and record the phase and intensity (amplitude) of the returning waves when they bounce back from the ground (Figure 3-14a) (Massonnet & Souyris, 2008). If the Earth's surface has moved between repeated radar acquisitions at the same location, the phases recorded before and after the ground movement will be different. Therefore, the amount of surface deformation between any two acquisitions can be estimated from the wavelengths and the phase differences. The phase differences are demonstrated as interferograms. The preliminary interferograms usually show the wrapped phase in cycles of 2π. In order to obtain the continuous phase difference, ϕ, an unwrapping process with a chosen reference point is applied to the interferograms. The continuous phase difference between any two acquisitions should be identical to the incremental phase changes of other interferograms between these two acquisitions. For example, if there are three acquisitions A, B, and C, the relationship of continuous phase differences between them should be $\phi_{AB} + \phi_{BC} = \phi_{AC}$. By using a network of interferograms across a couple of continuous years, we can obtain an incremental phase change within that period. By converting the incremental phase change into the amount of surface deformation, we can extract the mean velocities of the surface movement down to a few millimetres per year.

However, other factors besides surface deformation can cause a change in phase. The InSAR phase difference present in each interferogram can be described as the sum of the following components:

$$\phi = \phi_{def} + \phi_{atm(stra+tur)} + \phi_{orb} + \phi_{DEM} + \phi_{noise}$$

where ϕ_{def} is the phase change of the crustal surface deformation, $\phi_{atm(stra+tur)}$ is the atmospheric (atm) phase delays caused by the stratified (stra) components and turbulent (tur) components within the troposphere and the ionosphere on the path of the radar waves, ϕ_{orb} is the phase change due to the inaccuracy of the satellite orbits, ϕ_{DEM}, is the phase change from inaccuracies in the modelled topography (e.g. DEM), ϕ_{noise} is the residual phase from all other factors such as the instrumental noise, the unmodelled turbulent phase delay, etc.

In order to obtain ϕ_{def}, we have to correct for all the other factors involved in the phase change. For atmospheric phase delay, stratified components are usually associated with topography and seasonality whilst turbulent components appear randomly in space and time (Hanssen, 2001). Numerous approaches have been developed for correcting $\phi_{atm(stra+tur)}$ (e.g. Zebker et al., 1997; Doin et al., 2009, 2015; Jolivet et al., 2011; Walters et al., 2013; Fattahi & Amelung, 2014a; Bekaert et al., 2015; Yu et al., 2017, 2018; L. Shen et al., 2019). The recently launched Re-Analysis-5 (ERA-5) global atmospheric model from the European Centre for Medium-Range Weather Forecasts (ECMWF)

(https://www.ecmwf.int/en/forecasts/datasets/reanalysis-datasets/era5) is a powerful tool for correcting atmospheric phase delay. The ERA-5 model is a replacement and advanced version of the ERA-Interim model which was stopped being produced in August 2019 (Dee et al., 2011, 2014; Jolivet et al., 2014). The ERA-5 model provides estimates of atmospheric variables such as temperature and water vapour partial pressure. It provides hourly outputs and uncertainty estimates, with a global data coverage of 30 km × 30 km horizontal resolution and 137 levels from the surface to an elevation of 80 km. The complete dataset and the wide spatial and temporal resolution of the ERA-5 model make it well-suited to atmospheric phase delay correction. For the satellite orbit inaccuracy, there have been great improvements in the orbit controls for the new-generation satellites (e.g. Sentinel-1) due to their smaller perpendicular baseline, which is the satellite distance between the two acquisitions perpendicular to the satellite viewing direction (Figure 3-14b). The smaller perpendicular baseline can also decrease the inaccuracy of the modelled topography as ϕ_{DEM} scales with the perpendicular baseline (Ducret et al., 2013).

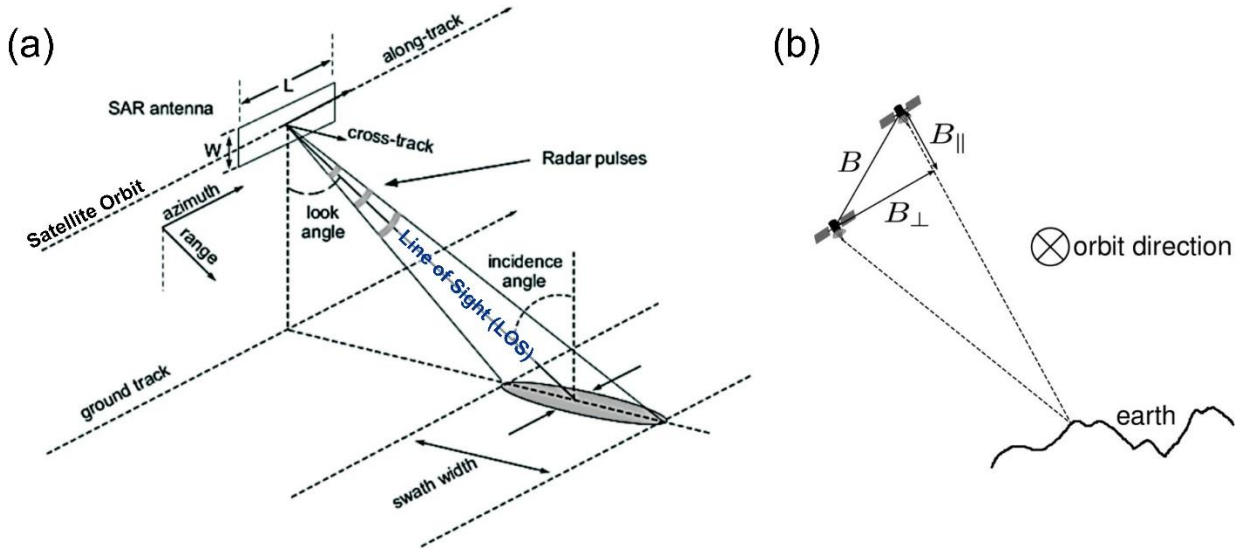

Figure 3-14. (a) Illustration of SAR acquisition geometry and the related terms. (adapted from Dawson (2008)). (b) Illustration of baseline (B), perpendicular baseline and parallel baseline. (from Rossi 2016)

3.4.2.2 Interferogram Generation

In this study, we processed SAR data from the archive of the European Space Agency (ESA) Sentinel-1 satellite which was launched in April 2014 and has been acquiring data every 24 days before November 2016 and every 12 days afterwards. This frequent data acquisition plus the wide coverage (> 250 km swath width in range) and high spatial resolution (averaged ground pixel size of 5 m (in range) ×

20 m (in azimuth) before multilooking) of Sentinel-1 SAR data make it a great tool for measuring fault movements and modern crustal deformation. We analysed data from descending track 063 (D063) and ascending track 012 (A012) with their overlapping area covering a length of ~175 km along the southern DZF (Figure 3-13).

The C-band (~5.5 cm) Sentinel-1 SAR data were obtained with acquisition periods between September 2014 and July 2019 for D063 and between June 2015 and March 2020 for A012. We processed the interferograms with the New Small Baselines Subset (NSBAS) processing chain, based on the ROI_PAC software (Rosen et al., 2004; Doin et al., 2011, 2015; Grandin et al., 2016; Yague-Martinez et al., 2016; Thollard et al., 2021). Fine registration based on precise orbits, the SRTM 30-m resolution DEM (Hooper et al., 2007), and an enhanced spectral diversity method as explained in Grandin et al. (2016), were applied to generate interferograms computed at 40 × 40 m resolution.

The initial networks for interferograms were built semi-automatically to contain all possible date pairs within three months and additional pairs across six months and one year for each epoch (acquisition) to ensure that interferograms within the same season and across different seasons were both included. For track D063, 89 epochs are available and 372 interferograms were generated; for track A012, 109 epochs are available and 561 interferograms were generated.

3.4.2.3 Unwrapping Strategy

We observed low interferometric phase coherence in our study area with obvious topographic-related fringes at the edges of the basins (Figure 3-15a,b,c). In addition, we observed some asymmetric and abrupt fringes within the basin areas especially among the agricultural fields or among the alluvial fans next to the fields (Figure 3-15b,c,d). Moreover, temporal decorrelation tends to appear in the mountainous areas (e.g. the Koguqin Range) and around Lake Alakol (Figure 3-15). This generally low InSAR phase coherence is likely caused by changes in humidity, vegetation coverage and snow across seasons, and by strong atmospheric delays, which poses great challenges in unwrapping in this Dzhungarian region. To unwrap both short and long-baseline interferograms and reduce phase decorrelation due to those parasite signals, we tested and applied different corrections on the wrapped phase.

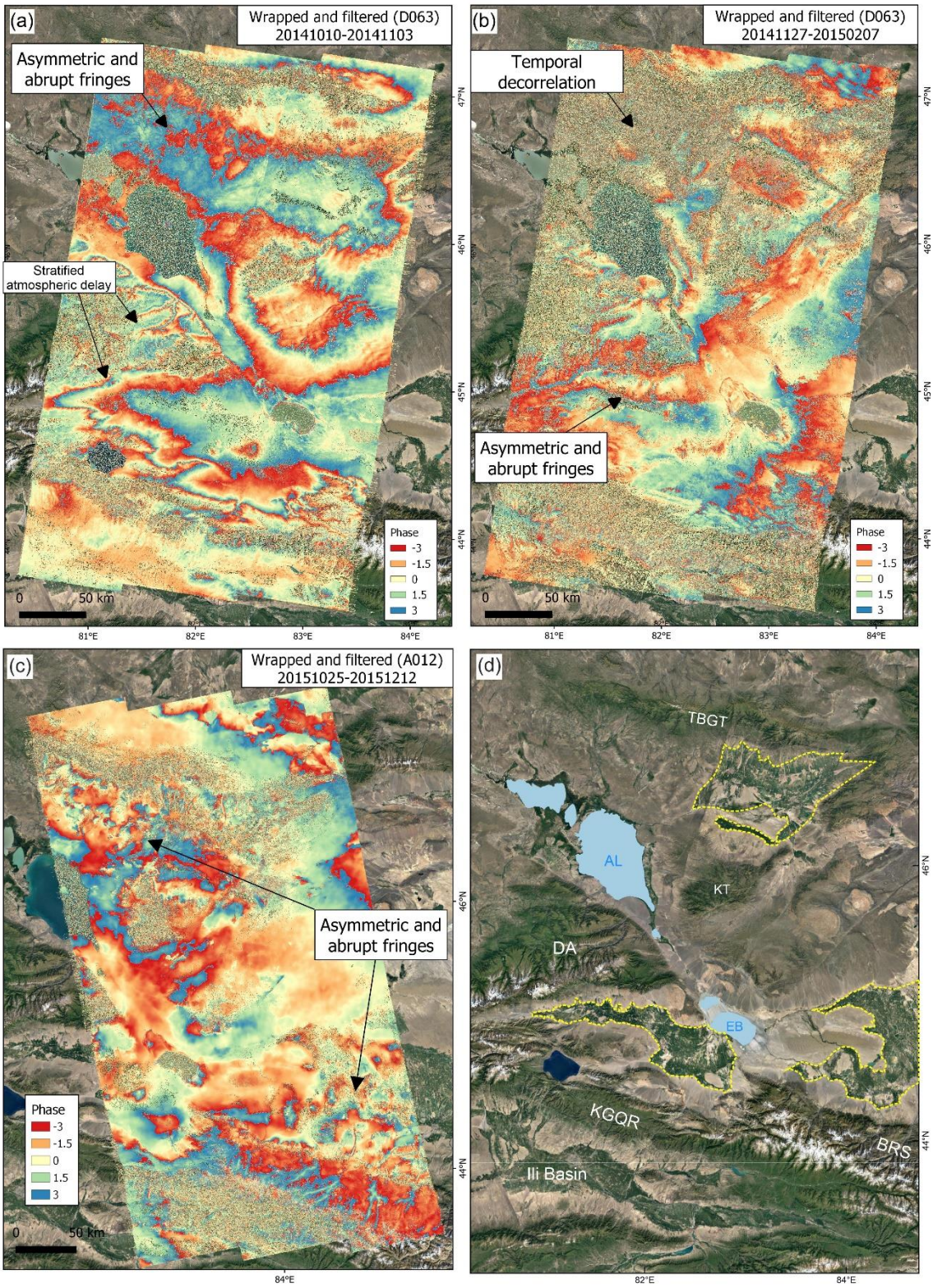

Figure 3-15. Example interferograms showing the signals that lead to unwrapping difficulties due to atmospheric delays. These signals include the topographic-related fringes, some asymmetric and abrupt fringes and temporal decorrelation. (d) has the same extent as (a) and (b). Major agricultural fields are

marked by yellow dashed lines. AL: Lake Alakol; EB: Lake Ebinur; BRS: Borohoro Shan; DA: Dzhungarian Alatau; KGQR: Koguqin Range; KT: Kertau Mountain; TBGT: Tarbagatay Mountain

3.4.2.3.1 Atmospheric Corrections

The high topographic relief (> 2500 m) between the mountainous ranges and the basins has impacts on the unwrapping capacity of the interferograms and also causes significant atmospheric stratified delays correlated with the topography. As we observed the variable performance of the predictive correction from atmospheric models, we first tried, on track D063, to estimate an empirical relationship between the wrapped phase and a crossed function of topography and azimuth. Different from a simple phase-elevation relationship, this attempts to capture the spatial complexity of the stratified delays that can strongly vary from north to south. However, we observed no significant improvement in the unwrapping quality, and there was even some deterioration after applying this correction (Figure 3-16). This is likely because some other parasite signals (such as local hydrological deformation) also correlate with the topography and are thus modified after applying this empirical correction. Therefore, we re-introduced the empirical correction previously removed from each interferogram after unwrapping to avoid deteriorating or modifying the tectonic signal. We then decided to correct for tropospheric delays using the ERA-5 atmospheric model provided by ECMWF for both tracks (Doin et al., 2009, 2015; Jolivet et al., 2011; Daout et al., 2020), which did show better unwrapping results (Figure 3-17).

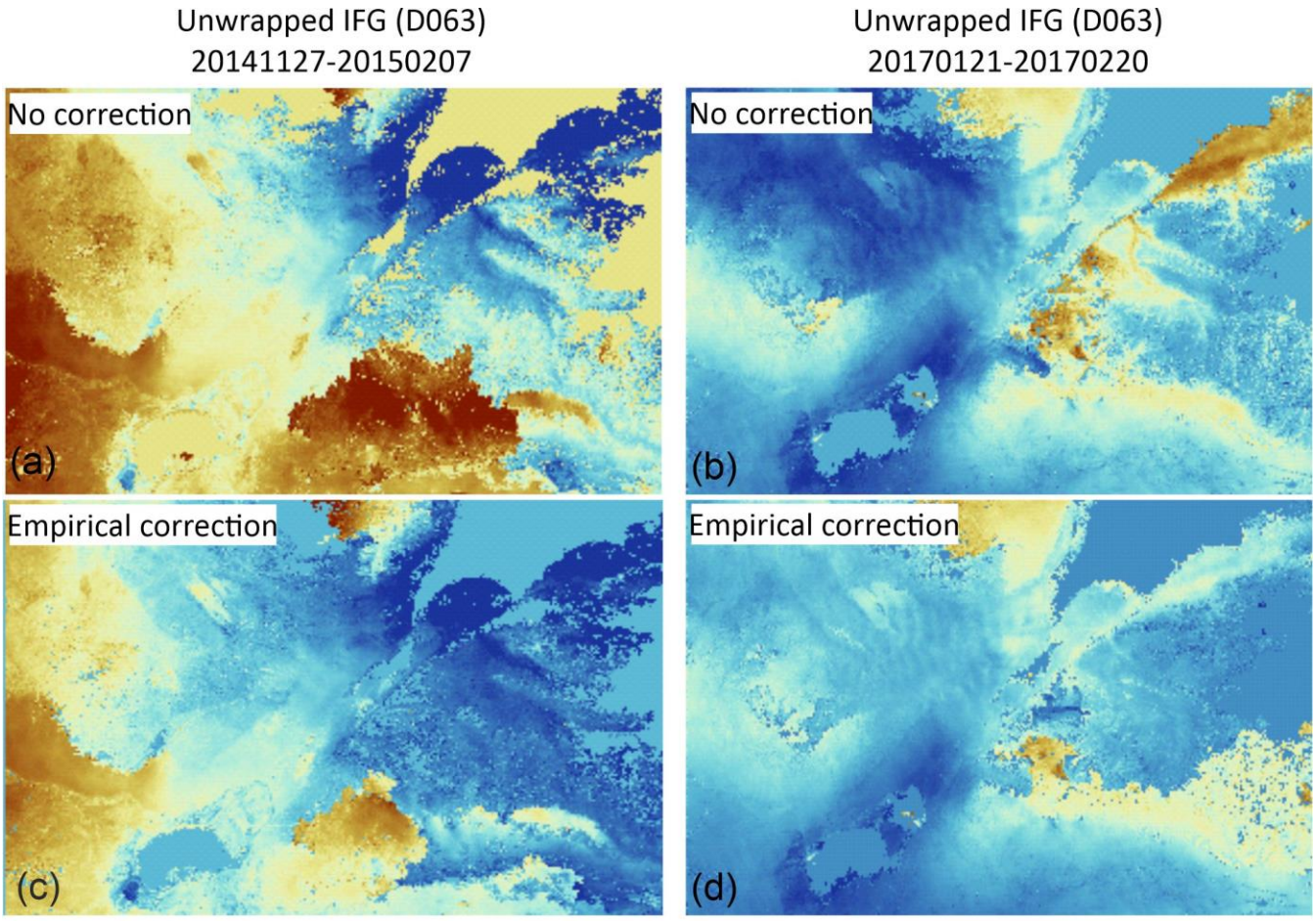

Figure 3-16. Unwrapping results for two example interferograms from D063. The top panels (a) and (b) show the results without any correction before the unwrapping. The middle panels (c) and (d) show the results with empirical phase-topography corrections before unwrapping. This correction seems to slightly improve the unwrapping in the left interferogram (c) but it deteriorates the results in the right interferogram (d).

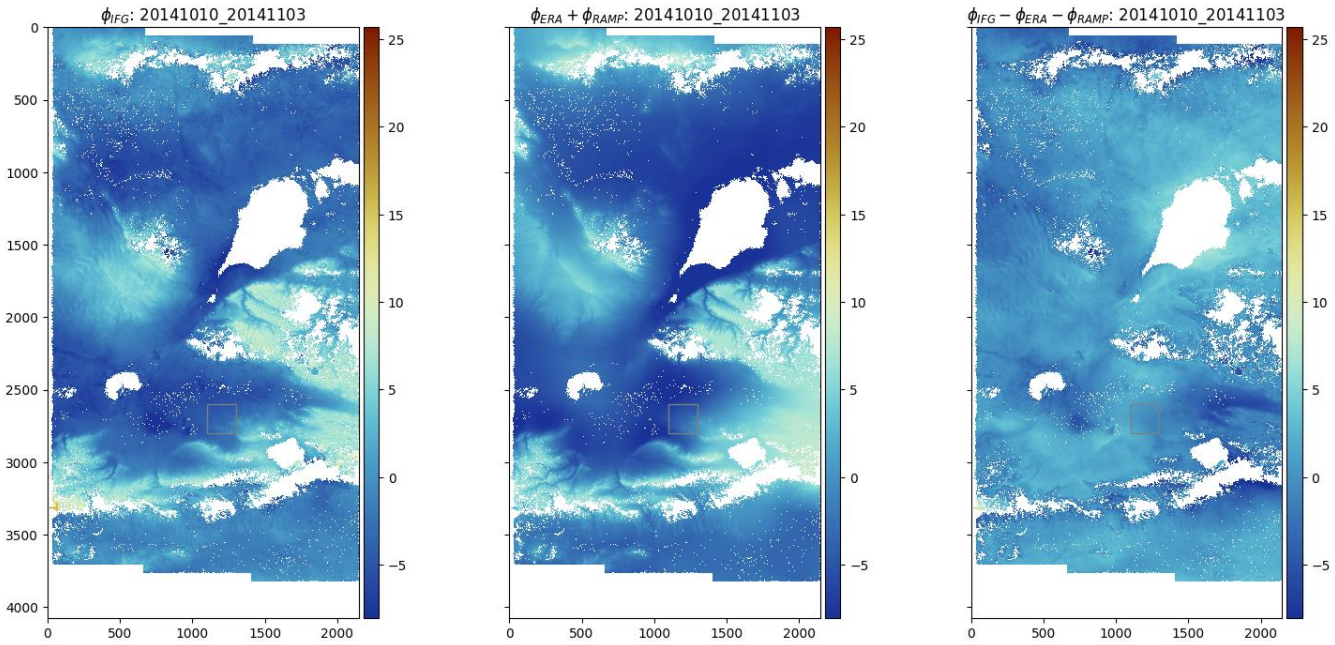

Figure 3-17. Example from the interferogram 20141010_20141103, in D063 radar geometry, demonstrating the tropospheric path-delay correction with ERA-5. Left panel shows the original unwrapped phase. Middle panel shows the phase analysed by the ERA-5 model with a linear phase ramp (see Section 3.4.2.3.3). Right panel shows the corrected unwrapped phase with tropospheric and ramp phases removed.

3.4.2.3.2 Filtering and Multilooking

To reduce the phase noise and the effect of decorrelation in the mountainous areas (Figure 3-15b), we replaced the amplitude of the interferograms by the phase colinearity measurement, which better distinguishes the non-noisy areas from the strength of backscatter of pixels (Pinel-Puysségur et al., 2011). We then multilooked the interferograms by 8 in azimuth (160 × 160 m) for D063 and by 6 in azimuth (120 × 120 m) for A012. We further applied a low-pass filter which is a complex phase average in sliding windows weighted by the phase colinearity (López-Quiroz et al., 2009; Pinel-Puysségur et al., 2011).

3.4.2.3.3 Unwrapping

Following Grandin et al. (2012), we imposed an unwrapping path from the high to low coherent areas, where the coherence is defined by the phase colinearity of the filtered phase. However, despite all the procedures described in the previous sections aimed at improving unwrapping capability, we still observed phase discontinuities, mostly located at the edge of the sedimentary basin or within the agricultural areas, that led to propagating unwrapping errors in the interferograms (Figure 3-15). This kind

of phase pattern mostly appeared in the interferogram pairs acquired across seasons with one or both of the pair in winter or early spring.

To overcome this last unwrapping obstacle, we created a template for each track that has the observed deformation signals. To extract this template, we computed a stack or principal component analysis (PCA) on some selected well-unwrapped interferograms that present the deformation pattern (Yun et al., 2007; López-Quiroz et al., 2009; Daout et al., 2017). The template extracted from PCA better depicted the deformation signals for D063 whereas the stack worked better for A012 (Figure 3-15 and Figure 3-18). We then used these templates to weight the phase colinearity of the filtered phase and to further guide the unwrapping path. The guidance from these templates reduces the colinearity in deforming areas so that these areas are unwrapped last to prevent crossing high phase gradients and propagating errors (Figure 3-19).

After unwrapping, we computed and removed a linear phase ramp in range and azimuth estimated on all unwrapped interferograms. Such ramps are likely caused by the ionospheric phases, orbital inaccuracies, solid earth tide and unmodelled tropospheric delays that are undesired non-tectonics signals (Fattahi & Amelung, 2014b; Gomba et al., 2017; Xiaohua Xu & Sandwell, 2020). The ramp parameters are inverted into time series to check for consistency within the interferometric network, and reconstructed parameters are used to correct all interferograms (Daout et al., 2019). The ramp also helps reference all the interferograms in to a 150 × 150 pixel area at western Bortala Basin (81.93°E, 44.83°N) for D063 and at the Dzhungarian Gate (82.41°E, 45.36°N), north of Lake Ebinur for A012 (Figure 3-13), where the coherence is high with low deformation signals and low topographic gradients.

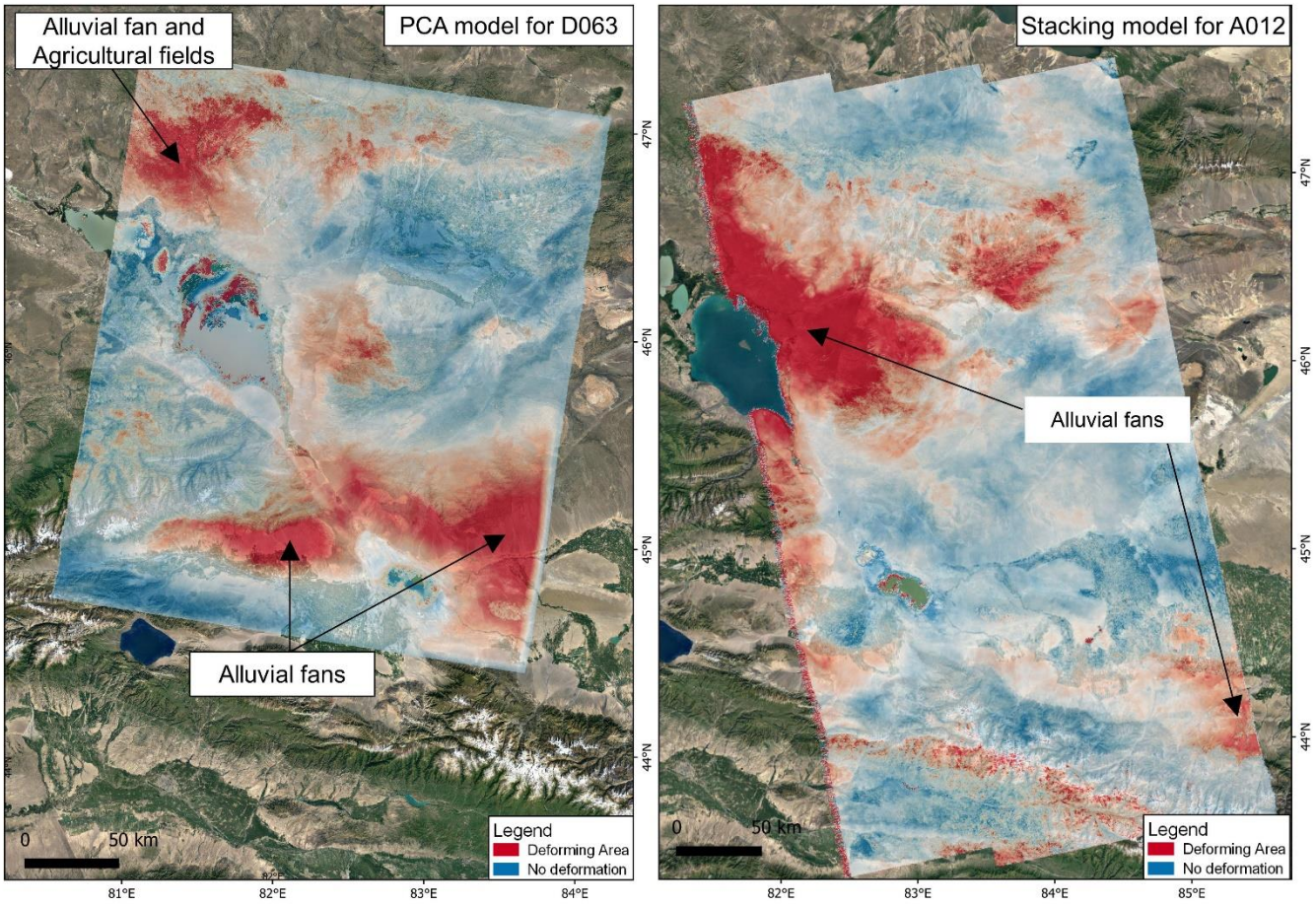

Figure 3-18. The templates depicting the deforming areas from the PCA (left panel) and stack (right panel) of the well-unwrapped interferograms. The deforming areas (red) mostly appear at the edge of basins and the alluvial fans.

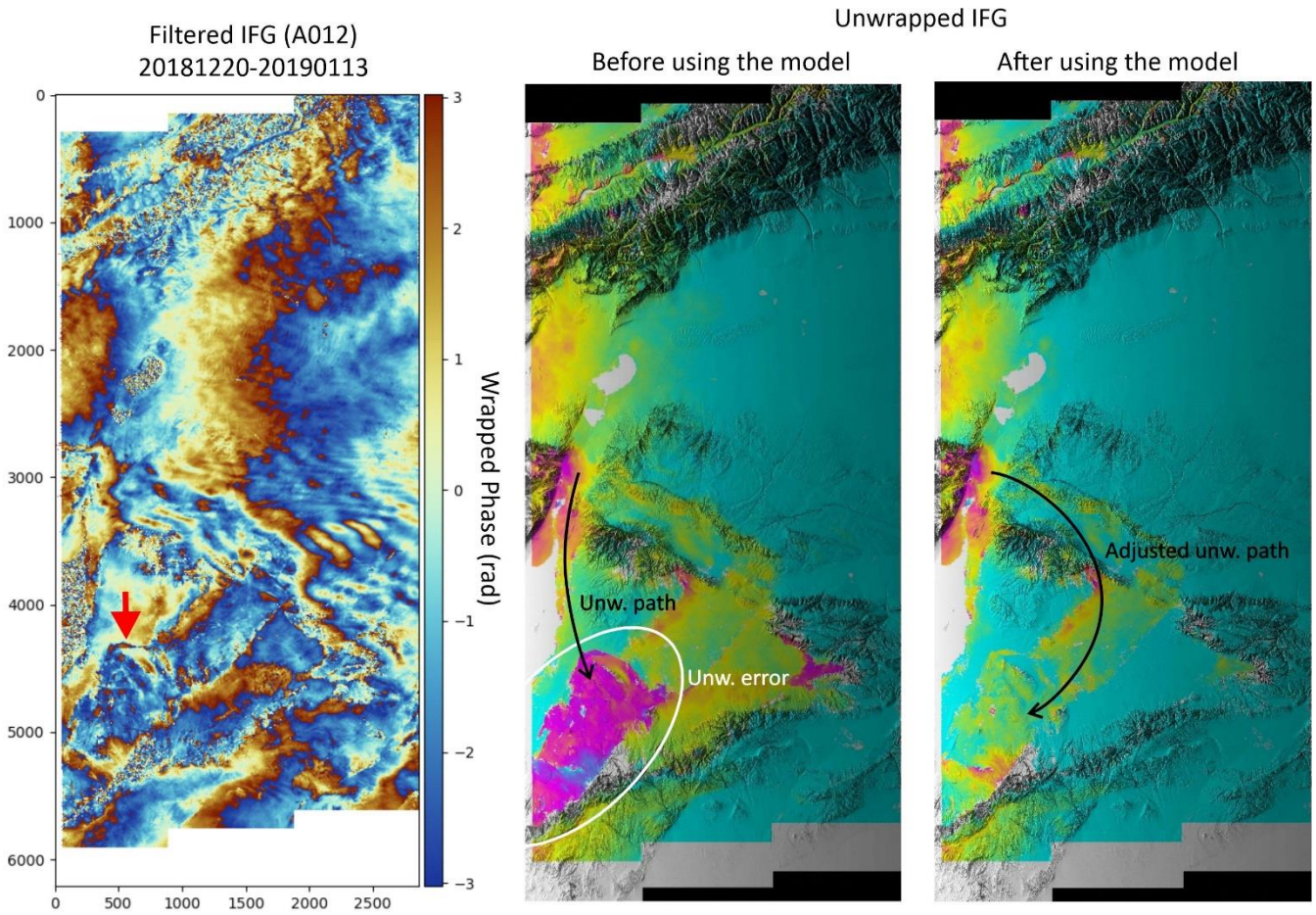

Figure 3-19. Improved unwrapping quality from the example of interferogram 20181220_20190113 of A012 in radar geometry. Left panel shows the original wrapped phase of the interferogram with red arrows pointing to abrupt fringes. Middle panel shows the unwrapping result before applying the stacking model. Right panel shows the improved unwrapping result after applying the model to adjust the unwrapping path.

3.4.2.3.4 Time-series Analysis and Unwrapping Iteration

After unwrapping, we constructed the cumulative time series from an inversion on a pixel-by-pixel basis (López-Quiroz et al., 2009; Doin et al., 2015):

(1)

$$\forall l \in [1, M] = \sum_{n=i}^{n=j-1} \delta\phi_n = \Phi_l$$

(2)

$$-\alpha W_1 \phi_1^s = 0$$

(3)

$$\forall k \in [2, N] \quad \alpha W_k \left(\sum_{n=1}^{n=k-1} \delta\phi_n - \phi_k^s \right) = 0$$

(4)

$$\forall k \in [1, N] \quad \frac{\Upsilon \omega_k \partial^2 \phi_k^s}{\partial t^2} = 0$$

where M and N are the total numbers of interferograms and epochs, respectively for each track. Φ_l is the phase delay of the lth unwrapped interferogram between epoch numbers i and j. $\delta\phi_n$ is the incremental phase delay of each date compared to its preceding dates and is solved from the inversion of Φ_l. ϕ_k is the total phase delay adding from the incremental phases assuming ϕ_1 is zero. α is a weight that is set small for only working on the occasion when missing links exist in the network and W_k is a weight that can be changed at each iteration during the inversion. ϕ_k^s is the evolution of deformation that we set to be smooth in time. Υ is the smoothing coefficient and ω_k equals the average time interval within the five epochs used to calculate the second derivative.

This inversion can first help detect the residual unwrapping errors. It produces products such as the initial LOS velocity map with the overall root-mean-square (RMS) values of every pixel, every interferogram and every epoch. We proceeded with the inversion with an iterative approach. In the first iteration, the RMS misclosure map per pixel, $\phi_{RMS_{pixel}}$, derived from the misclosure of the interferometric network, is used to check the quality of unwrapping for each pixel. The deviation maps, $\phi_{RMS_{ifg}}$, demonstrate the differences between every original interferogram and its reconstructed version after the inversion, which indicate the outlines of unwrapping errors in each interferogram, and help identify and discard the badly-unwrapped interferograms. The RMS map per epoch, $\phi_{RMS_{epoch}}$, averaged from all the deviation maps related to that epoch, can identify certain acquisition that cause mistakes in all their associated interferograms. The errors detected in this step are either corrected by imposing high-priority paths during new unwrapping iterations or discarded by removing the interferograms in the next time series analysis iteration until no large network inconsistency remained (López-Quiroz et al., 2009; Doin et al., 2011, 2015).

Nevertheless, after all the iterations and procedures mentioned above, significant unwrapping errors still exist in many interferograms from both tracks (e.g. Figure 3-20). For those regions with high topographic gradients or at the edge of the sedimentary basin, the unwrapping quality remained relatively

low for interferograms across certain seasons. The large regional moisture variation and the rough topography still pose great challenges for the unwrapping process in our study area.

To manage this issue, we had to find a balance between withdrawing low-quality unwrapped interferograms and maintaining sufficient networks for both tracks. Although interferograms with short temporal baselines (12 or 24 days) might cause systematic biases in time-series results (Ansari et al., 2021), we chose to retain them because these interferograms have good unwrapping qualities which are valuable in our study area. We kept all the short-baseline interferograms for D063 but we excluded 12-day interferograms for A012 since A012 has more available interferograms. Finally, we checked that the phase misclosure computed for the final networks is significantly reduced after several unwrapping iterations and the removal of badly-unwrapped interferograms (Figure 3-21). The final networks include 263 interferograms for D063 and 358 interferograms for A012 (Figure 3-22). The final networks were further inverted using the method with temporal smoothing and automatic correction (López-Quiroz et al., 2009).

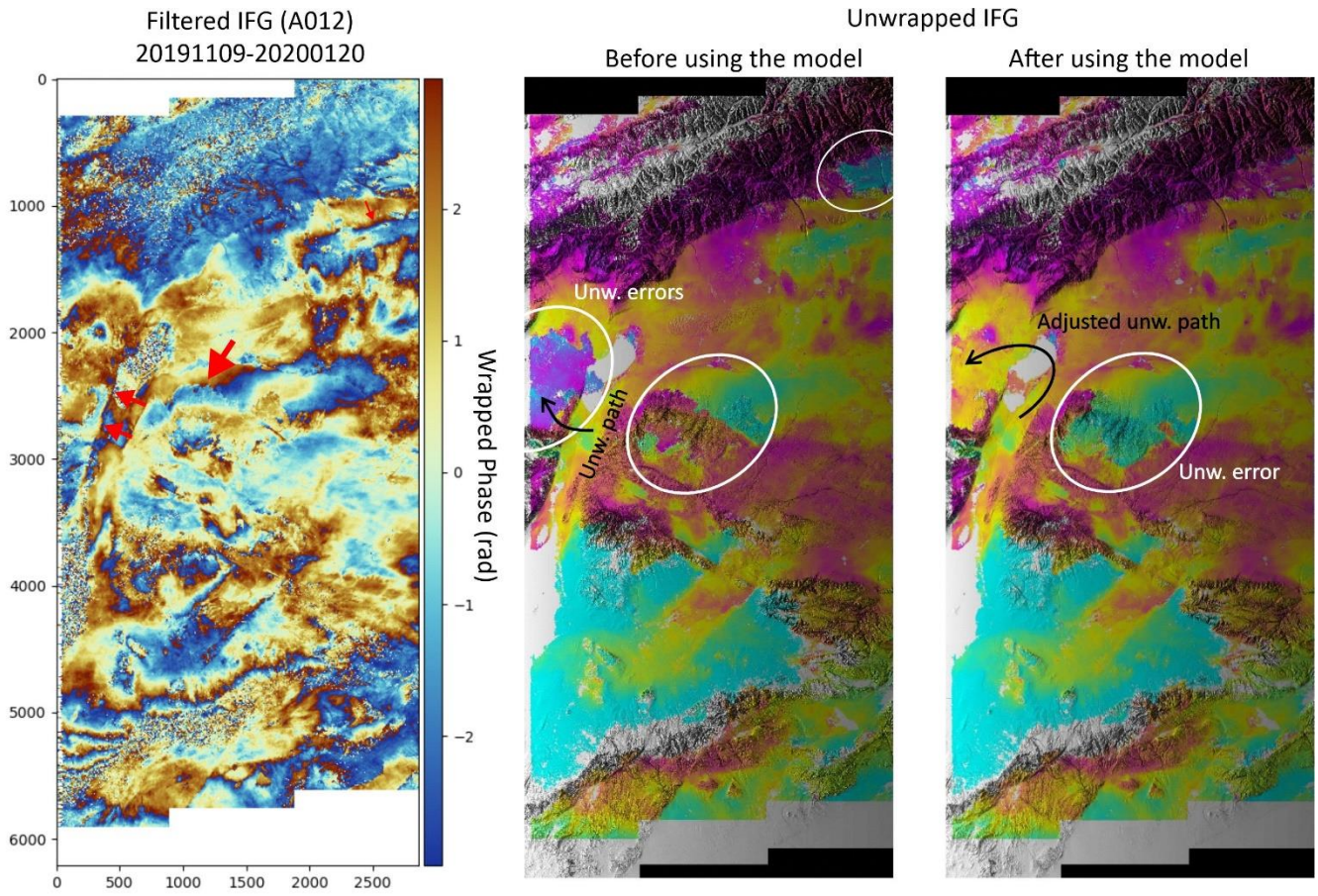

Figure 3-20. Example of interferogram 20191109_20200120 of A012 in radar geometry showing the limitation of the model in improving the unwrapping quality. Left panel shows the original wrapped phase

of the interferogram with red arrows pointing to the abrupt fringes. Middle panel shows several unwrapping errors (white circles) before applying the stacking model. Right panel shows large-area unwrapping errors still exist even after applying the model although some small ones are corrected.

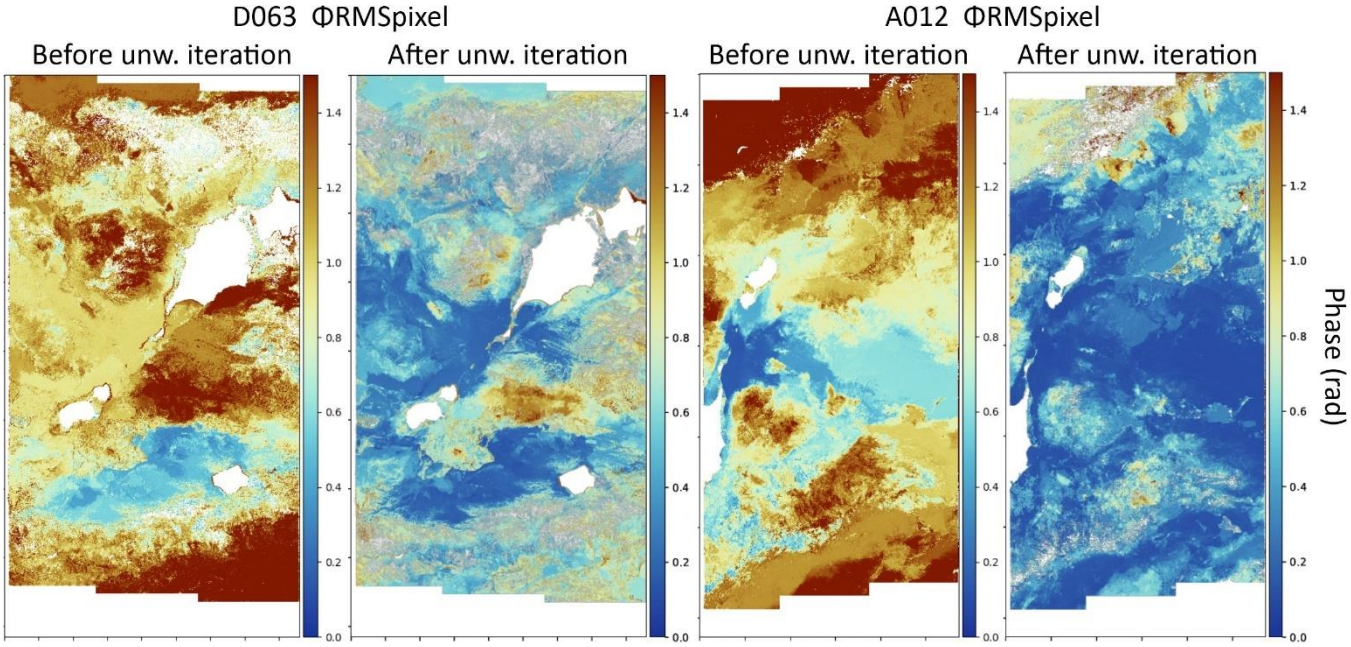

Figure 3-21. Illustration of the $\phi_{RMS_{pixel}}$ maps in radar geometry of both tracks before and after the unwrapping iterations and the removal of badly-unwrapped interferograms.

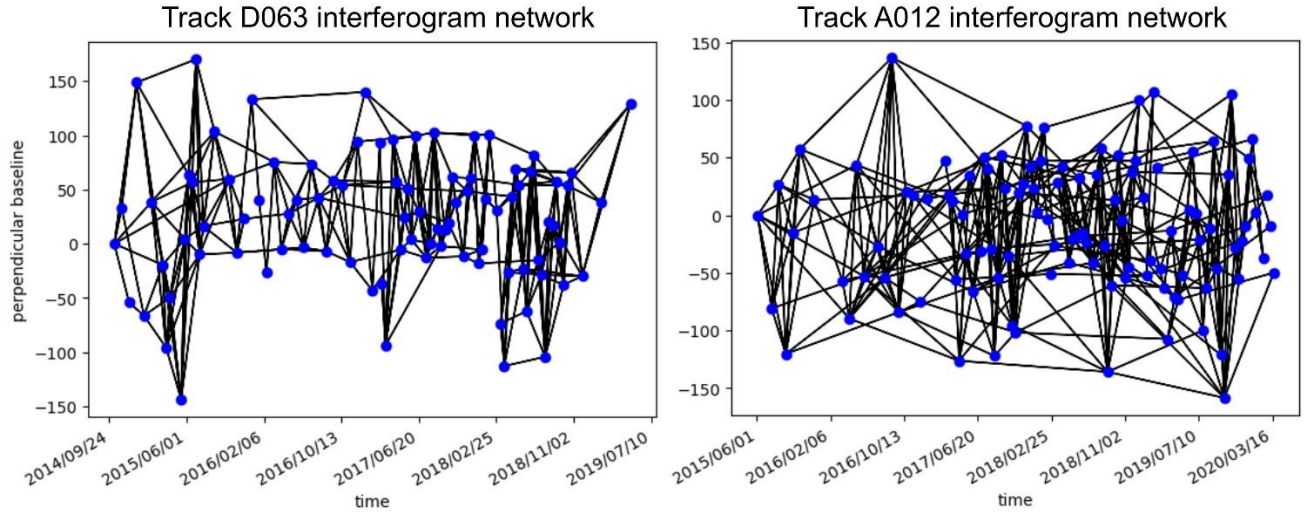

Figure 3-22. The final interferogram networks for the tracks D063 (left) and A012 (right). Blue dots are the epochs and black lines are the interferograms, with 263 for D063 and 358 for A012.

3.4.2.4 Temporal Decomposition

In a final step, we improve the time-series decomposition using an iterative procedure and extract a linear velocity and amplitudes of ground deformation. To reduce the effect of poorly-fit interferograms associated with certain dates on the derived velocity map, we performed a temporal decomposition of the cumulative time series weighted by $\phi_{RMS_{epoch}}$ and with two iterations. In the first iteration, we weighted the acquisitions by $\phi_{RMS_{epoch}}$ and in the second iteration, we weighted the acquisitions by the residual of the first iteration. Since the season-dependent unwrapping quality indicates there is likely non-tectonic seasonal ground deformation in the region, we added a sinusoidal term and a cosine term to the decomposition. Our inversion uses the following equation:

$$LOS(t) = V \times t + B\sin(\omega t) + C\cos(\omega t) \quad (5)$$

where $LOS(t)$, which we already had from the step in Section 3.4.2.3.4, is the phase change of a pixel over the cumulative time t from the first epoch, V is the linear velocity, and B and C are the amplitudes of the sinusoidal and cosine terms, respectively. Our seasonal amplitude map (Figure 3-23) has amplitude equal to $\sqrt{B^2 + C^2}$ and a temporal lag of $\tan^{-1}\frac{B}{C}$ (Daout et al., 2017). The LOS velocity map from this inversion (Equation 5) will, after cleaning, be our final LOS velocity map (V). The uncertainties (σV), displayed in Figure S3-6, in our final velocity measurements are equal to the standard deviation of the residual between $LOS(t)$ and the model-predicted V for each pixel. We solved this temporal decomposition as an inverse problem, $d = Gm$, where d is the data vector made of the cumulative phase displacements, and m is the vector of the model, with a sequential least-square algorithm. The uncertainty ($\sigma_m^{i,j}$) for each pixel i and each parameter j is computed by

$$\sigma_m^{i,j} = \sqrt{\frac{N}{N-M}\left(\sigma_d^i\right)^2 (G^T G)_j^{-1}} \quad (6)$$

where N is the number of data, M is the number of parameters, σ_d^i is the RMS phase residual for each pixel i, and $(G^T G)_j^{-1}$ is the variance of the model (Daout et al., 2017). An initial cleaning step was further applied to the LOS linear velocity maps (V) by masking out the pixels with $\phi_{RMS_{pixel}}$ higher than 0.6 rad (~ 2.7 mm) and with uncertainties (σV) > 1.78 mm/yr for D063 and > 2.00 mm/yr for A012. The different masking thresholds for the two tracks result from a compromise between removing bad-quality pixels and maintaining sufficient data around the fault.

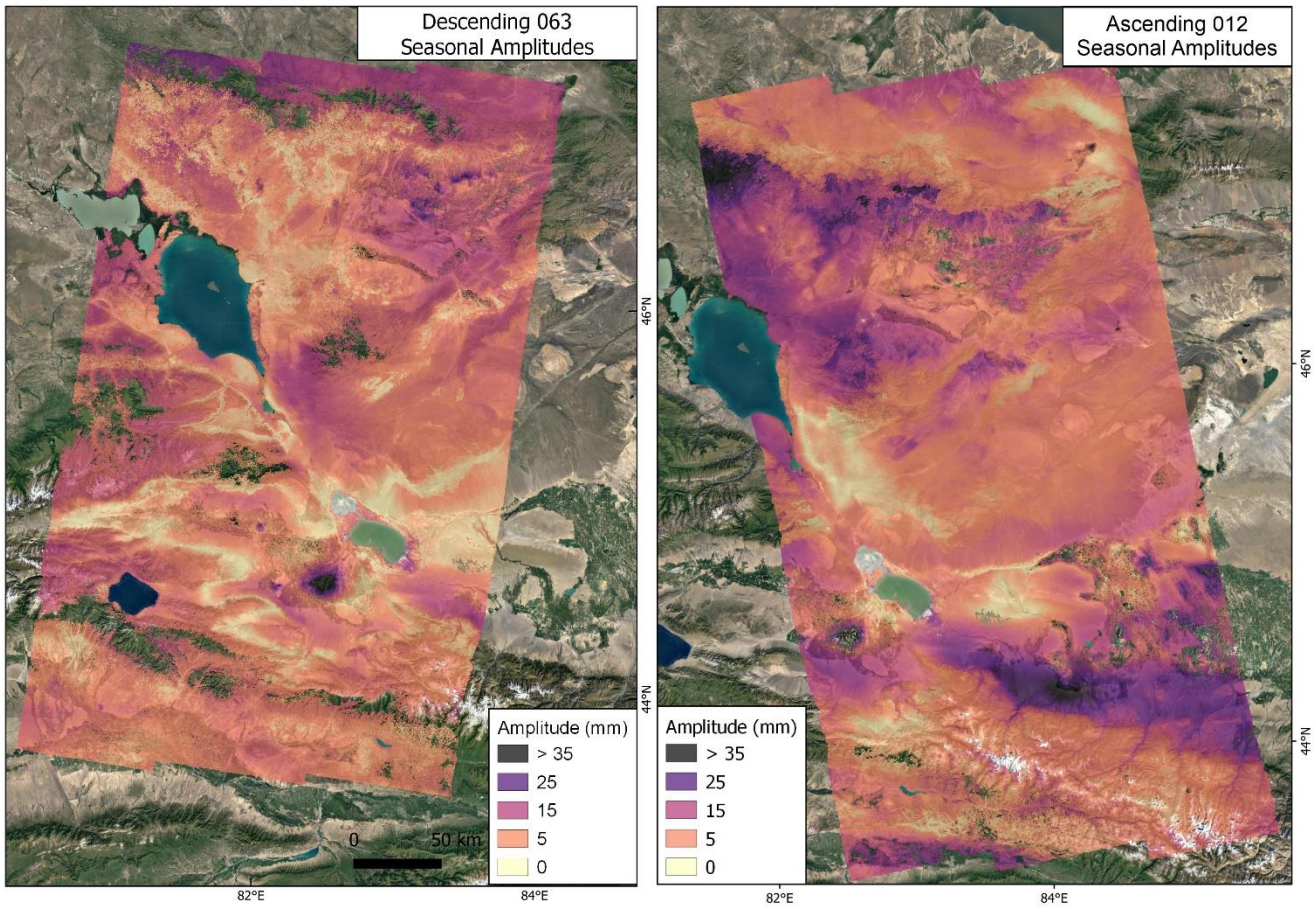

Figure 3-23. Amplitudes of seasonal signals for D063 (left) and A012 (right).

3.4.2.4.1 Seasonal Surface Displacements

The temporal decomposition shows strong seasonal signals mostly appear in agricultural areas, with amplitudes over 50 mm (Figure 3-24), and within several alluvial fan regions. Moreover, the results show the alluvial fans and the agricultural fields have opposite timing of maximum subsidence (Figure 3-25). The alluvial fans in this region regularly moved away from the satellite in both tracks during winter (January to February) (Location 2 and 3 in Figure 3-24), when the average temperature is below 0°C (Figure 3-25). We suggest a reduction in the supply of water from melting snow in the high mountains might cause this relative subsidence effect in the alluvial fans in winter, whilst in spring the fans show relative uplift due to groundwater recharge from increased meltwater volume. The agricultural areas north of the Borohoro Shan and west of Lake Ebinur moved away from the satellite in summer (July to September) in both tracks (Location 1 and 0 in Figure 3-24). This might be due to the extraction of groundwater during the period for irrigation. Since repeated ground water recharge and extraction might cause soil compaction and fissures over time (e.g. Guo et al., 2015; J. Xu et al., 2019), we masked out

pixels with seasonal amplitudes > 16 mm for both tracks (Figure 3-23) to remove secular hydrological signals (e.g. the long-term subsidence at Location 1 in Figure 3-24) from the tectonic deformation maps.

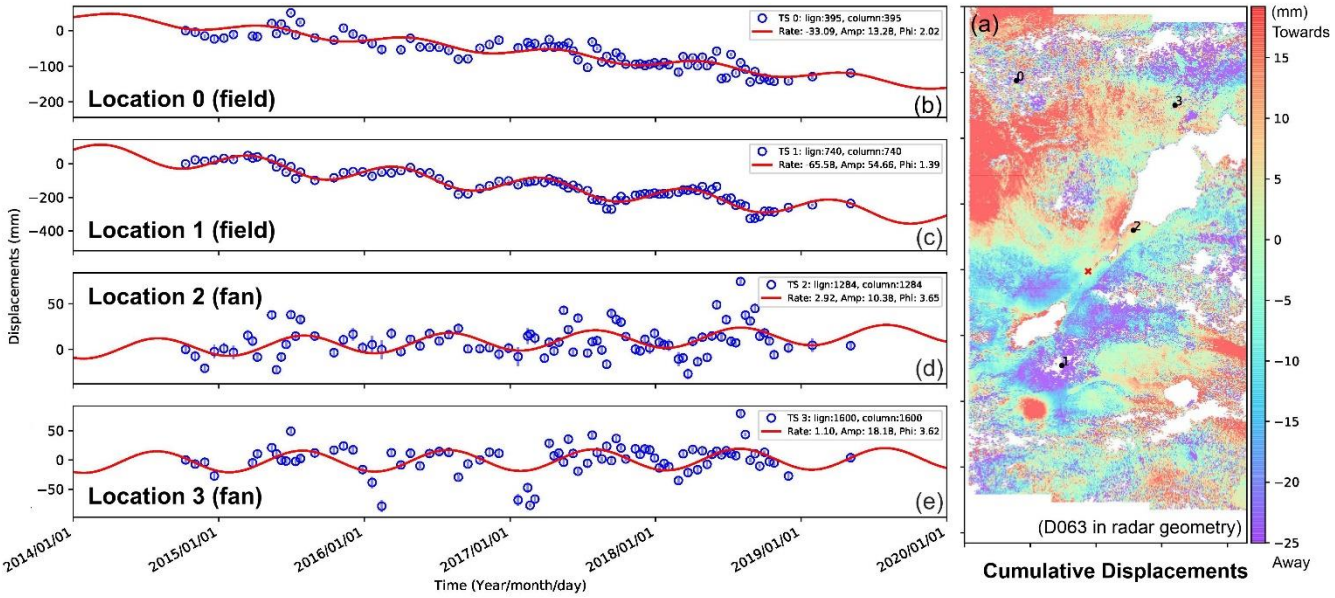

Figure 3-24. (a) InSAR time-series showing the cumulative displacements for D063 (Red cross is the referencing point for the temporal decomposition). (b)-(e) The fitted linear and seasonal displacements for the agricultural fields and the alluvial fan regions for D063. Blue dots are the amount of displacement. Red lines are the fitted displacements, modelled with Equation (5). Locations 0 (b) and 1 (c) are in agricultural fields that show clear secular displacements away from the satellite superimposed on strong seasonal signals. Locations 2 (d) and 3 (e) are in alluvial fans that also show seasonal signals but with the opposite direction of movements to the fields.

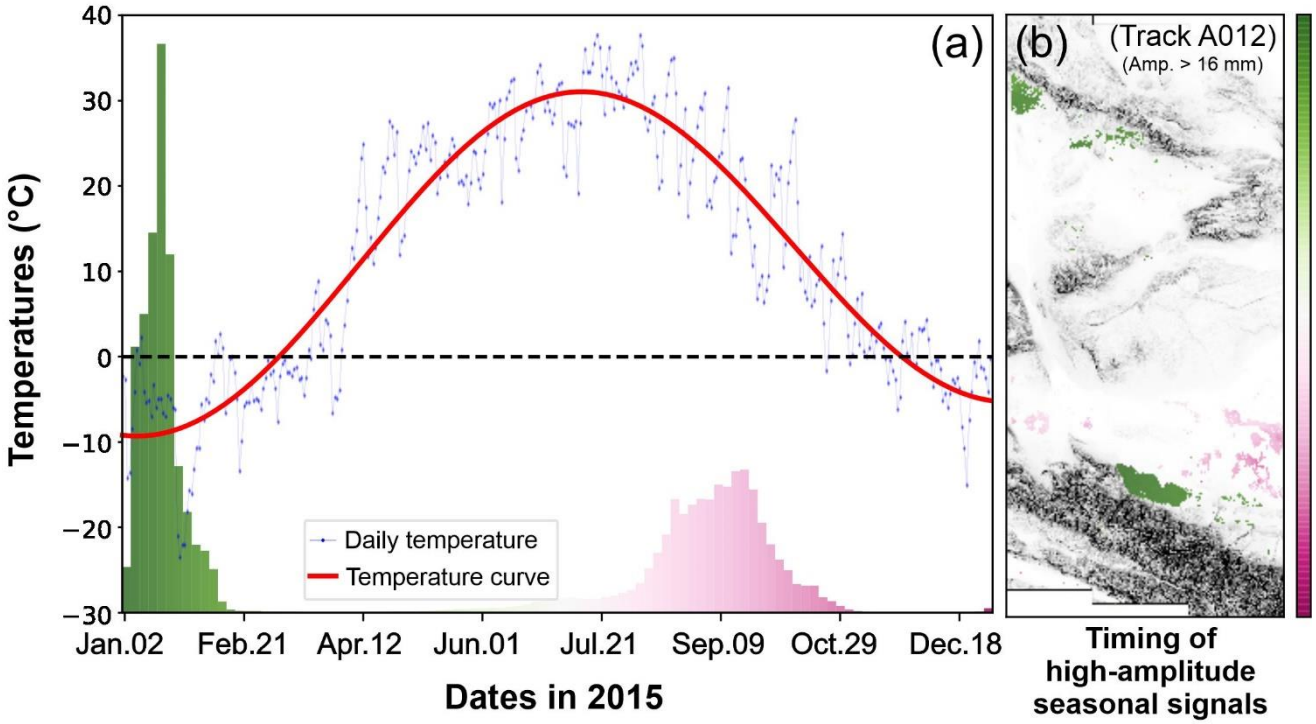

Figure 3-25. (a) Time series of air temperature at 47.45°N, 80.20°E based on the ERA-5 model in 2015. The histogram shows the timing of high-amplitude (>16 mm) seasonal signals moving away from the satellite of A012 and their corresponding regions in (b). The agricultural fields (pink) show movement away from the satellite from late summer to early autumn. The alluvial fans (green) show movement away from the satellite in mid-winter.

3.4.2.4.2 The 2017 Mw 6.3 Jinghe Earthquake

From the inverted LOS velocity and displacement maps, we also observed a coseismic deformation signal from the 2017 Mw 6.3 Jinghe Earthquake (Figure 3-26 and Figure 3-27) (W. Gong et al., 2019; Z. Hu, Li, et al., 2021). This earthquake occurred on the 8th of August in 2017 and is thought to have ruptured a blind thrust with a magnitude of Mw 6.3 (Z. Hu, Li, et al., 2021). Previous InSAR analysis indicates the maximum coseismic slip is ~ 25 cm at a depth of ~14 km (W. Gong et al., 2019). To inspect the coseismic signals, we performed a separated temporal decomposition with a step function, such as:

$$LOS(t) = A \times H(t - t_{eq}) + V_{cos} \times t \quad (7)$$

where t is the SAR acquisition time, t_{eq} is the timing of the earthquake (8th Aug. 2017), V_{cos} is the linear LOS velocity from this Equation (7), and A is the amplitude of the Heaviside step functions (H) for the 2017 Jinghe Earthquake. The coseismic displacement map (A from the equation) shows a smooth long-wavelength uplift signal of ~ 40 km long and no subsidence, as expected from a deep thrust rupture (Figure 3-26). We also inspected some cumulative time series surface displacements around the earthquake, but

observed no post-seismic decays associated with afterslip or possible relaxation of the crust, and thus concluded an absence of post-seismic motion. We decided to mask out the coseismic area with a radius of ~ 20 km to exclude the coseismic deformation signals from the final velocity map (V). This avoids the need to include a step function in our initial temporal decomposition (Equation 5), which would increase the variance of the model.

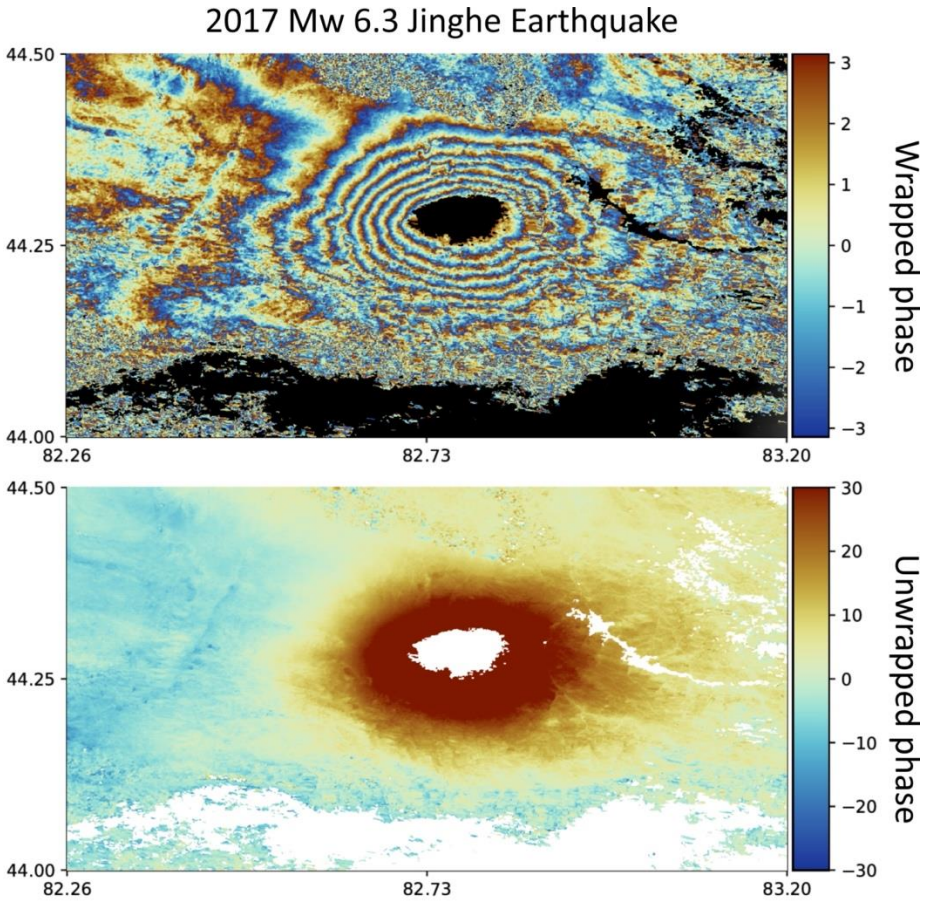

Figure 3-26. Coseismic deformation of the 2017 Mw 6.3 Jinghe Earthquake, revealed by the temporal decomposition of Equation (7), shown in the wrapped phase in the upper panel and unwrapped phase in the lower panel.

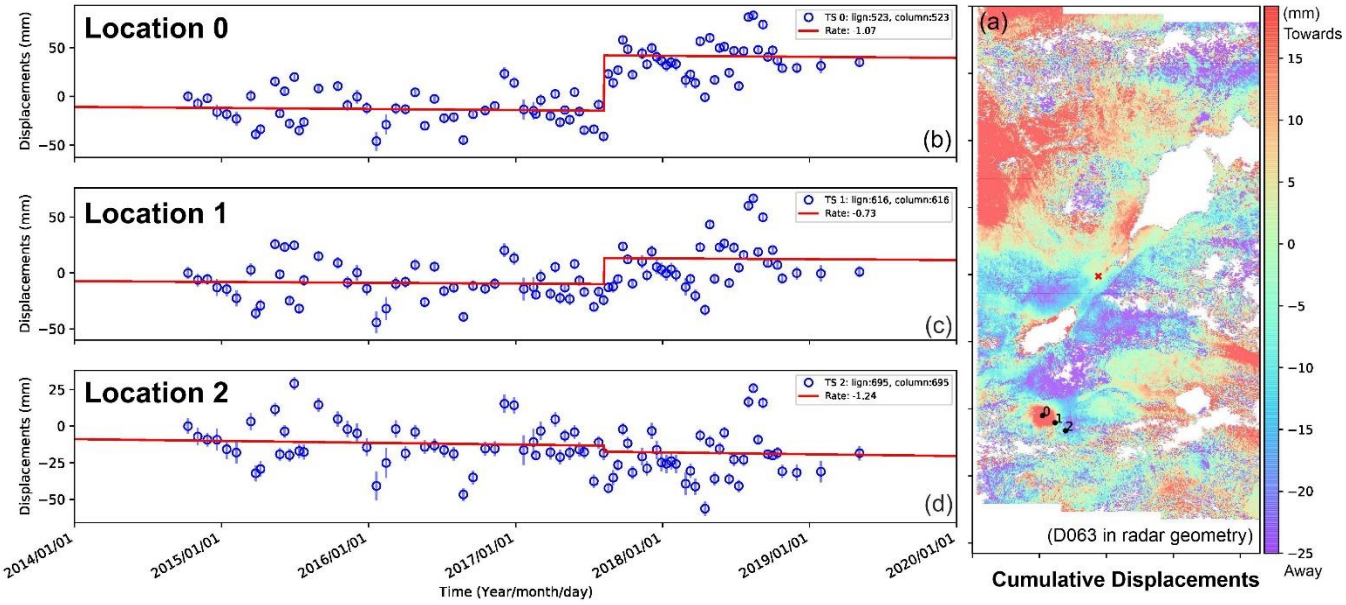

Figure 3-27. (a) InSAR time-series showing the cumulative displacements for D063 (Red cross is the referencing point for the temporal decomposition). (b), (c) and (d) show the coseismic deformation for the 2017/08/08 Jinghe Earthquake at Locations 0, 1 and 2 from the temporal decomposition. Blue dots are the amount of displacement. Red lines are the fitted step functions.

3.4.3 Results and Discussion

3.4.3.1 Interseismic LOS Velocity Fields

Interseismic surface displacements are mainly due to elastic deformation caused by steady-state slip on deep structures. If the shallower faults are fully locked, then the spatial variation of surface strain is very smooth, reflecting the deep strain accumulation. In this case, the long-wavelength tectonic signal might be hardly distinguishable and masked out by shallow surface processes (hydrological, soil creep, etc.). In contrast, if fault locking depths are shallower or if some fault segments exhibit creep close to the surface, then the strain map will show higher spatial variation (centred around fault segments with shallow slip), easily visible on the InSAR deformation field.

From an overview of the LOS velocity fields, we observe no sharp velocity gradients associated with shallow slip, suggesting a large locking depth. A long wavelength signal associated with the right-lateral motion across the DZF is observed in both tracks (Figure 3-28). The interseismic LOS velocity fields are broadly similar to the patterns we expect to observe (sketched in Figure 3-29), considering the DZF is the main active fault with the highest slip rate in this region. Since most of the data in the Dzhungarian Alatau were masked out in the cleaning process, it is difficult to quantify the uplift and

shortening motion across this mountain range from our results. The NE-SW trending faults between the Dzhungarian Basin and the Tacheng Basin are left-lateral strike-slip faults (Zelenin et al., 2021). However, they have either little evidence of Holocene activity, such as the Dalabute Fault (K. Wu et al., 2018) or very low (< 1 mm/yr) slip rates, such as the East Tacheng Fault (~ 0.7 mm/yr) (J. Yu et al., 2021). We, therefore, suggest that those faults are either fully locked with a smooth and long-wavelength strain field indistinguishable from other non-tectonic signals, or accumulating hardly strain in the present time.

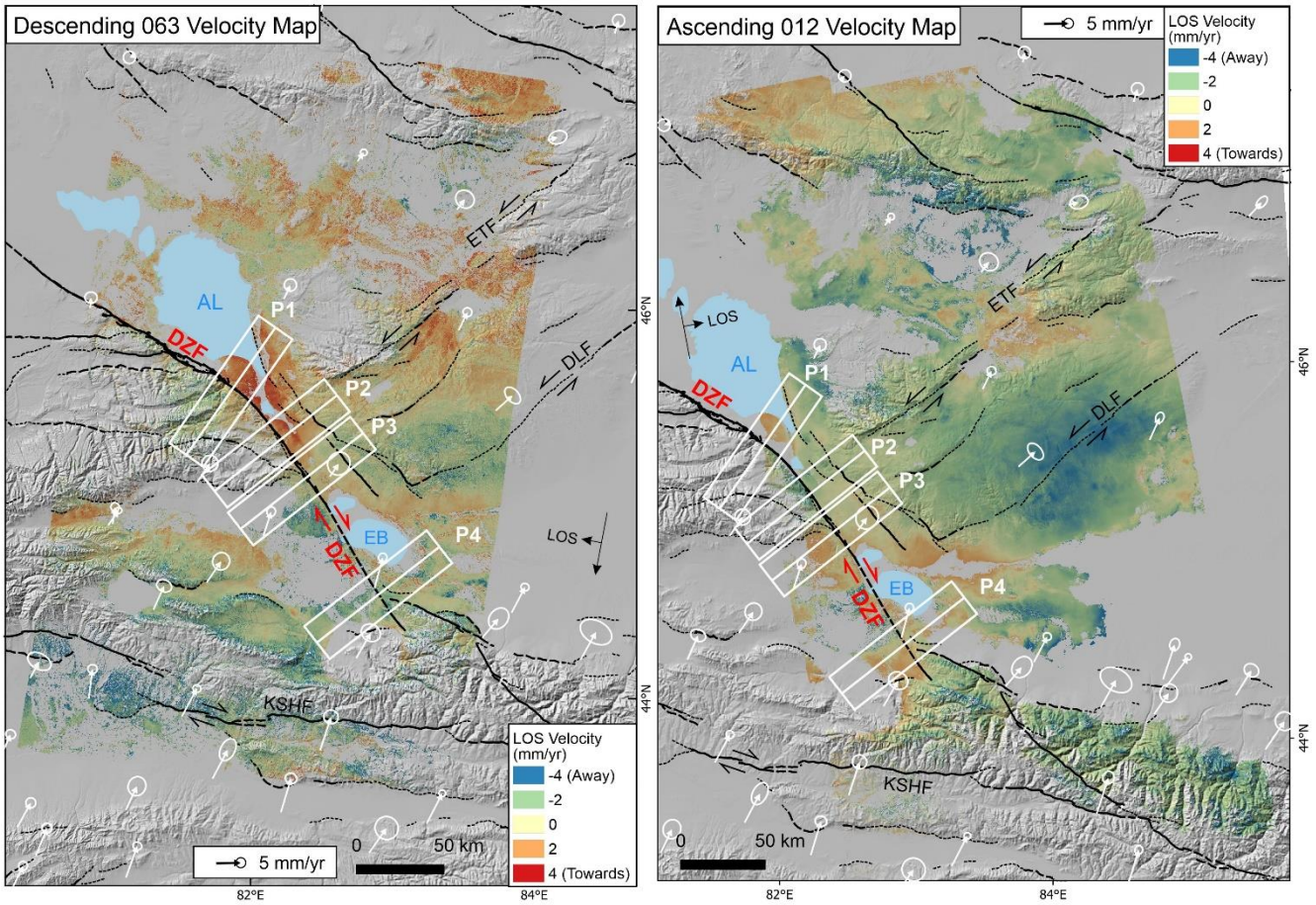

Figure 3-28. LOS velocity maps of the D063 track (left panel) and the A012 track (right panel). The Dzhungarian Fault (DZF) is mapped by this study. The other fault traces and slip rates are from the Active Faults of Eurasia Database (AFEAD) (Zelenin et al., 2021). Other faults with slip rates higher and lower than 1 mm/yr are delineated by black solid and dashed lines respectively. Faults delineated by thinner dashed lines have lower reliability of activity. Locations of the three fault-perpendicular profiles (P1, P2, P3 and P4) are labelled in white on the map with a swath width of 25 km each. Directions of LOS are annotated for each track. GPS velocity vectors are shown with white arrows (Zheng et al., 2017). AL: Lake Alakol; EB: Lake Ebinur; DLF: Dalabute Fault; ETF: East Tacheng Fault; KSHF: Kashihe Fault

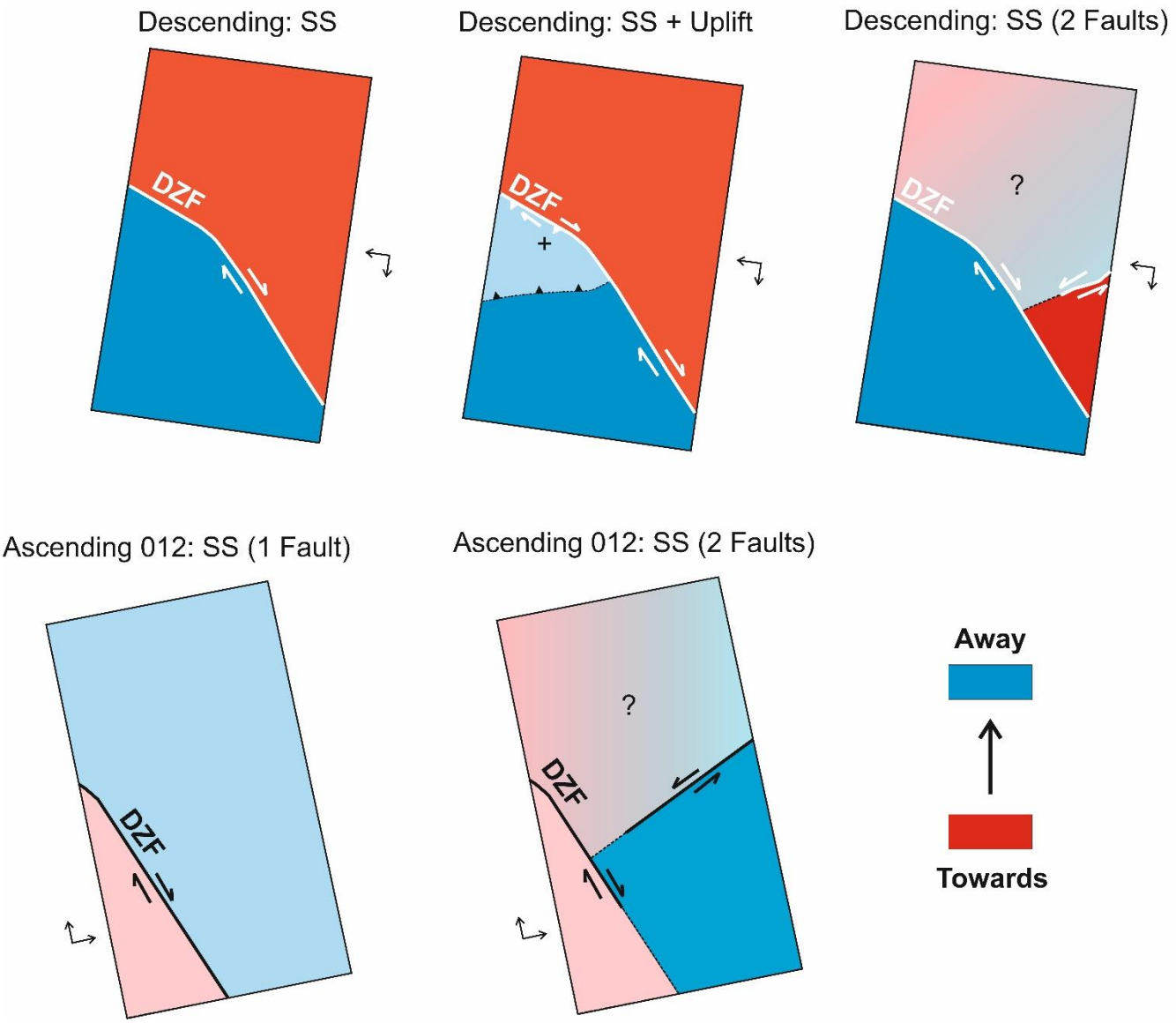

Figure 3-29. Sketch of the expected LOS observations from the right-lateral motion along the DZF. "SS" means only considering the strike-slip component of the DZF. "SS+Uplift" means considering both the strike-slip component of the DZF and the uplift motion of the Dzhungarian Alatau. "SS (2 Faults)" means considering the strike-slip motion of the DZF and the DLF. The "SS" scenario is the most similar sketch to our LOS velocity field.

We make four fault-perpendicular profiles (P1 to P4) across the DZF, avoiding agricultural fields and lakes, in order to examine the LOS velocity changes. The profiles are arranged from north to south along the fault strike and have a length of 90 km and a width of 25 km each (Figure 3-28 and Figure 3-30). The profiles are all centred on our mapped DZF fault trace and are located within the sections we presume to be purely strike-slip. Although the LOS data of A012 is limited in Profiles P1 and P2, all the

profiles show opposite LOS velocity gradients across the DZF in both tracks, demonstrating the expected tectonic signals of right-lateral motion along the fault (Figure 3-31). Note that P1 and P2 show a large increase in velocity in both tracks across the DZF, which will be discussed later. Profile P3 demonstrates a stepwise LOS velocity change of 2 – 3 mm/yr and 1 – 2 mm/yr in D063 and A012, respectively (Figure 3-31). The velocity gradient is greater in D063 than in A012 as expected, since the orientation and the dextral motion of the DZF are more optimally aligned to the descending LOS vector. Profile P4 also demonstrates an opposite direction of LOS velocity gradient in both tracks, but with a similar step of 1 – 2 mm/yr in both tracks. We notice that the LOS velocity changes are not centred on our mapped DZF in P3 and P4 (Figure 3-31). This might be related to the fact that the fault is dipping and locked at large depths, shifting the horizontal position of the strain gradient. It is also likely that our mapped location of the DZF is incorrect due to the less prominent surface ruptures when the fault enters the Bortala Basin. Indeed, the LOS velocity-indicated fault position in P3 is ~ 4 km west of our mapped fault, which could correspond to another possible DZF fault trace mapped by Zelenin et al. (2021) (Figure 3-30). The LOS velocity-indicated fault position in P4 is ~ 7 km east of our mapped fault, which might again be explained by the diffuse and obscure surface trace of the DZF south of Lake Ebinur.

Many non-tectonic signals are also observed in the LOS velocity fields. Although most of the agricultural field areas have been masked out due to the strong seasonal deformation and larger uncertainties, we still observe strong subsidence signals from the remaining data in those regions with similar LOS signals from both tracks (Figure 3-28), which could be attributed to long-term water extraction for irrigation. Although Profiles P1, P2 and P3 cover some small faults distributed in the east of the DZF, we suggest their interseismic strain accumulation is not visible in our LOS velocity fields since those faults also have low slip rates and little Holocene activity, or are fully locked to large depths. Moreover, the LOS velocity fields either disagree with or show no evidence for the movements on those small faults (Figure 3-30) (Zelenin et al., 2021), suggesting noise or non-tectonic signals in our data are higher than their interseismic strain accumulation. We note that there are multiple short-wavelength signals and some of them are localised in specific regions, especially in fans near the lakes and agricultural fields (Figure 3-28 and Figure 3-30). For example, in Profile P1, the velocity step change across the DZF is up to ~ 3 mm/yr in both tracks but this increased velocity drops at the boundary between the alluvial fans and the lake, which is about 18 km NE of the DZF (Figure 3-31). We suggest the large increase in velocity in both tracks across the DZF in profiles P1 and P2 is a result of short-wavelength positive LOS signals from the alluvial fans south of Lake Alakol rather than tectonic deformation. Such short-

wavelength and high-amplitude signals might reflect surface hydrological deformation of the ground surface or residual moisture/turbulent signals. This non-tectonic fan uplift could also explain the V-shape velocity bounce in A012 across the DZF in Profile P1 and P2 (Figure 3-31). Other short-wavelength LOS velocities east of the DZF mostly follow the same trend in both tracks, which suggests vertical movements are dominating in those areas, possibly caused by hydrological processes. These short-wavelength signals in both tracks may also be the result of stratified atmospheric delays. In addition, there are some apparent topographic-correlated signals in the southwestern edges of the Bortala Basin and north of Lake Ebinur in D063 (Figure 3-13 and Figure 3-28). This means some residual stratified atmospheric delays might still be included in the velocity map.

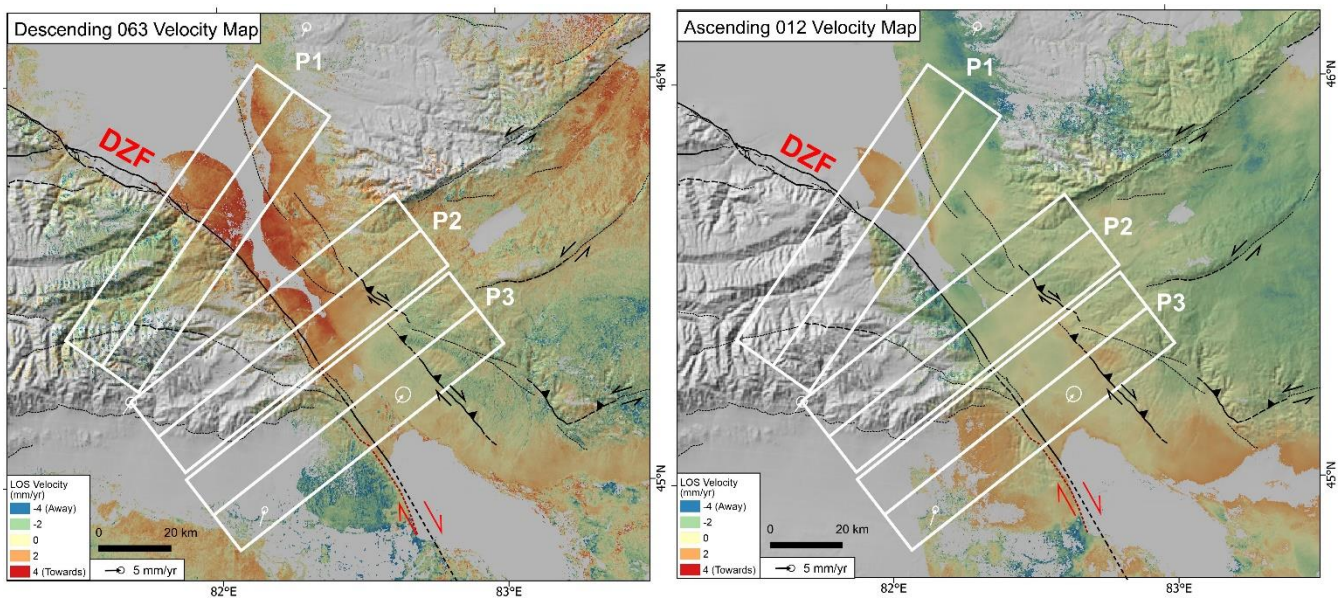

Figure 3-30. Zoomed-in LOS velocity fields and the profile locations for P1, P2 and P3. The brown dashed line is another possible DZF fault trace mapped by Zelenin et al. (2021).

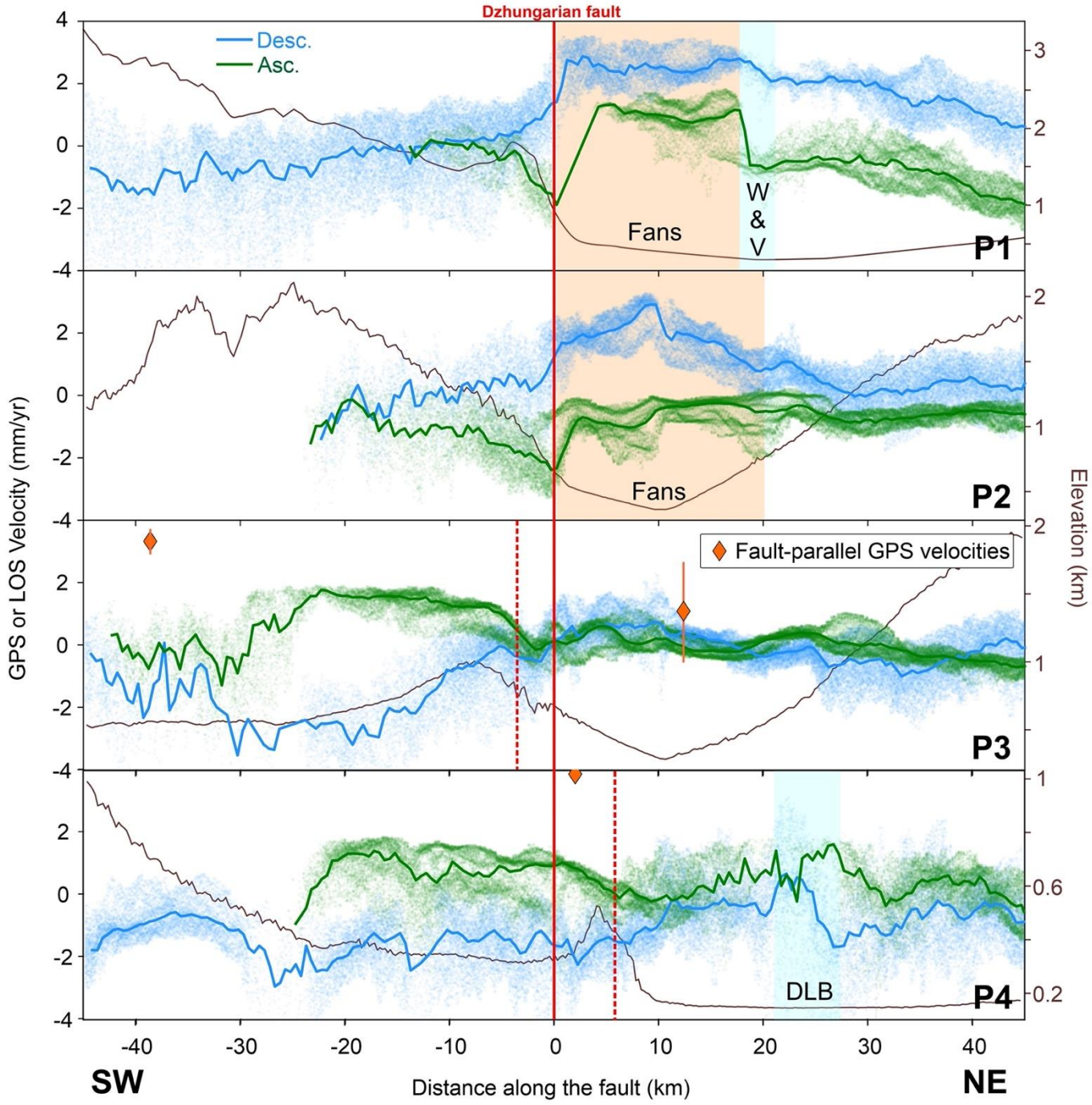

Figure 3-31. Four LOS velocity (blue and green dots), fault-parallel GNSS (orange diamonds) and elevation (brown lines) profiles. Blue and green lines are the mean LOS velocity for D063 and A012, respectively. Red lines are our mapped location of the DZF. Dashed-red lines in P3 and P4 are the DZF fault locations inferred from the LOS velocity. GNSS data are the absolute values from Zheng et al. (2017). Light orange colours in P1 and P2 are the alluvial fan areas in the south of Lake Alakol. W & V: Water and vegetation; DLB: Dry lakebed

3.4.3.2 Fault-parallel LOS Velocity Profiles

We implemented a decomposition of the LOS velocities into N142°E horizontal and vertical directions, within the overlapping area of both tracks, to better analyse the InSAR results and to reduce the noise in the data. The LOS data are down-sampled to a 90-m grid before the decomposition. We further assumed no displacements in the dip-slip direction of the DZF for the decomposition, which fits with geological observations along the southern DZF (Tsai et al., 2022), and which has the advantage of being independent of interpolations of the scarce GNSS data in this area. We took the azimuth and look angle for every overlapped pixel in both tracks and used the derived velocity uncertainty in the modelled linear velocity (σV) as a prior uncertainty matrix to help solve the associated least-square uncertainties of each pixel for the inversion (Figure 3-14a and Figure S3-6) (Wright et al., 2004). In this decomposition, the velocity vectors with opposite directions in ascending and descending tracks were projected to the N142°E horizontal component.

The preliminary observations from the LOS velocity fields are mostly consistent with the decomposed fault-parallel and vertical components (Figure 3-32a,b). The alluvial fans around the lakes and the agricultural areas have positive vertical velocities (uplift) whilst the agricultural fields, although mostly masked out, have negative vertical velocities (Figure 3-32b), in agreement with our previous interpretation from the seasonal analysis. From the fault-parallel component map, the velocity pattern agrees with the known right-lateral DZF movements; however, there is a short-wavelength velocity gradient north of the location of profile P3, which could be caused by residual moisture/turbulent signals considering the high seasonal amplitudes of the alluvial fan in this region and the high topographic relief at the Dzhungarian Gate (Figure 3-13 and Figure 3-32a). Therefore, we only examine the fault-parallel velocities from profiles P3 and P4.

Profiles P3 and P4 both show a long-wavelength velocity gradient across the DZF, which is consistent with the right-lateral displacement of the fault and the decomposed fault-parallel velocities are similar to the GNSS velocities (Figure 3-33). The velocity gradients in P3 and P4 indicate the lateral slip rate of the DZF is ~ 4 – 7 mm/yr and ~ 2 – 5 mm/yr respectively (Figure 3-33). We further used a simple arctangent function to fit these two fault-parallel velocity profiles with a model in a 2-D elastic half-space (Weertman & Weertman, 1964; Savage & Burford, 1973), specifically:

$$v = \frac{S}{\pi}\tan^{-1}\left(\frac{x}{LD}\right) \quad (8)$$

where v is the surface fault-parallel velocities (in mm/yr), S is the fault strike-slip rate (in mm/yr), x is the distance (in km) to the fault and LD is the locking depth (in km) of the fault. The fitting was implemented using the non-linear least squares method in SciPy (Virtanen et al., 2020). During the fitting, we assigned a prior range for each parameter: strike-slip rate, locking depth and fault location.

We first set the ranges encompassing 0 – 7 mm/yr for the slip rate, 0 – 30 km for the locking depth and -20 – 20 km for the DZF location. The best fit for P4 shows a strike-slip rate of 3.60 ± 1.03 mm/yr and a locking depth of 12.37 ± 47.44 km (Figure 3-34c). However, the best fit for P3, under this prior range, produces a poorly fitting curve with an unconvincing shallow locking depth of 0.5 km, which disagrees with our observation of no sharp velocity gradient (Figure 3-34a). We thus adjust the prior ranges of the locking depth to be 5 – 25 km for P3. We further exclude the data in P3 that are > 30 km away from our mapped DZF in the west since they are far-field velocities with a noisy pattern suggesting a possible non-tectonic origin (Figure 3-32a). The best fit for P3 under the adjusted prior ranges shows a better fitting curve with a slip rate of 6.51 ± 0.46 mm/yr and a locking depth of 5.14 ± 2.24 km (Figure 3-34b). We could not get a well-constrained locking depth for P4 under any prior ranges, but earthquake catalogues do show seismicity with depths over 12 km around the region (e.g. the 2017 Jinghe Earthquake) (Sloan et al., 2011; ISC, 2021, 2022; U. S. Geological Survey, 2022).

The modelled slip-rate results of P3 and P4 do not overlap with each other. The geodetic lateral slip rate of 3.60 ± 1.03 mm/yr derived from P4 is comparable to the previously-derived geodetic slip rate of ~ 4.8 mm/yr by G. Li et al. (2016) from GNSS measurements near Alashankou, whilst the slip rate of ~ 6.5 mm/yr derived from P3 is higher than any of the previously-reported rates. These discrepancies of the locking depths and the slip rates along the southern DZF might be due to the variation in frictional strength of the underlying crust, which could be a result of the varying lithology, geothermal and fluid conditions, or the transient temporal variation of interseismic slip throughout the seismic cycle (Hetland & Hager, 2006; K. Wang et al., 2012; Meade et al., 2013; Loveless & Meade, 2016; Diao et al., 2019). However, we note that extra uncertainties exist since these inferred geodetic slip rates and locking depths are under the assumption of no dip-slip along the fault, which is unlikely due to the natural complexity of fault geometry. In addition, there is at least ~ 2 mm/yr of uncertainty in the decomposed velocity (Figure S3-7). Thus, more geodetic data with wider coverage and lower uncertainty will be needed in the future to better constrain the geodetic slip rate of the DZF.

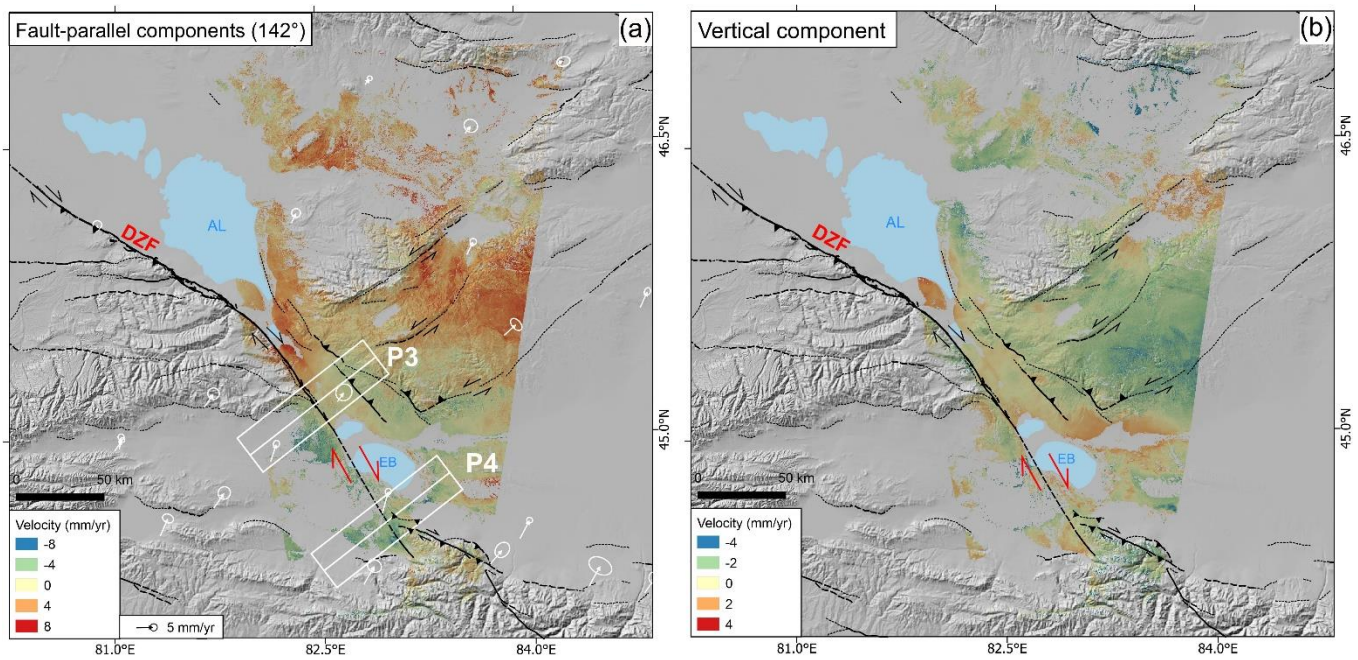

Figure 3-32. Decomposition of the LOS velocity fields into DZF fault-parallel (N142°E) (a) and vertical components (b). GPS velocity vectors are shown as white arrows (Zheng et al., 2017). AL: Lake Alakol; EB: Lake Ebinur.

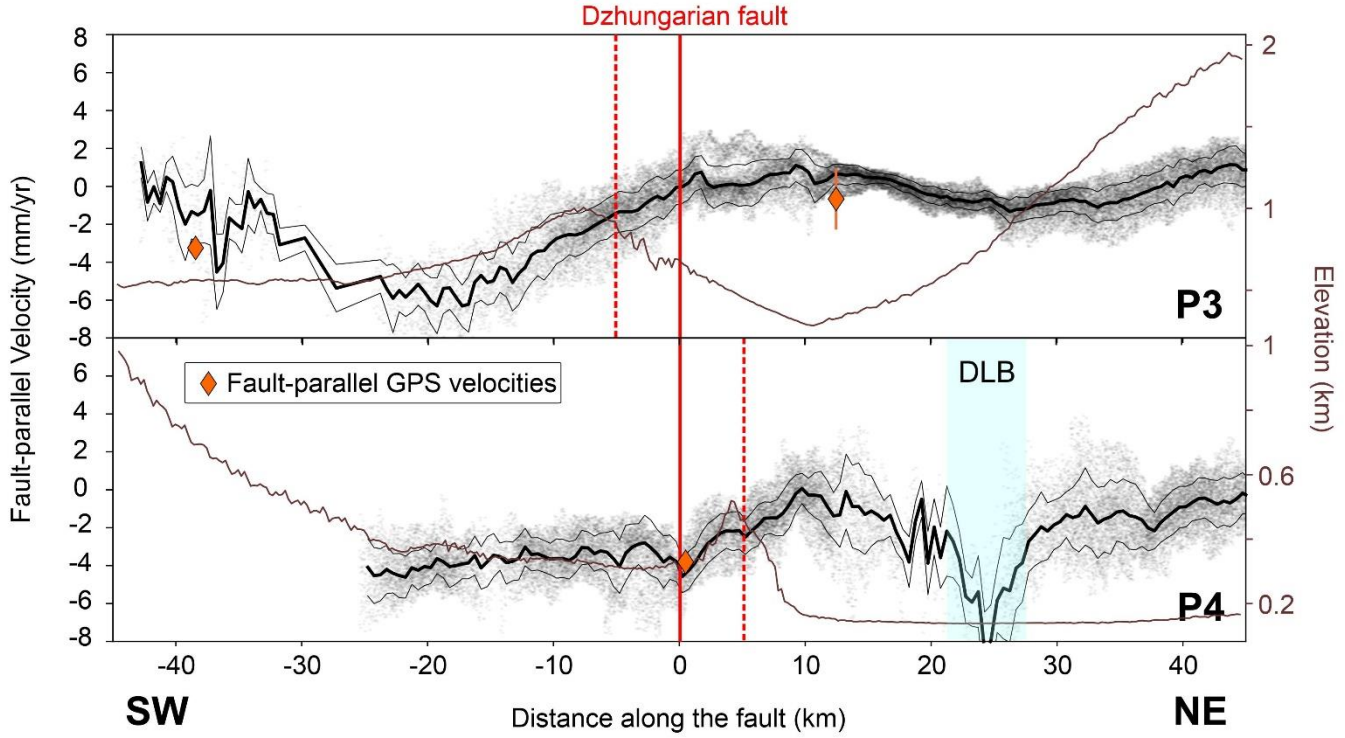

Figure 3-33. Fault-parallel velocity (black) and elevation (brown) profiles for P3 and P4 across the DZF. GNSS data (orange diamonds) are from Zheng et al. (2017). Positive velocity means movement towards the direction of N142°E. Negative velocity means movement away from the direction of N142°E. The red

line is our mapped DZF fault trace. Dashed-red lines in P3 and P4 are the centres of the velocity change. DLB: Dry lakebed

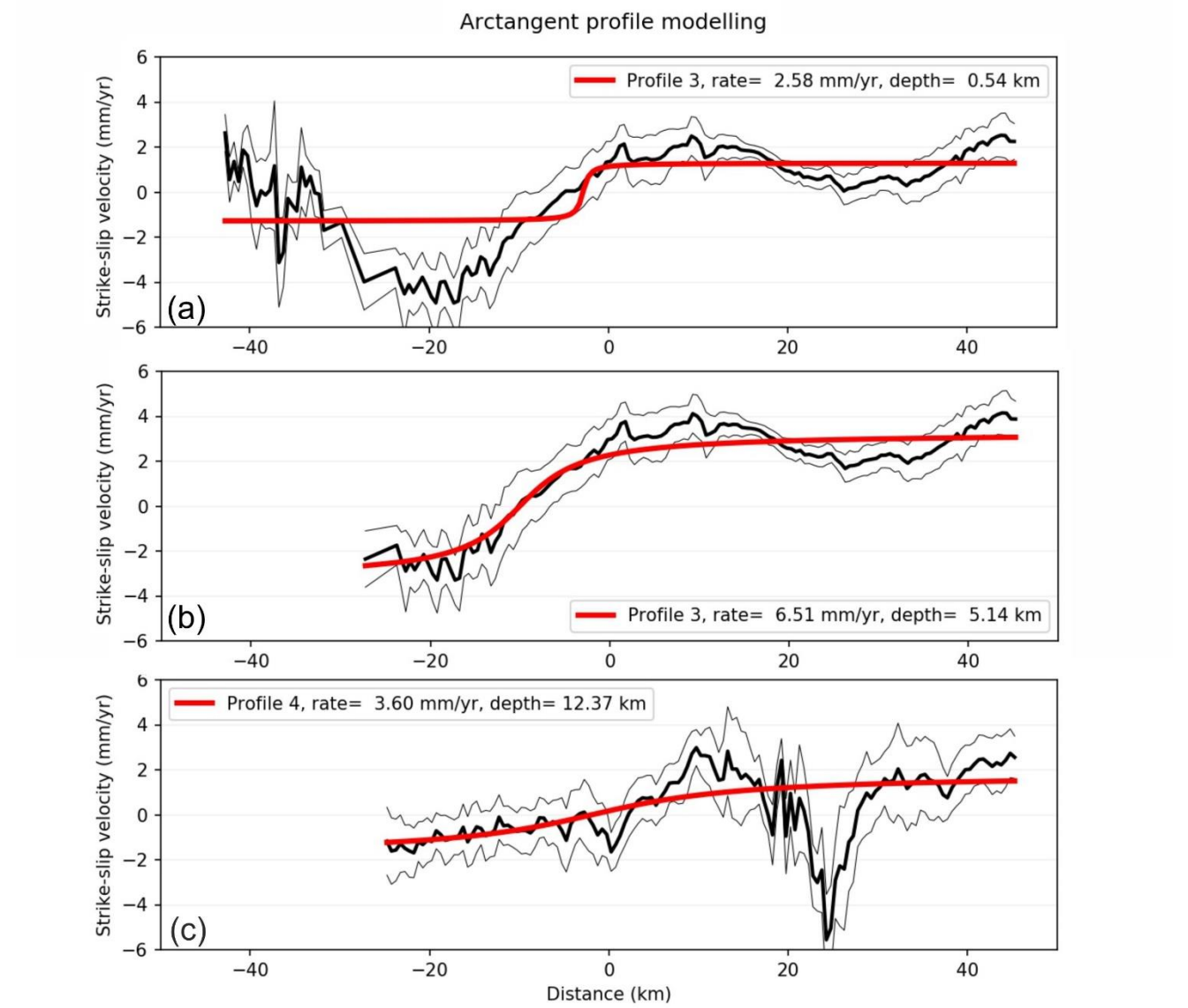

Figure 3-34. Arctangent curve fitting (red lines) for profiles P3 and P4. Thick black lines are the mean value of the fault-parallel velocities and thin black lines are the standard deviation of the velocities. (a) and (c) The best fits for P3 and P4, respectively, with prior ranges encompassing 0 – 30 km for the locking depth. (b) The best fits for P3 with prior ranges encompassing 5 – 25 km for the locking depth.

3.5 Discussions

3.5.1 Comparison of Geological and Geodetic Slip Rates

We estimate a lateral geological slip rate on the southern DZF of 3.4 ± 1.3 mm/yr based on the TCN ages. This rate is consistent with the geodetic strike-slip rate of 3.60 ± 1.03 mm/yr derived from the modelling of InSAR profile P4 (Figure 3-35). It is worth noting that larger uncertainty might exist for both geological and geodetic results due to the essential assumptions and the limited spatial and temporal resolution of sampling. Nevertheless, the geological and geodetic lateral slip rates are comparable within error through the southern DZF, from the Rygayty River to the Jinghe River East. The slip rate of ~ 6.5 mm/yr derived from InSAR profile P3 might be an outlier because the estimated slip rates from this work and previous studies are all within the range of 1 – 5 mm/yr. Thus, we can summarise that all the geological and geodetic lateral slip rates result on the southern DZF overlap at ~ 3.5 mm/yr with the range of 2.1 – 4.7 mm/yr covering all the uncertainties.

The similar geological and geodetic slip rates indicate that strain has been accumulated at a constant rate in this area since ~ 100 ka and that there could be quasi-periodic earthquake occurrence on the southern DZF (Chéry & Vernant, 2006). A consistency between geological and geodetic slip rates has been observed in other major continental strike-slip faults such as the Doruneh Fault (Mousavi et al., 2021), the Haiyuan Fault (J. Liu et al., 2022), the Altyn Tagh Fault (He et al., 2013) and the Main Kopetdag Fault (Dodds, Daout, et al., 2022), with most of them recorded as having hosted large and lethal historical earthquakes. The lateral slip rates we calculated also support the previously proposed counterclockwise block rotation kinematics in the northern Tien Shan, which require a total lateral slip rate of ~ 3.5 mm/yr on the DZF (Campbell et al., 2013; C. Wu et al., 2020).

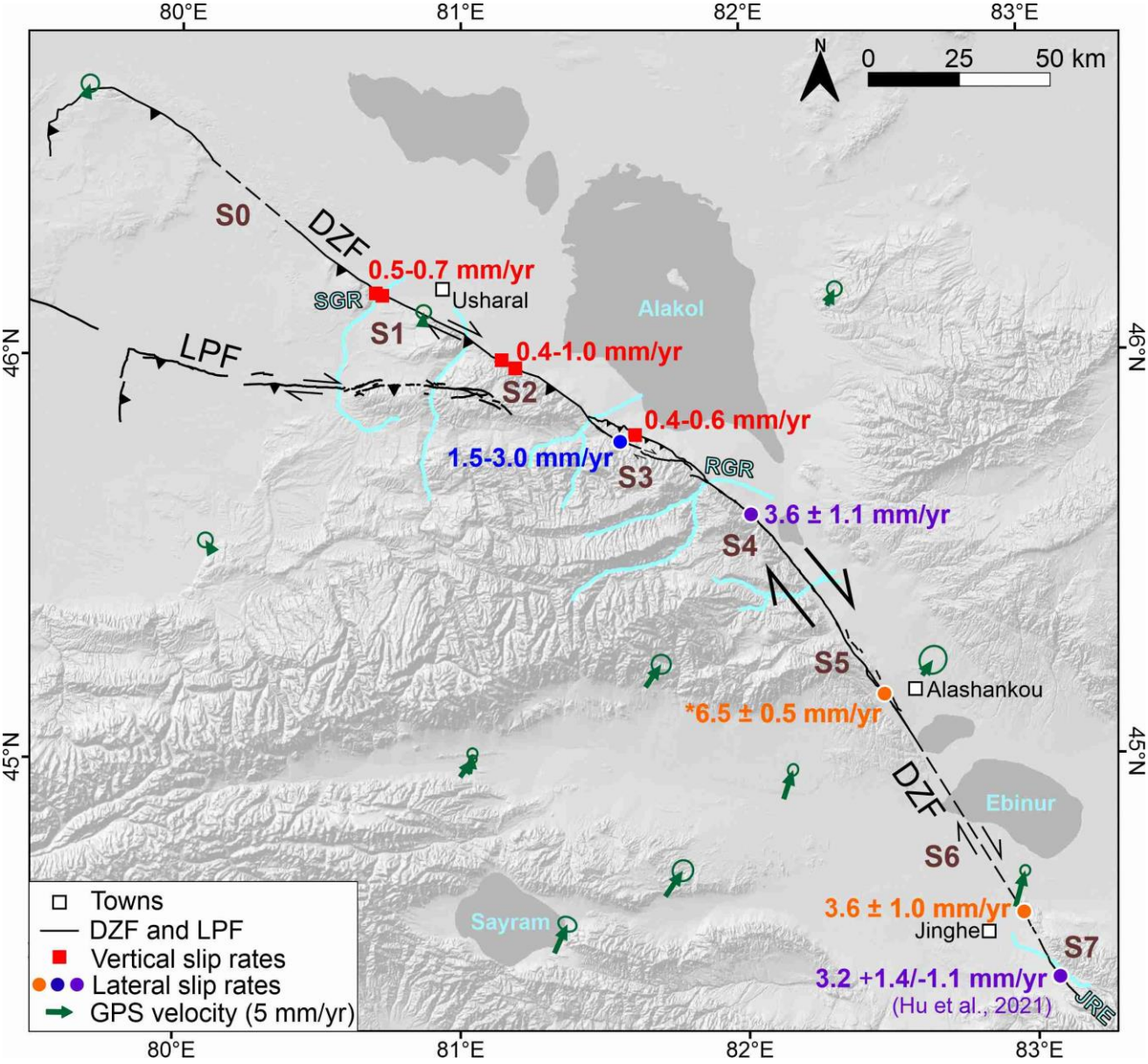

Figure 3-35. Overview of the geological and geodetic slip rates from this study and Hu et al. (2021) and their sampling site on the DZF. Uplift rates are labelled with red squares. Strike-slip rates are labelled in blue for those calculated from luminescence samples, in purple for those calculated from TCN ages and in orange for those derived from the InSAR time-series, with "*" indicating the possible outlier. GNSS velocities are from Zheng et al. (2017). LPF: Lepsy Fault; SGR: Shynzhyly River; RGR: Rygayty River; JRE: Jing River East.

3.5.2 Slip Rates along the DZF and Its Implications

3.5.2.1 Kinematics and Crustal Shortening along the DZF with Its Adjacent Faults

Considering the fault orientation, the 2.1 – 4.7 mm/yr strike-slip rate yields a N-S component of 1.8 – 4.0 mm/yr across the southern DZF. This N-S shortening rate could correspond to the geodetic N-S velocity change of 1.4 – 3.9 mm/yr calculated from the GNSS velocity vectors at Alashankou Town and Jinghe County (Zheng et al., 2017) (Figure 3-1a and Figure 3-35). The strike-slip rates from this study also support the suggestion that the southern DZF is accommodating about 25 ± 10% of the total crustal shortening (~10 mm/yr) between the Tarim and Dzhungarian Basins (M. Wang & Shen, 2020; Z. Hu, Yang, et al., 2021).

Taking a simplified DZF fault geometry and assuming a consistent slip vector azimuth along the DZF (Tsai et al., 2022), the 2.1 – 4.7 mm/yr strike-slip rate of the southern DZF yields an uplift rate of 0.8 – 3.2 mm/yr on the northern DZF. The rate of 0.6 ± 0.2 mm/yr calculated from the uplifted terraces in the northern DZF only fits the lower bound of this inferred uplift rate, suggesting the total slip rate on the northern DZF might be lower than the rate in the south.

By assuming a fault dip of 39° – 55° with a uniform strike of 330° for the northern DZF (Tsai et al., 2022), the 0.6 ± 0.2 mm/yr uplift rate yields a N-S shortening across the DZF of 0.1 – 0.5 mm/yr and a fault-perpendicular shortening of 0.3 – 1.0 mm/yr. These shortening rates are much lower than those on the southern DZF and the 1 – 3 mm/yr N-S crustal shortening across the Dzhungarian Alatau inferred from the GNSS velocities (Zubovich et al., 2010; Zheng et al., 2017) (Figure 3-1c). This indicates either that lateral slip on the northern DZF is accommodating a component of the shortening with a strike-slip rate of ~ 3 – 4 mm/yr, or that other faults are accommodating the rest of the total crustal shortening in the northern Dzhungarian Alatau. Based on the GNSS velocity vectors, the lateral slip rate of the northern DZF is unlikely to reach 3 mm/yr. For example, the GPS station (TEN4 at 80.866°E, 46.081°N) on the hanging wall of the DZF near Usharal Town shows a maximum net velocity of 3.2 mm/yr with a vector azimuth of N17°E (Zheng et al., 2017) (Figure 3-35), meaning the velocity component towards the northeast along the strike of the northern DZF is only ~ 0.9 mm/yr. Considering the crustal deformation on the footwall of the DZF should be slower than the hanging wall and assuming there is minimal discrepancy between the geological and geodetic slip rates, the lateral slip rate of the northern DZF should be less than 0.9 mm/yr, if neglecting the impact of locking depth on the GNSS station close to the fault.

Therefore, the northern DZF is likely accommodating less than 25% of the total N-S crustal shortening across the Dzhungarian Alatau. The remaining ~75% of the shortening must then be accommodated by other faults and/or folding, which would explain the topography of the E-W oriented ridges and uplifted peneplains in the Dzhungarian Alatau. Although most of the faults in the Alatau demonstrate little activity from a lack of continuous fault lineaments with significant offsets, the approximately E-W striking Lepsy Fault shows clear palaeo-earthquake ruptures with a total length of ~120 km in the northern Dzhungarian Alatau. Based on the geometry of the Dzhungarian and Lepsy Faults and assuming a consistent slip vector azimuth (Tsai et al., 2022), the strike-slip rate of the southern DZF yields an uplift rate of over 1.9 mm/yr and an N-S shortening component of at least 1.8 mm/yr on the Lepsy Fault. Even if the northern DZF is accommodating parts (up to 0.5 mm/yr) of this total shortening (1.8 mm/yr), the Lepsy Fault could still be accommodating at least one-third of the N-S shortening across the Dzhungarian Alatau, which is much higher than the proportion accommodated by the northern DZF. These results further support the hypothesis that the Lepsy Fault is the primary mountain-building structure in northern Alatau and it might be able to cause joint ruptures with the DZF and large-magnitude earthquakes in this region (Tsai et al., 2022).

3.5.2.2 Possible Termination and Recurrence Interval of the DZF

The lower slip rates are calculated on the northern DZF, especially north of Section S3 (Figure 3-35). We suggest that the DZF is significantly less active to the NW of Usharal, based on the low topographic relief on Section S0. Thus, the lower slip rate of the northern DZF is likely not only due to the presence of the LPF, but also due to its proximity to the fault tip, where the fault slip should theoretically terminate at. More investigations are needed to reveal the fault behaviour on the ~ 100 km-long Section S0 of the DZF to better explain this slip rate variation. In contrast, the consistent slip rate of the southern DZF (from the Rygayty River to Jinghe) indicates the DZF indeed does not terminate at Jing River East but continues through the Borohoro Shan, although the fault trace is unclear in the NW Borohoro Shan (Figure 3-1a and Figure 3-2).

Using a strike-slip rate of 2.1 – 4.7 mm/yr with an average single-event horizontal offset of 6 – 9 m (Tsai et al., 2022) yields a recurrence interval of 1300 – 4300 years with an average of ~ 2200 years on the southern DZF, which is shorter than the average recurrence time of ~ 4 – 6 ka inferred from the investigation of trenches by Hu et al. (2021). If the ~ 50-m offset fan on Section S4 results from 5 – 8 earthquakes, our estimated recurrence interval here is compatible with the dated age (~14 ka) of the fan.

More importantly, this estimated recurrence interval is within the timing of the last event (after ~ 6.6 ka) on the southern DZF (Z. Hu, Yang, et al., 2021), which indicates a high probability for a large earthquake occurring on this fault in the near future. Using a possible single-event scarp height of 6 – 8 m from the Bear River Site on Section S2 (Tsai et al., 2022) with an uplift rate of 0.6 ± 0.2 mm/yr yields an average recurrence interval of ~ 12000 years on the northern DZF. However, the average recurrence interval is only ~ 4200 years if the average vertical fault slip of 2 – 3 m suggested by Campbell et al., (2013) is used. Further investigations, such as trenching with geochronological data, on the northern DZF could help provide better constraints for the recurrence intervals.

3.6 Conclusions

We have provided the first long-term geological uplift rates on the northern DZF, from the Shynzhyly River to the Rygayty River, which we find to be a uniform 0.6 ± 0.2 mm/yr over the last ~ 5 – 60 ka. We also conclude that the geological strike-slip rates on the southern DZF, from the Rygayty River to the Jing River East, are a uniform 3.4 ± 1.3 mm/yr over the last ~ 100 ka based on the better-constrained TCN ages. We further estimated the first present-day geodetic strike-slip rate derived from the InSAR time-series analysis on the southern DZF and it is consistent with the geological strike-slip rate, which is in a range of 2.1 – 4.7 mm/yr. Based on the fault orientation, our estimated strike-slip rates imply the southern DZF is accommodating ~ 25 ± 10% of the total crustal shortening between the Tarim and Dzhungarian Basins. However, the total slip rates on the DZF seem to decrease on the northern sections (S2 to S0), which is likely due to the proximity to the NW fault tip and the presence of other fast-moving structures accommodating most of the crustal shortening in the northern Dzhungarian Alatau. Combining our estimated slip rates and the suggested average single-event fault slip from our previous findings, we calculated a recurrence interval of ~ 12000 years on the northern DZF and 1300 – 4300 years on the southern DZF. Considering the long elapsed time since the last event of ~ 6.6 ka (Hu et al. 2021) on the southern DZF and the possible occurrence of Mw > 8 earthquakes (Tsai et al., 2022), our study highlights the potentially high seismic hazard posed by the DZF in this region.

3.7 Appendices
Part1: Luminescence Dating

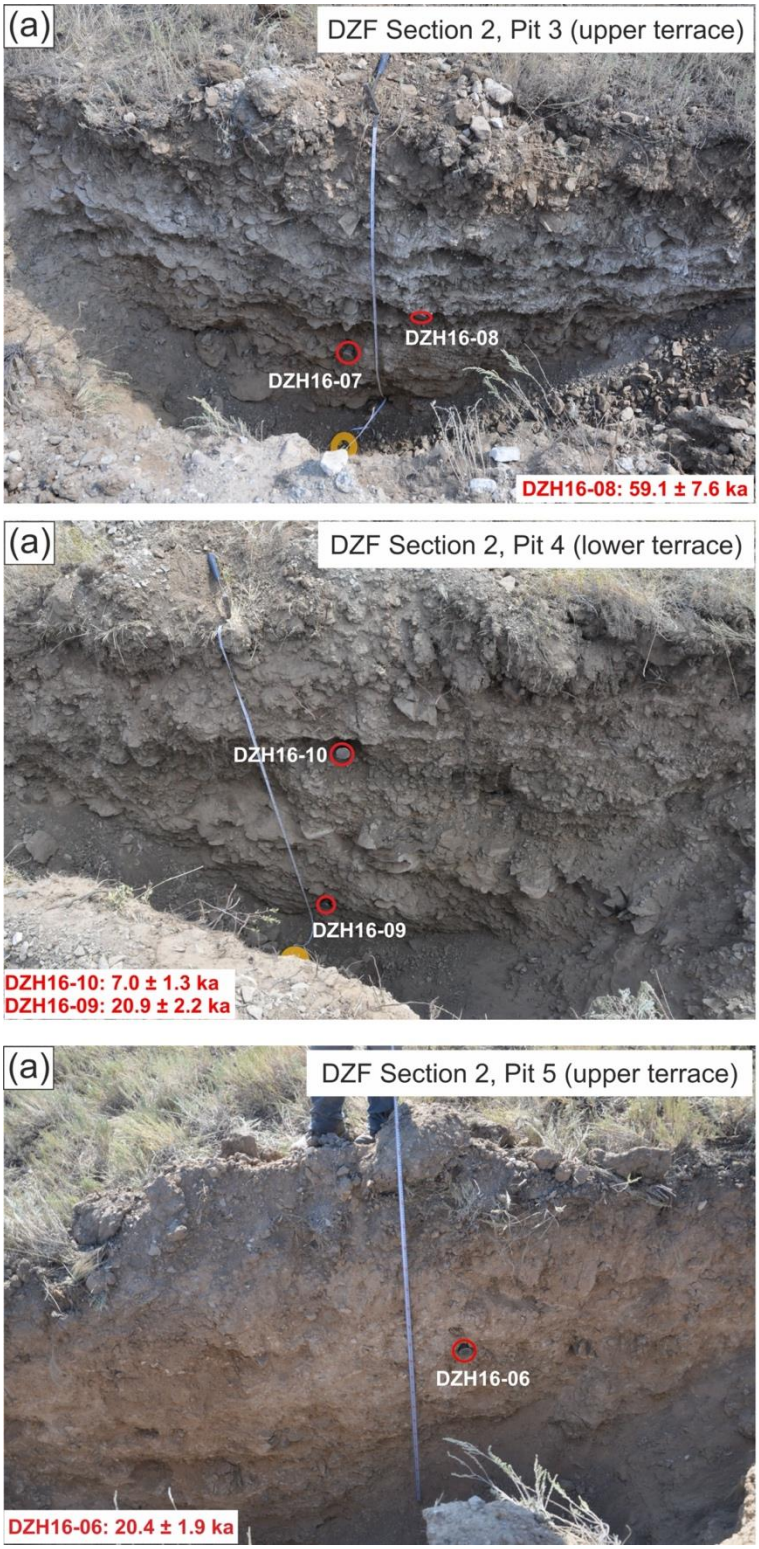

Figure S3-1. Field photographs of the sampling Pits 3, 4 and 5 on Section S2.

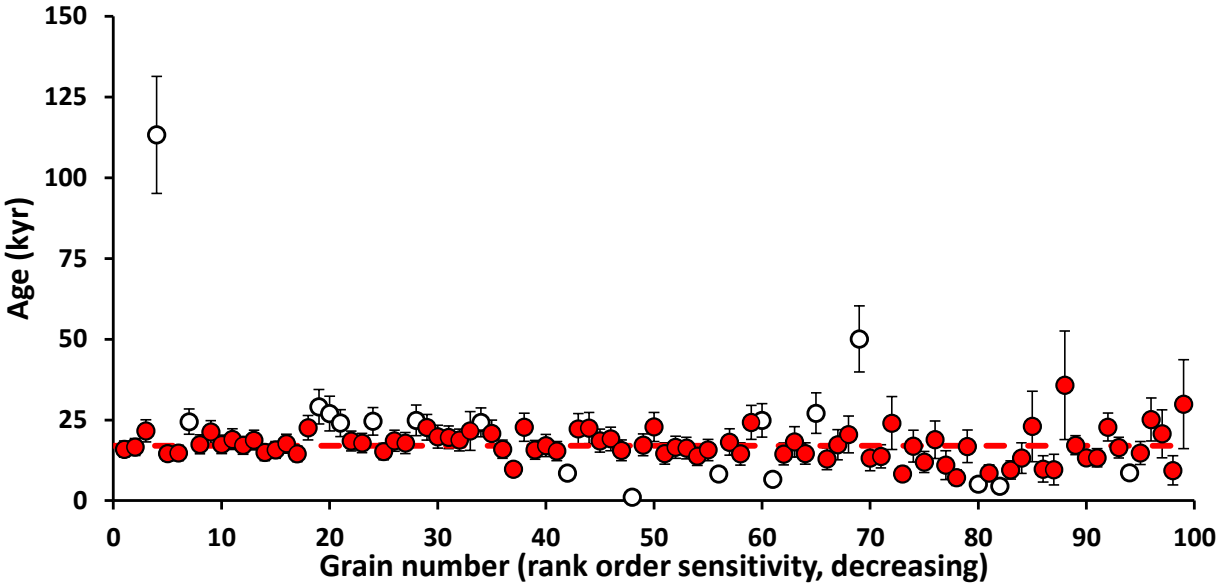

Figure S3-2. Age distribution of sample KAZ19-DZH1(Shfd 19200).
Age estimate = 17.0 ± 1.1 ka / 400/99/81/7 (grains measured/response/included/young rejected)

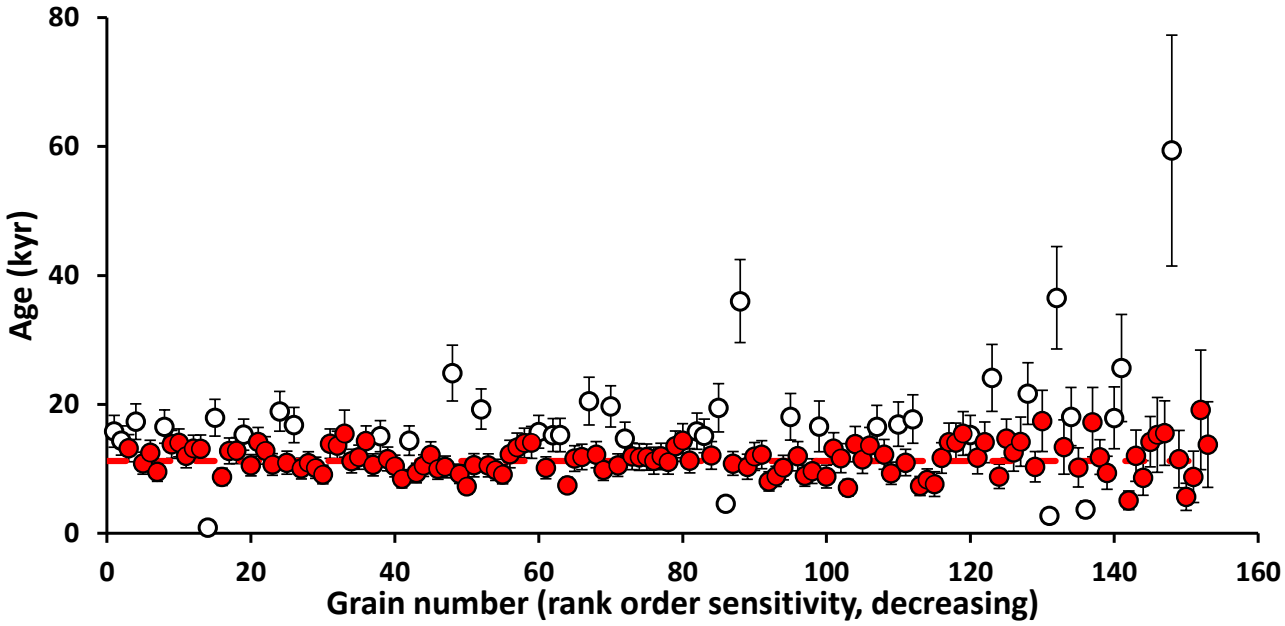

Figure S3-3. Age distribution of sample KAZ19-DZH2(Shfd 19201).
Age estimate = 11.2 ± 0.8 ka / 200/153/114/4 (grains measured/response/included/young rejected)

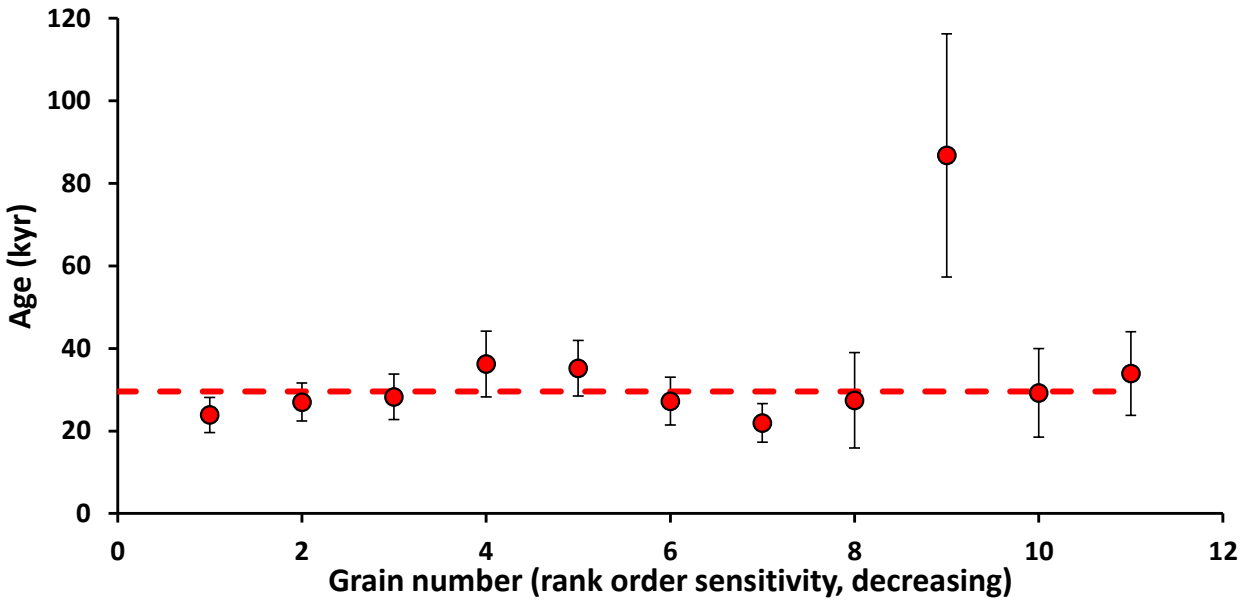

Figure S3-4. Age distribution of sample KAZ19-DZH3(Shfd 19202).
Age estimate = 29.6 ± 2.8 ka / 600/11/11/0 (grains measured/response/included/young rejected)

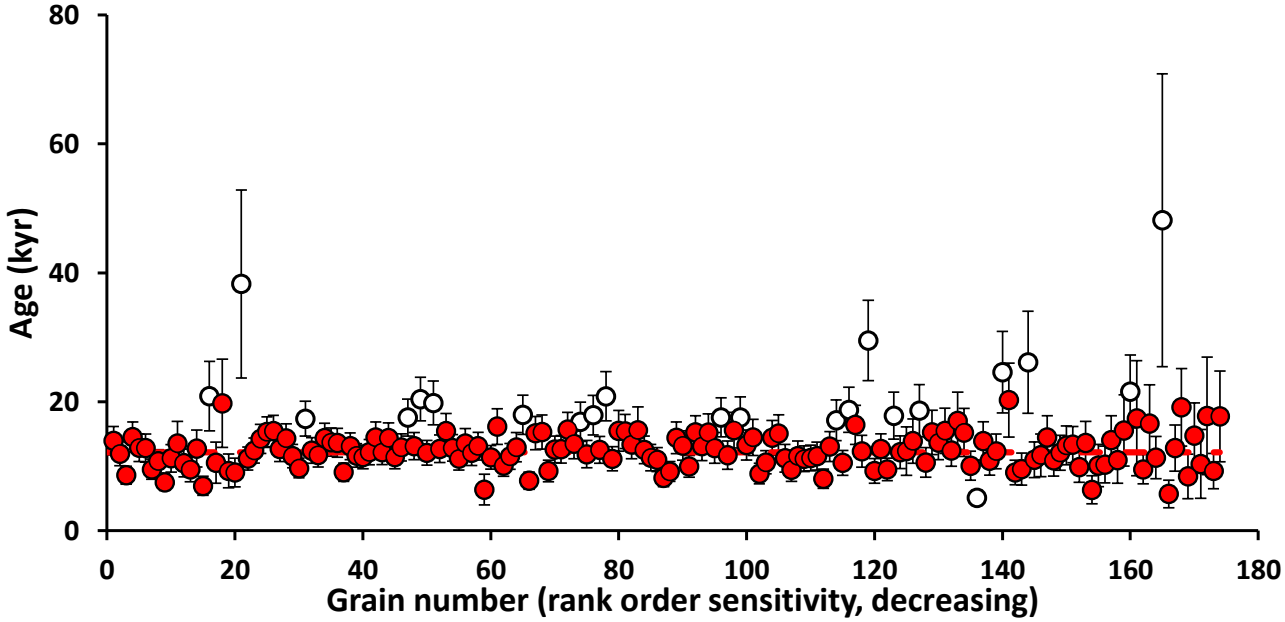

Figure S3-5. Age distribution of sample KAZ19-DZH4(Shfd 19203).
Age estimate = 12.2 ± 0.9 ka 200/174/153/1 (grains measured/response/included/young rejected)

Part 2. Cosmogenic Nuclide Dating Results

Table S3-1. Full parameters used for cosmogenic sample data reduction.

Sample ID	AMS ID	Quartz (g)	Be carrier (g)	$^{10}Be/^{9}Be$	1σ	[^{10}Be] atoms/g	1σ
DZH-1	XBE1530	7.820	0.3348	2.628E-14	8.60E-16	5.39E+04	1.98E+03
DZH-2	XBE1531	15.859	0.3377	7.771E-14	1.79E-15	8.36E+04	1.99E+03
DZH-3	XBE1532	11.769	0.3337	5.362E-14	1.33E-15	7.59E+04	1.98E+03
DZH-4	XBE1533	9.332	0.3373	5.357E-14	1.28E-15	9.67E+04	2.44E+03
DZH-5	XBE1534	7.617	0.3353	5.056E-14	1.29E-15	1.11E+05	2.99E+03
DZH-6	XBE1535	11.765	0.3366	5.553E-14	1.33E-15	7.94E+04	2.00E+03
DZH-7	XBE1536	16.411	0.3361	9.221E-14	2.07E-15	9.58E+04	2.21E+03
DZH-8	XBE1537	7.492	0.3363	4.380E-14	1.52E-15	9.73E+04	3.57E+03
DZH-8R	XBE1538	9.545	0.3370	5.291E-14	1.35E-15	9.32E+04	2.50E+03
DZH-9	XBE1539	14.346	0.3379	9.900E-14	2.21E-15	1.18E+05	2.71E+03
STDA220322	XBE1540	0.493	0.3379	9.627E-13	1.86E-14	3.41E+07	6.61E+05
BLK220322	XBE1529	-	0.3375	1.944E-15	2.35E-16	-	-

Notes:

Be carrier solution has a measured Be concentration of 775.23 ug/g.

AMS measured ratios were normalized to standard KN 01-5-2 with an assumed $^{10}Be/^{9}Be$ ratio of 8.558×10^{-12} (Nishiizumi et al., 2007).

^{10}Be total number of atoms in samples are blank corrected by subtracting the ^{10}Be total number of atoms in the process blank (BLK220322) with uncertainties in sample and blank propagated in quadrature.

Sample DZH-8R is a replicate of DZH-8. The average ^{10}Be concentration and standard deviation of concentration calculated in DZH-8 and DZH-8R were used in age calculations.

Reported concentration value of CRONUS-A (STDA220322) is $3.42 \times 10^{-7} \pm 0.1 \times 10^{-7}$ (1 SD) atoms/gram (Jull et al., 2013).

Table S3-2. Cosmogenic sample exposure age calculation inputs and outputs

Sample name	Latitude (DD)	Longitude (DD)	Elevation (m)	Elv/pressure flag	Thickness (cm)	Density (g cm^{-2})	Shielding correction	Erosion (cm yr^{-1})	[^{10}Be] (atoms g^{-1})	+/- (atoms g^{-1})	Be AMS standard	[^{26}Al] (atoms g^{-1})	+/- (atoms g^{-1})	Al AMS standard	Exposure Age (yr)	1σ internal (yr)
DZH-1	45.60588	82.02567	644	std	2	2.7	0.985	0	53933	1978	07KNSTD	0	0	KNSTD	8036	295
DZH-2	45.60597	82.02575	640	std	4	2.7	0.985	0	83574	1989	07KNSTD	0	0	KNSTD	12717	304
DZH-3	45.60597	82.02584	640	std	2	2.7	0.985	0	75868	1978	07KNSTD	0	0	KNSTD	11352	297
DZH-4	45.60614	82.02654	632	std	5	2.7	0.985	0	96656	2441	07KNSTD	0	0	KNSTD	14939	379
DZH-5	45.60515	82.02511	658	std	3	2.7	0.985	0	110824	2989	07KNSTD	0	0	KNSTD	16487	446
DZH-6	45.60612	82.02650	637	std	5	2.7	0.985	0	79406	1997	07KNSTD	0	0	KNSTD	12212	308
DZH-7	45.60603	82.02660	637	std	2	2.7	0.985	0	95757	2215	07KNSTD	0	0	KNSTD	14375	334
DZH-8	45.60590	82.02569	642	std	3	2.7	0.985	0	95258	2899	07KNSTD	0	0	KNSTD	14357	439
DZH-9	45.60521	82.02410	637	std	2	2.7	0.985	0	118423	2714	07KNSTD	0	0	KNSTD	17793	410

Notes:

Sample thickness measured in field when sample was collected.

DZH-7, DZH-8 and DZH-9 are amalgamated samples of small quartz clasts collected from areas that are around their locations noted in the table with assumed elevations

Ages are calculated using a constant production rate model and scaling scheme for spallation (Lal, 1991; Stone, 2000) and production rate of 4.132±0.218 atoms g^{-1} yr^{-1}.

Muonogenic ^{10}Be production modelled after Heisinger et al. (2002a; 2002b).

The average ^{10}Be concentration and standard deviation of concentration calculated in DZH-8 and DZH-8R was used in age calculations.

Version 3 of the online exposure age calculator described by Balco et al. (2008), and subsequently updated, was used for calculations. Exposure ages were calculated using a ^{10}Be production rate of 4.132 ± 0.218 atoms g^{-1} yr^{-1},

Part 3: InSAR Processing

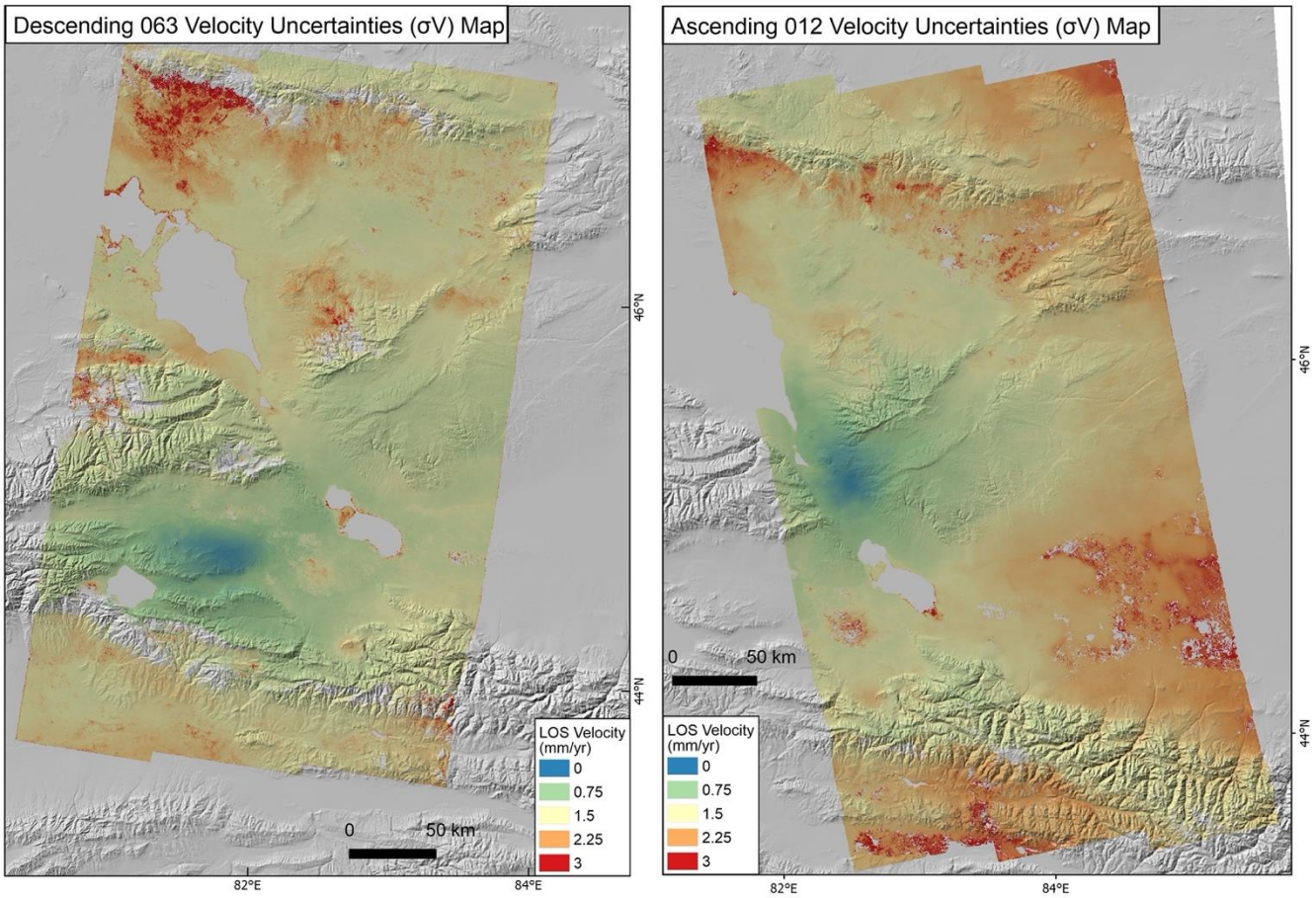

Figure S3-6. Uncertainty maps (σV) of the LOS velocity.

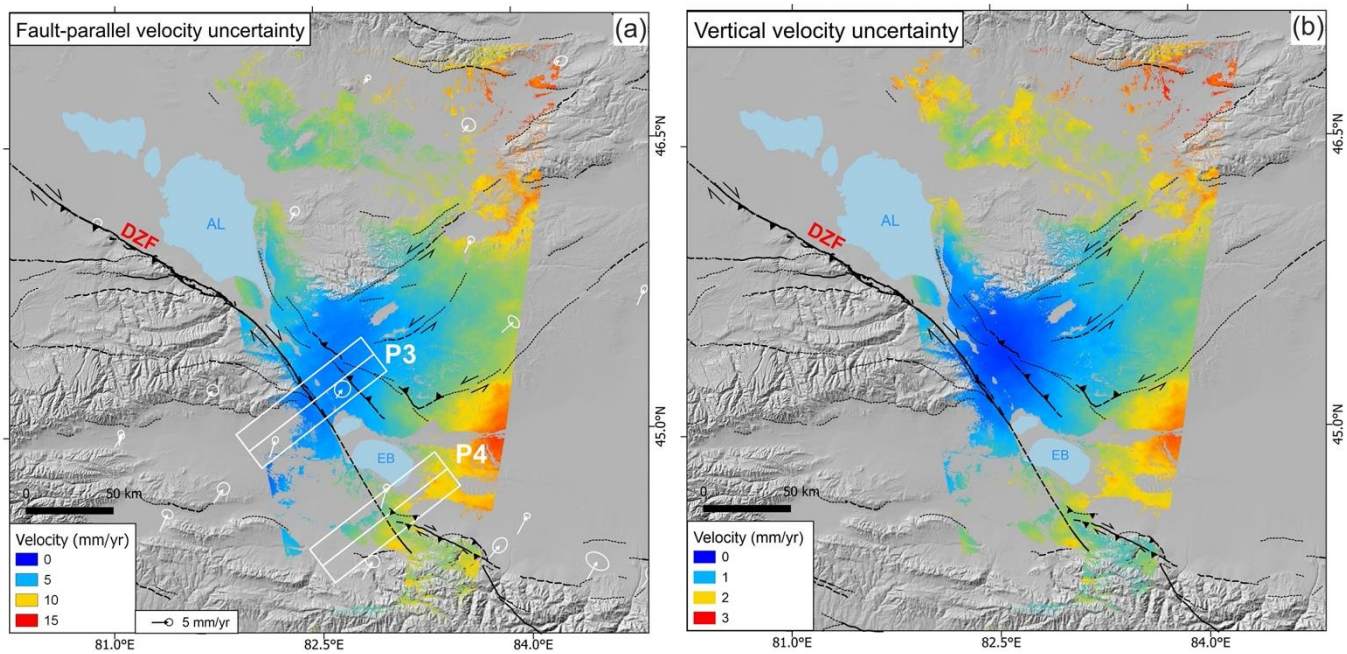

Figure S3-7. Uncertainty maps for the decomposed fault-parallel (a) and vertical (b) components.

Statement of Authorship for joint/multi-authored papers for PGR thesis

To appear at the end of each thesis chapter submitted as an article/paper

The statement shall describe the candidate's and co-authors' independent research contributions in the thesis publications. For each publication there should exist a complete statement that is to be filled out and signed by the candidate and supervisor **(only required where there isn't already a statement of contribution within the paper itself).**

Title of Paper	Geological and Geodetic Constraints on Average Quaternary Rates of the Dzhungarian Fault Slip
Publication Status	□Published □ Accepted for Publication □Submitted for Publication ■Unpublished and unsubmitted work written in a manuscript style
Publication Details	Tsai, C.-H., Grützner, C., Daout, S., Abdrakhmatov, K., Mukambayev, A., Fitzsimmons, K., Carr, A. S., Rhodes, E., Ivester, A., Rood, A. H., Rood D. H., Wilkinson, R., & Walker, R. T. Geological and Geodetic Constraints on Average Quaternary Rates of the Dzhungarian Fault Slip.

Student Confirmation

Student Name:	Chia-Hsin Tsai		
Contribution to the Paper	Processed the InSAR data and modelling, interpreted all the data, made figures, wrote manuscript		
Signature		Date	06.03.2023

Supervisor Confirmation

By signing the Statement of Authorship, you are certifying that the candidate made a substantial contribution to the publication, and that the description described above is accurate.

Supervisor name and title: Prof. Richard T. Walker		
Supervisor comments		
Signature 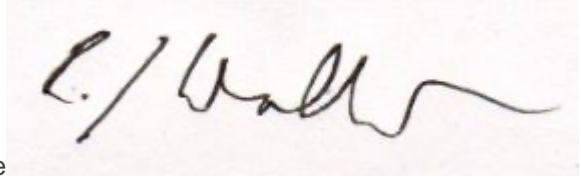	Date	7/3/2023

This completed form should be included in the thesis, at the end of the relevant chapter.

Chapter 4

Source Parameters of the 1906 Manas (Mw 7.7), 1944 Xinyuan (Mw 7.2) and 1812 Nilke Earthquakes and Seismotectonics of the Borohoro Shan, Western China

4.1 Introduction

The 23rd December 1906 Manas Earthquake occurred at the northern tip of the Chinese Tien Shan, along the northern margin of the Borohoro Shan and the southern margin of the Dzhungarian basin (Figure 4-1) (Molnar & Deng, 1984; Institute of Geophysics, SSB & Institute of Chinese Historical Geography, 1990; Avouac et al., 1993; P. Zhang, Deng, Xu, Peng, et al., 1994). It is one of the largest (Ms ≈ 8) reverse faulting earthquakes known on the continents, potentially involving the rupture of multiple segments, and with inferred complexities of rupture with depth (Avouac et al., 1993; Deng et al., 1996; Burchfiel et al., 1999; Deng et al., 2000; C. Y. Wang et al., 2004; Stockmeyer et al., 2014). As such, it potentially holds insights into the occurrence of large and complex intraplate earthquakes in general, as well as providing results of relevance to understanding the regional active tectonics of central Asia, and the earthquake hazard to nearby cities, including Urumqi which has a population of over 3.5 million. Although the 1906 earthquake is well recorded in historical documents and has a wide coverage of recorded intensities (Institute of Geophysics, SSB & Institute of Chinese Historical Geography, 1990), the surface ruptures inferred to be caused by this event are scarce and widely distributed (Avouac et al., 1993). Moreover,

estimates of its epicentre and magnitude vary widely (Figure 4-2 and Table 4-1), with magnitude anywhere in the range of 7.2 to 8.3 under various magnitude scales and input data. Therefore, the responsible fault and the earthquake mechanism of the 1906 Manas Earthquake remain unclear. In our study we reinvestigate the Manas Earthquake, reviewing previously published information, and combining this with seismological analysis of digitized seismic records, and remote sensing analysis of tectonic geomorphology.

Other large-magnitude earthquakes have occurred within the Borohoro Shan (Figure 4-1b and 4-2). The 1944 Xinyuan Earthquake (Mw 7.1 from USGS) is thought to have occurred within the southwestern part of the range, but with reported epicentre locations differing by up to ~100 km (Z. Yang, 1992; Shen et al., 2003; Chinese Earthquake Network Center (CENC)), meaning that the causative fault, or faults, are unknown (Figure 4-2). The other one is the 1812 Nilke Earthquake which is suggested to have even higher intensity than the 1906 Manas Earthquake but with little information about its magnitude and earthquake mechanism (Z. Yang et al., 1985; G. Yin et al., 2009). These three events highlight the non-negligible seismic hazards around the Borohoro Shan but all with unclarified magnitudes, epicentres or causative faults that are critical to understanding the seismotectonics of the Borohoro Shan and the future earthquakes in this region. Furthermore, the regions bordering the Borohoro Shan have seen dramatic population increase and urban growth over past decades, bringing an increased need to investigate the potential sources of future earthquakes through an understanding of examples from recent history, and through evidence preserved in the late Quaternary geology.

In this study, we analyse the 1906 and 1944 earthquake source parameters and integrate them with geological observations from the published literature. We located and compiled the previously reported surface ruptures caused by the 1812, 1906 and 1944 earthquakes and summarised them with our own examination from open-access high-resolution modern satellite imagery. We then relocated the hypocentres for the 1906 and 1944 earthquakes and re-estimated their magnitudes by analysing the digitised analogue seismic data collected globally. [#] This seismological approach has been successfully applied to large intra-continental historical earthquakes in Asia (Kulikova & Krüger, 2015; Ou et al., 2020). Finally, we integrated the geological observations, isoseismic maps and sub-surface seismic reflection profiles with our seismological analysis results to propose the likely responsible faults and the kinematics for these three historical events and to highlight the seismotectonics of the Borohoro Shan.

[#]The seismological analysis and related data collection/calculations in this chapter for the 1906 Manas and 1944 Xinyuan Earthquakes were all conducted by Dr. Galina Kulikova and not by the author of this thesis.

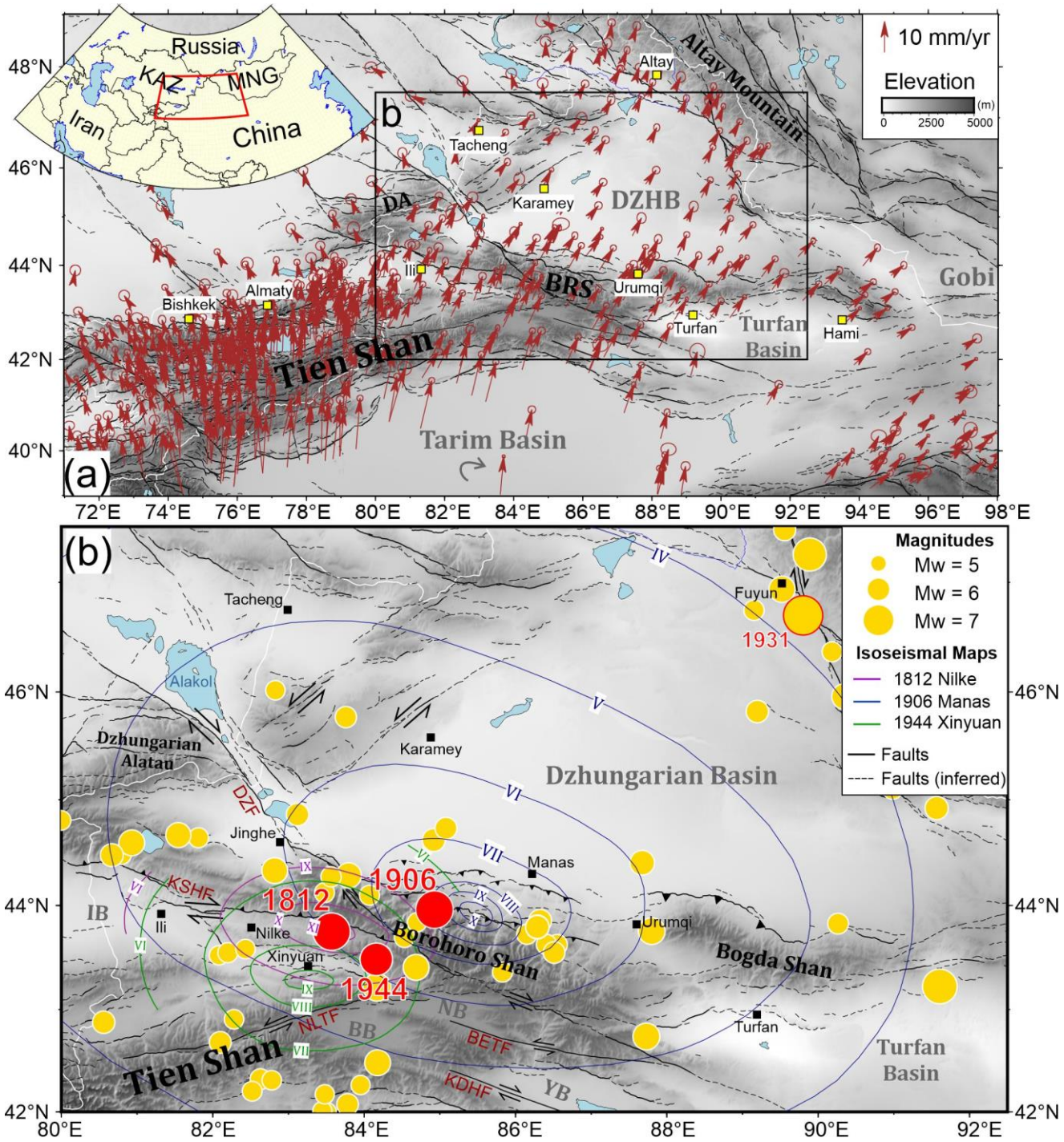

Figure 4-1. (a) Overview of the Tien Shan with its surrounding mountains and basins. GPS velocities vector (brown) are from Zubovich et al., (2010) and M. Wang & Shen, (2020). Cities and towns are labelled with yellow squares. International borders are in white. BR: Borohoro Shan; DA: Dzhungarian Alatau; DZHB: Dzhungarian Basin; KAZ: Kazakhstan; MNG: Mongolia. (b) Overview of seismicity around the Dzhungarian Basin. Yellow circles are earthquakes with magnitudes above 5.5 between 1904 and 2017 in the ISC-GEM catalogue (ISC, 2021). The 1812 Nilke, 1906 Manas and 1944 Xinyuan events are highlighted in red circles with the epicentre locations explained in the context below. The isoseismal maps of the 1812, 1906 and 1944 earthquakes are displayed in purple, blue and green lines with the

intensity labelled in *New Chinese Intensity Scale* (Institute of Geophysics, SSB & Institute of Chinese Historical Geography, 1990; Z. Yang, 1992; G. Yin et al., 2009). The 1931 Mw 7.6 Fuyun Earthquake (Klinger et al. 2011) is highlighted by a red frame. Cities and towns are labelled in black squares. Fault locations are based on the mapping in Avouac et al. (1993) and the online database from Zelenin et al. (2021). The names of the main strike-slip faults are noted in brown: DZF: Dzhungarian Fault; KSHF: Kashihe Fault; NLTF: Nalati Fault; BETF: Baoertu Fault; KDHF: Kaiduhe Fault. IB: Ili Basin; NB: Nalati Basin; BB: Bayanbuluk Basin; YB: Yangqi Basin.

4.2 Tectonic Settings and Earthquakes of the Borohoro Shan

The Tien Shan is a ~2500-km-long E-W trending mountain range that straddles western China, SE Kazakhstan and Kyrgyzstan (Figure 4-1a). It has a long geological history, with initial deformation in the late Palaeozoic, and with Cenozoic reactivation related to the India-Eurasian collision (Molnar & Tapponnier, 1975b; Windley et al., 1990, 2007; Abdrakhmatov et al., 2001; De Grave et al., 2007). The Borohoro Shan is a sub-range connecting the NW and the NE Tien Shan, which also separates the Dzhungarian (Junnggar) Basin in the north from the Tarim basin in the south (Figure 4-1). A prominent fold and thrust belt along the northern margin of the Borohoro Shan has deformed the thick Mesozoic and Cenozoic sedimentary strata of the Dzhungarian Basin (Figure 4-2) (Avouac et al., 1993; Burchfiel et al., 1999; Deng et al., 2000; Daëron et al., 2007; Charreau et al., 2008; Stockmeyer et al., 2017; Lu et al., 2018). This fold and thrust belt consists of three main subparallel anticlines formed in the Cenozoic with active reverse faults in listric geometries at their fronts (C. Y. Wang et al., 2004; Stockmeyer et al., 2014; Lu et al., 2018; Su et al., 2018). From south to north, these are the Qigu, Tugulu-Manas-Huoerguos and Anjihai-Dushanzi anticlines and their corresponding faults (Figure 4-3a). The Holocene shortening rate is ~ 2.2 – 3.3 mm/yr at the Tugulu-Manas-Houergous Fault and ~ 1.3 – 2.0 mm/yr at the Anjihai-Dushanzi Fault (Fu et al., 2017; Su et al., 2018).

Besides those reverse structures accommodating the crustal deformation via shortening, large strike-slip faults accommodate the counterclockwise rotation of the NW Tien Shan tectonic blocks and left-lateral shear in the eastern Tien Shan (Figure 4-2) (Cunningham, 2007; C. Wu et al., 2021). The right-lateral strike-slip Dzhungarian Fault (also called the Bolokenu-Aqikekuduk Fault, or Bo-A, Fault, e.g. Shen et al., 2003; Z. Hu et al., 2021) enters the Borohoro Shan from the northwest and probably merges with the right-lateral and reverse Kashihe Fault (Kashi River Fault) that is ~ WNW-ESE trending and located at the southwestern margin of the Borohoro Shan (Figure 4-2) (C. Wu et al., 2020; Z. Hu, Yang, et al., 2021). The dextral slip rate of the Kashihe Fault is ~ 2.4 mm/yr with a shortening of ~ 0.6 mm/yr (C. Wu et al., 2020), whereas the Dzhungarian Fault has a right-lateral slip rate of 2.1 – 4.7 mm/yr in the

south with an uplift rate of 0.6 ± 0.2 mm/yr in the north (Campbell et al., 2013; Z. Hu, Yang, et al., 2021, this study) (Figure 4-2). Another WNW-ESE trending right-lateral strike-slip fault is the Kaiduhe Fault which is located in the southeastern Borohoro Shan with a dextral slip rate of 1.2 – 1.6 mm/yr (Huang, 2015) (Figure 4-1b). The WSW-ENE trending left-lateral and reverse Nalati Fault elongates from the southern margin of the Borohoro Shan to the Kyrgyz Tien Shan with a strike-slip rate of 1.4 – 1.8 mm/yr and a shortening rate of 1.4 ± 0.7 mm/yr (Charreau et al., 2017). Another left-lateral strike-slip fault is the ~ E-W trending Baoertu Fault that is located at the southeastern Borohoro Shan with a sinistral slip rate of ~ 0.65 ± 0.16 mm/yr with shortening of ~ 0.07 ± 0.01mm/yr (Ren et al., 2021) (Figure 4-1b). These left-lateral strike-slip faults are considered to be parts of the Gobi-Tien Shan fault system that is accommodating the left-lateral shearing across the NE Tien Shan and Gobi region (Cunningham, 2007) (Figure 4-1a).

Almost 80 earthquakes with magnitudes ≥ 5.0 (C. Y. Wang et al., 2004) and at least 19 events with magnitudes ≥ 6.0 in any magnitude scale (Z. Hu, Yang, et al., 2021; ISC, 2022b) have occurred around the Borohoro Shan in the past three centuries. Most of the historical events in the northern Borohoro Shan fold and thrust belt are reverse or thrust events such as the latest 2017 Mw 6.3 Jinghe and the 2016 Mw 6.0 Hutubi Earthquakes (Figure 4-2) (Dziewonski et al., 1981; Ekström et al., 2012; ISC, 2022b). The 2017 Jinghe Earthquake occurred on the lower ramp of the south-dipping Jinghenan Fault with the maximum slip at a depth of ~ 14 km but without surface rupture (Figure 4-2) (W. Gong et al., 2019; Z. Hu, Li, et al., 2021). The 2016 Hutubi Earthquake occurred under the Qigu-Qingshuihe Anticline at a depth of ~16 km along the Tugulu-Manas-Huoerguos Fault or on a north dipping back-thrust of it (Figure 4-2 and 4-3) (Lu et al., 2018; X. Wang et al., 2019). This 2016 earthquake did not cause surface rupture but it did lead to a destruction of infrastructures and serious economic losses. Most of the past events in the southern Borohoro Shan have prominent strike-slip mechanisms compared to the northern ones such as the recent 2012 Mw 6.3 Xinyuan Earthquake (Dziewonski et al., 1981; Ekström et al., 2012). This 2012 earthquake is a right-lateral strike-slip event and possibly ruptured the Kashihe Fault, with a depth of ~ 28 km (Figure 4-2) (Q. Wang et al., 2015).

The three largest earthquakes recorded around the Borohoro Shan, with magnitudes > 7.0, are the 1906 Manas Earthquake in the north, and the 1944 Xinyuan and 1812 Nilke Earthquakes in the south, which all have the highest intensity above IX in *New Chinese Intensity Scale* (Figure 4-1b) (Institute of Geophysics, SSB & Institute of Chinese Historical Geography, 1990; Z. Yang, 1992). The 1906 and the 1812 events have similar degrees of damage and have been initially estimated to have magnitudes above

or approaching Ms 8 (Table 4-1) (Richter, 1958; Bai & Fang, 1981; Z. Yang et al., 1985). The 1944 event is a smaller event with a better-estimated magnitude of Mw 7.1 – 7.3 and has been reported to be a double-event earthquake (https://www.usgs.gov/natural-hazards/earthquakes), but it has widely distributed estimates of epicentres compared to the other two (Figure 4-2).

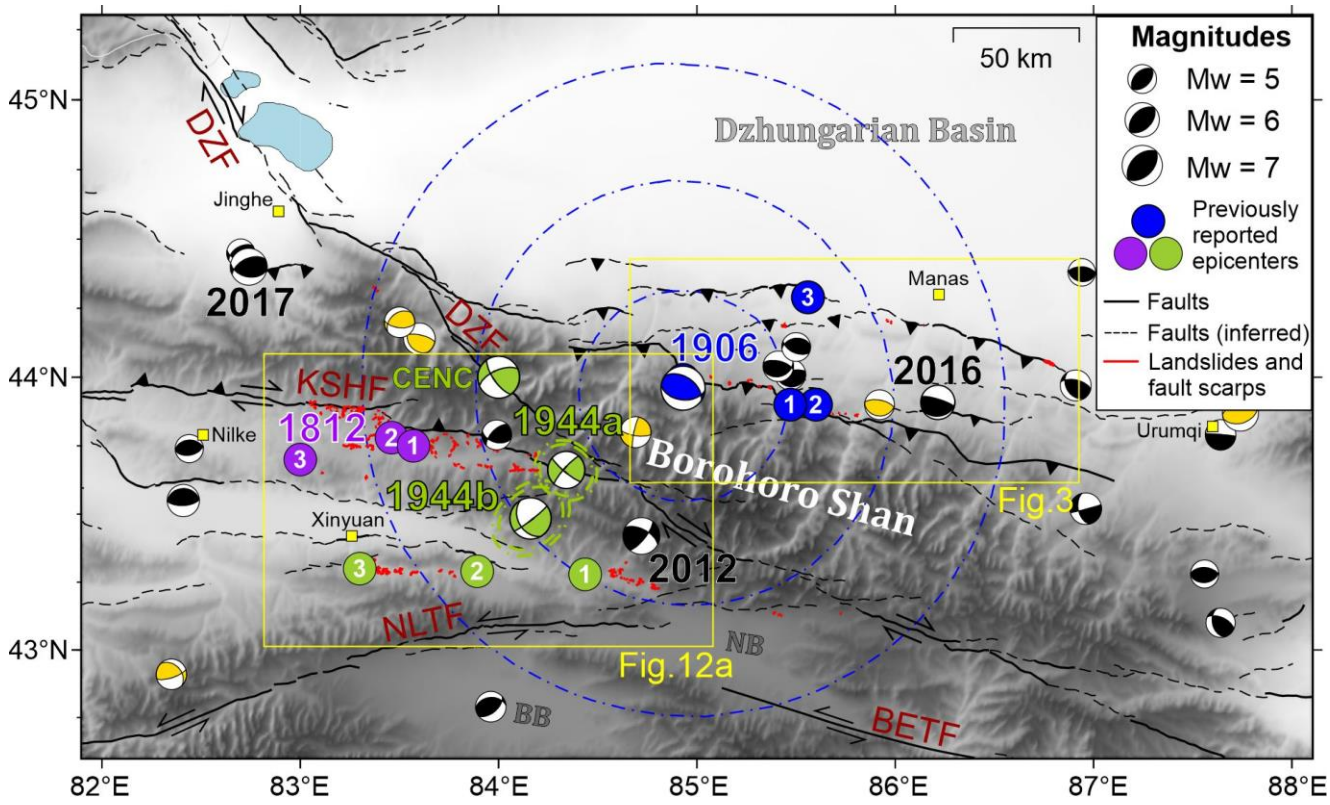

Figure 4-2. Tectonic overview of the Borohoro Shan and the 1812, 1906 and 1944 earthquakes. Focal mechanisms of historical earthquakes are shown in yellow for those analysed by Sloan et al. (2011) and in black for those from 1976 to June of 2021 with Mw > 5 from the Global Centroid-Moment-Tensor (GCMT) data (Dziewonski et al., 1981; Ekström et al., 2012). The previously reported epicentres for the 1812 event (purple circles) are numbered "1" by Yin et al. (2009), "2" by Z.Yang et al. (1985) and "3" by China Earthquake Administration (1971). The previously reported epicentres for the 1906 event (blue circles) are numbered "1" by Xie and Cai (1986), "2" by the Institute of Geophysics, SSB & Institute of Chinese Historical Geography (1990) and "3" by Storchak et al. (2013). The focal mechanism for the 1906 event (in blue) is re-estimated by this study with the relocated epicentre and its error ellipses in 3 sigmas (blue dotted-dash lines). The previously reported epicentres for the 1944 event (green circles) are numbered "1" and "2" by the USGS catalogue for the 1944a and 1944b events respectively, and "3" by Z. Yang (1992). The 1944 epicentre and fault plane solutions from China Earthquake Networks Center (CENC) and this study, with error ellipses in 3 sigmas (green dotted-dash lines), are also labelled in green. Cities and towns are labelled in yellow squares. Fault locations are from Avouac et al. (1993), Ren et al., (2021) and Zelenin et al. (2021). Possibly earthquake-induced landslides and fault scarps mapped by the previous work and this study are labelled in red (Z. Yang et al., 1985; Feng, 1990; Z. Yang, 1992; Avouac et al., 1993; P. Zhang, Deng, Xu, Peng, et al., 1994; G. Yin et al., 2009). The 2012 Mw 6.3 Xinyuan, the

2017 Mw 6.3 Jinghe, and the 2016 Mw 6.0 Hutubi earthquakes are annotated in black. DZF: Dzhungarian Fault; KSHF: Kashihe Fault; NLTF: Nalati Fault; BETF: Baoertu Fault; NB: Nalati Basin; BB: Bayanbuluk Basin.

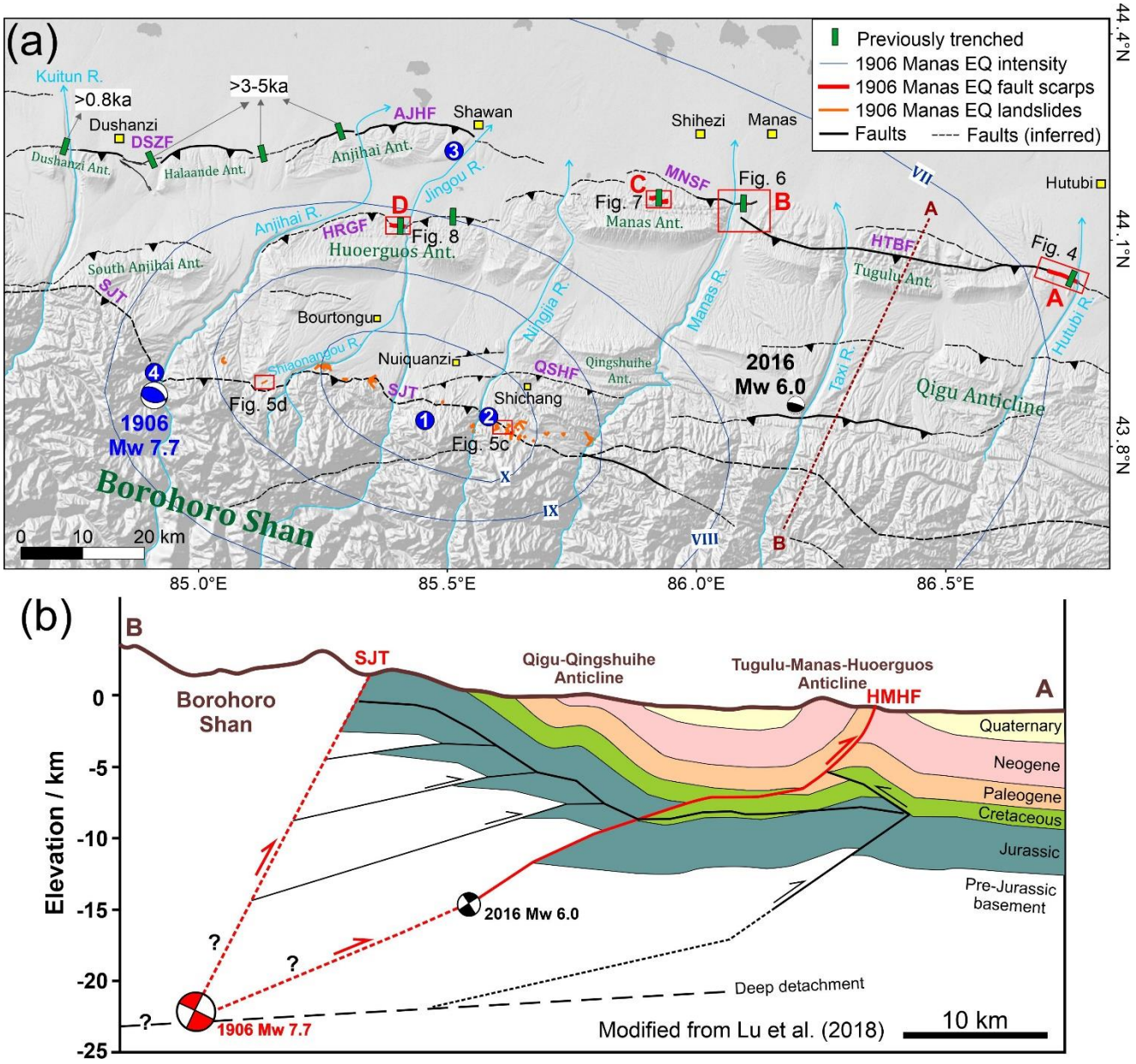

Figure 4-3. (a) Topographic map showing the fold and thrust belt at the northern range front of the Borohoro Shan from the shaded ESRI world relief imagery. A (Hutubi River west), B (Manas River east), C (Aweitan) and D (Jinguo River west) are the four regions where the 1906 possible fault scarps (red lines) are found. The detached scarps and landslides likely caused by the 1906 event are labelled in orange. Previous trenching sites (green rectangles) (Deng et al., 1996; Su et al., 2018) are shown with the ages of their latest earthquakes summarized and noted. Names of the anticlines (Ant.) and mountain ranges are annotated in green text. Isoseismal map (blue lines) of the 1906 earthquake is displayed with the intensity in *New Chinese Intensity Scale* (Institute of Geophysics, SSB & Institute of Chinese Historical Geography,

1990). Previously-located epicentres are in blue circles with the number "4" from the ISC-GEM catalogue (ISC, 2021) and the others described in the caption of Figure 4-2. The focal mechanism of the 1906 event (in blue) from this study and the 2016 Mw 6.0 Hutubi Earthquake from Lu et al. (2018) are marked. Cities and towns arelabelled in yellow and noted by black text. Major rivers arelabelled in light blue with arrows. The brown dashed line mark the path of the seismic-reflection profile (A-B) shown in (b). Names of the reverse faults are annotated by purple text. SJT: Southern Junggar Thrust; QSHF: Qingshuihe Fault; HRGF: Huoergous Fault; DSZF: Dushanzi Fault; AJHF: Anjihai Fault; MNSF: Manas Fault; HTBF: Hutubi Fault. Fault locations are compiled from Avouac et al. (1993), Zelenin et al. (2021) and our own mapping results. (b) Seismotectonic model modified from Lu et al. (2018), based on a ~ 15 km-deep seismic-reflection profile of the Borohoro range front, for the 1906 Manas Earthquake and the 2016 Hutubi Earthquake. Red lines represent the likely ruptured faults during the 1906 Manas Earthquake. (Dashed red lines are the inferred faults.) Brown lines represent the topography. HMHF: Tugulu-Manas-Huoerguos Fault.

4.3 The 1906 Manas Earthquake

4.3.1 Background and Macroseismic Data

The Manas Earthquake occurred at 18:21:12 UTC on 23rd December 1906. It caused the collapse of more than 2100 houses and at least 305 fatalities (P. Zhang, Deng, Xu, Peng, et al., 1994). The estimated magnitudes for this earthquake range from M 7.2 – 8.3 in various scales (Table 4-1). (Gutenberg & Richter, 1954; Richter, 1958; Bai & Fang, 1981; Abe & Noguchi, 1983; Gongxu Gu, 1983; Molnar & Deng, 1984; Xie & Cai, 1986; Abe, 1988; Institute of Geophysics, SSB & Institute of Chinese Historical Geography, 1990; Avouac et al., 1993; Burchfiel et al., 1999; Stockmeyer et al., 2014; ISC, 2021). It is the latest and the most destructive historical event with a magnitude > 7 at the northern range front of the Borohoro Shan and further aftershocks were recorded in the following six years until 1912 (Institute of Geophysics, SSB & Institute of Chinese Historical Geography, 1990). The first detailed investigation of the surface ruptures and isoseismal map of this earthquake was conducted from 1972 – 1980 by the Seismological Bureau of Xinjiang Uygur Autonomous Region (Bai & Fang, 1981; Institute of Geophysics, SSB & Institute of Chinese Historical Geography, 1990). According to those studies, ground shaking reached X in the *New Chinese Intensity Scale* for the area near Nuiquanzi, reached VI at the capital city Urumqi and reached V or IV for regions near Turfan, Yining, Tacheng and Lake Alakol (Figure 4-1b). The most damaged area is in the southwest of the current Manas County including Shichang, Nuiquanzi and Bourtongu where all the mud-built houses and 90% of the wooden houses were destroyed (Institute of Geophysics, SSB & Institute of Chinese Historical Geography, 1990) (Figure 4-3). The epicentre inferred from the isoseismal map is near 43.9°N, 85.6°E (Institute of Geophysics, SSB & Institute of Chinese Historical Geography, 1990) or 43.9°N, 85.47°E (Xie & Cai, 1986). On the other hand, the International

Seismological Centre (ISC) has provided epicentral locations at 44.29°N, 85.56°E (Storchak et al., 2013) and 43.99°N, 84.93°E (ISC, 2021) (Figure 4-3).

Most of the inferred surface ruptures from the 1906 event are landslides and fractures triggered by shaking and gravity instead of the direct movements of the fault (Bai & Fang, 1981; Seismological Bureau of Xinjiang, 1985; J. Hu & Bai, 1988; P. Zhang, Deng, Xu, Peng, et al., 1994). Several fault scarps possibly ruptured by the 1906 Manas Earthquake are all sited 30 – 90 km northeast of the inferred epicentres (Figure 4-3a) (Avouac et al., 1993; P. Zhang, Deng, Xu, Peng, et al., 1994; Deng et al., 1996; Pang et al., 2021), albeit some authors disagree with those distant scarps being products of the 1906 event (Burchfiel et al., 1999), highlighting the continued challenges in identifying the responsible fault. Based on the isoseismal map and the epicentres inferred from it, some studies have attributed the 1906 earthquake to the Qingshuihe Fault or the Southern Junggar Thrust (SJT) (also called the Junggar Frontal Thrust or the Junggar Southern Marginal Fault), which is a ~ E-W trending reverse fault dipping to the south (Figure 4-3a) (Bai & Fang, 1981; J. Hu & Bai, 1988; Avouac et al., 1993; C. Y. Wang et al., 2004). Others attribute the earthquake to a blind fault underneath the range front of the Borohoro Shan (P. Zhang, Deng, Xu, Peng, et al., 1994; Deng et al., 1996), though this does not rule out rupture at depth on the SJT (X. Yang et al., 1998). A number of studies have further revealed the complicated subsurface structures of this fold and thrust belt with two levels of decollements and several structural wedges with listric geometries and back thrusts, which certainly increases the number of candidates for the responsible fault of the 1906 Manas Earthquake (X. Yang et al., 2002; C. Y. Wang et al., 2004; C. X. Li et al., 2011; Stockmeyer et al., 2014; Lu et al., 2018).

4.3.2 Surface Ruptures

According to the previous literature (Bai & Fang, 1981; Seismological Bureau of Xinjiang, 1985; Avouac et al., 1993; Deng et al., 1994; Zhang, Deng, Xu, Peng, et al., 1994; Deng et al., 1996), the possible 1906 surface ruptures expressed as fault scarps or flexural scarps have only been found in four places and the landslides caused by this earthquake are mostly found along the northern hills of the Borohoro Shan near Shichang (Figure 4-3a). We assess these sites from east to west.

4.3.2.1 Western Terraces of the Hutubi River

The northward-flowing Hutubi River is located at the eastern end of the E-W trending Hutubi Fault that penetrates the Tugulu Anticline (Figure 4-3a). From the eastern part of the Tugulu Anticline to the western terraces of the Hutubi River, prominent fault scarps can be recognised up to 8 km long but no fault scarps are found on the eastern side of the river (P. Zhang, Deng, Xu, Peng, et al., 1994) (Figure 4-59). From a road cut at the eastern flank of Tugulu Anticline, Stockmeyer et al. (2014) observed at least two south-dipping fault splays underneath the fault scarp and suggested them to be the splays of the SJT from the interpretation of seismic-reflection profiles. In this study, we mapped the Hutubi River terraces and the Hutubi Fault scarps based on the 30-m DEM from Copernicus imagery (Opentopography.org) and optical satellite imagery from Yandex Maps, Bing Maps and Google Earth (European Space Agency Sinergise, 2021) (Figure 4-4d). The terraces from high to low are labelled from T6 to T1 in this study with their approximate elevations as 890 m (T6), 820 m (T5), 816 m (T4), 813 m (T3), 796 m (T2), 776 m (T1) and 766 m (T0, riverbed) (Figure 4-4). Terrace T3 is the largest hanging-wall terrace surface cut by the fault with braided rivers still developing on it and T3' is defined as the corresponding terrace surfaces on the footwall of the western bank that are flat and widely spread (Figure 4-4). We recognised from the 2019 Google Earth imagery that the hanging wall of T3 has been modified with concentric agricultural facilities so that the original topography is no longer preserved (Figure 4-4a,b). However, Avouac et al. (1993), Zhang, Deng, Xu, Peng, et al. (1994) and Deng et al. (1996) presented *in situ* measurements for these fault scarps and some trench data in the 1990s before the artificial modification.

The average height of fault scarps between T3 and T3' is 8.5 ± 0.2 m (Avouac et al., 1993) with a hinge graben preserved on the upper parts of some scarps. The scarp is typically composite, with the lowest scarp heights of 1.1 m (Avouac et al., 1993) or 0.30-0.58 m (Deng et al., 1994; Zhang, Deng, Xu, Peng, et al., 1994; Deng et al., 1996), inferred to represent the most recent surface rupture (Figure 4-5a,b). The fault scarps between T4 and T3' are all composite scarps, suggestive of accumulated vertical offset, with an average height of 11.1 ± 0.6 m (Avouac et al., 1993). Deng et al. (1996) excavated a large trench (HUTc-1) consisting of nine stepped subtrenches on terrace T3 near 86.794°E, 44.045°N and they found three south-dipping reverse faults (F1, F2 and F3) and one north-dipping normal fault (F4) (Figure 4-4c). This normal fault is interpreted to be the fault that forms the hinge graben mentioned in Avouac et al. (1993). The reverse fault F1 dips 53° and has ~ 2 m vertical displacement; the reverse fault F2 dips ~ 45° and has ~ 0.78 m vertical displacement. The reverse fault F3 has a variable dip angle from 39° to 73° and penetrates the surface with a ~ 0.3 m high free face (Deng et al., 1996). Combining the trench log with the

thermal luminescence dating results from the offset sediments, Deng et al. (1996) suggest only two Holocene earthquakes are identified and fault F3 had ruptured during the 1906 Manas Earthquake.

Fresh fault scarps are found on the youngest terrace T1 with a single-step and no beveling, indicating they are single-event scarps (Avouac et al., 1993; P. Zhang, Deng, Xu, Peng, et al., 1994). Nevertheless, their measured heights vary in the literature. All estimated from the topographic profiles, Avouac et al. (1993) reported the average height of T1 fault scarps is 0.83 ± 0.15 m whereas Zhang, Deng, Xu, Peng, et al. (1994)and Deng et al. (1996) reported the heights to be only 0.2 – 0.3 m. Zhang, Deng, Xu, Peng, et al. (1994) presented trench data across the fault scarp on terrace T1 showing one fault plane dipping 25 – 30° to the south with underlying strata displaced only about 0.35 m. Although there is variation in height, both the lower scarps (0.3 – 1.1m) at the foot of the composite scarps on T3 and the fresh < 1 m scarps on T1 are all compatible with slip in the 1906 Manas Earthquake

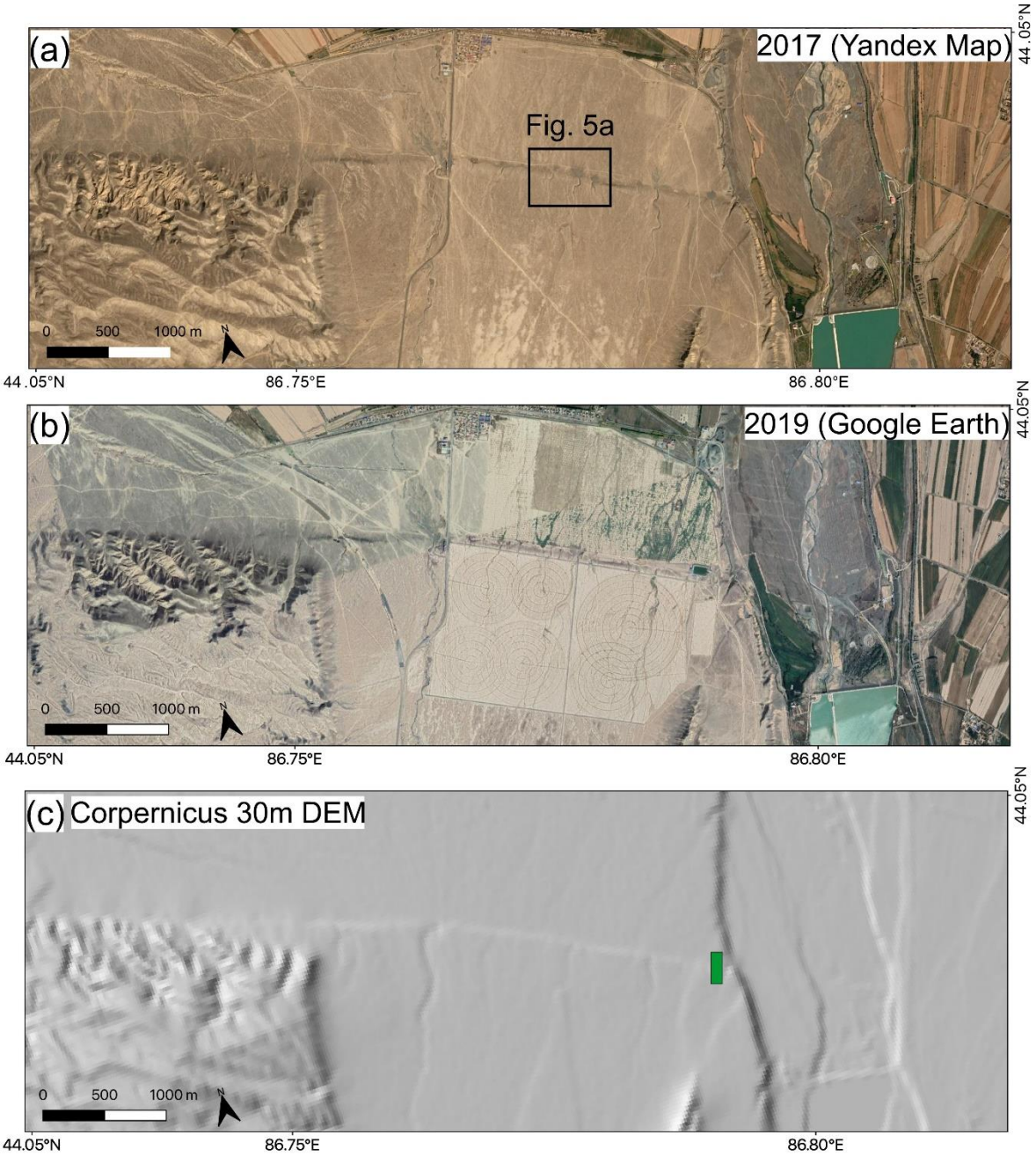
(a)
2017 (Yandex Map)
Fig. 5a
0 500 1000 m
N
44.05°N
86.75°E
86.80°E
(b)
2019 (Google Earth)
(c) Corpernicus 30m DEM
(d)
100 m
T3'
Hutubi fault
T1
Hutubi river
T6
T3
T4
T0
T2
T5
Dam

Figure 4-4. Fault scarps along the Hutubi Fault on the western bank of the Hutubi River. (a) and (b) Optical satellite imagery from Yandex and Google Earth Map respectively with the years when the imagery was taken. Artificial irrigation and farming system can be seen from the 2019 imagery which has modified the original landscape. (c) Shaded topographic relief from the 30-m Corpernicus DEM (European Space Agency Sinergise, 2021). The green square marks the location of the trench (HUTc-1) in Deng et al. (1996). (d) Mapping and interpretations from this study with faults marked in red.

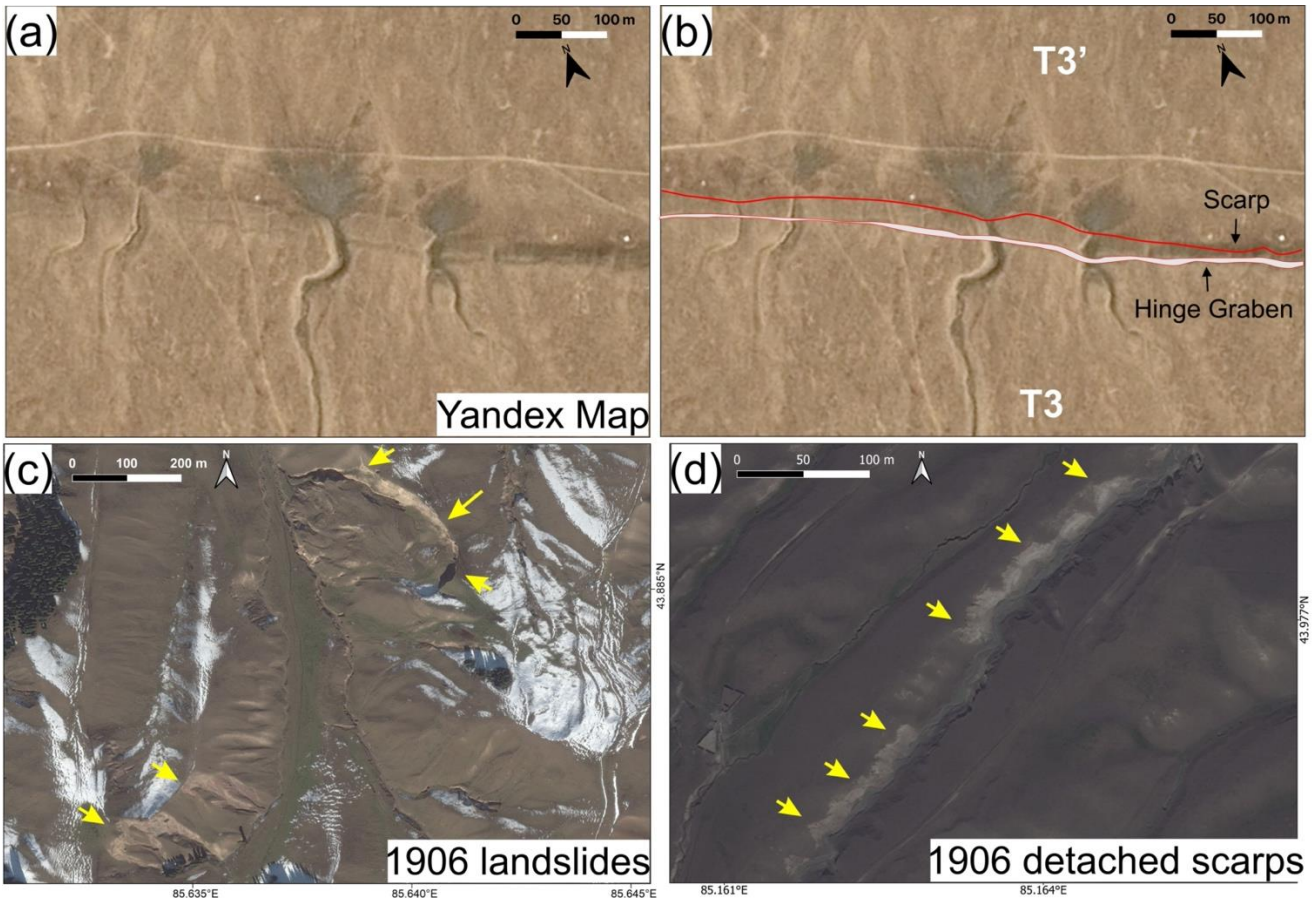

Figure 4-5. (a) and (b) Zoomed-in view of the Hutubi Fault scarps (in red) and hinge graben across T3 and T3' shown in Figure 4-4a. (c) The landslides near Shichang, shown in Bing Map, possibly caused by the 1906 Manas Earthquake (d) A possibly detached scarp, sliding to the southeast, caused by the 1906 shaking near the Shiaonanguo River shown in Bing Map. Locations of (c) and (d) are labelled in Figure 4-3a.

4.3.2.2 Eastern Terraces of the Manas River

The northward-flowing Manas River is located between the Tugulu Anticline and the Manas Anticline (Figure 4-3a). On the eastern bank of the main Manas River, there are six major terrace levels recognised, T6 to T1 from high to low, with terraces T5 and T6 being intensively deformed by the two faults that have a ~ 2 km interval between each other (Z. Gong et al., 2015) (Figure 4-6). The western extension of the Hutubi Fault terminates at terrace T5 of the Manas River and has produced 3 – 5 m high scarps on it near 86.1251°E, 44.1698°N (Avouac et al., 1993; Z. Gong et al., 2015) (Figure 4-6c). The Manas Fault, bounding the north side of the Manas Anticline, terminates on terrace T6 and has produced 7 – 10 m high scarps on both T5 and T6 near 86.1417°E, 44.1883°N, north of the Hutubi Fault scarps (Avouac et al., 1993; Z. Gong et al., 2015) (Figure 4-6). Some previous studies do not associate these two scarp series with the 1906 Manas Earthquake due to the highly-degraded scarp surfaces and the lack of scarp continuity to the younger terraces (Avouac et al., 1993; P. Zhang, Deng, Xu, Wu, et al., 1994); however, trenching data from this site are interpreted to show the possible influence of the 1906 Manas Earthquake. Deng et al. (1996) excavated a trench (MTc-4), at the Manas Fault scarp on T5, and they revealed no surface rupture, but the top three layers, including soil and gravels, are warped, suggesting recent deformation. Gong et al. (2015) reported a very fresh surface rupture of the Manas Fault within the T5 surface at 86.1329°E, 44.1885°N (site MNS2); however, they did not associate it with any historical event, and we further suggest this rupture is probably an artificial scarp since it is at the edge of a small man-made trail. Apart from trench MTc-04 and site MNS2, the other trenches or outcrops observed by Deng et al. (1994), Deng et al. (1996) and Gong et al. (2015) in this region do not show recent surface rupture.

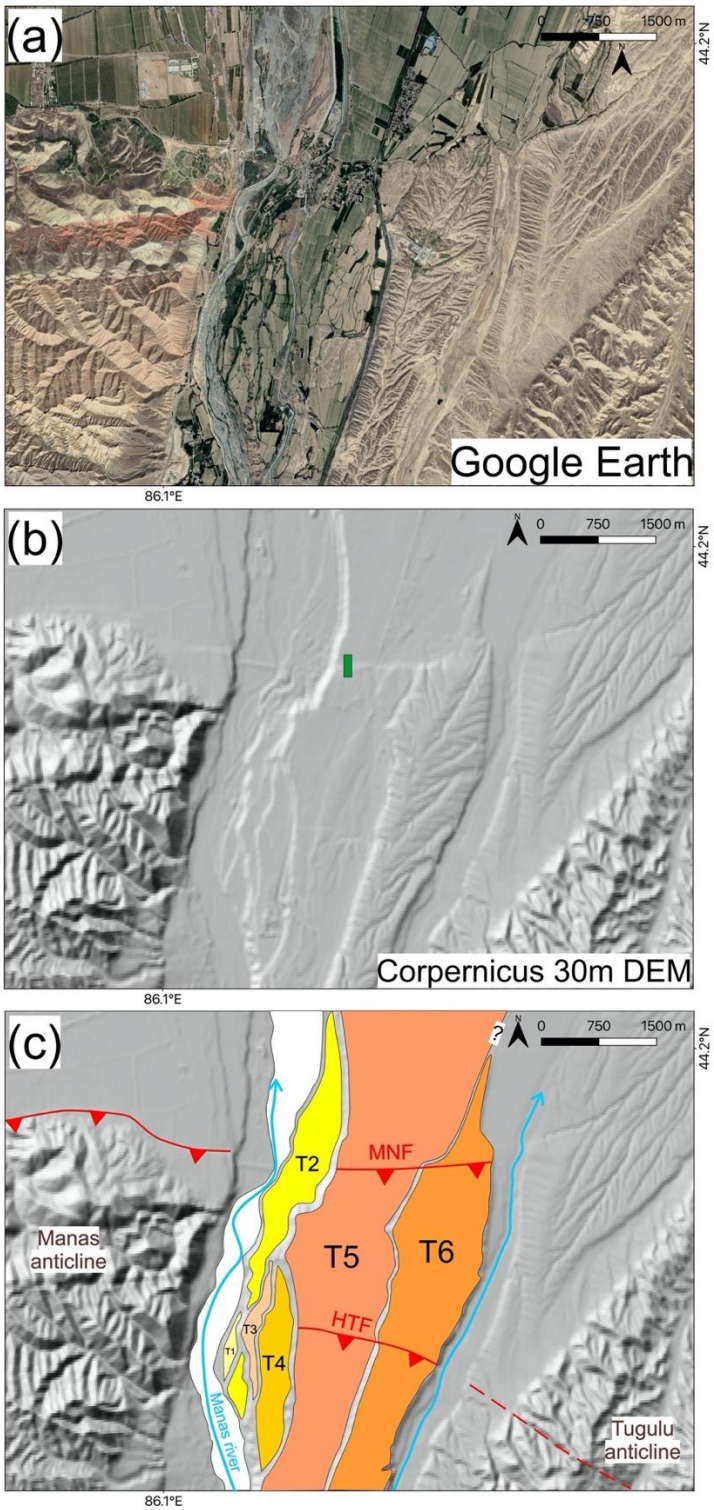

Figure 4-6. Two series of fault scarps (in red) along the Manas River between the Tugulu and Manas Anticlines shown in (a) optical satellite imagery in Google Earth Map in 2019 and (b) shaded topographic relief from the Corpernicus DEM (European Space Agency Sinergise, 2021). The green rectangle marks the location of the trench (MTc-4) in Deng et al. (1996). (c) Mapping and interpretations from this study. MNF: Manas Fault; HTF: Hutubi Fault.

4.3.2.3 Aweitan Gulley (the Central Section of the Manas Fault)

Zhang et al. (1994) reported a ~ 300 m long fault scarp at the Aweitan Gulley which is a 4 – 5 m high composite scarp with the latest vertical offset around 0.6 m (Profile III therein). A trench (MTc-3) dug at this site indicated this scarp is the product of an underlying fault (Deng et al., 1996). However, there is no description in that literature of the precise locations of the Aweitan Gulley, the scarps and the trench. According to the previous mapping from Zhang, Deng, Xu, Wu, et al., (1994) and Deng et al. (1996), we infer the site to be south of Aweitan village near 85.987°E, 44.198°N, which is ~ 7 km southeast of the Shihezi Airport (Figure 4-3a), where a series of fresh scarps are visible in satellite imagery (Figure 4-7). Quite a few unnamed gullies in this region now contain water dams, quarries, or roads that have obscured or degraded the previously identified fault scarps. We suggest the most likely scarps mentioned in Zhang et al. (1994) might be either in the west of the Aweitan Gulley at 85.9543°E, 44.2053°N or on the Aweitan terrace at 85.9757°E, 44.1987°N, which has now been destroyed by quarry construction (Figure 4-7).

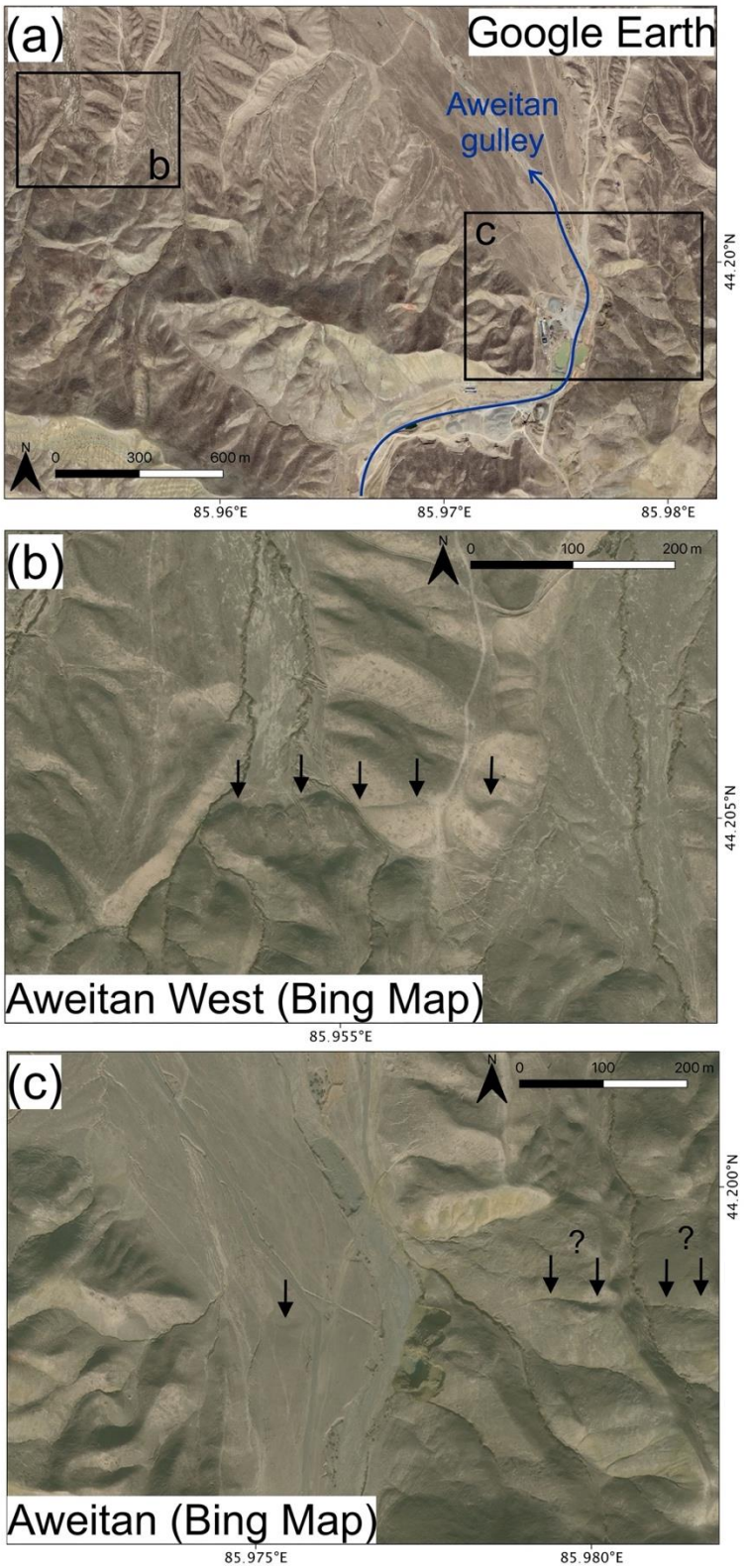

Figure 4-7. (a) The likely 1906 surface ruptures (pointed by black arrows) at the Aweitan Gulley shown in optical satellite imagery with two specific sites shown in (b) and (c). A quarry infrastructure can be seen in the 2019 Google Earth Map in (a) but Bing Map in (c) caught the landscape before the exploitation.

4.3.2.4 Western Terraces of the Jingou River

The northward-flowing Jingou River (also called the Huoerguos River) cuts throw the E-W trending Huoergous Anticline and the Huoergous Fault (Figure 4-3a). Prominent fault scarps along the Huoergous Fault can be easily recognised for ~ 2.5 km on the western side of the Jingou River, and displace all the five terrace levels that are present (Avouac et al., 1993; P. Zhang, Deng, Xu, Peng, et al., 1994; Pang et al., 2021). The terraces are labelled T5 – T1 from high to low in this study (Figure 4-8). The morphology of the Huoergous Fault scarps is similar to the Hutubi Fault scarps as having a hinge graben at the top and showing distinct lower scarps at the bottom of the main scarp that is interpreted as resulting from the most recent surface rupture. The average heights of fault scarps on terraces T5 and T4 are ~ 11 m and 4.6 ± 0.5 m, respectively, and both with hinge graben (Avouac et al., 1993; Pang et al., 2021). On terrace T3, the average scarp height is 4.0 ± 0.4 m (Pang et al., 2021). A secondary fault on T3, and a distinct step at the bottom of the T3 composite scarps have similar heights measured at 0.9 m by Avouac et al. (1993) and 0.5 – 0.7 m by J. Li et al., (1992) and Zhang, Deng, Xu, Peng, et al. (1994). These < 1 m vertical offsets are similar to those found at the Hutubi River terraces and the freshness (outlined by turf and rodent holes) of them observed in the field suggests they are less than hundreds of years old (Avouac et al., 1993; P. Zhang, Deng, Xu, Peng, et al., 1994). The composite scarps measured on terrace T2 are 2.8 ± 0.3 m high with a hinge graben at the top (Pang et al., 2021). No scarp data were reported from terrace T1 since there is a hydrological infrastructure built on it (Figure 4-8a). Deng et al. (1996) excavated a trench (HOTc-1) in the youngest terrace of the Jingou River that should be located on the terrace T1 mapped in this study, although no precise location was provided. A reverse fault dipping 40° to the south was found in this trench and the top sediment layer, dated at ~ 6900 cal. year B. P., has been warped by the latest earthquake event which is interpreted to be the 1906 Manas Earthquake (Deng et al., 1996).

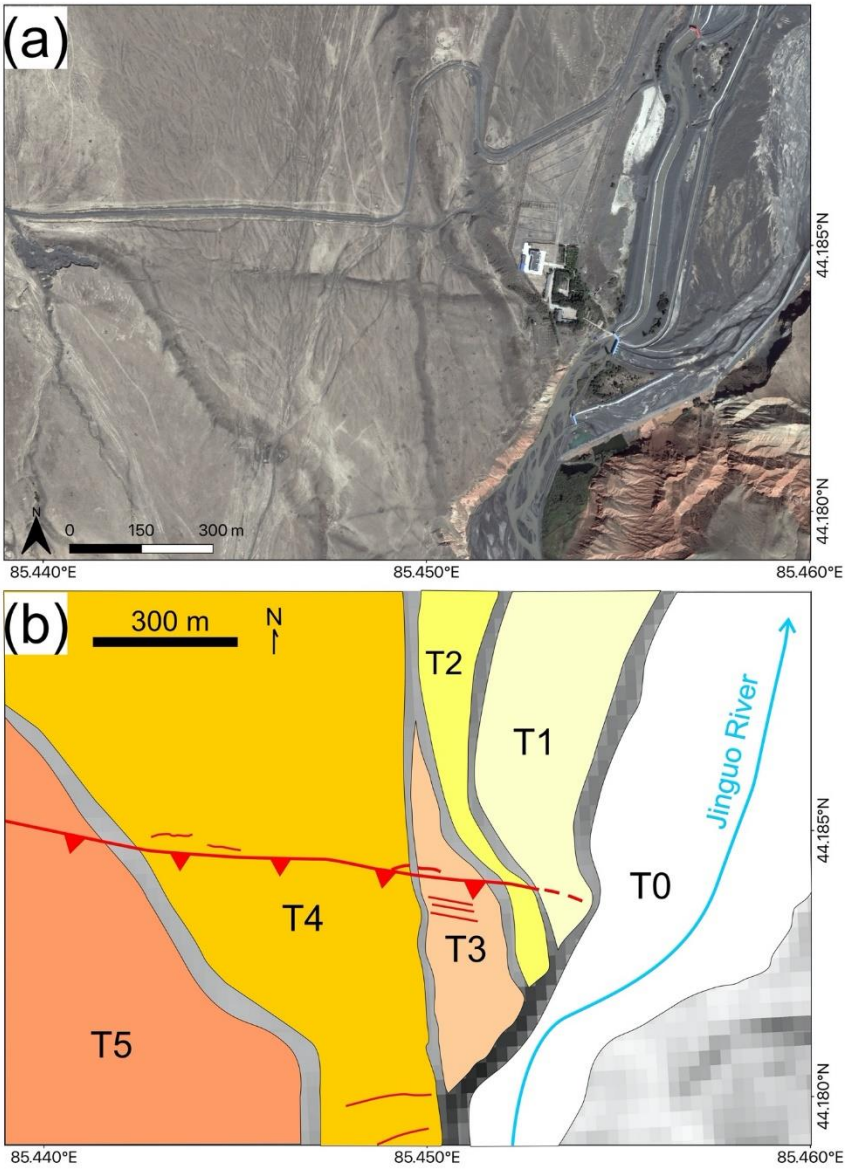

Figure 4-8. The Huoerguos Fault scarps in the western bank of the Jinguo River shown in optical satellite imagery from Bing Map. (b) Mapping and interpretations with faults marked in red based on the shaded topographic relief from the Corpernicus DEM (European Space Agency Sinergise, 2021). The trench (HOTc-1) was dug into the youngest terrace which is now obscured by infrastructure (Deng et al., 1996).

4.3.2.5 The Northern Hills of the Borohoro Shan

Previous surveys have shown that the most damaged area during the 1906 Manas Earthquake extends for ~ 40 km along the range front of the Borohoro Shan from the Manas River to the Shiaonangou River (Seismological Bureau of Xinjiang, 1985) (Figure 4-3a). Most of the ruptures in this region are gravity-triggered landslides, fissures and detached scarps instead of compressional ruptures (Bai & Fang, 1981; P. Zhang, Deng, Xu, Peng, et al., 1994). In this study, "landslides" are defined to be U-shaped mass wasting with obvious crowns and sliding bodies. "Fissures" are shaking-triggered tensional cracks that do not display offset. Unlike the scarps that show obviously hanging-wall and foot-wall offsets within the stratigraphy, "detached scarps" are gravity-triggered linear scarps that only offset the loose surface materials, like soil or loess, but not the bedrock (P. Zhang, Deng, Xu, Peng, et al., 1994). From the Manas River to the Ningjia River, the type of surface ruptures is mostly large landslides with their crowns up to hundreds of meters wide (P. Zhang, Deng, Xu, Peng, et al., 1994) (Figure 4-3a and Figure 4-5c). From the Ningjia River to Nuiquanzi (Figure 4-3a), most ruptures are fissures longer than 100 m with a depth of 0.1 – 0.2 m and a width of 0.3 – 0.4 m developed along the gulleys (P. Zhang, Deng, Xu, Peng, et al., 1994). Nevertheless, it is difficult to recognise these fissures from the imagery nowadays, probably due to their relatively small sizes and post-earthquake erosion. Some smaller landslides with tens of meters sliding and 1 – 2 m-high head scarps are also recognised from the Ningjia River to Nuiquanzi (P. Zhang, Deng, Xu, Peng, et al., 1994). From the Jinguo River to the Shiaonangou River, most ruptures are detached scarps developed along the secondary loess layer on the sides of gulleys (P. Zhang, Deng, Xu, Peng, et al., 1994) (Figure 4-3 and Figure 4-5d). These detached scarps are usually tens to hundreds of meters long and 0.5 – 1 m high with a SE sliding direction (P. Zhang, Deng, Xu, Peng, et al., 1994) (Figure 4-5d). Some trenches were dug across the detached scarps and they showed no fault nor offset within the bedrock but some fissures within the secondary loess layers, indicating they are shaking-induced mass wasting (Seismological Bureau of Xinjiang, 1985; P. Zhang, Deng, Xu, Peng, et al., 1994). Bai & Feng (1981) mentioned several 2.5 m dextral displacements along the right-stepping en echelon reverse cracks in this region but we have no information about their locations. A possible fault scarp at the northern hills of the Borohoro Shan is reported by the Institute of Geophysics, SSB & Institute of Chinese Historical Geography, (1990), who include a photo showing the ~ 2 m-high scarp in the south of Bourtongu, but without giving a precise location and we could not identify this scarp from modern satellite imagery (Figure 4-3a).

4.3.2.6 Anjihai-Dushanzi Anticline

Along the Anjihai Anticline (Figure 4-3a), no fresh fault scarps have been reported in the previous studies. Between the Halaande Anticline and the Dushanzi Anticline, left-stepping en echelon faults are recognised on the river terraces (Figure 4-3a), indicating some dextral fault movements in this region (Deng et al., 1991; Avouac et al., 1993). The trench data along the Anjihai Anticline and across those en-echelon faults indicate two Holocene earthquakes in the intervals 6-8 ka and 3-5 ka respectively, but no earthquake evidence could be found within the last 3000 years (Deng et al., 1991) (Figure 4-3a). On the western bank of the Kuitun River, which cuts through the Dushanzi Anticline, several < 3 m-high fault scarps are found on the high-level terraces (Deng et al., 1996; Su et al., 2018). However, the trench data collected from these Dushanzi scarps also infer the thrust here has not ruptured the surface for at least the past 800 years (Figure 4-3a) (Y. Li et al., 2012; Su et al., 2018). These all indicate the 1906 Manas Earthquake did not cause surface rupture from Anjihai to Dushanzi Anticlines. In sum, the surface ruptures of the Manas Earthquake can only be observed between the east of the Anjihai River and the west of the Hutubi River, which is 120-140 km long (Figure 4-3a).

4.3.3 Previously Estimated Magnitudes

A summary of the previously reported magnitudes is shown in Table 4-1 with the corresponding references and methods. The largest magnitudes for the 1906 Manas Earthquake were estimated to be Ms 8.3 by Richter, (1958) and Molnar & Deng, (1984) and lower magnitudes were also reported to be M 8 (Bai & Fang, 1981; Gongxu Gu, 1983; ISC, 2021), Ms 7.9 (Gutenberg & Richter, 1954), Mw 7.8±0.2 (Storchak et al., 2013), and M 7.7 (Institute of Geophysics, SSB & Institute of Chinese Historical Geography, 1990; P. Zhang, Deng, Xu, Peng, et al., 1994; Deng et al., 1996; X. Yang et al., 1998, 2002; W. Zhou et al., 2003; C. Y. Wang et al., 2004; Lu et al., 2018). Some even suggested the magnitudes were only Ms 7.3 (Abe, 1988) or Ms 7.2 (Abe & Noguchi, 1983) from the implication that the surface wave magnitudes inferred from the seismograms of 1897 – 1912 events might be systematically overestimated. However, Avouac et al. (1993) disagreed with these low magnitudes from the comparison with other better-estimated historical events. Avouac et al. (1993) further added their field survey results with certain assumptions to calculate the magnitude as Ms 8 ± 0.2, based on the surface rupture length of 150 km and the assumed fault slip, dip and depth of 3.5 ± 2 m, 45°S and 15 – 40 km respectively, which is the most detailed implication of the fault geometry. It is also worth noticing that Chinese studies after 1990 all use

Ms 7.7 as referring to the Institute of Geophysics, SSB & Institute of Chinese Historical Geography (1990) or Zhang et al. (1994).

Table 4-1. Reported Magnitudes, Depths and Surface Rupture Length of the 1906 Manas Earthquake

Magnitudes	Reference	Method
Ms 7.9	Gutenberg & Richter (1954) and Abe (1981)	Surface wave amplitudes measured at 20s period
Ms 8.3	Richter (1958)	Surface wave amplitudes
m_B 7.5	Abe (1981)	Body wave measured on broad-band instruments in periods of ~ 4s – 12s.
M 8	Bai & Fang, (1981)	Unspecified
Ms 8	Gu (1983)	Referred to Gutenberg & Richter (1954) but with corrections based on Chinese seismological data
Ms 7.2	Abe & Noguchi (1983)	Surface wave amplitudes with a factor of the effective gain
Ms 8.3	Molnar & Deng (1984)	Rupture area based on the observations in Bai & Fang, (1981)
Ms 7.3	Abe (1988)	Revised from Abe & Noguchi (1983)
Ms 8 ± 0.2	Avouac et al. (1993)	Rupture area from field observations and associated assumptions
Ms 7.7	Institute of Geophysics, SSB & Institute of Chinese Historical Geography, (1990); Zhang, Deng, Xu, Peng, et al. (1994); Deng et al. (1996); X.Yang et	Either unspecified or refer to the field survey conducted by the Seismological Bureau of Xinjiang Uygur Autonomous Region in 1973

	al. (1998); X. Yang et al. (2002); Zhou et al. (2003); Wang et al. (2004); Lu et al. (2018)	
Mw 7.8 ± 0.2	Storchak et al. (2013)	Estimation from a bibliographical search of references (1900 – 1979) that feature a reliable direct estimation of M_0
Mw 7.95	ISC-GEM (2021)	Original amplitude-period measurements (Bondár et al., 2015)
m_B 7.4 ± 0.3 M_S 7.9 ± 0.2 Mw 7.7 ± 0.2	This study	Methods elaborated in this study based on Kulikova (2016)
Depth	Reference	Method
12 km	Gu (1983)	Unspecified but should be related to the formula in Gutenberg & Richter (1942) and Liu (1961)
24 km	Xie and Cai (1986)	Referring to the Chinese earthquake catalogue in 1977
15 – 40 km	Avouac et al. (1993)	Compilation of the depths from historical seismicities in the northern Tien Shan
~ 15 km	Yang et al. (2002)	Tomography profiles and the depths from historical seismicities
20 km	Wang et al. (2004)	The median focal depth from 110 well-located earthquakes in

		the northern Tien Shan since 1980.
18 km	This study	Methods elaborated in this study based on Kulikova (2016)
Surface Rupture Length	Reference	Method
65 km	Bai & Fang, (1981)	Observation of ruptures from the Shiaonangou River to the east of the Manas River
40 km	Molnar & Deng (1984)	The most concentrated area of ruptures mentioned in Bai & Fang, (1981)
150 km	Avouac et al. (1993)	The length from South Anjihai Anticline to Tugulu Anticline
130 km	This study	Distance between the east of the Anjihai River and the west of the Hutubi River
110-120 km	This study	Source duration of P-wave

4.3.4 Seismological Analysis and Earthquake Mechanism[#]

4.3.4.1 Data Acquisition

We collected 14 seismic records of the Manas earthquake from 8 stations to relocate the epicentre, construct the focal mechanism and re-estimate the magnitude. The station distribution is presented in Figure 4-9. The majority of the seismograms were collected from seismic stations located in Europe, due to better preservation of records and easier accessibility. Considering the epicentral distance (about ~ 5000 km), the European stations altogether can be considered as a large aperture distant seismic array, which allows stacking of the traces to improve the signal-to-noise ratio (Kulikova & Krüger, 2015). Seismograms from seismic station HNG, Tokyo, Japan and Chinese station ZKW (ZiKaWei) were added

[#]The seismological analysis and related data collection/calculations in this chapter for the 1906 Manas and 1944 Xinyuan Earthquakes were all conducted by Dr. Galina Kulikova and not by the author of this thesis. The majority of the content in Section 4.3.4 is written by Dr. Galina Kulikova.

to the data collection providing observations from different azimuths. The 1906 Manas Earthquake has been recorded by analogue seismic instruments with the seismograms existing either as original paper recordings or as reproductions on microfilm, or as photographs in books. For further processing, the analogue seismograms were digitized manually using the path tool of GIMP (GNU Image Manipulation Program) (Kimball et al., 2013) and the technique described by Kulikova (2016) and Ou et al. (2020). Examples of digitized seismic waveforms of the Manas Earthquake are presented in Figure 4-10. The records show clear P phase arrival followed by impulsive S wave, especially on the N component of the European stations. In addition, both direct P and S phases are followed by dominant larger amplitude arrivals, which are attributed to the surface reflections PP and SS accordingly.

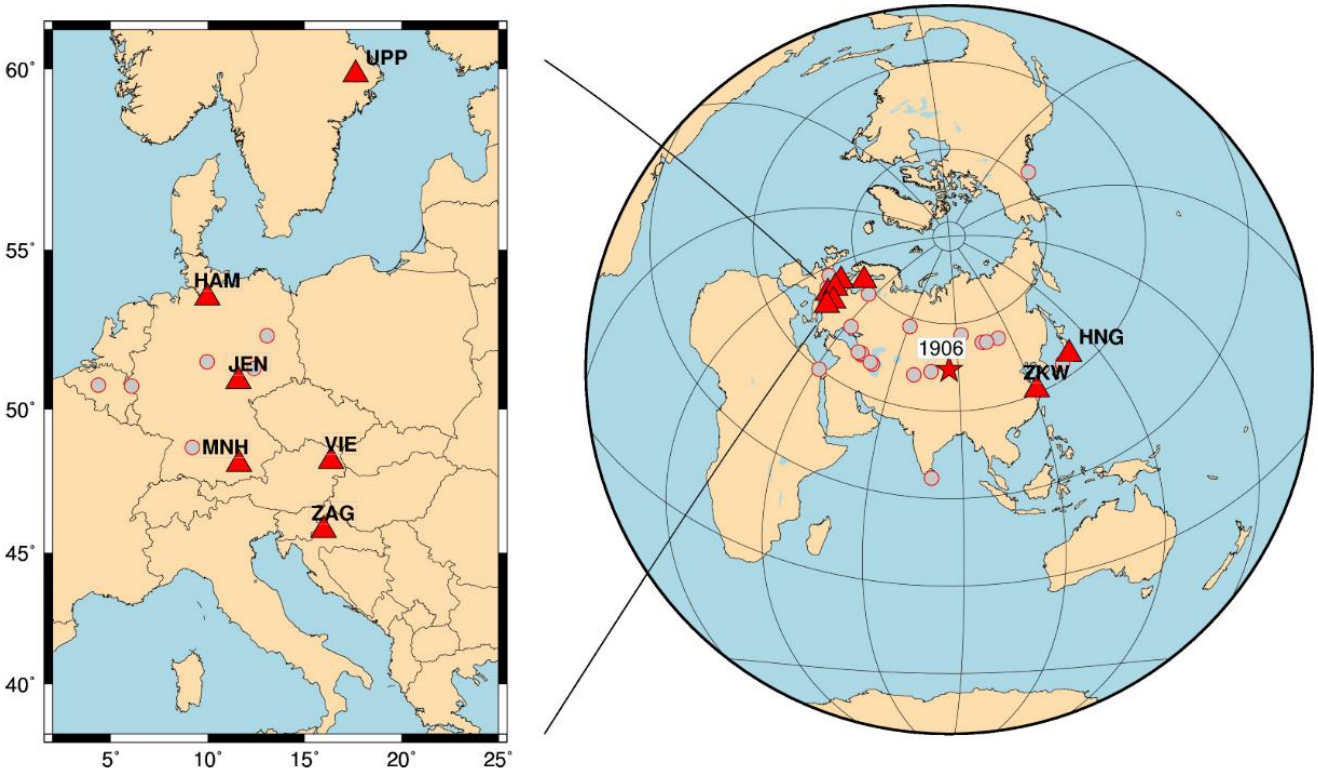

Figure 4-9. Station distribution map for the 1906 Manas Earthquake. Red star shows the epicentre location of this event; Grey circles show the seismic stations, from which the bulletins, including different phase arrival times, were available; Red triangles show the stations from which seismic records were obtained.

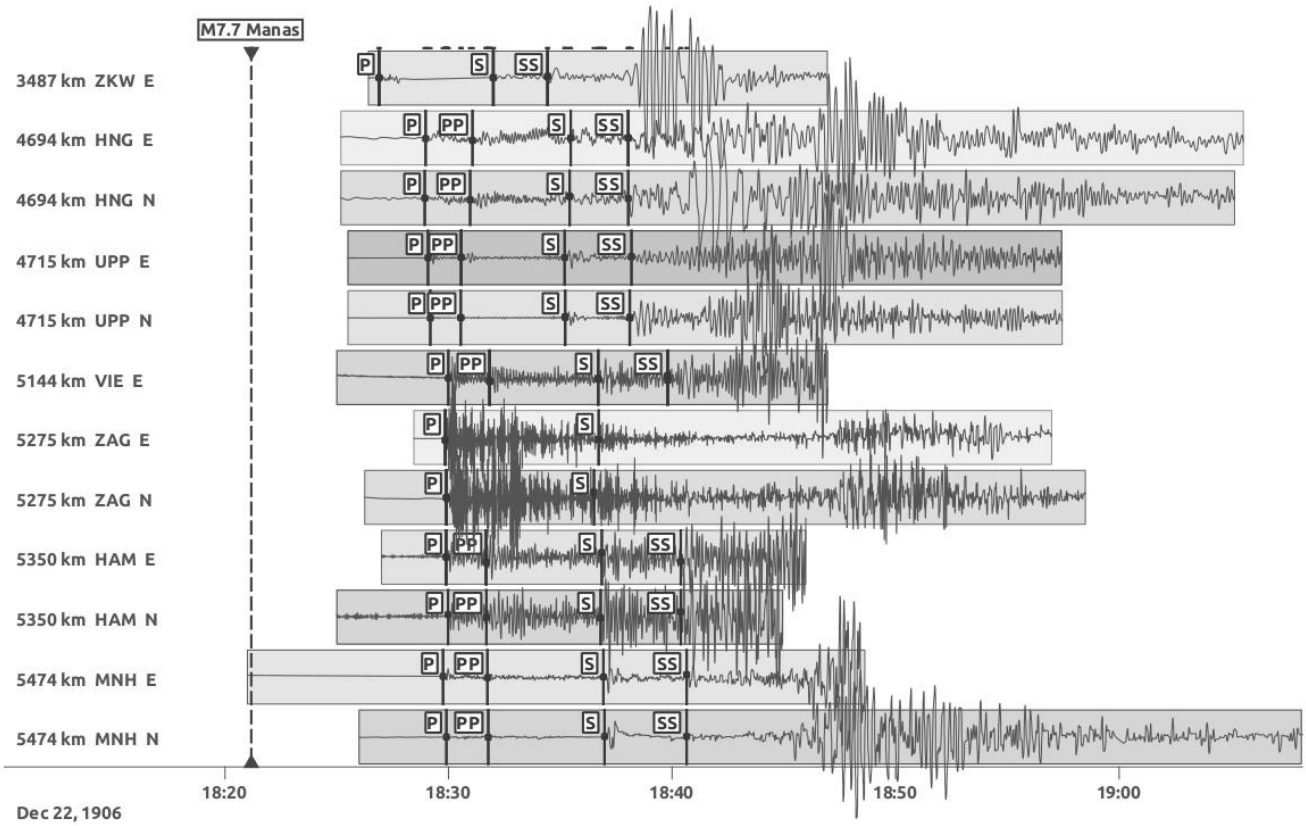

Figure 4-10. Digitised seismic records of the 1906 Manas Earthquake from the 8 seismic stations (Figure 4-9). The curvature was corrected using the method in Cadek (1987) and the traces are normalised. The dominant P, PP, S and SS phases are marked accordingly.

4.3.4.2 Epicentre Relocation

The poor azimuthal coverage and a limited number of stations lead to high uncertainties in the epicentre location based on the waveform data since we only have available seismograms from 14 seismic stations that are mainly located in Europe. Therefore, 24 local and teleseismic bulletins were employed in the epicentre location procedure in addition to the 14 digitized seismograms. A total of 58 onset times of all identified phases and 21 arrival time differences were inverted in the HYPOSAT program with a modified crustal structure based on the CRUST 5.1 model and the AK135 global velocity model (Kennett et al., 1995; Mooney et al., 1998; Schweitzer, 2001, 2012). Three different epicentres were determined from the inversion (see Table 4-2 and Figure S4-1): 1- at 44.09°N, 85.16°E using arrival times picked from the digitized waveforms, 2- at 44.04°N, 84.61°E using the bulletin arrivals only, and 3- at 43.96°N, 84.93°E using a combination of the two datasets. All solutions are in good agreement with each other and

place the epicentre about 100 km southwest of Manas County. Although all available arrivals were employed, the dataset did not include any depth phase arrivals. Thus, the hypocentre depth could not be determined and was fixed at 20 km in the HYPOSAT inversion.

Table 4-2. Epicentre Locations

Number	Location type	Origin time (hh:mm:ss.s)	Latitude	Longitude	Depth (km)
1	Waveforms only	18:21:08.3±2.0	44.093±0.6691	85.158±0.3850	20.00-Fixed
2	Bulletins only	18:21:09.6±3.9	44.039±0.6560	84.608±0.6011	20.00-Fixed
3	Preferred location	18:21:10.6±1.9	43.958±0.5214	84.926±0.2954	20.00-Fixed

4.3.4.3 Focal Mechanism

The amplitude ratios comparison method was used for focal mechanism determination of the 1906 Manas Earthquake (Kulikova & Krüger, 2015; Ou et al., 2020). Amplitude ratios of different phases (body waves only: P, PP, S and SS phases were used) were compared in a grid search procedure to the synthetic records amplitude ratios for different focal mechanisms to determine the best amplitude ratios fit. All combinations of strike, dip and rake (0° <strike<360°, 0° <dip<90°, -180° <rake<180°, with 2° step for all) for a double couple source were tested considering a point source. Grid search was performed over different test depths from 0 to 60 km with a 2 km step (Figure 4-11). The minimum misfit, corresponding to the best, was observed for the combination strike/dip/rake: 96°/46°/70°. Although the minimum misfit defined 96° strike, the 5% best solutions varied in strike between 96° and 116°, which would mean the strike is likely to be around 106 ± 10°. The minimum misfit for dip angle is at 46° from the best solutions varied between 46° and 56°, implying the earthquake has likely occurred on a steeply dipping fault (51° ± 5°). Based on the overall tectonic regime of the region we suggest the ruptured fault plane is the south-dipping plane (see Figure 4-3 Figure 4-11). Unfortunately, with the available limited dataset, the method proved itself rather insensitive to the change of depth. The calculation for different tested depths shows a very low dynamic with a misfit minimum of 18 km (Figure 4-11).

4.3.4.4 Magnitude Estimation

We determined magnitudes m_B and M_S using the amplitudes and periods of body and surface waves from seismic bulletins and digitized waveforms. Moment magnitude M_W was also determined based on waveform modelling. Broadband body wave magnitude m_B was determined using the Gutenberg & Richter, (1956) formula corrected for geometric spreading and distance-dependent attenuation (Bormann et al., 2013). For the case of the 1906 Manas Earthquake, the broadband body wave magnitude m_B is especially important since the seismic instruments operating at that time mostly had limited dynamic range and were frequently not able to record the full amplitude of surface waves. Moreover, the period of the instruments was more suitable for recording the shorter period of body waves than surface waves. The amplitudes and period data used for m_B estimation are presented in Table 4-3. It is subdivided into two parts showing the data found in seismic bulletins and the values measured on digitized waveforms. Although the amplitude values from bulletins and waveforms differ, even for the same station (possibly due to the unknown method used to convert from mm on paper to µm of displacement by the analysts at that time), the average magnitude for all stations remains the same and equals to m_B 7.4 ± 0.3. The estimation of surface wave magnitude was based on the maximum amplitudes of surface waves using the "Moscow-Prague 1962 formula" (Kárník, 1962). Results of M_S estimation are presented in Table 4-4, with separation for bulletins and waveforms amplitudes as well, resulting in M_S 7.9 ± 0.2. This value is similar to Ms 8.0 ± 0.2 in Avouac et al. (1993), supporting that Ms 7.2 – 7.3 should be underestimated whereas Ms 8.3 is likely overestimated (Table 4-1).

After the focal mechanism was determined with amplitude ratio comparison, forward waveform modelling was used to estimate the moment magnitude Mw. For the fixed focal mechanism, the synthetic seismograms were simulated for different Mw and compared in a grid search with the observed data, in order to determine the best waveform fit. For this procedure, only true-scale seismograms (full scans, no microfilms) with precisely known instrument parameters were used. In our case, these were the seismograms from the European stations. The best waveform fit was observed for an average magnitude Mw 7.7 with ± 0.2 magnitude deviation for different stations. This agrees with the Mw 7.8 ± 0.2 in Storchak et al. (2013) and further implies the Mw 7.95 from the latest ISC-GEM catalogue could be the upper bound (ISC, 2021). A magnitude of ~ Mw 7.7 for a thrust earthquake suggests a rupture width of 20 – 40 km (Blaser et al., 2010). This means it is reasonable to have a broad misfit minimum of the seismic depth; however, this also implies the low possibility of the 1906 hypocentre being > 60 km in depth (Figure 4-11), which could also be inferred from the strong shaking of this crustal earthquake.

An approximate source time duration of the earthquake can be directly estimated from the P-wave record. The majority of the seismograms obtained for this study were recorded on seismic stations in Europe (about ~5000 km away from the epicentre). To estimate the source time duration from the European stations, P-waves were aligned and stacked together, to improve the signal-to-noise ratio (see Figure S4-2, it should be noted that P-wave duration was measured on the horizontal E-component since the preferred vertical component was not available). The overall maximum P-wave source duration was ~ 37 – 40 seconds, which would produce ~ 110 – 120 km rupture considering the case of unilateral rupture and taking the average rupture velocity as 2.9 km/s. Empirical scaling relations suggest a magnitude Mw 7.7 – 7.8 for this rupture length (Wells & Coppersmith, 1994; Blaser et al., 2010).

Table 4-3. Amplitudes and Periods of Different Phases Used for m_B Calculation for the 1906 Event

Station	Phase	T[sec]	Amp[mm]	Amp[μm]	m_B
Bulletins					
JEN	P	8.5		29	7.7
JEN	PP	8.6		49	7.6
JEN	S	13		67	7.4
GTT	P	9		17	7.4
GTT	PP	9		30	7.3
GTT	S	17		60	7.3
ZKW	P	2.4		70	8.4
ZKW	S	15		266	8.1
UPP	P	8		20	7.1
UPP	PP	10		19	7
UPP	S	10		27	6.9
AAC	S	12		41	7
LEI	P	7.5		14	7.5
LEI	PP	7.5		20	7.2
LEI	S	9		26	7.2
UCC	P	1	0.3	2	7.2
UCC	S	10	5	24	6.9
				Average	7.4 ± 0.4
Waveforms					
HAM	P	9	7.8	39.1	7.8
HAM	PP	9	11.9	59.5	7.6
HAM	S	7	19.4	97.1	7.8
UPP	P	8	6.1	22.5	7.1
UPP	PP	11	5.1	25.5	7.1
UPP	S	13	10.3	74.3	7.3
JEN	P	8	3.8	12.7	7.4

JEN	PP	8	6.5	21.7	7.2
JEN	S	18	10.2	211.3	7.8
MNH	P	10	6.8	22.8	7.5
MNH	PP	11	3.7	12.5	6.9
MNH	S	12	18.5	68.6	7.5
VIE	P	8.7	8.4	32.7	7.7
VIE	PP	8.7	7.2	28.1	7.3
VIE	S	8.7	9	35.1	7.2
				Average	7.4 ± 0.3

Table 4-4. Amplitudes and Periods of Different Phases Used for M_S Calculation for the 1906 Event

Station	T[sec]	Amp[mm]	Amp[μm]	M_s
Bulletins				
AAC	20		1200	7.9
HOH	13	80	690	8.2
LEI	24		2200	8
UCC	15	130	873	7.9
ZKW	19		3865	8.1
UPP	20		650	7.5
JEN	20		1861	8.1
ZKW	19		3865	8.1
GTT	21		700	7.6
OSK	19.8		1285	7.8
			Average	7.9 ± 0.2
Waveforms				
UPP	20	81	1516	7.9
JEN	22	75	2415	8.1
MNH	20.5	76	840	7.7
			Average	7.9 ± 0.2

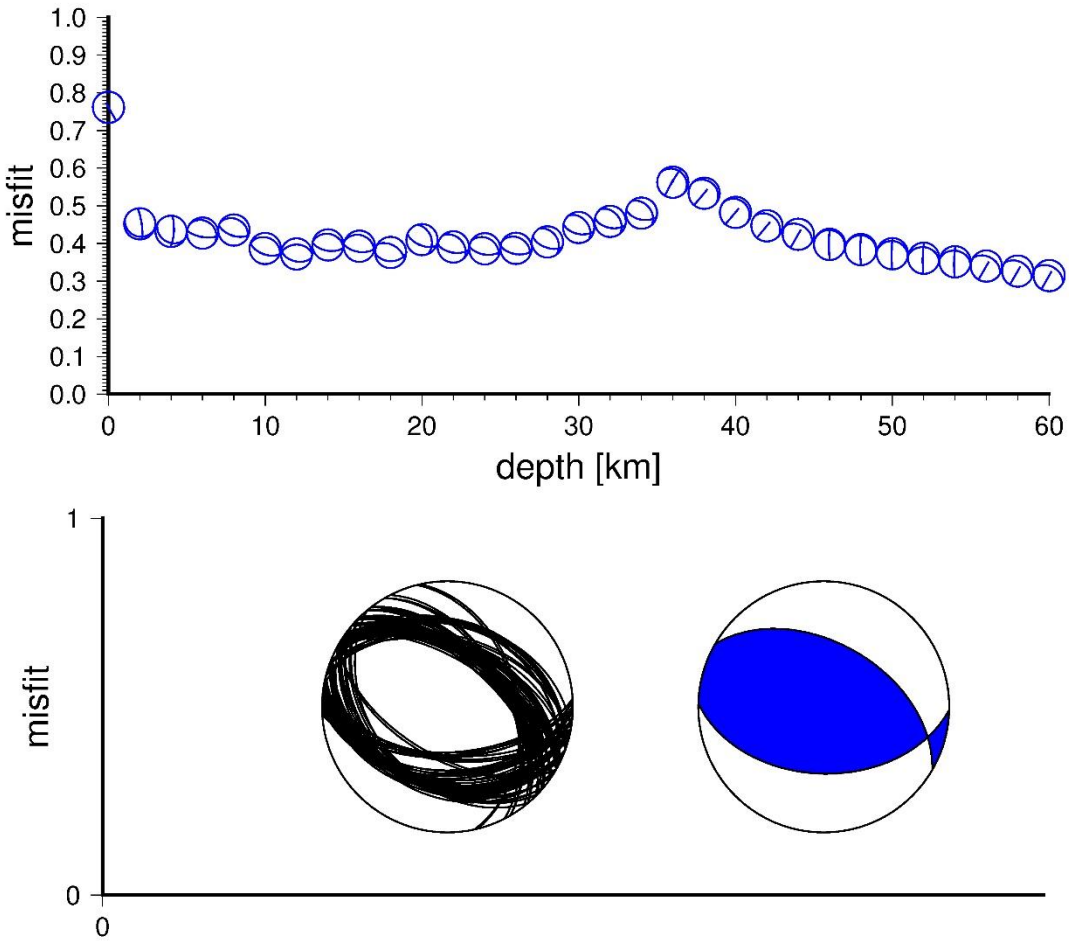

Figure 4-11. Focal mechanism determination of the 1906 Manas Earthquake. The top panel shows the mechanism determination for different tested depths; the bottom panel shows the 5% best solutions and the solution with the minimum misfit.

4.3.5 Seismogenic Faulting

The strike (96°) and rake (70°) of our modelled focal mechanism suggests predominantly thrusting parallel to the northern margin of the Borohoro Shan. The epicentral location indicates that it nucleated beneath the northern Borohoro range, though we do not have a direct constraint on nucleation depth, and with a relatively steep dip of ~ 51° to the south. The surface ruptures, however, are found along the northern margin of a series of folds ~ 10 km north of the Borohoro Shan range front, with a total length of ~ 125 km for the three ruptured segments.

We first exclude the Anjihai-Dushanzi Fault to be the responsible fault for the 1906 event since most of the reported epicentres are far away from it and the trenching data indicate the Anjihai-Dushanzi Fault has not ruptured at least in the past 800 years (Figure 4-3a) (Deng et al., 1991; Y. Li et al., 2012; Su

et al., 2018). According to what we have observed, analysed and compiled for the 1906 Manas Earthquake, the responsible fault for this event should be the SJT. Moreover, we notice that definitions of the SJT vary in different literature, which could cause confusion and has complicated the debate on the responsible fault (P. Zhang, Deng, Xu, Peng, et al., 1994; Deng et al., 1996; Stockmeyer et al., 2014; Lu et al., 2018; G. Hu et al., 2021). In this study, we define the SJT to be the major thrust closest to the northern Borohoro Shan and the others (e.g. the Hutubi-Houergous Fault) as the branches of the SJT (Figure 4-3b).

Interpretations of seismic reflection data suggest there are two layers of detachments under the Qingshuihe and Qigu Anticlines, with the shallower one (~ 7 km at depth) being a branch of the SJT that propagates to the north and penetrates to the surface as the Hutubi-Houergous Fault (Figure 4-3b) (C. Y. Wang et al., 2004; Stockmeyer et al., 2014; Lu et al., 2018). Since this branch starts to dip down to the south at ~ 22°±5° under the Qigu Anticline (Stockmeyer et al., 2014; Lu et al., 2018), it can reach a depth of > 15 km beneath the Borohoro Shan, which is consistent with our compilation for the depth of the 1906 event (Table 4-1). However, the dip of ~ 22° does not match the dip of 51°±5° from our modelled focal mechanism. Therefore, we suggest the 1906 Manas Earthquake is likely to have ruptured on the SJT at depth beneath its connection to the Hutubi-Houergous splay, with slip then transferred onto that splay to reach the surface to the north (Figure 4-3b). The absence of deformed Quaternary strata and the unclear geomorphic expression of the SJT fault trace (Avouac et al., 1993; P. Zhang, Deng, Xu, Peng, et al., 1994) suggests that slip did not propagate to the surface along the range-front fault. Ground deformations along the range-front appear to be related to gravitational movements, rather than tectonic faulting, although 2-m high fresh fault scarps were reported by the Institute of Geophysics, SSB & Institute of Chinese Historical Geography, (1990), that we cannot confirm, and without precise reporting of location. Our modelled focal mechanism of the 1906 event is similar to the 2016 Mw 6.0 Hutubi Earthquake which is suggested to occur on the Hutubi-Houergous Fault (Figure 4-3), but with different dips albeit both epicentres are close to the SJT (Lu et al., 2018). This might further support that the 1906 event is associated with a major structure that has different geometry and could host larger-magnitude earthquakes than the Hutubi-Houergous Fault itself only. However, we could not exclude the possibility that the Hutubi-Houergous Fault is the only ruptured fault for the 1906 event and that it has a steeper dipping angle in the west of the Qigu Anticline.

From earthquake scaling relations (Wells & Coppersmith, 1994; Wesnousky, 2008), the dip of ~ 51°, the magnitude Mw ~ 7.7 and the ~ 125 km surface rupture length of the 1906 event yield a total slip

of ~7 – 9 m. Considering the absence of large surface displacements, this implies that most of the surface deformation is accommodated either by folding or dissipated at depth.

4.4 The 1944 Xinyuan Earthquake

4.4.1 Background and Macroseismic Data

The 1944 Xinyuan Earthquake occurred on 10th March (local date) in the southern Borohoro Shan. There are two versions of the isoseismal map with quite different coverage and inferred epicentres (Figure 4-12a). The earlier version was made in 1973 and depicted the area of intensity VII and VIII and an inferred epicentre at 44°N, 84°E which is inside the Borohoro Shan and is catalogued in the CENC database with a recorded magnitude of Ms 7.3 (Figure 4-12a) (Z. Yang, 1992 and CENC). A later version was proposed by Z. Yang (1992) who identified the likely most damaged area with an intensity of IX in the southeast of Xinyuan Town with prominent landslides and an inferred epicentre at 43.3°N, 83.3°E (Figure 4-12a) (Z. Yang, 1992). However, based on the USGS earthquake catalogue, the epicentre of the 1944 Xinyuan Earthquake is a double event that has a smaller Mw 6.9 foreshock at 43.28°N, 84.43°E, which occurred ten minutes before the Mw 7.1 main shock at 43.29°N, 83.89°E (Figure 4-2 and Figure 4-12a).

4.4.2 Seismological Analysis[#], Surface Ruptures and Discussion

We performed a seismological analysis for the 1944 Xinyuan Earthquake using exactly the same approach as for the 1906 Manas Earthquake described in Section 4.3.4. Therefore we skip redundant information about the methods in this section. We re-estimated the magnitudes and relocated the hypocentre using 26 digitised seismograms from 11 stations and bulletin information from over 60 stations. Our results confirm the 1944 Xinyuan Earthquake was a double event but with different locations of epicentres from those reported by USGS and the previous studies. The Mw 6.5 ± 0.3 foreshock (1944a) occurred at 22:03:43 UTC on 9th March. The epicentre was located at 43.66°N, 84.34°E.The Mw 7.2 ± 0.2 main shock (1944b) occurred 9 minutes later (22:12:57 UTC) at 43.48°N, 84.16°E. Both events occurred at 24-km depth. (Figure 4-12a).

[#]The seismological analysis and related data collection/calculations in this chapter for the 1906 Manas and 1944 Xinyuan Earthquakes were all conducted by Dr. Galina Kulikova and not by the author of this thesis.

Z. Yang (1992) interpreted landslides clustered along the Qiakebo River (now called Qiapu River), which are covered by trees growing after 1944, as resulting from the 1944 Earthquake (Figure 4-12a and Figure 4-13a,b). Nevertheless, other places in the southern Borohoro Shan also have clustered landslides such as those spreading along the Kashi River, which have been mostly referred to the 1812 Nilke Earthquake (Feng, 1990, see Section 4.5), and those along the Kunes River that we identify here for the first time (Figure 4-13c,d). It is worth noticing that none of these landslide clusters fit well with our relocated epicentres for the 1944 double-event although the Kunes River landslides could align with the NW-SE fault strike inferred from the 1944b focal mechanism (Figure 4-12a). According to our relocated epicentres, the landslides along the Qiakebo River should be least likely caused by the 1944 events since they are located furthest from the epicentres.

The relocated foreshock (1944a) epicentre and its focal mechanism (strike/dip/rake=220/70/-10) are consistent with the Kashihe Fault trace and its right-lateral strike-slip component (Figure 4-12a) (Feng, 1987; C. Wu et al., 2020). Thus, it is possible that the 1944a event occurred on the Kashihe Fault or one of its branches, although the Dzhungarian Fault still remains a candidate for the responsible fault considering its similar kinematics and its vicinity with the 1944a event (J. Shen et al., 2003). Our re-estimated focal mechanism for the 1944a event is similar to the event estimated by CENC which is also a mainly strike-slip event, but the inferred fault strike and epicentre location from CENC is more consistent with the Dzhungarian Fault (Figure 4-12a). Our relocated epicentre of the main shock (1944b) is inside the Awulale Shan with a focal mechanism (strike/dip/rake=50/80/-50) indicating an oblique slip consisting of normal and strike-slip components, either with right-lateral slip on an NW-SE trending and SW-dipping fault or on a near-vertical left-lateral fault trending NE-SW. No prominent fault trace could be recognised near the 1944b epicentre except the inferred range front structure of the Awulale Shan and some elusive fault branches within the mountains (Figure 4-12a). Considering the Awulale range front structure should be a reverse fault, it is less likely to be the ruptured fault for the 1944b event, which is dominated by normal components. There should be other strike-slip faults that are responsible for the 1944b earthquake, which are likely branches of the Kashihe Fault as well. The 2012 Mw 6.3 events with similar focal mechanisms of mostly strike-slip movement are present near the 1944b event (Figure 4-12a) (Dziewonski et al., 1981; Ekström et al., 2012; Fang et al., 2014), again indicating such fault kinematics are dominating within the eastern Awulale Shan.

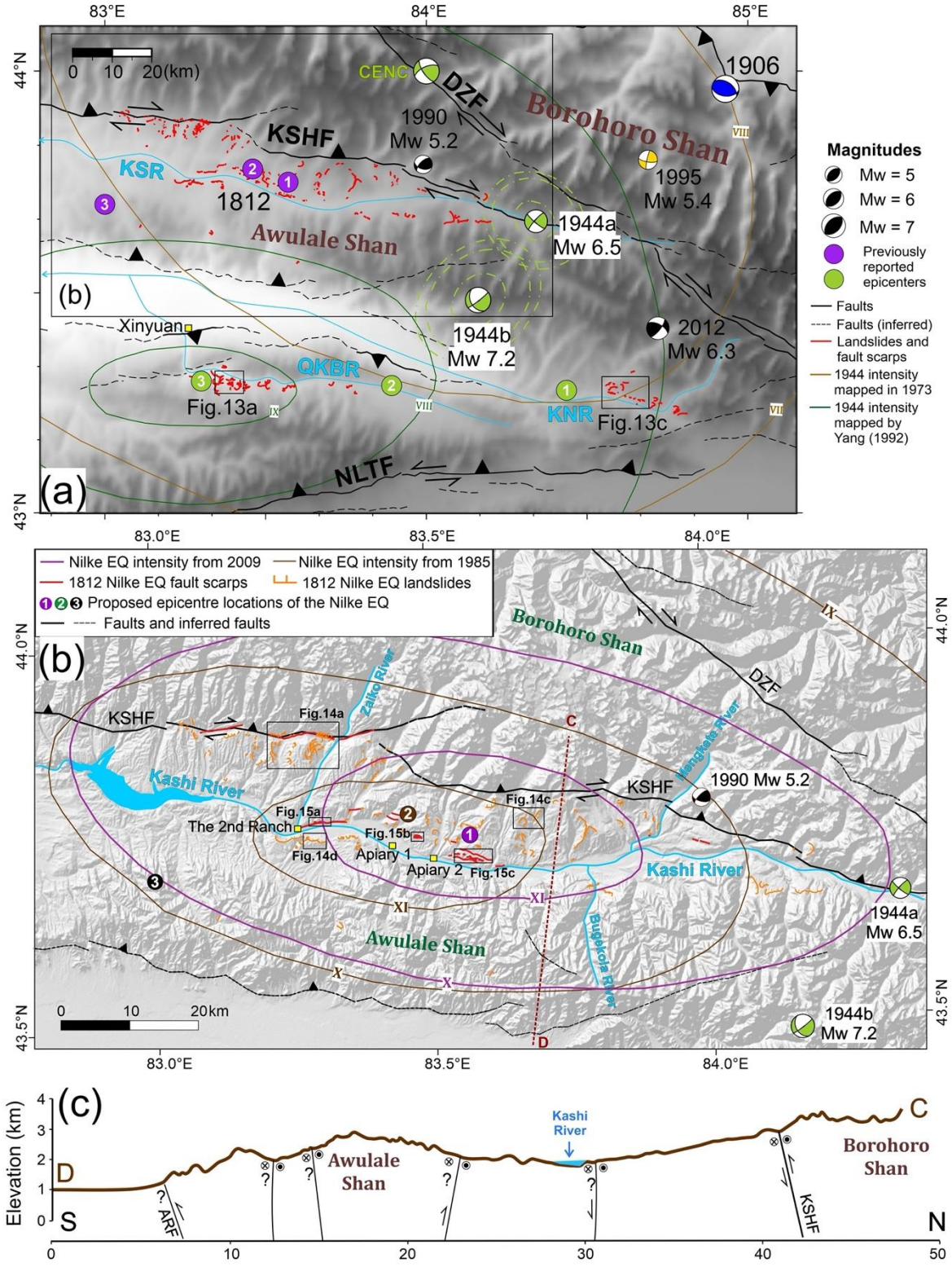

Figure 4-12. (a) Overview of the southern Borohoro Shan with epicentres of the 1944 (light green), 1906 (blue) and 1812 (purple) earthquakes. The 1944 Xinyuan Earthquake double-event focal mechanisms and epicentres relocated by this study are shown with the error ellipses in green dashed lines. Colour-filled circles are the previously reported epicentres with the numbers described in the caption of Figure 4-2. The

likely earthquake-induced landslides are marked in red. Focal mechanisms of earthquakes from 1976 to June of 2021 with Mw ≥ 5 are displayed and labelled based on the GCMT data (Dziewonski et al., 1981; Ekström et al., 2012) except for the 1995 Mw 5.4 event (in yellow) which is from Sloan et al. (2011). Isoseismal maps for the 1944 event are marked in light brown for the version mapped in 1973 and in dark green for the version mapped in 1992, both in *New Chinese Intensity Scale*. Xinyuan Town is annotated by the yellow square. KSHF: Kashihe Fault; DZF: Dzhungarian Fault; NLTF: Nalati Fault; KSR: Kashi River; QKBR: Qiakebo River; KNR: Kunes River. (b) Overview of the 1812 Nilke Earthquake with ESRI shaded relief imagery. Isoseismal maps from Z.Yang et al. (1985) and Yin et al. (2009) are shown in brown and purple respectively and labelled in *New Chinese Intensity Scale*. Colour-filled circles are the previously reported epicentres with detailed descriptions in the caption of Figure 4-2. Landslides and fault scarps possibly related to the 1812 event are labelled in orange and red respectively. Rivers are delineated in light blue. Faults are in black (Zelenin et al., 2021). (c) Seismotectonic section with along the profile C-D in the southwestern Borohoro Shan interpreted by this study inspired by the mapping database in http://www.ngac.org.cn/Map/Document?guid=EC7E1A7A79E71954E0430100007F182E. ARF: Awulale Range Front Fault

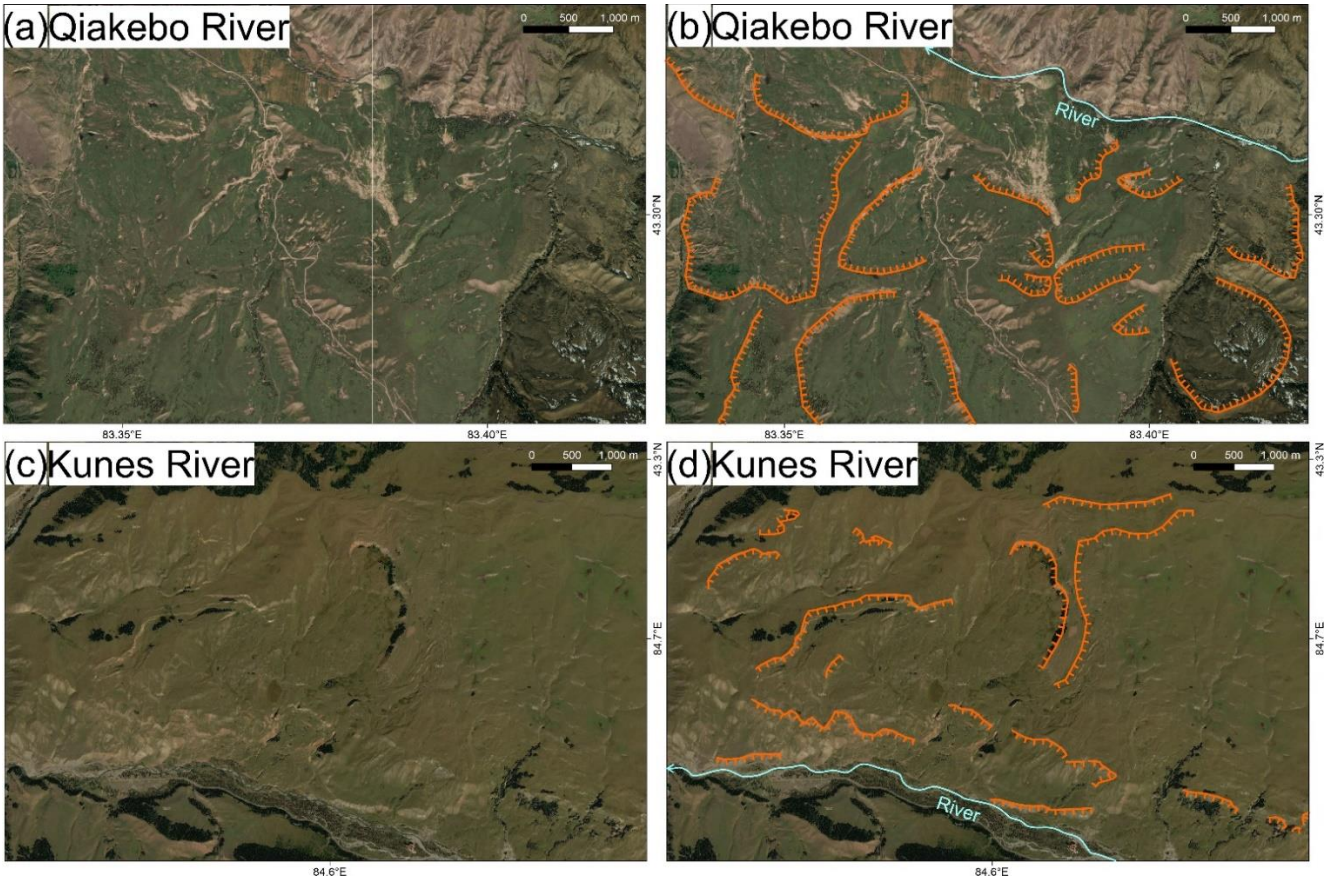

Figure 4-13. Landslides possibly caused by historical earthquakes found in the southern Borohoro Shan along (a) the Qiakebo River and (b) The Kunes River. Locations are labelled in Figure 4-12a.

4.5 The 1812 Nilke Earthquake

4.5.1 Background and Macroseismic Data

The Nilke Earthquake occurred in the evening on 8th March 1812 local time near Nilke County (Figure 4-1and Figure 4-2). The magnitude of this earthquake was estimated to be Ms 8 and it caused at least 58 fatalities and over five thousand deaths of livestock, mainly due to landslides (China Earthquake Administration, 1971; Z.Yang et al., 1985; Institute of Geophysics, SSB & Institute of Chinese Historical Geography, 1990). A detailed survey of the surface ruptures of the Nilke Earthquake began in the 1970s and these ruptures are dominated by landslides and are distributed along the Kashi River, especially on its northern bank (Z. Yang et al., 1985; Feng, 1990; G. Yin et al., 2001, 2006; C. Wu et al., 2020) (Figure 4-12b). The first isoseismal map of the 1812 Nilke Earthquake was made by Z. Yang et al. (1985) based on contemporary Qing Dynasty damage records, and the size and distribution of earthquake-induced landslides. The intensity reached XI on the *New Chinese Intensity Scale* from Zaiko River to the west of Bugekola River and reached VI near Ili City (Figure 4-1b and 4-Figure 4-12b) (Z. Yang et al., 1985). However, Yin et al. (2009) re-evaluated the distribution of surface ruptures from modern airborne photos and relocated the isoseismal contours ~ 15 km to the east of the 1985 one, suggesting the area of XI intensity extended from the east of the Zaiko River to the west of the Mengkete River (Figure 4-12b). The epicentre of the earthquake was reported to be near 43.7°N, 83.0°E by China Earthquake Administration (1971) but it has been relocated to 43.78°N, 83.46°E by Z. Yang et al. (1985) and 43.75°N, 83.57°E by Yin et al. (2009) according to their isoseismal maps (Figure 4-12b). Despite the discrepancy in the epicentre and intensity coverage, they all suggest the most severe ground shaking appeared in the Apiary area, and had a broadly east-west elongation (Figure 4-12b). Based on the intensity and the distribution of surface ruptures, the 1812 Nilke Earthquake has been implied to have occurred on the Kashihe Fault (Z. Yang et al., 1985; Feng, 1987, 1990; G. Yin et al., 2002; C. Wu et al., 2020). However, reverse fault scarps and lateral offsets are scarce whilst numerous landslides and normal fault scarps can be observed in the most damaged area, which is ~ 10 km south of the Kashihe fault trace (Figure 4-12b).

4.5.2 Surface Ruptures

The surface ruptures of the 1812 Nilke Earthquake can be categorized into four main types: landslides, normal fault scarps, fissures and reverse fault scarps. The most widely distributed are the landslides. Thousands of landslides have been observed with 365 of them having widths larger than 500 m with the widest ones reaching 5 km (G. Yin et al., 2001) (Figure 4-14b,c,d). The previous studies have identified earthquake-induced landslides based on their clustered distribution, and also on the steepness of their main scarps and the sliding surfaces, with inferred earthquake-induced landslides having shallower dips and occurring on gentle hill slopes of only 6° – 19° (G. Yin et al., 2001, 2006). The density of landslides decreases noticeably away from the high-intensity region (Z. Yang et al., 1985; Feng, 1990; G. Yin et al., 2001, 2006) (Figure 4-12b).

The second commonly observed ruptures are normal fault scarps, mostly distributed in the XI isoseismal area (Figure 4-12b and Figure 4-15). Ninety-two sites have been identified, with 28 of them also showing right-lateral displacements (G. Yin et al., 2006). These normal fault scarps mostly dip to the south although several north-dipping ones are also recognised (Figure 4-15c) (Feng, 1990; G. Yin et al., 2002, 2006). The majority of these normal faults are formed by E-W striking faults with several of them having listric geometry with steep (60 – 80°) slopes at the top that are shallow towards the bottom (Feng, 1990; G. Yin et al., 2002, 2006). East of Apiary 2, ~ 200-m-wide grabens are also found to be bounded by the normal faults (Figure 4-15c). Compared to the landslides, these normal fault scarps have good linearity and their extension is not constrained by topography (G. Yin et al., 2006). Furthermore, trenching results show some of these normal faults only cut through the thick loess and soil layer at the surface but not the bedrock underneath (Feng, 1987). The vertical offsets of these normal fault scarps are 2 – 10 m with the largest offset up to 15 m with right-lateral offsets of 1.5 – 4 m (Feng, 1990; G. Yin et al., 2002) (Figure 4-15a,b,d). The third commonly found ruptures are tensional fissures that do not have offsets and are mostly N-S striking, which means they tend to be perpendicular to the fault scarps (G. Yin et al., 2002, 2006). Nevertheless, there is a lack of information on the locations of these fissures in the literature.

Only 12 reverse fault scarps were reported to be produced by the Nilke Earthquake but only four of them were described in detail, and no precise locations were provided (Feng, 1990; G. Yin et al., 2002). These four reverse scarps are in the east of Apiary 2 which are ~ 2 m high with scarp surfaces facing to the north and with underlying faults dipping 56° – 62° to the south as constrained by palaeoseismic trenching, although no precise scarp nor trench locations were provided (Feng, 1990; G. Yin et al., 2002). There is also a ~ 70 m high cumulative reverse escarpment in the east of Apiary 2 (C. Wu et al., 2020)

(Figure 4-15c). In the southwest of this cumulative escarpment, there is a ~ 4 km long S-shape north-facing fault scarp which is 2 – 15 m high with 2.5 – 4 m right-lateral displacements (Feng, 1990) (Figure 4-15c). From the previous trenching data and the field outcrop, this north-facing scarp is a steeply-dipping dextral-slip fault with the 1812 surface ruptures cutting the top loess layer (Feng, 1990; C. Wu et al., 2020). West of the Zaiko River, there is a series of south-facing scarps at the range front and they are considered to be the Kashihe Fault trace (Figure 4-14a, b, e) (C. Wu et al., 2020). Landslides inferred to be from the 1812 earthquake are widespread on both the northern and southern sides of these scarps (G. Yin et al., 2001, 2002) (Figure 4-14b, e).

We digitized the previously reported 1812 surface ruptures with our own mapping results in Figure 4-12b. Although we could not locate all the previously mapped ruptures due to a lack of precise locations given in the literature, most of the large landslides and the prominent normal and reverse fault scarps could still be recognised from the present-day satellite imagery. However, fissures and other reverse fault scarps are not easily distinguished due to the image resolution and the long-term erosion. According to our compilation, the majority of the Nilke Earthquake surface ruptures are located north of the Kashi River but they generally have distances from the main Kashihe Fault trace (C. Wu et al., 2020; Zelenin et al., 2021), with the prominent inferred ruptures within the highest-intensity area distributed in a zone 7 – 10 km south of the main Kashihe Fault trace (Figure 4-12b). WNW of the highest intensity area, oblique-slip ruptures are identified along the main Kashihe Fault trace (Figure 4-14a,b, e).

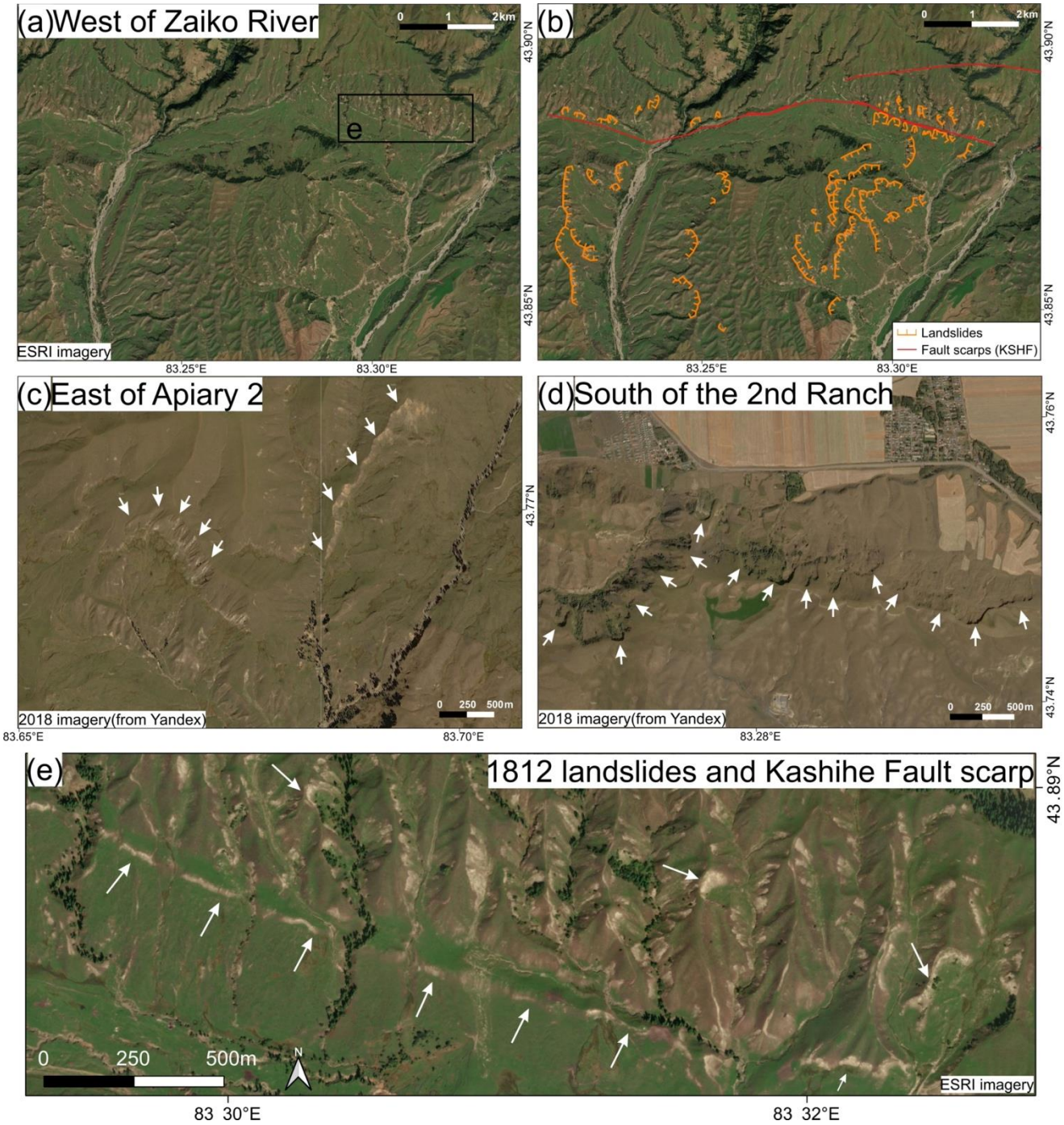

Figure 4-14. (a) ESRI optical satellite imagery showing the likely 1812 landslides and fault scarps in the west of the Zaiko River with annotations in (b). (c) and (d) Optical satellite imagery from Yandex Map showing the likely 1812 landslides in the east of Apiary 2 and the south of The 2nd Ranch. (e) the Kashihe Fault trace with a prominent fault scarp in the west of the Zaiko River, which has been visited and measured by Wu et al. (2020). Fault scarps and landslide crowns are pointed by white arrows. Locations of each panel are labelled in Figure 4-12b.

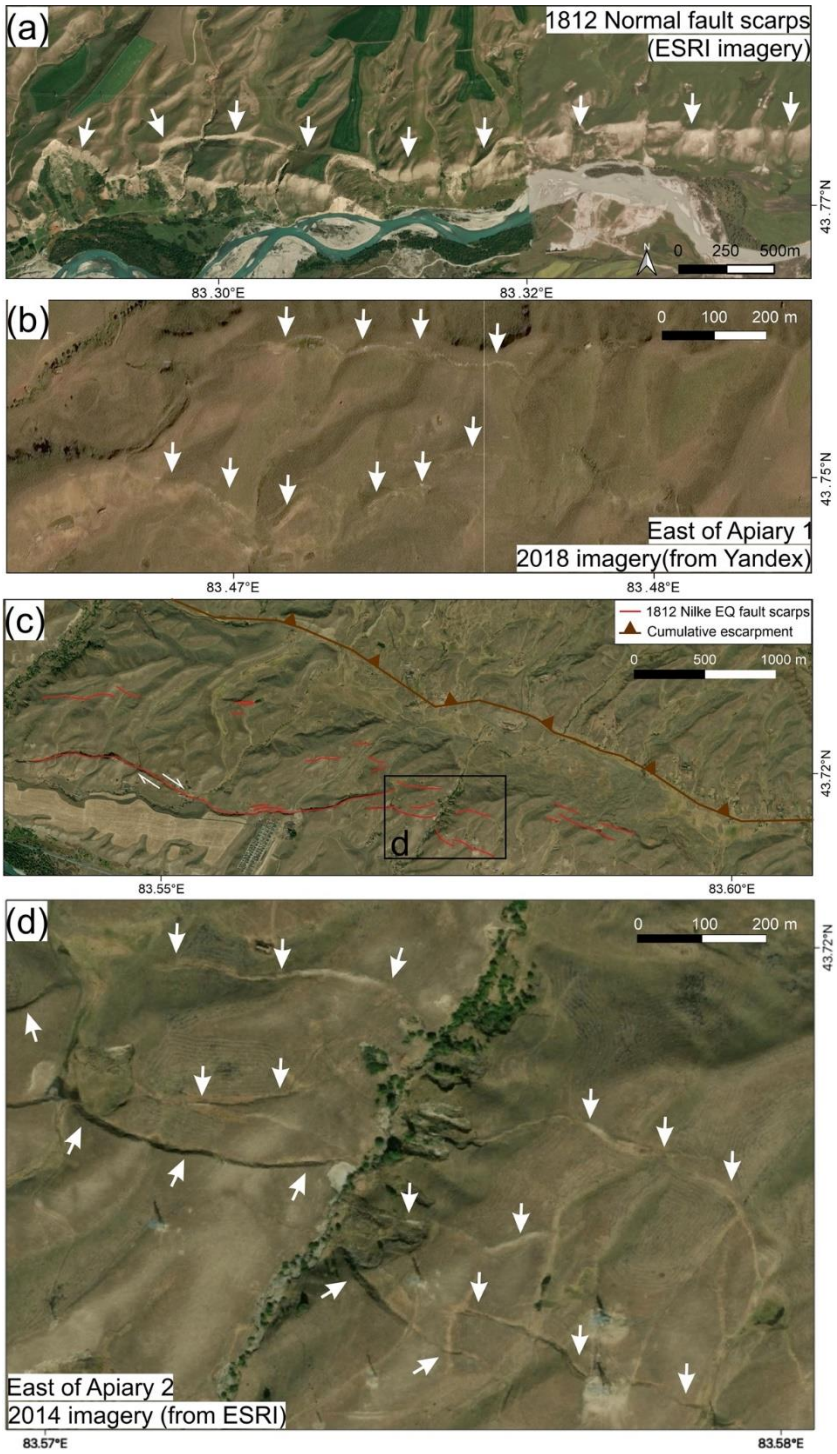

Figure 4-15. (a) A large normal fault scarp with ~ 15 m offset near The 2nd Ranch likely produced by the 1812 event. (b) The likely 1812 normal scarps mentioned in Feng (1990) and Yin et al. (2002) in the east of Apiary 1. (c) Reverse, strike-slip and normal fault scarps near Apiary 2. The ~70 m high cumulative reverse scarp measured by Wu et al. (2020) is marked in brown. The 4-km-long Z-shape fault scarp (red) with dextral movements is trenched and described by Feng (1990). (c) Grabens that are likely formed in the 1812 event by the normal scarps. A profile of this graben has been illustrated in Feng (1990). Locations of each panel are labelled in Figure 4-12b.

4.5.3 Earthquake Magnitude and Mechanism

The estimated magnitude of the 1812 Nilke Earthquake is Ms 8.0 – 8.1 based on intensity-magnitude relationships (China Earthquake Administration, 1971; Z. Yang et al., 1985). However, recent seismological investigation of several of the large earthquakes of the early to mid-20th century have indicated that the magnitudes derived from seismic intensities may be overestimated (Kulikova & Krüger, 2015; Ou et al., 2020), with the seismology-derived magnitudes in broad agreement with geologically derived estimates from rupture length and slip distribution (Klinger et al., 2011; Ou et al., 2020). Pre-instrumental earthquake magnitudes derived from intensity information may, therefore, be similarly overestimated (e.g. Middleton et al., 2015; Feng et al., 2020), with the discrepancy likely arising from the use of Gutenberg surface wave magnitude in the formulation of the intensity-magnitude relationship (Ou et al., 2020), such that the approximate Mw would be ~ 7.7.

The surface rupture of the Nilke Earthquake could extend up to 124 km (G. Yin et al., 2009), though from our own mapping, the length of surface ruptures is approximately 100 km (Figure 4-12b). Z.Yang et al (1985) calculated the depth of the Nilke Earthquake to be ~ 25 km from the isoseismal distribution (C.-J. Liu, 1961), which is consistent with the nearby recent earthquake depths of 20.4 – 40.6 km (ISC, 2022a). Using the scaling relationship from Wells and Coppersmith (1994) and Blaser et al. (2010), the 100 – 124 km surface rupture length yields a magnitude of Mw 7.5 – 7.7 and Mw 7.6 – 7.8, respectively. Using the scaling relationship from Wesnousky (2008), this surface rupture length yields a magnitude of Mw 7.3 – 7.4 and Mw 7.9 – 8.0 for strike-slip and reverse faulting respectively. A magnitude of Mw 7.8 – 7.9 is estimated from the likely rupture area, assuming a depth of 25 km, length of 100 – 124 km, average displacement of 7.5 m from the mean offset of the scarps (G. Yin et al., 2006) and an assumed fault dipping of 60° (Aki, 1966; Kanamori, 1977). In sum, the 1812 Nilke Earthquake magnitudes implied from both scaling relationships and the rupture area are no larger than Mw 8, which is lower than the magnitudes inferred from the intensity in the previous studies (China Earthquake Administration, 1971; Z. Yang et al., 1985).

Z. Yang et al. (1985) suggested the ruptured fault plane strikes 280° and dips 68° to the north with a rake of ~ 95°, indicating this is a mainly reverse faulting event. The regional N-S convergence and the behaviour of the Kashihe Fault are consistent with the reverse mechanism of the Nilke Earthquake. Our interpretation of the observed ruptures and other surface deformation is that the 1812 Nilke Earthquake more likely had components of both right-lateral and reverse faulting and that it could have a focal mechanism similar to the 1990 Mw 5.2 event near the Kashihe Fault (Figure 4-12b). A number of the

faults within this southern rupture zone show right-lateral displacements, which highlights the strike-slip motion of the responsible faults. The majority of the 1812 ruptures are found ~ 10 km occurring on another fault or branches that are in the south of the recently mapped main Kashihe Fault (C. Wu et al., 2020; Zelenin et al., 2021), with an alignment that is parallel to it (Figure 4-12b,c). The 1812 Nilke Earthquake likely ruptured both the Kashihe Fault and another splay to the south of it.

The Awulale Shan and its surrounding regions are accommodating not only the N-S shortening but also a rotation with westwards extrusion, inferred from the fact that they are bounded by a dextral strike-slip fault in the north and a sinistral strike-slip fault in the south (Figure 4-12a, Figure 4-16). Several historical events show strike-slip mechanisms within the Awulale Shan (see Section 4.5.2), also suggesting the overall oblique slip on the faults. The fault pattern and geometry could be complex in this area with predominantly oblique slip during earthquakes, which is likely able to produce the diverse types of surface ruptures of the 1812 event. The normal component of the 1944b event might also result from the complicated kinematics of crustal deformation within the Awulale Shan. Grützner et al. (2019) have suggested a zigzag pattern of strike-slip faults, with right-lateral faulting on NW-SE planes and left-lateral faulting on NE-SW planes, which are accommodating the shortening in the west of the Ili Basin (Figure 4-16). Different scales of this zigzag fault pattern might also exist in the eastern Ili Basin with the same fault kinematics observed from the historical events in the Awulale Shan (Figure 4-12a, Figure 4-16). However, it is difficult to map the faults in this region merely from the remote sensing imagery. Field surveys and the associated *in situ* investigations will be essential to unravel the detailed seismogenic structures in the southwest Borohoro Shan.

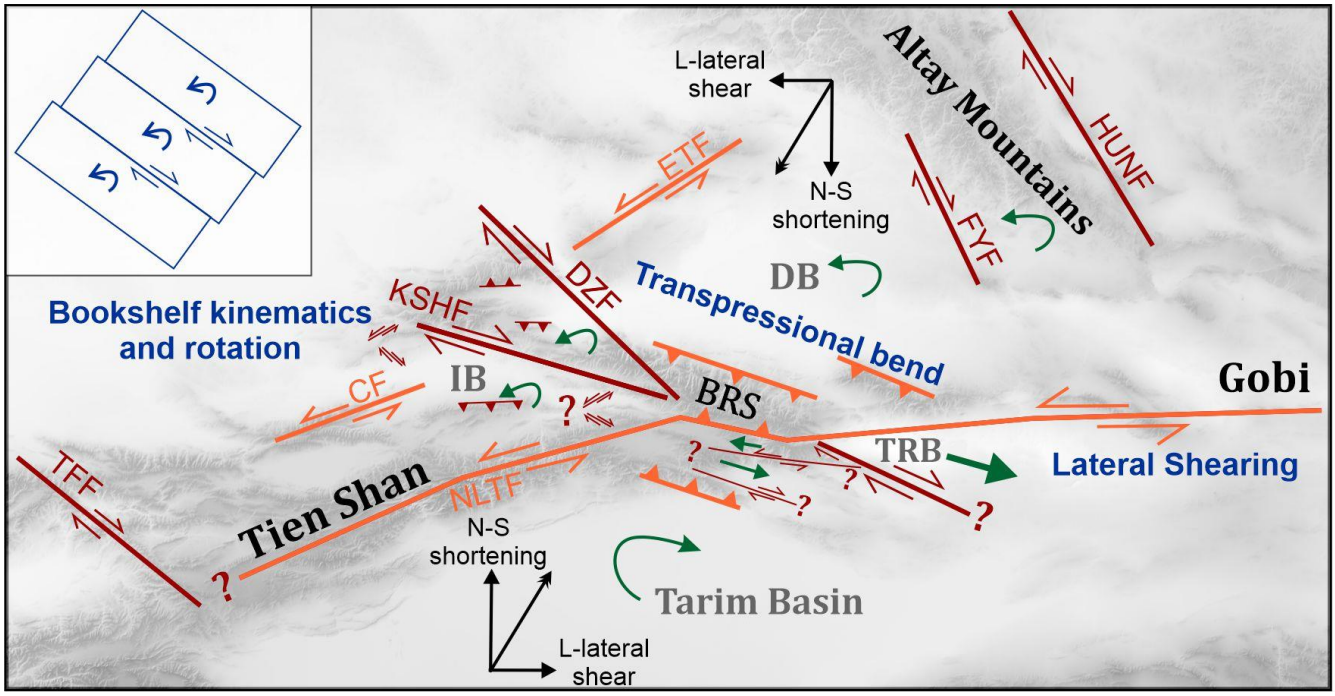

Figure 4-16. Simplified crustal deformation kinematics around the Borohoro Shan (BRS). Main left-lateral strike-slip faults and transpressional bend are displayed in orange. Main right-lateral faults and other smaller faults are displayed in brown with the fault kinematics labelled. Black arrows show the shortening and shearing directions. Green arrows show the crustal/block motion with respect to the BRS. Types of deformation are annotated in blue with a model in the upper right showing bookshelf deformation. NLTF: Nalati Fault; CF: Chilik Fault; ETF: East Tacheng Fault; TFF: Talas-Fergana Fault; KSHF: Kashihe Fault; DZF: Dzhungarian Fault; FYF: Fuyun Fault; HUNF: Har-Us-Nuur Fault; DB: Dzhungarian Basin; IB: Ili Basin; TRB: Turfan Basin

4.6 Discussion

Our investigation of the 1812 Nilke, 1906 Manas, and 1944 Xinyuan Earthquakes has helped to refine our knowledge of likely source parameters of all three events. We interpret the 1812 earthquake as having a moment magnitude in the range of Mw 7.3 – 8.0, with most of the estimates over Mw 7.5 (see Section 4.5.3). This 1812 earthquake possibly involved oblique reverse and right-lateral slip along the Kashihe Fault, and also a splay from it that projects to the surface near the Kashi River (Figure 4-12c). The 1906 Manas Earthquake likely ruptured a steeply-dipping thrust at depth beneath the Borohoro Shan margin, but with a slip that was transferred across a decollement to rupture the surface for a distance of 125 km along the Huoerguos, Manas, and Tugulu anticline segments (see Section 4.3.5)(Figure 4-3). The 1906 earthquake nucleated at the lower western corner of the fault plane and ruptured unilaterally eastwards. The 1944 Xinyuan Earthquake is confirmed to be two earthquakes closely spaced in time and location, with an Mw 6.5 earthquake being followed by an Mw 7.2 earthquake ~ 25 km to the southwest

(Figure 4-12a). Both events have similar strike-slip mechanisms, with right-lateral faulting on an NW-SE plane, or left-lateral faulting on a NE-SW plane. There is remaining ambiguity in the causative faults, though the segment right-lateral Kashihe Fault southeast of the 1812 rupture is possible (Figure 4-12a).

Several recent studies have drawn attention to the apparent over-estimation of magnitude from intensity measurements for Chinese earthquakes of historical and early instrumental periods (Kulikova & Krüger, 2015; Middleton et al., 2015; Kulikova, 2016; Feng et al., 2020; Ou et al., 2020). The discrepancy has been interpreted to result from the use of Gutenberg surface wave magnitude in the intensity-magnitude relationship (e.g. Ou et al., 2020), though may also relate to bias in intensity measurements from densely populated basin regions that may be susceptible to enhanced shaking. Our results from the Borohoro Shan agree with the pattern, with the 1906 Manas Earthquake having a well-defined moment magnitude of Mw 7.7 that is substantially smaller than previously stated magnitudes from intensity X. The length and slip amount in the 1812 Nilke Earthquake also suggests a likely upper bound of a magnitude of Mw 7.8 – 7.9, rather than the M 8+ estimates obtained from the intensities.

In the northern range front of the Borohoro Shan, the surface topography only reflects the structures less than 10 km deep in the crust as inferred from the wavelength of anticlines and the seismic-reflection profile (Figure 4-3). The likely coseismic slip for the 1906 Mana Earthquake is less than 1 m, observed from the fault scarps among the terraces. Both the seismic depth and the fault slip indicated solely by the surficial features are less than the seismological re-estimated results for the 1906 event as > 15 km of depth and ~ 7 – 9 m of slip. This indicates that surface geomorphology could disguise the sub-surface structural complexity (Mackenzie et al., 2016). For example, the seemingly shallow faults may have a large down-dip extension or may be connected with hidden deeper structures like the case of the 1906 event. Furthermore, in some cases, rupture starting at the deeper part of the fault would not propagate upwards, which prohibits the surface rupture but retains the seismic risk in the shallow unruptured portion (Z. Hu, Li, et al., 2021). The example of the 1906 Manas Earthquake provides another lesson that surface topography may not fully reflect the depth extent of seismogenic faulting and that additional information, such as seismic-reflection profiles, is needed to help interpret the seismotectonics. In the southern range front of the Borohoro Shan, the complex strike-slip fault system could pose great seismic hazards, but it is less identifiable from the surface geomorphology. More *in situ* investigations are needed to help reveal the active faulting in this region.

In terms of local earthquake hazards, an important feature of all three earthquakes is the widespread occurrence of landslides. Landsliding was responsible for much of the destruction and loss of life in, for

example, the 1920 Haiyuan, 2005 Kashmir and 2008 Wenchuan Earthquakes (Daniell et al., 2017; Nowicki Jessee et al., 2020). Thousands of people died due to the collapse of loess cliffs, where they resided, and the landslides caused by shaking during the 1556 Huaxian Earthquake in central China (Feng et al., 2020). Many of the landslides possibly triggered by the earthquakes in the Borohoro Shan occurred in relatively low-relief regions in areas of thick loess cover too, with identification aided by the study of tree shapes and additional radiocarbon dating (Z. Yang, 1988, 1992). The widespread and damaging landslide points to the potentially damaging effects that might be expected in future large earthquakes. Although there are difficulties in distinguishing seismically-induced landslides from those caused by other factors, the occurrences within the three known earthquakes form distinct clusters. The identification of landslide clusters may provide an efficient means of palaeoseismic investigation in such mountainous and loess-covered landscapes, particularly as the ruptures may fail to reach the surface, or be hard to identify. The landslide clusters shown in Figure 4-13a and c may relate to earthquakes that are not known from the historical record and thus are worth further investigation.

The earthquakes highlight some important features of the seismotectonics of the Borohoro Shan. The northern margin is dominated by ~ east-west reverse faulting, whereas the southern margins include oblique right-lateral faults with a WNW-ESE trend and left-lateral faults with a WSW-ENE trend (Figure 4-2 and Figure 4-16). The interior of the range contains the southern extension of the Dzhungarian right-lateral fault (Campbell et al., 2013; Z. Hu, Yang, et al., 2021). Left-lateral shearing parallel to the Tien Shan range is introduced due to the motion of the Tarim Basin relative to Eurasia (Figure 4-1a and Figure 4-16) (Zubovich et al., 2010; M. Wang & Shen, 2020). The Borohoro Shan form at a transpressional bend within the through-going left-lateral fault system, which eastwards extends into Mongolia as the Gobi-Tien Shan Faults, and westwards extend into the high mountainous interior of the Kyrgyz Tien Shan (Figure 4-16). The right-lateral Dzhungarian and Kashihe Faults splay northwards from this transpressional bend and other right-lateral faults with an NW-SE to NNW-SSE trend are present throughout the Tien Shan and Altay ranges, from the Talas-Fergana Fault of western Tien Shan to the Fuyun and Har-Us-Nuur Faults of western Mongolia (Figure 4-16: Nissen et al., 2009; Xu et al., 2012; Bande et al., 2017). These right-lateral faults are consistent with a bookshelf kinematic model, where they can both accommodate N-S shortening related to the overall India-Eurasia collision, whilst also enabling distributed range-parallel left-lateral shear in this region (Cobbold & Davy, 1988; Bayasgalan et al., 2005; Cunningham, 2005, 2007; Campbell et al., 2015; C. Wu et al., 2020, 2021). Southeast of the Borohoro Shan seems to have eastwards block extrusion kinematics, consistent with the overall left-lateral shearing,

with the deformation concentrated at the deep crust-cutting strike-slip faults (e.g. Ren et al., 2021) (Figure 4-16). Since the Borohoro Shan is an important feature of the India-Eurasia collision zone, involving reverse faulting and both left- and right-lateral strike-slip faulting just like a smaller scale of the Tien Shan, unravelling the tectonic history of the Borohoro Shan hence has the potential to unravel the tectonic history of the wider Tien Shan and surroundings.

4.7 Conclusions

We analysed the source parameters of the 1906 Manas, 1944 Xinyuan and the 1812 Nilke Earthquakes in the Borohoro Shan, eastern Tien Shan region, by combining published data, remote sensing and seismological analysis of the 1906 and the 1944 events. We found that the most common surface deformations associated with these three historical earthquakes are landslides instead of fault scarps, especially for those in the southern Borohoro Shan. Based on the re-estimated seismic magnitude (Mw 7.7 ± 0.2), the relocated hypocentre and the occurrence of coseismic surface ruptures of the 1906 Manas Earthquake, we suggest this event nucleated on a steeply-dipping basement reverse fault and propagated to the surface across a shallow decollement. Our seismological analysis of the 1944 Xinyuan Earthquake implies it is a double-event consisting of an Mw 6.5 ± 0.3 foreshock and an Mw 7.2 ± 0.2 main shock at a depth of ~24 km, both dominated by strike-slip motion, and possibly on the major right-lateral Kashihe Fault. The 1812 Nilke Earthquake is likely to have involved oblique right-lateral slip on the Kashihe Fault, on the section northwest of the 1944 earthquakes, and also on a splay 10 km to the south. Its magnitude was likely smaller than previously suggested. The earthquakes highlight the importance of right-lateral and reverse faulting in the seismotectonics of the Borohoro Shan, which has formed at an intersection between both left-lateral and right-lateral faults, and which likely accommodate a combination of N-S shortening and range-parallel left-lateral shear by bookshelf faulting and block extrusion.

4.8 Appendices[2]

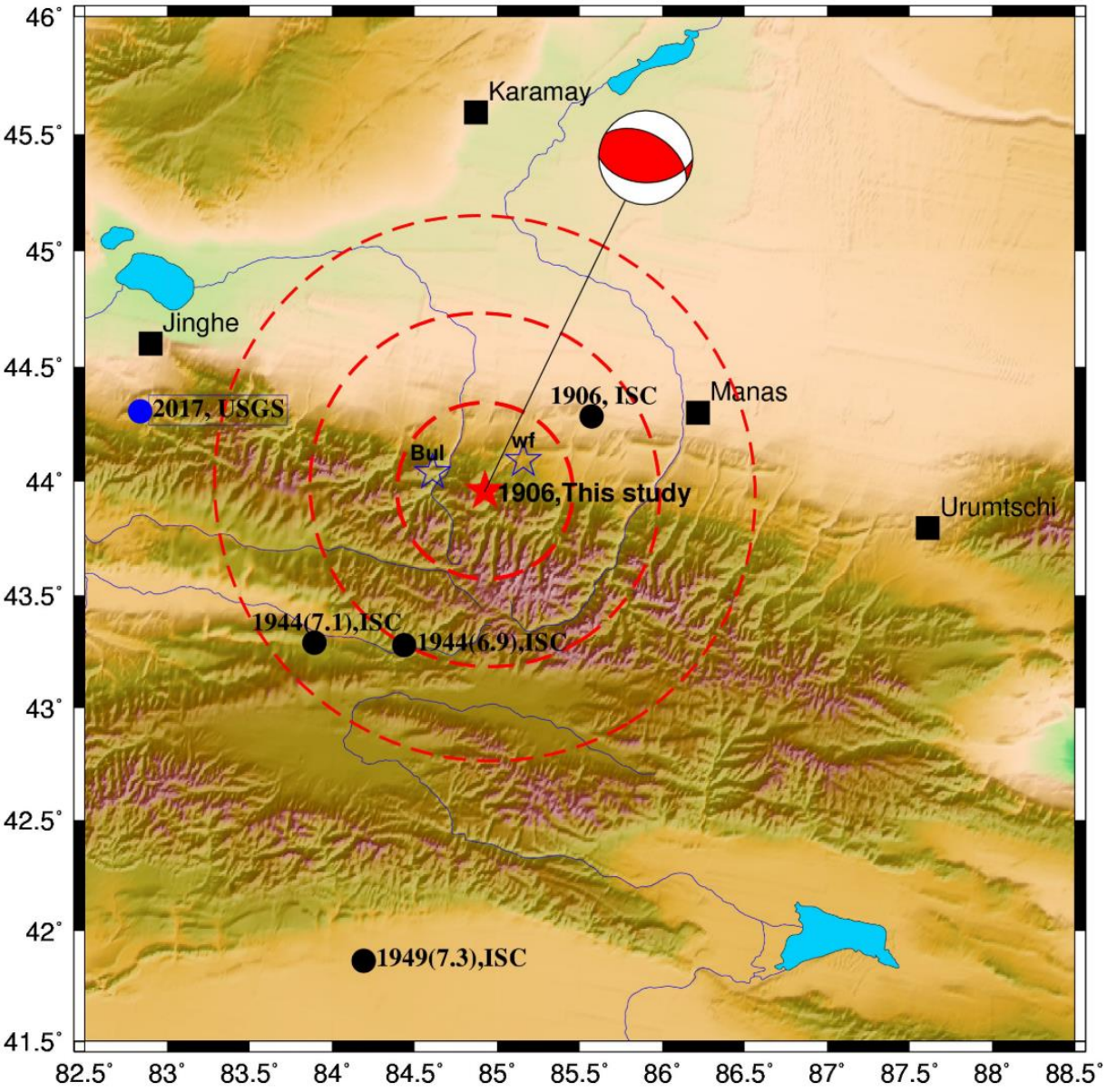

Figure S4-1. Tectonic map of the eastern Tien Shan region, black rectangles show the main cities in the area, shows epicentre locations (black circles) for the Manas earthquake from GEM - Storchak et al. (2013), additional black circles show other significant earthquakes in the area with the year of occurrence based on Storchak et al. (2013). Epicentre determined in this study is marked as a red star with a corresponding error ellipse, two blue stars show alternative epicentres determined in this study based on waveform data (wf) and bulletin information (Bul). Blue circle shows the USGS (USGS, 2018) epicentre of the M 6.3 earthquake which occurred on August 8, 2017. Red beach ball shows the focal mechanism of the Manas earthquake determined in this study.

[2] The content in Appendices 4.8 are from Dr Galina Kulikova.

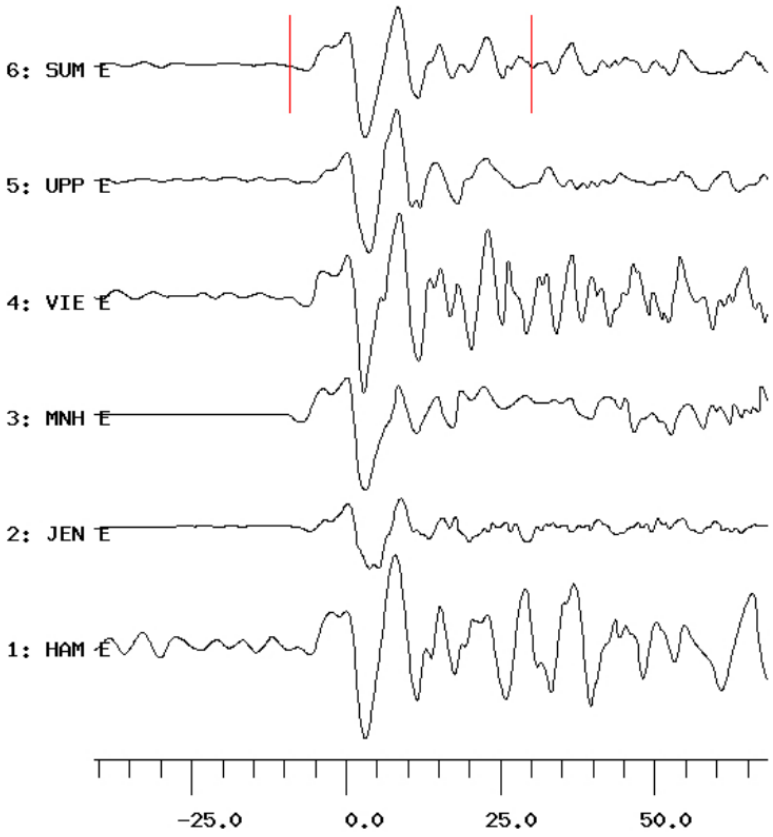

Figure S4-2. Stack of all P-wave records from the European stations with their names and components noted. The top trace shows the summation record with P-wave duration, marked with red lines.

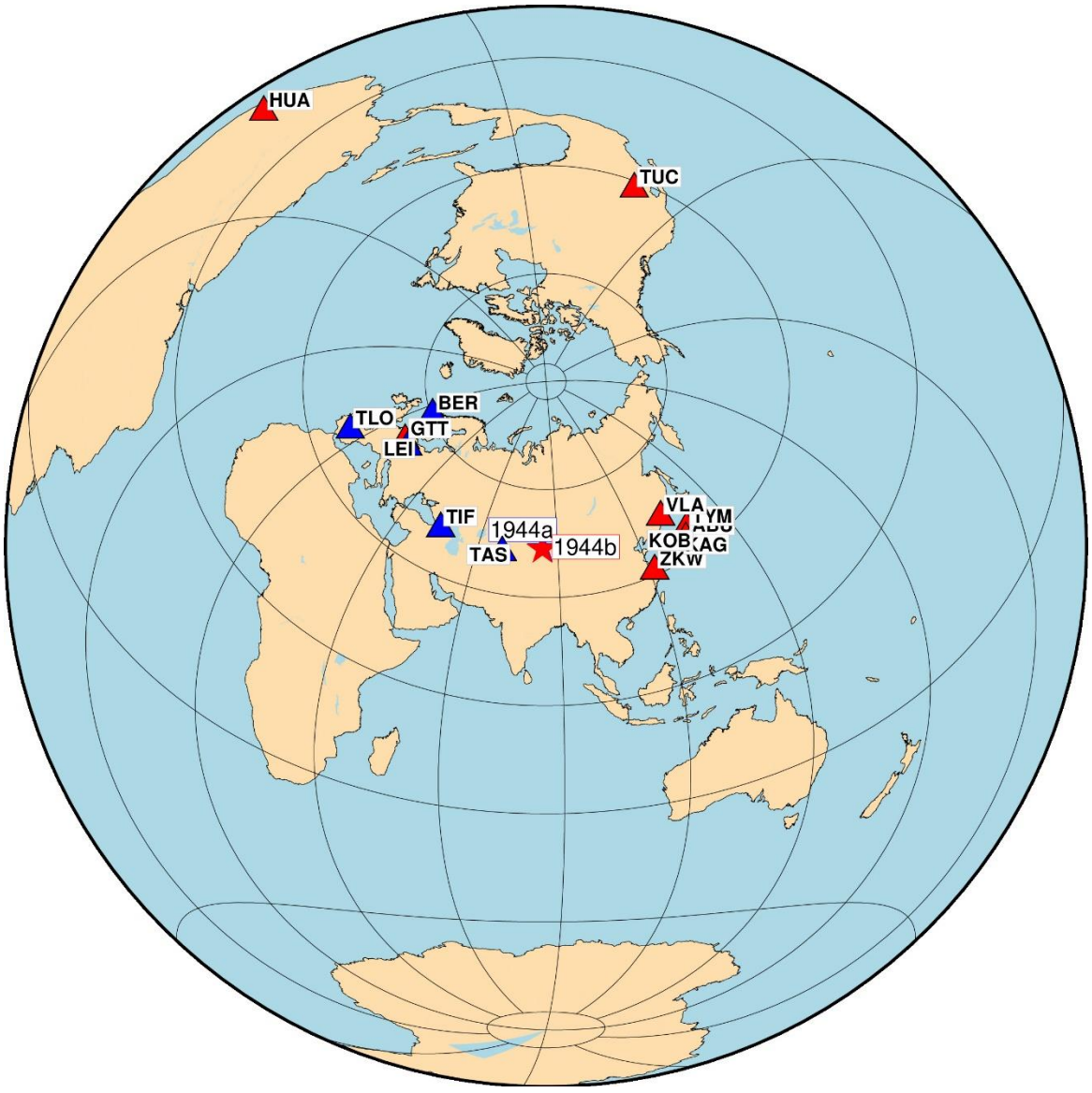

Figure S4-3. Station distribution map for the 1944 Xinyuan Earthquake. Red star shows the epicentre location of this event; Blue triangles show those used for estimating the 1944a event; Red triangles show those used for estimating the 1944b event.

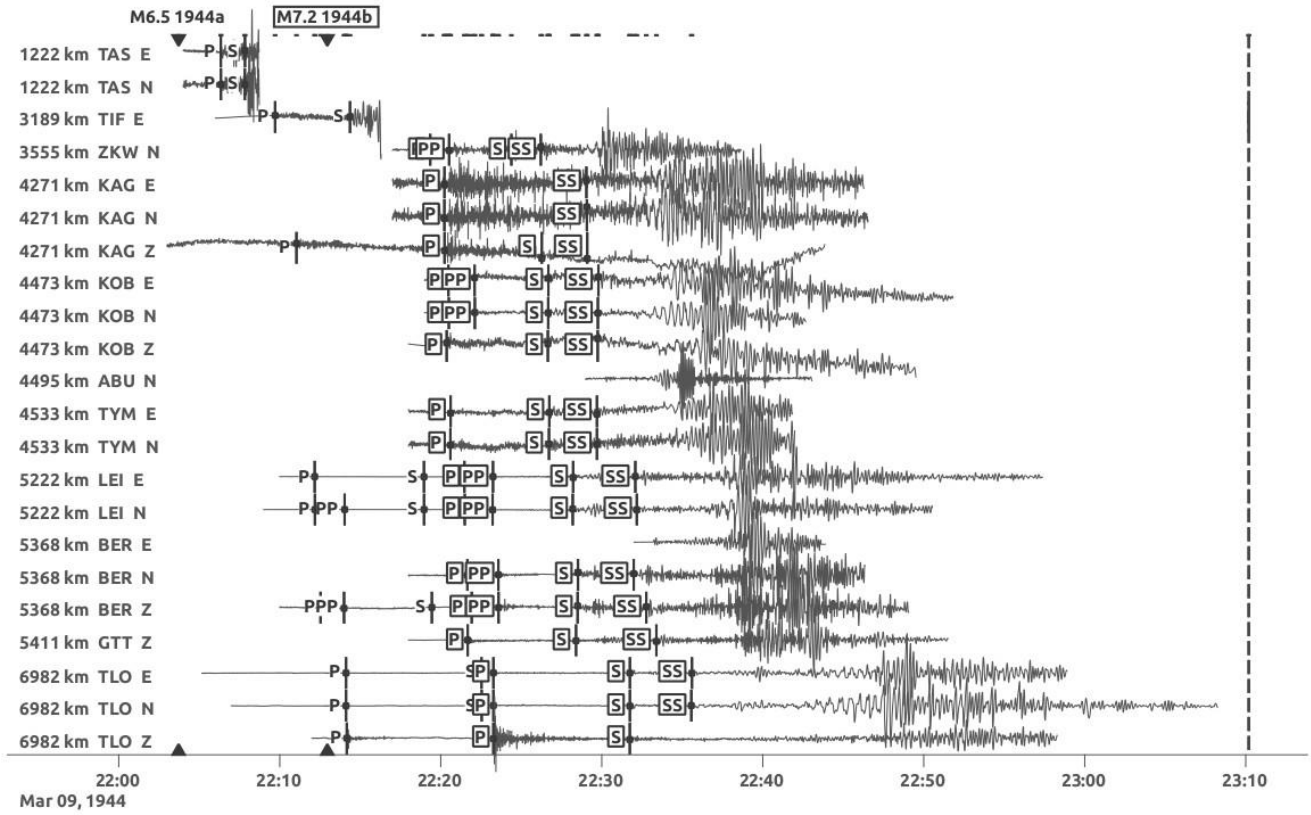

Figure S4-4. Digitized seismic records of the 1944 Xinyuan Earthquakes.

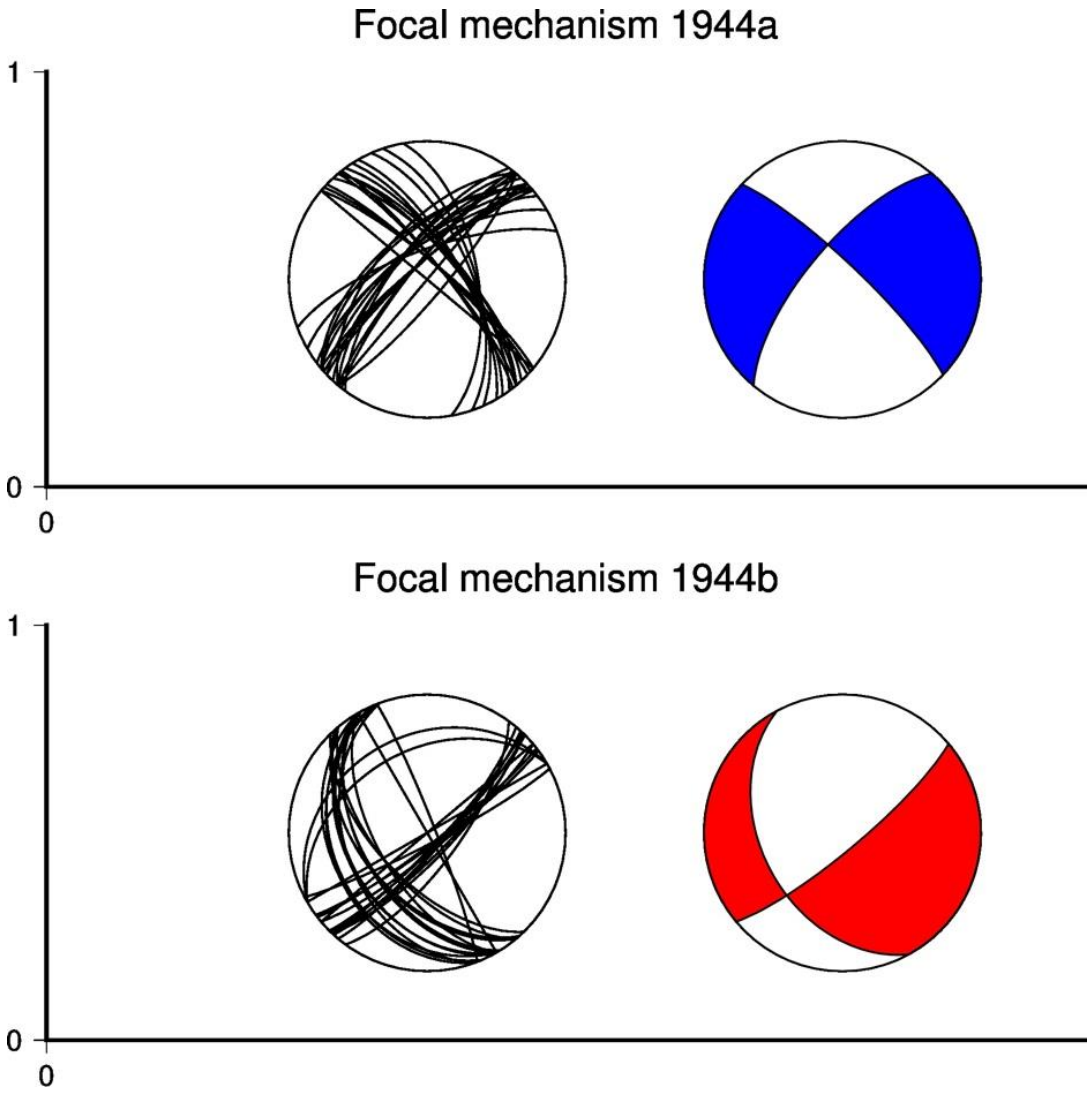

Figure S4-5. Focal mechanism determination of the 1944 Xinyuan Earthquakes.

Table S4-1. Amplitudes and Periods of different phases used for m_B calculation of 1944a

Station	Phase	T[sec]	Amp[mm]	Amp[μm]	m_B
Waveforms					
BER	P	2	0.6	1.3	6.7
TIF	P	5	0.8	6.6	6.9
TIF	S	7	3.3	27.0	6.9
LEI	P	2	0.1	0.4	6.5
LEI	S	8	1.1	3.4	6.2
TLO	P	2	3.0	1.8	6.9
TLO	S	10	2.5	4.2	6.3
				Average	6.6 ± 0.3

Table S4-2. Amplitudes and Periods of different phases used for M_s calculation of 1944a

Station	Phase	T[sec]	Amp[mm]	Amp[μm]	M_s
Waveforms					
HYD_Bul_N		12		68	6.5

Table S4-3. Amplitudes and Periods of different phases used for m_B calculation of 1944b

Station	Phase	T[sec]	Amp[mm]	Amp[μm]	m_B
Waveforms					
BER	P	3	2.52	5.5	7.2
BER	PP	4	2.08	2.7	6.6
BER	S	5	4.23	18	7.2
LEI	P	3	0.46	1.7	7.0
ZKW	P	2	1.41	8.8	7.5
ZKW	S	3	3.72	22.1	7.4
TLO	P	2	12.17	7.2	7.5
TLO	S	9	7.9	12.9	6.8
GTT	P	2	0.73	3.6	7.0
TYM	P	5	2.5	32.7	7.5
TYM	S	6	4	49.6	7.5
				Average	7.2 ± 0.3

Table S4-4. Amplitudes and Periods of different phases used for M_s calculation of 1944b

Station	Phase	T[sec]	Amp[mm]	Amp[μm]	M_s
Waveforms					
HYD_Bul_N		13		310	7.1
BER_Bul_E		11		60	6.8
				Average	6.9 ± 0.2

Statement of Authorship for joint/multi-authored papers for PGR thesis

To appear at the end of each thesis chapter submitted as an article/paper

The statement shall describe the candidate's and co-authors' independent research contributions in the thesis publications. For each publication there should exist a complete statement that is to be filled out and signed by the candidate and supervisor **(only required where there isn't already a statement of contribution within the paper itself).**

Title of Paper	Source Parameters of the 1906 Manas (Mw 7.7), 1944 Xinyuan (Mw 7.2) and 1812 Nilke Earthquakes and Seismotectonics of the Borohoro Shan, Western China.
Publication Status	□Published □ Accepted for Publication □Submitted for Publication ■Unpublished and unsubmitted work written in a manuscript style
Publication Details	Tsai, C.-H., Kulikova, G., Krüger, F. & Walker, R. T. Source Parameters of the 1906 Manas (Mw 7.7), 1944 Xinyuan (Mw 7.2) and 1812 Nilke Earthquakes and Seismotectonics of the Borohoro Shan, Western China.

Student Confirmation

Student Name:	Chia-Hsin Tsai		
Contribution to the Paper	Compiled previous data, performed mapping via satellite imagery, interpreted data, wrote manuscript		
Signature	蔡佳欣	Date	06.03.2023

Supervisor Confirmation

By signing the Statement of Authorship, you are certifying that the candidate made a substantial contribution to the publication, and that the description described above is accurate.

Supervisor name and title: Prof. Richard T. Walker		
Supervisor comments		
Signature 	Date	7/3/2023

This completed form should be included in the thesis, at the end of the relevant chapter.

Chapter 5

Synthesis of Earthquake Scaling and Regional Kinematics

5.1 Overview

This chapter provides updated earthquake scaling relationships for intra-continental earthquakes and synthesises the earthquake occurrence and kinematics of the Dzhungarian Basin, from the findings in this thesis and previous studies. We have presented the characteristics of the faults bounding the Dzhungarian Alatau (see Chapters 2 and 3) and the seismotectonics of the Borohoro Shan (see Chapter 4). In this chapter, we further present other less-studied prominent palaeo-earthquake ruptures in the west of the Dzhungarian Basin, including a brief overview of the two major faults bounding the northern and eastern basin. We then compile the displacements, magnitudes, and surface rupture lengths of both palaeo- and historical intra-continental earthquakes in Central Asia and other regions worldwide. Updated earthquake scaling relationships are provided for the earthquakes we have compiled, and differences in earthquake scaling between different intra-continental settings are also revealed. Based on the types of faulting we observe around the Dzhungarian Basin, as well as their slip rates determined in this work and previous studies, we summarise the regional fault patterns and propose a kinematic model for the mechanism by which N-S crustal shortening and left-lateral shearing are accommodated by the Dzhungarian Basin and its surroundings.

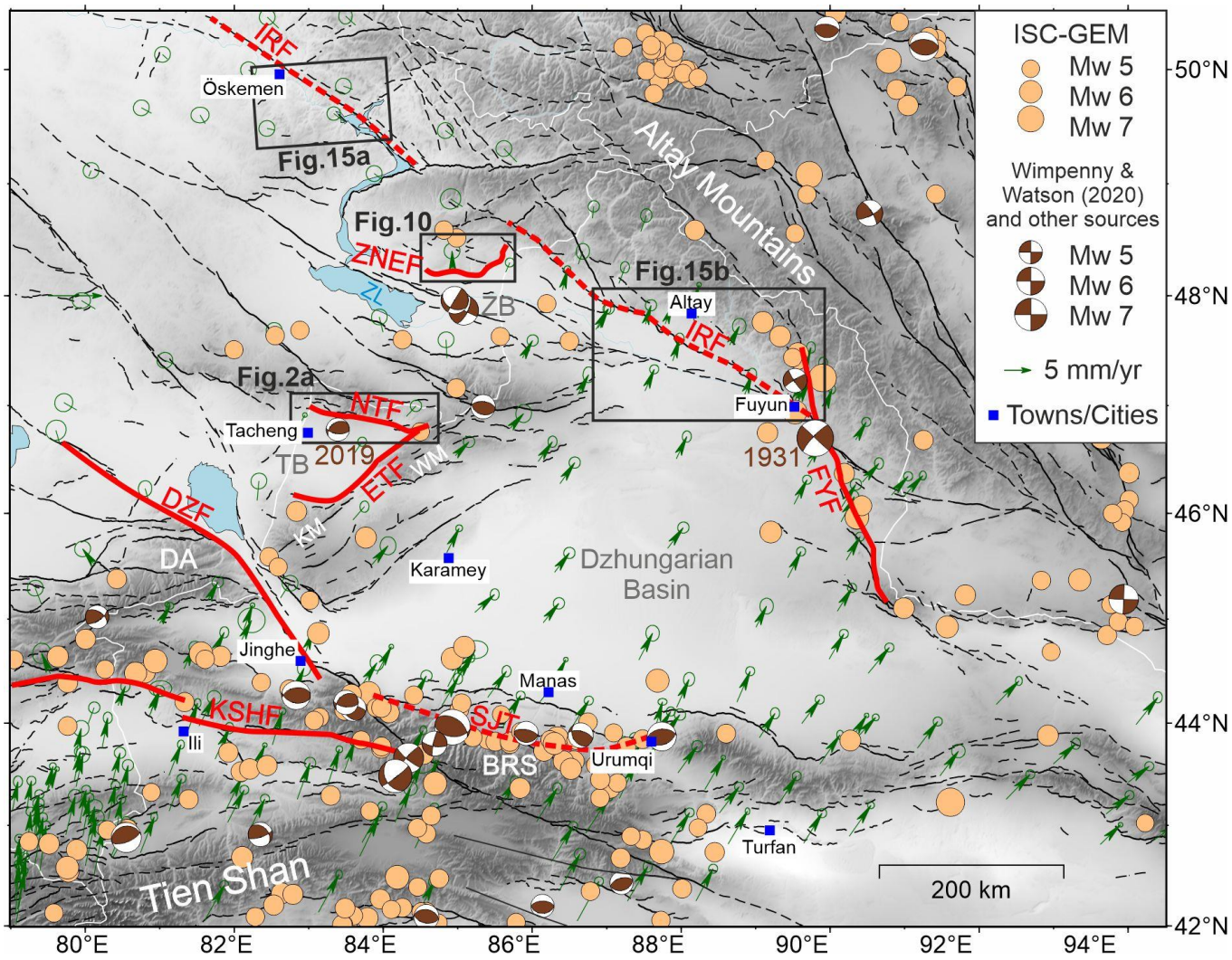

Figure 5-1. Seismicity, faults and GNSS velocities around the Dzhungarian Basin. The fault database is from Zelenin et al. (2021) with confidence levels A and B (as defined in the database) delineated in solid black lines and levels C and D delineated in dashed black lines. Thick red/red-dashed lines are the faults mentioned in this study with either prominent palaeo-earthquake ruptures or large historical events. Beige circles are the Mw > 5.0 seismicity from 1904 to 2017 from the ISC-GEM catalogue (ISC, 2021). Focal mechanisms are from Wimpenny and Watson (2020) except for the 2019 Tacheng event, from USGS, and the 1906 and 1944 events in Borohoro Shan, which are analysed in this study. IRF: Irtysh Fault; ZNEF: Zaisan NE Fault; FYF: Fuyun Fault; NTF: North Tacheng Fault; ETF: East Tacheng Fault; DZF: Dzhungarian Fault; KSHF: Kashihe Fault; SJT: South Junggar Fault; ZB: Zaisan Basin; TB: Tacheng Basin; DA: Dzhungarian Alatau; BRS: Borohoro Shan; WM: Wuerkashier Mountains; KM: Kertau Mountains ZL: Lake Zaisan

5.2 Other significant palaeo-earthquake ruptures

5.2.1 The North Tacheng Fault

The North Tacheng Fault (NTF) (also called the Taketai Fault) is located at the northern edge of the Tacheng Basin, which is a triangular basin sitting between the western Dzhungaria and Lake Alakol (Figure 5-1). The Tacheng Basin is bounded by the Tarbagatay Mountains (also called the Taketai Mountains) in the north, the Wuerkashier Mountains in the east and the Kertau Mountains (also called the Baerluke Mountains) in the south. These mountains consist of various strata that mostly incorporate Devonian and Carboniferous rocks with granitoid intrusions and represent amalgamation of multiple oceanic island arcs and continental fragments (Xiao et al., 2012; D. Zhang et al., 2017). Compared to the Tien Shan, these mountains mostly have lower relief and more extensive peneplain surfaces preserved at their summit, suggesting a relatively less intense Late Cenozoic uplift and tectonic activity in this region. However, seismicity, with magnitudes up to M_b 5.3, have occurred near the edges of the Tacheng Basin and several clear fault traces and surface ruptures can also be found bounding the basin, such as the East Tacheng Fault (also called the Dongbielike Fault), the Wuerkaishier Fault and the Baerluke Fault in the east, and the NTF in the north (Figure 5-1) (J. Yu et al., 2021). Several studies have investigated the slip rates and palaeo-earthquake occurrence on the faults located in the eastern basin (Luo et al., 2015; Yao et al., 2015, 2020; J. Yu et al., 2021), but little is known about the NTF. The NTF is a ~ E-W trending fault, with both right-lateral and reverse components, located at the southern range front of the Tarbagatay Mountains and extending for ~ 125 km (J. Yu et al., 2021; Zelenin et al., 2021). The fault separates Palaeozoic basement from Quaternary strata within the Tacheng Basin (Luo et al., 2015; D. Zhang et al., 2017). Fault scarps up to 8-m high and trenches revealing a fault dipping angle of 35° – 75° have been found among the Late Quaternary terraces on the western NTF with a roughly estimated uplift rate of 0.25 mm/yr (Luo et al., 2015) (Figure 5-2). From remote sensing, we interpret fresh surface ruptures in the section of the NTF east of 83.8°E. Thus, we use open-access satellite imagery and Pléiades optical imagery and DEMs derived from it to examine the palaeo-earthquake ruptures along the eastern ~ 50 km of the NTF in this study (Figure 5-2b).

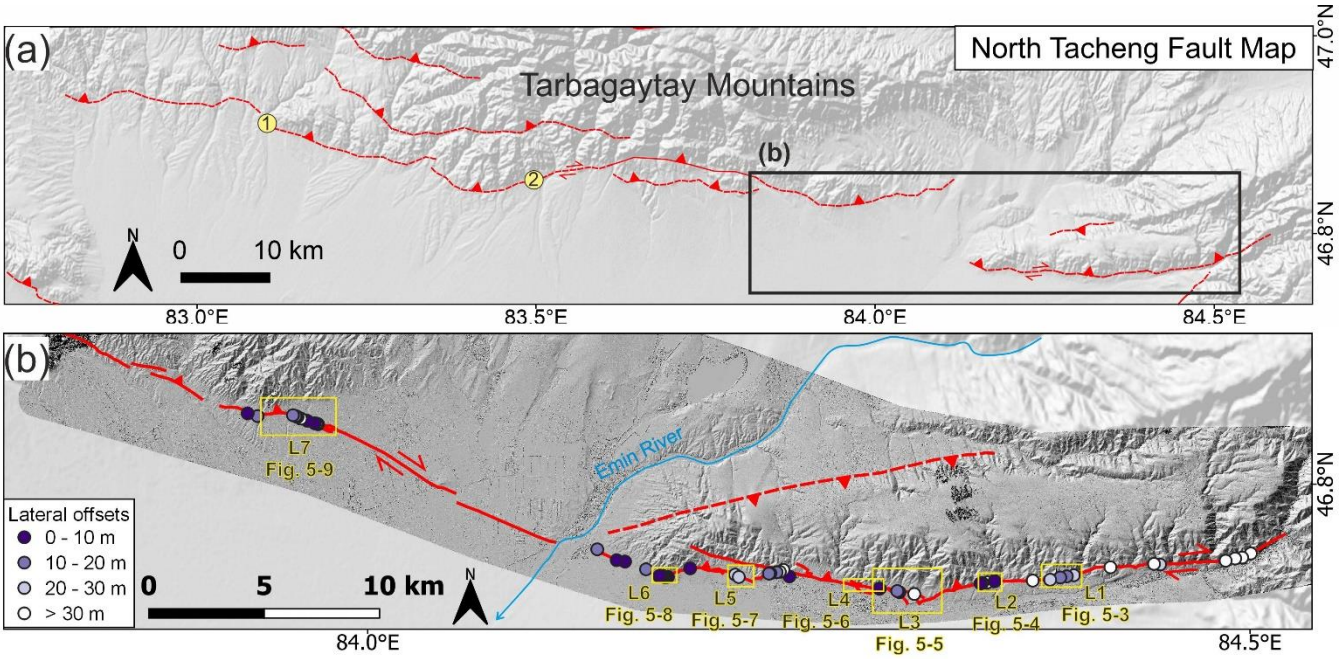

Figure 5-2. (a) Map of the North Tacheng Fault with ESRI shaded relief and the fault traces (red dashed lines) from Zelenin et al. (2021). Yellow circles annotated "1" and "2" are the rough locations where 8-m high fault scarps were found and trenches were excavated, respectively, by Luo et al. (2015). (b) Shaded-relief DEMs derived from Pléiades imagery showing the eastern NTF. Fault traces (red lines) are mapped by this study. Lateral offset measurements are labelled by dots. Seven locations in which we have provided detailed examinations are framed by yellow boxes with L1 to L7 annotated and correspond to the figures shown below. The Emin River is labelled in blue.

We characterise the geomorphological features showing the right-lateral and reverse offsets from seven locations (L1 to L7) along the eastern NTF (Figure 5-2b). We find little evidence for scarps lower than a height of 2 m whereas fault scarps with a height of 2 – 3.5 m are widely distributed, from L1 to L7, on this section of the fault (Figure 5-3, Figure 5-5, Figure 5-6 and Figure 5-9). For example, at L3, 2 – 3.5 m-high scarps appear on both lower (T1) and higher (T2) terraces (Figure 5-5b). At L5, 2 – 3.5 m-high scarps appear on the lower terraces (T1) whilst 5 – 6 m-high scarps appear on the higher terraces (T2), indicating the latter ones are cumulative scarps (Figure 5-7c). (Note that the labelling of T1 and T2 is site specific, such that there is no necessity for T1 and T2 mapped at L3 to correlate in age with the two levels mapped at site L5). We also discovered cumulative right-lateral displacements and possible single-event lateral offsets. At L2, cumulative displacements of over 80 m are measured from the offset channels (Figure 5-4b) and laterally-offset channels that have displacements of at least ~ 15 m are found at L1, L6 and L7 (Figure 5-3b, Figure 5-8c and Figure 5-9c,d). Meanwhile, several < 10 m lateral offsets are found among the narrower channels. For example, right-lateral displacements of 5 – 6 m are measured at both

L2 and L3 (Figure 5-4d and Figure 5-5d). It is worth noting that < 5 m lateral displacements appear on the 2 – 3.5 m-high fault scarps at L6 (Figure 5-8). The smallest lateral offsets at L6 are ~ 3 – 4 m (Figure 5-8c). Moreover, profile N14 demonstrates a pattern of double scarps, each has a height of ~ 2 – 3.5 m and each corresponds to a fault strand (Figure 5-8b, N14).

As the surface ruptures with similar amounts of offsets can be traced continuously for ~ 50 km and there are few gaps in preservation along the east NTF except at the Emin River crossing, and at a few < 1 km-long step-overs, we suggest the surface ruptures may be produced by the most recent earthquake (MRE) with a total rupture length of 50 km. Using a surface rupture length of 50 km and the empirical earthquake scaling relationship for all fault types yields an earthquake magnitude of Mw 7.1 (Wells & Coppersmith, 1994). The widely-spread smallest scarp heights and channel lateral displacements are 2 – 3.5 m and 3 – 6 m, respectively, which might be the single-event offsets in MRE; however, we do not observe these smallest vertical and lateral offsets at the same locus except at L6. The presence of up to ~ 30-m lateral offsets at L6 suggests either that the MRE is overprinted on pre-existing lateral displacements, or that the complex fault geometry and the natural river curvature might have affected some river patterns here. By assuming a vertical strike-slip fault plane with a maximum lateral displacement of 6 m, we can estimate a magnitude of Mw 7.4 from the earthquake scaling relationship for strike-slip faults (Wells & Coppersmith, 1994). Using an averaged dip of 55° and a maximum vertical displacement of 3.5 m, we can estimate another magnitude of Mw 7.4 as well from the scaling relationship for reverse faults (Wells & Coppersmith, 1994; Luo et al., 2015). Moreover, if assuming that the offsets at L6 best represent the fault slip in the MRE, we can calculate a maximum total fault slip of 6.1 m from the maximum vertical (3.5 m) and lateral (4.3 m) displacements with the same 55° dipping angle at L6. This further yields an earthquake magnitude of Mw 7.3 from the empirical scaling relationship for all types of faults (Wells & Coppersmith, 1994). Therefore, the east NTF is likely to produce an earthquake with a magnitude over Mw 7.0 and with possible maximum earthquake magnitudes of Mw 7.3 – 7.4.

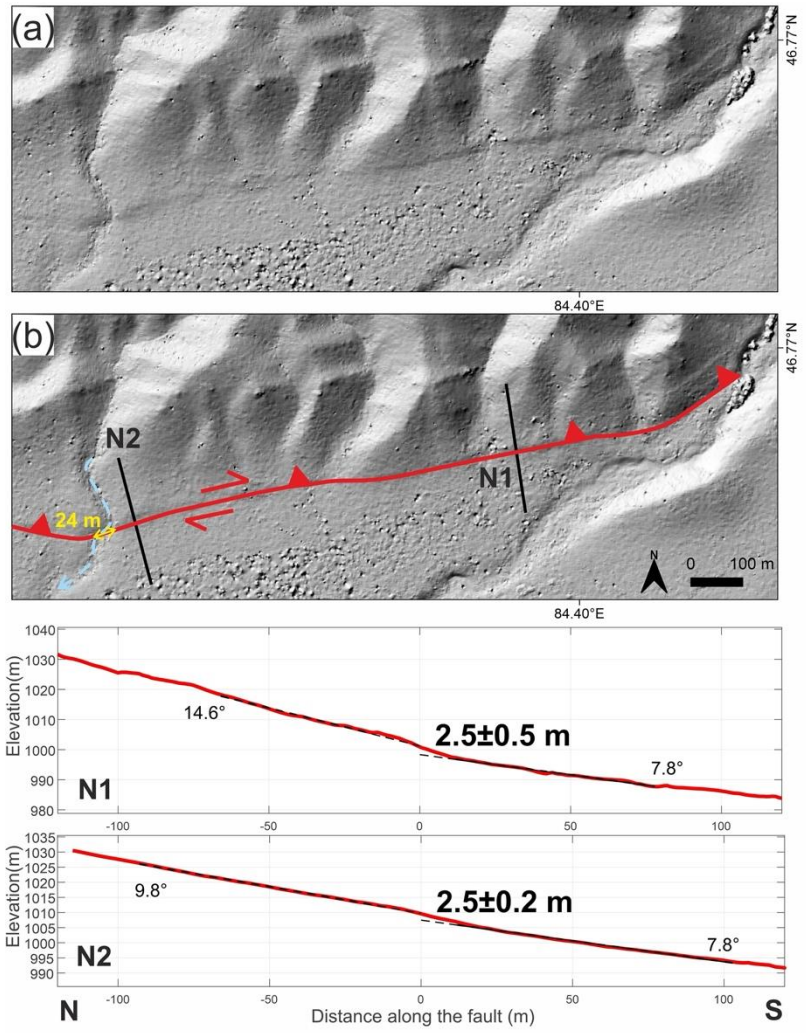

Figure 5-3. Location 1 (L1) (near 84.396°E, 46.768°N) on the NTF. (a) Shaded-relief Pléiades DEMs with interpretations in (b) where profiles N1 and N2 are marked by black lines and the NTF is mapped in red. A ~ 24-m laterally-offset channel (in light blue) is also labelled. The extracted topographic profiles N1 and N2 are shown below with annotated vertical offsets and fan slopes.

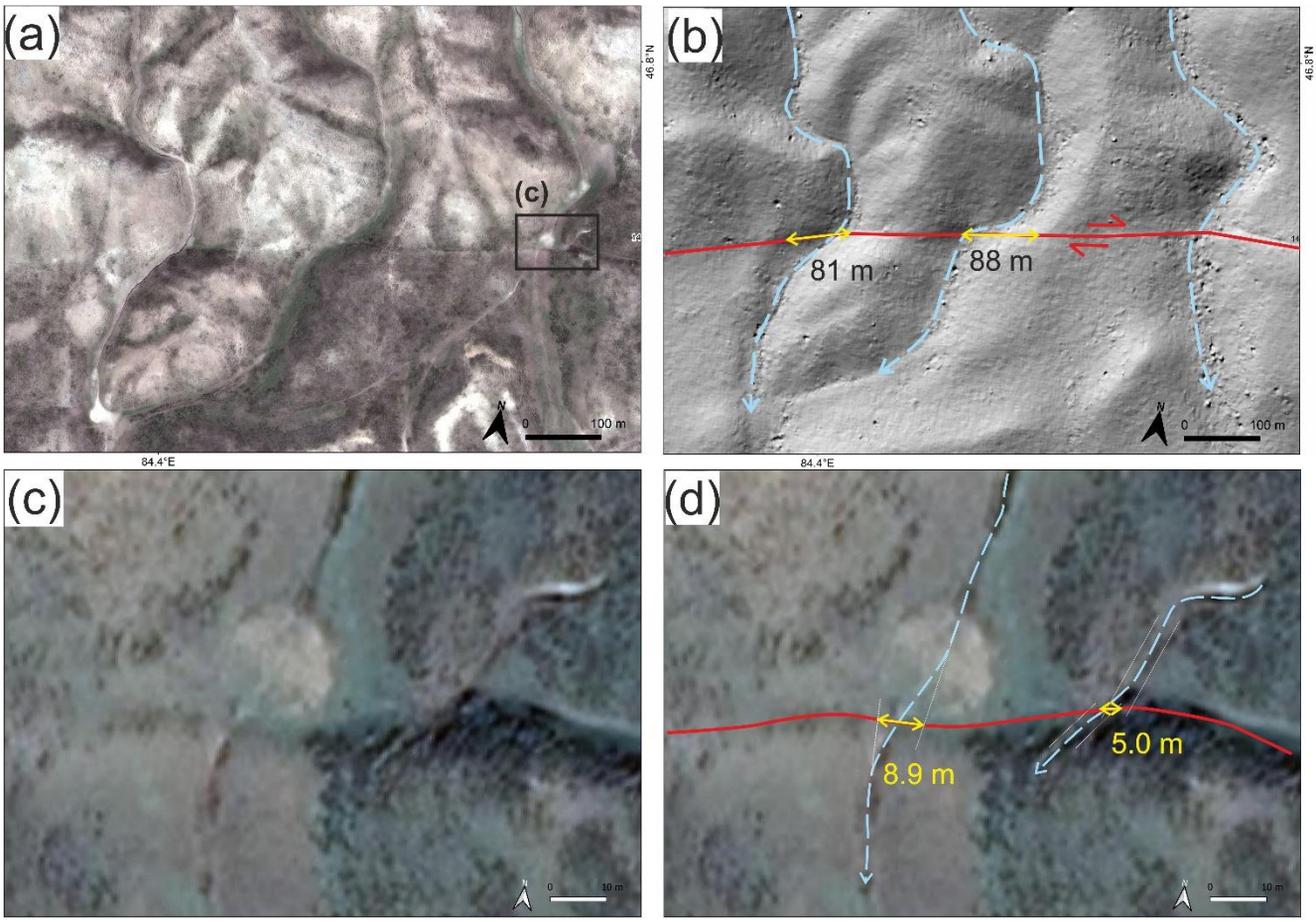

Figure 5-4. Location 2 (L2) (near 84.353°E, 46.767°N) on the NTF. Pléiades optical imagery (a) and shaded-relief DEMs (b) showing the offset channels with interpretations. (c) and (d) Google Earth imagery showing two < 10-m laterally-offset channels. Faults are in red; channels are in light blue; amounts of offsets are in yellow arrows.

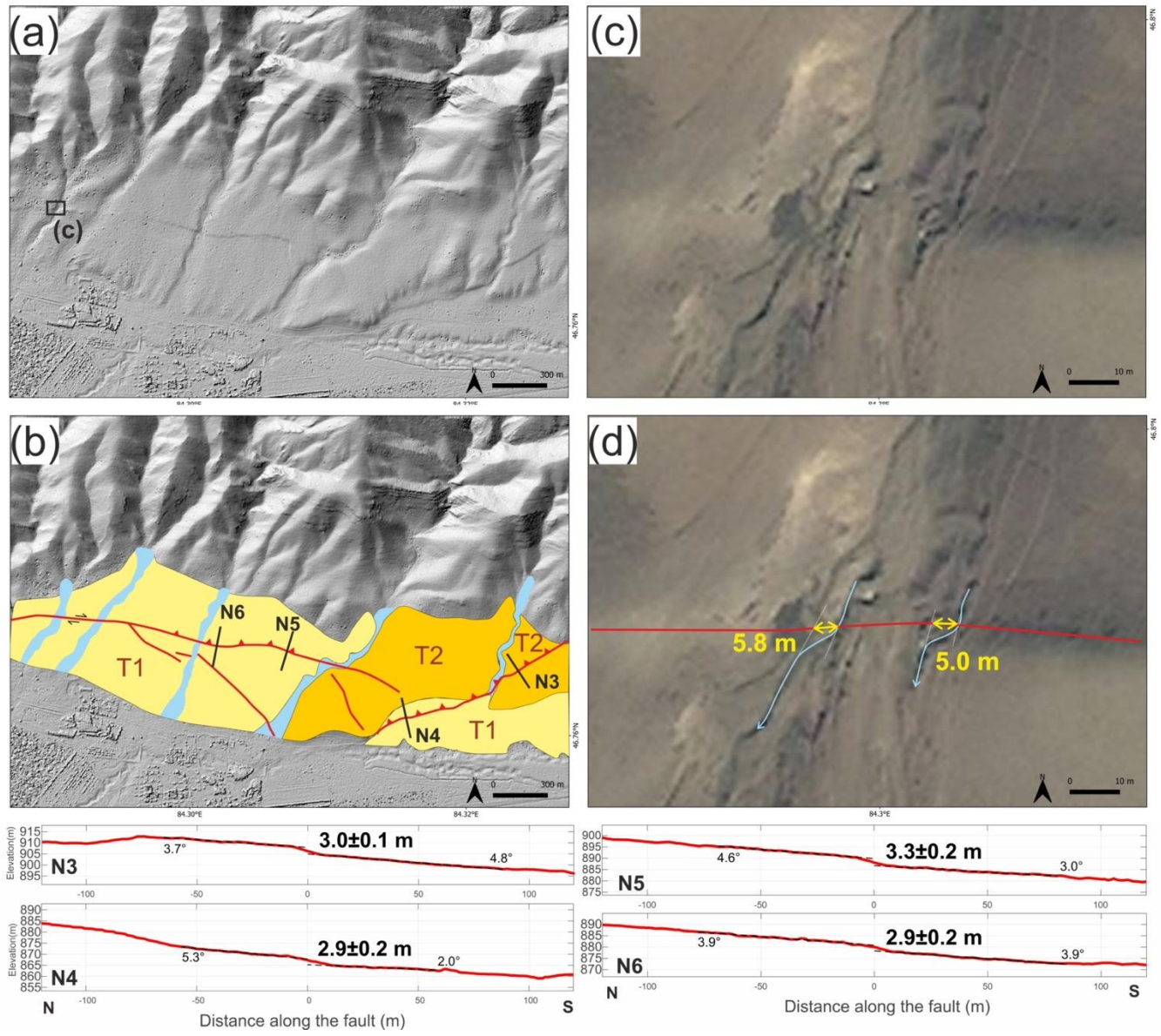

Figure 5-5. Location 3 (L3) (near 84.307°E, 46.765°N) on the NTF. (a) Shaded-relief Pléiades DEMs with interpretations in (b) where profiles N3 – N6 are marked by black lines and the NTF is mapped in red. Lower and higher terraces are labelled as T1 and T2, respectively. The extracted topographic profiles N1 and N2 are shown below with annotated vertical offsets and fan slopes. (c) and (d) Bing Map imagery showing two < 10-m laterally-offset channels. Faults are in red; channels are in light blue; amounts of lateral offsets are marked by yellow arrows.

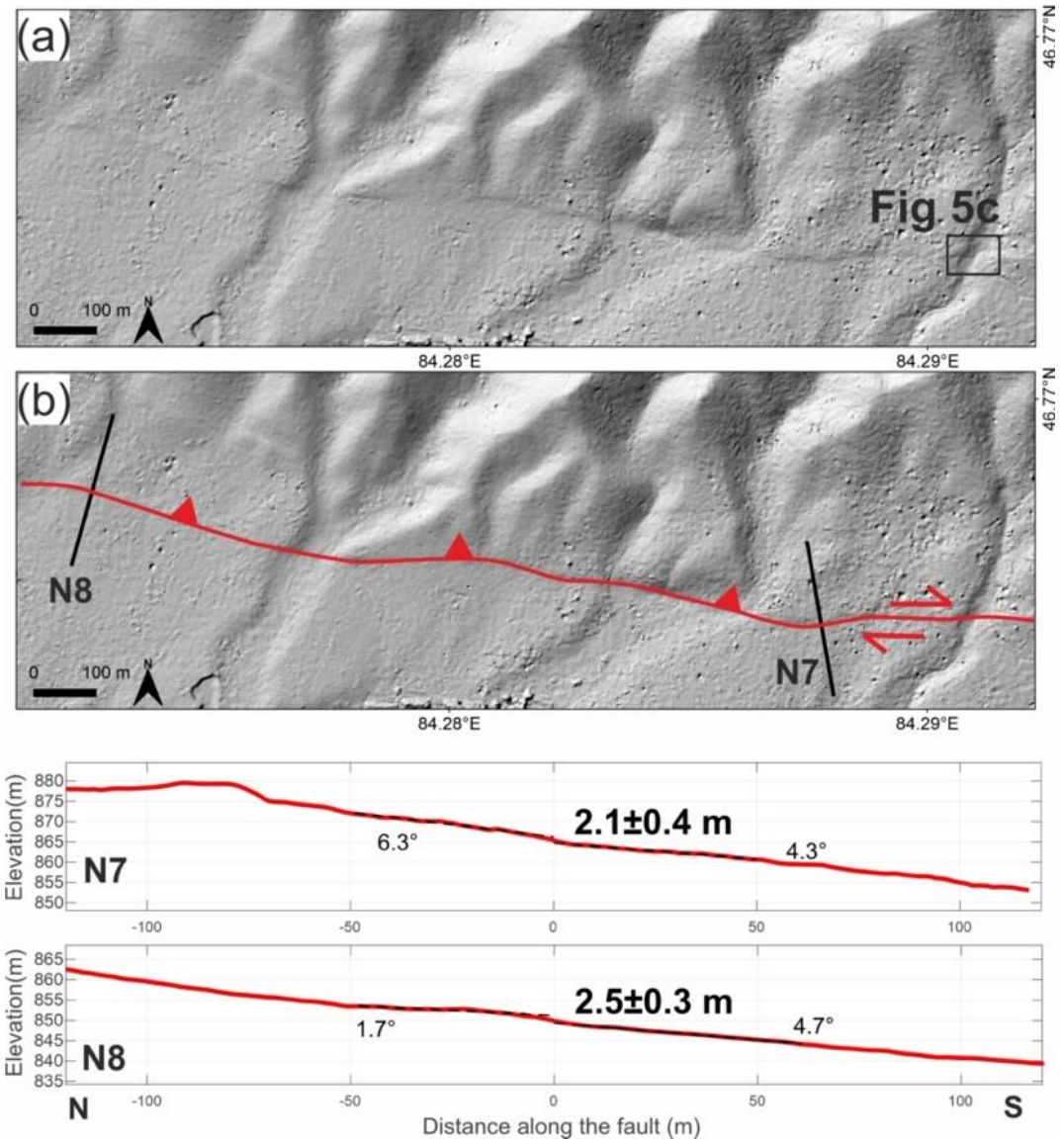

Figure 5-6. Location 4 (L4) (near 84.282°E, 46.768°N) on the NTF. (a) Shaded-relief Pléiades DEMs with interpretations in (b) where profiles N7 and N8 are marked by black lines and the NTF is mapped in red. The extracted topographic profiles N7 and N8 are shown below with vertical offsets and fan slopes annotated.

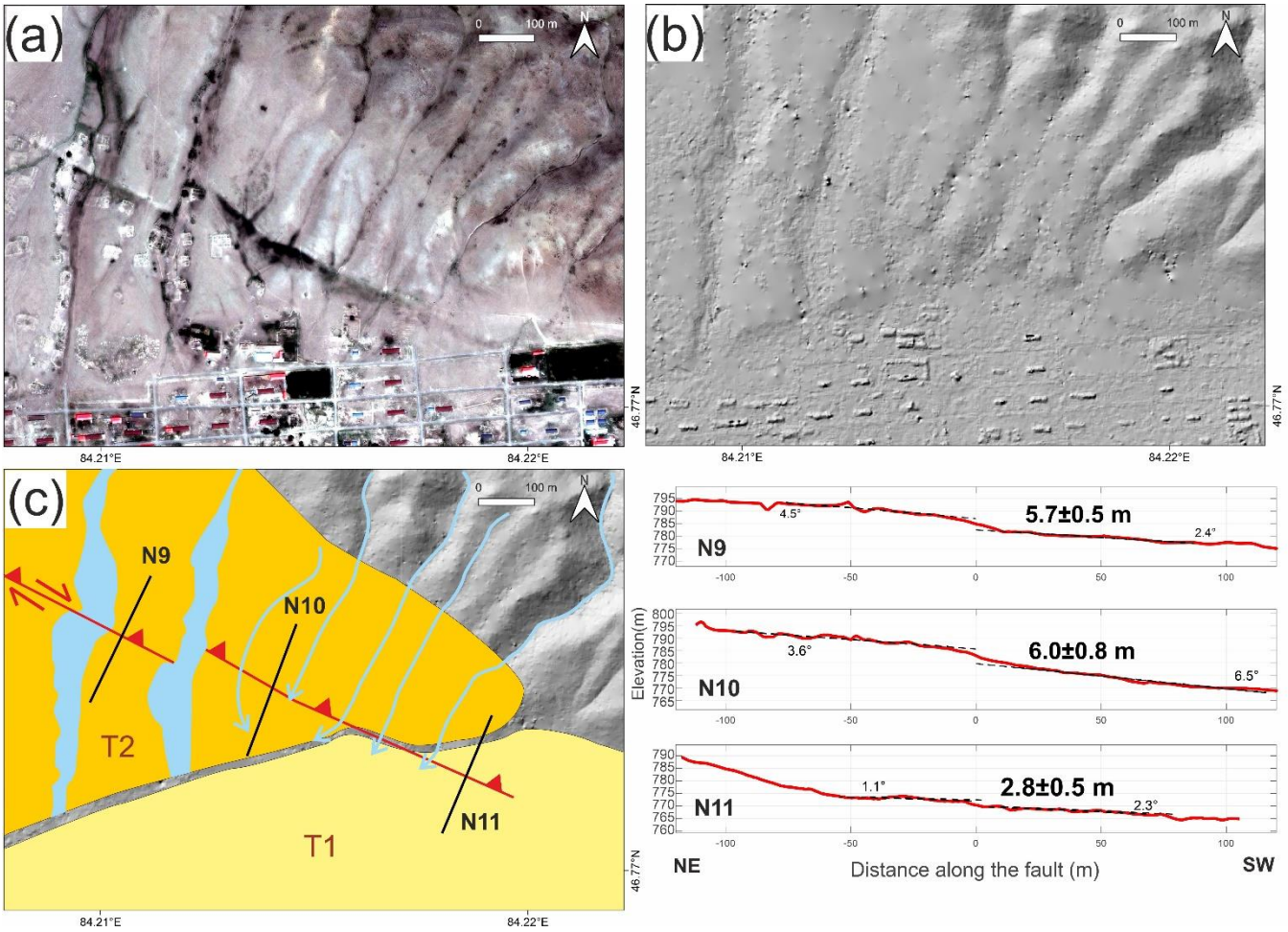

Figure 5-7. Location 5 (L5) (near 84.216°E, 46.773°N) on the NTF. Pléiades optical imagery (a) and shaded-relief DEMs (b) showing the fault scarps and the offset channels with interpretations in (c) where profiles N9 – N11 are marked by black lines and the NTF is mapped in red. Lower and higher terraces are labelled as T1 and T2, respectively. The extracted topographic profiles N9 – N11 are shown in the bottom right with vertical offsets and fan slopes annotated.

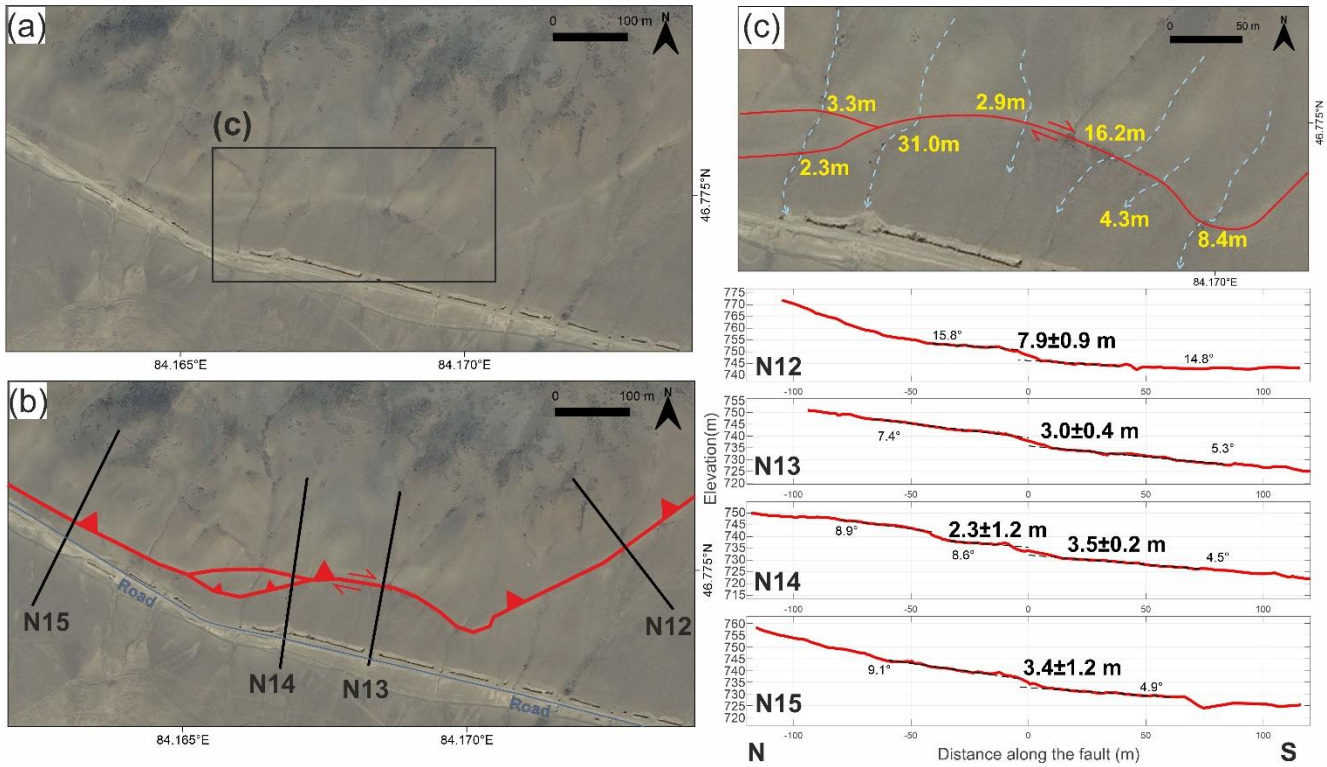

Figure 5-8. Location 6 (L6) (near 84.169°E, 46.775°N) on the NTF. (a) Bing Map imagery showing the fault scarps with interpretations in (b) where profiles N12 – N15 are marked by black lines and the NTF is mapped in red. The extracted topographic profiles N12 – N15 are shown in the bottom right with vertical offsets and fan slopes annotated. (c) Bing Map imagery showing the offset channels (in light blue) across the scarps and their laterally-offset amounts (in yellow).

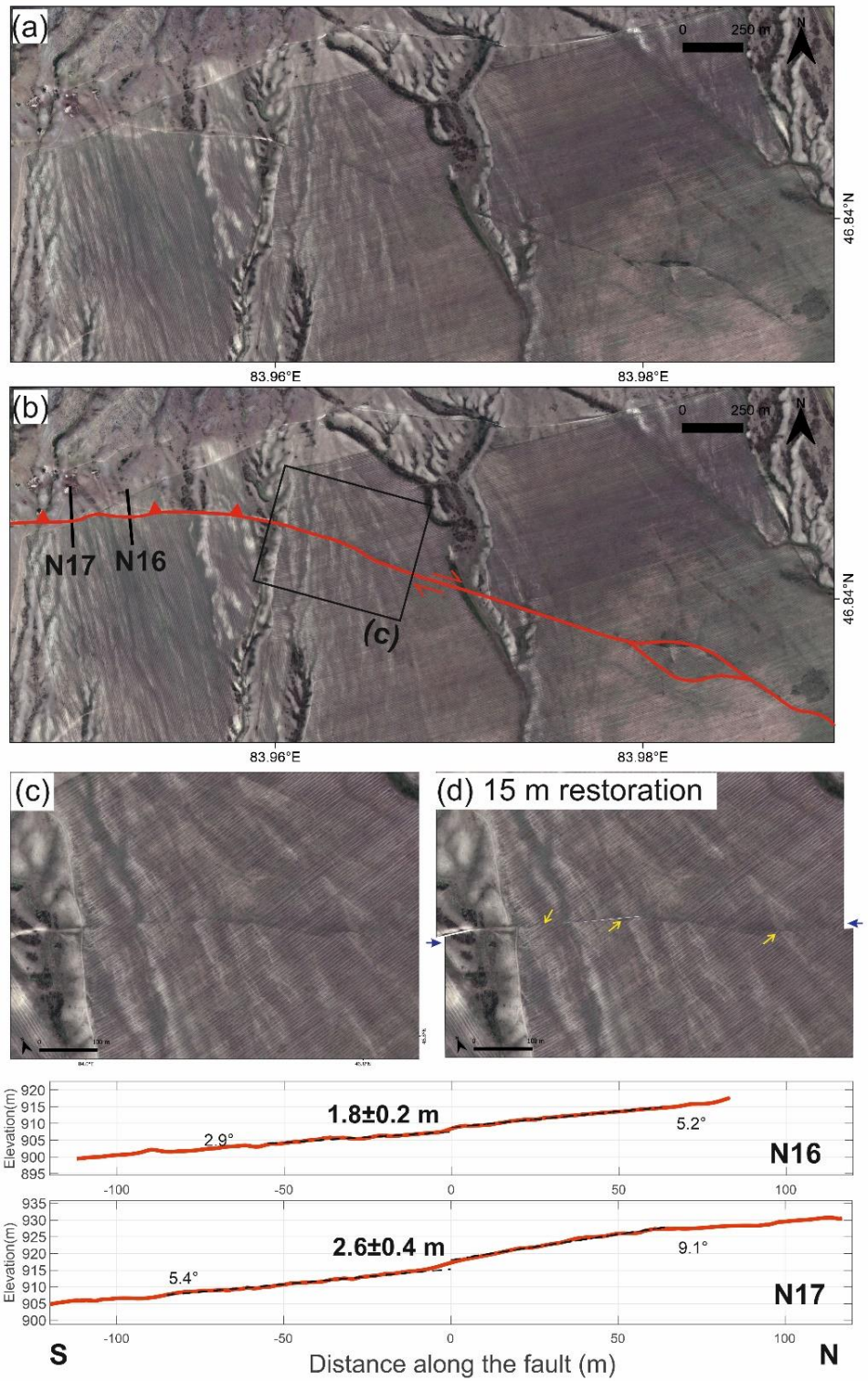

Figure 5-9. Location 7 (L7) (near 83.963°E, 46.843°N) on the NTF. (a) Bing Map imagery showing the fault scarps and displaced channels with interpretations in (b) where profiles N16 and N17 are marked by black lines and the NTF is mapped in red. The extracted topographic profiles N12 – N15 are shown below with annotated vertical offsets and fan slopes. (c) The zoomed-in version for the laterally-offset channels and a ~ 15-m restoration shown in (d) with yellow arrows pointing to the matching lineament.

5.2.2 Northeast of Lake Zaisan

Lake Zaisan is in the middle of the Zaisan Basin which is located north of the Tacheng Basin between the Tarbagatay Mountains and the NW Altay Mountains (Figure 5-1). The maximum N-S shortening across the Zaisan Basin from the GNSS velocities is only ~ 1 mm/yr (Zheng et al., 2017). Several well-recorded deep earthquakes (21 – 34 km) with magnitudes ranging from Mw 4.9 to Mw 6.4 occurred along reverse faults at the southern edge of the basin and on a right-lateral strike-slip fault within the basin (Thomas et al., 2002; Wimpenny & Watson, 2020; ISC, 2022a), but less seismicity has occurred in the northern part of the basin (Figure 5-1). However, northeast of Lake Zaisan along the northern basin edge, we have found palaeo-earthquake ruptures extending for at least 90 km long at the range front of the Qalschyr Mountains (named in this study and part of the Altay Mountains) (Figure 5-10). These ruptures have been mapped by Thomas et al. (2002) as reverse faults but without a specific name or further descriptions. Thus, here we name it the Zaisan Northeast Fault (ZNEF) and we investigate the fault using DEMs, covering from ~ 84.6°E to ~ 85.6°E, derived from the Pléiades imagery (Figure 5-10). The ZNEF can be separated into two main portions with a nearly 90° bend in between – the northeast portion has a ~ NE-SW trending whereas the west portion is E-W trending. From the preliminary observation, the ruptures along the ZNEF are mostly fault scarps among uplifted alluvial fan surfaces without prominent laterally-offset geomorphic features. Unlike the NTF which generally has a quite straight fault trace in many places, the fault traces of the ZNEF are mostly sinuous and non-continuous, which fits with the property of reverse fault ruptures. Although fault scarps, or scarp-like features, are recognisable along the ZNEF, some features possibly either have complicated fault geometry or are not caused by faults as they seem to be. We show them in the figures with detailed descriptions in the paragraphs below.

A series of range-facing scarp extends for ~ 20 km along the northeast portion of the ZNEF (Figure 5-10 and Figure 5-11). Profiles Z1 and Z2 show various heights (~ 7 m to ~ 19 m) of these range-facing scarps and a continuous asymmetric bulge with steeper range-facing scarps and smoother SE-facing slopes Figure 5-11d, Z1, Z2). A SE-dipping back thrust of the ZNEF could produce this kind of topography. However, this asymmetric bulge might merely be the beddings of basement strata since the colours of rocks shown in the satellite optical imagery seem to follow the trend of this bulge (48.270°N, 85.465°E) (Figure 5-11b). In this case, the ZNEF should be located much closer to the range, but fault scarps are barely recognised in those areas and only one straight lineament can be found, which, is possibly a strike-slip fault cutting through the hills (Figure 5-11a, c). Another possibility is that the feature is related wholly, or in part with a palaeo-shoreline of Lake Zaisan, though the heights of these bulges are slightly varied

and the corresponding palaeo-shoreline is hardly found on the counter part of the lake. Due to a lack of detailed large-scale geological maps and the history of Lake Zaisan, we require *in situ* investigations to reveal the cause of this topography and to locate the exact location of the ZNEF here. On the other hand, Profile Z3 shows a more plausible morphology of fault scarps among the alluvial fans and so do Profiles Z4 and Z5, which are ~ 7 – 10 km southwest of Profile Z3 (Figure 5-11c, Z3 and Figure 5-12). Nevertheless, there is also a bulge-like and bumpy surface on the hanging wall of the Profile Z5 scarp series (Figure 5-12b, Z5), which again makes them possible to be bedrock features instead of fault scarps.

There is another continuous bulge with range-facing scarps (Profile Z6) extending for ~ 5 km long in the west of the Qalschyr River on the west portion of ZNEF (Figure 5-13a, b, Z6). Unlike those on the northeast portion, both scarps along this bulge have similar steepness and each has a more consistent height along the strike. Again, a back thrust likely exists here to create such topography; however, there could be non-tectonic causes as well, such as bedrock or river terrace risers. Profiles Z7 – Z10, ~ 7 km west of Profile Z6, show plausible morphology of fault scarps among the alluvial fans with scarp heights decreasing from the fan apex (Figure 5-13c, Z7-Z10). The heights of higher scarps here are 7 – 10 m whereas those of lower scarps are 2 – 3 m, which are the lowest scarps measured along the ZNEF. This series of fault scarps extend further west and clearly cut through the alluvial fans at the range front until ~ 84.714°E. These scarps' heights vary from ~ 5 m to ~ 20 m (Figure 5-14).

In sum, we found many bulging topographic features along the ZNEF which might or might not be fault scarps, and we need further field investigations to reveal their entities. The ZNEF might have quite complicated fault geometry considering its abrupt change in the strike and its various geomorphology. It is difficult to tell the single-event fault slip based on the current observations since the scarp heights are various and there seems to be a quite uniform terrace level among the alluvial fans at the Qalschyr range front. If considering a maximum rupture length of ~ 85 km based on the surface ruptures recognised along this range front, the ZNEF can cause earthquakes with an average displacement of ~ 1 m and a magnitude of Mw 7.4 from the empirical scaling relationship for reverse faults (Wells & Coppersmith, 1994). Further investigations such as trenching and Quaternary dating are needed to unravel the palaeo-earthquake history and occurrence of the ZNEF, which could be a precious example of extremely slowly moving intra-continental reverse faults.

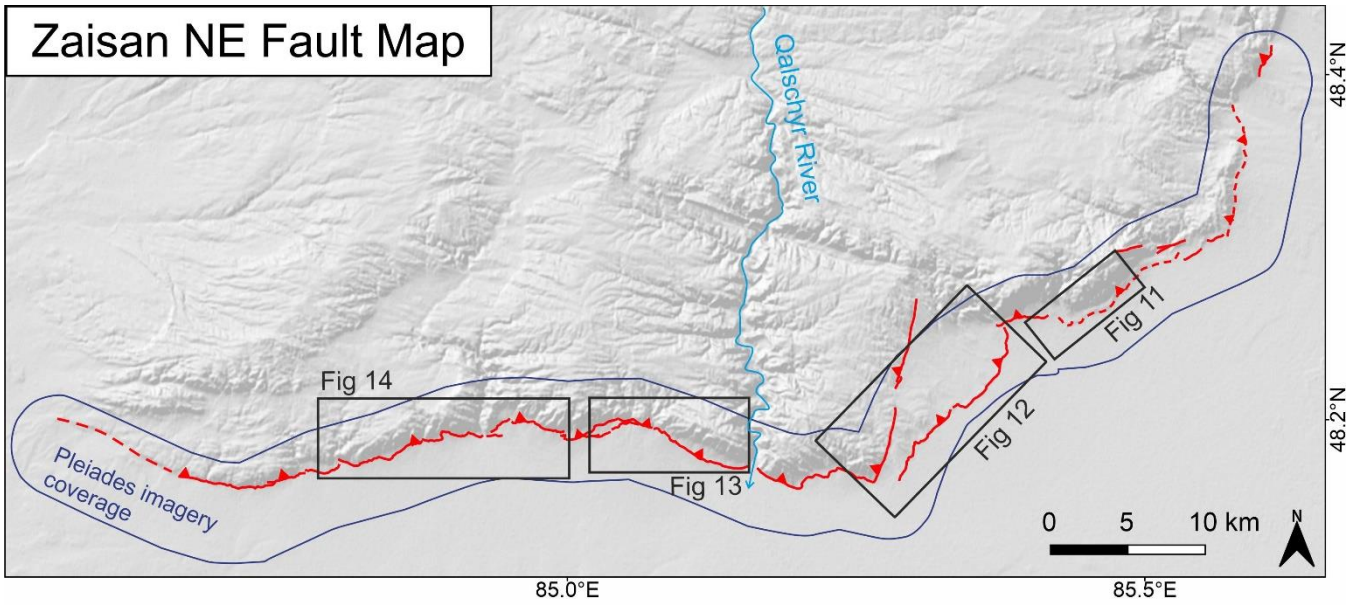

Figure 5-10. The Zaisan NE Fault (in red) mapped by this study with ESRI shaded-relief DEMs. The dark blue frame shows the coverage of the Pléiades imagery in this study.

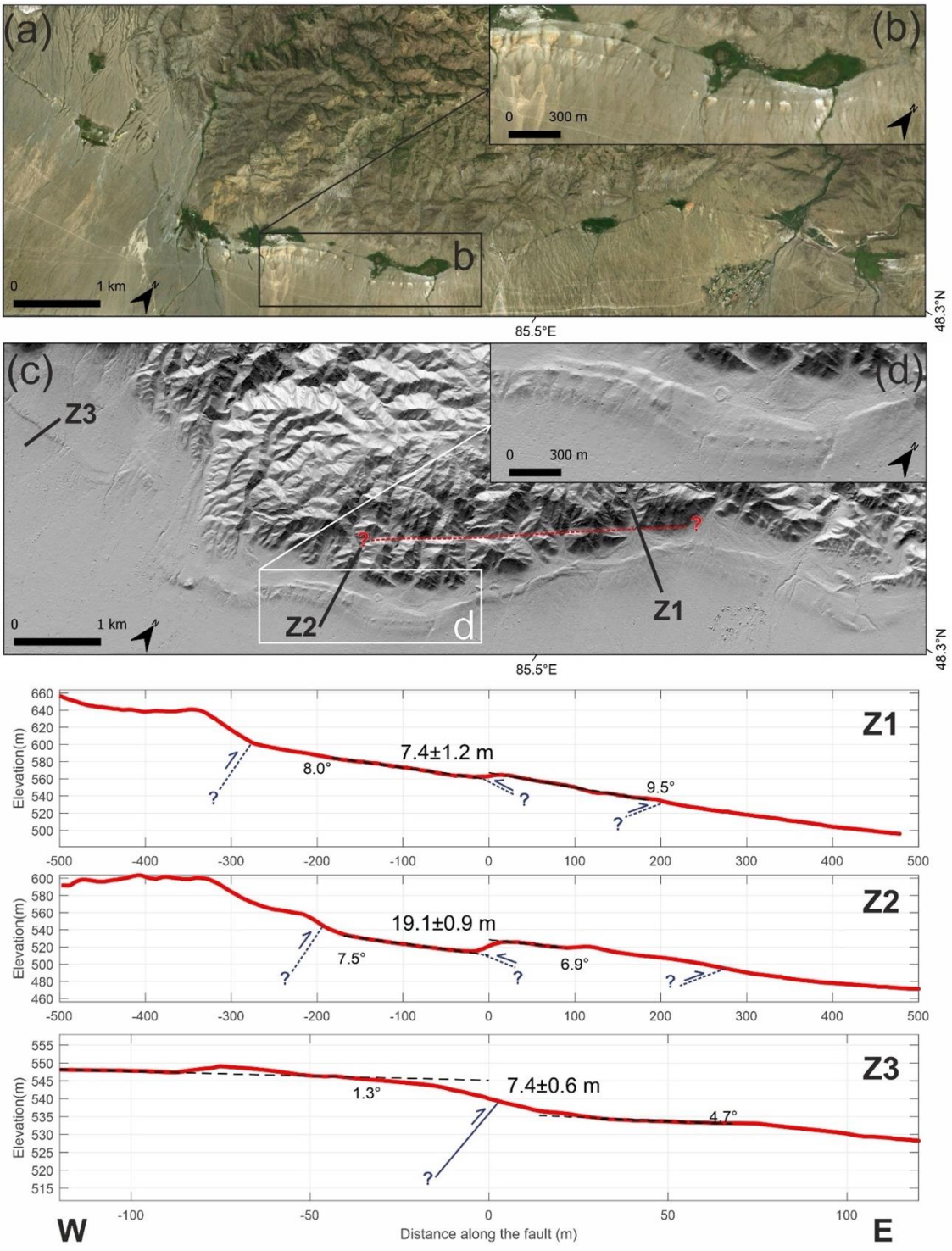

Figure 5-11. The range-facing scarps and the asymmetric bulge on the northeast portion of the ZNEF shown in Bing Map imagery (a) and Pléiades shaded-relief DEMs (c). (b) The zoomed-in Bing Map showing the possibly colourful bedrock. (d) The zoomed-in shaded-relief DEMs showing the shape and morphology of this bulge. The extracted topographic profiles Z1 – Z3 are labelled in (c) and shown below with vertical offsets and fan slopes annotated, and possible underneath faults sketched with question marks. A possible E-W trending strike-slip fault is also labelled by a red-dashed line with question marks in (c).

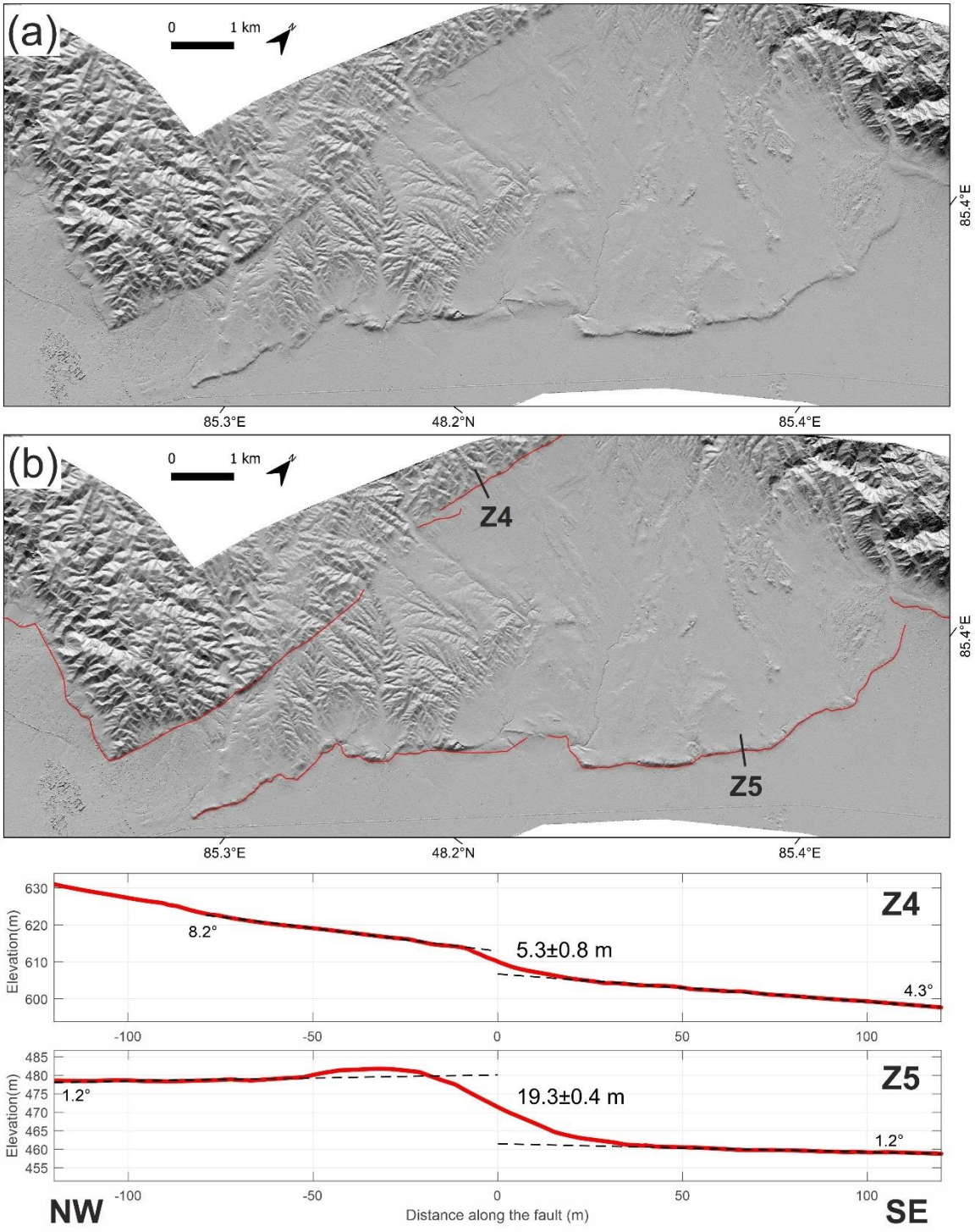

Figure 5-12. Pléiades shaded-relief DEMs (a) showing the possible fault scarps with interpretations in (b) where profiles Z4 and Z5 are marked by black lines and the ZNEF is mapped in red. The extracted topographic profiles Z4 and Z5 are shown below with vertical offsets and fan slopes annotated.

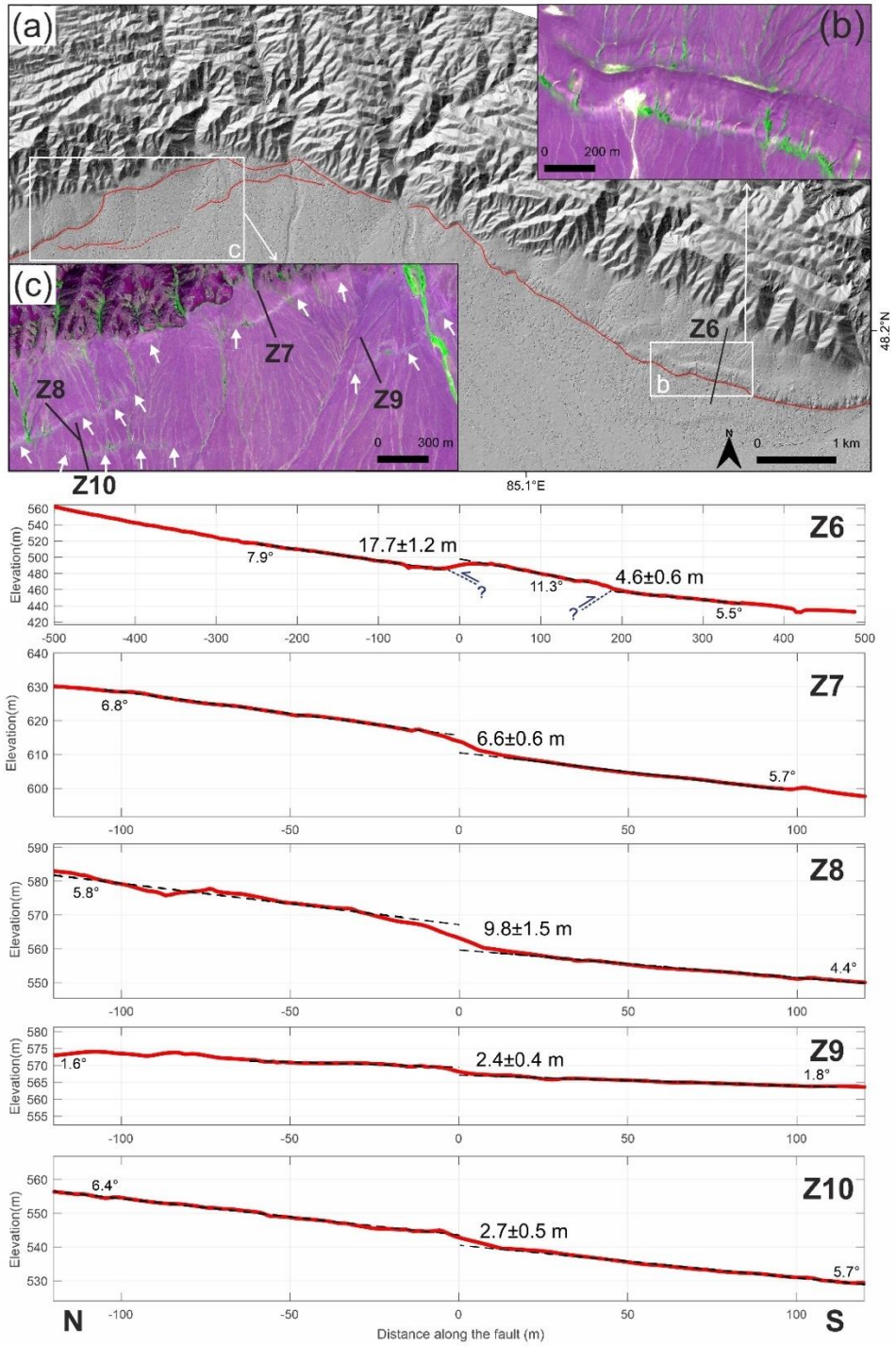

Figure 5-13. (a) Pléiades shaded-relief DEMs showing the fault scarps and those with bulging topography on the west portion of the ZNEF (in red). (b) Pléiades optical imagery, with near-infrared (IR) band demonstrated in green, showing the bulging topography. (c) The same type of Pléiades optical imagery showing the fault scarps (pointed by white arrows, among the alluvial fans. The extracted topographic profiles Z6 – Z10 are marked by black lines in (a) and (c) and are shown below with annotated vertical offsets and fan slopes. The possibly underlying fault arrangement for Profile Z6 is sketched with question marks.

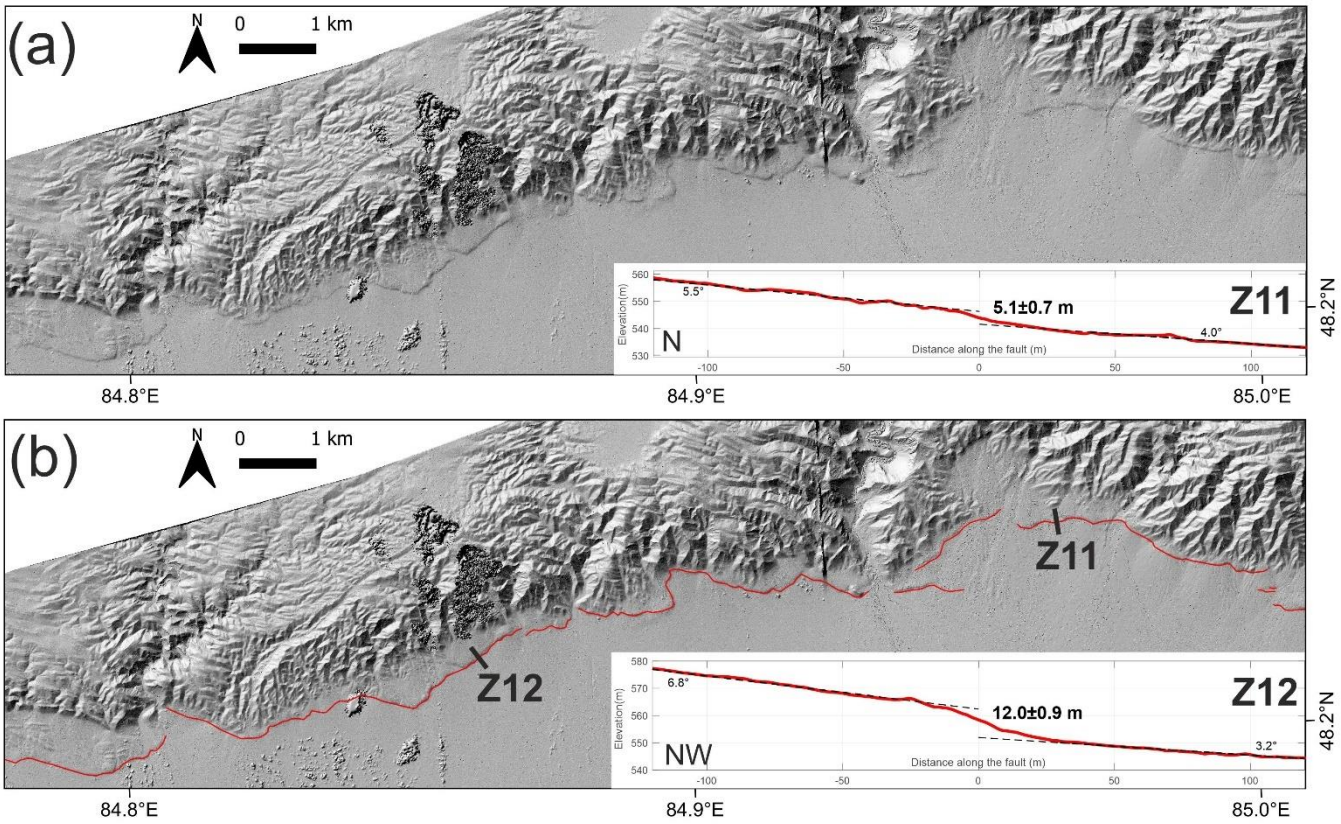

Figure 5-14. Pléiades shaded-relief DEMs (a) showing the possible fault scarps on the west portion of the ZNEF (in red) with interpretations in (b) where profiles Z12 and Z11 are marked by black lines. The extracted topographic profiles Z12 and Z11 are shown in attached panels with vertical offsets and fan slopes annotated.

5.2.3 Northern and Eastern Dzhungarian Basin

5.2.3.1 The Irtysh Fault

The Irtysh Fault (or the Irtysh Fault Zone) is a > 300-km-long NW-SE trending dextral strike-slip fault with reverse components. This fault sits between the NW-SE trending Altay Mountains and the northern Dzhungarian Basin and separates the Palaeozoic igneous basement with the Mesozoic-Cenozoic sedimentary cover (W. Hu et al., 2020; Zelenin et al., 2021) (Figure 5-1). Similar to other major strike-slip faults in Central Asia, the Irtysh Fault is an inherited structure which originated from the Siberian-Kazakh craton collision in the Late Palaeozoic and was reactivated due to the India-Eurasia collision (Glorie et al., 2012; W. Hu et al., 2020). The northwest part of the Irtysh Fault has a historical earthquake in 1761 with a magnitude of ~ M 6.5 whereas there is no recorded significant earthquake along the southeast part (Baize et al., 2019). Although possible fault lineament and escarpments can be recognised

from the satellite imagery (Figure 5-15), the potential Quaternary activity of the Irtysh Fault has been addressed only by Baize et al. (2019), who performed a preliminary palaeo-earthquake investigation of the NW Irtysh Fault near Öskemen City (Figure 5-15a). From trenching and tectonic-morphological analysis, they confirm the fault has ruptured the Holocene deposits with no more than two past events in the last 10000 years. A displacement of 0.25 – 1.5 m has been observed from the trenches, suggesting an earthquake magnitude of Mw 6 – 7, and a ~ 190 km active Irtysh Fault map has been proposed as well (Baize et al., 2019).

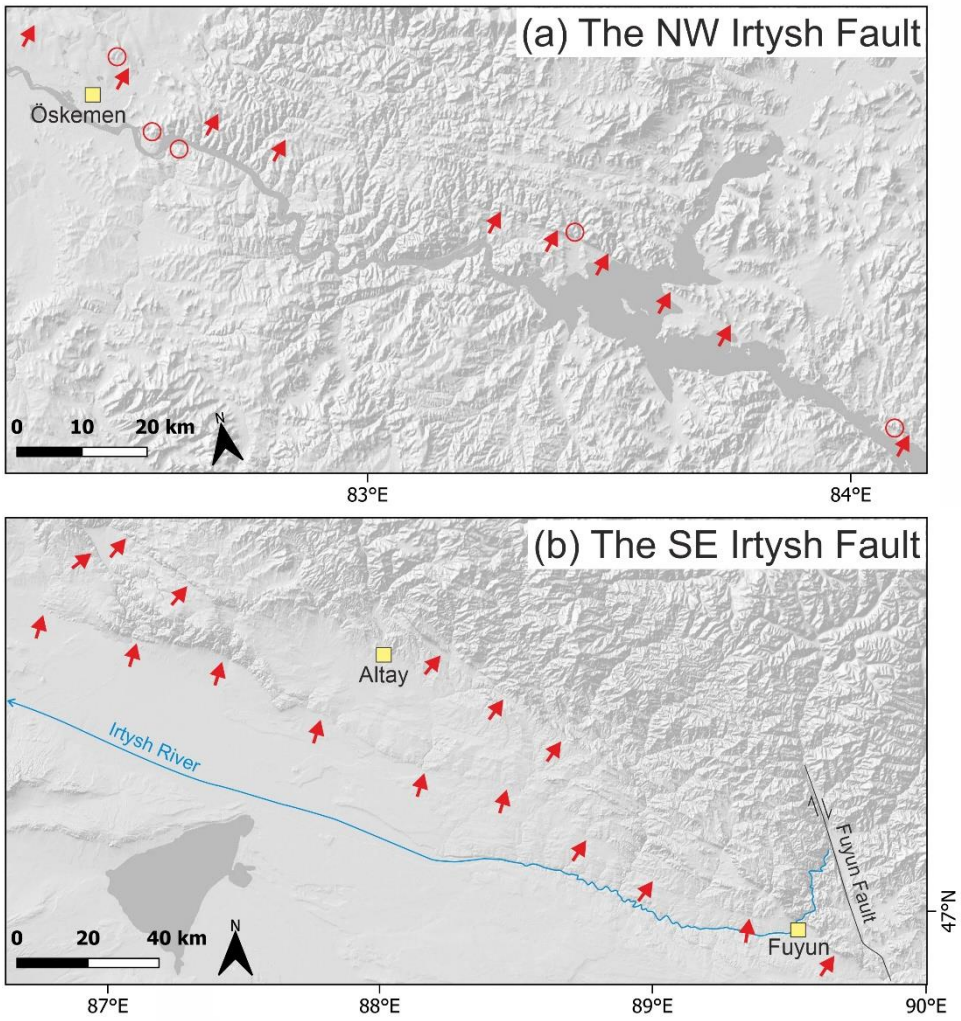

Figure 5-15. Possible fault lineaments and scarps (pointed by red arrows) of the NW (a) and (SE) Irtysh Fault with ESRI topography in shaded relief. Field sites along the NW Irtysh Fault where Baize et al. (2019) visited and trenched are marked by red circles. Towns and counties are labelled with yellow squares. The Irtysh River is delineated in blue.

5.2.3.2 The Fuyun Fault

The Fuyun Fault is a ~ 176-km-long NNW-SSE trending right-lateral strike-slip fault located at the eastern edge of the Dzhungarian Basin (Figure 5-1). The 1931 Fuyun Earthquake ruptured on this fault with a magnitude of Ms 7.9 – 8.0, which is the most recent earthquake with a magnitude ~ M 8 around the Dzhungarian Basin (Klinger et al., 2011; Xiwei Xu et al., 2012) (Figure 5-1). Due to this 1931 earthquake and the prominent surface ruptures, the Fuyun Fault is relatively well-studied in comparison to the neighbouring Irtysh Fault. Horizontal offsets of river channels along the Fuyun Fault can be recognised from the satellite imagery and previous studies conclude an average co-seismic slip of 6.3 m during the 1931 event which is similar to the other five palaeo-earthquake events from the observed cumulative displacements, suggesting a characteristic slip model on this fault (Klinger et al., 2011). A long-term lateral slip rate of 0.76 ± 0.24 mm/yr is calculated from the ^{10}Be exposure ages of the offset river terraces (Xiwei Xu et al., 2012). A recent study also reveals six palaeo-earthquakes with potential magnitudes of Ms ≥ 8.0 as well as three additional potential Ms ≥ 7.0 past events and 11 potential Ms ≥ 5.5 palaeo-earthquakes all within ~ 28,000 cal. yr BP from the lacustrine strata and radiocarbon dating of an adjacent lake (Fan et al., 2022). These lacustrine records indicate, in contrast, a weakly periodic recurrence interval of the fault with an average of 5303 years for the Ms ≥ 8.0 events (Fan et al., 2022), which is much shorter than the 9300 ± 3300 years estimated from the average co-seismic slip and the lateral slip rate. (Klinger et al., 2011; Xiwei Xu et al., 2012).

5.3 Earthquake Scaling

5.3.1 Earthquakes in Dzhungaria, the Tien Shan and Mongolia

We first compile the fault parameters from the palaeo-earthquakes and the large (Mw > 7.0) historical earthquakes in Central Asia around the Dzhungarian Basin, the Tien Shan and Mongolia in Table 5-1 to reveal the scaling of intra-continental earthquakes. The displacement to surface rupture length (SRL) ratio compiled from these historical and palaeo-earthquake examples is ~ 2.7×10^{-5} for average displacement (AD) and ~ 4.0×10^{-5} for maximum displacement (MD) (Figure 5-16). These ratios are inconsistent with the ratio of ~ 6×10^{-5} for intraplate events suggested by Scholz et al. (1986). We also plot AD against SRL for several large and renowned interplate earthquakes globally, and they yield a ratio of 1.1×10^{-5} (Figure 5-16a) (Table 5-2), which is similar to the ratio of ~ 1×10^{-5} estimated by Scholz et al. (1986). The similarity in slip to length ratios between intraplate and interplate faults from our results

implies that their stress drops and frictional strength do not vary as much (six times) as previously suggested (Scholz et al., 1986). We also compare the displacement and SRL relationships of the data in Central Asia with those estimated from all types of faults globally by Wells and Coppersmith (1994). Our data yield regressions of $log_{10}(AD) = -0.12 + 0.36log_{10}(SRL)$ and $log_{10}(MD) = 0.49 + 0.16log_{10}(SRL)$ with both 95% confidence intervals overlap with the results calculated by Wells and Coppersmith (1994) (Figure 5-16c,d). However, we are aware that our data are scattered and our examples in Table 5-1 have a very limited sample size. Thus, in the following section, we expand the sample size by adding more historical intra-continental earthquakes.

5.3.2 Earthquakes in SCRs, TCRs and Worldwide

We include intra-continental earthquakes, whose AD, MD and SRL are revealed from direct measurements instead of modelling, listed in Lettis et al. (1997), Moss & Ross (2011), Clark et al. (2020), Yang et al. (2021), .etc (Table 5-2). Based on the global strain rate model (Kreemer et al., 2014), we further categorise them into stable continental regions (SCR), for those with strain rates of $\approx 1 \times 10^{-9} yr^{-1}$, such as Australia, central India and NE America, and tectonically active continental regions (TCR) where the strain rates are $> 1 \times 10^{-9} yr^{-1}$, such as Central Asia, China and Iran. From the scaling relationships between SRL and Mw, it seems that the TCR earthquakes have a slightly larger SRL than the SCR earthquakes of comparable Mw (within this study) when Mw > ~ 6.5, but are consistent with the SCR events of the same Mw range compiled by Leonard (2010) and global events compiled by Wells and Coppersmith (1994) (Figure 5-17). Global strike-slip and dip-slip faults also have slightly larger SRL than SCR and TCR faults of comparable Mw (Leonard, 2010). However, the null hypothesis of various tectonic settings having the same regression coefficients of SRL on Mw cannot be rejected, because the 95% confidence intervals of SCR and TCR overlap with others (Figure 5-17) (Wells & Coppersmith, 1994; Leonard, 2010).

Since records of MD for intra-continental earthquakes are more complete than records of AD, we only discuss the displacement-related scaling relationships for MD in this section. Similar scaling relationships are found between MD and SRL and between MD and Mw for earthquakes from various tectonic settings as the 95% confidence intervals of SCR and TCR mostly overlap with each other, and also with the regression compiled by Wells and Coppersmith (1994) (Figure 5-18). Nevertheless, Figure 5-18a demonstrates that the TCR earthquakes generally have larger SRL than the SCR earthquakes of comparable MD. Figure 5-18b also demonstrates that the TCR earthquakes have larger Mw, in a range of

Mw 6 – 8, than the other earthquakes of comparable MD. In other words, the TCR earthquakes have smaller MD than the other earthquakes of comparable Mw (Figure 5-18b). These all indicate that the TCR earthquakes seem to have larger rupture areas, especially when compared to the SCR ones, which is consistent with the conclusion made by Somerville (2021).

In summary, earthquake scaling relationships of SRL and Mw are consistent within various tectonic settings, whereas the relationships related to MD are more variable between different tectonic settings. This indicates that displacements might be a more critical parameter than SRL regarding the estimation of earthquake magnitude in various tectonic settings. Moreover, both SCR and TCR faults seem to have distinct earthquake scaling, and thus should be discussed separately rather than considered as a uniform intra-continental setting in terms of fault behaviours.

Table 5-1. Observations of intra-continental earthquakes in Tien Shan, Mongolia and Dzhungaria.

Historical or Paleo-events	Responsible Fault	PD (m)	MD (m)	AD (m)	MND (m)	SRL (km)	Mw	Slip type	Displacement and SRL references	Displacement estimation	Mw estimation and references
1812 Nilke	Kashihe Fault	15	-	-	-	112	7.5-7.9*	RL	This study & Yin et al. (2006)	Field Observations	This study / EES
1889 Chilik	Chon-Kemin-Chilik	10†	-	-	-	175	8.0	RL	Abdrakhmatov et al. (2016)	Mapping and/or field observation	Kruger et al. (2017)
1911 Chon-Kemin	Chon-Kemin-Chilik	14	5.5	4	3	188	8.0	R	Rizza et al. (2019) & Arrowsmith et al. (2017)	Mapping and/or field observation	Galina and Kruger (2015)
1905 Bulnay	Bulnay Fault	-	9.5	8.9	8.3	375	8.3-8.5	L	Rizza et al. (2015)	Mapping and/or field observation	Schlupp and Cisternas (2007)
1906 Manas	South Junggar Thrust	-	9*	8*	7*	125	7.7	R	This study	From EES	This study from seismological reanalysis
1931 Fuyun	Fuyun Fault	-	7.5	6.3	5.1	160	7.9	L	Klinger et al. (2011)	Mapping and/or field observation	USGS
1957 Gobi-Altay	Bogd Fault	-	4.8	3.5	2.2	360	8.1	RL	Kurtz et al. (2018)	Mapping and/or field observation	USGS
1992 Suusamyr	Suusamyr Fault	4.2	-	-	-	7.6	7.2	RL	Ainscoe et al. (2019)	Mapping and/or field observation	USGS
DZF and LPF (RS1)	Dzhungarian and Lepsy Fault	-	19.9	14.1	8.2	375	8.1-8.4*	RL	This study	Mapping and/or field observation	This study / EES
DZF (RS2)	Dzhungarian Fault	-	19.9	14.4	8.8	248	7.9-8.2*	RL	This study	Mapping and/or field observation	This study / EES
North Tacheng Fault	North Tacheng Fault	-	6.1	4.3	2.4	50	7.0-7.4*	RL	This study	Mapping and/or field observation	This study / EES
East Tacheng Fault	East Tacheng Fault	-	6	3.65	1.3	67	6.4-7.6*	L	Yu et al. (2021)	Mapping and/or field observation	Yu et al. (2021) / EES
Zaisan NE Fault	Zaisan NE Fault	-	-	1*	-	85	7.4*	R	This study	From EES	This study / EES
Irtysh Fault	Irtysh Fault	-	1.5	0.75	0.25	200	6.0-7.0*	RL	Baize et al. (2019)	Observation from trenches	Baize et al. (2019) / EES

PD: Peak displacement; MD: Maximum displacement; AD: Average displacement; MND: Minimum displacement; SRL: Surface rupture length; EES: Empirical earthquake scaling relationship

†Excluded from MD plotting due to the uncertain corresponding rupture of the 1889 Chilik Earthquake

*Examples excluded from plotting since they are inferred from previously-reported earthquake scaling

Slip type: R = Reverse slip; RL = Reverse and lateral slip

Table 5-2. Other Earthquakes Included in Scaling Plotting

Event	Year	MD (m)	AD (m)	SRL (km)	Mw	References	Country	TS
Wairarapa	1855	18.3	16	145	8.1-8.2	(Rodgers & Little, 2006)	NZ	Interplate
Landers	1992	3	2.5	85	7.3	(Sieh et al., 1993; Freymueller et al., 1994)	USA	Interplate
Chi-Chi	1999	-	2	100	7.6	(Ma & Mori, 2000)	Taiwan	Interplate
Sumatra	2004	11	10.5	1200	9	(Catherine et al., 2005)	IND	Interplate
Chile	2010	-	6.8	650	8.8	(Pollitz et al., 2011)	Chile	Interplate
Darfield	2010	5.8	2.5	29.5	7.1	(Quigley et al., 2012)	NZ	Interplate
Tohoku	2011	25	9.5	550	9	(Satake et al., 2013)	Japan	Interplate
New Madrid (Reelfoot Thrust)	1812	2	-	61	7.25	(Clark et al., 2020)	USA	SCR
Kutch	1819	8	-	90	7.75	(Clark et al., 2020)	India	SCR
Meckering	1968	3.7	1.67	39	6.6	(H. Yang et al., 2021)	AUS	SCR
Calingiri	1970	1.3	0.31	4	5	(H. Yang et al., 2021)	AUS	SCR
Cadoux	1979	1.8	0.47	23	6.1	(H. Yang et al., 2021)	AUS	SCR
Marryat Creek	1986	1.1	0.31	14	5.7	(H. Yang et al., 2021)	AUS	SCR
Kunayungku	1988	1.4	0.58	9.2	6.3	(H. Yang et al., 2021)	AUS	SCR
Lake Surprise west	1988	2.3	1.08	8.3	6.4	(H. Yang et al., 2021)	AUS	SCR
Lake Surprise east	1988	3.6	1.15	17.2	6.6	(H. Yang et al., 2021)	AUS	SCR
Ungava	1989	0.8	-	8.5	6.3	(Clark et al., 2020)	CAN	SCR
Killari	1993	0.5	-	3	6.1	(Clark et al., 2020)	India	SCR
Katanning	2007	0.3	0.17	2.5	4.7	(H. Yang et al., 2021)	AUS	SCR
Pukatja	2012	1	0.26	1.6	5.2	(H. Yang et al., 2021)	AUS	SCR
Petermann	2016	1.9	0.35	22	6.1	(H. Yang et al., 2021)	AUS	SCR
Lake Muir	2018	0.75	0.28	7.1	5.3	(H. Yang et al., 2021)	AUS	SCR
Montelimar	2019	0.08	-	1	4.9	(Clark et al., 2020)	France	SCR
Silakhar	1909	2.5	-	45	7.23	(Lettis et al., 1997)	Iran	TCR
Raver	1911	0.5	-	15	6.29	(Lettis et al., 1997)	Iran	TCR
Haiyuan	1920	6	4	237	7.9	(Ou et al., 2020)	China	TCR
Baghan	1929	2.1	-	60	7.51	(Lettis et al., 1997)	Iran	TCR
Salmas	1930	6.4	-	30	7.6	(Lettis et al., 1997)	Iran	TCR
Changma	1932	4.6	-	15	7.8	(Lettis et al., 1997)	China	TCR
Behabad	1933	1	-	5	6.29	(Lettis et al., 1997)	Iran	TCR
Dari	1947	5	-	150	7.89	(Lettis et al., 1997)	China	TCR

Turad	1953	1.4	-	1	6.67	(Lettis et al., 1997)	Iran	TCR
Farsinaj-Sahjneh	1957	1	-	20	6.91	(Lettis et al., 1997)	Iran	TCR
Ipak	1962	0.8	-	99	7.42	(Lettis et al., 1997)	Iran	TCR
Qir	1972	0.1	-	20	6.8	(Lettis et al., 1997)	Iran	TCR
Songpan	1976	-	-	60	6.9	(Lettis et al., 1997)	China	TCR
Tangshan	1976	2.5	-	47	7.5	(Hui Guo et al., 2011)	China	TCR
Khurgu	1977	-	-	30	6.7	(Lettis et al., 1997)	Iran	TCR
Naghan	1977	-	-	80	6	(Lettis et al., 1997)	Iran	TCR
Mangya	1977	0.3	-	21	6.1	(Lettis et al., 1997)	China	TCR
Tabas	1978	3	-	85	7.4	(Lettis et al., 1997)	Iran	TCR
Golbaf Gowk	1981	0.11	-	15	6.6	(Lettis et al., 1997)	Iran	TCR
Sirch	1981	0.5	-	65	7.1	(Lettis et al., 1997)	Iran	TCR
Armenia	1988	2	-	25	6.8	(Lettis et al., 1997)	Armenia	TCR
Rudbar-Tarom	1990	1	-	80	7.4	(Lettis et al., 1997)	Iran	TCR
Kokoxili	2001	8	5.5	450	7.8	(Klinger et al., 2005)	China	TCR
Wenchuan	2008	6	2	304	7.9	(Liu-Zeng et al., 2009; Tong et al., 2010)	China	TCR
Balochistan	2013	10	6	200	7.7	(Avouac et al., 2014)	PKS	TCR
Madou	2021	2.1	-	158	7.3	(Liu-Zeng et al., 2022)	China	TCR

TS: Tectonic settings; SCR: Stable continental region; TCR: Tectonically active continental region; NZ: New Zealand; IND: Indonesia; AUS: Australia; CAN: Canada; PKS: Pakistan

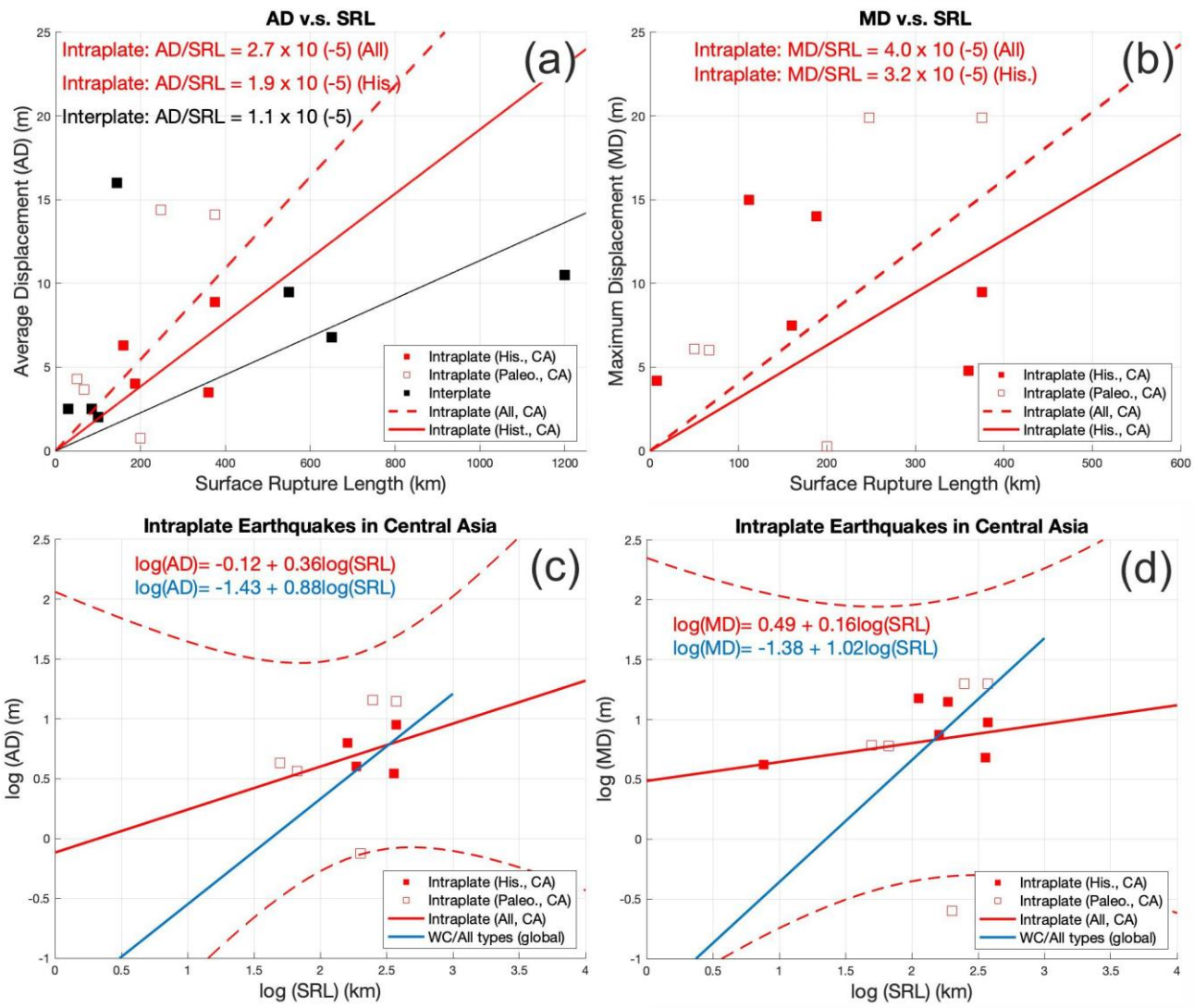

Figure 5-16. (a) Regression of average displacement (AD) on surface rupture length (SRL) for intraplate (red) earthquakes in Central Asia (CA) and interplate (black) earthquakes compiled in this study. (b) Regression of maximum displacement (MD) on SRL for intraplate earthquakes in CA compiled in this study. (c) and (d) Regressions of AD/MD on SRL in $\log_{10}$ scale for intraplate earthquakes in CA compiled in this study and the empirical earthquake scaling (blue) estimated from all types of faults globally by Wells and Coppersmith (1994) (WC). Red dashed lines in (c) and (d) indicate 95% confidence intervals of the regression of intraplate data. Hist.: Historical earthquakes; Paleo.: Paleo-earthquakes. (MD is replaced by peak displacement (PD) for plotting for those having PD reported in Table 5-1.)

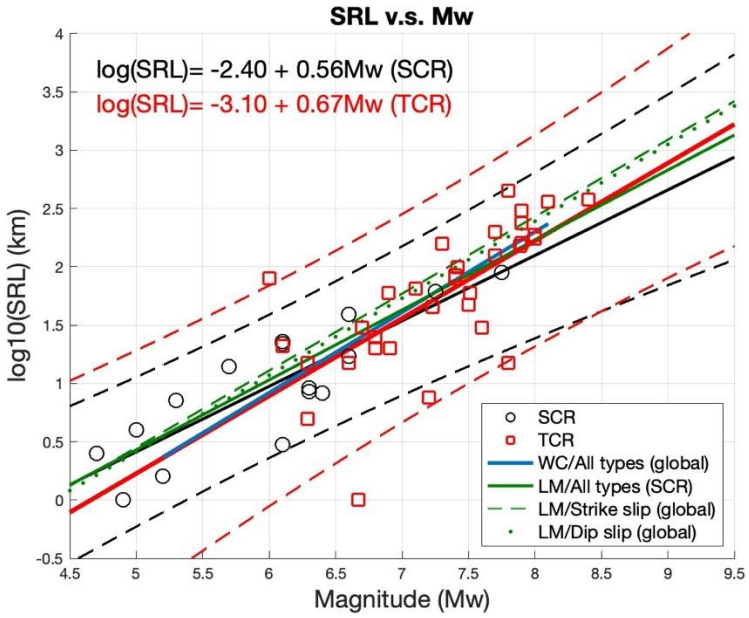

Figure 5-17. (a) Regression of SRL in $\log_{10}$ scale on magnitude (Mw) for SCR (black) and TCR (red) earthquakes with global earthquakes of all/various fault types. WC: Wells and Coppersmith (1994); LM: Leonard (2010). Black-dashed and Red-dashed lines indicate 95% confidence intervals of the regressions of SCR and TCR earthquakes, respectively.

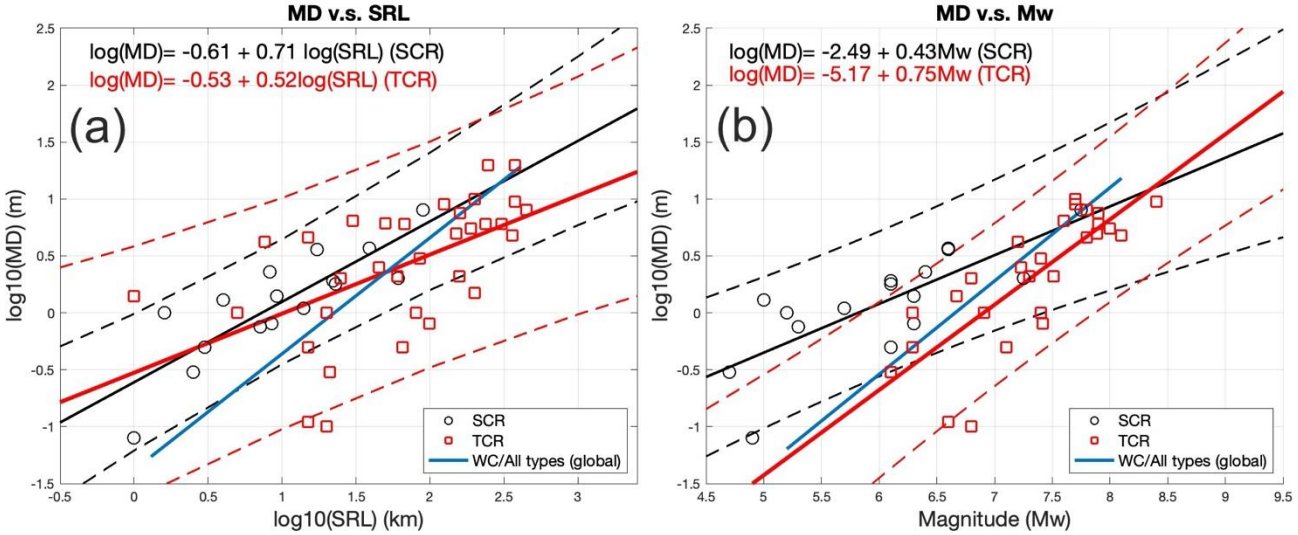

Figure 5-18. (a) Regression of MD in $\log_{10}$ scale on SRL $\log_{10}$ scale and (b) regression of MD in $\log_{10}$ scale on magnitude (Mw) for SCR (black) and TCR (red) earthquakes with global earthquakes of all fault types (blue) compiled by Wells and Coppersmith (1994). (MD is replaced by peak displacement (PD) for plotting for those having PD reported in Table 5-1.)

5.4 Seismic Depths

The palaeo-earthquakes investigated in this study and the historical events demonstrate that large earthquakes with magnitudes approaching Mw 8.0 could occur around the Dzhungarian Basin, especially for the DZF which we suggest is capable of producing large displacements (> 15 m) and multi-fault rupture. From the earthquake scaling relationships, we also find that the TCR earthquakes, including those in Central Asia, seem to have larger rupture areas but not necessarily larger SRL than other earthquakes of comparable Mw, especially in a range of ~ Mw 6 – 8. This infers that the large rupture areas of large TCR earthquakes might result from increased seismic depths.

The seismic depths from instrumental records reach over 30 km near Lake Zaisan and within the Borohoro Shan for earthquakes with Mw > 6, according to the better-constrained instrumental earthquake depths from Sloan et al. (2011) and Wimpenny & Watson (2020) (Figure 5-19). We also examine the seismicity around the Dzhungarian Basin from the ISC-EHB catalogue which has teleseismically well-constrained events and minimal errors in the estimated seismic depths. Figure 5-19 demonstrates the L1 events (< 5 km standard error of depths) and the L2 events (5-15 km standard error of depths) from the ISC-EHB catalogue. We can see the > 30 km-deep earthquakes distributed mostly near the range front or near the boundary between the mountainous ranges and the flat basin/platform areas. This is consistent with the observation mentioned by Sloan et al. (2011) who further suggest that the lower crust under the rigid forelands in compressional Central Asian areas is anhydrous and, thus, strong and seismogenic. Although there is little deep seismicity along the DZF from the instrumental records, the lower crust under the DZF might also have the same anhydrous property since it is located at the range front of the Dzhungarian Alatau.

There is one event in 2009 (Mw 4.5) in the south of the LPF in the northern Dzhungarian Alatau with a depth of ~ 31 km (Figure 5-19). Although it is an L2 event, it highlights the possibility for deep (> 30 km) earthquakes to occur near this region. From the InSAR-derived velocity profiles P3 and P4 in Chapter 3, we also find that the modelled seismic depths deepen towards the Borohoro Shan from the Bortala Basin (from ~ 5 km to > 12 km), despite the large uncertainty within the data, further supporting that the seismogenic layer under the boundary between mountains and basins does deepen. The widespread deep (> 20 km) seismicity within the Borohoro Shan again underlines the potential occurrence of earthquakes with large rupture area and, thus, large magnitudes in this region (Figure 5-19). The deep epicentres may explain the rarity of surface ruptures but widespread shaking-induced mass wasting in the Borohoro Shan.

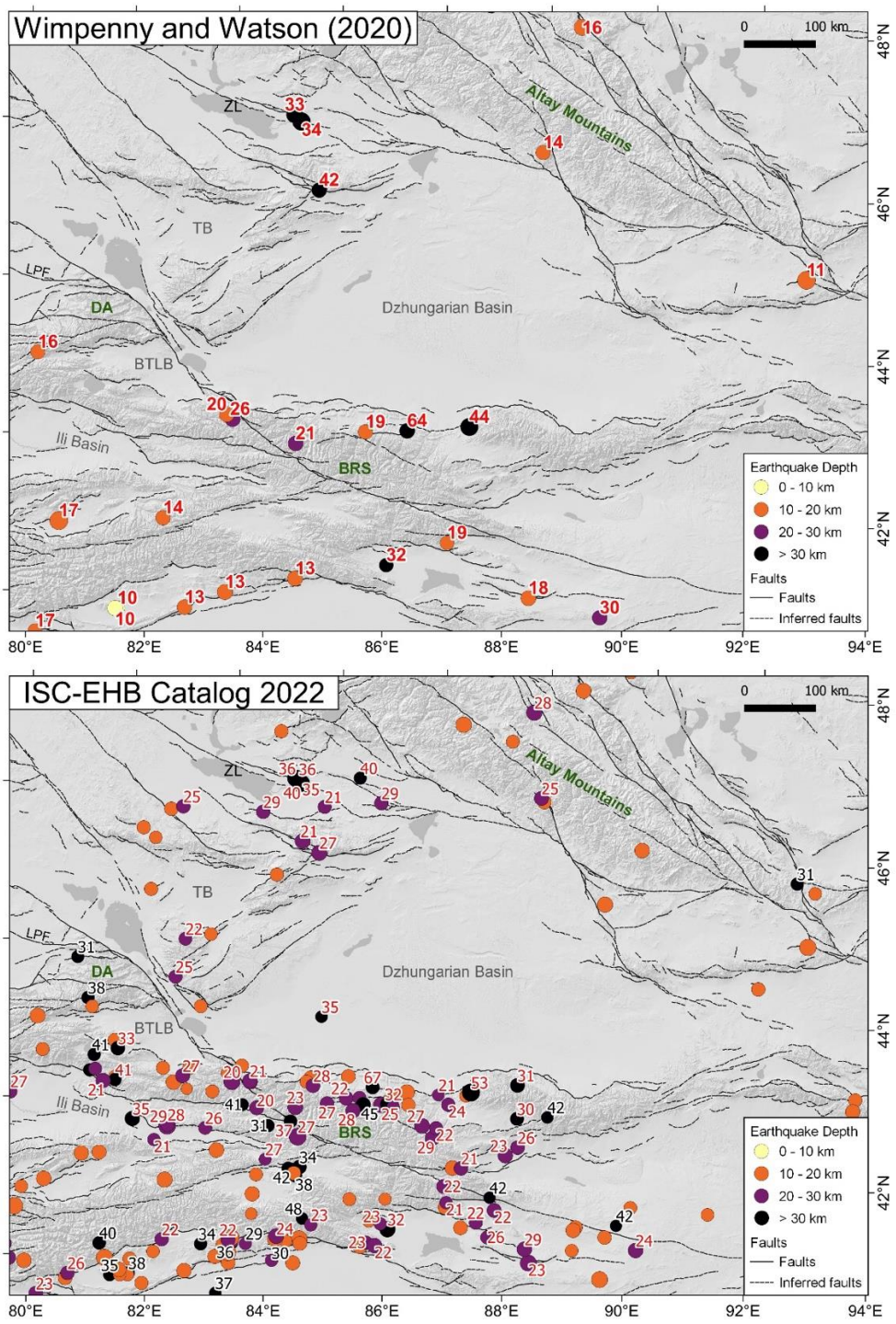

Figure 5-19. Seismic depths from instrumental records around the Dzhungarian Basin. Upper panel is the database from Wimpenny and Watson (2020) with the depths annotated in red near the events. Lower panel is the database from the ISC-EHB catalogue with L1 and L2 events' depths annotated in red and black, respectively. (Seismicity with depths of 0 – 10 km is not shown in the lower panel.) The fault database is from Zelenin et al. (2021) with confidence levels A and B (as defined in the database) delineated in solid black lines and levels C and D delineated in dashed black lines. ZL: Lake Zaisan; TB: Tacheng Basin; DA: Dzhungarian Alatau; BRS: Borohoro Shan; BTLB: Bortala Basin; LPF: Lepsy Fault.

5.5 Regional Kinematics

5.5.1 Slip Rates of Faults and Accommodation of Crustal Shortening

We compile the Quaternary slip rates of the faults around the Dzhungarian Basin determined in this thesis and previous studies in Figure 5-20. Charreau et al. (2017) have estimated a N-S shortening rate of ~ 1.4 mm/yr across the Nalati Fault (NLTF). Wu et al. (2020) have calculated a lateral slip rate of ~ 2.4 mm/yr and an across-fault shortening of ~ 0.6 mm/yr on the Kashihe Fault (KSHF). Using a fault strike of 280°, these will contribute an average N-S shortening rate of ~ 1.03 mm/yr across the KSHF. An average N-S shortening rate of ~ 2.9 mm/yr on the southern DZF has been proposed in Chapter 3 from the lateral slip rate of ~ 3.4 mm/yr. Yu et al. (2021) have estimated a N-S shortening rate of ~ 0.35 mm/yr on the East Tacheng Fault (ETF). The overall N-S shortening accommodated by these four faults is ~ 5.7 mm/yr on average. Considering that the western Dzhungarian Basin, at the longitude of 83°E, is currently accommodating ~ 6 – 7 mm/yr of N-S crustal shortening as measured by GNSS (Figure 5-21 and Figure 5-22A) (Zheng et al., 2017), the four faults mentioned above accommodate a significant portion of the total N-S shortening, assuming consistent geological and geodetic shortening rates. The remaining shortening should be accommodated by other reverse or strike-slip structures.

We notice that the across-fault N-S shortening rates inferred from the GNSS velocities have some discrepancies with the rates mentioned above, especially for the NLTF and the ETF whose GNSS shortening rates seem to be twice those determined from geology (Figure 5-22A). This indicates that other reverse faults in the southern Ili Basin may also contribute to the accommodation of N-S convergence. The strike-slip and reverse faults bounding the Kertau Mountain are likely contributing to the shortening (Figure 5-21), though at rates that are not identifiable from the InSAR analysis (see Chapter 3). Nevertheless, this discrepancy might merely be the discrepancy between the geodetic and geological slip rates. More detailed fault mapping and field investigations are needed to better understand the fault activities in the region.

Despite the discrepancy between geological and GNSS rates, the southern DZF has the highest N-S shortening rate among the other faults, which again indicates this fault is a primary structure with relatively fast movement. This further indicates that the strike-slip faults accommodate more N-S shortening than the reverse faults in the western Dzhungaria. Similar kinematics of deformation are observed in the eastern Dzhungaria where most of the N-S shortening seems to be accommodated by the right-lateral strike-slip Fuyun Fault (FYF). From the GNSS velocity, the east of the Dzhungarian Basin, at the longitude of 90.1°E,

accommodates ~ 2 – 3 mm/yr of N-S crustal shortening and there is a N-S velocity drop of ~ 1.5 – 2 mm/yr across the FYF (Figure 5-21 and Figure 5-22D). Xu et al. (2012) estimated a Late Quaternary lateral slip rate of 0.76 ± 0.24 mm/yr on the FYF, which is lower than a lateral slip rate of at least 1.5 mm/yr inferred from the GNSS velocity (Figure 5-22E,F). A ~ 9700 year of recurrence interval calculated from the rate of ~ 0.76 mm/yr in Xu et al. (2012) also contradicts with a shorter interval of ~ 5300 years recently inferred from the lacustrine records of the FYF (Fan et al., 2022). Thus, we note that the slip rate of the FYF might be higher than 0.76 ± 0.24 mm/yr but should lower than the rate of the DZF based on the GNSS velocity.

In the south of the Dzhungarian Basin, at the longitude of 85.4°E, the GNSS velocity shows ~ 5 – 6 mm/yr of N-S crustal shortening between the Tarim and Dzhungarian Basin across the Borohoro Shan (Figure 5-22B). A significant N-S GNSS velocity drop of ~ 2 – 4 mm/yr is observed across the Borohoro Shan range front, which fits with a shortening rate of 2 – 4 mm/yr calculated on the Tugulu-Manas-Huoerguos Anticline (Fu et al., 2017; Su et al., 2018). No obvious N-S GNSS velocity drop is observed across the strike-slip faults, such as the Baoertu Fault whose geological N-S shortening rate is < 1 mm/yr, in the SE Borohoro Shan (Figure 5-22B). Thus, in the southern Dzhungarian Basin, the fold and thrust belt at the range front of the Borohoro Shan is accommodating most of the N-S shortening by reverse faulting.

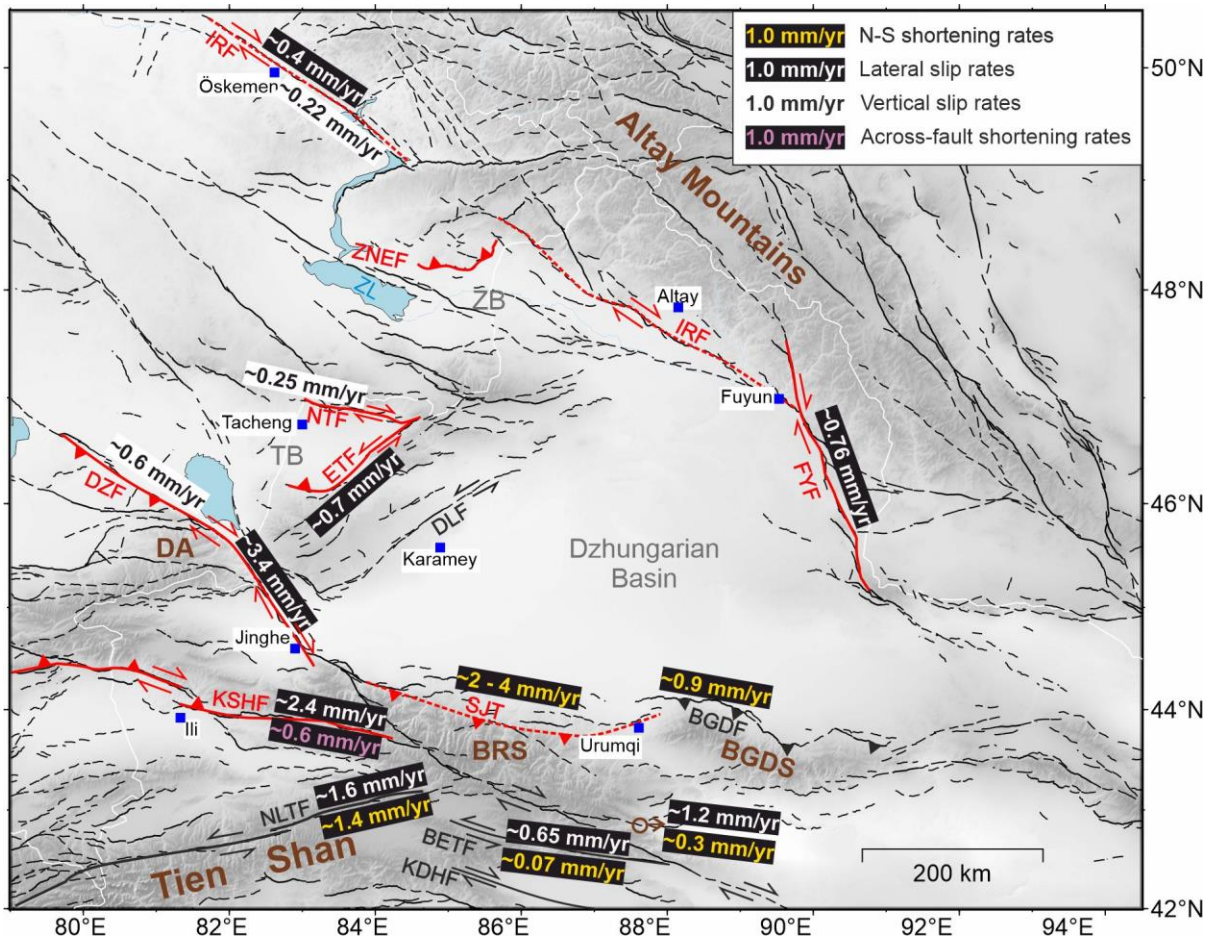

Figure 5-20. Slip rates of the faults around the Dzhungarian Basin. The fault database is from Zelenin et al. (2021) with confidence levels A and B (as defined in the database) delineated in solid black lines and levels C and D delineated in dashed black lines. Faults highlighted in red are mentioned in the previous sections and chapters with either prominent palaeo-earthquake ruptures or large historical events. Slip rates of the DZF are determined in this study. Slip rates of other faults are determined by Luo et al. (2015) for the North Tacheng Fault (NTF), Yu et al. (2021) for the East Tacheng Fault (ETF), Wu et al. (2020) for the Kashihe Fault (KSHF), Charreau et al. (2017) and Ren et al. (2021) for the Nalati Fault (NLTF), Fu et al. (2017) and Su et al. (2018) for the Borohoro Shan range front structure, Ren et al. (2021) for the Baoertu Fault (BETF) and the right-lateral fault in the NE of the BETF, Wu et al. (2016) for the Bogda Fault (BGDF), Xu et al. (2012) for the Fuyun Fault (FYF), Baize et al. (2019) for the Irtysh Fault (IRF). City and towns are labelled with blue squares. ZNEF: Zaisan NE Fault; KDHF: Kaiduhe Fault; TB: Tacheng Basin; ZB: Zaisan Basin; DA: Dzhungarian Alatau; BRS: Borohoro Shan; BGDS: Bogda Shan; ZL: Lake Zaisan.

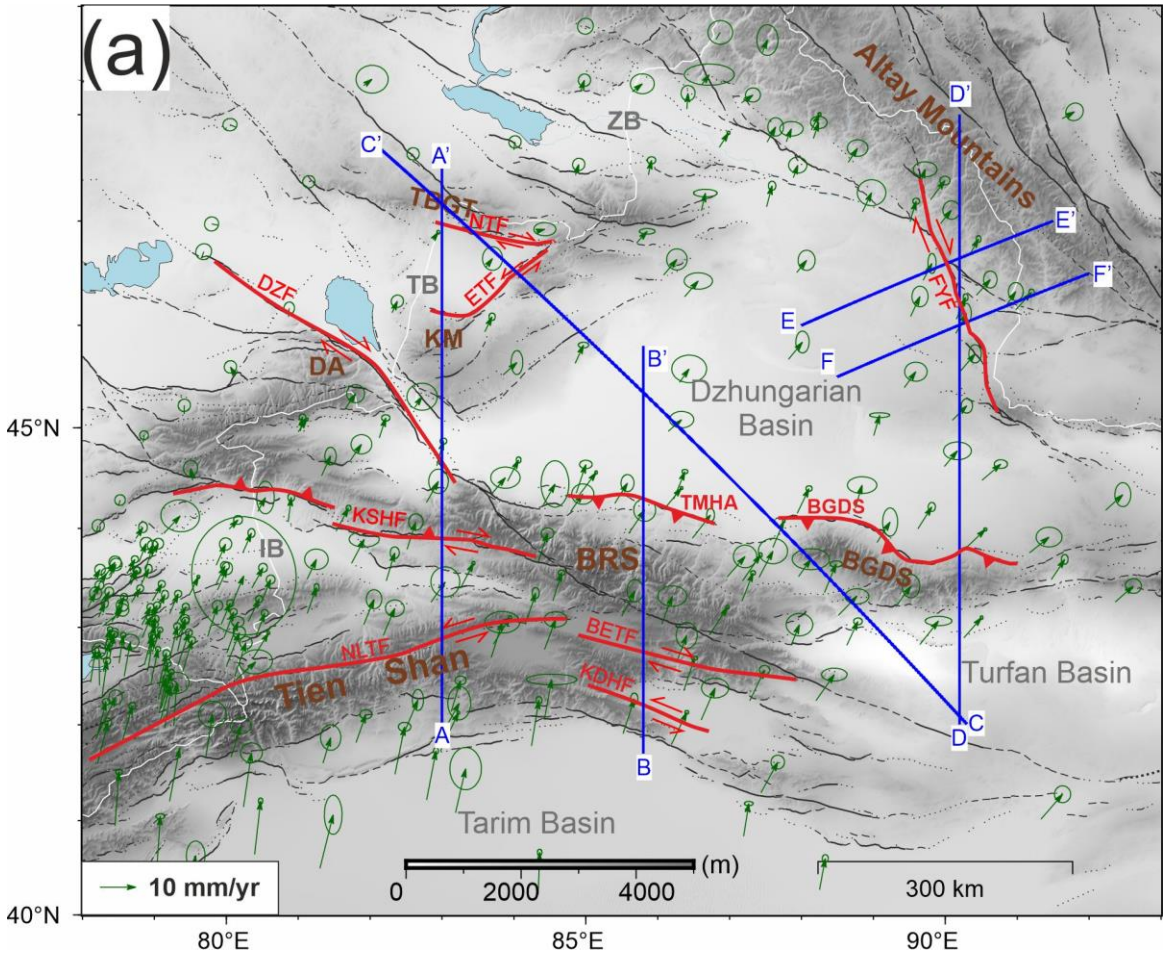

Figure 5-21. GNSS velocity from Zheng et al. (2017) around the Dzhungarian Basin. Blue lines are the GNSS velocity profiles A, B, C, D, E, F (in blue) shown in Figure 5-22. The fault database is from Zelenin et al. (2021) with confidence levels A and B (as defined in the database) delineated in solid black lines and levels C and D delineated in dashed black lines. Faults in red are hightlighted in Figure 5-22. IB: Ili basin; TB: Tacheng Basin; ZB: Zaisan Basin; DA: Dzhungarian Alatau; KM: Kertau Mountains; BRS: Borohoro Shan; BGDS: Bogda Shan; TMHA: Tugulu-Manas-Huoerguos Anticline. (Other abbreviations of faults can be referred to Figure 5-20.)

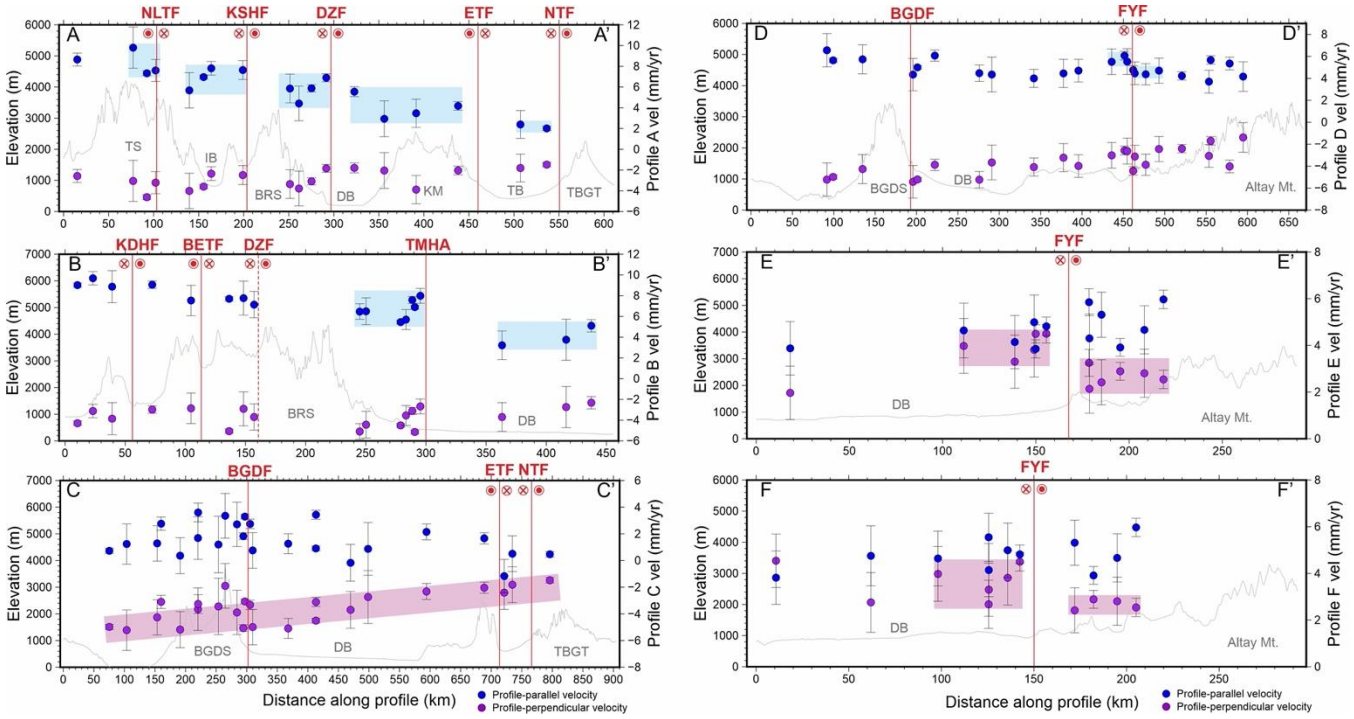

Figure 5-22. GNSS velocity profiles A – F with locations shown in Figure 5-21. Elevation data are from GEBCO (https://www.gebco.net/data_and_products/gridded_bathymetry_data/) and are plotted in grey. Fault locations are plotted in red. Blue dots show the components parallel to the profiles, and purple dots show the components perpendicular to the profiles. Blue and purple squares are the visually fitted range of the GNSS velocities. Positive numbers show the velocity vectors towards the north and the west. Abbreviations of faults are as in Figure 5-20.

5.5.2 The Kinematic Model of the Dzhungarian Basin

After analysing the results and interpretations of this study and previous research, we have developed a simplified kinematic model of the Dzhungarian Basin and explored how different observations can be incorporated into it. The region from the southwestern end of the Tien Shan to the Altay Mountains is accommodating both N-S convergence and left-lateral shearing, which are mainly caused by the northwards movement of the India Plate combined with the clockwise rotation of the Tarim Basin (Zubovich et al., 2010; Zheng et al., 2017; M. Wang & Shen, 2020). We refer to this region as the "TS-AM Zone" in this thesis. The TS-AM Zone is confined between the stable Kazakh Platform in the northwest and the Tarim Basin, a rigid block with little internal deformation, in the southeast. It is worth noting that the TS-AM Zone widens towards the northeast and has several large ~ NW-SE trending right-lateral strike-slip faults cutting through it. Within the TS-AM Zone, the Dzhungarian Basin is a large, triangular-shaped, rigid tectonic block whose basement strength has increased overtime since the Palaeozoic (Allen & Vincent, 1997). In the southwest of the Dzhungarian Basin, there are two smaller

triangular basins which are the Bortala Basin and the Ili Basin. These two smaller basins also behave more or less like rigid blocks with shortening localised at their northern and southern margins. However, internal block rotation is thought to occur within the Ili Basin (Grützner et al., 2019), suggesting that it might be starting to deform internally. Counter-clockwise block rotation has been proposed for the tectonic blocks and units bounded by the right-lateral strike-slip faults in the TS-AM Zone (Rizza et al., 2019; C. Wu et al., 2021). The DZF, bordering the Bortala and Dzhungarian Basins, is thought to accommodate N-S shortening and left-lateral shearing via a counter-clockwise rotation with a rate of ~ 0.45°/Myr (Campbell et al., 2013). Similar kinematics is also proposed for the KSHF which bounds the Bortala and Ili Basins (C. Wu et al., 2020). At the NE end of the TS-AM Zone, the Mongolian Altay is bounded by the FYF in the west and the Har-Us-Nuur Fault (HUNF) in the east and is thought to rotate anticlockwise due to the left-lateral shearing as well (Bayasgalan et al., 2005).

We propose that the TS-AM Zone consists of both rigid and non-rigid zones based on observed fault types, regional topography, and previous rotation models and tectonic units. Figure 5-23 illustrates the deformation kinematics within the TS-AM Zone. The Dzhungarian Basin and the Bortala Basin are considered rigid blocks, whilst the Ili Basin is considered a failing rigid block with potential for internal deformation. The Altay Mountains and the Tien Shan are considered tectonic units consisting of non-rigid materials at a macro level, as there are several smaller and rigid-like intramontane basins within the Tien Shan such as the Issyk-Kul Basin (De Grave et al., 2013). These rigid blocks and tectonic units are rotating counter-clockwise due to the overall left-lateral shearing strain in the TS-AM Zone (Figure 5-23b). The right-lateral DZF in the SW and the FYF in the NE of the Dzhungarian Basin favour the anticlockwise rotation of a triangular rigid block in between. The right-lateral KSHF in the SW and the DZF in the NE of the Bortala Basin also indicate the same rotating kinematics.

The triangular shape of the Dzhungarian and Bortala basins, which are rotating anticlockwise and experiencing N-S shortening strain, suggests that the TS-AM Zone is narrowing and experiencing compression at the NW and southern edges of the basins (Figure 5-23b). The narrowing rate should decrease towards the NE as indicated from the decreasing GNSS N-S shortening rates (Figure 5-21 and Figure 5-22A,D), which may contribute to the NE-widening shape of the TS-AM Zone. Wedge-shaped mountains, as observed in the Dzhungarian Alatau, should be present at the NW edges of the two basins due to compression (Figure 5-23b), but this is not the case in the NW Dzhungarian Basin. We suggest that the topographic development in the NW Dzhungarian Basin may have been influenced by the kinematics of the Tacheng and Zaisan Basins, although more data, such as surrounding fault activities and geodetic

information, is needed to confirm this hypothesis. Nevertheless, the reverse ZNEF, which experiences a ~ 90° change in strike and indicates a slip vector towards the SE, supports the compression suggested at the NW corner of the Dzhungarian Basin. In this kinematic model, the southern basin margins, which trend ~ NEE-SWW or E-W, will be dominated by compression and shortening instead of lateral shearing (Figure 5-23b). This aligns with the prominent reverse faulting in the Borohoro Shan and in the south of the Bortala and Ili Basins. As a result of N-S shortening, the non-rigid regions in the TS-AM Zone, such as the Tien Shan and Altay Mountains, experience compression and uplift, leading to their high-relief topography and intense internal deformation compared to the rigid blocks.

The proposed kinematic model presented in Figure 5-23 is consistent with the observed fault kinematics around the Dzhungarian Basin. The N-S crustal shortening is accommodated mainly by the strike-slip faulting in the western and eastern parts of the basin but by reverse faulting in the south. As expected from the greater N-S convergence rate towards the southwest, the slip rate of the DZF should be higher than the rate of the FYF, which is in line with the observation (see Section 5.5.1). Transpressional counterclockwise rotation of the Dzhungarian Basin is thought to have occurred during the Mesozoic as well (Y. Yu et al., 2016). It is likely that the major inherited strike-slip faults (e.g. the DZF, the FYF and the KSHF) continue to play a significant role in accommodating crustal strain in the Cenozoic as pre-existing weak zones and boundaries of tectonic units within the TS-AM Zone. GNSS velocity data indicates a left-lateral shearing rate of ~3-4 mm/yr across the Dzhungarian Basin (Figure 5-22C), which is expected to be primarily accommodated by rotation.

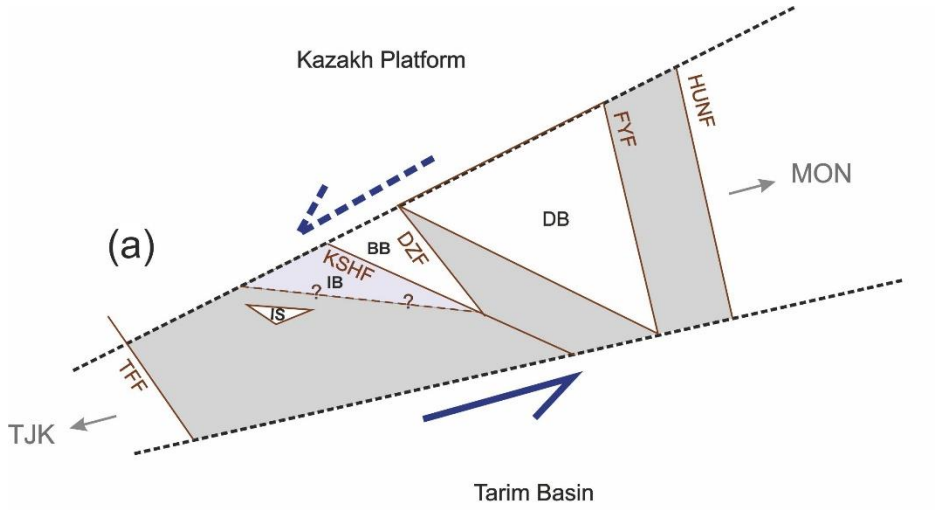
Kazakh Platform
HUNF
FYF
MON
(a)
DB
DZF
BB
KSHF
IB
IS
TFF
TJK
Tarim Basin

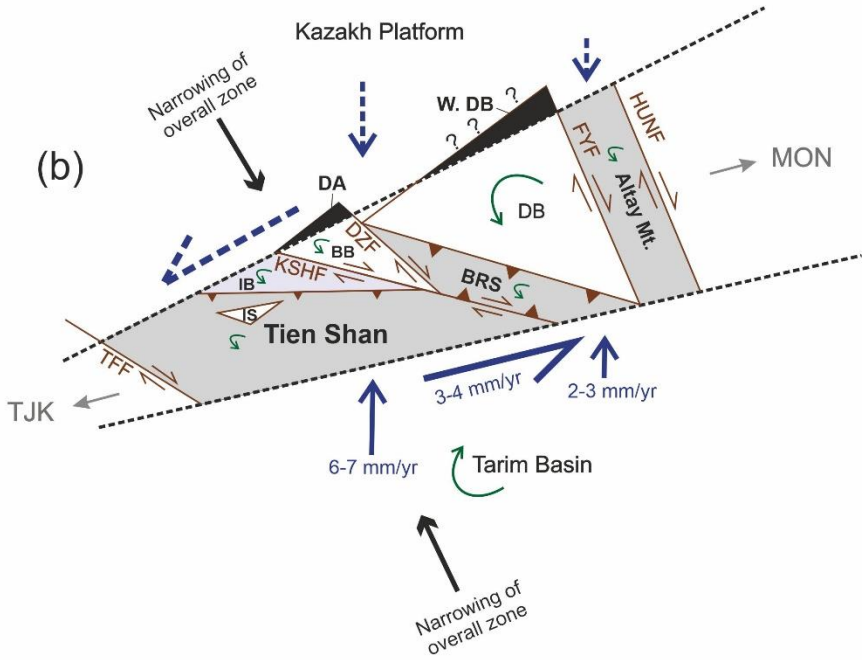
Kazakh Platform
Narrowing of overall zone
W. DB
HUNF
FYF
MON
(b)
DA
DB
Altay Mt.
DZF
BB
KSHF
IB
BRS
IS
Tien Shan
TFF
TJK
3-4 mm/yr
2-3 mm/yr
6-7 mm/yr
Tarim Basin
Narrowing of overall zone

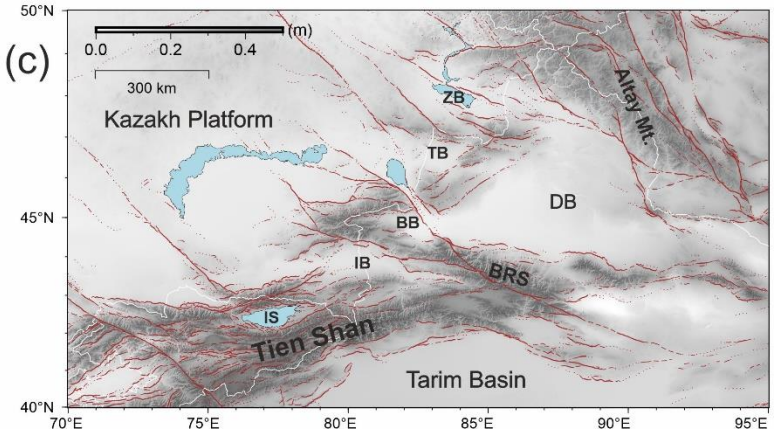
50°N
(m)
0.0
0.2
0.4
300 km
(c)
Kazakh Platform
ZB
Altay Mt.
TB
DB
45°N
BB
IB
BRS
IS
Tien Shan
Tarim Basin
40°N
70°E
75°E
80°E
85°E
90°E
95°E

Figure 5-23. (a) and (b) Schematic kinematics of the TS-AM Zone. The Dzhungarian Basin (DB), the Bortala Basin (BB), and the Issyk-Kul Basin (IS) are considered as rigid blocks (white triangles). Black area represents the compressive regions at the NW sides of the rigid blocks. DA: Dzhungarian Alatau; W. DB: Western DB. The Ili Basin (IB) (in pink) is considered as a failing rigid block which might have internal deformation. The Tien Shan, Borohoro Shan (BRS), and the Altay Mountains are considered as non-rigid tectonic units (in grey). Brown lines in (a) and (b) show the major faults or fault zones with their sense of movement. TFF: Talas-Ferghana Fault; KSHF: Kashihe Fault; DZF: Dzhungarian Fault; FYF: Fuyun Fault; HUNF: Har-Us-Nuur Fault. Dark blue lines indicate the direction of N-S shortening and left-lateral shearing with the rates annotated. Black arrows indicate the overall zone narrowing. Note that the black dashed lines do not represent any specific left-lateral faults, but rather demonstrate the regional left-lateral shearing. Green arrows indicate the rotation of each tectonic unit. Grey arrows show the corresponding geographical locations. TJK: Tajikistan; MON: Mongolia. (c) The reference map of the schetch with brown lines showing the fault database from Zelenin et al. (2021) with confidence levels A and B (as defined in the database) delineated in solid lines and levels C and D delineated in dotted lines. TB: Tacheng Basin; ZB: Zaisan Basin

5.6 Conclusions

We report on the lateral and vertical displacements of surface ruptures of ~ 50 km in length on the NTF, which indicate the occurrence of a palaeo-earthquake with a magnitude at least Mw 7.0. Furthermore, we have identified surface ruptures of ~ 85 km in length on the ZNEF, suggesting that an earthquake with a magnitude of Mw 7.4 may have occurred at the northwest corner of the Dzhungarian Basin. Our analysis of earthquake scaling relationships, derived from global plate-boundary and intra-continental earthquakes, indicates that the scaling relationships between surface rupture length (SRL) and magnitude (Mw) are similar across various tectonic settings. However, the empirical relationships between maximum displacement (MD) and magnitude may differ among different tectonic settings. Moreover, our findings reveal that different earthquake scaling relationships exist in intra-continental fault settings between stable continental region (SCR) and tectonically active continental region (TCR). This suggests that intraplate faults behave differently under different intra-continental settings. Our study of regional kinematics reveals that N-S convergence is mainly accommodated by strike-slip faulting in the west and east of the Dzhungarian Basin, whilst reverse faulting dominates along the southern edge of the basin. The pattern of faulting and topography indicate a counterclockwise rotation of the triangular Dzhungarian Basin and its surrounding tectonic units, in a zone under compression and left-lateral shearing that extends from the southwestern Tien Shan to the Altay Mountains.

Chapter 6

Concluding Remarks

6.1 Conclusions from the Whole Thesis

This thesis aims to expand our knowledge and understanding of the intra-continental earthquakes from investigating the palaeo-earthquake ruptures and historical seismicity in the northern Tien Shan and Dzhungaria.

In Chapters 2 and 3, my focus was on earthquake occurrences and slip rates along the boundary strike-slip fault in northern Tien Shan. I examined the ~ 400 km long palaeo-earthquake ruptures on the Dzhungarian Fault, a significant intra-continental fault bounding the Dzhungarian Alatau with the Lepsy Fault. The analysis indicates that the total fault slip of the most recent event along the Dzhungarian Fault could be up to ~20 m at one site on its northern oblique-slip sections and 6–9 m on its southern pure strike-slip section. I further interpreted a likely combined rupture of the Dzhungarian and Lepsy Faults with a magnitude that could reach up to Mw 8.4, placed among the largest known intra-continental earthquakes. Using Quaternary dating techniques and InSAR time-series analysis, I determined geological and geodetic slip rates of the Dzhungarian Fault. Displacements of the terraces and their abandonment ages determined from luminescence dating indicate the vertical slip rate on the northern Dzhungarian Fault is 0.6 ± 0.2 mm/yr over the last ~ 5–60 ka. On the southern Dzhungarian Fault, the geological strike-slip rate determined from ^{10}Be exposure ages is consistent with the geodetic strike-slip rate derived from the InSAR time-series analysis, which is in a range of 2.1–4.7 mm/yr since ~ 100 ka. Combining the average single-event fault slip suggested in this study, I estimated a recurrence interval of ~ 12000 years on the northern Dzhungarian Fault and 1300–4300 years on the southern Dzhungarian Fault. The observed

decrease in slip rates towards the NW of the fault indicates that the Dzhungarian Fault terminates towards its northwest. This further suggests that other faults, such as the Lepsy Fault, might accommodate more N-S shortening in the NW corner of the Tien Shan.

In Chapter 4, I re-investigated the 1812 Nilke, 1906 Manas and 1944 Xinyuan Earthquakes in the Borohoro Shan by integrating published data, seismological analysis, and remote sensing imagery. I presented the re-located hypocentres and the re-estimated seismic magnitudes of the 1906 Earthquake (Mw 7.7 ± 0.2) and the 1944 Xinyuan Earthquake (double-event, Mw 6.5 ± 0.3 and Mw 7.2 ± 0.2). The seismological analysis results, along with the type and distribution of coseismic surface ruptures, suggest the 1906 earthquake occurred on a reverse fault plane, whereas the 1812 and the 1944 earthquakes likely had prominent oblique right-lateral components on the fault plane. These three historical earthquakes highlight the important role in which both reverse and strike-slip faulting play in the seismotectonic in the region, which further reflects the deformation kinematics of the Borohoro Shan as located at a transpressional zone.

Chapter 5 of this study begins by presenting notable palaeo- and historical earthquake ruptures around the Dzhungarian Basin. I then collated fault parameters, such as displacements, magnitudes, and surface rupture lengths, of intra-continental earthquakes in Central Asia and other regions worldwide. Using this dataset, I updated earthquake scaling relationships for intraplate faults and emphasised the differences between stable continental regions (SCR) and tectonically active continental regions (TCR). The findings suggest that TCR earthquakes tend to have larger rupture areas, which I suggest being related to the increased seismic depth, particularly in the range front areas in the Dzhungarian region. Lastly, I concluded that most of the observations and results support a kinematic model in which the Dzhungarian Basin and surrounding tectonic units rotate counterclockwise within a large-scale zone of N-S shortening and left-lateral shearing from the southwestern Tien Shan to the Altay Mountains.

6.2 Suggestions for Future Work

The findings of this thesis suggest the need for several lines of research to be pursued. Firstly, I have demonstrated the utility of remote-sensing high-resolution satellite imagery in identifying and analysing surface ruptures of palaeo- and historical earthquakes. To gain a more comprehensive understanding of fault patterns and distributions, wider coverage of such imagery can be utilised to efficiently investigate additional surface ruptures, such as those in the Dzhungarian Alatau and the western Dzhungarian Basin. However, this thesis also highlights the need for more *in situ* field investigations in

the region. Determining the timing of the most recent earthquake along the Dzhungarian Fault, for instance, requires further trenching, sampling, and dating to obtain better age constraints on the ruptures. Field survey is also necessary to examine the fault scarps and geometry of the Zaisan NE Fault and to reveal the fault patterns and landslide formation in the southern Borohoro Shan and Ili Basin, complementing the findings from remote sensing data.

This study has demonstrated the challenges inherent from the unwrapping process of interferograms in the Dzhungarian region, which limits the availability of interferograms and the completeness of InSAR network for time-series analysis. The use of a much longer record of satellite acquisitions in the future may facilitate the retention of more available interferograms for time-series processing. Additionally, the development of SAR-bearing satellites traveling more parallel to the equator, rather than from north to south, such as NISAR, may improve estimates of interseismic strain across the Dzhungarian Fault and other structures in the region due to their fault strikes and the dominant N-S shortening. The incorporation of additional geodetic data sources with longer time scales, such as SAR and GNSS measurements, will also enhance the understanding of regional deformation kinematics, particularly in the northwest part of the Dzhungarian Basin.

There is still a need for further research to advance our understanding of intra-continental earthquakes. Whilst this thesis focused on faults around the Dzhungarian Basin, there is still much to be learned about the behaviours of other intra-continental faults, particularly those in regions with even slower deformation rates, such as the Kazakh Platform. This thesis has improved our knowledge of intra-continental earthquake scaling, but the sample size of the compiled earthquake examples is still limited due to the infrequent occurrence of these types of earthquakes. Given the potential seismic hazards associated with intra-continental faults and the rapid urban developments in the regions, it is imperative to continue studying these faults using both innovative and well-developed techniques.

Bibliography

Abdrakhmatov, K. E., Aldazhanov, S. A., Hager, B. H., Hamburger, M. W., Herring, T. A., Kalabaev, K. B., Makarov, V. I., Molnar, P., Panasyuk, S. V., Prilepin, M. T., Reilinger, R. E., Sadybakasov, I. S., Souter, B. J., Trapeznikov, Y. A., Tsurkov, V. Y., & Zubovich, A. V. (1996). Relatively recent construction of the Tien Shan inferred from GPS measurements of present-day crustal deformation rates. *Nature*, *384*(6608), 450–453. https://doi.org/10.1038/384450a0

Abdrakhmatov, K. E., Djanuzakov, K. D., & Delvaux, D. (2002). Active Tectonics and Seismic Hazard of the Issyk-Kul Basin in the Kyrgyz Tian-Shan. In J. Klerkx & B. Imanackunov (Eds.), *Lake Issyk-Kul: Its Natural Environment* (pp. 147–160). Springer Netherlands. https://doi.org/10.1007/978-94-010-0491-6_11

Abdrakhmatov, K. E., Walker, R. T., Campbell, G. E., Carr, A. S., Elliott, A. J., Hilleman, C., Hollingsworth, J., Landgraf, A., Mackenzie, D., Mukambayev, A., Rizza, M. A., & Sloan, R. A. (2016). Multisegment rupture in the 11 July 1889 Chilik earthquake (Mw 8.0-8.3), Kazakh Tien Shan, interpreted from remote sensing, field survey, and paleoseismic trenching. *Journal of Geophysical Research: Solid Earth*, *1*, 1–17. https://doi.org/10.1002/2013JB010776.Received

Abdrakhmatov, K. E., Weldon, R. J., Thompson, S. C., Burbank, D. W., Ch, R., Miller, M., & Molnar, P. (2001). Origin, direction, and rate of modern compression of the central Tien Shan (Kyrgyzstan). *Russian Geology and Geophysics*, *42*(10), 1585–1609.

Abe, K. (1981). Magnitudes of large shallow earthquakes from 1904 to 1980. *Physics of the Earth and Planetary Interiors*, *27*(1), 72–92. https://doi.org/10.1016/0031-9201(81)90088-1

Abe, K. (1988). Magnitudes and origin times from Milne seismograph data: earthquakes in China and California, 1898-1912. *Symposium on Historical Seismograms and Earthquakes*, 37–50.

Abe, K., & Noguchi, S. (1983). Revision of magnitudes of large shallow earthquakes, 1897-1912. *Physics of the Earth and Planetary Interiors*, *33*(1), 1–11. https://doi.org/10.1016/0031-9201(83)90002-X

Adamiec, G., & Aitken, M. (1998). Dose rate conversion factors. In *Health Physics* (Vol. 16, Issue 2, pp. 37–50).

Ainscoe, E. A., Abdrakhmatov, K. E., Baikulov, S., Carr, A. S., Elliott, A. J., Grützner, C., & Walker, R. T. (2019). Variability in surface rupture between successive earthquakes on the Suusamyr Fault, Kyrgyz Tien Shan: Implications for palaeoseismology. *Geophysical Journal International*, *216*(1), 703–725. https://doi.org/10.1093/gji/ggy457

Aki, K. (1966). Generation and Propagation of G Waves from the Niigata Earthquake of June 16, 1964. : Part 2. Estimation of earthquake moment, released energy, and stress-strain drop from the G wave spectrum. In *Bulletin of the Earthquake Research Institute, University of Tokyo* (Vol. 44, Issue 1, pp. 73–88). The Earthquake Research Institute, University of Tokyo. https://ci.nii.ac.jp/naid/120000871042/en/

Alinaghi, A., & Krüger, F. (2014). Seismic array analysis and redetermination of depths of earthquakes in Tien-Shan: implications for strength of the crust and lithosphere. *Geophysical Journal International*, *198*(2), 1111–1129. https://doi.org/10.1093/gji/ggu141

Allen, M. B., & Vincent, S. J. (1997). Fault reactivation in the Junggar region, northwest China: the role of basement structures during Mesozoic-Cenozoic compression. *Journal of the Geological Society*, *154*(1), 151–155. https://doi.org/10.1144/gsjgs.154.1.0151

Allmann, B. P., & Shearer, P. M. (2009). Global variations of stress drop for moderate to large earthquakes. *Journal of Geophysical Research: Solid Earth*, *114*(1), 1–22. https://doi.org/10.1029/2008JB005821

Amey, R. M. J., Elliott, J. R., Hussain, E., Walker, R. T., Pagani, M., Silva, V., Abdrakhmatov, K. E., & Watson, C. S. (2021). Significant Seismic Risk Potential From Buried Faults Beneath Almaty City, Kazakhstan, Revealed From High-Resolution Satellite DEMs. *Earth and Space Science*, *8*(9), 1–25. https://doi.org/10.1029/2021EA001664

Ansari, H., De Zan, F., & Parizzi, A. (2021). Study of Systematic Bias in Measuring Surface Deformation With SAR Interferometry. *IEEE Transactions on Geoscience and Remote Sensing*, *59*(2), 1285–1301. https://doi.org/10.1109/TGRS.2020.3003421

Argus, D. F., Gordon, R. G., Heflin, M. B., Ma, C., Eanes, R. J., Willis, P., Peltier, W. R., & Owen, S. E. (2010). The angular velocities of the plates and the velocity of Earth's centre from space geodesy. *Geophysical Journal International*, *180*(3), 913–960. https://doi.org/10.1111/j.1365-246X.2009.04463.x

Arrowsmith, J. R., Crosby, C. J., Korzhenkov, A. M., Mamyrov, E., Povolotskaya, I., Guralnik, B., & Landgraf, A. (2017). Surface rupture of the 1911 Kebin (Chon–Kemin) earthquake, Northern Tien Shan, Kyrgyzstan. *Geological Society, London, Special Publications*, *432*(1), 233–253. https://doi.org/10.1144/SP432.10

Avouac, J.-P., Ayoub, F., Wei, S., Ampuero, J. P., Meng, L., Leprince, S., Jolivet, R., Duputel, Z., & Helmberger, D. (2014). The 2013, Mw 7.7 Balochistan earthquake, energetic strike-slip reactivation of a thrust fault. *Earth and Planetary Science Letters*, *391*, 128–134. https://doi.org/https://doi.org/10.1016/j.epsl.2014.01.036

Avouac, J.-P., Tapponnier, P., Bai, M., You, H., & Wang, G. (1993). Active Faulting and Folding Along the Northern Tien Shan and Late Cenozoic Rotation of the Tarim Relative to Dzungaria and Kazakhstan. *Journal of Geophysical Research*, *98*(B4), 6755–6804.

Bai, M., & Fang, Z. (1981). Relationship between phenomena of surface breaking and geological studies of the Manas southwestern earthquake (M=8) in 1906 in the Xinjiang region (in Chinese). *Northwestern Seismological Journal*, *3*(2), 100–102.

Baize, S., Reicherter, K., Avagyan, A., Belyashov, A., Pestov, E., Vittori, E., Arakelyan, A., & Decker, K. (2019). First assessment of recent tectonics and paleoearthquakes along the Irtysh fault (eastern Kazakhstan). *Geomorphology*, *326*, 90–106. https://doi.org/10.1016/j.geomorph.2018.09.013

Balco, G., Stone, J. O., Lifton, N. A., & Dunai, T. J. (2008). A complete and easily accessible means of calculating surface exposure ages or erosion rates from 10Be and 26Al measurements. *Quaternary Geochronology*, *3*(3), 174–195. https://doi.org/10.1016/j.quageo.2007.12.001

Bande, A., Sobel, E. R., Mikolaichuk, A., & Torres Acosta, V. (2017). Talas–Fergana Fault Cenozoic timing of deformation and its relation to Pamir indentation. *Geological Society, London, Special Publications*, *427*(1), 295 LP – 311. https://doi.org/10.1144/SP427.1

Bayasgalan, A., Jackson, J. A., & McKenzie, D. (2005). Lithosphere rheology and active tectonics in Mongolia: Relations between earthquake source parameters, gravity and GPS measurements. *Geophysical Journal International*, *163*(3), 1151–1179. https://doi.org/10.1111/j.1365-246X.2005.02764.x

Bekaert, D. P. S., Walters, R. J., Wright, T. J., Hooper, A. J., & Parker, D. J. (2015). Statistical comparison of InSAR tropospheric correction techniques. *Remote Sensing of Environment*, *170*, 40–47. https://doi.org/10.1016/j.rse.2015.08.035

Bi, H., Zheng, W., Lei, Q., Zeng, J., Zhang, P., & Chen, G. (2020). Surface Slip Distribution Along the West Helanshan Fault, Northern China, and Its Implications for Fault Behavior. *Journal of Geophysical Research: Solid Earth*, *125*(7), 1–20. https://doi.org/10.1029/2020JB019983

Bilham, R., & England, P. (2001). Plateau 'pop-up' in the great 1897 Assam earthquake. *Nature*, *410*(6830), 806–809. https://doi.org/10.1038/35071057

Bindi, D., Parolai, S., Gómez-Capera, A., Locati, M., Kalmeteva, Z. A., & Mikhailova, N. (2014). Locations and magnitudes of earthquakes in Central Asia from seismic intensity data. *Journal of Seismology*, *18*(1), 1–21. https://doi.org/10.1007/s10950-013-9392-1

Bird, P. (2003). An updated digital model of plate boundaries. *Geochemistry, Geophysics, Geosystems*, *4*(3). https://doi.org/10.1029/2001GC000252

Blaser, L., Krüger, F., Ohrnberger, M., & Scherbaum, F. (2010). Scaling relations of earthquake source parameter estimates with special focus on subduction environment. *Bulletin of the Seismological Society of America*, *100*(6), 2914–2926. https://doi.org/10.1785/0120100111

Bogdanovich, K. I., Kark, I. M., Korolkov, B. Y., & Mushketov, D. I. (1914). Earthquake in Northern District of Tien Shan, 22 December 1910. *Communications of the Geological Community, St Petersburg, Russia (in Russian)*.

Bollinger, L., Klinger, Y., Forman, S., Chimed, O., Bayasgalan, A., Munkhuu, U., Davaasuren, G., Dolgorsuren, T., Enkhee, B., & Sodnomsambuu, D. (2021). 25,000 Years Long Seismic Cycle in a Slow Deforming Continental Region of Mongolia. *Scientific Reports*. https://doi.org/https://doi.org/10.21203/rs.3.rs-310793/v1

Bondár, I., Engdahl, E. R., Villaseñor, A., Harris, J., & Storchak, D. (2015). ISC-GEM: Global Instrumental Earthquake Catalogue (1900-2009), II. Location and seismicity patterns. *Physics of the Earth and Planetary Interiors*, *239*, 2–13. https://doi.org/10.1016/j.pepi.2014.06.002

Borchers, B., Marrero, S., Balco, G., Caffee, M. W., Goehring, B., Lifton, N. A., Nishiizumi, K., Phillips, F., Schaefer, J. M., & Stone, J. O. (2016). Geological calibration of spallation production rates in the CRONUS-Earth project. *Quaternary Geochronology*, *31*, 188–198. https://doi.org/10.1016/j.quageo.2015.01.009

Bormann, P., Wendt, S., & DiGiacomo, D. (2013). Seismic sources and source parameters. In *New Manual of Seismological Observatory Practice 2 (NMSOP2)* (pp. 1–259). German Research Centre for Geosciences (GFZ).

Bosboom, R., Dupont-Nivet, G., Huang, W., Yang, W., & Guo, Z. (2014). Oligocene clockwise rotations along the eastern Pamir: Tectonic and paleogeographic implications. *Tectonics*, *33*(2), 53–66. https://doi.org/https://doi.org/10.1002/2013TC003388

Bøtter-Jensen, L., Bulur, E., Duller, G. A. T., & Murray, A. S. (2000). Advances in luminescence measurement systems. *Radiation Measurements*, *32*, 523–528. https://ac.els-cdn.com/S1350448700000391/1-s2.0-S1350448700000391-main.pdf?_tid=59d7ff0e-0665-4ed0-ad3a-18d268a28765&acdnat=1522418437_118cb0422d9cedbfc9e26c4244650ea9

Burchfiel, B. C., Brown, E. T., Deng, Q., Feng, X., Li, J., Molnar, P., Shi, J., Wu, Z., & Yu, H. (1999). Crustal Shortening on the Margins of the Tien Shan, Xinjiang, China. *International Geology Review*, *41*(8), 665–700. https://doi.org/10.1080/00206819909465164

Burtman, V. (1975). Structural geology of variscan Tien Shan, USSR. *Am. J. Sci*, *275*(January 1975), 157–186.

Burtman, V. (2008). Nappes of the southern Tien Shan. *Russian Journal of Earth Sciences*, *10*(1).

Buylaert, J. P., Murray, A. S., Thomsen, K. J., & Jain, M. (2009). Testing the potential of an elevated temperature IRSL signal from K-feldspar. *Radiation Measurements*, *44*(5–6), 560–565. https://doi.org/10.1016/j.radmeas.2009.02.007

Cadek, O. (1987). Studying earthquake ground motion in Prague from Wiechert seismograph records. *Gerlands Beiträge Zur Geophysik*, *96*(5), 438–447.

Campbell, G. E., Walker, R. T., Abdrakhmatov, K. E., Carolin, S., Carr, A. S., Elliott, J. R., Jackson, J. A., Mackenzie, D., Rizza, M. A., & Rodes, A. (2019). Rapid Late Quaternary Slip, Repeated Prehistoric Earthquake Rupture, and Widespread Landsliding Associated With the Karakudzhur Thrust, Central Kyrgyz Tien Shan. *Tectonics*, *38*(11), 3740–3764. https://doi.org/10.1029/2018TC005433

Campbell, G. E., Walker, R. T., Abdrakhmatov, K. E., Jackson, J. A., Elliott, J. R., Mackenzie, D., Middleton, T., & Schwenninger, J. (2015). Great earthquakes in low strain rate continental interiors : An example from SE Kazakhstan. *Journal of Geophysical Research : Solid Earth*, *120*, 5507–5534. https://doi.org/10.1002/2015JB011925

Campbell, G. E., Walker, R. T., Abdrakhmatov, K. E., Schwenninger, J., Jackson, J. A., Elliott, J. R., & Copley, A. (2013). The Dzhungarian fault: Late Quaternary tectonics and slip rate of a major right-lateral strike-slip fault in the northern Tien Shan region. *Journal of Geophysical Research: Solid Earth*, *118*(10), 5681–5698. https://doi.org/10.1002/jgrb.50367

Carson, M. A., & Kirkby, M. J. (1972). *Hillslope form and process* (3rd ed.). Cambridge University Press.

Catherine, J. K., Gahalaut, V. K., & Sahu, V. K. (2005). Constraints on rupture of the December 26, 2004, Sumatra earthquake from far-field GPS observations. *Earth and Planetary Science Letters*, *237*(3), 673–679. https://doi.org/https://doi.org/10.1016/j.epsl.2005.07.012

Cerling, T. E., & Craig, H. (1994). Geomorphology and In-situ Cosmogenic Isotopes. *Annual Review of Earth and Planetary Sciences*, *22*, 273–317.

Charreau, J., Avouac, J.-P., Chen, Y., Dominguez, S., & Gilder, S. (2008). Miocene to present kinematics of fault-bend folding across the Huerguosi anticline, northern Tianshan (China), derived from structural, seismic, and magnetostratigraphic data. *Geology*, *36*(11), 871–874. https://doi.org/10.1130/G25073A.1

Charreau, J., Saint-Carlier, D., Dominguez, S., Lavé, J., Blard, P. H., Avouac, J.-P., Jolivet, M., Chen, Y., Wang, S., Brown, N. D., Malatesta, L. C., & Rhodes, E. J. (2017). Denudation outpaced by crustal thickening in the eastern Tianshan. *Earth and Planetary Science Letters*, *479*, 179–191. https://doi.org/10.1016/j.epsl.2017.09.025

Chen, W.-P., & Molnar, P. (1983). Focal depths of intracontinental and intraplate earthquakes and their implications for the thermal and mechanical properties of the lithosphere. *Journal of Geophysical Research: Solid Earth*, *88*(B5), 4183–4214. https://doi.org/https://doi.org/10.1029/JB088iB05p04183

Chéry, J., & Vernant, P. (2006). Lithospheric elasticity promotes episodic fault activity. *Earth and Planetary Science Letters*, *243*(1–2), 211–217. https://doi.org/10.1016/j.epsl.2005.12.014

China Earthquake Administration. (1971). *Catalogue of Earthquakes in China (in Chinese)*. Science Press, Beijing. https://books.google.co.uk/books?id=Cb2CmgEACAAJ

Chuang, R. Y., & Johnson, K. M. (2011). Reconciling geologic and geodetic model fault slip-rate discrepancies in Southern California: Consideration of nonsteady mantle flow and lower crustal fault creep. *Geology*, *39*(7), 627–630. https://doi.org/10.1130/G32120.1

Clark, D. J., Brennand, S., Brenn, G., Garthwaite, M. C., Dimech, J., Allen, T. I., & Standen, S. (2020). Surface deformation relating to the 2018 Lake Muir earthquake sequence, southwest Western Australia: New insight into stable continental region earthquakes. *Solid Earth*, *11*(2), 691–717. https://doi.org/10.5194/se-11-691-2020

Clarke, M. L., & Rendell, H. M. (1998). Climate change impacts on sand supply and the formation of desert sand dunes in the south-west U.S.A. *Journal of Arid Environments*, *39*(3), 517–531. https://doi.org/https://doi.org/10.1006/jare.1997.0372

Cobbold, P. R., & Davy, P. (1988). Indentation tectonics in nature and experiment. 2. Central Asia. *Bull. Geol. Inst. Univ. Uppsala, NS*, *14*(June), 143–162.

Colman, S. M., & Watson, K. E. N. (1983). Ages estimated from a diffusion equation model for scarp degradation. *Science*, *221*(4607), 263–265. https://doi.org/10.1126/science.221.4607.263

Copley, A., Avouac, J.-P., Hollingsworth, J., & Leprince, S. (2011). The 2001 Mw 7.6 Bhuj earthquake, low fault friction, and the crustal support of plate driving forces in India. *Journal of Geophysical Research: Solid Earth*, *116*(B8). https://doi.org/https://doi.org/10.1029/2010JB008137

Corbett, L. B., Bierman, P. R., & Rood, D. H. (2016). An approach for optimizing in situ cosmogenic 10Be sample preparation. *Quaternary Geochronology*, *33*, 24–34. https://doi.org/10.1016/j.quageo.2016.02.001

Cording, A., Hetzel, R., Kober, M., & Kley, J. (2014). 10Be exposure dating of river terraces at the southern mountain front of the Dzungarian Alatau (SE Kazakhstan) reveals rate of thrust faulting over the past ~400ka. *Quaternary Research (United States)*, *81*(1), 168–178. https://doi.org/10.1016/j.yqres.2013.10.016

Cowgill, E., Gold, R. D., Chen, X., Wang, X. F., Arrowsmith, J. R., & Southon, J. R. (2009). Low Quaternary slip rate reconciles geodetic and geologic rates along the Altyn Tagh fault northwestern Tibet. *Geology*, *37*(7), 647–650. https://doi.org/10.1130/G25623A.1

Cunningham, W. D. (2005). Active intracontinental transpressional mountain building in the Mongolian Altai: Defining a new class of orogen. *Earth and Planetary Science Letters*, *240*(2), 436–444. https://doi.org/10.1016/j.epsl.2005.09.013

Cunningham, W. D. (2007). Structural and topographic characteristics of restraining bend mountain ranges of the Altai, Gobi Altai and easternmost Tien Shan. *Geological Society Special Publication*, *290*, 219–237. https://doi.org/10.1144/SP290.7

Daëron, M., Avouac, J.-P., & Charreau, J. (2007). Modeling the shortening history of a fault tip fold using structural and geomorphic records of deformation. *Journal of Geophysical Research: Solid Earth*, *112*(3), 1–19. https://doi.org/10.1029/2006JB004460

Daniell, J. E., Schaefer, A. M., & Wenzel, F. (2017). Losses Associated with Secondary Effects in Earthquakes. *Frontiers in Built Environment*, *3*. https://doi.org/10.3389/fbuil.2017.00030

Daout, S., Dini, B., Haeberli, W., Doin, M. P., & Parsons, B. (2020). Ice loss in the Northeastern Tibetan Plateau permafrost as seen by 16 yr of ESA SAR missions. *Earth and Planetary Science Letters*, *545*, 116404. https://doi.org/10.1016/j.epsl.2020.116404

Daout, S., Doin, M. P., Peltzer, G., Socquet, A., & Lasserre, C. (2017). Large-scale InSAR monitoring of permafrost freeze-thaw cycles on the Tibetan Plateau. *Geophysical Research Letters*, *44*(2), 901–909. https://doi.org/10.1002/2016GL070781

Daout, S., Sudhaus, H., Kausch, T., Steinberg, A., & Dini, B. (2019). Interseismic and Postseismic Shallow Creep of the North Qaidam Thrust Faults Detected with a Multitemporal InSAR Analysis. *Journal of Geophysical Research: Solid Earth*, 1–21. https://doi.org/10.1029/2019JB017692

Darvill, C. M. (2013). Cosmogenic nuclide analysis. *Geomorphological Techniques (Online Edition)*, *10*(2008), 1–25. http://www.geomorphology.org.uk/sites/default/files/geom_tech_chapters/4.2.10_CosmogenicNuclideAnalysis.pdf

Dawson, J. H. (2008). *Satellite radar interferometry with application to the observation of surface deformation in Australia*. Australian National University Canberra,, Australia.

De Grave, J., Buslov, M. M., & Van den haute, P. (2007). Distant effects of India–Eurasia convergence and Mesozoic intracontinental deformation in Central Asia: Constraints from apatite fission-track thermochronology. *Journal of Asian Earth Sciences*, *29*(2), 188–204. https://doi.org/https://doi.org/10.1016/j.jseaes.2006.03.001

De Grave, J., Glorie, S., Buslov, M. M., Stockli, D. F., McWilliams, M. O., Batalev, V. Y., & Van den haute, P. (2013). Thermo-tectonic history of the Issyk-Kul basement (Kyrgyz Northern Tien Shan, Central Asia). *Gondwana Research*, *23*(3), 998–1020. https://doi.org/10.1016/j.gr.2012.06.014

Dee, D. P., Balmaseda, M. A., Balsamo, G., Engelen, R., Simmons, A. J., & Thépaut, J.-N. (2014). Toward a Consistent Reanalysis of the Climate System. *Bulletin of the American Meteorological Society*, *95*(8), 1235–1248. https://doi.org/10.1175/BAMS-D-13-00043.1

Dee, D. P., Uppala, S. M., Simmons, A. J., Berrisford, P., Poli, P., Kobayashi, S., Andrae, U., Balmaseda, M. A., Balsamo, G., Bauer, P., Bechtold, P., Beljaars, A. C. M., van de Berg, L., Bidlot, J., Bormann, N., Delsol, C., Dragani, R., Fuentes, M., Geer, A. J., … Vitart, F. (2011). The ERA-Interim reanalysis: configuration and performance of the data assimilation system. *Quarterly Journal of the Royal Meteorological Society*, *137*(656), 553–597. https://doi.org/https://doi.org/10.1002/qj.828

Delvaux, D., Abdrakhmatov, K. E., Lemzin, I. N., & Strom, A. L. (2001). Landslide and surface breaks of the 1911 Ms 8.2 Kemin earthquake, Kyrgyzstan. *Landslides*, *42*(10), 1583–1592.

Deng, Q., Feng, X., Yang, X., Peng, S., Zhang, P., & Xu, X. (1994). Study on Holocene Paleoearthquakes by Large Trench in the Manas-Tugulu Reverse Fault and Fold Zone along Northern Margin of the Tianshan Mountain, in Xinjiang (in Chinese). In *Research on Active Fault (3)* (pp. 1–16). Seismological Press, Beijing.

Deng, Q., Feng, X., Yu, H., Chen, J., Li, J., Zhang, Y., Xu, X., Wu, Z., & Zhang, H. (1991). Paleoseismology and Late Quaternary Activity of the Dushanzi-Anjihai Reverse Fault Zone, Xinjiang (in Chinese). In *Research on Active Fault (1)* (pp. 37–56). Science Press, Beijing.

Deng, Q., Feng, X., Zhang, P., Xu, X., Yang, X., Peng, S., & Li, J. (2000). *Active Tectonics of the Chinese Tianshan Mountains (in Chinese)*. Seismological Press, Beijing.

Deng, Q., Zhang, P., Xu, X., Yang, X., Peng, S., & Feng, X. (1996). Paleoseismology of the northern piedmont of Tianshan Mountains, northwestern China. *Journal of Geophysical Research B: Solid Earth*, *101*(3), 5895–5920. https://doi.org/10.1029/95jb02739

Diao, F., Xiong, X., Wang, R., Walker, R. T., Wang, Y., & Wang, K. (2019). Slip Rate Variation Along the Kunlun Fault (Tibet): Results From New GPS Observations and a Viscoelastic Earthquake-Cycle Deformation Model. *Geophysical Research Letters*, *46*(5), 2524–2533. https://doi.org/10.1029/2019GL081940

Dixon, T. H., Norabuena, E., & Hotaling, L. (2003). Paleoseismology and global positioning system: Earthquake-cycle effects and geodetic versus geologic fault slip rates in the Eastern California shear zone. *Geology*, *31*(1), 55–58. https://doi.org/10.1130/0091-7613(2003)031<0055:PAGPSE>2.0.CO;2

Dodds, N., Begenjev, G., Bezmenov, Y., Grützner, C., Mirzin, R., Rhodes, E. J., Walker, R. T., & Wordsworth, P. (2022). A Major Medieval Earthquake on the Main Köpetdag (Kopeh Dagh) Fault , Turkmenistan. *Bulletin - Seismological Society of America*. https://doi.org/10.1785/0120210195

Dodds, N., Daout, S., Walker, R. T., Begenjev, G., Bezmenov, Y., Mirzin, R., & Parsons, B. (2022). Interseismic deformation and strain-partitioning along the Main K opetdag Fault , Turkmenistan , with Sentinel-1 InSAR time-series. *Geophysical Journal International*, *230*, 1612–1629.

Doin, M. P., Lasserre, C., Peltzer, G., Cavalié, O., & Doubre, C. (2009). Corrections of stratified tropospheric delays in SAR interferometry: Validation with global atmospheric models. *Journal of Applied Geophysics*, *69*(1), 35–50. https://doi.org/10.1016/j.jappgeo.2009.03.010

Doin, M. P., Lodge, F., Guillaso, S., Jolivet, R., Lasserre, C., Ducret, G., Grandin, R., Pathier, E., & Pinel, V. (2011). Presentation of the small baseline NSBAS processing chain on a case example: the Etna deformation monitoring from 2003 to 2010 using Envisat data. *Proceedings of the ESA "Fringe 2011 Workshop", Frascati, Italy, (19-23 September 2011)*, *2011*(January), 19–23. http://www.geologie.ens.fr/~grandin/upload/Doin_2012_NSBAS.pdf%5Cnhttp://www.gps.caltech.edu/~jolivetr/jolivetr/Publications_files/Proceedings_of_the_Fringe_symposium_2011_Doin.pdf

Doin, M. P., Twardzik, C., Ducret, G., Lasserre, C., Guillaso, S., & Sun, J. (2015). InSAR measurement of the deformation around Siling Co Lake: Inferences on the lower crust viscosity in central Tibet. *Journal of Geophysical Research: Solid Earth*, *120*(7), 5290–5310. https://doi.org/10.1002/2014JB011768

Dolan, J. F., & Meade, B. J. (2017). A Comparison of Geodetic and Geologic Rates Prior to Large Strike-Slip Earthquakes: A Diversity of Earthquake-Cycle Behaviors? *Geochemistry, Geophysics, Geosystems*, *18*(12), 4426–4436. https://doi.org/10.1002/2017GC007014

Ducret, G., Doin, M. P., Grandin, R., Lasserre, C., & Guillaso, S. (2013). DEM corrections before unwrapping in a small baseline strategy for InSAR time series analysis. *IEEE Geoscience and Remote Sensing Letters*, *11*(3), 696–700. https://doi.org/10.1109/LGRS.2013.2276040

Dunai, T. J. (2010). *Cosmogenic nuclides: principles, concepts and applications in the earth surface sciences*. Cambridge University Press.

Dunne, J., Elmore, D., & Muzikar, P. (1999). Scaling factors for the rates of production of cosmogenic nuclides for geometric shielding and attenuation at depth on sloped surfaces. *Geomorphology*, *27*(1–2), 3–11. https://doi.org/10.1016/S0169-555X(98)00086-5

Durcan, J. A., & Duller, G. A. T. (2011). The fast ratio: A rapid measure for testing the dominance of the fast component in the initial OSL signal from quartz. *Radiation Measurements*, *46*(10), 1065–1072. https://doi.org/10.1016/j.radmeas.2011.07.016

Duvall, A. R., & Clark, M. K. (2010). Dissipation of fast strike-slip faulting within and beyond northeastern Tibet. *Geology*, *38*(3), 223–226. https://doi.org/10.1130/G30711.1

Dziewonski, A. M., Chou, T.-A., & Woodhouse, J. H. (1981). Determination of earthquake source parameters from waveform data for studies of global and regional seismicity. *Journal of Geophysical Research: Solid Earth*, *86*(B4), 2825–2852. https://doi.org/https://doi.org/10.1029/JB086iB04p02825

Ekström, G., Nettles, M., & Dziewonski, A. M. (2012). The global CMT project 2004–2010: Centroid-moment tensors for 13,017 earthquakes. *Physics of the Earth and Planetary Interiors*, *200–201*, 1–9. https://doi.org/https://doi.org/10.1016/j.pepi.2012.04.002

Elliott, A. J., Oskin, M. E., Liu-zeng, J., & Shao, Y. X. (2015). Rupture termination at restraining bends: The last great earthquake on the Altyn Tagh Fault. *Geophysical Research Letters*, *42*(7), 2164–2170. https://doi.org/10.1002/2015GL063107

Elliott, J. R., Biggs, J., Parsons, B., & Wright, T. J. (2008). InSAR slip rate determination on the Altyn Tagh Fault, northern Tibet, in the presence of topographically correlated atmospheric delays. *Geophysical Research Letters*, *35*(12), 1–5. https://doi.org/10.1029/2008GL033659

England, P., & Jackson, J. A. (2011). Uncharted seismic risk. *Nature Geoscience*, *4*(6), 348–349. https://doi.org/10.1038/ngeo1168

England, P., & Molnar, P. (1997). The field of crustal velocity in Asia calculated from Quaternary rates of slip on faults. *Geophysical Journal International*, *130*(3), 551–582. https://doi.org/10.1111/j.1365-246X.1997.tb01853.x

European Space Agency Sinergise. (2021). *Copernicus Global Digital Elevation Model.* Distributed by OpenTopography. https://doi.org/https://doi.org/10.5069/G9028PQB Accessed: 2021-11-01

Fan, J., Xu, H., Shi, W., Guo, Q., Zhang, S., Wei, X., Cai, M., Huang, S., Wang, J., & Xiao, J. (2022). A ~28-kyr Continuous Lacustrine Paleoseismic Record of the Intraplate, Slow-Slipping Fuyun Fault in Northwest China. *Frontiers in Earth Science*, *10*(January), 1–16. https://doi.org/10.3389/feart.2022.828801

Fang, L., Wu, J., Wang, C., Wang, W., & Yang, T. (2014). Relocation of the 2012 M s6.6 Xinjiang Xinyuan earthquake sequence. *Science China Earth Sciences*, *57*(2), 216–220. https://doi.org/10.1007/s11430-013-4755-6

Fattahi, H., & Amelung, F. (2014a). InSAR bias and uncertainty due to the systematic and stochastic tropospheric delay. *Journal of Geophysical Research, Solid Earth*, *119*(iv), 3076–3095. https://doi.org/10.1002/2015JB012419.Received

Fattahi, H., & Amelung, F. (2014b). InSAR uncertainty due to orbital errors. *Geophysical Journal International*, *199*(1), 549–560. https://doi.org/10.1093/gji/ggu276

Feng, X. (1987). Paleoseismological study for Kaxhe fault zone, Xinjiang. *Seismology and Geology*, *9*(2), 75–77.

Feng, X. (1990). The Nilka Earthquake Fault Zone in Xinjiang (in Chinese). *Inland Earthquake*, *4*(3), 5.

Feng, X., Ma, J., Zhou, Y., England, P., Parsons, B., Rizza, M. A., & Walker, R. T. (2020). Geomorphology and Paleoseismology of the Weinan Fault, Shaanxi, Central China, and the Source of the 1556 Huaxian Earthquake. *Journal of Geophysical Research: Solid Earth*, *125*(12). https://doi.org/10.1029/2019JB017848

Fletcher, J. M., Oskin, M. E., & Teran, O. J. (2016). The role of a keystone fault in triggering the complex El Mayor–Cucapah earthquake rupture. *Nature Geoscience*, *9*(4), 303–307. https://doi.org/10.1038/ngeo2660

Freymueller, J., King, N. E., & Segall, P. (1994). The co-seismic slip distribution of the Landers earthquake. *Bulletin of the Seismological Society of America*, *84*(3), 646–659.

Fu, X., Li, S. H., Li, B., & Fu, B. (2017). A fluvial terrace record of late Quaternary folding rate of the Anjihai anticline in the northern piedmont of Tian Shan, China. *Geomorphology*, *278*(October), 91–104. https://doi.org/10.1016/j.geomorph.2016.10.034

Galbraith, R. F., Roberts, R. G., Laslett, G. M., Yoshida, H., & Olley, J. M. (1999). Optical dating of single and multiple grains of quartz from Jinmium rock shelter, northern Australia: Part I, experimental design and statistical models. *Archaeometry*, *41*(2), 339–364. https://doi.org/10.1111/j.1475-4754.1999.tb00987.x

Gatinsky, Y. G., & Prokhorova, T. V. (2014). Superficial and Deep Structure of Central Asia as Example of Continental Lithosphere Heterogeneity. *Universal Journal of Geoscience*, *2*(2), 43–52. https://doi.org/10.13189/ujg.2014.020202

Ghose, S., Mellors, R. J., Korjenkov, A. M., Hamburger, M. W., Pavlis, T. L., Pavlis, G. L., Omuraliev, M., Mamyrov, E., & Muraliev, A. R. (1997). The MS = 7.3 1992 Suusamyr, Kyrgyzstan, earthquake in the tien shan: 2. Aftershock focal mechanisms and surface deformation. *Bulletin of the Seismological Society of America*, *87*(1), 23–38.

Glorie, S., De Grave, J., Delvaux, D., Buslov, M. M., Zhimulev, F. I., Vanhaecke, F., Elburg, M. A., & Van den haute, P. (2012). Tectonic history of the Irtysh shear zone (NE Kazakhstan): New constraints from zircon U/Pb dating, apatite fission track dating and palaeostress analysis. *Journal of Asian Earth Sciences*, *45*, 138–149. https://doi.org/10.1016/j.jseaes.2011.09.024

Gomba, G., Rodriguez Gonzalez, F., & De Zan, F. (2017). Ionospheric phase screen compensation for the Sentinel-1 TOPS and ALOS-2 ScanSAR modes. *IEEE Transactions on Geoscience and Remote Sensing*, *55*(1), 223–235. https://doi.org/10.1109/TGRS.2016.2604461

Gong, W., Zhang, Y., Li, T., Wen, S., Zhao, D., Hou, L., & Shan, X. (2019). Multi-sensor geodetic observations and modeling of the 2017 Mw 6.3 jinghe earthquake. *Remote Sensing*, *11*(18). https://doi.org/10.3390/rs11182157

Gong, Z., Li, S. H., & Li, B. (2015). Late Quaternary faulting on the Manas and Hutubi reverse faults in the northern foreland basin of Tian Shan, China. *Earth and Planetary Science Letters*, *424*, 212–225. https://doi.org/10.1016/j.epsl.2015.05.030

Goode, J. K., Burbank, D. W., & Ormukov, C. (2014). Pliocene-Pleistocene initiation, style, and sequencing of deformation in the central Tien Shan. *Tectonics*, *33*(4), 464–484. https://doi.org/https://doi.org/10.1002/2013TC003394

Gosse, J. C., Evenson, E. B., Klein, J., Lawn, B., & Middleton, R. (1995). Precise cosmogenic 10 Be measurements in western North America: support for a global Younger Dryas cooling event. *Geology*, *23*(10), 877–880. https://doi.org/10.1130/0091-7613(1995)023<0877:PCBMIW>2.3.CO;2

Gosse, J. C., & Philips, F. M. (2001). Terrestrial in situ cosmogenic nuclides:theory and application. *Quaternary Science Reviews*, *20*, 1475–1560. http://www.ees.nmt.edu/outside/courses/hyd558/downloads/Set_14b_InSitu/Gosse_Phillips.pdf

Grandin, R., Doin, M. P., Bollinger, L., Pinel-Puysségur, B., Ducret, G., Jolivet, R., & Sapkota, S. N. (2012). Long-term growth of the Himalaya inferred from interseismic InSAR measurement. *Geology*, *40*(12), 1059–1062. https://doi.org/10.1130/G33154.1

Grandin, R., Klein, E. C., Métois, M., & Vigny, C. (2016). Three-dimensional displacement field of the 2015 Mw8.3 Illapel earthquake (Chile) from across- and along-track Sentinel-1 TOPS interferometry. *Geophysical Research Letters*, *43*(6), 2552–2561. https://doi.org/10.1002/2016GL067954

Grützner, C., Campbell, G. E., Walker, R. T., Jackson, J. A., Mackenzie, D., Abdrakhmatov, K. E., & Mukambayev, A. (2019). Shortening Accommodated by Thrust and Strike-Slip Faults in the Ili Basin, Northern Tien Shan. *Tectonics*. https://doi.org/10.1029/2018TC005459

Grützner, C., Carson, E., Walker, R. T., Rhodes, E. J., Mukambayev, A., Mackenzie, D., Elliott, J. R., Campbell, G. E., & Abdrakhmatov, K. E. (2017). Assessing the activity of faults in continental interiors: Palaeoseismic insights from SE Kazakhstan. *Earth and Planetary Science Letters*, *459*, 93–104. https://doi.org/10.1016/j.epsl.2016.11.025

Grützner, C., Walker, R. T., Abdrakhmatov, K. E., Mukambayev, A., Elliott, A. J., & Elliott, J. R. (2017). Active Tectonics Around Almaty and along the Zailisky Alatau Rangefront. *Tectonics*, *36*(10), 2192–2226. https://doi.org/10.1002/2017TC004657

Gu, Gongxu. (1983). *Catalogue of Chinese Earthquakes, 1831 B.C.-1969 A.D. (in Chinese)*. Science Press, Beijing.

Gu, Guohua, & Wang, W. (2013). Advantages of GNSS in Monitoring Crustal Deformation for Detection of Precursors to Strong Earthquakes. *Positioning*, *04*(01), 11–19. https://doi.org/10.4236/pos.2013.41003

Guérin, I., Mercier, N., & Adamiec, G. (2011). Volume 29 No.1 June 2011. *Ancient TL*, *29*(1), 5–8.

Guo, Haipeng, Zhang, Z., Cheng, G., Li, W., Li, T., & Jiao, J. J. (2015). Groundwater-derived land subsidence in the North China Plain. *Environmental Earth Sciences*, *74*(2), 1415–1427. https://doi.org/10.1007/s12665-015-4131-2

Guo, Hui, Jiang, W. L., & Xie, X. S. (2011). Late-Quaternary strong earthquakes on the seismogenic fault of the 1976 Ms7.8 Tangshan earthquake, Hebei, as revealed by drilling and trenching. *Science China Earth Sciences*, *54*(11), 1696–1715. https://doi.org/10.1007/s11430-011-4218-x

Gutenberg, B., & Richter, C. F. (1942). Earthquake magnitude, intensity, energy and accelaration. *Bulletin of the Seismological Society of America*, *32*(3), 163–190. https://doi.org/10.1086/622062

Gutenberg, B., & Richter, C. F. (1954). *Seismicity of the Earth and Associated Phenomena, 2nd ed.* Princeton University Press, Princeton, NJ.

Gutenberg, B., & Richter, C. F. (1956). Magnitude and energy of earthquakes: Annali di. *Annali Di Geofisic*, *9*(1), 1–15. https://doi.org/10.4401/ag-5590

Haeussler, P. J., Schwartz, D. P., Dawson, T. E., Stenner, H. D., Lienkaemper, J. J., Sherrod, B., Cinti, F. R., Montone, P., Craw, P. A., Crone, A. J., & Personius, S. F. (2004). Surface Rupture and Slip Distribution of the Denali and Totschunda Faults in the 3 November 2002 M 7.9 Earthquake, Alaska. *Bulletin of the Seismological Society of America*, *94*(6B), S23–S52. https://doi.org/10.1785/0120040626

Hamiel, Y., & Fialko, Y. (2007). Structure and mechanical properties of faults in the North Anatolian Fault system from InSAR observations of coseismic deformation due to the 1999 Izmit (Turkey) earthquake. *Journal of Geophysical Research: Solid Earth*, *112*(B7). https://doi.org/https://doi.org/10.1029/2006JB004777

Hanks, T. C. (2000). The Age of Scarplike Landforms From Diffusion-Equation Analysis. In J. S. Noller, J. M. Sowers, & W. R. Lettis (Eds.), *Quaternary Geochronology: methods and applications* (Vol. 4, pp. 313–338). American Geophysical Union.

Hanssen, R. F. (2001). *Radar interferometry: data interpretation and error analysis* (Vol. 2). Springer Science \& Business Media.

Hay, M. B. (1888). The Earthquakes of May and June, 1887, in the Verny (Vernoe) District, Russian Turkestan, and Their Consequences. *Proceedings of the Royal Geographical Society and Monthly Record of Geography*, *10*(10), 638–646. https://doi.org/10.2307/1800851

He, J., Vernant, P., Chéry, J., Wang, W., Lu, S., Ku, W., Xia, W., & Bilham, R. (2013). Nailing down the slip rate of the Altyn Tagh fault. *Geophysical Research Letters*, *40*(20), 5382–5386. https://doi.org/10.1002/2013GL057497

Hendrix, M. S., GRAHAM, S. A., CARROLL, A. R., Sobel, E. R., McKNIGHT, C. L., SCHULEIN, B. J., & Wang, Z. (1992). Sedimentary record and climatic implications of recurrent deformation in the Tian Shan: Evidence from Mesozoic strata of the north Tarim, south Junggar, and Turpan basins, northwest China. *GSA Bulletin*, *104*(1), 53–79. https://doi.org/10.1130/0016-7606(1992)104<0053:SRACIO>2.3.CO;2

Hetland, E. A., & Hager, B. H. (2006). Interseismic strain accumulation: Spin-up, cycle invariance, and irregular rupture sequences. *Geochemistry, Geophysics, Geosystems*, *7*(5). https://doi.org/10.1029/2005GC001087

Hetzel, R. (2013). Active faulting, mountain growth, and erosion at the margins of the Tibetan Plateau constrained by in situ-produced cosmogenic nuclides. *Tectonophysics*, *582*, 1–24. https://doi.org/10.1016/j.tecto.2012.10.027

Hollingsworth, J., Walker, R. T., Abdrakhmatov, K. E., Campbell, G. E., Mukambayev, A., Rhodes, E. J., & Rood, D. H. (2016). Active fault slip and potential large magnitude earthquakes within the stable Kazakh Platform (Central Kazakhstan). *AGU Fall Meeting Abstracts*, *2016*, T32B-05. https://ui.adsabs.harvard.edu/abs/2016AGUFM.T32B..05H

Hollingsworth, J., Ye, L., & Avouac, J.-P. (2017). Dynamically triggered slip on a splay fault in the Mw 7.8, 2016 Kaikoura (New Zealand) earthquake. *Geophysical Research Letters*, *44*(8), 3517–3525. https://doi.org/10.1002/2016GL072228

Hooper, A. J., Segall, P., & Zebker, H. A. (2007). Persistent scatterer interferometric synthetic aperture radar for crustal deformation analysis, with application to Volcán Alcedo, Galápagos. *Journal of Geophysical Research: Solid Earth*, *112*(7), 1–21. https://doi.org/10.1029/2006JB004763

Hu, G., Chen, J., Zhang, W., Di, N., Li, Y., & Li, S. H. (2021). Out-of-Sequence Backthrusting Since the Middle Pleistocene Revealed by the Jiangnanmiao Thrust Fault Along the Northern Tian Shan, China. *Tectonics*, *40*(4), 1–18. https://doi.org/10.1029/2020tc006662

Hu, J., & Bai, M. (1988). The rupture zone of Manas earthquake, Xingjiang, Research on earthquake Faults in China (in Chinese), edited by Seismological Bureau of Xingjiang. *Xingjiang Press, Urumqi, China*, 61–65.

Hu, W., Li, P., Rosenbaum, G., Liu, J., Jourdan, F., Jiang, Y., Wu, D., Zhang, J., Yuan, C., & Sun, M. (2020). Structural evolution of the eastern segment of the Irtysh Shear Zone: Implications for the collision between the East Junggar Terrane and the Chinese Altai Orogen (northwestern China). *Journal of Structural Geology*, *139*(April), 104126. https://doi.org/10.1016/j.jsg.2020.104126

Hu, Z. (2019). *Activity of the Jinghe Section of the Boluokenu-Aqikekuduke Fault since the Late Pleistocene (Master Thesis)*. Beijing, China: Institute of Geology, China Earthquake Administration.

Hu, Z., Li, T., Thompson Jobe, J., & Yang, X. (2021). Lower Portion Rupture of a Thrust Fault during the 2017 Mw 6.3 Jinghe Earthquake: Implications to Seismic Hazards in the Tian Shan Region. *Seismological Research Letters*. https://doi.org/10.1785/0220200295

Hu, Z., Yang, X., Yang, H., Huang, W., Wu, G., Miao, S., & Zhang, L. (2021). Slip Rate and Paleoseismology of the Bolokenu-Aqikekuduk (Dzhungarian) Right-Lateral Strike-Slip Fault in the Northern Tian Shan, NW China. *Tectonics*, *40*(8), e2020TC006604. https://doi.org/https://doi.org/10.1029/2020TC006604

Huang, W. L. (2015). *Crustal shortening rates across the Yanqi basin, TianShan during Mid-late Quaternary (in Chinese)*. Institute of Geology, China Earthquake Administration Beijing.

Hubert-Ferrari, A., Armijo, R., King, G., Meyer, B., & Barka, A. (2002). Morphology, displacement, and slip rates along the North Anatolian Fault, Turkey. *Journal of Geophysical Research: Solid Earth*, *107*(B10), ETG 9-1-ETG 9-33. https://doi.org/10.1029/2001jb000393

Huntley, D. J., & Baril, M. R. (1997). The K content of the K-feldspars being measured in optical dating or in thermoluminescence dating. *Ancient Tl*, *15*(1), 11–13.

Huntley, D. J., Godfrey-Smith, D. I., & Thewalt, M. L. W. (1985). Optical dating of sediments. *Nature*, *313*(5998), 105–107. https://doi.org/10.1038/313105a0

Huntley, D. J., & Lamothe, M. (2001). Ubiquity of anomalous fading in K-feldspars and the measurement and correction for it in optical dating. *Canadian Journal of Earth Sciences*, *38*(7), 1093–1106. https://doi.org/10.1139/cjes-38-7-1093

Hussain, E., Hooper, A. J., Wright, T. J., Walters, R. J., & Bekaert, D. P. S. (2016). Interseismic strain accumulation across the central North Anatolian Fault from iteratively unwrapped InSAR measurements. *Journal of Geophysical Research: Solid Earth*, *121*(12), 9000–9019. https://doi.org/10.1002/2016JB013108

Hütt, G., Jaek, I., & Tchonka, J. (1988). Optical dating: K-feldspars optical response stimulation spectra. *Quaternary Science Reviews*, *7*(3–4), 381–385. https://doi.org/10.1016/0277-3791(88)90033-9

Institute of Geophysics, SSB & Institute of Chinese Historical Geography, F. U. (1990). *Atlas of the Historical Earthquakes in China (The Qing Dynasty Period) (in Chinese)*. China Cartographic Publishing House.

ISC. (2021). *ISC-GEM Earthquake Catalogue*. https://doi.org/10.31905/d808b825

ISC. (2022a). *ISC-EHB dataset*. https://doi.org/https://doi.org/10.31905/PY08W6S3

ISC. (2022b). *On-line Bulletin*. https://doi.org/10.31905/D808B830

Jackson, J. A., McKenzie, D., & Priestley, K. (2021). Relations between earthquake distributions, geological history, tectonics and rheology on the continents. *Philosophical Transactions of the Royal Society A: Mathematical, Physical and Engineering Sciences*, *379*(2193), 20190412. https://doi.org/10.1098/rsta.2019.0412

Jain, M., Buylaert, J. P., Thomsen, K. J., & Murray, A. S. (2015). Further investigations on "non-fading" in K-Feldspar. *Quaternary International*, *362*, 3–7. https://doi.org/10.1016/j.quaint.2014.11.018

Jolivet, R., Agram, P. S., Lin, N. Y., Simons, M., Doin, M. P., Peltzer, G., & Li, Z. (2014). Improving InSAR geodesy using Global Atmospheric Models. *Journal of Geophysical Research: Solid Earth*, *119*(3), 2324–2341. https://doi.org/10.1002/2013JB010588

Jolivet, R., Grandin, R., Lasserre, C., Doin, M. P., & Peltzer, G. (2011). Systematic InSAR tropospheric phase delay corrections from global meteorological reanalysis data. *Geophysical Research Letters*, *38*(17), 1–6. https://doi.org/10.1029/2011GL048757

Jull, A. J. T., & Burr, G. S. (2014). *Treatise on geochemistry 2nd edn (eds Holland, H. D. & Turekian, K. K.)*. Elsevier Amsterdam, The Netherlands:

Kalmeteva, Z. A., Mikolaichuk, A., Moldobekov, B. D., Meleshko, A. V, Jantaev, M. M. M., Zubovich, A. V., & Havenith, H. B. (2009). Atlas of earthquakes in Kyrgyzstan. In *CAIAG, Bishkek* (Issue January).

Kanamori, H. (1977). The energy release in great earthquakes. *Journal of Geophysical Research (1896-1977)*, *82*(20), 2981–2987. https://doi.org/https://doi.org/10.1029/JB082i020p02981

Kanamori, H., & Anderson, D. L. (1975). Theoretical Basis of Some Empirical Relations in Seismology. *Bulletin - Seismological Society of America*, *65*(5), 1073–1095.

Kárník, V. (1962). Amplitude-distance curves of surface waves at short epicentral distances (Δ<2000 km). *Studia Geophysica et Geodaetica*, *6*(4), 340–346. https://doi.org/10.1007/BF02585233

Kennett, B. L. N., Engdahl, E. R., & Buland, R. (1995). Constraints on seismic velocities in the Earth from traveltimes. *Geophysical Journal International*, *122*(1), 108–124. https://doi.org/10.1111/j.1365-246X.1995.tb03540.x

Kimball, S., Mattis, P., Natterer, M., & Neumann, S. (2013). *GIMP: G image manipulation program*. Version 2.8. http://www.gimp.org/

King, T. R., Quigley, M., & Clark, D. (2019). Surface-Rupturing Historical Earthquakes in Australia and Their Environmental Effects: New Insights from Re-Analyses of Observational Data. In *Geosciences* (Vol. 9, Issue 10). https://doi.org/10.3390/geosciences9100408

Klinger, Y., Etchebes, M., Tapponnier, P., & Narteau, C. (2011). Characteristic slip for five great earthquakes along the Fuyun fault in China. *Nature Geoscience*, *4*(6), 389–392. https://doi.org/10.1038/ngeo1158

Klinger, Y., Xu, X., Tapponnier, P., Van der Woerd, J., Lasserre, C., & King, G. (2005). High-resolution satellite imagery mapping for the surface rupture and slip distribution of the Mw ~7.8, 14 November 2001 Kokoxili earthquake, Kunlun fault, northern Tibet, China. *Bulletin of the Seismological Society of America*, *95*(5), 1970–1987. https://doi.org/10.1785/0120040233

Kondorskaya, N. V, & Shebalin, N. (1977). *New catalog of strong earthquakes in the USSR from ancient times through 1977*. Academy of Sciences, Moscow (English translation, updated through 1977, available as Report SE-31, World Data Center A for Solid Earth Geophysics, Boulder, CO).

Kreemer, C., Blewitt, G., & Klein, E. C. (2014). A geodetic plate motion and Global Strain Rate Model. *Geochemistry, Geophysics, Geosystems*, *15*, 3849–3889. https://doi.org/10.1002/2014GC005407.Received

Krüger, F., Kulikova, G., & Landgraf, A. (2017). Instrumental magnitude constraints for the 11 July 1889, Chilik earthquake. *Geological Society, London, Special Publications*, *432*(1), 41–72. https://doi.org/10.1144/SP432.8

Kulikova, G. (2016). *Source parameters of the major historical earthquakes in the Tien-Shan region from the late 19th to the early 20th century*. University of Potsdam.

Kulikova, G., & Krüger, F. (2015). Source process of the 1911 M8.0 Chon-Kemin earthquake: investigation results by analogue seismic records. *Geophysical Journal International*, *201*(3), 1891–1911. https://doi.org/10.1093/gji/ggv091

Kurtz, R., Klinger, Y., Ferry, M., & Richter, C. F. (2018). Horizontal surface-slip distribution through several seismic cycles: The Eastern Bogd fault, Gobi-Altai, Mongolia. *Tectonophysics*, *734–735*(March), 167–182. https://doi.org/10.1016/j.tecto.2018.03.011

Lal, D. (1991). Cosmic ray labeling of erosion surfaces: in situ nuclide production rates and erosion models. *Earth and Planetary Science Letters*, *104*(2), 424–439. https://doi.org/https://doi.org/10.1016/0012-821X(91)90220-C

Lamothe, M., Auclair, M., Hamzaoui, C., & Huot, S. (2003). Towards a prediction of long-term anomalous fading of feldspar IRSL. *Radiation Measurements*, *37*(4–5), 493–498. https://doi.org/10.1016/S1350-4487(03)00016-7

Lee, J.-C., Chu, H.-T., Angelier, J., Chan, Y.-C., Hu, J.-C., Lu, C.-Y., & Rau, R.-J. (2002). Geometry and structure of northern surface ruptures of the 1999 Mw=7.6 Chi-Chi Taiwan earthquake: influence from inherited fold belt structures. *Journal of Structural Geology*, *24*(1), 173–192. https://doi.org/https://doi.org/10.1016/S0191-8141(01)00056-6

Leonard, M. (2010). Earthquake fault scaling: Self-consistent relating of rupture length, width, average displacement, and moment release. *Bulletin of the Seismological Society of America*, *100*(5 A), 1971–1988. https://doi.org/10.1785/0120090189

Lettis, W. R., Wells, D. L., & Baldwin, J. N. (1997). Empirical observations regarding reverse earthquakes, blind thrust faults, and quaternary deformation: Are blind thrust faults truly blind? *Bulletin of the Seismological Society of America*, *87*(5), 1171–1198. https://doi.org/10.1785/bssa0870051171

Li, C. X., Guo, Z., & Dupont-Nivet, G. (2011). Late Cenozoic tectonic deformation across the northern foreland of the Chinese Tian Shan. *Journal of Asian Earth Sciences*, *42*(5), 1066–1073. https://doi.org/10.1016/j.jseaes.2010.08.009

Li, G., Sun, X., Wang, X. Q., Liu, D., Chen, S., Li, J., Ailixiati, Y., & Chen, L. (2016). Analysis on Activity of Bolokenu-Aqikekuduke Fault Based on GNSS (in Chinese). *Inland Earthquake*, *30*(4).

Li, Jie, Wang, X. Q., Tan, K., Liu, D., Paerhati, Jiang, J., & Fang, W. (2010). Analysis of Movement Characters of Present-day Active Tectonics of Northern TianShan Region (in Chinese). *Journal of Geodesy and Geodynamics*, *30*(6), 5.

Li, Jun, Feng, X., Chen, J., Zhao, R., Deng, Q., Tang, W., Zhang, P., Xu, X., Wu, Z., & Yang, X. (1992). Activity of the Huoerguos Active Fold and Thrust Fault Zone (in Chinese). In *Research on Active Fault (2)* (pp. 105–116).

Li, Q., Liu, M., & Stein, S. (2009). Spatiotemporal complexity of continental intraplate seismicity: Insights from geodynamic modeling and implications for seismic hazard estimation. *Bulletin of the Seismological Society of America*, *99*(1), 52–60. https://doi.org/10.1785/0120080005

Li, Y., Si, S., Lu, S., & Wang, Y. (2012). Tectonic and climatic controls on the development of the Kuitun River terraces in the northern piedmont of Tianshan Mountains (in Chinese). *Quaternary Sciences*, *32*(5), 880–890.

Lifton, Z. M., Lee, J., Frankel, K. L., Newman, A. V., & Schroeder, J. M. (2020). Quaternary slip rates on the White Mountains fault zone, eastern California: Implications for comparing geologic to geodetic slip rates across the Walker Lane. *Bulletin of the Geological Society of America*, *133*(1–2), 307–324. https://doi.org/10.1130/B35332.1

Liu-Zeng, J., Yao, W., Liu, X., Shao, Y., Wang, W., Han, L., Wang, Y., Zeng, X., Li, J., Wang, Z., Liu, Z., & Tu, H. (2022). High-resolution structure-from-motion models covering 160 km-long surface ruptures of the 2021 MW 7.4 Madoi earthquake in northern Qinghai-Tibetan Plateau. *Earthquake Research Advances*, *2*(2), 100140. https://doi.org/10.1016/j.eqrea.2022.100140

Liu-zeng, J., Zhang, Z., Wen, L., Tapponnier, P., Sun, J., Xing, X., Hu, G., Xu, Q., Zeng, L., Ding, L., Ji, C., Hudnut, K. W., & Van der Woerd, J. (2009). Co-seismic ruptures of the 12 May 2008, Ms 8.0 Wenchuan earthquake, Sichuan: East-west crustal shortening on oblique, parallel thrusts along the eastern edge of Tibet. *Earth and Planetary Science Letters*, *286*(3–4), 355–370. https://doi.org/10.1016/j.epsl.2009.07.017

Liu, C.-J. (1961). A Graticule for the Macroseismic Determination of the Depth of Focus of an Earthquake. *Chinese Journal of Geophysics*, *10*(2), 114–119.

Liu, J., Ren, Z., Zhang, H., Li, C., Zhang, Z., Zheng, W., Li, X., & Liu, C. (2022). Slip Rates Along the Laohushan Fault and Spatial Variation in Slip Rate Along the Haiyuan Fault Zone. *Tectonics*, *41*(2), 1–29. https://doi.org/10.1029/2021TC006992

Liu, M., & Stein, S. (2016). Mid-continental earthquakes: Spatiotemporal occurrences, causes, and hazards. *Earth-Science Reviews*, *162*, 364–386. https://doi.org/https://doi.org/10.1016/j.earscirev.2016.09.016

Liu, M., Stein, S., & Wang, H. (2011). 2000 years of migrating earthquakes in North China: How earthquakes in midcontinents differ from those at plate boundaries. *Lithosphere*, *3*(2), 128–132. https://doi.org/10.1130/L129.1

López-Quiroz, P., Doin, M. P., Tupin, F., Briole, P., & Nicolas, J. M. (2009). Time series analysis of Mexico City subsidence constrained by radar interferometry. *Journal of Applied Geophysics*, *69*(1), 1–15. https://doi.org/10.1016/j.jappgeo.2009.02.006

Loveless, J. P., & Meade, B. J. (2016). Two decades of spatiotemporal variations in subduction zone coupling offshore Japan. *Earth and Planetary Science Letters*, *436*, 19–30. https://doi.org/10.1016/j.epsl.2015.12.033

Lu, R., He, D., Xu, X., Wang, X., Tan, X., & Wu, X. (2018). Seismotectonics of the 2016 M 6.2 Hutubi Earthquake: Implications for the 1906 M 7.7 Manas Earthquake in the Northern Tian Shan Belt, China. *Seismological Research Letters*, *89*(1), 13–21. https://doi.org/10.1785/0220170123

Luo, F.-Z., Yao, Y., Tang, L.-H., Ge, M., & Liu, Z.-J. (2015). Characteristics of Late Quaternary Faults in Tacheng Basin, Xinjiang (in Chinese). *Inland Earthquake*, *29*(3), 197–202.

Ma, K. F., & Mori, J. (2000). Rupture Porcess of the 1999 Chi-Chi,Taiwan Earthquake from Direct Observations and Joint Inversion of Strong Motion, GPS and Teleseismic data. *2000 Western Pacific Geophysics Meeting*.

Mackenzie, D., & Elliott, A. J. (2017). Untangling tectonic slip from the potentially misleading effects of landform geometry. *Geosphere*, *13*(4), 1310–1328. https://doi.org/10.1130/GES01386.1

Mackenzie, D., Elliott, J. R., Altunel, E., Walker, R. T., Kurban, Y. C., Schwenninger, J., & Parsons, B. (2016). Seismotectonics and rupture process of the MW 7.1 2011 Van reverse-faulting earthquake, eastern Turkey, and implications for hazard in regions of distributed shortening. *Geophysical Journal International*, *206*(1), 501–524. https://doi.org/10.1093/gji/ggw158

Manighetti, I., Campillo, M., Bouley, S., & Cotton, F. (2007). Earthquake scaling, fault segmentation, and structural maturity. *Earth and Planetary Science Letters*, *253*(3–4), 429–438. https://doi.org/10.1016/j.epsl.2006.11.004

Massonnet, D., & Souyris, J.-C. (2008). *Imaging with synthetic aperture radar*. EPFL press.

McCalpin, J. P., & Carver, G. A. (2009). Paleoseismology. *International Geophysics*, *95*, 315–419.

McKenzie, D., & Jackson, J. A. (1983). The relationship between strain rates, crustal thickening, palaeomagnetism, finite strain and fault movements within a deforming zone. *Earth and Planetary Science Letters*, *65*(1), 182–202. https://doi.org/10.1016/0012-821X(83)90198-X

Meade, B. J., Klinger, Y., & Hetland, E. A. (2013). Inference of multiple earthquake-cycle relaxation timescales from irregular geodetic sampling of interseismic deformation. *Bulletin of the Seismological Society of America*, *103*(5), 2824–2835. https://doi.org/10.1785/0120130006

Mejdahl, V. (1979). Thermoluminescence dating: beta-dose attenuation in quartz grains. *Archaeometry*, *21*(pt1), 61–72. http://inis.iaea.org/search/search.aspx?orig_q=RN:10451974

Middleton, T., Walker, R. T., Parsons, B., Lei, Q., Zhou, Y., & Ren, Z. (2015). A major, intraplate, normal-faulting earthquake: The 1739 Yinchuan event in northern China. *Journal of Geophysical Research : Solid Earth*, *4*, 293–320. https://doi.org/10.1002/2015JB012355.

Middleton, T., Walker, R. T., Rood, D. H., Rhodes, E. J., Parsons, B., Lei, Q., Elliott, J. R., Ren, Z., & Zhou, Y. (2016). The tectonics of the western Ordos Plateau, Ningxia, China: Slip rates on the Luoshan and East Helanshan Faults. *Tectonics*, *35*(11), 2754–2777. https://doi.org/10.1002/2016TC004230

Molnar, P., & Deng, Q. (1984). Faulting associated with large earthquakes and the average rate of deformation in central and eastern Asia. *Journal of Geophysical Research: Solid Earth*, *89*, 6203–6227.

Molnar, P., & Ghose, S. (2000). Seismic moments of major earthquakes and the rate of shortening across the Tien Shan. *Geophysical Research Letters*, *27*(16), 2377–2380. https://doi.org/10.1029/2000GL011637

Molnar, P., & Tapponnier, P. (1975a). Cenozoic tectonics of Asia: Effects of a continental collision, Science. *Science*, *30*(3), 213–219.

Molnar, P., & Tapponnier, P. (1975b). Cenozoic Tectonics of Asia: Effects of a Continental Collision. *Science*, *189*(4201), 419–426. http://www.jstor.org/stable/1740465

Mooney, W. D., Laske, G., & Masters, T. G. (1998). CRUST 5.1: A global crustal model at 5° x 5°. *Journal of Geophysical Research: Solid Earth*, *103*(B1), 727–747.

Mosca, I., Baptie, B., Sargeant, S., & Walker, R. T. (2019). Integrating outcomes from probabilistic and deterministic seismic hazard analysis in the Tien Shan. *Bulletin of the Seismological Society of America*, *109*(2), 688–715. https://doi.org/10.1785/0120180081

Moss, R. E. S., & Ross, Z. E. (2011). Probabilistic fault displacement hazard analysis for reverse faults. *Bulletin of the Seismological Society of America*, *101*(4), 1542–1553. https://doi.org/10.1785/0120100248

Mousavi, Z., Fattahi, M., Khatib, M., Talebian, M., Pathier, E., Walpersdorf, A., Sloan, R. A., Thomas, A. L., Rhodes, E. J., Clive, F., Dodds, N., & Walker, R. T. (2021). Constant Slip Rate on the Doruneh Strike-Slip Fault, Iran, Averaged Over Late Pleistocene, Holocene, and Decadal Timescales. *Tectonics*, *40*(6). https://doi.org/10.1029/2020TC006256

Murray, A. S., & Roberts, R. G. (1997). Determining the burial time of single grains of quartz using optically stimulated luminescence. *Earth and Planetary Science Letters*, *152*(1–4), 163–180. https://doi.org/10.1016/s0012-821x(97)00150-7

Murray, A. S., & Wintle, A. G. (2000). Luminescence dating of quartz using an improved single-aliquot regenerative-dose protocol. *Radiation Measurements*, *32*(1), 57–73. https://doi.org/10.1016/S1350-4487(99)00253-X

Murray, A. S., & Wintle, A. G. (2003). The single aliquot regenerative dose protocol: Potential for improvements in reliability. *Radiation Measurements*, *37*(4–5), 377–381. https://doi.org/10.1016/S1350-4487(03)00053-2

Mushketov, I. V. (1890). Le tremblement de terre de Verny, 28 Mai (9 Juin) 1887. *Memoires Du Comite Geologique*, *X*(1).

Mushketov, I. V, & Orlov, A. P. (1893). Catalog of earthquakes of the Russian Empire. *Russian Geoglogical Society, St. Petersburg (in Russian)*.

Nash, D. B. (1980). Morphologic dating of degraded normal fault scarps. *The Journal of Geology*, *88*(3), 353–360.

Negishi, H., Mori, J., Sato, T., Singh, R., Kumar, S., & Hirata, N. (2002). Size and orientation of the fault plane for the 2001 Gujarat, India earthquake (Mw7.7) from aftershock observations: A high stress drop event. *Geophysical Research Letters*, *29*(20), 10–14. https://doi.org/https://doi.org/10.1029/2002GL015280

Nishiizumi, K., Imamura, M., Caffee, M. W., Southon, J. R., Finkel, R. C., & McAninch, J. (2007). Absolute calibration of 10Be AMS standards. *Nuclear Instruments and Methods in Physics Research, Section B: Beam Interactions with Materials and Atoms*, *258*(2), 403–413. https://doi.org/10.1016/j.nimb.2007.01.297

Nissen, E., Walker, R. T., Bayasgalan, A., Carter, A., Fattahi, M., Molor, E., Schnabel, C., West, A. J., & Xu, S. (2009). The late Quaternary slip-rate of the Har-Us-Nuur fault (Mongolian Altai) from cosmogenic 10Be and luminescence dating. *Earth and Planetary Science Letters*, *286*(3–4), 467–478. https://doi.org/10.1016/j.epsl.2009.06.048

Nowicki Jessee, M. A., Hamburger, M. W., Ferrara, M. R., McLean, A., & FitzGerald, C. (2020). A global dataset and model of earthquake-induced landslide fatalities. *Landslides*, *17*(6), 1363–1376. https://doi.org/10.1007/s10346-020-01356-z

Ou, Q., Daout, S., Weiss, J. R., Shen, L., Lazecky, M., Wright, T. J., & Parsons, B. (2022). Large-Scale Interseismic Strain Mapping of the NE Tibetan Plateau From Sentinel-1 Interferometry. *Journal of Geophysical Research: Solid Earth*, *127*(6). https://doi.org/10.1029/2022JB024176

Ou, Q., Kulikova, G., Yu, J., Elliott, A. J., Parsons, B., & Walker, R. T. (2020). Magnitude of the 1920 Haiyuan Earthquake Reestimated Using Seismological and Geomorphological Methods. *Journal of Geophysical Research: Solid Earth*, *125*(8). https://doi.org/10.1029/2019JB019244

Pang, L., Lu, H., Wu, D., Guan, X., Zhao, J., Zheng, X., & Li, Y. (2021). Late Pleistocene Uniform Rate of Thrusting Along the Fault's Strike: A Case Study From the Northern Tian Shan Foreland. *Tectonics*, *40*(4), 1–23. https://doi.org/10.1029/2021tc006726

Pantosti, D., Schwartz, D. P., & Valensise, G. (1993). Paleoseismology along the 1980 surface rupture of the Irpinia fault: implications for earthquake recurrence in the southern Apennines, Italy. *Journal of Geophysical Research: Solid Earth*, *98*(B4), 6561–6577.

Papanikolaou, I. D., Roberts, G. P., & Michetti, A. M. (2005). Fault scarps and deformation rates in Lazio-Abruzzo, Central Italy: Comparison between geological fault slip-rate and GPS data. *Tectonophysics*, *408*(1–4), 147–176. https://doi.org/10.1016/j.tecto.2005.05.043

Pierce, I., Wesnousky, S. G., Owen, L. A., Bormann, J. M., Li, X., & Caffee, M. W. (2021). Accommodation of Plate Motion in an Incipient Strike-Slip System: The Central Walker Lane. *Tectonics*, *40*(2). https://doi.org/10.1029/2019TC005612

Pierce, K. L., & Colman, S. M. (1986). Effect of height and orientation (microclimate) on geomorphic degradation rates and processes, late-glacial terrace scarps in central Idaho. *Geological Society of America Bulletin*, *97*(7), 869–885. https://doi.org/10.1130/0016-7606(1986)97<869:EOHAOM>2.0.CO;2

Pinel-Puysségur, B., Michel, R., & Avouac, J.-P. (2011). Multi-link SAR interferograms: Enhancement of a wrapped interferometric database. *International Geoscience and Remote Sensing Symposium (IGARSS)*, *5*(3), 1627–1629. https://doi.org/10.1109/IGARSS.2011.6049543

Pollitz, F. F., Brooks, B., Tong, X., Bevis, M. G., Foster, J. H., Bürgmann, R., Smalley, R., Vigny, C., Socquet, A., Ruegg, J., Campos, J., Barrientos, S., Parra, H., Soto, J. C. B., Cimbaro, S., & Blanco, M. (2011). Coseismic slip distribution of the February 27, 2010 Mw 8.8 Maule, Chile earthquake. *Geophysical Research Letters*, *38*(9), 1–5. https://doi.org/10.1029/2011gl047065

Prescott, J. R., & Hutton, J. T. (1994). Cosmic ray contributions to dose rates for luminescence and ESR dating: Large depths and long-term time variations. *Radiation Measurements*, *23*(2–3), 497–500. https://doi.org/10.1016/1350-4487(94)90086-8

Quigley, M., Jiménez, A., Duffy, B., & King, T. R. (2019). Physical and Statistical Behavior of Multifault Earthquakes: Darfield Earthquake Case Study, New Zealand. *Journal of Geophysical Research: Solid Earth*, *124*(5), 4788–4810. https://doi.org/10.1029/2019JB017508

Quigley, M., Van Dissen, R., Litchfield, N., Villamor, P., Duffy, B., Barrell, D. J. A., Furlong, K., Stahl, T., Bilderback, E., & Noble, D. (2012). Surface rupture during the 2010 Mw 7.1 Darfield (Canterbury) earthquake: Implications for fault rupture dynamics and seismic-hazard analysis. *Geology*, *40*(1), 55–58. https://doi.org/10.1130/G32528.1

Ren, G., Li, C., Wu, C., Zhang, H., Wang, S., Ren, Z., Lei, Q., & Li, X. (2021). Late Quaternary Slip Rate and Kinematics of the Baoertu Fault, Constrained by 10Be Exposure Ages of Displaced Surfaces within Eastern Tian Shan. *Lithosphere*, *2021*(1), 1–19. https://doi.org/10.2113/2021/7866920

Rhodes, E. J. (1988). Methodological considerations in the optical dating of quartz. *Quaternary Science Reviews*, *7*(3–4), 395–400. https://doi.org/10.1016/0277-3791(88)90035-2

Rhodes, E. J. (2011). Optically Stimulated Luminescence Dating of Sediments over the Past 200,000 Years. *Annual Review of Earth and Planetary Sciences*, *39*(1), 461–488. https://doi.org/10.1146/annurev-earth-040610-133425

Rhodes, E. J. (2015a). Dating sediments using potassium feldspar single-grain IRSL: Initial methodological considerations. *Quaternary International*, *362*, 14–22. https://doi.org/10.1016/j.quaint.2014.12.012

Rhodes, E. J. (2015b). Dating sediments using potassium feldspar single-grain IRSL: Initial methodological considerations. *Quaternary International*, *362*, 14–22. https://doi.org/10.1016/j.quaint.2014.12.012

Rhodes, E. J., Fanning, P. C., & Holdaway, S. J. (2010). Developments in optically stimulated luminescence age control for geoarchaeological sediments and hearths in western New South Wales, Australia. *Quaternary Geochronology*, *5*(2), 348–352. https://doi.org/https://doi.org/10.1016/j.quageo.2009.04.001

Richter, C. F. (1958). *Elementary Seismology*. W.H. Freeman, San Francisco.

Rizza, M. A., Abdrakhmatov, K. E., Walker, R. T., Braucher, R., Guillou, V., Carr, A. S., Campbell, G. E., McKenzie, D., Jackson, J. A., Aumaître, G., Bourlès, D. L., & Keddadouche, K. (2019). Rate of Slip From Multiple Quaternary Dating Methods and Paleoseismic Investigations Along the Talas-Fergana Fault: Tectonic Implications for the Tien Shan Range. *Tectonics*, *38*(7), 2477–2505. https://doi.org/10.1029/2018TC005188

Rizza, M. A., Richter, C. F., Prentice, C., Vassallo, R., Braucher, R., Larroque, C., Arzhannikova, A., Mahan, S. A., Massault, M., Michelot, J. L., Todbileg, M., Arnold, M., Aumaître, G., Bourlès, D. L., & Keddadouche, K. (2015). Earthquake

geology of the Bulnay fault (Mongolia). *Bulletin of the Seismological Society of America*, *105*(1), 72–93. https://doi.org/10.1785/0120140119

Rodgers, D. W., & Little, T. A. (2006). World's largest coseismic strike-slip offset: The 1855 rupture of the Wairarapa Fault, New Zealand, and implications for displacement/length scaling of continental earthquakes. *Journal of Geophysical Research: Solid Earth*, *111*(B12), 1–19. https://doi.org/10.1029/2005JB004065

Rogozhin, E. A., Shen, J., Chen, Q., & Shen, X. (2015). Paleoseismic ruptures in the potential seismic source of major earthquakes in the Dzhungar Tien Shan. *Seismic Instruments*, *51*(2), 99–110. https://doi.org/10.3103/s0747923915020073

Rood, A. H., Rood, D. H., Stirling, M. W., Madugo, C. M., Abrahamson, N. A., Wilcken, K. M., Gonzalez, T., Kottke, A., Whittaker, A. C., Page, W. D., & Stafford, P. J. (2020). Earthquake Hazard Uncertainties Improved Using Precariously Balanced Rocks. *AGU Advances*, *1*(4). https://doi.org/10.1029/2020av000182

Rosen, P. A., Hensley, S., Peltzer, G., & Simons, M. (2004). Updated repeat orbit interferometry package released. *EOS, Transactions American Geophysical Union*, *85*(5), 47. https://doi.org/10.1029/2004EO050004

Ross, Z. E., Idini, B., Jia, Z., Stephenson, O. L., Zhong, M., Wang, X., Zhan, Z., Simons, M., Fielding, E. J., Yun, S.-H., Hauksson, E., Moore, A. W., Liu, Z., & Jung, J. (2019). Hierarchical interlocked orthogonal faulting in the 2019 Ridgecrest earthquake sequence. *Science*, *366*(6463), 346–351. https://doi.org/10.1126/science.aaz0109

Rossi, C. (2016). *Uncertainty assessment of single-pass TanDEM-X DEMs in selected applications*. DLR, Deutsches Zentrum für Luft-und Raumfahrt.

Rust, D. J., Korzhenkov, A. M., & Tibaldi, A. (2018). Geologic Slip-Rate Determinations on the Talas-Fergana Fault: Mismatch With Geodetic Slip Rate. *Geophysical Research Letters*, *45*(9), 3880–3888. https://doi.org/10.1002/2017GL076990

Salditch, L., Stein, S., Neely, J., Spencer, B. D., Brooks, E. M., Agnon, A., & Liu, M. (2020). Earthquake supercycles and Long-Term Fault Memory. *Tectonophysics*, *774*(July 2019), 228289. https://doi.org/10.1016/j.tecto.2019.228289

Satake, K., Fujii, Y., Harada, T., & Namegaya, Y. (2013). Time and space distribution of coseismic slip of the 2011 Tohoku earthquake as inferred from tsunami waveform data. *Bulletin of the Seismological Society of America*, *103*(2B), 1473–1492.

Savage, J. C., & Burford, R. O. (1973). Geodetic Determination of Relative Plate Motion in Central California. *Journal of Geodesy and Geodynamics*, *78*(5), 832–845.

Savage, J. C., & Prescott, W. H. (1978). Asthenosphere readjustment and the earthquake cycle. *Journal of Geophysical Research: Solid Earth*, *83*(B7), 3369–3376. https://doi.org/10.1029/jb083ib07p03369

Schaefer, J. M., Codilean, A. T., Willenbring, J. K., Lu, Z.-T., Keisling, B., Fülöp, R.-H., & Val, P. (2022). Cosmogenic nuclide techniques. *Nature Reviews Methods Primers*, *2*(1). https://doi.org/10.1038/s43586-022-00096-9

Schlupp, A., & Cisternas, A. (2007). Source history of the 1905 great Mongolian earthquakes (Tsetserleg, Bolnay). *Geophysical Journal International*, *169*(3), 1115–1131. https://doi.org/10.1111/j.1365-246x.2007.03323.x

Schmidt, D. A., & Bürgmann, R. (2006). InSAR constraints on the source parameters of the 2001 Bhuj earthquake. *Geophysical Research Letters*, *33*(2). https://doi.org/https://doi.org/10.1029/2005GL025109

Scholz, C. H. (1982). Scaling laws for large earthquakes: consequences for physical models. *The Geographical Journal*, *48*(4), 348. https://doi.org/10.2307/1779766

Scholz, C. H. (2002). *THe Mechanics of Earthquakes and Faulting* (2nd ed.). Cambridge University Press, Cambridge.

Scholz, C. H., Aviles, C. A., & Wesnousky, S. G. (1986). Scaling differences between large interplate and intraplate earthquakes. *Bulletin of the Seismological Society of America*, *76*(1), 65–70.

Schweitzer, J. (2001). HYPOSAT – An Enhanced Routine to Locate Seismic Events. *Pure and Applied Geophysics*, *158*(1), 277–289. https://doi.org/10.1007/PL00001160

Schweitzer, J. (2012). User manual for HYPOSAT and HYPOMOD. In *New Manual of Seismological Observatory Practice 2 (NMSOP-2)* (pp. 1–38). German Research Centre for Geosciences (GFZ). http://gfzpublic.gfz-potsdam.de/pubman/item/escidoc:4135:3/component/escidoc:4136/PD11.1rev1.pdf

Seismological Bureau of Xinjiang. (1985). *Compilation of Seismic Data in Xinjiang Uygur Autonomous Region (in Chinese)* (pp. 38–44). Seismological Press, Beijing.

Selander, J., Oskin, M. E., Ormukov, C., & Abdrakhmatov, K. E. (2012). Inherited strike-slip faults as an origin for basement-cored uplifts: Example of the Kungey and Zailiskey ranges, northern Tian Shan. *Tectonics*, *31*(4), 1–22. https://doi.org/10.1029/2011TC003002

Shean, D. (2017). *High Mountain Asia 8-meter DEM Mosaics Derived from Optical Imagery, Version 1. [Indicate subset used]. Boulder, Colorado USA.* NASA National Snow and Ice Data Center Distributed Active Archive Center. https://doi.org/10.5067/KXOVQ9L172S2

Shen, J., Wang, Y., & Li, Y. (2011). Characteristics of the Late Quaternary right-lateral strike-slip movement of Bolokenu-Aqikekuduk fault in northern Tianshan Mountains, NW China. *Geoscience Frontiers*, *2*(4), 519–527. https://doi.org/10.1016/j.gsf.2011.05.004

Shen, J., Wang, Y., Li, Y., Jiang, H., & Xiang, Z. (2003). Late Quaternary Right-lateral Strike-slip Faulting along the Bolokenu-Aqikekuduke Fault in Chinese Tian Shan. *Seismology and Geology*, *25*(2), 183–194.

Shen, L., Hooper, A. J., & Elliott, J. R. (2019). A Spatially Varying Scaling Method for InSAR Tropospheric Corrections Using a High-Resolution Weather Model. *Journal of Geophysical Research: Solid Earth*, *124*(4), 4051–4068. https://doi.org/https://doi.org/10.1029/2018JB016189

Shimazaki, K., & Nakata, T. (1980). Time-predictable recurrence model for large earthquakes. *Geophysical Research Letters*, *7*(4), 279–282. https://doi.org/https://doi.org/10.1029/GL007i004p00279

Sieh, K. (1978). Prehistoric large earthquakes produced by slip on the San Andreas fault at Pallett Creek, California. *Journal of Geophysical Research: Solid Earth*, *83*(B8), 3907–3939.

Sieh, K. (1996). The repetition of large-earthquake ruptures. *Proceedings of the National Academy of Sciences*, *93*(9), 3764–3771. https://doi.org/10.1073/pnas.93.9.3764

Sieh, K., Jones, L., Hauksson, E., Hudnut, K., Eberhart-Phillips, D., Heaton, T., Hough, S., Hutton, K., Kanamori, H., Lilje, A., Lindvall, S., McGill, S. F., Mori, J., Rubin, C. M., Spotila, J. A., Stock, J., Thio, H. K., Treiman, J., Wernicke, B., & Zachariasen, J. (1993). Near-field Investigations of the Landers Earthquake Sequence, April to July 1992. *Science (New York, N.Y.)*, *260*(5105), 171–176. https://doi.org/10.1126/science.260.5105.171

Simpson, D. W., Hamburger, M. W., Pavlov, V. D., & Nersesov, I. L. (1981). Tectonics and seismicity of the Toktogul Reservoir Region, Kirgizia, USSR. *Journal of Geophysical Research: Solid Earth*, *86*(B1), 345–358. https://doi.org/https://doi.org/10.1029/JB086iB01p00345

Sloan, R. A., Jackson, J. A., McKenzie, D., & Priestley, K. (2011). Earthquake depth distributions in central Asia, and their relations with lithosphere thickness, shortening and extension. *Geophysical Journal International*, *185*(1), 1–29. https://doi.org/10.1111/j.1365-246X.2010.04882.x

Smedley, R. K., Duller, G. A. T., Pearce, N. J. G., & Roberts, H. M. (2012). Determining the K-content of single-grains of feldspar for luminescence dating. *Radiation Measurements*, *47*(9), 790–796. https://doi.org/10.1016/j.radmeas.2012.01.014

Smedley, R. K., Duller, G. A. T., & Roberts, H. M. (2015). Bleaching of the post-IR IRSL signal from individual grains of K-feldspar: Implications for single-grain dating. *Radiation Measurements*, *79*, 33–42. https://doi.org/10.1016/j.radmeas.2015.06.003

Somerville, P. (2021). Scaling relations between seismic moment and rupture area of earthquakes in stable continental regions. *Earthquake Spectra*, *37*(1_suppl), 1534–1549. https://doi.org/10.1177/8755293020988024

Spelz, R. M., Fletcher, J. M., Owen, L. A., & Caffee, M. W. (2008). Quaternary alluvial-fan development, climate and morphologic dating of fault scarps in Laguna Salada, Baja California, Mexico. *Geomorphology*, *102*(3–4), 578–594. https://doi.org/10.1016/j.geomorph.2008.06.001

Sreejith, K. M., Sunil, P. S., Agrawal, R., Saji, A. P., Ramesh, D. S., & Rajawat, A. S. (2016). Coseismic and early postseismic deformation due to the 25 April 2015, Mw 7.8 Gorkha, Nepal, earthquake from InSAR and GPS measurements. *Geophysical Research Letters*, *43*(7), 3160–3168. https://doi.org/https://doi.org/10.1002/2016GL067907

Stahl, T. A., Cowgill, E., Boichenko, G., Vasey, D. A., & Godoladze, T. (2022). Recent Surface Rupturing Earthquakes along the South Flank of the Greater Caucasus near Tbilisi, Georgia. *Bulletin of the Seismological Society of America*, 1–19. https://doi.org/10.1785/0120210267

Stein, S., Liu, M., Calais, E., & Li, Q. (2009). Mid-continent earthquakes as a complex system. *Seismological Research Letters*, *80*(4), 551–553. https://doi.org/10.1785/gssrl.80.4.551

Stewart, N., Gaudemer, Y., Manighetti, I., Serreau, L., Vincendeau, A., Dominguez, S., Mattéo, L., & Malavieille, J. (2018). "3D_Fault_Offsets," a Matlab Code to Automatically Measure Lateral and Vertical Fault Offsets in Topographic Data: Application to San Andreas, Owens Valley, and Hope Faults. *Journal of Geophysical Research: Solid Earth*, *123*(1), 815–835. https://doi.org/10.1002/2017JB014863

Stockmeyer, J. M., Shaw, J. H., Brown, N. D., Rhodes, E. J., Richardson, P. W., Wang, M., Lavin, L. C., & Guan, S. (2017). Active thrust sheet deformation over multiple rupture cycles: A quantitative basis for relating terrace folds to fault slip rates. *Bulletin of the Geological Society of America*, *129*(9–10), 1337–1356. https://doi.org/10.1130/B31590.1

Stockmeyer, J. M., Shaw, J. H., & Guan, S. (2014). Seismic Hazards of Multisegment Thrust-Fault Ruptures: Insights from the 1906 Mw 7.4-8.2 Manas, China, Earthquake. *Seismological Research Letters*, *85*(4), 801–808. https://doi.org/10.1785/0220140026

Stone, J. O. (2000). Air pressire and cosmogenic isotpoe production. *Journal of Geophysical Research*, *105*(1), 753–759.

Storchak, D., Di Giacomo, D., Bondár, I., Engdahl, E. R., Harris, J., Lee, W. H. K., Villaseñor, A., & Bormann, P. (2013). Public Release of the ISC–GEM Global Instrumental Earthquake Catalogue (1900–2009). *Seismological Research Letters*, *84*(5), 810–815. https://doi.org/10.1785/0220130034

Su, P., He, H., Wei, Z., Lu, R., Shi, F., Sun, H., Tan, X., & Hao, H. (2018). A new shortening rate across the Dushanzi anticline in the northern Tian Shan Mountains, china from lidar data and a seismic reflection profile. *Journal of Asian Earth Sciences*, *163*(June), 131–141. https://doi.org/10.1016/j.jseaes.2018.06.008

Suvorov, A. I. (1964). Contribution to the description of the aktas fault zone, central kazakhstan. *International Geology Review*, *6*(3), 507–518. https://doi.org/10.1080/00206816409473927

Tapponnier, P., & Molnar, P. (1979). Active faulting and cenozoic tectonics of the Tien Shan, Mongolia, and Baykal Regions. *Journal of Geophysical Research: Solid Earth*, *84*(B7), 3425–3459. https://doi.org/https://doi.org/10.1029/JB084iB07p03425

Thatcher, W. (2009). How the continents deform: The evidence from tectonic geodesy. *Annual Review of Earth and Planetary Sciences*, *37*, 237–262. https://doi.org/10.1146/annurev.earth.031208.100035

Thingbaijam, K. K. S., Mai, P. M., & Goda, K. (2017). New empirical earthquake source-scaling laws. *Bulletin of the Seismological Society of America*, *107*(5), 2225–2246. https://doi.org/10.1785/0120170017

Thollard, F., Clesse, D., Doin, M. P., Donadieu, J., Durand, P., Grandin, R., Lasserre, C., Laurent, C., Deschamps-ostanciaux, E., Pathier, E., Pointal, E., Proy, C., & Specht, B. (2021). FLATSIM : The ForM @ Ter LArge-Scale Multi-Temporal. *Remote Sensing*, *13*(3734), 1–29.

Thomas, J. C., Lanza, R., Kazansky, A., Zykin, V., Semakov, N., Mitrokhin, D., & Delvaux, D. (2002). Paleomagnetic study of Cenozoic sediments from the Zaisan basin (SE Kazakhstan) and the Chuya depression (Siberian Altai): Tectonic implications for central Asia. *Tectonophysics*, *351*(1–2), 119–137. https://doi.org/10.1016/S0040-1951(02)00128-2

Thompson, S. C. (2001). *Active tectonics in the central Tien Shan, Kyrgyz Republic (Doctoral Dissertation)*. University of Washington.

Thompson, S. C., Weldon, R. J., Rubin, C. M., Abdrakhmatov, K. E., Molnar, P., & Berger, G. W. (2002). Late Quaternary slip rates across the central Tien Shan, Kyrgyzstan, central Asia. *Journal of Geophysical Research: Solid Earth*, *107*(B9), 7-1-7–31. https://doi.org/10.1029/2001jb000596

Timar, A., Vandenberghe, D., Panaiotu, E. C., Panaiotu, C. G., Necula, C., Cosma, C., & Van den haute, P. (2010). Optical dating of Romanian loess using fine-grained quartz. *Quaternary Geochronology*, *5*(2–3), 143–148. https://doi.org/10.1016/j.quageo.2009.03.003

Tong, X., Sandwell, D. T., & Fialko, Y. (2010). Coseismic slip model of the 2008 Wenchuan earthquake derived from joint inversion of interferometric synthetic aperture radar, GPS, and field data. *Journal of Geophysical Research*, *115*(B4), 1–19. https://doi.org/10.1029/2009jb006625

Tong, X., Smith-Konter, B., & Sandwell, D. T. (2014). Is there a discrepancy between geological and geodetic slip rates along the San Andreas Fault System? *AGU: Journal of Geophysical Research, Solid Earth*, *119*(iv), 3076–3095. https://doi.org/10.1002/2013JB010765.Received

Trauerstein, M., Lowick, S. E., Preusser, F., Rufer, D., & Schlunegger, F. (2012). Exploring fading in single grain feldspar IRSL measurements. *Quaternary Geochronology*, *10*, 327–333. https://doi.org/10.1016/j.quageo.2012.02.004

Trauerstein, M., Lowick, S. E., Preusser, F., & Schlunegger, F. (2014). Small aliquot and single grain IRSL and post-IR IRSL dating of fluvial and alluvial sediments from the Pativilca valley, Peru. *Quaternary Geochronology*, *22*, 163–174. https://doi.org/10.1016/j.quageo.2013.12.004

Tsai, C.-H., Abdrakhmatov, K. E., Mukambayev, A., Elliott, A. J., Elliott, J. R., Grützner, C., Rhodes, E., Ivester, A., Walker, R. T., & Wilkinson, R. (2022). Probing the upper end of intra-continental earthquake magnitude: a prehistoric example from the Dzhungarian and Lepsy faults of Kazakhstan. *Tectonics*, *41*(e2022TC007300).

Tsai, C.-H., Walker, R. T., Daout, S., Abdrakhmatov, K. E., Mukambayev, A., Grützner, C., Rhodes, E. J., & Kulikova, G. (2021). Great Earthquakes in the Dzhungarian Region Interpreted from Palaeo-and Historical Sources: Implications for Intraplate Earthquake Occurrence and Scaling. *AGU Fall Meeting 2021*.

U. S. Geological Survey. (2022). *Search Earthquake Catalog, accessed Dec., 2022 at URL https://earthquake.usgs.gov/earthquakes/search/*.

Vilgelmzon, P. M. (1947). Kemin-Chu Earthquake of July 21, 1938. *Academy of Sciences of the Kazakh, Almaty SSR*, 40.

Virtanen, P., Gommers, R., Oliphant, T. E., Haberland, M., Reddy, T., Cournapeau, D., Burovski, E., Peterson, P., Weckesser, W., Bright, J., van der Walt, S. J., Brett, M., Wilson, J., Millman, K. J., Mayorov, N., Nelson, A. R. J., Jones, E., Kern, R., Larson, E., … SciPy 1.0 Contributors. (2020). SciPy 1.0: Fundamental Algorithms for Scientific Computing in Python. In *Nature Methods* (Vol. 17, pp. 261–272). https://doi.org/10.1038/s41592-019-0686-2

Visocekas, R. (1985). Tunnelling radiative recombination in labradorite: Its association with anomalous fading of thermoluminescence. *Nuclear Tracks and Radiation Measurements (1982)*, *10*(4–6), 521–529. https://doi.org/10.1016/0735-245X(85)90053-5

Voytovich, V. S. (1965). Development of dzhungar deep fault. *International Geology Review*, *7*(5), 874–883. https://doi.org/10.1080/00206816509474154

Voytovich, V. S. (1969). Nature of the Dzungarian deep fault (in Russian). *Trans. Geol. Inst., Acad. Sci. USSR*, *183*, 189.

Walker, R. T., Bezmenov, Y., Begenjev, G., Carolin, S., Dodds, N., Grützner, C., Jackson, J. A., Mirzin, R., Mousavi, Z., & Rhodes, E. J. (2021). Slip-rate on the Main Köpetdag (Kopeh Dagh) Strike-slip fault, Turkmenistan, and the active tectonics of the South Caspian. *Tectonics*, 1–27. https://doi.org/10.1029/2021tc006846

Walker, R. T., Wegmann, K. W., Bayasgalan, A., Carson, R. J., Elliott, J. R., Fox, M., Nissen, E., Sloan, R. A., Williams, J. M., & Wright, E. (2017). The egiin davaa prehistoric rupture, central mongolia: A large magnitude normal faulting earthquake on a reactivated fault with little cumulative slip located in a slowly deforming intraplate setting. *Geological Society Special Publication*, *432*(1), 187–212. https://doi.org/10.1144/SP432.4

Wallace, R. (1970). Earthquake recurrence intervals on the San Andreas fault. *Bulletin of the Geological Society of America*, *81*(10), 2875–2889. https://doi.org/10.1130/0016-7606(1970)81[2875:ERIOTS]2.0.CO;2

Wallace, R. (1977). Profiles and ages of young fault scarps, north-central Nevada. *GSA Bulletin*, *88*(9), 1267–1281. https://doi.org/10.1130/0016-7606(1977)88<1267:PAAOYF>2.0.CO;2

Walters, R. J., Elliott, J. R., Li, Z., & Parsons, B. (2013). Rapid strain accumulation on the Ashkabad fault (Turkmenistan) from atmosphere-corrected InSAR. *Journal of Geophysical Research: Solid Earth*, *118*(7), 3674–3690. https://doi.org/10.1002/jgrb.50236

Walters, R. J., Holley, R. J., Parsons, B., & Wright, T. J. (2011). Interseismic strain accumulation across the North Anatolian Fault from Envisat InSAR measurements. *Geophysical Research Letters*, *38*(5), 1–5. https://doi.org/10.1029/2010GL046443

Wang, C. Y., Yang, Z. E., Luo, H., & Mooney, W. D. (2004). Crustal structure of the northern margin of the eastern Tien Shan, China, and its tectonic implications for the 1906 M∼7.7 Manas earthquake. *Earth and Planetary Science Letters*, *223*(1–2), 187–202. https://doi.org/10.1016/j.epsl.2004.04.015

Wang, K., Hu, Y., & He, J. (2012). Deformation cycles of subduction earthquakes in a viscoelastic Earth. *Nature*, *484*(7394), 327–332. https://doi.org/10.1038/nature11032

Wang, M., & Shen, Z. K. (2020). Present-Day Crustal Deformation of Continental China Derived From GPS and Its Tectonic Implications. *Journal of Geophysical Research: Solid Earth*, *125*(2). https://doi.org/10.1029/2019JB018774

Wang, Q., Ji, Z., Zhao, C., Wang, H., Nie, X., & Li, Z. (2015). Research on source rupture process of Ms 6.6 earthquake of June 30, 2012, in the border area of Xinyuan and Hejing County, Xinjiang (in Chinese). *Seismology and Geology*, *37*(1), 33–43.

Wang, X., Xu, C., Wen, Y., Wang, S., Xu, G., Xiao, Z., & Fang, L. (2019). The 2016 Mw 6.0 Hutubi earthquake: A blind thrust event along the northern Tian Shan front. *Journal of Asian Earth Sciences*, *173*(December 2018), 79–87. https://doi.org/10.1016/j.jseaes.2019.01.011

Weertman, J., & Weertman, J. R. (1964). *Elementary dislocation theory*. Macmillan.

Weiss, J. R., Walters, R. J., Morishita, Y., Wright, T. J., Lazecky, M., Wang, H., Hussain, E., Hooper, A. J., Elliott, J. R., Rollins, C., Yu, C., González, P. J., Spaans, K., Li, Z., & Parsons, B. (2020). High-Resolution Surface Velocities and Strain for Anatolia From Sentinel-1 InSAR and GNSS Data. *Geophysical Research Letters*, *47*(17). https://doi.org/10.1029/2020GL087376

Wells, D. L., & Coppersmith, K. J. (1994). New empirical relationships among magnitude, rupture length, rupture width, rupture area, and surface displacement. *Bulletin - Seismological Society of America*, *84*(4), 974–1002.

Wesnousky, S. G. (2008). Displacement and geometrical characteristics of earthquake surface ruptures: Issues and implications for seismic-hazard analysis and the process of earthquake rupture. *Bulletin of the Seismological Society of America*, *98*(4), 1609–1632. https://doi.org/10.1785/0120070111

Westoby, M. J., Brasington, J., Glasser, N. F., Hambrey, M. J., & Reynolds, J. M. (2012). "Structure-from-Motion" photogrammetry: A low-cost, effective tool for geoscience applications. *Geomorphology*, *179*, 300–314. https://doi.org/10.1016/j.geomorph.2012.08.021

Wilcken, K. M., Fink, D., Hotchkis, M. A. C., Garton, D., Button, D., Mann, M., Kitchen, R., Hauser, T., & O'Connor, A. (2017). Accelerator Mass Spectrometry on SIRIUS: New 6MV spectrometer at ANSTO. *Nuclear Instruments and Methods in Physics Research Section B: Beam Interactions with Materials and Atoms*, *406*, 278–282. https://doi.org/https://doi.org/10.1016/j.nimb.2017.01.003

Wimpenny, S., & Watson, C. S. (2020). gWFM: A global catalog of moderate-magnitude earthquakes studied using teleseismic body waves. *Seismological Research Letters*, *92*(1), 212–226. https://doi.org/10.1785/0220200218

Windley, B. F., Alexeiev, D., Xiao, W., Kröner, A., & Badarch, G. (2007). Tectonic models for accretion of the Central Asian Orogenic Belt. *Journal of the Geological Society*, *164*(1), 31–47.

Windley, B. F., Allen, M. B., Zhang, C., Zhao, Z.-Y., & Wang, G.-R. (1990). Paleozoic accretion and Cenozoic redeformation of the Chinese Tien Shan Range, central Asia. *Geology*, *18*(2), 128–131. https://doi.org/10.1130/0091-7613(1990)018<0128:PAACRO>2.3.CO;2

Wintle, A. G. (1973). Anomalous Fading of Thermo-luminescence in Mineral Samples. *Nature*, *245*, 143–144.

Wintle, A. G., & Murray, A. S. (2006). A review of quartz optically stimulated luminescence characteristics and their relevance in single-aliquot regeneration dating protocols. *Radiation Measurements*, *41*(4), 369–391. https://doi.org/10.1016/j.radmeas.2005.11.001

Wright, T. J., Parsons, B., & Lu, Z. (2004). Toward mapping surface deformation in three dimensions using InSAR. *Geophysical Research Letters*, *31*(1), 1–5. https://doi.org/10.1029/2003GL018827

Wu, C., Ren, G., Yu, J., Zheng, W., Li, X., Liu, J., Wang, S., Li, C., Zhang, Z., Yang, H., & Zhang, D. (2020). Oblique Right-Lateral Faulting Along the Northern Margin of the Ili Basin in the Northern Tian Shan, Northwest China. *Tectonics*, *39*(10), 1–22. https://doi.org/10.1029/2020TC006061

Wu, C., Wang, W., Zheng, W., Zhang, P., & Yu, Z. (2021). Opposite Sense of Strike-Slip Faulting and Crustal Rotation Accommodating Left-Lateral Shear Between the Tianshan Mountains and Kazakh Platform. *Geophysical Research Letters*, *48*(24), 1–8. https://doi.org/10.1029/2021GL096442

Wu, C., Wu, G., Shen, J., Dai, X., Chen, J., & Song, H. (2016). Late Quaternary tectonic activity and crustal shortening rate of the Bogda mountain area, eastern Tian Shan, China. *Journal of Asian Earth Sciences*, *119*, 20–29. https://doi.org/10.1016/j.jseaes.2016.01.001

Wu, K., Pei, Y., Li, T., Wang, X., Liu, Y., Liu, B., Ma, C., & Hong, M. (2018). Structural characteristics and implication on tectonic evolution of the Daerbute strike-slip fault in West Junggar area, NW China. *Frontiers of Earth Science*, *12*(3), 555–568. https://doi.org/10.1007/s11707-018-0686-z

Xiao, W., Li, S., Santosh, M., & Jahn, B. ming. (2012). Orogenic belts in Central Asia: Correlations and connections. *Journal of Asian Earth Sciences*, *49*, 1–6. https://doi.org/10.1016/j.jseaes.2012.03.001

Xie, Y. S., & Cai, M. B. (1986). *Collections of historical records of earthquakes in China (in Chinese)*. Science Press, Beijing, China.

Xu, J., Peng, J., & An, H. (2019). Experimental study on Su-Xi-Chang earth fissures induced by repeated groundwater pumping and impounding. *Geomatics, Natural Hazards and Risk*, *10*(1), 2051–2068. https://doi.org/10.1080/19475705.2019.1676832

Xu, W., Feng, G., Meng, L., Zhang, A., Ampuero, J. P., Bürgmann, R., & Fang, L. (2018). Transpressional Rupture Cascade of the 2016 Mw 7.8 Kaikoura Earthquake, New Zealand. *Journal of Geophysical Research: Solid Earth*, *123*(3), 2396–2409. https://doi.org/10.1002/2017JB015168

Xu, Xiaohua, & Sandwell, D. T. (2020). InSAR : Correcting for Earth Tides and Phase. *IEEE Transactions on Geoscience and Remote Sensing*, *58*(1), 726–733.

Xu, Xiaohua, Sandwell, D. T., & Smith-Konter, B. (2020). Coseismic displacements and surface fractures from Sentinel-1 InSAR: 2019 Ridgecrest earthquakes. *Seismological Research Letters*, *91*(4), 1979–1985.

Xu, Xiwei, Sun, X. Z., Tan, X., Li, K., Yu, G., Etchebes, M., Klinger, Y., Tapponnier, P., & Van der Woerd, J. (2012). Fuyun fault: Long-term faulting behavior under low crustal strain rate (in Chinese). *Seismology and Geology*, *34*(4), 606–617. https://doi.org/10.3969/j.issn.0253-4967.2012.04.007

Yague-Martinez, N., Prats-Iraola, P., Gonzalez, F. R., Brcic, R., Shau, R., Geudtner, D., Eineder, M., & Bamler, R. (2016). Interferometric Processing of Sentinel-1 TOPS Data. *IEEE Transactions on Geoscience and Remote Sensing*, *54*(4), 2220–2234. https://doi.org/10.1109/TGRS.2015.2497902

Yang, H., Quigley, M., & King, T. R. (2021). Surface slip distributions and geometric complexity of intraplate reverse-faulting earthquakes. *Bulletin of the Geological Society of America*, *133*(9–10), 1909–1929. https://doi.org/10.1130/B35809.1

Yang, X., Deng, Q., Zhang, P., Xu, X., Yu, G., & Feng, X. (1998). Active reverse fault-fold zones and estimation of potential earthquake sources in northern Tianshan (in Chinese). *Seismology and Geology*, *20*(3), 194–200.

Yang, X., Gu, M., Sun, Z., Zhao, C., & Zhou, Q. (2002). Multilayered Reverse Faults and Deep Structures in the Manas Earthquake Area, Northern TianShan (in Chinese). *Seismology and Geology*, *24*(3), 304–314.

Yang, X., & Shen, J. (2000). Late quaternary activity of Jinghe-Alashankou section of the Boluokenu Fault, interior Tianshan. *Seismology and Geology*, *22*(3), 305–315.

Yang, Z. (1988). The preliminary study of the landslides triggered by historial earthquakes in Xinjiang (in Chinese). *Journal of Seismology*, *3*, 1–8.

Yang, Z. (1992). Discussion on the Epicentral Position of Xinyuan Earthquake with Magnitude 7.25 on March 10. 1944 (in Chinese). *Earthquake Research in China*, *8*(2), 29–37.

Yang, Z., Cheng, X., Yin, G., Li, J., & Zhang, Y. (1985). The Nilke Great Earthquake (M=8.0), March 8, 1812, Xinjiang) (in Chinese). *Northwestern Seismological Journal*, *7*(1), 60–65.

Yang, Z., Guo, H.-Z., Ding, D.-X., & Xu, D.-Z. (1988). Finding of Tekes-Zhaosu Earthquake Faults in Xinjiang and Some Discussion (in Chinese). *Seismology and Geology*, *10*(3), 6.

Yao, Y., Li, S., Huang, S., & Jia, H. (2020). Late Quaternary activity characteristics of the strike-slip Dongbielieke Fault in West Junggar, China. *Arabian Journal of Geosciences*, *13*(11). https://doi.org/10.1007/s12517-020-05423-6

Yao, Y., Wu, C., & Luo, F.-Z. (2015). Characteristics of Late Quaternary Activity on Dongbielieke Fracture Located Eastern Margin of Tacheng Basin in Xinjiang (in Chinese). *Inland Earthquake*, *29*(1), 71–76.

Yin, A. (2010). Cenozoic tectonic evolution of Asia: A preliminary synthesis. *Tectonophysics*, *488*(1), 293–325. https://doi.org/https://doi.org/10.1016/j.tecto.2009.06.002

Yin, G., Jiang, J. X., & Pei, H. D. (2006). The fault and the maximal displacement of Nilike earthquake in 1812 (in Chinese). *Inland Earthquake*, *20*(4).

Yin, G., Jiang, J. X., & Wu, G. (2009). Research of the Macro-epicenter location on 1812 Nilka Earthquake (in Chinese). *Inland Earthquake*, *23*(4), 425–429.

Yin, G., Jiang, J. X., Zhang, Y., & Li, J. (2002). The Character of Seismic Fault of 1812 Nileke Earthquake (in Chinese). *Northwestern Seismological Journal*, *24*(2), 4. https://doi.org/10.18907/jjsre.4.Special_87_1

Yin, G., Li, J., Zhang, Y., & Yang, Z. (2001). Statistical Analysis and Research of Landslides Caused by Nileke Earthquake (in Chinese). *Inland Earthquake*, *15*(1), 57–63.

Yu, C., Li, Z., Penna, N. T., & Crippa, P. (2018). Generic Atmospheric Correction Model for Interferometric Synthetic Aperture Radar Observations. *Journal of Geophysical Research: Solid Earth*, *123*(10), 9202–9222. https://doi.org/10.1029/2017JB015305

Yu, C., Penna, N. T., & Li, Z. (2017). Generation of real-time mode high-resolution water vapor fields from GPS observations. *Journal of Geophysical Research*, *122*(3), 2008–2025. https://doi.org/10.1002/2016JD025753

Yu, J., Walker, R. T., Rhodes, E. J., Zhang, P., Li, C., Wang, S., Wang, Y., Liu, F., & Hao, Y. (2021). East Tacheng (Qoqek) Fault Zone: Late Quaternary Tectonics and Slip Rate of a Left-Lateral Strike-Slip Fault Zone North of the Tian Shan. *Tectonics*, *40*(2), 1–25. https://doi.org/10.1029/2020TC006377

Yu, Y., Wang, X., Rao, G., & Wang, R. (2016). Mesozoic reactivated transpressional structures and multi-stage tectonic deformation along the Hong-Che fault zone in the northwestern Junggar Basin, NW China. *Tectonophysics*, *679*, 156–168. https://doi.org/10.1016/j.tecto.2016.04.039

Yun, S. H., Zebker, H. A., Segall, P., Hooper, A. J., & Poland, M. (2007). Interferogram formation in the presence of complex and large deformation. *Geophysical Research Letters*, *34*(12), 1–6. https://doi.org/10.1029/2007GL029745

Zebari, M., Preusser, F., Grützner, C., Navabpour, P., & Ustaszewski, K. (2021). Late Pleistocene-Holocene Slip Rates in the Northwestern Zagros Mountains (Kurdistan Region of Iraq) Derived From Luminescence Dating of River Terraces and Structural Modeling. *Tectonics*, *40*(8), 1–24. https://doi.org/10.1029/2020TC006565

Zebker, H. A., Rosen, P. A., & Hensley, S. (1997). Atmospheric effects in interferometric synthetic aperture radar surface deformation and topographic maps. *Journal of Geophysical Research: Solid Earth*, *102*(B4), 7547–7563. https://doi.org/https://doi.org/10.1029/96JB03804

Zelenin, E., Bachmanov, D., Garipova, S., Trifonov, V., & Kozhurin, A. (2021). *The Database of the Active Faults of Eurasia (AFEAD): Ontology and Design behind the Continental-Scale Dataset*. https://doi.org/10.5194/essd-2021-312

Zhang, D., Zhou, T., Yuan, F., White, N., Hollings, P., Xiao, W., Deng, Y., Zhao, B., & Wang, J. (2017). Genesis of late carboniferous granitoid intrusions in the Dayinsu area, West Junggar, Northwest China: evidence of an arc setting for the western CAOB. *International Geology Review*, *59*(9), 1082–1096. https://doi.org/10.1080/00206814.2016.1271290

Zhang, P., Deng, Q., Xu, X., Peng, S., Yang, X., Feng, X., Zhao, R., & Li, J. (1994). Blind Thrust, Folding Earthquake, and the 1906 Manas Earthquake, Xinjiang (in Chinese). *Seismology and Geology*, *16*(3), 193–204.

Zhang, P., Deng, Q., Xu, X., Wu, Z., Li, J., Chen, W., Zhao, R., & Tang, W. (1994). Tectonic Deformation, Crustal Shortening, and Slip Rate Estimation along the Manas Reverse Fault-Fold Zone (in Chinese). In *Research on Active Fault (3)* (pp. 18–31). Seismological Press, Beijing.

Zhang, P., Deng, Q., Yang, X., Feng, X., Peng, S., & Zhao, R. (1995). Glaciofluvial geomorphology and neotectonics along the rangefront of the northern Tianshan (in Chinese). *Research on Active Faults*, *4*, 63–78.

Zhang, P., Min, W., Deng, Q., & Mao, F. (2005). Paleoearthquake rupture behavior and recurrence of great earthquakes along the Haiyuan fault, northwestern China. *Science in China Series D: Earth Sciences*, *48*(3), 364–375. https://doi.org/10.1360/02yd0464

Zheng, G., Wang, H., Wright, T. J., Lou, Y., Zhang, R., Zhang, W., Shi, C., Huang, J., & Wei, N. (2017). Crustal Deformation in the India-Eurasia Collision Zone From 25 Years of GPS Measurements. *Journal of Geophysical Research: Solid Earth*, *122*(11), 9290–9312. https://doi.org/10.1002/2017JB014465

Zhou, W., Yang, Z. E., Sun, J., & Zhao, R. (2003). Numerical modeling of the generation process of the 1906 Manas Ms 7.7 earthquake (in Chinese). *Seismology and Geology*, *25*(4), 610–616.

Zhou, Y., Parsons, B., Elliott, J. R., Barisin, I., & Walker, R. T. (2015). Assessing the ability of Pleiades stereo imagery to determine height changes in earthquakes: A case study for the El Mayor-Cucapah epicentral area. *Journal of Geophysical Research: Solid Earth*, *120*(12), 8793–8808. https://doi.org/10.1002/2015JB012358

Zielke, O., & Arrowsmith, J. R. (2012). LaDiCaoz and LiDARimager-MATLAB GUIs for LiDAR data handling and lateral displacement measurement. *Geosphere*, *8*(1), 206–221. https://doi.org/10.1130/GES00686.1

Zielke, O., Arrowsmith, J. R., Ludwig, L. G., & Akciz, S. O. (2010). Slip in the 1857 and earlier large earthquakes along the Carrizo Plain, San Andreas Fault. *Science*, *327*(February), 1119–1123.

Zinke, R., Dolan, J. F., Rhodes, E. J., Van Dissen, R., & McGuire, C. P. (2017). Highly Variable Latest Pleistocene-Holocene Incremental Slip Rates on the Awatere Fault at Saxton River, South Island, New Zealand, Revealed by Lidar Mapping and Luminescence Dating. *Geophysical Research Letters*, *44*(22), 11,301-311,310. https://doi.org/https://doi.org/10.1002/2017GL075048

Zubovich, A. V., Wang, X. Q., Scherba, Y. G., Schelochkov, G. G., Reilinger, R. E., Reigber, C., Mosienko, O. I., Molnar, P., Michajljow, W., Makarov, V. I., Li, J., Kuzikov, S. I., Herring, T. A., Hamburger, M. W., Hager, B. H., Dang, Y. M., Bragin, V. D., & Beisenbaev, R. T. (2010). GPS velocity field for the Tien Shan and surrounding regions. *Tectonics*, *29*(6), 1–23. https://doi.org/10.1029/2010TC002772